

# A multiscale study of microstructural evolutions in hot-deformed two-phase titanium alloys

Matheus Brozovic Gariglio

▶ **To cite this version:**

Matheus Brozovic Gariglio. A multiscale study of microstructural evolutions in hot-deformed two-phase titanium alloys. Materials Science [cond-mat.mtrl-sci]. Université Paris sciences et lettres, 2023. English. ⟨NNT : 2023UPSLM033⟩. ⟨tel-04308336⟩

**HAL Id: tel-04308336**

**https://pastel.hal.science/tel-04308336v1**

Submitted on 27 Nov 2023

**HAL** is a multi-disciplinary open access archive for the deposit and dissemination of scientific research documents, whether they are published or not. The documents may come from teaching and research institutions in France or abroad, or from public or private research centers.

L'archive ouverte pluridisciplinaire **HAL**, est destinée au dépôt et à la diffusion de documents scientifiques de niveau recherche, publiés ou non, émanant des établissements d'enseignement et de recherche français ou étrangers, des laboratoires publics ou privés.



HAL Authorization

PSL UNIVERSITÉ PARIS

THÈSE DE DOCTORAT
DE L'UNIVERSITÉ PSL

Préparée à MINES Paris

# ÉTUDE MULTI-ÉCHELLE DES ÉVOLUTIONS MICROSTRUCTURALES DANS LES ALLIAGES DE TITANE BIPHASÉS DÉFORMÉS À CHAUD

## A MULTISCALE STUDY OF MICROSTRUCTURAL EVOLUTIONS IN HOT-DEFORMED TWO-PHASE TITANIUM ALLOYS


Soutenue par

**Matheus BROZOVIC GARIGLIO**


Le 02 février 2023

École doctorale n° 364

**Sciences Fondamentales et Appliquées**

Spécialité

**Mécanique Numérique et Matériaux**

Composition du jury :

| | |
|---|---|
| Frédéric, PRIMA<br>Professeur, PSL Chimie Paris | *Président* |
| Maria Cecilia, POLETTI<br>Professeur, Graz University of Technology | *Rapporteur* |
| Olivier, CASTELNAU<br>Directeur de Recherche, École Nationale Supérieure d'Arts et Métiers | *Rapporteur* |
| Jérôme, DELFOSSE<br>Dr. Ingénieur, SafranTech | *Examinateur* |
| Christian, DUMONT<br>Dr. Ingénieur, Aubert & Duval | *Examinateur* |
| Daniel, PINO MUÑOZ<br>Chargé de Recherche, PSL MINES Paris | *Examinateur* |
| Nathalie, BOZZOLO<br>Professeur, PSL MINES Paris | *Directrice de thèse* |

MINES PARIS | PSL

**MINES Paris**
**Centre de Mise en Forme des Matériaux (CEMEF)**
CNRS UMR 765
1 rue Claude Daunesse, CS 10207, Sophia Antipolis Cedex, France
https://www.cemef.minesparis.psl.eu

# ACKNOWLEDGEMENTS

First and foremost, I would like to thank Nathalie Bozzolo and Daniel Pino Muñoz, my PhD supervisors, for having given me this opportunity. Since the beginning, their constant guidance, original ideas and patience were crucial for me to conclude this work. It was extremely enriching to have one supervisor (Nathalie) for the metallurgical and experimental aspects, while another (Daniel) for the mechanical and simulations ones.

I would like to thank the industrial partners (Airbus, Aubert & Duval, Timet and Safran) for funding this PhD work and putting their trust in me. The opportunity to frequently exchange ideas and receive the industrial point of view was tremendously useful during those three years. I am grateful for my industrial supervisors, Jérôme Delfosse, Benjamin Dod, Christian Dumont, Yvon Millet and Michael Piellard, towards their constant participation, collaboration and support. I would also like to thank the academic partners, Patrick Villechaise, Frédéric Prima and Samuel Hémery for the great suggestions to my PhD work from different perspectives.

My sincere thanks to the jury members, Prof. Maria Cecilia Poletti (Graz University of Technology), Prof. Olivier Castelnau (École Nationale Supérieure d'Arts et Métiers) and Sheldon Lee Semiatin (US Air Force), for accepting to review this PhD work with great discussions to improve it.

I had the pleasure to work with people who have highly contributed to tackle different challenges of this work, which was only possible because of the experimental team at CEMEF, especially during the pandemic. I would like to express my gratitude to Suzanne Jacomet for training me on SEM and EBSD. Gilbert Fiorucci for all the support and talks during the thermomechanical tests. Cyrille Collin for training me in the metallurgical preparation. Also, Alexis Nicolaÿ and Franco Jaime for all their help during the three-dimensional characterizations.

My gratitude also goes to Pierre-Olivier Bouchard and Katia Mocellin for their guidance in the use of the *FORGE* software, regarding the optimization of the double-cone samples. Francis Fournier, Marc Bouyssou and Eric Brotons for their support in the sample machining. Marie-Françoise and Sylvie Massol for always handling the administrative issues with such kindness. Hallem Ben Aissa, Jérôme Dupré, Emmanuel Levrat, Sélim Kraria and the entire IT team at CEMEF for all their support during those three years. Furthermore, I would also like to thank Florence Morcamp for her useful advices during the Prix Laffitte competition, as also to Elie Hachem for creating this amazing prize.

My sincere thanks to all my friends and colleagues from CEMEF for their support and sharing moments of happiness. Ilusca, Ghaniyya, Victor C, Victor G, Oswaldo, Brayan, Diego, Federico, Antonio, Yacine, David, Medhi, Sacha, Claude, Pablo and others. I also would like to thank Tiphaine and Ioannis from Institut P' and Chimie Paris, respectively, for all the good times we shared together during the consortium meetings.

A special thanks to all my friends outside the lab that were tremendously important for me during these years. The friends that I have since my university in Brazil, Gabriel C and Asaph. The friendships that were formed in my double-

degree in Clermont-Ferrand, Laura, Igor, Camila, Gabriel F, Guilherme, Felipe, Danilo and Isaías. I also wish to thank all my friends from Paris, Bruno, Aline, Marina, Artur, Guilherme, Luís and Tulio. Also, to all the new friendships I formed in Nice, Marcelina, Bruna, Reynan, Oscar, Fernando, Maxime, Gabriel M and Luigi. To all my friends, the support you gave me was extremely important in this journey, thank you for always being there for me, to talk and laugh about everything. I consider you all as my family in France.

Finally, I would like to express my deepest gratitude to the most special people in my life. The biggest thanks to my parents, Evanio and Andréa, for always believing in me and serving as inspiration. Without you I would never have come this far. I want to extend special thanks to my grandparents, aunts, uncles and cousins, for all the love they have granted me while growing up and until now, through our constant calls. A huge thanks to my sister Giovanna, who is always cheering for me and sharing the funniest stories. Even though 9.000 km apart, home is where the heart is.

# SUMMARY

**GENERAL INTRODUCTION ..... 1**

Industrial context ..... 2
Objectives and scientific approach of the thesis ..... 3
Characterization of as-received and initial (prior to deformation) microstructures...3
Microscopic approach: Microstructural evolution during hot deformation ..... 4
Macroscopic approach: Rheological analysis based on compression tests ..... 4
Full field simulation of the deformation of two-phase microstructures ..... 4

**1. LITERATURE BACKGROUND ON MICROSTRUCTURE EVOLUTION DURING HOT DEFORMATION ..... 7**

1.1 Titanium alloys ..... 8
1.1.1 Characteristics and general information ..... 8
1.1.2 Crystal structure ..... 8
1.1.3 Alloying elements and categories ..... 9
1.1.4 The β→α phase transformation and the Burgers orientation relationship ..... 10
1.1.5 α phase fraction ..... 10
1.1.6 Microstructures ..... 11
1.2 Microstructural evolution during hot deformation ..... 14
1.2.1 Plasticity, recovery and recrystallization ..... 14
1.2.2 Deformation in the β domain and the influence of microstructural/ thermomechanical parameters ..... 17
1.2.3 Deformation in the α+β domain and the influence of microstructural/ thermomechanical parameters ..... 19
1.2.4 Summary of microstructure evolution mechanisms and influence of microstructural/ thermomechanical parameters ..... 24
1.3 Industrial thermomechanical processing of titanium alloys ..... 25
1.4 Résumé en Français ..... 28

**2. MATERIALS AND METHODS ..... 29**

2.1 Received material ..... 30
2.2 Sampling directions ..... 31
2.3 Heat treatments ..... 32
2.4 Sample preparation ..... 32
2.5 Verification of possible azimuthal and radial heterogeneities ..... 33
2.5.1 Primary α phase quantification ..... 34
2.6 Scanning electron microscopy (SEM) ..... 36
2.6.1 BSE imaging ..... 36
2.6.2 EBSD map analysis ..... 37
2.7 EBSD data analysis and conventions ..... 38
2.7.1 Parent β grain reconstruction ..... 40
2.7.2 Quantification of α/β boundaries respecting BOR ..... 41
2.7.3 LAGB and HAGB density ..... 42
2.7.4 LAGB density as a function of grain orientation ..... 43
2.7.5 Dislocation density estimation from EBSD maps ..... 44
2.8 3D characterization of the Ti64 lamellar microstructures ..... 50
2.9 Thermomechanical tests ..... 54
2.9.1 Samples geometries ..... 54

2.9.2 Sampling ..... 55
2.9.3 Double-cone samples ..... 56
2.9.4 Cylindrical samples ..... 57
2.10 Summary and Conclusions ..... 58
2.11 Résumé en Français ..... 60

**3. CHARACTERIZATION OF AS-RECEIVED AND INITIAL (PRIOR TO HOT DEFORMATION) MICROSTRUCTURES ..... 61**

3.1 Verification of possible azimuthal and radial heterogeneities ..... 62
3.2 Characterization of as-received microstructures ..... 64
3.3 Grain size and phase fractions of initial microstructures ..... 66
3.3.1 EBSD phase maps and local misorientation analysis ..... 68
3.3.2 GND density of the initial states ..... 70
3.3.3 Complementary 3D analysis of the Ti64_CL and Ti64_FL microstructures 72
3.4 Summary and Conclusions ..... 76
3.5 Résumé en Français ..... 77

**4. MICROSCOPIC APPROACH: MICROSTRUCTURAL EVOLUTION DURING HOT DEFORMATION ..... 79**

4.1 Comparison of different initial microstructures for a given set of deformation conditions ..... 80
4.1.1 Topological evolutions ..... 81
4.1.2 Crystallographic texture evolution ..... 84
4.1.3 LAGB and HAGB density ..... 90
4.1.4 Orientation dependency of substructure formation in α grains ..... 102
4.1.5 GND density estimation ..... 104
4.1.6 3D characterization of deformed Ti64_FL ..... 107
4.2 Influence of temperature and strain rate on microstructure evolution ..... 110
4.2.1 Topological evolutions ..... 111
4.2.2 Crystallographic texture evolution ..... 114
4.2.3 LAGB and HAGB density ..... 116
4.2.4 Orientation dependency of substructure formation in α grains ..... 125
4.2.5 Quantification of α/ß boundaries respecting BOR ..... 127
4.2.6 GND density estimation ..... 128
4.3 Summary and Conclusions ..... 132
4.4 Résumé en Français ..... 137

**5. MACROSCOPIC APPROACH: RHEOLOGICAL ANALYSIS BASED ON COMPRESSION TESTS ..... 141**

5.1 A rule of mixtures (ROM) as a ground assumption ..... 142
5.2 Selected initial microstructures ..... 143
5.3 Experimental setup and thermomechanical parameters for *in*- and *off*-equilibrium conditions ..... 143
5.4 Phase fraction measurements ..... 144
5.5 Analysis of rheological data ..... 147
5.5.1 Experimental stress-strain curves ..... 147
5.5.2 α and ß-phase flow stresses obtained by the rule of mixtures ..... 149
5.6 Estimation of average dislocation density per phase from the estimated phase flow stress ..... 154
5.7 Comparison between the Macroscopic and Microscopic approaches ..... 156

5.8 Summary and Conclusions ....159
5.9 Résumé en Français ....161

**6. FULL FIELD SIMULATION OF TWO-PHASE MICROSTRUCTURE DEFORMATION 165**

6.1 Introduction to crystal plasticity ....166
6.2 Constitutive model for crystal plasticity finite element method ....167
6.2.1 Flow and hardening rules ....167
6.3 Simulation ....169
6.3.1 Computational domain ....169
6.3.2 Constitutive laws ....177
6.3.3 Boundary conditions and limitations ....178
6.4 Results, comparison to experimental data and discussions ....179
6.4.1 Equiaxed α morphology ....179
6.4.2 Lamellar α morphology ....185
6.4.3 Stress-strain curves ....187
6.5 Summary, Conclusions and Perspectives ....189
6.6 Résumé en Français ....191

**7. GENERAL CONCLUSIONS AND PERSPECTIVES .... 193**

7.1 Conclusions, perspectives and synthesis ....194
7.1.1 Methodology and characterization of microstructures ....194
7.1.2 Microscopic approach: Microstructural evolution during hot deformation. 194
7.1.3 Macroscopic approach: Rheological analysis based on compression tests ..196
7.1.4 Full field simulation of the deformation of two-phase microstructures ....197
7.1.5 Summary of the comparison between the three different approaches and final considerations ....199
7.2 Preliminary experiments addressing perspectives of this work related to the industrial process ....201
7.2.1 Tests followed by slow cooling ....201
7.2.2 Influence of the thermomechanical path ....207

**APPENDIXES .... 213**

A. Analyzed microstructures that were not selected for further studies in this PhD work ....214
B. About dislocation density estimation and dislocation mode analysis from EBSD data: application to hot-deformed titanium alloys ....216
B.1 Introduction ....216
B.2 Experimental orientation maps ....217
B.3 Synthetic orientation maps ....219
B.4 Results ....222
B.5 Discussions ....225
B.6 Conclusions ....226
C. An optimized geometry of double-cone compression test samples for a better control of strain rate ....227
C.1 Introduction ....228
C.2 Finite Element Model ....228
C.3 Methodology and resulting optimized geometry ....230
C.4 Evaluation of the new geometry ....234
C.5 Conclusions ....242
D. Hansel-Spittel smoothing parameters for the rheological analysis ....243

**SCIENTIFIC COMMUNICATIONS AND PRIZES** ..... **245**
**BIBLIOGRAPHY** ..... **247**

# LIST OF ABBREVIATIONS

| Abbreviation | Meaning |
|---|---|
| BCC | Body-Centered Cubic |
| BOR | Burgers Orientation Relationship |
| BSE | Backscattered Electron |
| CEMEF | Centre de Mise en Forme des Matériaux |
| CD | Compression Direction |
| CDRX | Continuous Dynamic Recrystallization |
| CPFEM | Crystal Plasticity Finite Element Method |
| DDRX | Discontinuous Dynamic Recrystallization |
| Def. | Deformation |
| DRV | Dynamic Recovery |
| DRX | Dynamic Recrystallization |
| EBSD | Electron Backscatter Diffraction |
| FCC | Face-Centered Cubic |
| FE | Finite Element |
| FEG | Field Emission Gun |
| GB | Grain Boundary |
| GBL | Grain Boundary Length |
| GND | Geometrically Necessary Dislocations |
| GS | Grain Size |
| H | Height |
| HAGB | High Angle Grain Boundary/ Grain Boundaries ($\theta \geq 10°$) |
| HCP | Hexagonal Close-Packed |
| HT | Heat Treatment |
| IPF | Inverse Pole Figure |
| L | Length |
| LAGB | Low Angle Grain Boundary/ Subgrain Boundaries ($\theta \geq 1°$) |
| MLI | Mean Linear Intercept |
| MRD | Multiples of The Random Distribution |
| OM | Optical Microscopy |
| P-D | Post-Deformation |
| PF | Pole Figure |
| RVE | Representative Volume Element |
| ROI | Region of Interest |
| ROM | Rule of Mixtures |
| RX | Recrystallization |
| SEM | Scanning Electron Microscopy |
| SR | Sampling Region |
| SSD | Statistically Stored Dislocations |

*continued on next page*

| | |
|---|---|
| Th | Thickness |
| Ti64 | Ti-6Al-4V alloy ($\alpha$+$\beta$) |
| Ti1023 | Ti-10V-2Fe-3Al alloy (metastable-$\beta$) |
| WQ | Water Quenched |

## LIST OF SYMBOLS

| Symbol | Meaning |
|---|---|
| $\alpha$ | Alpha phase (HCP) – stable below the $\beta$ transus |
| $\beta$ | Beta phase (BCC) – stable above the $\beta$ transus |
| $\varphi$ | Phase |
| $\alpha_P$ | Primary alpha phase |
| $\alpha_S$ | Secondary alpha phase |
| $\alpha_{GB}$ | Grain boundary alpha |
| $\rho_{EBSD}$ | Dislocation density estimated by EBSD analysis |
| $\rho_{\sigma}$ | Dislocation density estimated by rheological analysis |
| $\rho_{sim}$ | Dislocation density estimated by full field simulations |
| $f_{\alpha}$ | $\alpha$ phase fraction |
| $f_{\alpha_P}$ | Primary $\alpha$ phase fraction |
| $f_{\beta}$ | $\beta$ phase fraction |
| $T$ | Temperature |
| $T_{\beta}$ | $\beta$ transus temperature |
| $\sigma_{macro}$ | Macroscopic stress |
| $\varepsilon_{macro}$ | Macroscopic strain |
| $\varepsilon$ | Equivalent strain (local value) |
| $\dot{\varepsilon}_{macro}$ | Macroscopic strain rate |
| $\dot{\bar{\varepsilon}}$ | Average equivalent strain rate (local value) |
| $\theta$ | Misorientation angle |
| $\rho_{GB}$ | Grain boundary density |
| $\rho_{LAGB}$ | LAGB density |
| $\rho_{HAGB}$ | HAGB density |
| $f_{GB_{\alpha/\beta}}^{BOR}$ | Fraction of $\alpha/\beta$ boundaries respecting the BOR |
| $\overline{GS}$ | Average grain size |
| $t$ | Time |
| $\emptyset$ | Diameter |
| $\sigma_{SR}$ | Standard deviation related to the sampling region |
| $\bar{\sigma}_M$ | Average standard deviation in a micrograph |
| $\boldsymbol{\mu}$ | Mean value |
| $SS$ | Slip systems |
| $\parallel$ | Parallel |
| $\perp$ | Perpendicular |

# GENERAL INTRODUCTION

# Industrial context

One of the main challenges for the future of the aeronautical industry is to reduce $CO_2$ emissions. Increasing the operating temperature of the engines and reducing the weight of the aircraft are the main solutions to improve fuel efficiency [1]. Titanium alloys play a fundamental role in this reduction, thanks to their temperature resistance and corrosion properties, but above all their low density which gives them a particularly high specific resistance (**Figure 1**). To reduce the weight of aircrafts, composite materials are also increasingly used, yet metallic materials remain essential for structural parts. The question then arises of the compatibility of the alloys and composites used. Titanium alloys are also excellent candidates here, with thermal expansion properties in particular close to those of composites.

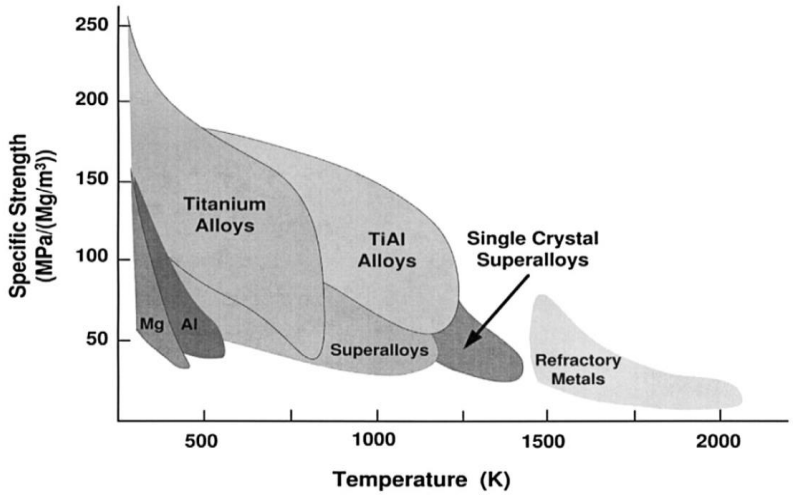



*Figure 1. Specific resistance as a function of temperature for different classes of alloys* [2].

Consequently, titanium alloys are increasingly used in aircrafts and will be for a long time to come. The two-phase ($\alpha/\beta$) nature of these alloys is particularly interesting since it offers, for a given grade, a very wide variety of possible microstructures with morphologies ranging from lamellar to globular (equiaxed), with different characteristic sizes. Therefore, a certain flexibility in the adjustment of properties.

The properties are in fact strongly linked to the microstructure, which itself results from forging operations. Optimizing the properties therefore requires knowing as accurately as possible the relationships between the numerous thermomechanical parameters involved in the process and the microstructural evolutions. A literature background is presented in Chapter **1**, emphasizing on the substructure development in both phases (HCP-$\alpha$ and BCC-$\beta$).

This is such an important subject for the industrial sector that it has made it possible to bring together in an industrial consortium (CONTiNUUM) producers of materials and semi-finished products (*Timet* and *Aubert & Duval*), a manufacturer (*Safran*) and an aircraft manufacturer (*Airbus*) to deepen their knowledge of the metallurgical phenomena involved in the forging stages of titanium alloys. A multi-year work program (2019-2025) comprising a total of six PhD theses and involving three research laboratories (CEMEF Mines Paris,

Institut Pprime and Chimie Paris) has been established. This thesis is part of the consortium work program and aims to describe the evolutions of microstructure during the stages of hot deformation. Two titanium alloys are targeted: the Ti-6Al-4V ($\alpha$+$\beta$) alloy used in turbojets (up to 315°C [3]) and the Ti-10V-2Fe-3Al alloy (metastable-$\beta$) used in landing gears, hereafter referred to as Ti64 and Ti1023, respectively.

## Objectives and scientific approach of the thesis

The main objective of this work is to describe microstructure evolution during hot deformation in the two-phase domain, according to the thermomechanical parameters and initial microstructure. Plastic deformation is strongly associated with the creation and movement of dislocations in metallic materials. Microstructural evolutions require a driving force in order to take place. This driving force is often provided by the stored energy in the material, being tightly linked to the presence of dislocations. Consequently, analyzing how the dislocation density is distributed between the different phases ($\alpha$ and $\beta$) of the Ti64 and Ti1023, is of utmost importance in the correlation of thermomechanical parameters, initial microstructure and its evolution. Indeed, the dislocation density provides important information to understand several microstructural mechanisms (*e.g.*, crystallographic texture development, recovery and recrystallization).

However, the assessment of dislocation density in highly deformed materials is a challenging task. Currently, all the existing approaches only allow for obtaining partial or imprecise estimates of the dislocation density distribution, and the task is even more difficult when dealing with dual phase materials. To address this research question, a methodology was implemented in this work to combine multiscale laboratory experiments and numerical simulations. It involved the development of experimental methods and data processing adapted to the complexity of the underlying physical phenomena (presented in Chapter **2**). This thesis is divided into four different steps (**Figure 2**), which complement each other, described below and detailed in Chapters **3** to **6**.

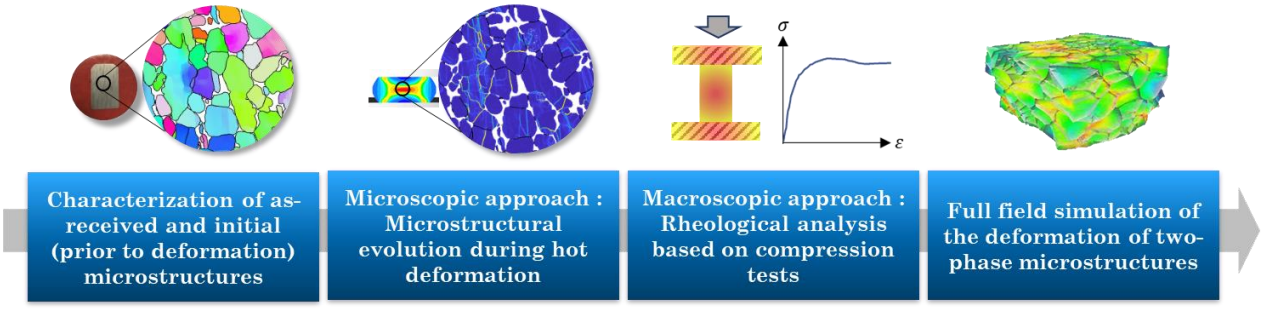



*Figure 2. Schematic of the different steps of the thesis.*

### *Characterization of as-received and initial (prior to deformation) microstructures*

The objective of this first step (Chapter **3**) is to characterize as-received and initial (prior to deformation) microstructures for each of the two alloys studied (Ti64 and Ti1023), varying the morphology of the phases (globular and lamellar)

and the characteristic sizes of each type of grain. The received microstructures were characterized in detail by optical microscopy (OM), scanning electron microscopy (SEM) and electron backscatter diffraction (EBSD). The aim was to analyze the evolution of phase fractions, size and characteristic morphology of grains during heating to deformation temperatures (leading to the initial state of the microstructure, *i.e.,* just before deformation). Furthermore, to better understand the nature of the titanium alloy microstructures, which are inherently three-dimensional, 3D EBSD studies were also performed in lamellar microstructures of the Ti64 alloy. This 3D analysis also helped to provide the most realistic input data possible for the full field simulations (Chapter **6**).

### *Microscopic approach: Microstructural evolution during hot deformation*

This approach (Chapter **4**) consists in the description of the formation of the substructures in the grains of each phase ($\alpha$ and $\beta$) as a function of their morphology, size and crystallographic orientation. To this end, double-cone samples [4] were subjected to hot-compression tests, allowing the study of fairly wide ranges of conditions, with the analysis of strain fields and different strain rates from a single test. These characterizations consisted in acquiring orientation maps by EBSD, which allow, by analyzing the measured intragranular misorientations, an assessment of the density field of geometrically necessary dislocations (GNDs) at the granular and intragranular scales, as well as the average dislocation density ($\rho_{EBSD}$) per phase [5].

### *Macroscopic approach: Rheological analysis based on compression tests*

A macroscopic approach (Chapter **5**) was implemented to estimate the dislocation density ($\rho_{\sigma}$) distribution based on stress-strain curves. Those curves then allowed to assess the macroscopic flow stress of each phase, by a simple rule of mixture, following the method proposed in [6]. An average dislocation density per phase was estimated from the phase flow stress values obtained, for comparison with those of Chapter **4**. With that aim, some of the compression test conditions applied for the double-cone samples were duplicated on cylindrical samples, with variable holding times before deformation, controlling the phase fractions independently of the deformation temperature.

### *Full field simulation of the deformation of two-phase microstructures*

Full field simulations (Chapter **6**) were implemented to help in the prediction of the dislocation density ($\rho_{Sim}$) and intragranular misorientation evolution of $\alpha$ and $\beta$ phases by using a Crystal Plasticity Finite Element Method (CPFEM). Meshes conforming to the measured phase topologies were generated (synthetically or by immersing real microstructures by 3D EBSD data) and statistically representative microstructures (morphologies and orientations) were also studied. The aim of these simulations is to verify whether the tendencies observed experimentally are reproduced by the simulations. This comparison was

mainly done in terms of dislocation density distribution in each phase and texture development.

Finally, Chapter **7** summarizes the main conclusions of this work and also discusses how far the different approaches can be compared to each other. Perspectives are suggested on how to connect these approaches to obtain a better estimation of dislocation densities, and therefore microstructural evolutions, in both $\alpha$ and $\beta$ phases of titanium alloys. This correlation is a key issue in the consortium's work program insofar as the deformed state conditions subsequent changes during cooling or heat treatments.

# 1. LITERATURE BACKGROUND ON MICROSTRUCTURE EVOLUTION DURING HOT DEFORMATION

# 1.1 Titanium alloys

## *1.1.1 Characteristics and general information*

Titanium is a metallic element well known for the excellent mechanical and corrosion resistance of its alloys, as well as low thermal and electrical conductivity. It is a transition metal with a high melting temperature (1668 °C) and a low density (4507 kg/m$^3$). These characteristics make titanium alloys widely used, especially in applications requiring high resistance to fatigue and high temperatures, which is the case notably in the aeronautical industry [7,8]. Among titanium alloys, the Ti64 is by far the most common. This alloy is widely used in the manufacture of fans and blades for the cold section (up to 315 °C) of aircraft engines, and in cockpit window frames, for example, due to potentially high loads. Developed in the early 1950s in the USA, the success of the Ti64 is due to two reasons [8,9]:

- It has the right balance of properties (mechanical strength, fatigue, ductility and fracture resistance);
- It is by far the most intensely developed and tested titanium alloy, which is a major advantage, especially in the aerospace industry.

The other alloy studied in this work is the Ti1023, which, besides its own industrial interest (widely used in the manufacture of aircraft landing gear components [3,9]), allows the direct assessment of the $\beta$ phase at room temperature.

## *1.1.2 Crystal structure*

Pure titanium (Ti) can crystallize in two crystal structures, each of which is stable within specific temperature ranges. The complete transformation from one crystalline structure to another is called allotropic transformation (term reserved for pure substances), the transformation temperature being called the transus temperature ($T_\beta$), equal to 882 ± 2 °C [9].

- $T > T_\beta$: Ti crystallizes in a body-centered cubic (BCC) structure called $\beta$;
- $T < T_\beta$: Ti crystallizes in a hexagonal close-packed (HCP) structure called $\alpha$.

The crystal structures of each of the two phases ($\alpha$ and $\beta$) are shown in **Figure 1.1** [9].

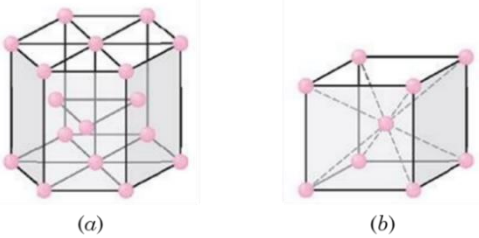



*Figure 1.1. Crystal structures of the: a) α (HCP); b) β (BCC) phases* [10].

This existence of two different crystalline structures is of paramount importance, since it is the basis of the great variety of properties exhibited by titanium alloys. Plastic deformation and diffusion rate are closely related to crystal structure. Moreover, the HCP crystal lattice induces elastic anisotropy in the

mechanical behavior of $\alpha$-titanium, where the elastic anisotropy is particularly pronounced. The Young's modulus of titanium single crystals (at room temperature) varies between 145 *GPa*, for a load normal to the base plane, and only 100 *GPa* parallel to this plane [9,11]. For alloys, the transus temperature $T_\beta$ (1000 °*C* and 800 °*C* for Ti64 and Ti1023, respectively) is defined as the temperature from which only the $\beta$ structure stable at high temperature remains. Below $T_\beta$, titanium alloys are generally two-phase. Furthermore, the $\beta$ phase is the more ductile, due to the greater number of slip systems in the BCC structure (48) [12] compared to the HCP structure (30), while the $\alpha$ phase is harder [13].

### *1.1.3 Alloying elements and categories*

The alloying elements in titanium are generally classified as $\alpha$ or $\beta$ stabilizers, depending on whether they increase or decrease the $T_\beta$ relative to that of pure Ti, respectively (**Figure 1.2**). Elements called $\alpha$-stabilizers, include Al, C, O and N. On the other hand, $\beta$-stabilizers can be divided into $\beta$-isomorphs (V, Mo, Ta and Nb) or $\beta$-eutectoids (Fe, Mn, Cr, Co, Ni, Cu and H), depending on whether or not an intermetallic compound is formed, respectively [8].

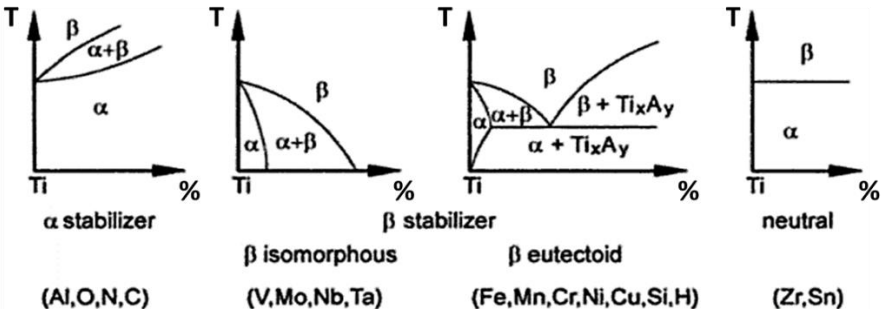



*Figure 1.2. The effect of alloying elements on the pseudo-binary phase diagrams of titanium alloys [3].*

Titanium alloys can be classified into four main categories: $\alpha$, $\alpha$+$\beta$, metastable-$\beta$ and stable-$\beta$ (**Figure 1.3**) [14].

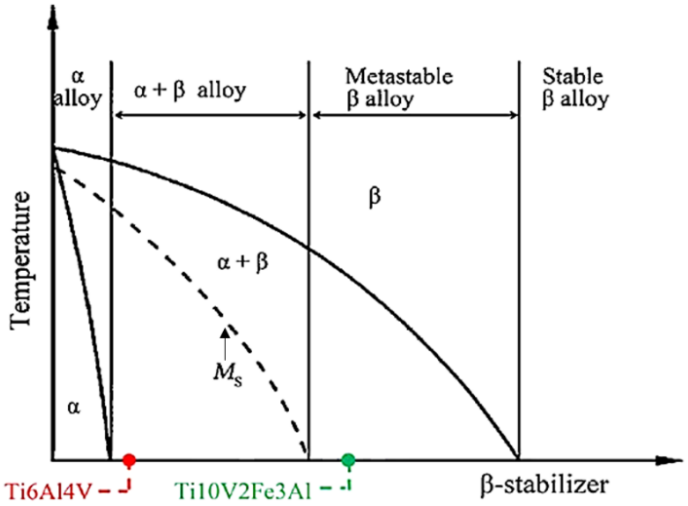



*Figure 1.3. Pseudo-binary phase diagram ($M_s$ being the martensite start) for titanium alloys, along with the alloy classification (schematic), showing the two alloys of interest (Ti64 in red and Ti1023 in green) in this work* [14].

In this work, the $\alpha$+$\beta$ and metastable-$\beta$ alloys will be detailed further, as these are the categories to which belong the alloys of interest: Ti64 ($\alpha$+$\beta$) and Ti1023 (metastable-$\beta$). A summary of both alloys characteristics is shown in **Table 1.1**.

| Alloy | Ti [%] | Al [%] | V [%] | Fe [%] | Category | $T_\beta$ [°C] |
|---|---|---|---|---|---|---|
| Ti64 | 90 | 6 | 4 | - | $\alpha + \beta$ | ~1000 |
| Ti1023 | 85 | 3 | 10 | 2 | Metastable-$\beta$ | ~800 |

*Table 1.1. Nominal compositions [wt.%], categories and β-transus temperatures of Ti64 and Ti1023 alloys [3,9].*

### 1.1.4 The $\beta \rightarrow \alpha$ phase transformation and the Burgers orientation relationship

Upon cooling from the $\beta$ domain, the $\alpha$ phase nucleates with the densest planes (in blue in **Figure 1.4**) and directions (in red in **Figure 1.4**) of the BCC structure aligned with those of the HCP structure.

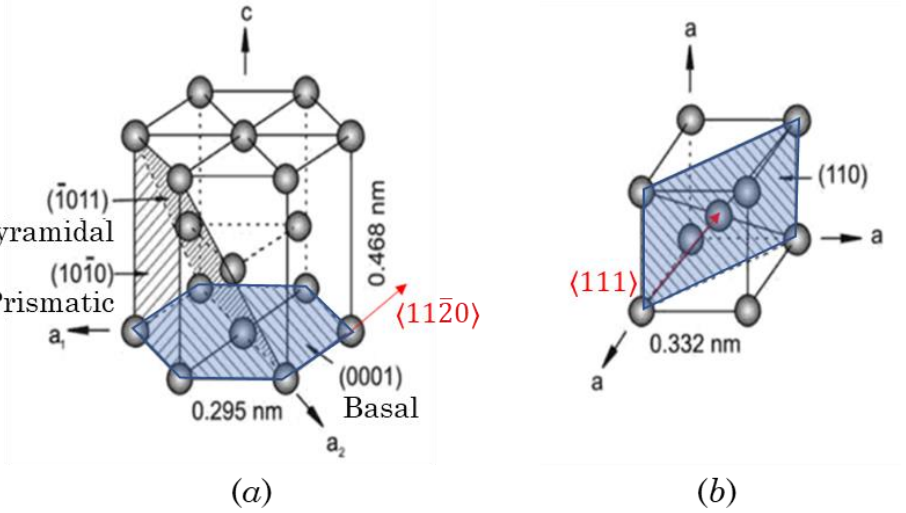



*Figure 1.4. Crystal structures of the: a) α; b) β phases; along with their respective densest planes (in blue) and directions (in red) involved in the BOR [3].*

Thus, this $\beta \rightarrow \alpha$ transformation fulfills the following orientation relation, known as Burgers orientation relationship (BOR) [15]:

$$(0001)_\alpha \parallel \{110\}_\beta$$
$$\langle 11\bar{2}0\rangle_\alpha \parallel \langle 111\rangle_\beta$$

The six $\{110\}_\beta$ planes and the two $\langle 111\rangle_\beta$ directions in each plane of the $\beta$ titanium unit cell give 12 variant orientations of the $\alpha$ phase after the allotropic transformation. Noteworthily, these planes and directions are also slip systems in both phases.

### 1.1.5 $\alpha$ phase fraction

The volume fraction of the $\alpha$ phase has great influence on the mechanical properties of titanium alloys [16]. The $\alpha$ phase percentage as a function of the temperature (between 700 and 1000 °C) for the Ti64 and Ti1023 alloys is shown in **Figure 1.5**.

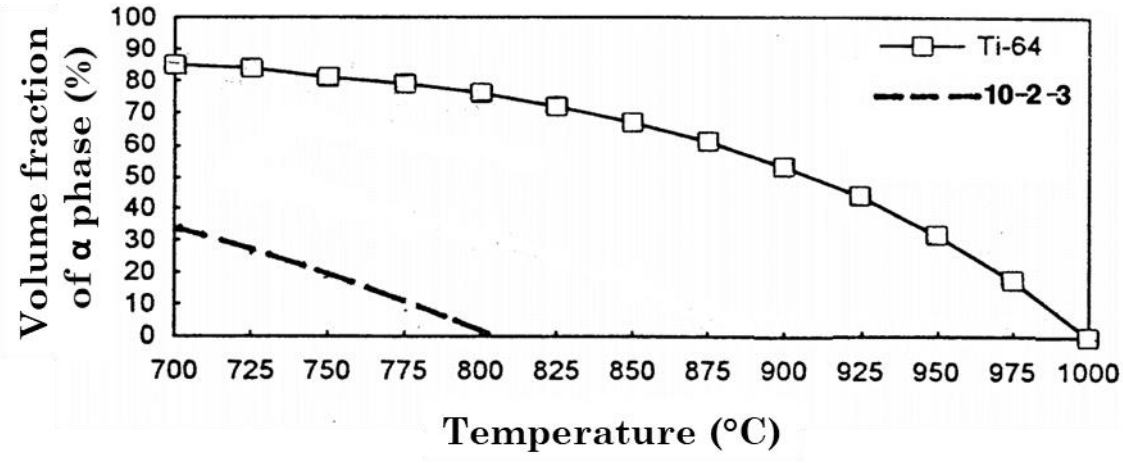



*Figure 1.5. Fraction of α phase (%) as function of temperature, for the Ti64 and Ti1023 alloys* [16].

Concerning the Ti64 alloy, the $\alpha$ phase volume fraction can phenomenologically be described as a function of temperature [17], as shown in equation **(1.1)**.

$$f_\alpha(T) = A(1 - e^{-b(T_\beta - T)}) \tag{1.1}$$

where $A = 0.925$ and $b = 0.0085$. No similar equation was found in the literature for the Ti1023 alloy, so these parameters ($A$ and $b$) were calculated in this work after specific heat treatments (section **2.3**) and based on the dotted line on **Figure 1.5** (obtained experimentally).

### *1.1.6 Microstructures*

The microstructures of conventional titanium alloys are mainly described by the size, shape and arrangement of the grains of the $\alpha$ and $\beta$ phases. A wide variety of microstructures can be obtained depending on the thermomechanical treatments owing to the $\beta \rightarrow \alpha$ phase transformation, the two extreme phase topologies being lamellar and equiaxed [9].

#### *1.1.6.1 Lamellar microstructure*

Lamellar microstructures are generated by cooling from the $\beta$ domain. Once the temperature is lowered below $T_\beta$, the $\alpha$ phase first forms at the grain boundaries and then develops as intragranular lamellae, according to the 12 previously defined orientation variants, within the $\beta$ grains (**Figure 1.6***a*) and/or as a grain boundary layer called $\alpha_{GB}$.

Then, for certain cooling conditions (slower), the lamellae appear in a colony of lamellae of the same orientation (**Figure 1.6***b*). The microstructures resulting from this transformation have a characteristic Widmanstätten-type morphology. The lamellae thickness depends on the cooling rate, becoming finer as the cooling rate increases (obtaining a basket-weave morphology, *e.g.*, **Figure 1.6***c*). Alloys with lamellar morphologies exhibit high toughness, good resistance to creep and fatigue crack growth, and are thus preferred in critical fracture toughness applications.

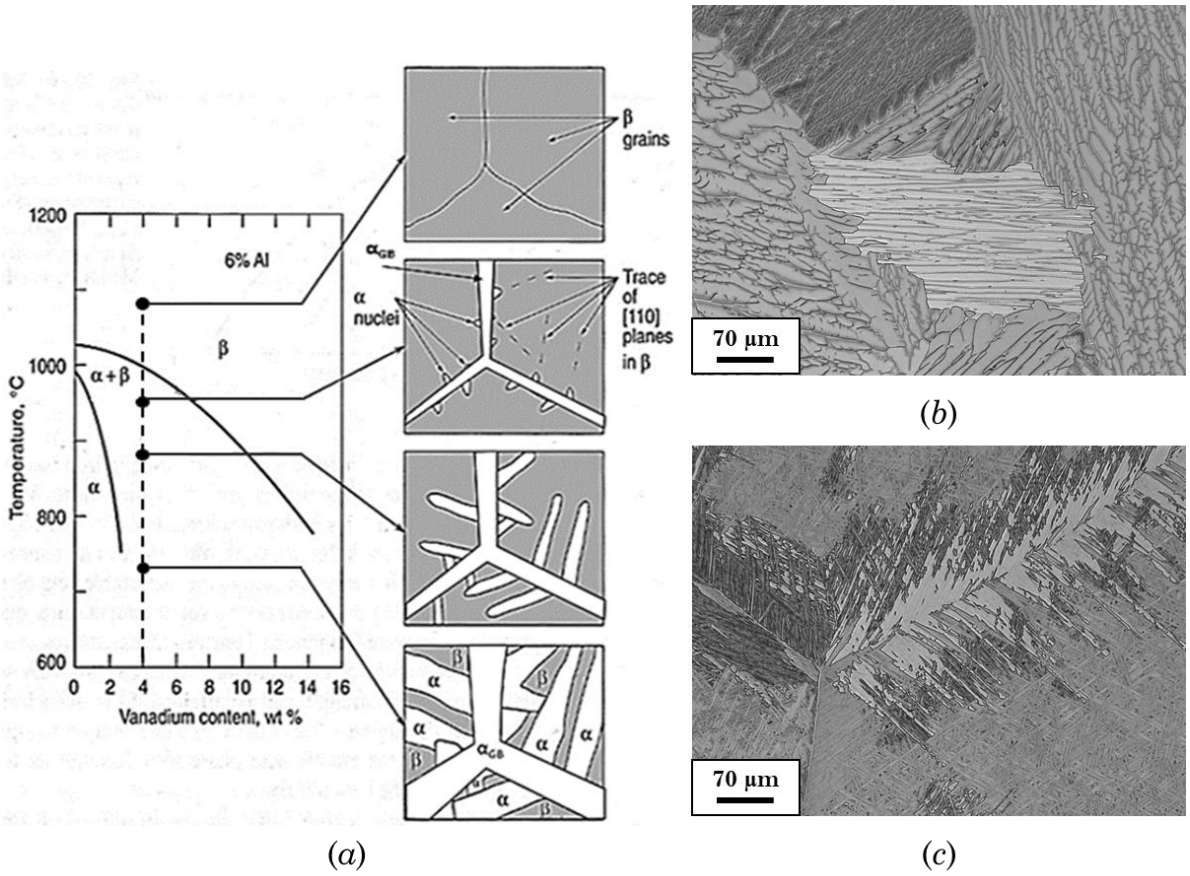



*Figure 1.6. a) Schematic evolution of lamellar α phase during slow cooling from the β domain [7]; The lamellar microstructures of Ti64 alloys resulting from: b) Slow cooling (~1°C/min); c) Faster cooling (air cooling).*

### *1.1.6.2 Equiaxed microstructure*

Equiaxed microstructures result from a process of globularization/ recrystallization of the $\alpha$ lamellae. Briefly, the alloy must first be strongly deformed in the $\alpha$+$\beta$ domain to introduce enough dislocations into the material. During a long duration holding at high temperatures in the two-phase range, a recrystallized and equiaxed (also called globular) microstructure can be obtained (**Figure 1.7**). Further, prolonged annealing enlarges the equiaxed microstructure and temperature determines the volume fraction of primary $\alpha$ phase ($\alpha_P$). Alloys with equiaxed $\alpha_P$ phase often have higher ductility and fatigue strength compared to lamellar morphologies, and thus are preferred in low cycle fatigue applications.

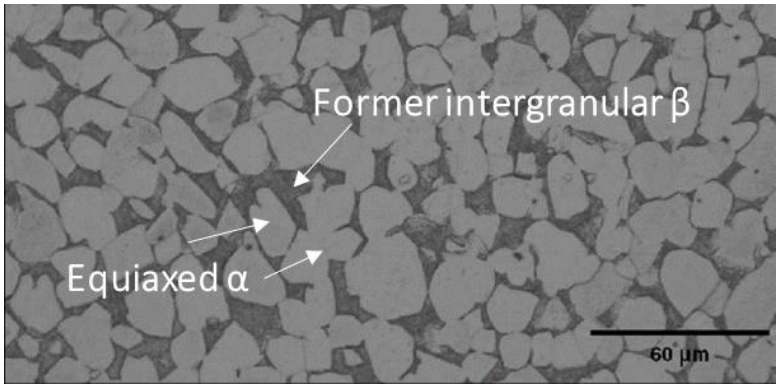



*Figure 1.7. Fully equiaxed α microstructure of a Ti-6Al-4V alloy [9].*

### *1.1.6.3 Bimodal microstructure*

Bimodal (duplex) microstructures exhibit both lamellar and equiaxed $\alpha_P$ phase (**Figure 1.8**), as bimodal microstructures combine the advantages of lamellar and equiaxed ones, they exhibit a well-balanced property profile.

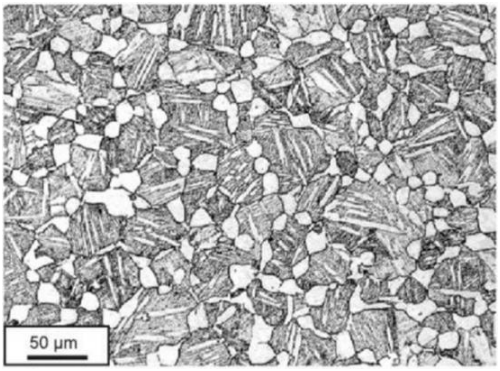



*Figure 1.8. Microstructure of a bimodal TIMETAL 834 alloy, showing the equiaxed α grains in a lamellar α+β matrix* [3].

### *1.1.6.4 α+β alloys*

The $\alpha$+$\beta$ alloys are widely used owing to their good combination of strength, toughness and formability, as they exhibit two-phase mixing at room temperature [18]. Rapid cooling from a temperature below $T_\beta$ transforms the $\beta$ phase into very fine laths, referred to as secondary $\alpha$ phase ($\alpha_S$), having strict BOR with the parent $\beta$ phase. The latter are then referred to as prior-$\beta$ grains. An example of this type of microstructure is shown in **Figure 1.9**.

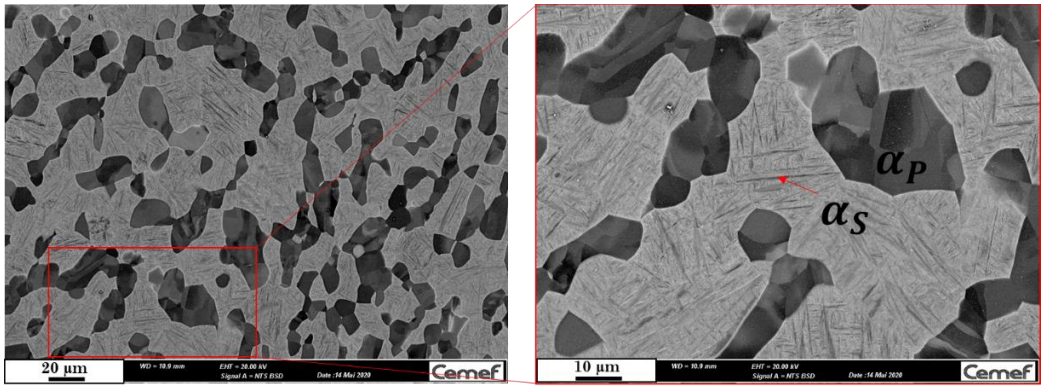



*Figure 1.9. Example of an α+β alloy (Ti64) water quenched (WQ) from 950°C ($T_\beta$-50°C), showing the equiaxed primary α phase ($\alpha_P$) with the very fine laths of the secondary α phase ($\alpha_S$) formed during quenching of the prior-β phase.*

However, if the content of $\beta$-stabilizing elements is high some fraction of $\beta$ phase may be retained at room temperature (**Figure 1.7**), which reduces mechanical strength but increases ductility. When cooled more slowly, the $\beta$ phase undergoes the transformation described in section **1.1.4**, leading to a two-phase ($\alpha$+$\beta$) lamellar microstructure.

### *1.1.6.5 Metastable-β alloys*

Unlike $\alpha$+$\beta$ alloys, $\beta$-metastable alloys do not undergo $\beta \rightarrow \alpha$ transformation when quenched, so the high temperature phase ($\beta$) can be retained at ambient temperature (**Figure 1.10**).

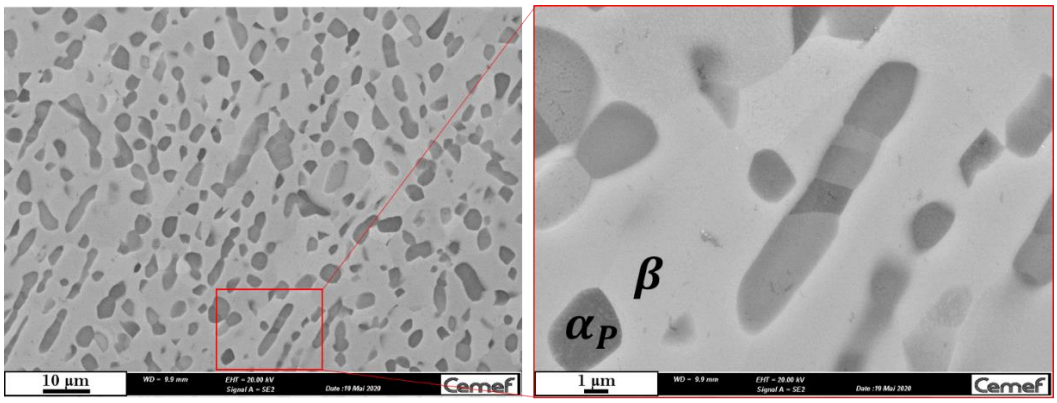



*Figure 1.10. Example of metastable-β alloy (Ti1023), water quenched (WQ) from 750°C ($T_\beta$-50°C), showing the equiaxed primary α phase ($\alpha_P$) and the retained β phase.*

An advantage of metastable-$\beta$ alloys is that they can be forged at lower temperatures than $\alpha$+$\beta$ alloys. This also possibilities the formation of substructures in the $\beta$ phase during a heat treatment. However, contrary to the $\alpha$+$\beta$ alloys, when the metastable-$\beta$ alloys are cooled at slower cooling rates, the $\alpha_s$ can nucleate and grow, thus forming a bimodal microstructure. Consequently, due to this high variety, it allows the design of alloys aiming to optimize high strength and toughness, as is the case for TIMETAL 10-2-3 (Ti1023).

## 1.2 Microstructural evolution during hot deformation

### *1.2.1 Plasticity, recovery and recrystallization*

When a metal is stressed beyond its yielding point, plastic deformation occurs, which is associated with the creation and movement of defects in the crystal [19]. These linear crystalline defects (dislocations) create local crystal distortion (**Figure 1.11**), at the atomic scale, and their energy is usually considered as the main contribution to the stored energy. Further details on dislocation types are given in section **2.7.5**.

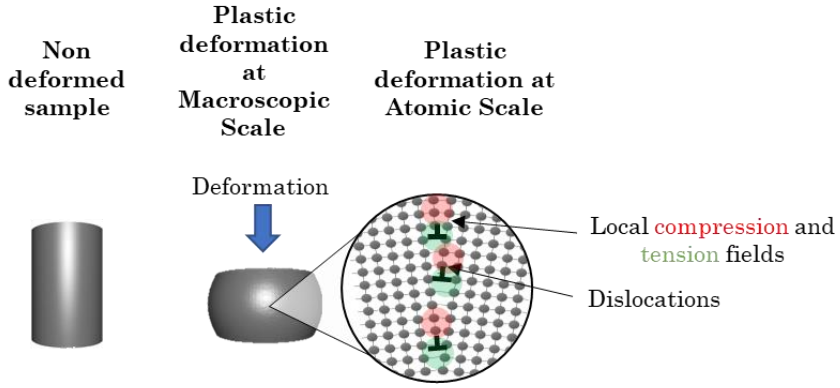



*Figure 1.11. Schematic of the plastic deformation on metals at different scales (macroscopic and atomic), with the local strain distortion created by the dislocations.*

The associated local stress fields lead to various interactions between dislocations, in addition to interactions between dislocations and other microstructural elements (grain boundaries, precipitates, atoms in solid solution, among others). This stored energy can be relaxed by a heat treatment at high temperature after the plastic deformation, to recover the initial properties through recovery and recrystallization mechanisms [19–22].

#### *1.2.1.1 Recovery*

Recovery is a thermally activated phenomenon, which precedes recrystallization, and allows a softening of the material by the rearrangement and the (generally partial) annihilation of the dislocations (**Figure 1.12**). The dislocations can annihilate and organize into sub-boundaries, subdividing the initial grains into subgrains (formation of substructures). There is thus a reduction in the dislocation density ($\rho$, defined as the total length of dislocation line per unit volume of crystal [23]), which accompanies a reduction in the stored energy.

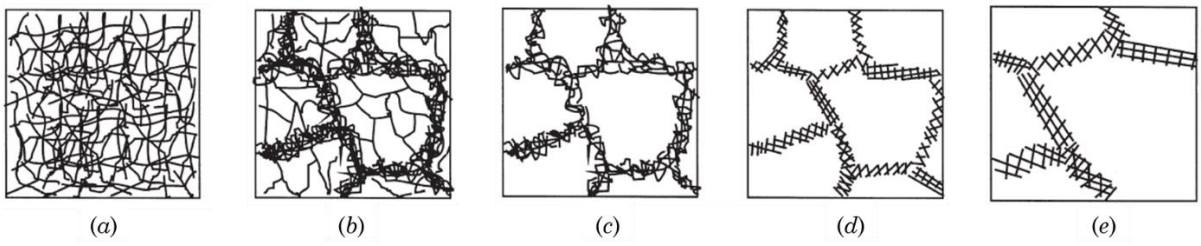



*Figure 1.12. Steps in the recovery of a plastically deformed metal: a) Dislocation tangles; b) Cell formation; c) Annihilation of dislocation within cells; d) Subgrain formation; Subgrain growth* [22].

#### *1.2.1.2 Recrystallization*

Recovery generally involves only a partial restoration of properties, as the dislocation structure is not completely removed (**Figure 1.13***b*). A further restoration process (recrystallization) can occur, where new dislocation-free grains are formed within the deformed or recovered microstructure [22]. This phenomenon consists in the profound evolution of the granular structure and can be divided into discontinuous or continuous recrystallization phenomena [24].

##### *1.2.1.2.1 Discontinuous recrystallization*

In this phenomenon, the applied plastic deformation is not uniformly distributed, where finer and denser (in terms of dislocation density) substructures are developed along the deformed grain boundaries. Coarser and less dense substructures are produced inside the grains [16,25]. Consequently, new small grains nucleate at the former grain boundaries and grow by "consuming" the dislocations inside the previous grain (under the effect of the driving force linked to the difference in stored energy), thus forming a “necklace” topology (**Figure 1.13***c*). These grains then grow and consume the old grains, resulting in a new grain structure (**Figure 1.13***d*) with low dislocation density (*i.e.,* no stored energy).

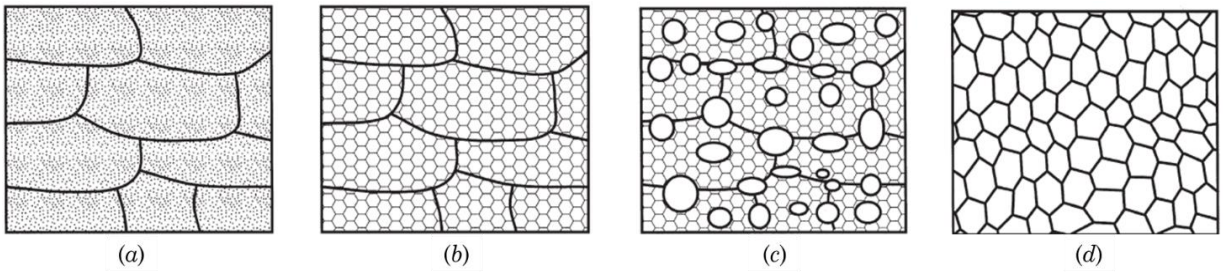



*Figure 1.13. Schematic diagram of the heat treatment of a plastically deformed alloy: a) Deformed state; b) Recovery (formation of substructures); c) Nucleation and growth of new grains leading to partial recrystallization; d) Full recrystallization* [22].

#### *1.2.1.2.2 Continuous recrystallization*

New grains can also be formed by progressive rotation of the subgrains, whose misorientation relative to each other increases with the deformation. When the angle between two adjacent subgrains becomes large enough, they are no longer considered as substructures (LAGB, low angle grain boundaries), being defined as grain boundaries (HAGB, high angle grain boundaries), as shown in **Figure 1.14** [25,26]. The microstructure evolves in a relatively homogeneous and, above all, progressive/ continuous way, without nucleation and growth of recrystallized grains, as occurs in the above described discontinuous process [22,27].

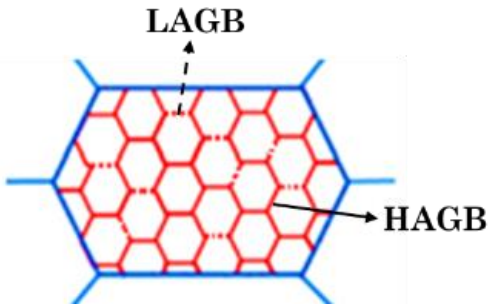



*Figure 1.14. Mechanism of continuous dynamic recrystallization (schematically), with LAGB (dashed red lines) gradually forming the HAGB (solid red lines) inside the former grain (in blue) by progressive evolution of the substructures* [28].

#### *1.2.1.2.3 Dynamic recovery and recrystallization*

The previously described processes of microstructure evolution (sections **1.2.1.1** and **1.2.1.2**) can occur statically (during a thermal treatment) or dynamically (during hot deformation), if the deformation takes place at a sufficiently high temperature). Then, they are referred to as: dynamic recovery (DRV), discontinuous dynamic recrystallization (DDRX) and continuous dynamic recrystallization (CDRX).

These three microstructural phenomena (DRV, CDRX and DDRX) are the main ones responsible for the microstructural evolutions in the $\alpha$ and $\beta$ phases during hot deformation. The following sections (**1.2.2** and **1.2.3**) describe how the initial microstructure and thermomechanical parameters influence these evolutions in the $\beta$ and $\alpha+\beta$ domain, respectively.

### *1.2.2 Deformation in the β domain and the influence of microstructural/ thermomechanical parameters*

During forging, the $\beta$ grains elongate, perpendicularly to the direction of the imposed deformation, and the grain boundaries become progressively more jagged with increasing deformation (**Figure 1.15**) [29,30].

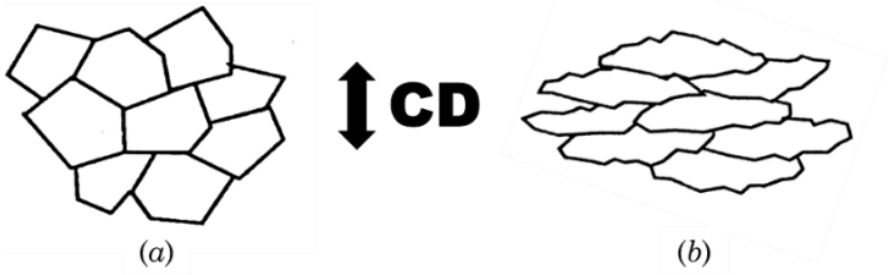



*Figure 1.15. Morphological evolution during the deformation of β grains above $T_\beta$, before (a) and after (b) compression (CD = Compression Direction)* [29].

For structures starting with coarse $\beta$ grains, typical of those encountered in ingots (cast microstructure), hot deformation is an important step for the homogenization of the microstructure. Different mechanisms can be observed in **Figure 1.16.** Partial discontinuous dynamic recrystallization by the typical "necklace" topology, while dynamic recovery of the $\beta$ phase is also observed inside the grains, with few continuously recrystallized grains.

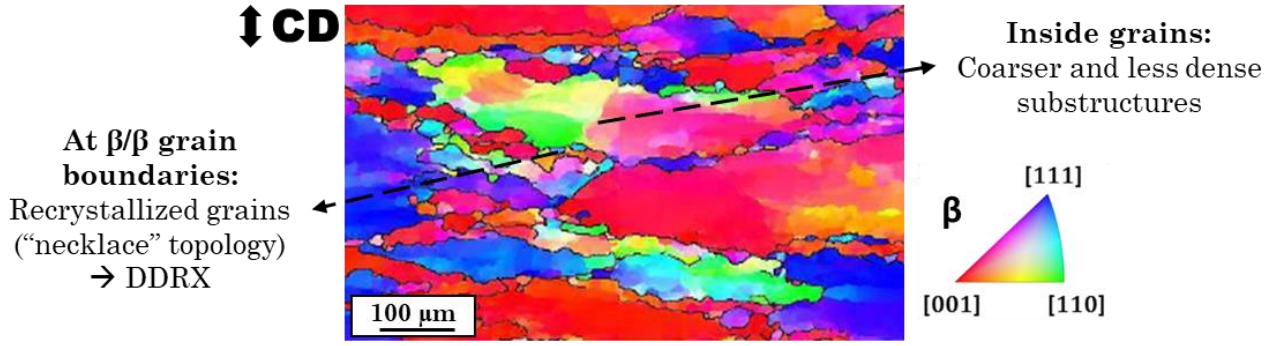



*Figure 1.16. Dynamic recrystallization in a Ti-17 alloy (metastable-β) deformed at 885°C and 0.01 $s^{-1}$* [31].

After understanding how the $\beta$ grains evolve above the $\beta$-transus, the influence of strain level, temperature and strain rate on those evolutions are discussed below (sections **1.2.2.1** to **1.2.2.3**).

#### *1.2.2.1 Strain level*

In the work of OuYang *et al.* [32] on a Ti1023 alloy deformed at $\dot{\varepsilon} = 0.01\ s^{-1}$ and 825°C (*i.e.,* above $T_\beta = 800°C$), with initial $\beta$ grain size of around 250 $\mu m$ (**Figure 1.17***a*), it was observed that at $\varepsilon < 0.5$, $\beta$ grains became serrated under the effect of deformation (**Figure 1.17***b*). Furthermore, for $0.5 < \varepsilon < 1$, a larger strain level (0.92) generate a "necklace" topology of very fine grains at the boundaries of the $\beta$ grains formed discontinuously, as well as grains recrystallized by continuous recrystallization (**Figure 1.17***c*). Finally, for $\varepsilon > 1$, the volume fraction of the

recrystallized grains increased to about 70% with an average grain size of 40$\mu m$ (**Figure 1.17***d*).

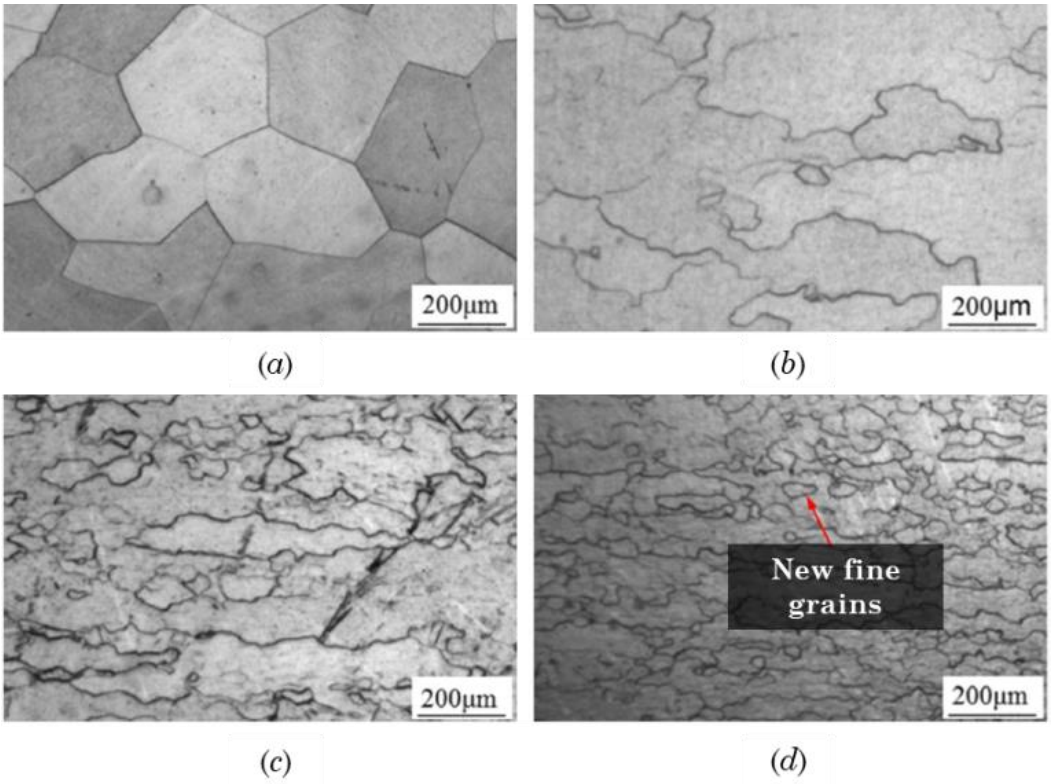



*Figure 1.17. Microstructures of a Ti1023 alloy deformed at 825°C and 0.01 $s^{-1}$ to ε of: a) 0; b) 0.51; c) 0.92; d) 1.61* [32].

### *1.2.2.2 Temperature*

For a strain level of 1.6 applied at 0.01 $s^{-1}$, the volume fraction and the size of the dynamically recrystallized $\beta$ grains of the Ti1023 alloy increase with deformation temperature [32]. At 825°C ($T_\beta$+25°C), there was 65% of recrystallized grains with an average size of 40.6 $\mu m$ (**Figure 1.18***a*). According to the overview work of Lee Semiatin [25], for temperatures up to about 50°C above the $T_\beta$, the volume fraction of grains discontinuously recrystallized is normally low (≤ 15%), the main mechanism being continuous dynamic recrystallization.

With increasing temperature (at 950°C), 79% of grains recrystallized, but with an average size of 61 $\mu m$, this increasing grain is favored by the higher temperature (**Figure 1.18***b*). Finally, at 1150°C, there were recrystallized grains with larger grain size, but no continuous dynamic recrystallization (**Figure 1.18***c*).

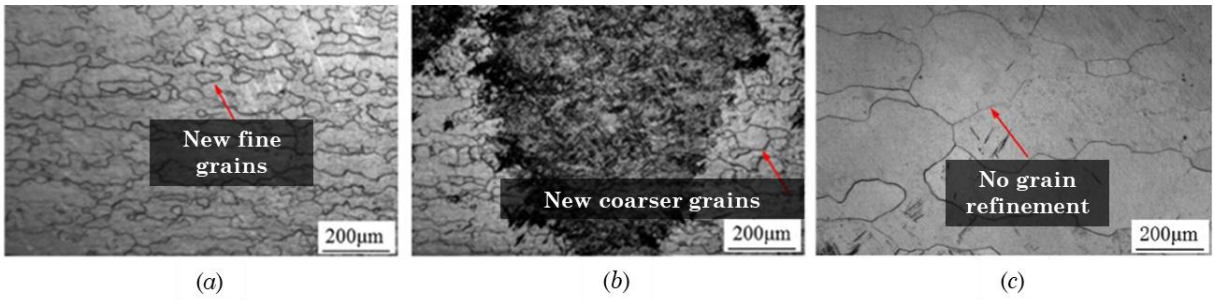



*Figure 1.18. Optical micrographs of Ti1023 samples after hot deformation to ε = 1.6 at $\dot{\varepsilon}$ = 0.01 $s^{-1}$ and: a) 825°C; b) 950°C; c) 1150°C* [32].

#### 1.2.2.3 Strain rate

The volume fraction and the size of recrystallized $\beta$ grains decrease with increasing strain rate above 0.1 $s^{-1}$ [32,33]. Tests were performed by OuYang *et al.* [32] with a strain level of 1.6 applied at different strain rates at 825°C. At a very low strain rate (0.001 $s^{-1}$), the presence of coarse grains can be observed (**Figure 1.18***a*). With increasing strain rate (*i.e.,* at 0.01 $s^{-1} < \dot{\varepsilon} < 0.1\ s^{-1}$), recrystallization of grains with a fine size was observed (**Figure 1.18***a* and **Figure 1.19***b*, respectively). Furthermore, at 1 $s^{-1}$, there was nearly no refinement of the microstructure (very rapid deformation). Recrystallization of small grains along the initially elongated $\beta$ grain boundaries ("necklace" structure) was observed, but with a low fraction of recrystallized grains (**Figure 1.19***c*).

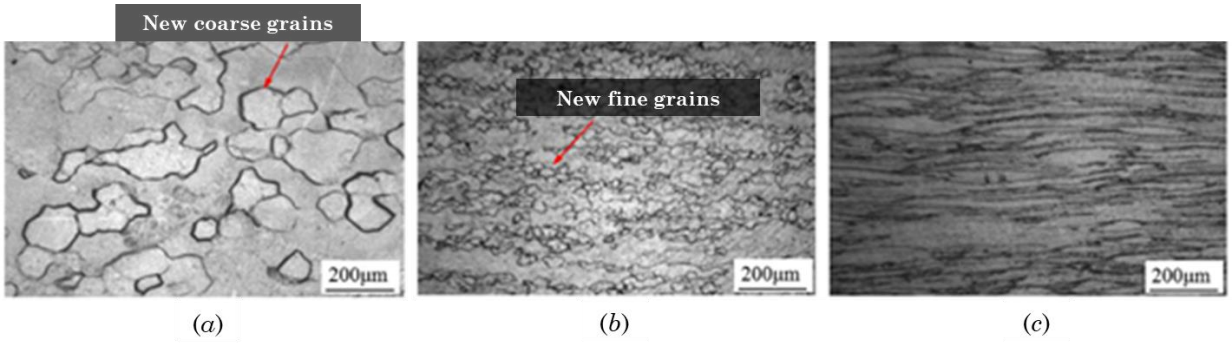



*Figure 1.19. Optical micrographs of Ti1023 specimens hot-deformed to ε = 1.6 at T = 825°C and: a) 0.001 $s^{-1}$; b) 0.1 $s^{-1}$; c) 1 $s^{-1}$* [32].

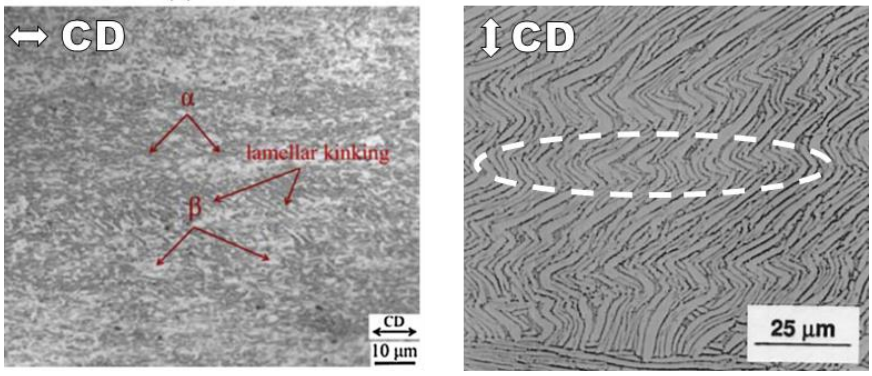
Furthermore, OuYang *et al.* [32] concluded that, in the case of Ti1023, very large strains ($\varepsilon \geq 2$) must be imposed at low strain rates (< 0.01 $s^{-1}$) and at temperatures well above $T_\beta$ to obtain a fully refined microstructure (~35 μ*m* grain size) via discontinuous dynamic recrystallization [25].

### 1.2.3 Deformation in the α+β domain and the influence of microstructural/ thermomechanical parameters

Below $T_\beta$, the two phases $\alpha$ and $\beta$ coexist during deformation, and the $\alpha$ phase will play a key role, not only in its own microstructural evolution, but also in the $\beta$ phase one. The main phenomena are discussed below.

#### 1.2.3.1 Kinking of α lamellae

Shearing and dislocation climb/glide process [23] lead to the kinking mechanism, by which lamellae, initially flat, bend. Two examples (for the Ti1023 and Ti64, respectively) of lamellae kinking are shown in **Figure 1.20.**



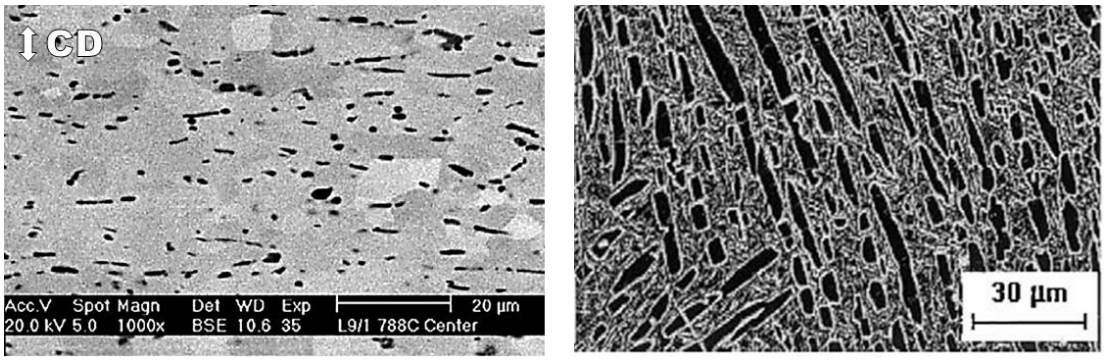

(a) (b)

*Figure 1.20. Kinking of α lamellae in the following alloys: a) Ti1023 deformed at 700°C/ 0.1 s-1/ 0.9 strain level [34]; b) Ti64 deformed at 900°C/ 0.1 s-1/ 0.7 strain level [35].*

The kinking mechanism has been observed in the Ti1023 [34,36] and Ti64 [35,37] alloys, being predominant at high $\dot{\varepsilon}$ (> 0.1 $s^{-1}$), at low $\varepsilon$ (< 0.5) and at low $T$ (< $T_\beta$ - 50°C), because there is limited diffusion (which in turn allows globularization). In addition, this mechanism is favored by a morphology with coarse lamellae, where there is formation of shear bands [26,35,38] across the $\alpha$ colonies (as in the ellipse in **Figure 1.20***b*).

### *1.2.3.2 Globularization of lamellar α*

In the case of globularization, the fragmentation and coarsening of the lamella fragments are controlled by bulk and interfacial diffusion [39]. Two examples (for the Ti1023 and Ti64, respectively) of lamellae fragmentation are shown in **Figure 1.21**.




(a) (b)

*Figure 1.21. Lamellae fragments in the following alloys: a) Ti1023 at 0.01 $s^{-1}$/788°C and 0.7 strain level, with elongated α grains which are aligned perpendicularly to the CD [40]; b) Ti64 at 0.005 $s^{-1}$/850°C at 0.7 strain level [34].*

The steps of the globularization mechanism are (**Figure 1.22**) [38]:

a) Shearing of lamellae due to an imposed stress;
b) Accumulation of dislocations along the shear band;
c) Formation of subgrain boundaries by recovery;
d) Migration of interfaces by diffusion (usually during long duration holding at high temperatures), to minimize the surface energy of globules.

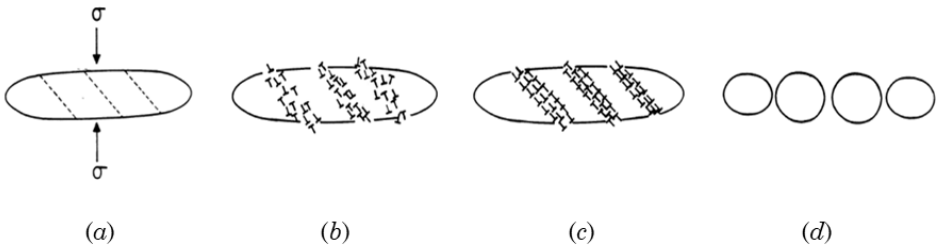



*Figure 1.22. Diagram (schematic) of the α globularization process* [38].

Dynamic globularization (during deformation) has been observed in Ti1023 [36] and in Ti64 [34], being favored at low $\dot{\varepsilon}$ (< 0.1 $s^{-1}$), at high $\varepsilon$ (> 0.5) and at high $T$ (close to $T_\beta$), as this promotes diffusion (more time and higher temperature). In addition, the globularization kinetics is faster for finer lamellae, because these lamellae are easier to be fragmented. During post-deformation holding in the $\alpha+\beta$ domain, they will then globularize, minimizing the $\alpha/\beta$ interface energy [26,37].

### *1.2.3.3 Continuous dynamic recrystallization of equiaxed α grains*

Souza *et al.* [41] have shown experimentally that continuous dynamic recrystallization of equiaxed $\alpha$ grains in the $\alpha+\beta$ domain can be classified into two different modes:

***a) Iso-stress mode***

The stress applied during deformation is considered to be uniform for all orientations and phases, which results in a variation of the strain rate between them. Therefore, $\alpha$-grains with orientations favorable to slip (*i.e.,* prismatic $\{10\bar{1}0\}$ and pyramidal $\{10\bar{1}1\}$ planes ∥ CD) and $\beta$-grains (more slip systems) form more dislocations. According to [41], this promotes the formation of substructures (and new equiaxed $\alpha$ grains) near the $\alpha/\alpha$ and $\alpha/\beta$ boundaries to maintain strain compatibility between adjacent grains/phases (**Figure 1.23***a*);

***b) Iso-strain rate mode***

The stress applied during deformation is distributed among different orientations and phases, which results in a uniform strain rate. However, the lower flow stresses for the $\alpha$ grains with orientations favorable to slip and for the $\beta$ phase lead to the deformation of the $\alpha$ phase with an unfavorable orientation (*i.e.,* the basal plane (0001) ∥ CD) to control the global deformation of the material ($\alpha+\beta$). The high resistance to deformation due to the unfavorable orientation of the initial $\alpha$ grains leads to the formation of substructures (and new equiaxed grains) mainly inside the $\alpha$ grains (**Figure 1.23***b*) [41].

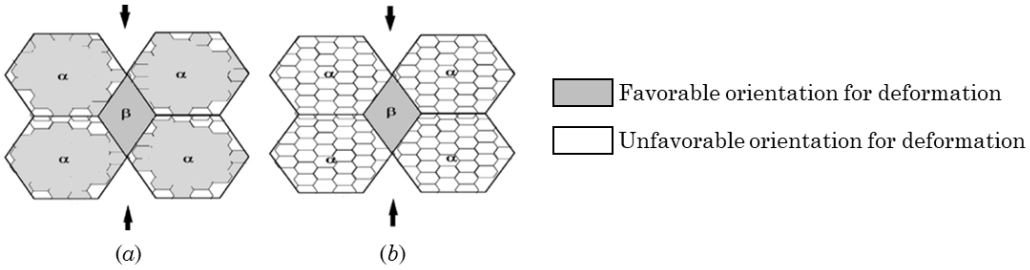



*Figure 1.23. Schematic representation of α grain dynamic recrystallization within the: a) iso-stress mode; b) iso-strain rate mode* [41].

According to the experimental observations of Souza *et al.* [41], the formation of substructures and equiaxed fine grains close to grain boundaries or in the initial $\alpha$ grains vary in the Ti64 alloy according to the following thermomechanical conditions (**Figure 1.24**):

- **At low *T* and high $\dot{\varepsilon}$,** substructures and equiaxed $\alpha$ fine grains develop close to the $\alpha/\alpha$ and especially $\alpha/\beta$ grain boundaries [42]. It was observed by [41] that the basal system becomes unfavorable at low temperatures and at high strain rates. Thus, the dislocations will mostly occur on the favorable planes (*i.e.,* prismatic and pyramidal ∥ CD). Those thermomechanical conditions favor the *Iso-stress mode*, as shown in the bottom part of **Figure 1.24**;

- **At high *T* and low $\dot{\varepsilon}$,** the basal plane becomes active [41], so the substructures and equiaxed $\alpha$ fine grains develop mainly inside the $\alpha$ grains. Those thermomechanical conditions favor the *Iso-strain rate mode*, as shown in the upper part of **Figure 1.24**.

In between the bold lines (bounds) in **Figure 1.24**, Ti64 undergoes both mechanisms to produce equiaxed α fine grains.

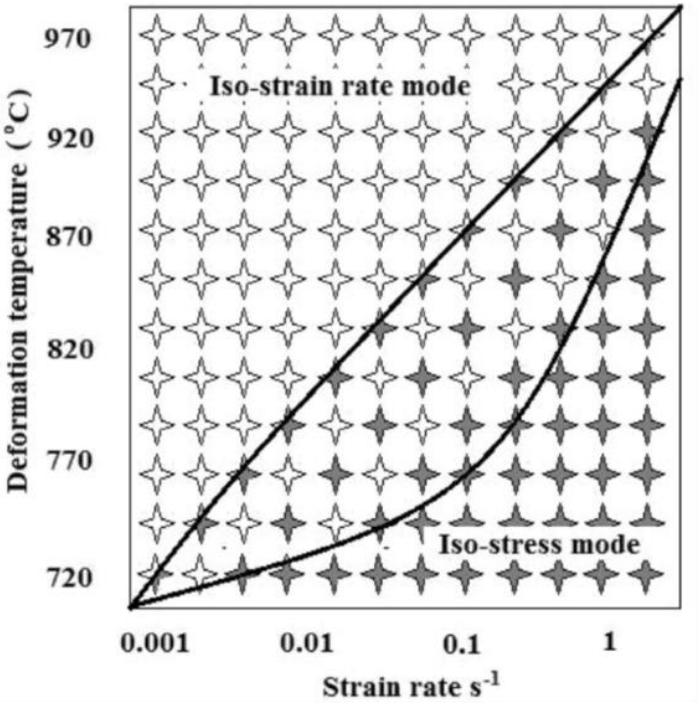



*Figure 1.24. Diagram of the continuous dynamic recrystallization mechanisms of the equiaxed α grains (Iso-stress or Iso-strain rate) as a function of the deformation temperature and the strain rate (in the Ti64 alloy)* [41].

### *1.2.3.4 Evolution of β grains*

During deformation in the two-phase domain, the $\alpha$ phase (lamellar or equiaxed) is gradually substructured (n°5 in **Figure 1.25)**. Also, the $\alpha$ phase generates an impingement effect on the $\beta$ phase at the $\alpha/\beta$ grain boundaries (n°4 in **Figure 1.25**), limiting the growth of $\beta$ grains. The $\beta$ grains accommodate the deformation mostly by becoming substructured (n°1 and 2 in **Figure 1.25**).

Furthermore, since the $\alpha$ phase deforms less than the $\beta$ phase, strain must concentrate, in the $\beta$ phase, in the vicinity of the $\alpha$ phase. This leads to the formation of small subgrains (n°1 in **Figure 1.25**) with larger misorientation compared to the subgrains produced in the rest of the $\beta$ matrix (n°2 of **Figure 1.25**).

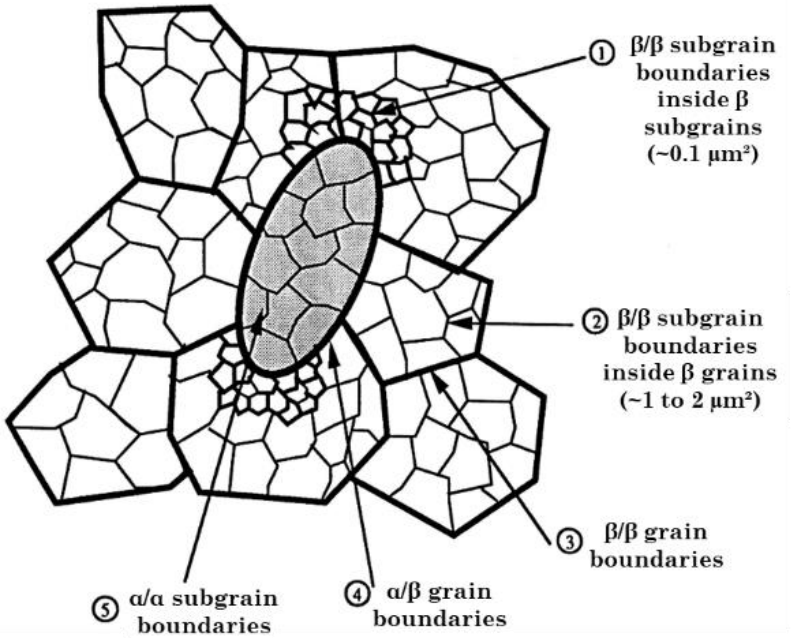



*Figure 1.25. Substructure formation in α and β grains/subgrains, during the deformation of β-CEZ (metastable-β with $T_\beta$ = 890°C) at 840°C and 0.3 $s^{-1}$* [16,29].

The $\beta$ matrix also undergoes microstructural changes associated with grain elongation (as shown in **Figure 1.15**) in addition to the formation of low angle grain boundaries (LAGB). With increasing deformation, those LAGB continuously increase their misorientation, hence creating high angle grain boundaries (HAGB), *i.e.,* continuous dynamic recrystallization, even if in very small quantities [16,43]. According to the work of Balachandran *et al.* [43] on the metastable-$\beta$ alloy Ti-5Al-5Mo-5V-3Cr, the $\beta$ phase recrystallizes continuously deformed at the following thermomechanical conditions: 765°C ($T_\beta$ = 845°C) to $\varepsilon$ of 0.5 at $\dot{\varepsilon}$ between 0.001 and 10 $s^{-1}$.

### *1.2.3.5 The α→β dynamic transformation*

It has been reported in the literature [34,44,45] that two-phase titanium alloys can undergo dynamic transformation from $\alpha$ phase (hard) to $\beta$ phase (soft) during hot deformation in the two-phase domain. This behavior was observed in both equiaxed and lamellar microstructures for the Ti64 alloy [46]. Furthermore, it was shown by Ding *et al.* [34] that this phenomenon is promoted by high temperature and slightly increases with increasing strain rate.

On the other hand, other research suggests on hot deformation of titanium alloys in the two-phase domain did not show any changes in phase fraction during deformation [32,36,39–41].

It appears that the thermomechanical parameters applied may be the main responsible of the occurrence of the $\alpha \rightarrow \beta$ dynamic transformation in some works.

For example, in the work of Semiatin *et al.* [44], with Ti64 and Ti-6Al-2Sn-4Zr-2Mo-0.1Si (Ti6242S) alloys, compression was applied at 0.1 $s^{-1}$ and at temperatures ranging approximately from $T_\beta$ - 100°$C$ to $T_\beta$ - 25°$C$. It was then shown [44] that the dynamic transformation only occurred when there was no sufficient holding time prior to deformation. Furthermore, in the work of Saby *et al.* [6], the dynamic transformation was observed in torsion tests of Ti64 alloy. Finally, Guo *et al.* [46] concluded that an appropriate strain rate for observing dynamic transformation lies in the range from 0.01 to 0.001 $s^{-1}$.

### 1.2.4 Summary of microstructure evolution mechanisms and influence of microstructural/ thermomechanical parameters

To summarize section **1.2**, the mechanisms that govern the microstructural evolutions during hot deformation, according to the literature review, are specific of the $\beta$ and $\alpha$+$\beta$ domains, occurring above and below $T_\beta$, respectively.

#### 1.2.4.1 In the β domain

The first mechanism is partial discontinuous dynamic recrystallization. Consisting in the formation of finer and denser substructures (as also small equiaxed grains) along deformed $\beta$ grain boundaries, with coarser and less dense substructures within the grains. This mechanism is favored by an initial coarse-grained microstructure, very high $T$, very high strain levels ($\varepsilon \geq 2$) and $\dot{\varepsilon} < 0.01 s^{-1}$.

Another observed mechanism is the continuous dynamic recrystallization, with formation of uniform substructures (continuously evolving into equiaxed $\beta$ grains during deformation) within the whole prior $\beta$ grains. This mechanism is favored by an initial fine-grained microstructure, $T < T_\beta$+50, $\varepsilon < 2$, and $\dot{\varepsilon} \geq 0.01\ s^{-1}$.

In both cases, there is elongation of $\beta$ grains and increasingly serrated grain boundaries as strain is increased.

#### 1.2.4.2 In the α + β domain

For the lamellar $\alpha$ phase, the first observed mechanism is the kinking, favored by a microstructure of coarse $\alpha$ lamellae, low $T$, high $\dot{\varepsilon}$ and low $\varepsilon$. The second mechanism is dynamic globularization (mainly controlled by diffusion), favored by a microstructure of fine $\alpha$ lamellae, high $T$, low $\dot{\varepsilon}$ and large $\varepsilon$.

Concerning the equiaxed $\alpha$ grains, continuous dynamic recrystallization of equiaxed $\alpha$ grains seems to be divided in two modes, so-called: *iso-stress* and *iso-strain rate* [41]. The former consists in the development of substructures (and equiaxed fine grains) close to the $\alpha/\alpha$ and $\alpha/\beta$ grain boundaries, being mainly observed at low $T$ and high $\dot{\varepsilon}$. While the latter consists in the development of substructures (and equiaxed fine grains) inside the grains, especially the ones with the basal plane parallel to the compression direction. The iso-strain rate mode was mostly observed at high $T$ and low $\dot{\varepsilon}$.

Regarding the $\beta$ grains evolution, the $\alpha$ grains generate an impingement effect at the $\alpha/\beta$ boundaries by limiting the growth of the $\beta$ grains, which accommodate the deformation by substructuring. With increasing deformation, the subgrain

boundaries (LAGB) can progressively become grain boundaries (HAGB), *i.e.,* continuous dynamic recrystallization, even if in limited amount.

Finally, **Table 1.2** summarizes the tendencies in the correlation between thermomechanical and microstructural parameters on the reported microstructure mechanisms. However, this analysis is rather indicative and must be taken with precaution, given that the mechanisms change depending on the different combined parameters (*e.g.,* morphology, texture, temperature, strain level and rate). The described mechanisms are favored or unfavored, respectively, by ↗ and ↘, according to the thermomechanical parameters.

| Domain | Morphology | Main mechanism | ↗ T | ↗ $\dot{\varepsilon}$ | ↗ $\varepsilon$ | Reference |
|---|---|---|---|---|---|---|
| $\alpha$+$\beta$ ($\alpha$ phase) | Fine lamellar $\alpha$ | Dynamic globularization | ↗ | ↘ | ↗ | [34,36,38–40] |
| | Coarse lamellar $\alpha$ | Kinking | ↘ | ↗ | ↘ | [26,36,37] |
| | Equiaxed $\alpha$ | Continuous dynamic recrystallization (Iso-stress) | ↘ | ↗ | ↗ | [41,42] |
| | | Continuous dynamic recrystallization (Iso-strain rate) | ↗ | ↘ | ↗ | [41] |
| $\alpha$+$\beta$ ($\beta$ phase) | Equiaxed $\beta$ | Dynamic recovery + Continuous dynamic recrystallization | ↗ | ↗ | ↗ | [16,29,43] |
| $\beta$ | Fine equiaxed $\beta$ | Continuous dynamic recrystallization | ↘ | ↗ | ↘ | [25,32,33] |
| | Coarse equiaxed $\beta$ | Partial discontinuous dynamic recrystallization | ↗ | ↘ | ↗ | [29–32] |

*Table 1.2. Summary assessment of the effects of the various thermomechanical and microstructural parameters on the mechanisms which govern the microstructural evolutions of titanium alloys.*

## 1.3 Industrial thermomechanical processing of titanium alloys

A typical thermomechanical processing route of titanium alloys, applied in the aeronautical industry, along with the microstructural mechanisms involved, are represented in **Figure 1.26**. Each processing step results in modifications in the microstructure. This thesis mostly focuses on microstructure evolution when deforming the alloys in the two-phase domain (green ellipses in **Figure 1.26**).

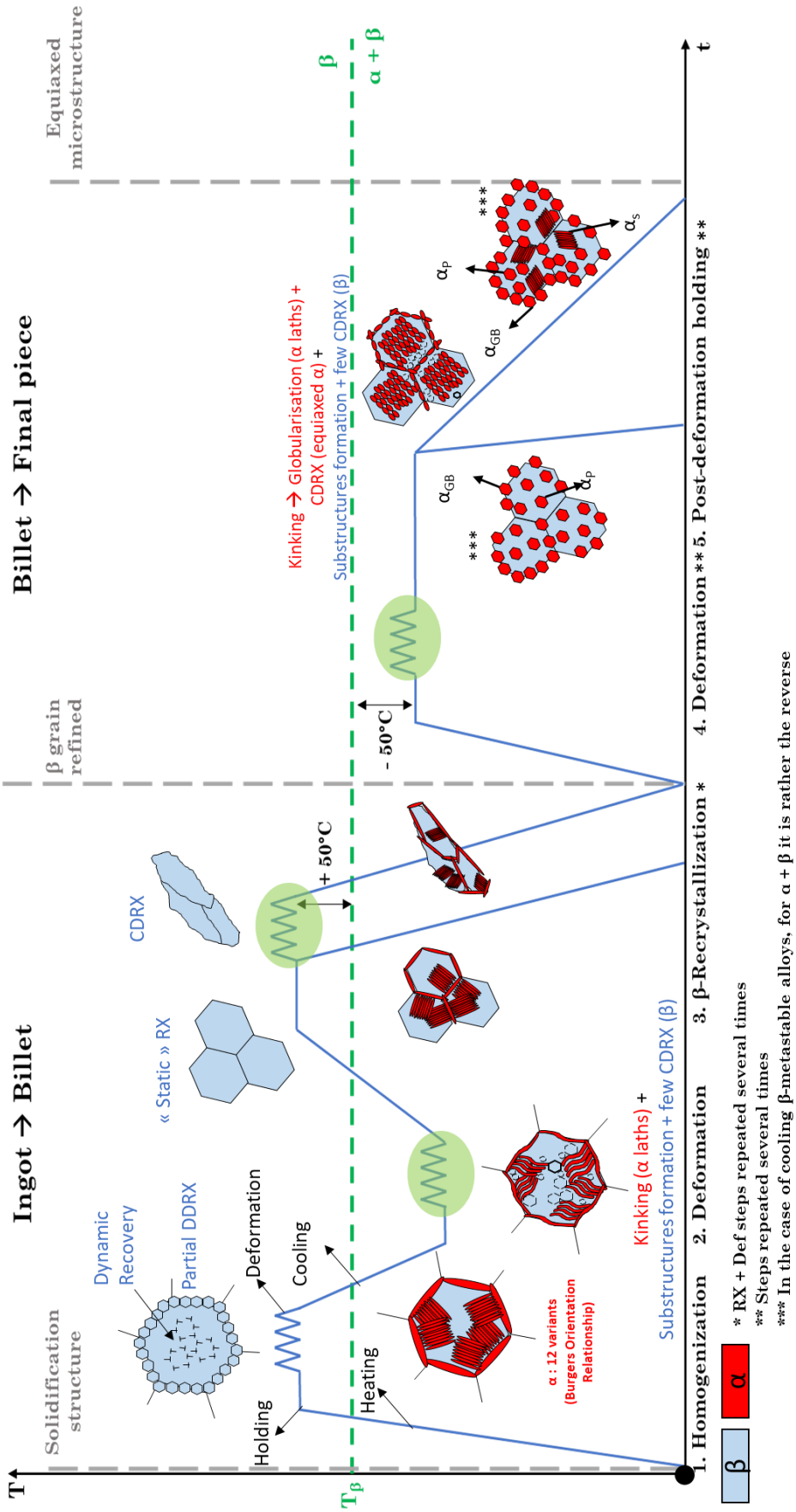



*Figure 1.26. Schematic representation of thermomechanical processing steps used for titanium alloys in the aeronautical industry, along with the microstructural evolutions.*

The different steps consist in:

- **Deformation and Homogenization in the $\beta$ domain**

Forging of the ingot to break the raw microstructure of solidification ($\beta$ grains of the order of a few millimeters) and help to homogenize the chemical composition. During cooling, colonies of $\alpha$ lamellae are formed according to the 12 possible BOR (BCC→HCP) described in section **1.1.4**.

- **Deformation in the two-phase domain**

Forging in the $\alpha$+$\beta$ domain causes the previously formed $\alpha$ lamellae to kink and break, surrounded by $\beta$ phase substructures (with low continuous dynamic recrystallization) [29].

- **"$\beta$-Recrystallization"**

This "$\beta$-recrystallization" is a process that is still insufficiently understood (subject of another ongoing thesis of the CONTiNUUM project), where the $\beta$ grains are refined. The temperature of this step is maintained between 30 to 50°$C$ above $T_{\beta,}$ to control $\beta$ grain size. Another important parameter of this step is the subsequent cooling rate, which will determine the thickness of the $\alpha$ lamellae generated inside the refined $\beta$ grains [9].

- **Deformation in the $\beta$ domain**

There is also an alternative of deforming in the $\beta$ domain the "$\beta$-recrystallized" microstructure, where the $\beta$ grains will be deformed and partially dynamically recrystallized. Cooling afterwards will form thin $\alpha$ lamellae as well, but with former $\beta$ grains elongated, perpendicularly to the CD, and serrated $\beta$/$\beta$ grain boundaries [30].

- **Deformation in the two-phase domain**

After obtaining a lamellar microstructure, if an equiaxed microstructure is desired, a deformation step in the two-phase domain will be necessary. There is then fragmentation of the $\alpha$ lamellae, followed by the formation of substructures and the initiation of the globularization of the lamellae [26]. The deformation temperature is maintained at high levels, approximately 50°$C$ below the $T_{\beta}$. In this step there will be no (or limited) growth of the $\beta$ grains, as the $\alpha$ phase will prevent it (impingement effect) [16].

- **Post-deformation holding in the two-phase domain**

This consists in the final step in the morphological evolution of the lamellae, to obtain an equiaxed microstructure (globularization). The temperature and the holding time fix the volume fraction and the grain size of the equiaxed $\alpha_P$. The cooling rate affects the formation of (or prevent its formation) the lamellar $\alpha_S$ (and its thickness), forming, respectively, a bimodal or fully equiaxed microstructure [3].

## 1.4 Résumé en Français

Dans ce chapitre, nous avons passé en revue les différents mécanismes qui régissent les évolutions microstructurales au cours de la déformation à chaud. Selon la revue de la littérature, ces évolutions sont spécifiques aux domaines $\beta$ et $\alpha+\beta$, intervenant respectivement au-dessus et au-dessous de $T_\beta$ (température du transus $\beta$).

- **Dans le domaine $\beta$ :**

Le premier mécanisme est la recristallisation dynamique discontinue partielle. Elle consiste en la formation de sous-structures fines et plus denses (ainsi que des grains petits et équiaxes) le long des joints de grains $\beta$ déformés, avec des sous-structures plus grossières et moins denses à l'intérieur des grains. Ce mécanisme est favorisé par une microstructure initiale à gros grains, par $T$ très élevée, par des niveaux de déformation très élevés ($\varepsilon \geq 2$) et par $\dot{\varepsilon} < 0.01\ s^{-1}$.

Un autre mécanisme observé est la recristallisation dynamique continue, avec formation de sous-structures uniformes (évoluant continuellement en grains $\beta$ équiaxes lors de la déformation) au sein de l'ensemble des grains $\beta$ antérieurs. Ce mécanisme est favorisé par une microstructure initiale à grains fins, par $T < T_\beta$ +50, par $\varepsilon < 2$, et par $\dot{\varepsilon} \geq 0.01\ s^{-1}$.

Dans les deux cas, il y a un allongement des grains $\beta$ et des joints de grains de plus en plus dentelés à mesure que la déformation augmente.

- **Dans le domaine $\alpha + \beta$ :**

Pour la phase $\alpha$ lamellaire, le premier mécanisme observé est le flambement, favorisé par une microstructure de lamelles $\alpha$ grossières, à $T$ faible, $\dot{\varepsilon}$ élevée et $\varepsilon$ faible. Le deuxième mécanisme est la globularisation dynamique (principalement contrôlée par la diffusion), favorisée par une microstructure de fines lamelles $\alpha$, $T$ élevée, $\dot{\varepsilon}$ faible et $\varepsilon$ importante.

Concernant les grains $\alpha$ équiaxes, la recristallisation dynamique continue des grains $\alpha$ équiaxes semble être divisée en deux modes, dits : contrainte homogène et vitesse de déformation homogène. Le premier est expliqué par le développement de sous-structures (et de grains fins équiaxes) proches des joints de grains $\alpha/\alpha$ et $\alpha/\beta$, principalement observés à faible $T$ et à $\dot{\varepsilon}$ élevée. Tandis que le deuxième est donné par le développement de sous-structures (et de grains fins équiaxes) à l'intérieur des grains, en particulier ceux dont le plan basal est parallèle à la direction de compression. Le mode de vitesse de déformation homogène a été principalement observé à $T$ élevée et à faible $\dot{\varepsilon}$.

Concernant l'évolution des grains $\beta$, les grains $\alpha$ limitent la croissance des grains $\beta$ (grâce aux joints $\alpha/\beta$), qui accommodent de la déformation par se sous-structurant. Avec l'augmentation de la déformation, les joints de sous-grains (LAGB) peuvent progressivement devenir des joints de grains (HAGB), c'est-à-dire une recristallisation dynamique continue, même en quantité limitée.

# 2. MATERIALS AND METHODS

The study of microstructural evolution occurring during the forging stages and the investigation of the relationship between microstructure and mechanical properties require the ability to finely characterize the microstructures. The objective of this chapter is to present the materials received from the industrial partners, along with the characterization methods and all the fundamental aspects to comprehend the microstructural analyses presented in the following chapters.

## 2.1 Received material

In total, seven slices of billets (20 *mm* thick) were received from industrial partners, with variable microstructures in terms of alloy, morphology and grain size. The objective of this variety is to study the influence of the initial microstructure on microstructural evolutions. To optimize the amount of analyzed microstructures, five of them were chosen as part of this thesis (**Table 2.1**), while the two remaining are detailed in the Appendix **A**, as they may be useful for further works in the consortium. The names chosen for each billet refer to the alloy grade and morphology.

| Billet name | Expected microstructure | Supplier | Ø [*mm*] | Th [*mm*] | Final thermomechanical treatment realized by the supplier |
|---|---|---|---|---|---|
| Ti1023_El$\beta$ | $\alpha$: Equiaxed and fine grains<br>$\beta$: Highly elongated grains | *Timet* | 128 | 20 | Deformed at 750°*C* \| Slow cooling |
| Ti1023_Eq | $\alpha$: Equiaxed and fine grains<br>$\beta$: Elongated grains | *Timet* | 285 | 20 | Deformed at 750°*C* \| Slow cooling |
| Ti64_Eq | $\alpha$: Equiaxed and coarse grains<br>prior-$\beta$: Highly elongated grains | *Timet* | 300 | 20 | No data |
| Ti64_FL | $\alpha$: Fine lamellae<br>prior-$\beta$: Coarse equiaxed grains | *Aubert & Duval* | 255 | 20 | 1050°*C* \| 1 hour \| Air cooling |
| Ti64_CL | $\alpha$: Coarse lamellae<br>prior-$\beta$: Coarse equiaxed grains | *Aubert & Duval* | 255 | 20 | 1050°*C* \| 1 hour \| Slow cooling (1°*C*/*min* up to 700°*C*) |

*Table 2.1. Summary of the as-received (AR) billet slices, supplied by industrial partners.*

In addition to the five selected as-received billets slices, another microstructure of the Ti1023 was selected to allow the comparison of a lamellar morphology with the one of the Ti64 alloy. Samples from Ti1023_Eq billet (the one with more available material) were heated (at ~ $3°C/s$) above the $T_\beta$ at $830°C$ for 1 hour, to homogenize the microstructure completely, then slow cooled (at ~ $5°C/min$) down to 300°, then WQ to room temperature. The monitoring of the temperature was done using a thermocouple with its sensor placed in the center of the sample. This heat treatment was selected with the industrial partners, aiming to obtain a microstructure that contains equiaxed $\beta$ grains with fine $\alpha$ lamellae, referred to as Ti1023_L.

## 2.2 Sampling directions

To obtain the ideal properties of interest for the aeronautical field, titanium alloys are subjected to several thermomechanical treatments: a complex sequence of heat treatments and hot deformation, as shown in **Figure 1.26**. During the initial forging steps, the billets, originally parallelepipedal blocks, become cylindrical (**Figure 2.1**).

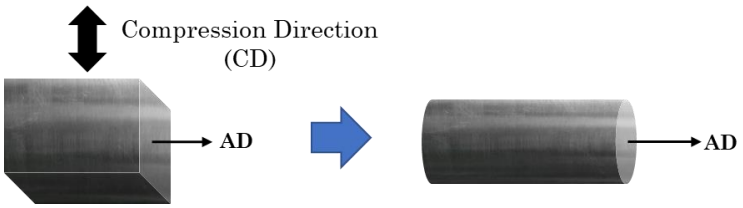



*Figure 2.1. Transformation of the shape of industrial billets by deformation.*

During this process, the $\beta$ grains elongate (cigar shaped [3]) along the axial direction of the billet (AD), perpendicular to the direction of the imposed strain (radial direction of the billet, RD or CD) [29,30]. Therefore, a sampling choice was made aiming to analyze this elongation of the $\beta$ or prior-$\beta$ grains, for the Ti1023 and Ti64 alloy, respectively. The aim is to reduce possible ambiguities that may appear by viewing the elongated $\beta$ grains in the transverse section, since they become globular on the micrographs (**Figure 2.2**).

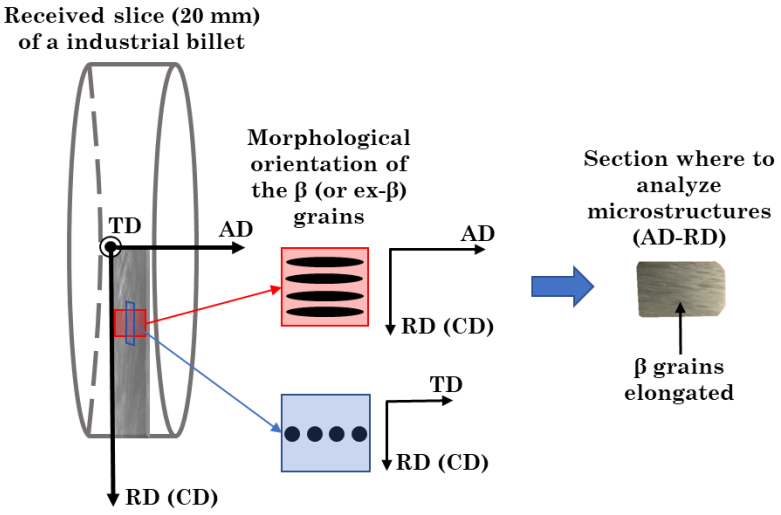



*Figure 2.2. Definition of the macroscopic reference, showing the chosen sampling direction from the industrial billets.*

Furthermore, the forging manufacturing process could lead to azimuthal and radial heterogeneities in the microstructure, especially in the region of the preliminary edges, 90° apart. Therefore, it is essential to determine whether the samples and specimens can be considered homogeneous (in the analysis scale), independently of the location of their sampling from the billet, which will be checked in section **3.1**.

## 2.3 Heat treatments

As the aim of this work is to study the hot deformation of titanium alloys, some heat treatments were performed to characterize the actual microstructures to be deformed (referred to as *initial microstructures/ states* in this work). The heat treatments were applied according to typical industrial forging temperatures (50°$C$ below the $T_\beta$, see **Figure 1.26**) and for one hour, followed by water quenching (WQ), thus with a cooling rate of about 75°$C/s$, value measured using a thermocouple inserted into a sample. A heat treatment at 750°$C$ was furtherly applied to the Ti64_Eq for comparison with the Ti1023 alloy at same temperature.

The as-received slices of billet, the applied heat treatments and the consequent initial states are shown in **Table 2.2**.

| As-received billet | Heat treatment | Initial state |
|---|---|---|
| Ti1023_El$\beta$ | 750° \| 1 hour \| WQ | Ti1023_El$\beta$ |
| Ti1023_Eq | 750°$C$ \| 1 hour \| WQ | Ti1023_Eq |
| Ti1023_Eq | 830°$C$ \| 1 hour \| Slow cooling at ~5°$C/min$, then 750°$C$ \| 1 hour \| WQ | Ti1023_L |
| Ti64_Eq | 750° \| 1 hour \| WQ | Ti64_750°$C$ |
| Ti64_Eq | 950° \| 1 hour\| WQ | Ti64_Eq |
| Ti64_FL | 950° \| 1 hour\| WQ | Ti64_FL |
| Ti64_CL | 950° \| 1 hour \| WQ | Ti64_CL |

*Table 2.2. Heat treatments applied to the as-received states for the characterization of the initial states.*

## 2.4 Sample preparation

Optical and scanning electron microscopy have been used for microstructure characterization. Observation and analysis of microstructures require careful surface preparation. Each of the samples analyzed in this work went through several preparation steps: mounting, pre-polishing (P320, P600 papers), mechanical polishing (9 $\mu m$ diamond) and mechanochemical polishing (90% colloidal $SiO_2$ solution with 10% $H_2O_2$).

Then, different final steps were applied depending on the microscopy technique to be used:

- For optical microscopy (OM), chemical etching was performed (Kroll solution: 2% HF, 3% $HNO_3$, 95% $H_2O$ for 25 seconds at 25°$C$);
- For scanning electron microscopy (SEM), the last step consisted of a vibratory polishing using 50% colloidal silica and 50% distilled water, for 2 hours under a load of 2 N. This finishing step provides a flat surface and

remove residual work hardening layer, enabling EBSD analysis to be performed.

## 2.5 Verification of possible azimuthal and radial heterogeneities

To analyze the possible azimuthal and radial microstructural heterogeneities in the slices of billet supplied by the industrial partners, the chosen method was optical microscopy (OM). For each slice of billet, several micrographs were taken, at different magnifications (as exemplified in **Figure 2.3**), to analyze the $\alpha$ and (ex-) $\beta$ grain sizes, as well as the $\alpha_P$ phase fraction (the $\alpha_S$ phase, composed of very fine lamellae, is not visible on OM micrographs) between the different sampling zones.

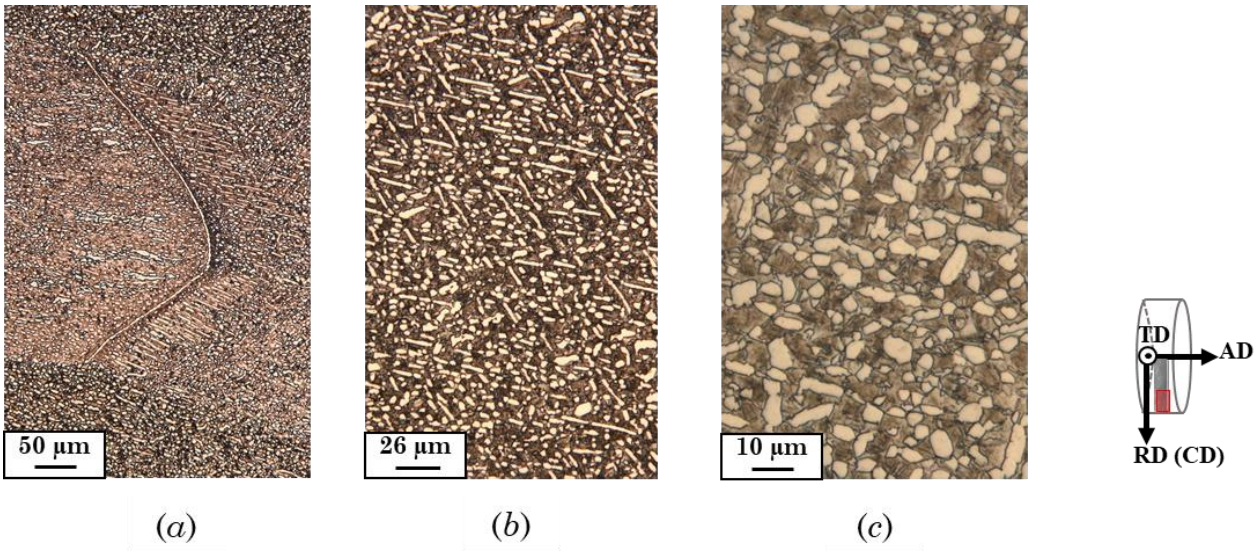



*Figure 2.3. Example of optical micrographs of the as-received Ti1023_Eq taken at different magnifications.*

To be able to measure the $\beta$ grains, given that their length were of the order of millimeters, a micrograph obtained by binocular magnifier (satisfactory scale) was taken per sample (Figure 2.4).

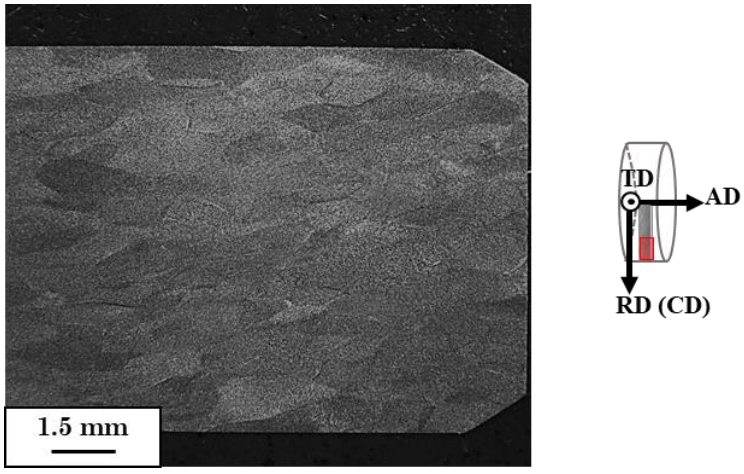



*Figure 2.4. Example of an optical binocular micrograph of the as-received Ti1023_Eq, where different β grains can be observed.*

Then, depending on the quantity and size of $\alpha_P$ grains in the micrographs, the ideal magnification was chosen (to have statistical representativeness) for the analysis of the micrographs with *ImageJ* [47]. This image analysis software allows the quantification of different microstructural characteristics (*e.g.,* phase fractions, particles/ grains sizes of the order of micrometers), as described in the following sections.

### *2.5.1 Primary α phase quantification*

Using the *ImageJ* software to quantify the phases or components in each micrograph, a method of noise reduction (Gaussian filtering) [48], grey level thresholding (*i.e.,* selecting the minimum and maximum grey levels for the $\alpha_P$ phase) has been implemented (after several manual tests for each of the microstructures), as exemplified for the Ti1023_El$\beta$ billet in **Figure 2.5**.

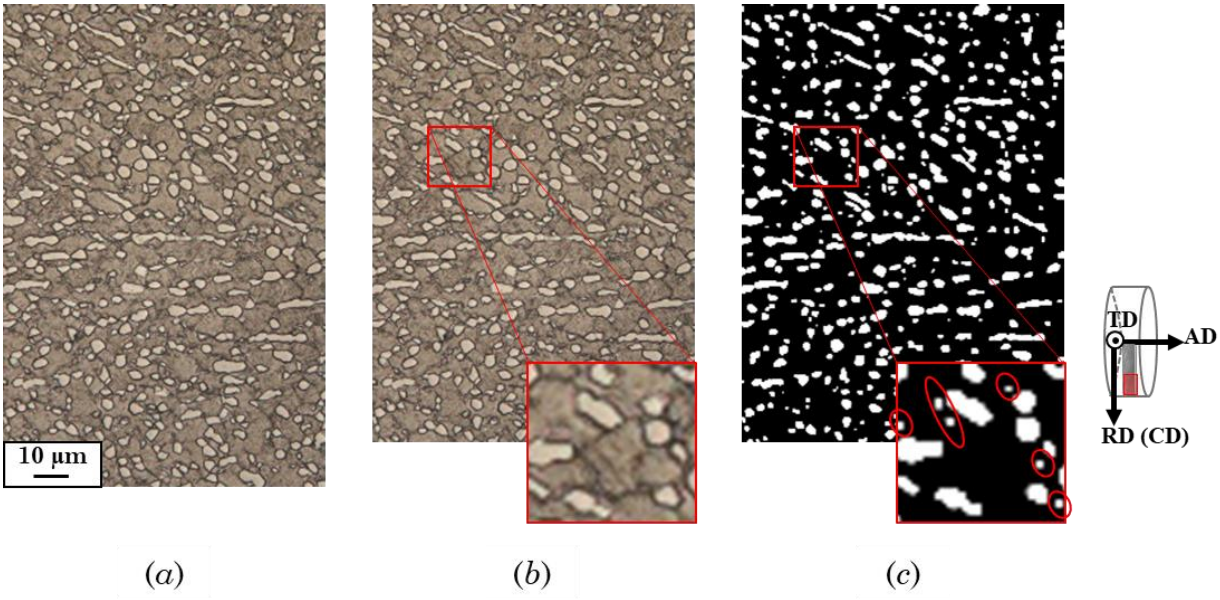



*Figure 2.5. Example (as-received Ti1023_Elβ billet) of primary α phase fraction quantification from optical micrographs; a) original micrograph; b) cropped micrograph (to remove scale bar); c) binarized micrograph; along with the macroscopic sample reference.*

The small white areas which do not correspond to real grains (as exemplified by the red ellipses in **Figure 2.5***c*) are removed based on a size criterion. Then, primary $\alpha$ phase fraction ($f_{\alpha_P}$) can be calculated by the fraction of the remaining white area divided by the total area of the micrograph. For each sample, ten micrographs were taken (in different zones), where an average of 400 $\alpha_P$ grains can be analyzed, to ensure statistical representativeness in the calculations.

Concerning the $\alpha$ grain size calculation, two different methods were implemented depending on the type of microstructure to be analyzed:

- **For microstructures with equiaxed $\alpha$:**

When the α grains are equiaxed (globular), they approach the shape of circles. Therefore, the average grain size ($\overline{GS}$), can be calculated as the average of the diameters of the circles with the same area as the considered grains [46], as shown in equation **(2.1)**. When analyzing the particles (*i.e.,* grains) with *ImageJ*, those on

the edges of the micrographs were ignored, as their shapes and dimensions are not completely defined.

$$\overline{GS} = \frac{\sum_{i=1}^{g} 2\sqrt{\frac{A_i^{\alpha_P}}{\pi}}}{g} \tag{2.1}$$

where $A_i^{\alpha_P}$ is the grain area and $g$ is the number of grains.

- **For microstructures with lamellar $\alpha$:**

In the case of lamellar microstructures, the mean linear intercept method [49] has been implemented to measure the average lamellar width. This method consists in drawing a line (perpendicular to the length of the lath colony) of length ($L$) on the micrograph, then counting the total number of grains ($N_T$) which are intercepted, entirely or partially, by this line.

**Figure 2.6** displays an example of an application of this method for the lamellar $\alpha$ phase. The entirely intercepted lamellae are marked in red, the grains whose line ends inside them are marked in green, and the grains whose boundaries are tangential to them, are marked in blue.

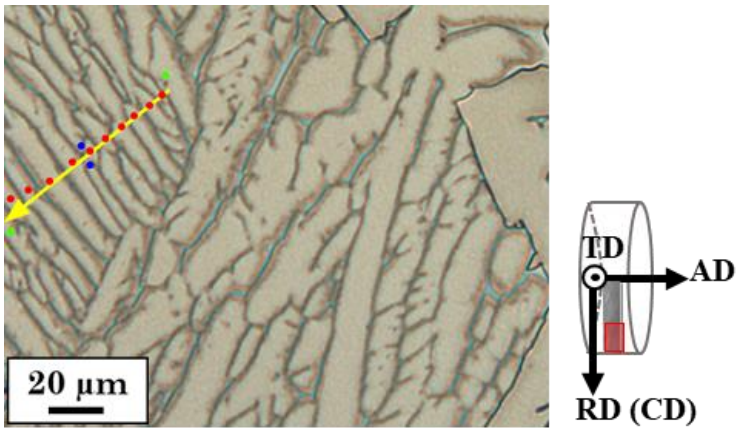



*Figure 2.6. Example of the method of the mean linear intercept for α lamellae (Ti64_CL) by optical micrograph.*

Dividing the length of this line by the number of grains gives the average grain size ($\overline{GS}$), as shown in equations **(2.2)** and **(2.3)**.

$$\overline{GS} = \frac{L}{N_T} \tag{2.2}$$

$$N_T = \sum_{i=1}^{g} N_i \tag{2.3}$$

The number of grains intercepted is calculated as follows. If the line:

- passes through the grain (entirely intercepted) → $N_i = 1$
- ends in the grain (partially intercepted) → $N_i = 0.5$
- is tangential to a grain boundary (partially intercepted) → $N_i = 0.5$

For each micrograph, one straight line was made in the finer lamellae colony observed, as shown in Figure 2.6. In fact, as explained in section **1.1.6.1**, the width of the $\alpha$ lamellae is controlled by the cooling rate, thus it is most probably equivalent throughout the different lamellae colonies. As those have a 3D platelet

shape [25], the finer lamellar colony observed in the microstructure is the closest to the true thickness of the microstructure, as those laths were cut transversally to their width. Coarser lamellae that were cut at a certain angle, give a false impression of a coarser lamellae morphology.

Lines for width measurement were placed perpendicularly to the morphological orientation of the lamellae (the choice of this direction is therefore user-dependent). This analysis determines the difference between fine or coarse $\alpha$ lamellae, since this morphological characteristic is important for the mechanisms of microstructural evolution [26]. Ten micrographs per sample (taken at different locations) were analyzed in order to calculate mean values and associated standard deviations.

- **For $\beta$ grains:**

In the case of elongated $\beta$ grains (**Figure 2.7***a*), with length of the order of millimeters, the same method was used, but with four lines per image of the sample (obtained by binocular magnifier). For the equiaxed $\beta$ grains (**Figure 2.7***b*), the straight lines were drawn along four distinct directions (two diagonal, one vertical and one horizontal).

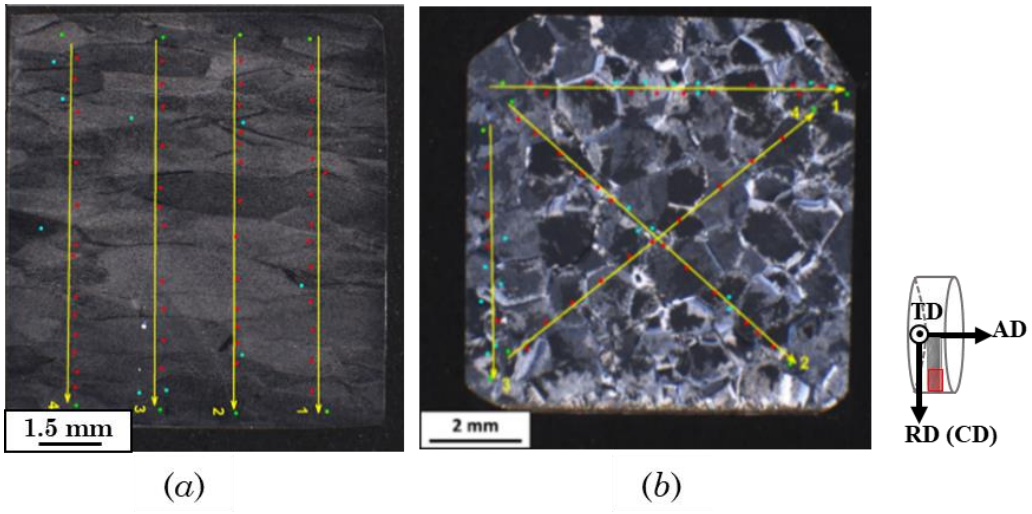



*Figure 2.7. Examples of the mean linear intercept method: a) For elongated (deformed) β grains; b) For equiaxed β grains; both by optical macrograph.*

## 2.6 Scanning electron microscopy (SEM)

In this work, the scanning electron microscope (SEM) is an instrument that has been widely used for the analysis of microstructures. The microstructural analyses were conducted on a ZEISS Supra40 microscope equipped with a field emission gun (FEG-SEM), and with EBSD system.

### *2.6.1 BSE imaging*

Backscattered electron (BSE) imaging was mainly used for microstructure observation and primary $\alpha$ phase fraction calculation of the microstructures (darker phase in **Figure 2.8***a*, lower average atomic number, as shown in section **1.1.3**). SEM settings consisted of an accelerating voltage of 20 $kV$, working distance between 10 and 12 $mm$ and aperture size of 60 $\mu m$. For all cases, five BSE

micrographs were taken at magnifications of 500 to 2500x (approximately 500 to 100 grains per image) and the area fraction of primary *α* phase was determined in the *ImageJ* software (**Figure 2.8**), using similar procedure described in section **2.5.1**.

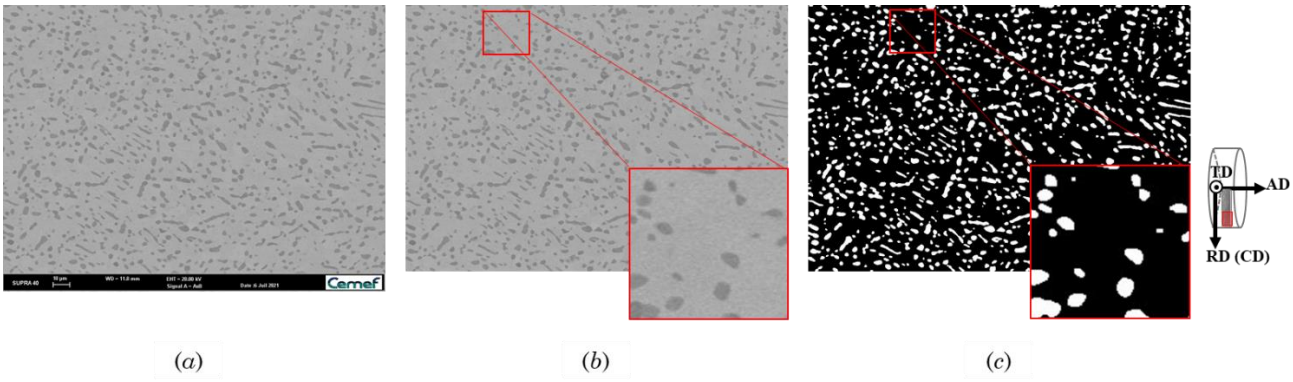



*Figure 2.8. Example (Ti1023_Eq billet) of the primary α phase fraction quantification from BSE images; a) original BSE micrograph; b) cropped micrograph (to remove scale bar); c) binarized micrograph.*

## *2.6.2 EBSD map analysis*

The electron backscattered diffraction (EBSD) technique was implemented to assess further information about the microstructure, by mapping crystallographic orientations. This is done by analyzing Kikuchi diffraction patterns collected on a detector for each point (pixel) of a regular discrete grid (square in this work) on the surface of the sample. The classical analysis and pattern indexing is performed by using the Hough transform [50], to detect the Kikuchi band positions, thus identify the local orientations of the crystals (**Figure 2.9**).

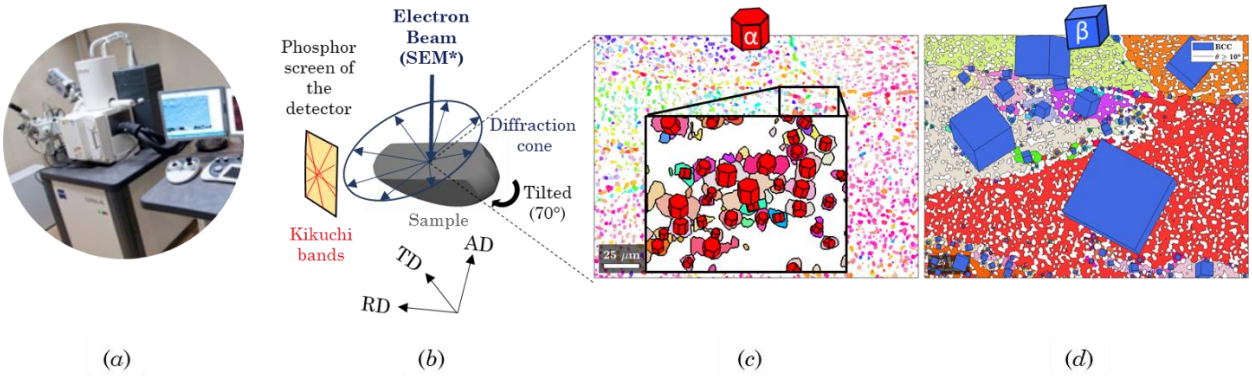



*Figure 2.9. Schematic of the EBSD analysis, showing the: a) ZEISS Supra40 microscope; b) Sample inside the microscope chamber along with the phosphor screen of the EBSD detector, which collects the Kikuchi diagrams, providing information on local orientations; b) α phase crystal orientation map; c) β phase crystal orientation map, both with their schematic crystal structures above.*

The EBSD data analysis and conventions are fully detailed in the following section (**2.7**).

## 2.7 EBSD data analysis and conventions

EBSD maps were acquired using a *Bruker Crystalign* system and a EBSD detector. The following SEM and EBSD detector settings were systematically applied for EBSD data acquisition: 70° sample tilt; 20 $kV$ acceleration voltage; working distance between 13 and 15 $mm$; 120 $\mu m$ aperture size.

The magnification and step size were adapted for the different microstructures (**Table 2.1**), finding a compromise between obtaining a statistically representative analysis zone and capturing the intragranular substructures in both $\alpha$ and $\beta$ phases. As mentioned in the general introduction section, the focus of this thesis is on the dislocation density, thus fine substructure development, in both phases. Consequently, the EBSD analysis needs high spatial resolution to capture those mechanisms. As the $\beta$ grains are of the order of millimeters long (**Figure 2.7**), this phase was mainly analyzed inside one or two different $\beta$ grains, focusing on the description of substructure evolutions.

The step sizes and analysis fields used for each initial microstructure are summarized in **Table 2.3**. Those microstructures represent the initial states (before deformation), *i.e.*, after the heat treatments applied to the as-received materials (see **Table 2.2**). These step sizes were maintained for the other metallurgical states obtained from each of the initial microstructures, for studying the effect of temperature, strain level and rate (Chapter **4**).

| Microstructure | Analysis field [$\mu m$ x $\mu m$] | Step size [$\mu m$] |
|---|---|---|
| Ti1023_El$\beta$ | 225 x 170 | 0.20 |
| Ti1023_Eq | 225 x 170 | 0.20 |
| Ti1023_L | 112.5 x 85 | 0.10 |
| Ti64_750$°C$ | 450 x 340 | 0.40 |
| Ti64_Eq | 1125 x 850 | 0.80 |
| Ti64_FL | 450 x 340 | 0.36 |
| Ti64_CL | 750 x 567 | 0.90 |

*Table 2.3. Summary of the step sizes and EBSD map dimensions used for each initial microstructure.*

The acquired EBSD data, have then been analyzed with the *MTEX* library [51], an open-source access *MATLAB* toolbox specifically developed for the post-processing of EBSD data. Several post-processing tools have been adapted or developed for the different microstructural characterizations presented in this work (*e.g.,* primary and secondary $\alpha$ phase separation, reduction of measurement noise, calculation of phase fraction, grain size and subgrain boundary density). Other tools, such as pole figures, orientation maps, intergranular and intragranular misorientations were also used.

The interest of this code development in the post-processing step is the ability to finely adapt the analysis for each specific microstructure, as it can vary depending on the alloy, morphology, heat treatment, deformation applied and other particularities. Furthermore, the post-processing methods will be used and improved throughout the different theses in the consortium.

Post-processing of EBSD data was performed in compliance with certain conventions, both for the definition of the microstructure elements and for the modes of representation. For the entire manuscript, unless stated otherwise, all EBSD maps are represented according to the following conventions (**Figure 2.10**):

- **Phase color coding**: $\alpha$ phase is shown in red, while $\beta$ in blue.
- **Grain boundaries**: High angle grain boundaries (HAGB) are defined when the misorientation angle between two neighboring points exceeds 10° ($\theta \geq 10°$). They are shown as yellow lines. While low angle grain boundaries (shown as black lines) are defined when the misorientation angle exceeds 1°, but remains below 10°.
- **Macroscopic reference**: All maps will be represented according to the macroscopic reference defined in **Figure 2.2**. The vertical direction corresponds to the compression direction (CD = RD of the billets) and the horizontal direction is the axial direction of the billets, also the $\beta$ grain elongation (when $\beta$ grains are elongated).
- **Orientation maps**: Orientation maps will be shown within a color coding defined in the standard triangle, so-called Inverse Pole Figure (IPF) coloring. The chosen standards were made according to the microstructural features observed in both phases and will be explained in the following chapters along with the results (section **4.1.2**). In this manner, for the $\alpha$ phase, the TD axis (transverse direction) was systematically projected into the standard triangle (reduced crystal reference due to the symmetries associated with the unit cell). For the $\beta$ phase, the CD axis was projected.

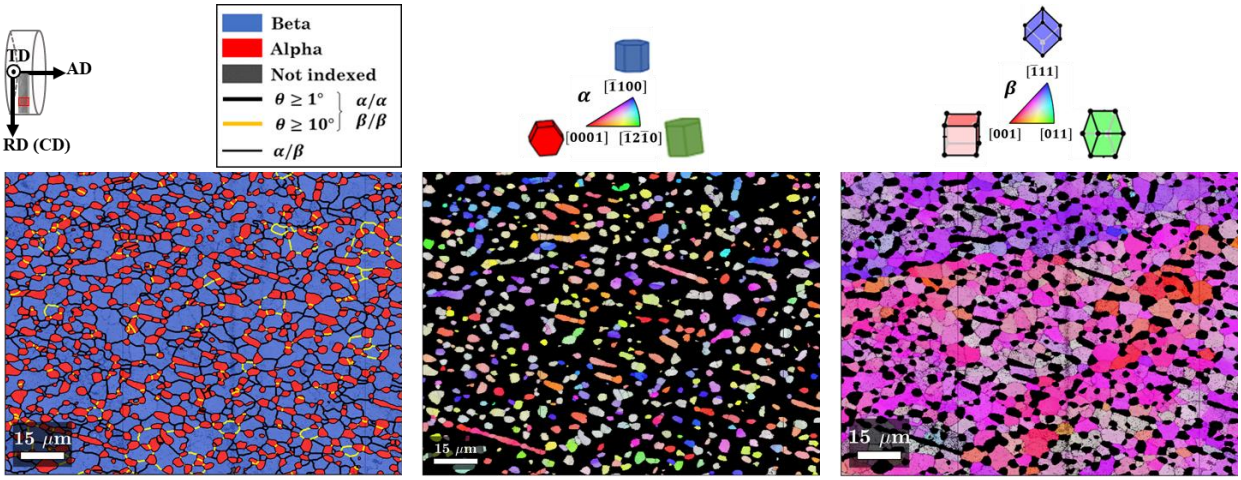



*Figure 2.10. EBSD maps example (Ti1023 alloy, WQ from 750°C) showing the conventions used for the representation of EBSD data: a) Phase map with LAGB (black lines) and HAGB (yellow lines) and the macroscopic reference above; b) Orientation map (TD-IPF color coding) of the α phase; c) Orientation map of the β phase (CD-IPF color coding); both orientation maps with their respective standard triangle above.*

From EBSD data, is it also possible to analyze local crystallographic texture, through pole figures and inverse pole figures (IPF), describing the preferential orientation of the crystallites within a polycrystalline sample.

- **Pole figures**: Those consist of poles of a family of crystallographic planes, represented in the form of stereographic projection in a plane of the macroscopic coordinate system (sample axes). In this work, this was the main representation mode for the $\alpha$ phase, along with the orientation maps. The family of planes chosen to be analyzed were (0001) and $\{11\bar{2}0\}$, since they were sufficient to describe the evolutions of texture. Plots are interpreted as a function of multiples of the random distribution (mrd) with respect to the distribution expected in a material with uniformly distributed orientations, *i.e.*, with no crystallographic texture.

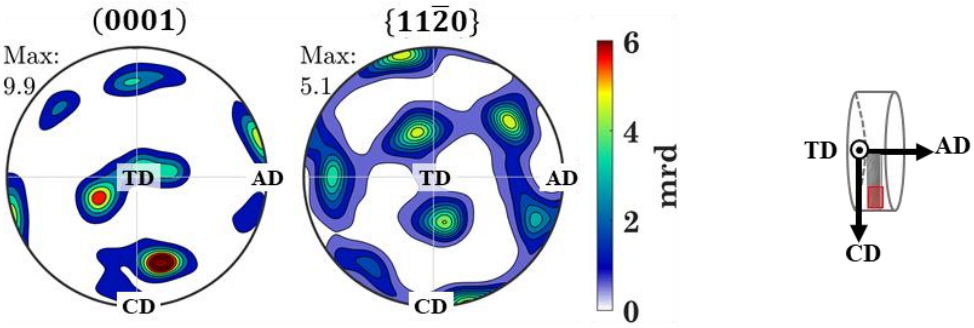



*Figure 2.11. Example of a pole figure representation for the α phase of a Ti1023 alloy WQ from 750°C. The (0001) and* $\{11\bar{2}0\}$ *pole densities are shown.*

- **Inverse pole figures (IPF)**: similar to pole figures, but the main difference is that orientations are plotted relative to crystal axes (and not the sample axes as in the case of a pole figure). This was the main representation mode for the $\beta$ phase orientations (along with the orientation maps). The aim is to analyze its texture evolution according to the CD, *i.e.,* the compression direction is projected into the standard triangle to show which crystal direction is parallel to it, as performed in [52].

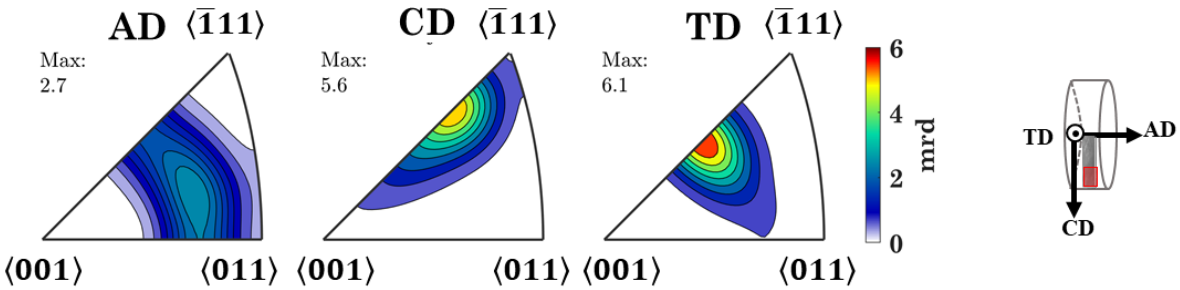



*Figure 2.12. Example of an inverse pole figure representation of the β phase of a Ti1023 sample (WQ from 750°C).*

### *2.7.1 Parent β grain reconstruction*

For the metastable-$\beta$ alloy (Ti1023), there is the direct possibility of analyzing the $\beta$ phase, as it is retained in the microstructure after quenching. However, for the $\alpha$+$\beta$ alloy (Ti64), the analysis of the $\beta$ phase is not straightforward, as the $\beta$ phase mostly transforms into secondary $\alpha$ ($\alpha_S$) upon cooling. To access the $\beta$ phase that was present at high temperatures of the Ti64, it was reconstructed using a routine available in *MTEX* from the $\alpha_S$ orientations, using the procedure proposed by [53,54]. This procedure assumes that the $\alpha_S$ crystallographic domains have a strict Burgers orientation relationship (BOR) with their parent $\beta$ grain (5° misfit

tolerance) [54]. Nevertheless, as the microstructures were water quenched from temperatures below $T_\beta$, they possess both primary and secondary $\alpha$ grains, being considered as a partially transformed microstructure. Thus, prior to the reconstruction of the $\beta$ phase, the $\alpha_S$ grains were first identified and separated based on several parameters, *e.g.*, size, shape factor and band contrast (related to the intensity and sharpness of the indexed Kikuchi bands). This automatic separation method can lead to some inaccuracy, as some primary $\alpha$ ($\alpha_P$) grains may present very similar parameters as the $\alpha_S$. Fortunately, the relative error of this separation (*i.e.,* incorrect $\alpha_P$ grains addressed to the $\alpha_S$ phase) was less than 0.5%. Furthermore, on the next step of the reconstruction, these incorrectly separated grains are not recognized as having a strict BOR, being discarded by the algorithm, and thus preventing miscalculation of the reconstructed $\beta$ phase orientation. An example of the reconstruction of the $\beta$ phase from partially transformed Ti64 alloys is summarized in **Figure 2.13**.

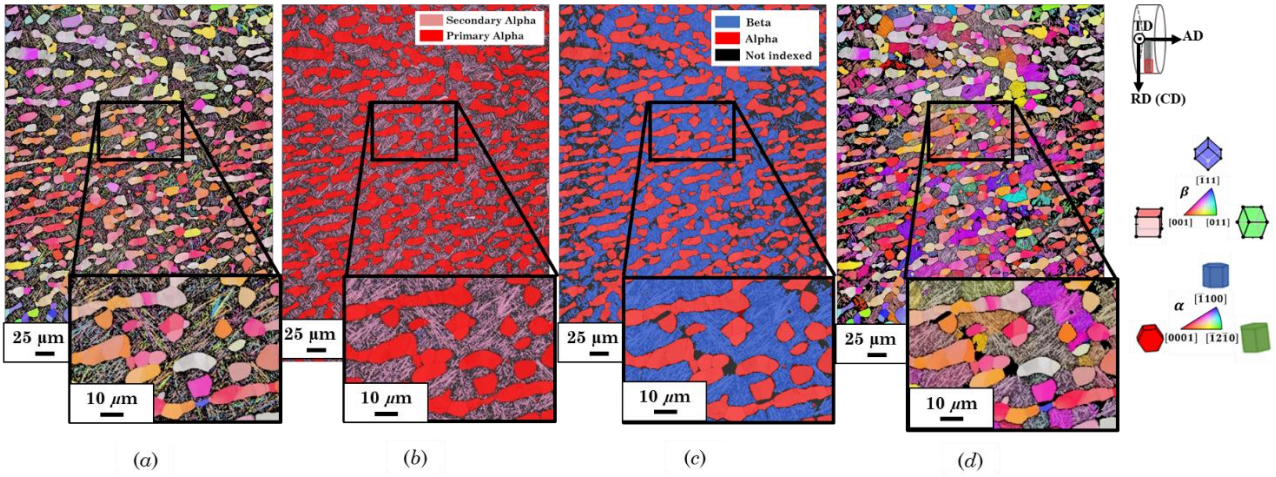



*Figure 2.13. Example of a parent β grain reconstruction from a partially transformed microstructure of Ti64 WQ from 950°C, showing: a) Original EBSD ($\alpha_P + \alpha_S$), TD-IPF color coding (α phase); b) Automatic separation of $\alpha_P$ and $\alpha_s$ grains; c) Parent β grains reconstruction; d) Reconstructed EBSD (α+β), TD-IPF color coding for both phases; all maps show the Band Contrast overlaid.*

Unfortunately, this reconstruction method could only be applied to the non-deformed states of the Ti64 alloys, as the deformed samples presented high residual stress in the microstructure, hence very poor measurement of the fine $\alpha_S$ laths (around 100 *nm* thick). Furthermore, the Burgers orientation relationship might be less respected in the deformed cases.

### *2.7.2 Quantification of α/β boundaries respecting BOR*

As mentioned in section **1.1.4**, the $\beta \rightarrow \alpha$ phase transformation follows the Burgers orientation relationship (BOR). Consequently, for a lamellar microstructure (arising from phase transformation) which was not deformed, all $\alpha/\beta$ grain boundaries follow this BOR. Throughout the deformation process, there is a loss of this relation, as both phase orientations are changed due to plastic activity and dislocation storage. A quantification of the amount of $\alpha/\beta$ grain boundaries (*i.e.,* $\alpha$ and $\beta$ crystal orientations on either side of the phase boundary) that follows the BOR was implemented following equation **(2.4)**.

$$f_{GB_{\alpha/\beta}}^{BOR} = \frac{GBL_{\alpha/\beta}^{BOR}\ [\mu m]}{GBL_{\alpha/\beta}^{Total}\ [\mu m]}\ x\ 100 \tag{2.4}$$

The principle is to calculate the $\alpha/\beta$ grain boundary length ($GBL$) that respect this BOR ($GBL_{\alpha/\beta}^{BOR}$), with a threshold of 5° of misorientation angle (θ) from the theorical relation, then divide by the total $\alpha/\beta$ grain boundary length ($GBL_{\alpha/\beta}^{Total}$). Thus, the fraction of those boundaries that corresponds to the BOR is obtained ($f_{GB_{\alpha/\beta}}^{BOR}$). An example of this BOR grain boundaries identification is show in **Figure 2.14**.

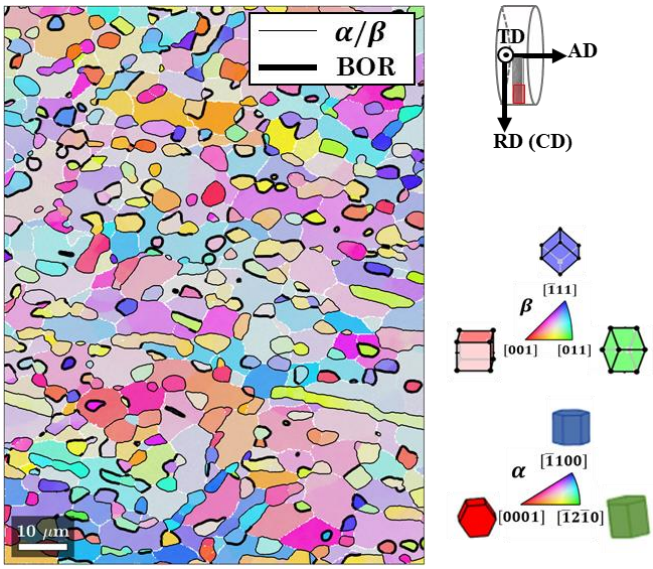



*Figure 2.14. EBSD maps of the Ti1023 alloy WQ from 750°C showing the orientation map (CD-IPF color coding) showing all α/β grain boundaries (thin black line) and the BOR α/β grain boundaries (thick black line).*

It is important to mention that the calculated value ($f_{GB_{\alpha/\beta}}^{BOR}$) is dependent of the chosen threshold. This value of 5° was chosen to admit a minor misorientation from the BOR, while remaining low. The same threshold was used for all microstructures and thermomechanical conditions for the sake of their comparison.

### *2.7.3 LAGB and HAGB density*

The description of the formation of new subgrains and grains is central to the understanding of many microstructural evolutions. Through **Figure 2.10***a*, it is possible to obtain a qualitative analysis of this phenomena. To obtain a quantification of the LAGBs and HAGBs in the microstructure (restricted to $\alpha/\alpha$ and $\beta/\beta$ boundaries) and to compare different material states, the following procedure was developed. The aim is to implement a cumulative analysis of grain boundary length ($GBL$) in a given grain area ($A_g$), depending on the misorientation angle (θ) of those boundaries (*i.e.,* the density of LAGBs and HAGBs), as shown in equation **(2.5)**.

$$\rho_{GB}(\geq \theta)[\mu m^{-1}] = \frac{GBL\ (\geq \theta)\ [\mu m]}{A_g\ [\mu m^2]} \tag{2.5}$$

This analysis not only gives information about the total LAGB and HAGB density ($\rho_{GB}$) in the microstructure, but also captures the dynamics of LAGBs turning into HAGBs, as shown in **Figure 2.15**.

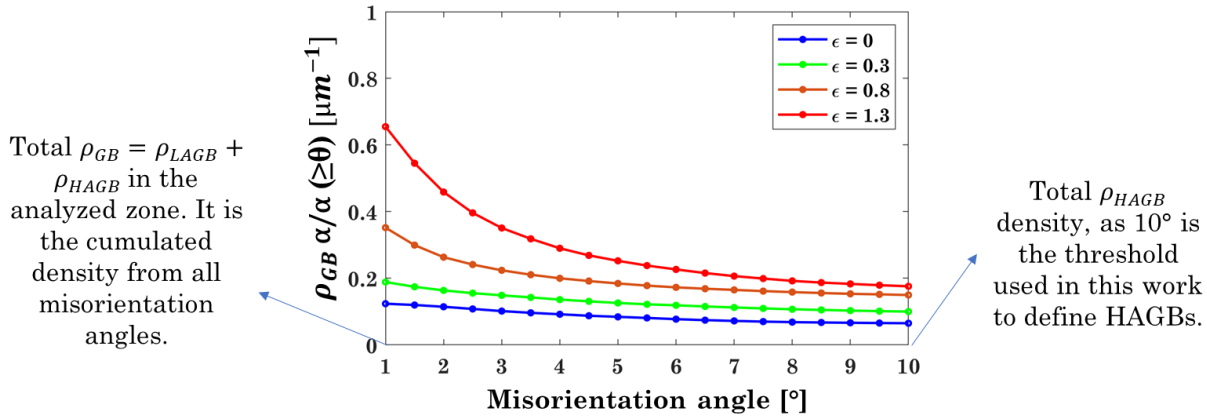



*Figure 2.15. Example for the α phase in Ti1023_Elβ WQ from 750°C, at different deformed states, of α/α grain boundary density ($\rho_{GB}$) analysis of all GBs with a misorientation angle ≥ θ.*

As the minimum misorientation angle used for the LAGB calculation is 1°, the leftmost value corresponds to the total $\rho_{GB}$ including all LAGBs and HAGBs, as it is a cumulative analysis. On the other hand, the rightmost values give the HAGB density, as 10° is the threshold used for defining a grain boundary. Furthermore, the shape of those curves and their evolution indicates how LAGBs transform into HAGBs during deformation. For example, the steeper and steeper slope as strain is increased up to 1.3 (**Figure 2.15**) shows that, in the *α* phase of the Ti1023_El*β*, the grains are being highly substructured during deformation (increase of the $\rho_{GB}$), while the $\rho_{HAGB}$ is only slightly increased.

### *2.7.4 LAGB density as a function of grain orientation*

In order to analyze the dependency of LAGB density ($\rho_{LAGB}$) on grain orientation, IPF maps were plotted (color coding by TD) showing the distribution of LAGB (substructures) inside different *α* grains. **Figure 2.16** shows an example of this analysis for the equiaxed Ti1023 deformed at 750 *°C*/ 0.1 *$s^{-1}$*/ 1.3 strain level.

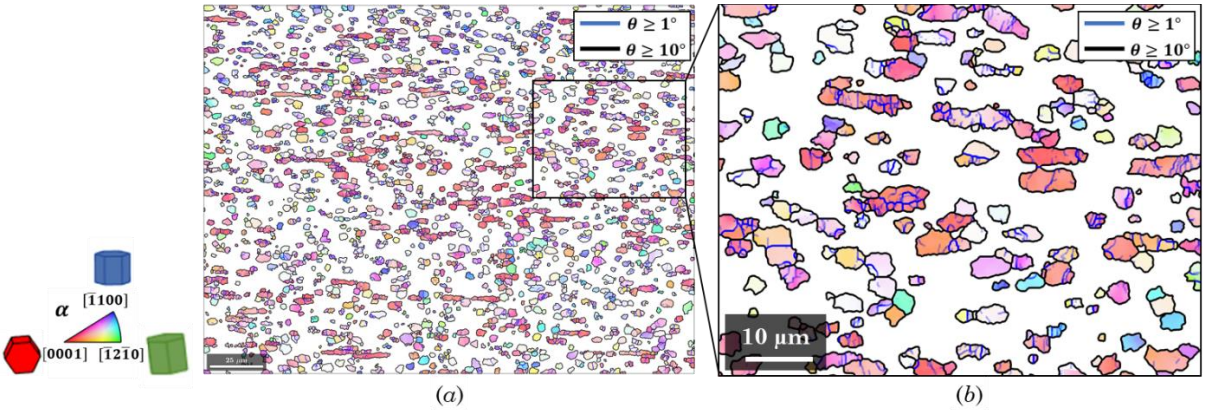



*Figure 2.16. a) TD-IPF map showing the distribution of LAGB (blue boundaries) for different grain orientations for a Ti1023 sample deformed at 750°C/ 0.1 $s^{-1}$/ 1.3 strain level; b) Zoomed area.*

To investigate the development of LAGBs, a similar analysis described in [41] was performed. The $\alpha$ grains were divided in three main populations according to the normal of the planes (0001), $\{\bar{1}100\}$ and $\{\bar{1}2\bar{1}0\}$ parallel ($\parallel$) to the TD, thus perpendicular ($\perp$) to the CD. A threshold of 15° was established to account for deviation from these specific orientations, yet small enough to avoid a grain belonging to two populations. Differently from the analysis in [41], as not all grains can be inserted in those three populations, a control was established with the other grains that have not been selected. The aim is to check if the non-inserted grains have an important substructure density that was not being perceived.

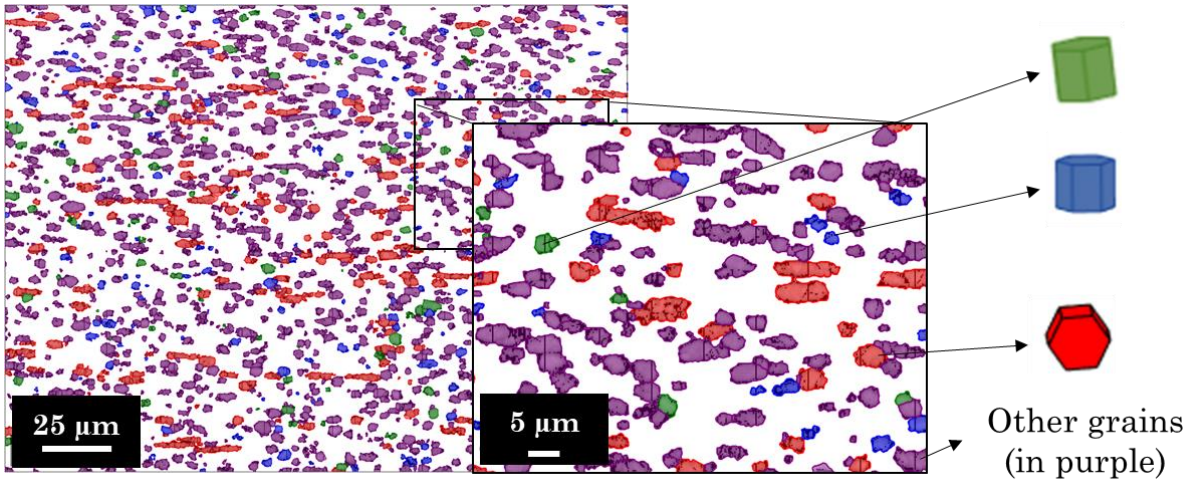



*Figure 2.17. Division of the α grains from* ***Figure 2.16*** *into four different populations according to their mean orientation: normal of the planes* (0001), $\{\bar{1}100\}$ *and* $\{\bar{1}2\bar{1}0\} \perp$ *to the CD, and the other grains.*

After assigning all the grains present in the analyzed zone to one of the four selected categories (**Figure 2.17**) the $\rho_{LAGB}$ was calculated per grain, as shown in equation **(2.6)**.

$$\rho_{LAGB}\ [\mu m^{-1}] = \frac{LAGB\ length\ [\mu m]}{A_g\ [\mu m^2]} \tag{2.6}$$

Finally, the average $\rho_{LAGB}$ value of each category was calculated to determine how $\alpha$ crystallographic orientation affects the formation of substructures inside its grains.

### *2.7.5 Dislocation density estimation from EBSD maps*

The accumulation of dislocations in a crystal produces crystal lattice rotations, which are referred to as an intragranular misorientation. A misorientation is defined as the rotation, from one orientation to another, which allows both crystal reference frames to be aligned. A given physical misorientation can be described by different equivalent crystal rotations, due to the crystal symmetry. By convention, the one which provides the smallest misorientation angle is considered. Intragranular misorientations can be used to estimate the *geometrically necessary dislocations* (GND) density.

The GND are defined here as the dislocations which are necessary to accommodate a given crystal misorientation, that is measurable by EBSD. The

minimum number of dislocations necessary to result in a given misorientation allow for an estimate of the GND density. At the microscopic level, internal energy minimization causes the GND to arrange themselves into energetically favorable configurations, thereby (possibly) dividing a grain into subgrains, or can continue to be entangled with each other and give rise to orientation gradients [55].

The deformed crystal may also include a number of dislocations which compensate each other in terms of lattice distortions, called *statistically-stored dislocations* (SSD), and lead to no cumulated misorientation measurable by EBSD (**Figure 2.18***c*).

The different scales at stake in the assessment of GND density from EBSD maps are schematized in **Figure 2.18**, showing:

a) **Microscopic scale:** shows the microstructure of the material, where both phase in the two phases of the polycrystal can be observed with a color coding according to crystallographic orientation;
b) **Mesoscopic scale:** a grain has been selected to exhibit the intragranular misorientation, interpreted as a substructure, and an orientation gradient;
c) **Atomic scale:** shows rotation of the crystal lattice induced by the presence of several dislocations (GND). The SSD are also shown, which cause no such rotation. The approach correlates those generated misorientations with the quantity of dislocations that were necessary to produce it (GND). The red and green circles represent the compression and tension fields generated by the presence of each dislocation.

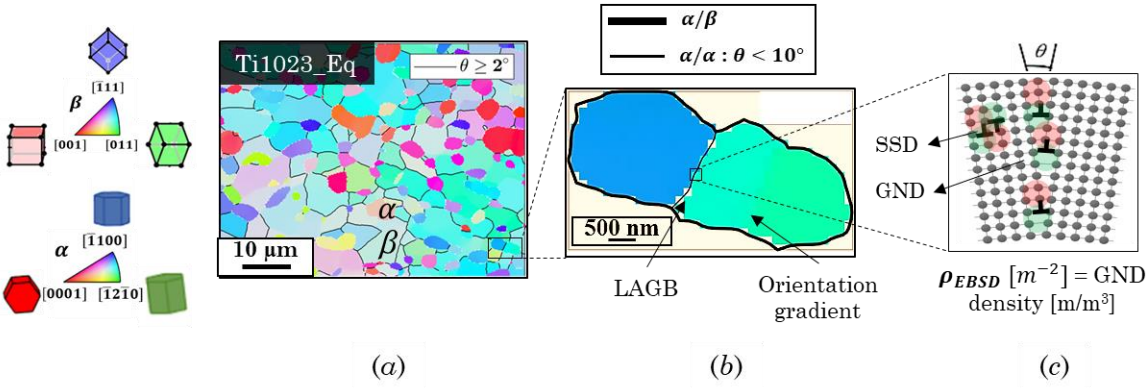



*Figure 2.18. Simplified schematic of the dislocation density estimation from EBSD maps approach, showing different scales.*

### *2.7.5.1 From orientations to GND densities*

Two approaches can be used to estimate the GND density from EBSD data (referred to as $\rho_{EBSD}$): by analyzing the misorientation angle between two points at a given distance, or the GND tensor.

The KAM is defined as the average misorientation angle of a given acquisition point on an EBSD map with its neighbors (at a given kernel radius, defined by the user), being used to estimate the local misorientation level. Several models exist to obtain a $\rho_{EBSD}$ value from a misorientation angle, the simplest being derived from the classical model of Read & Shockley [56] that correlates the misorientation angle of a low-angle tilt grain boundary (made of edge dislocations) to the dislocation amount necessary to cause this rotation (**Figure 2.18***c*). According to this model, the $\rho_{EBSD}$ between two pixels is given by equation **(2.7)**:

$$\rho_{EBSD} = \frac{a\theta}{bx} \tag{2.7}$$

where $\theta$ is the misorientation angle, $b$ the norm of the Burgers vector and $x$ the distance over which the misorientation is measured (step size, if the 1st neighbors are considered). The value of the constant $a$ depends on the type of boundary, thus dislocation structure, that would be needed to create the rotation [57]: $a$ = 1 (for tilt subgrain boundaries made of edge dislocations) or 2 (for twist subgrain boundaries made of screw dislocations). This geometrical approach is very simple to implement, though it considers only the misorientation angle, omitting the misorientation axis, thus lacking part of the information of the misorientation.

The second approach (GND tensor) is based on the continuum dislocation theory. Despite the discrete nature of crystal lattices, continuum defect theories have been proposed [58,59] and summarized by [60], being considered in this work. The two important quantities in this theory are the elastic curvature tensor ($\underline{\boldsymbol{\kappa}}_{el}$), hereafter abbreviated as elastic curvature, and the GND rank-2 tensor ($\underline{\boldsymbol{\alpha}}$), hereafter referred to as GND tensor. The elastic curvature is a rank-2 tensor that describes the heterogeneity of orientations. The rank 1 is associated with the misorientation vector representing the change in orientation between two pixels, while the rank 2 relates to the sample direction along the considered orientation variations. Nevertheless, 2D EBSD data do not assess the orientation changes along the normal direction to the sample surface, so the orientations along this direction are considered as uniform. From the misorientation angles between two measurement pixels, separated spatially by $\Delta\vec{x}$, the elastic curvature can be expressed as the equation **(2.8)** [61]:

$$\underline{\boldsymbol{\kappa}}_{el} \approx \frac{\theta_i}{\Delta x_j} \tag{2.8}$$

where the subscripts $(i,j)$ are taken in $i \in \{1,2,3\}$ and $j \in \{1,2\}$. This method of calculating the elastic curvature from orientation data gathered on a square grid aligned with the sample coordinate system is sketched in **Figure 2.19**.

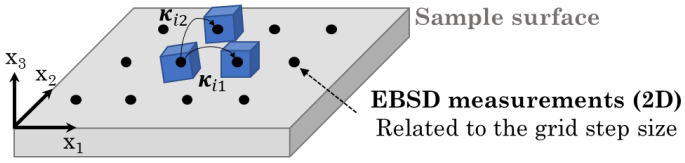



*Figure 2.19. Sketch of the sample coordinate system used for the 2D EBSD data acquisition. The local orientations are determined at each of the black points (pixels) arranged in a square grid on the surface of the specimen.*

As local lattice orientations are determined only in the plane of analysis (*i.e.*, along $x_1$ ad $x_2$), but not perpendicular to it (along $x_3$), the components $\boldsymbol{\kappa}_{i3}$ cannot be obtained. Hence, only six curvature components can be obtained from the EBSD data, as shown (in blue) in equation **(2.9)**.

$$\underline{\boldsymbol{\kappa}}_{el} = \begin{bmatrix} \kappa_{11} & \kappa_{12} & \kappa_{13} \\ \kappa_{21} & \kappa_{22} & \kappa_{23} \\ \kappa_{31} & \kappa_{32} & \kappa_{33} \end{bmatrix} \tag{2.9}$$

From the six accessible curvature components, five of the dislocation densities ($\underline{\underline{\boldsymbol{\alpha}}}$) can be recovered from the measured curvatures ($\alpha_{12}, \alpha_{13}, \alpha_{21}, \alpha_{23}, \alpha_{33}$) in the current sample reference frame [61]:

$$\alpha_{12} = \kappa_{21};\ \alpha_{13} = \kappa_{31}; \alpha_{21} = \kappa_{12};\ \alpha_{23} = \kappa_{32};\ \alpha_{33} = -\kappa_{21} - \kappa_{22} \tag{2.10}$$

A number of authors [61–63] have employed Nye's dislocation tensor formulation ($\underline{\underline{\boldsymbol{\alpha}}}$) when resolving $\rho_{EBSD}$ from the lattice curvature tensor. Details of this calculation are given in [5]. The elastic stress field can be neglected, as Hough analysis of diffraction patterns cannot recover local elastic strain induced by dislocations and no long-range elastic strain (loading boundary conditions) is applied. The total dislocation density tensor relates all possible dislocation modes, as defined in equation **(2.11)**.

$$\underline{\underline{\boldsymbol{\alpha}}} = \sum_{m=1}^{M} \rho_{EBSDm}\, \boldsymbol{b}_m \otimes \boldsymbol{l}_m \tag{2.11}$$

where $\rho_{EBSDm}$, $\boldsymbol{b}_m$ and $\boldsymbol{l}_m$ are respectively defined as the dislocation density, the Burgers vector and the unitary line vector of the $m^{\text{th}}$ physically and crystallographically possible dislocation mode. $M$ is the total number of possible dislocation modes. $M$ is larger than the number of slip systems because the definition of modes in this approach accounts for the edge or screw character of the dislocations.

The number of possible dislocation modes for the HCP is 39 (30 edge-type + 9 screw-type [64]), while for the BCC is 52 (48 edge-type + 4 screw-type [12]), as presented in **Figure 2.20** and **Figure 2.21**, respectively.

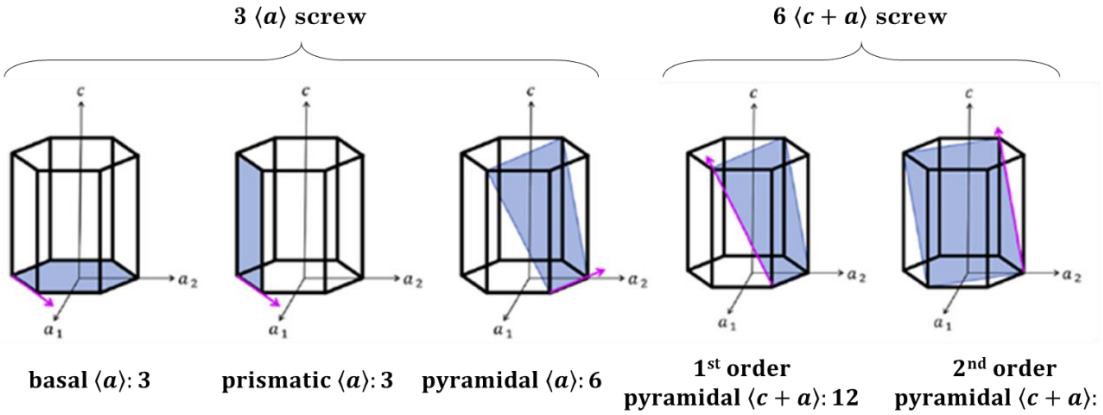



*Figure 2.20. Slip systems and dislocation modes in a HCP crystal [13].*

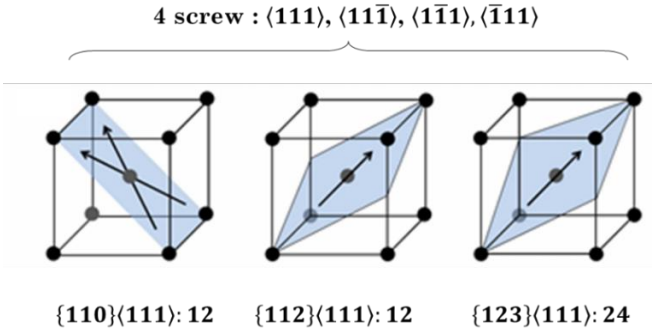



*Figure 2.21. Slip systems and dislocation modes in a BCC crystal [12].*

For the cases of the HCP and BCC crystal structures, several sets of dislocations densities satisfy equation **(2.11)** [61], in other words, a given rotation of the crystal lattice could be caused by different combinations of dislocations modes. Among all sets of dislocation densities satisfying equation **(2.11)**, the one that minimizes the internal energy due to dislocations is considered [61]. The internal energy per unit length ($e_L$) of the $m^{\text{th}}$ dislocation mode of screw dislocations can be calculated by equation **(2.12)** [23], while the ratio between the energies of edge and screw dislocations is given by equation **(2.13)** [55]:

$$e_{Lm}^{screw} \cong G_\varphi b_m^2 \tag{2.12}$$

$$e_{Lm}^{edge} \cong e_{Lm}^{screw}(1-\nu)^{-1} \tag{2.13}$$

where $G_\varphi$ is the shear modulus (of the phase $\varphi$), $b_m$ is the norm of Burgers vector (dependent on the dislocation mode) and $\nu$ is the Poisson coefficient.

The complete definition of the GND density $\rho_{EBSD}$ is then equation **(2.11)** such that

$$(\rho_{EBSDm})_{m=1\ldots M} \text{ minimizes } \sum_{m=1}^{M} |\rho_{EBSDm}| e_{Lm}^{edge/screw} \tag{2.14}$$

The shear modulus is a highly important parameter which appears in the energy of dislocation estimation. It is difficult to describe the evolution of such a quantity as a function of temperature since the macroscopic alloy shear modulus depends on the composition but also on $\alpha$ and $\beta$ phase fractions. Frost and Ashby [65] proposed an equation **(2.15)** for titanium alloys:

$$G_\varphi = G_{0_\varphi}\left[1 + \left(\frac{T-300}{T_M}\right)\left(\frac{T_M}{G_{0_\varphi}}\frac{\partial G_\varphi}{\partial T}\right)\right] \tag{2.15}$$

where, for titanium:

- $\alpha$ phase: $G_{0_\alpha} = 43.6\ GPa$ and $\frac{T_M}{G_{0_\alpha}}\frac{\partial G_\alpha}{\partial T}$ = -1.2;
- $\beta$ phase: $G_{0_\beta} = 20.5\ GPa$ and $\frac{T_M}{G_{0_\beta}}\frac{\partial G_\beta}{\partial T}$ = -0.5.

In the two-phase domain, by making the Voigt hypothesis (homogeneous deformation), we obtain equation **(2.16)**:

$$G = f_\alpha G_{0_\alpha} + (1-f_\alpha)G_{0_\beta} + \left(\frac{T-300}{T_M}\right)\left[f_\alpha G_{0_\alpha}\left(\frac{T_M}{G_{0_\alpha}}\frac{\partial G_\alpha}{\partial T}\right) + (1-f_\alpha)G_{0_\beta}\left(\frac{T_M}{G_{0_\beta}}\frac{\partial G_\beta}{\partial T}\right)\right] \tag{2.16}$$

where $f_\alpha$, considered at thermodynamic equilibrium, is given in **Figure 1.5** [16].

The dislocation density is calculated through *MTEX* [66] by means of the *MATLAB* function *linprog* designed to solve the linear programming problem while additionally satisfying the imposed constraints. The constraint imposed being equation **(2.11)** which minimizes equation **(2.14)**. It is important to mention that this method finds the first minimized solution satisfying equation **(2.14)**, where a number of equivalent solutions might exist.

To summarize, EBSD data provides orientation over a spatial grid that allows the calculation of local misorientations ($\theta$), leading to the partial computation of elastic curvature ($\underline{\underline{\boldsymbol{\kappa}}}_{el}$), giving access to almost all the components of the GND tensor ($\underline{\underline{\boldsymbol{\alpha}}}$) and finally to the $\rho_{EBSD}$.

### *2.7.5.2 EBSD data filtering*

Post-processing (filtering) of the raw EBSD orientation data is performed using the half-quadratic filter [67] available in the *MTEX* library, that preserves the substructures while reducing the orientation measurement noise (induced by experimental inaccuracy sources, *e.g.,* in the Kikuchi band positions detection) [68]. The purpose of this filtering step is to avoid the overestimation of the GND density, as it is shown in **Figure 2.22**. Other methods were also developed in the literature [5], which leads to similar results.

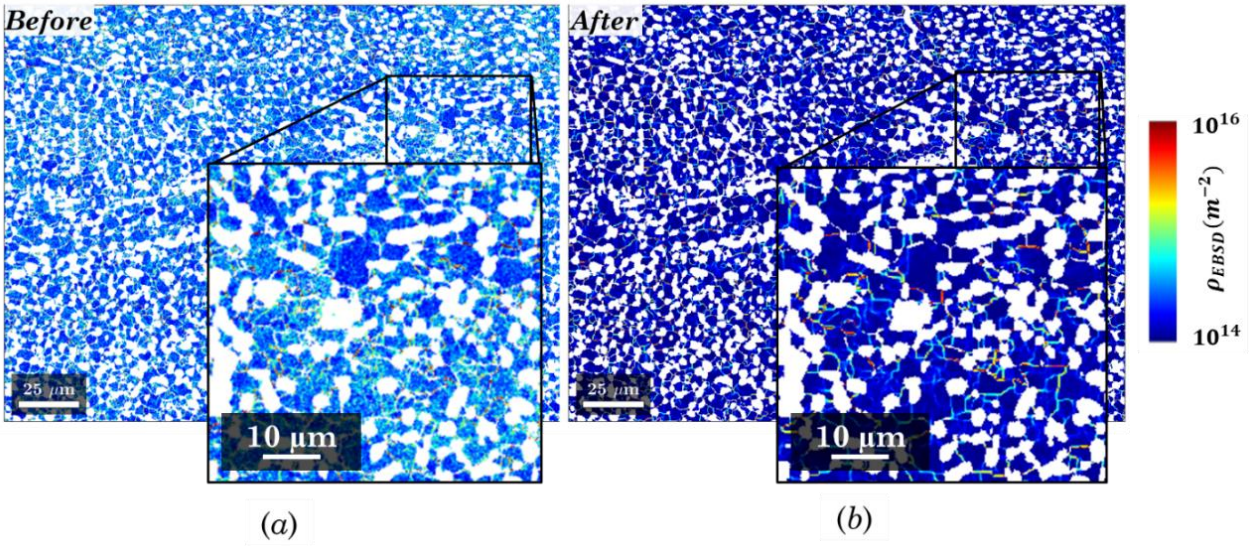



*Figure 2.22. Dislocation density maps of the β phase of a Ti1023 sample, WQ from 750°C: a) Raw data; b) After filtering with a half quadratic filter of the EBSD orientation data.*

The same misorientation angle threshold of 10° defined for high-angle grain boundary (HAGB) is used for the filtering and in the calculation of the dislocation density inside the grains (to exclude the grain boundaries, which have much higher misorientation angles).

After the filtering process, the GND tensor method [58,59], explained in section **2.7.5.1**, is applied separately for the $\alpha$ and $\beta$ phases, with respect to the crystal structures implicated in the calculation. The arithmetic mean of all measurements across the microstructure is then calculated for each phase ($\varphi = \alpha, \beta$), providing the average dislocation density per unit area for each phase ($\rho_{EBSD}^{\varphi}$), as estimated by the EBSD method.

It is worth mentioning that this post-processing tool was adapted for the filtering of the $\beta$ grains in the Ti1023, to maintain some not-indexed zones (where not sufficient EBSD data was acquired), avoiding miscalculations. Furthermore, different strain levels required adapted parameters, as there were microstructural changes from the initial states, as also larger not-indexed zones.

#### *2.7.5.3 Stored energy*

Among all physical parameters controlling microstructure evolutions, the amount of strain energy stored in the material in the form of crystalline defects is of utmost importance as it provides the thermodynamic driving force for recovery, recrystallization and more generally intervenes interface migration. For each phase $\varphi$, the stored energy ($E_{D_\varphi}$ $[J \cdot m^{-3}]$) is calculated by equation **(2.11)** [22].

$$E_{D_\varphi} = C\rho_\varphi G_\varphi b_\varphi^2 \tag{2.17}$$

where $C$ is a constant usually equal to 0.5 [22] (related to a supposed average quantity of edge and screw dislocations), $\rho_\varphi$ is the dislocation density, $G_\varphi$ the shear modulus and $b_\varphi$ the dislocation Burgers vector of each phase (φ).

Nevertheless, it was shown in **Figure 2.20** and **Figure 2.21** that multiple dislocation modes can be responsible for slip in the crystal. This is especially true for the HCP structure, where the $b$ depends on the different dislocation modes activated ($\langle a \rangle$-type or $\langle c + a \rangle$-type). It was also shown in equations **(2.12)** and **(2.13)** that the stored energy is dependent of the type of dislocation (edge or screw). Therefore, the $C$ constant value and the proportion of edge and screw dislocation could be deduced from an analysis of the dislocation modes.

In this manner, to correctly estimate the stored energy in the microstructure, it sounds relevant to analyze how the dislocation density is distributed amongst the different dislocation modes for both phases. Consequently, a in-depth study was performed to assess the influence of the EBSD dataset, through experimental and synthetic data, in the evaluation of the dislocation density in both phases (Appendix **B**). This study concluded that the analysis of the most active dislocation modes is orientation-dependent. Thus, 3D EBSD data would be necessary to avoid the detrimental assumption that orientations along the normal plane of the 2D EBSD data are considered as uniform (**Figure 2.19**).

Consequently, the stored energy was not estimated in this work, as assuming the constant $C$ is equal to 0.5 is a very strong assumption. Furthermore, the assessment of how the dislocation density is distributed in the different dislocation modes seems to lead to possible misinterpretations according to the analysis detailed in Appendix **B**.

## 2.8 3D characterization of the Ti64 lamellar microstructures

Given the great importance of phase morphology, 3D studies are also needed to better understand the nature of the titanium alloy microstructures, which are inherently three-dimensional. To address the topological ambiguities raised by the 2D observations, in order to provide the most realistic input data possible for the full field simulations (Chapter **6**), selected samples were subjected to 3D characterizations.

Only the lamellar microstructures of the Ti64 alloy (Ti64_FL and Ti64_CL) were submitted to 3D characterization (as there are less 2D *vs* 3D ambiguities for the equiaxed microstructures). Indeed, the comprehension of the 3D morphology

of those lamellae, and their behavior throughout deformation, is not well-known in the literature, as stated in the overview work of Lee Semiatin [25].

To perform 3D characterization in the lamellar Ti64 alloys, a TESCAN FERA 3 Plasma Focused Ion Beam–Scanning Electron Microscope (PFIB-FEG-SEM) was used. Volumes were acquired using a FIB serial sectioning approach. This tomography technique consists in alternatively removing a thin layer of material from a region of interest (ROI) with the ion beam, and acquiring an image of the new surface with the electron beam. These slicing and imaging steps are sequentially repeated until the predetermined volume to be analyzed is achieved (*i.e.*, has been totally sputtered by the ion beam). The plasma FIB technology offers the possibility of covering typical volume dimensions up to 100 $\mu m$, which is a great advantage to former gallium ($Ga^+$) FIB technology.

**Figure 2.23** represents the serial sectioning procedure in the PFIB-SEM microscope. Firstly, the sample is tilted at 55° from the horizontal so that its top surface is perpendicular to the FIB column axis and the cross section can be scanned with the electron beam. A deposition of a protective layer is then usually performed on the top surface of the ROI (**Figure 2.23***a*), aiming to reduce the well-known curtaining effect [69]. This milling artifact can make the analysis of the microstructure difficult or even impossible. Therefore, it needs to be minimized by optimizing the PFIB milling conditions. Also, the curtaining effect introduces some problems in 3D reconstruction [70]. The curtaining effect arises mostly from the spatial variation of the sputtering rate of the sample and increase with increasing ion beam current. Concerning the physical characteristics of the sample, several factors can favor the curtaining, such as the topology of the top surface (*e.g.,* scratches), the presence of different phases or orientations, as well as porosity [69]. Two methods have been employed for reducing the curtaining effect in this work: Platinum (Pt) deposition and Silicon (Si) mask deposition.

Secondly, the stair milling step consists in revealing the cross-section to be analyzed (**Figure 2.23***b*), being performed at a very high FIB current (around 1-2 $\mu A$). The main objective is to rapidly remove a huge amount of material from the surroundings of the ROI, to enable the electron beam scanning in the subsequent imaging step. As the milling step is performed at a very high current, the cross-section can be highly affected by the curtaining effect. Hence, several steps of polishing are performed (**Figure 2.23***c*), progressively reducing the ion beam current (typically from 300 to 100 $nA$), until obtaining the desired cross-section quality in terms of curtaining effect. Finally, the serial sectioning starts (**Figure 2.23***d*), being composed of two steps: milling, to remove a slice of material with the ion beam, followed by imaging with the electron beam.

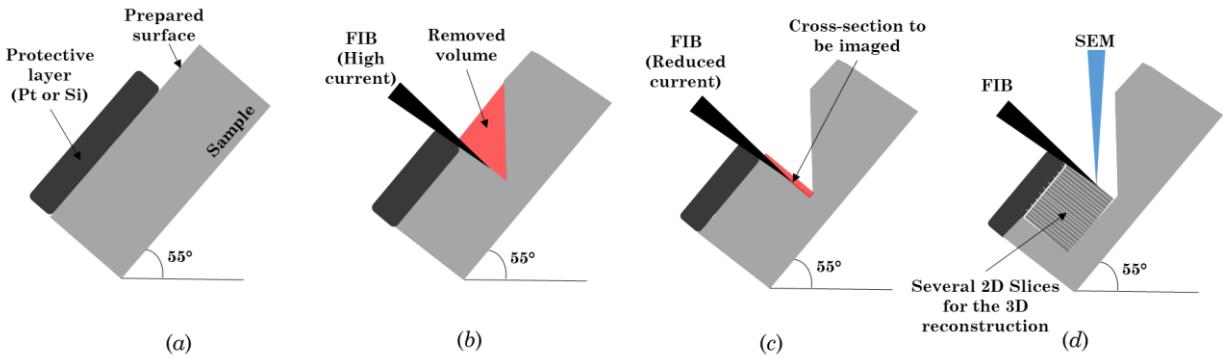



*Figure 2.23. Schematic diagram of PFIB-SEM tomography process: a) Protection layer deposition in the tilted sample; b) Cross-section opening; c) Cross-section polishing; d) FIB slicing and SEM imaging.*

**Figure 2.24** shows the real sample after the cross-section polishing step, with the different components involved in this 3D analysis.

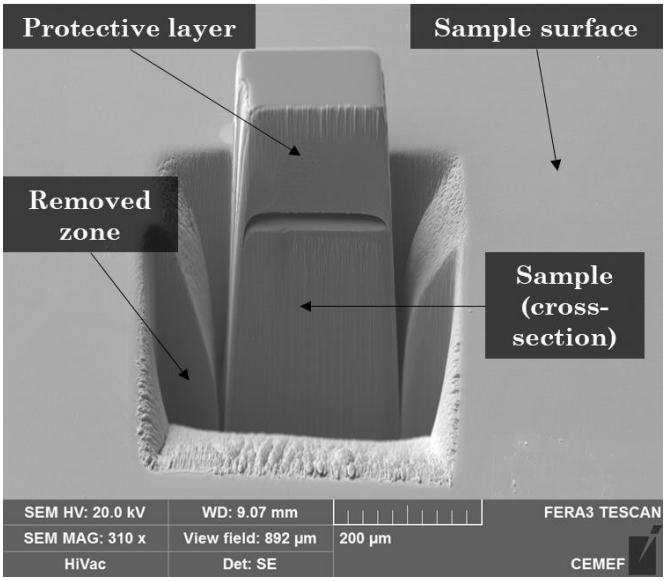



*Figure 2.24. SEM image of the real sample after the polishing step, showing the different components involved, to exemplify the schema in **Figure 2.23**.*

The sputtering rate for the Ti64 alloy (0.41 $\mu m^3 n A^{-1} s^{-1}$) was evaluated by measuring the volume of material removed, after scanning a well-defined area with the FIB at a certain current and for a certain time.

As mentioned previously, two different curtaining effect reduction methods were considered for the selected microstructures: Pt deposition and Si mask deposition. Pt deposition involves precursor release near the sample surface followed by adsorption of chemical precursors onto the sample surface. Then, the deposition of energy by the focused ion beam. In this way, the Pt layer is deposited on the top surface, as shown in **Figure 2.25***a*. The deposition of the Si mask involves placing a monocrystalline Si mask on the top surface of the sample. The steps to perform this deposition include extracting the Si mask from the platform, by attaching it to a nanomanipulator, then placing it in the ROI (**Figure 2.25***b*). Once the mask is placed, a milling step is performed to stich it to the sample by redeposition. The nanomanipulator is then cut from the mask.

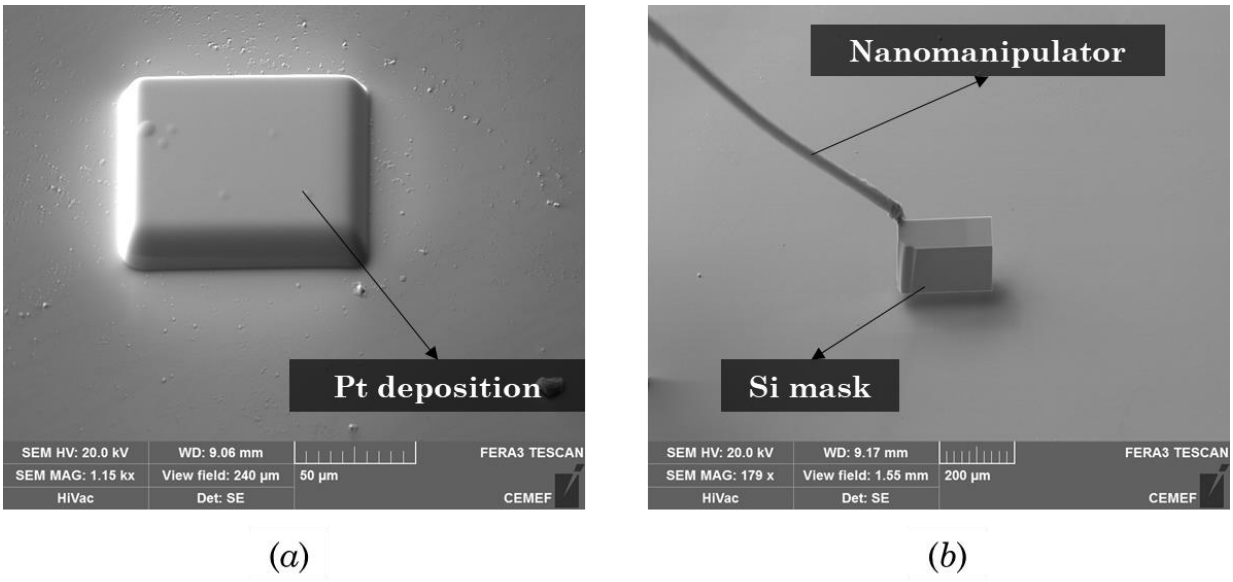



*Figure 2.25. SEM images of the: a) Pt deposition; b) Silicon mask deposition.*

**Figure 2.26** shows the polishing steps for both alloys, where the Pt deposition can be observed for the Ti64_FL (**Figure 2.26***a*) and the Si mask for the Ti64_CL (**Figure 2.26***b*). Both microstructures can be observed within these images, where minor curtaining effect is seen near the mask, while on the bottom, the curtaining effect can be clearly observed as black stripes. This indicates the efficiency of the respective depositions.

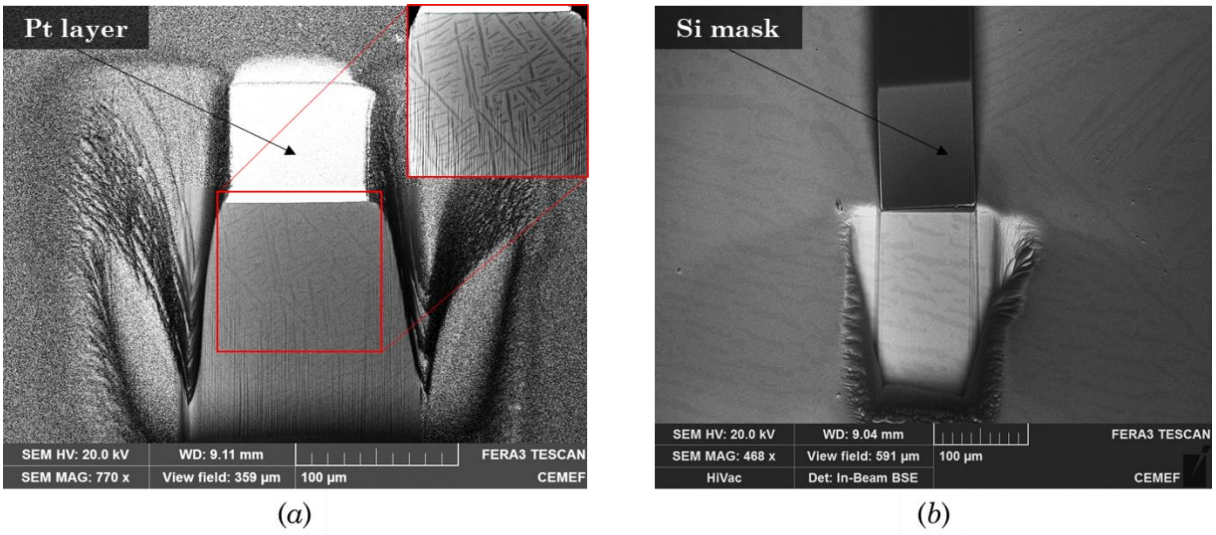



*Figure 2.26. SEM images of the cross-section after the polishing at 100 nA and 30 kV for the: a) Ti64_FL; b) Ti64_CL microstructures, with their respective Pt protective layer and Si mask.*

The FIB parameters used are summarized in **Table 2.4**.

| Microstructure | Deposition | Accelerating Voltage [$kV$] | Current [$\mu A$] | Layer step size [$\mu m$] |
|---|---|---|---|---|
| Ti64_FL | Pt | 30 | 0.1 | 0.20 |
| Ti64_CL | Si mask | 30 | 1 | 0.25 |

*Table 2.4. PFIB parameters used for the serial sectioning of the Ti64 alloys.*

The higher current for the Ti64_CL was implemented to obtain a faster milling rate, which was not implemented for the Ti64_FL, because of its finer laths. Also, at 1 $\mu A$ with the Pt deposition, the curtaining effect is more severe. As the volume is smaller (Ti64_FL), there is the possibility to perform the analysis at 100 $nA$, not penalizing in terms of time, compared to a large volume at 1 $\mu A$. The smaller step size for the latter was also implemented due to its morphology. After acquiring the raw BSE images (**Figure 2.27***a*), several steps were applied in *ImageJ* to improve the 3D reconstruction (**Figure 2.27***b* to *e*).

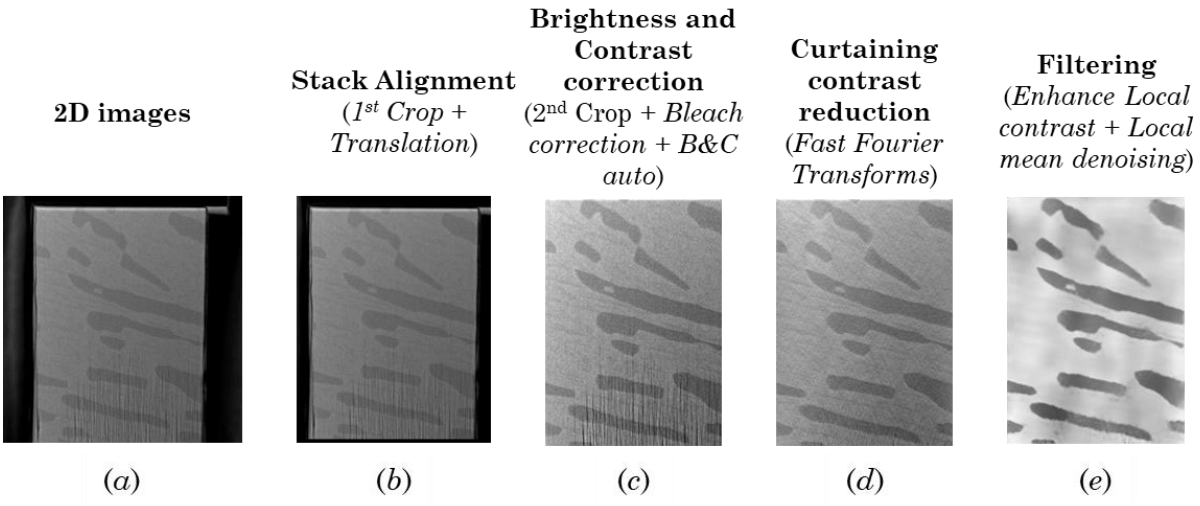



*Figure 2.27. The different BSE image treatment steps applied (in bold) in the ImageJ software (used functions in italic) for Ti64 alloys, aiming to an improved 3D reconstruction.*

## 2.9 Thermomechanical tests

The thermomechanical tests for the study of the microstructural evolution and its correlation with the thermomechanical parameters were performed in a MTS Landmark® machine, with a maximum capacity of 250 $kN$. Compression is performed by controlling the displacement of the upper tool as a function of time, while the bottom tool remains static. Compression tools ($\emptyset$ = 80 $mm$), designed and manufactured in the laboratory, were mounted in this compression machine. To achieve isothermal compression, the tools are surrounded by an LGTEC tube furnace with electronics also designed in the laboratory. Nevertheless, instrumenting a compression sample with a thermocouple is very difficult to achieve because of the montage and the applied deformation. It is therefore the compression tools that have each been instrumented with a thermocouple. Boron nitride was used as lubricant.

### *2.9.1 Samples geometries*

For the hot compression tests, two sample geometries (double-cone and cylindrical) were used depending on the purpose of the analysis. The advantage of the double-cone sample is that it allows the analysis of different strain levels from a single sample, reducing drastically the experimental campaigns. The geometry of the double-cone samples has been optimized within the framework of this thesis, thanks to finite element simulations [4]. The new geometry provides a better stable

equivalent strain rate ($\dot{\bar{\varepsilon}}$) during the compression test. This improvement is particularly true at the center of the sample, where the $\dot{\bar{\varepsilon}}$ variation for the other tested geometries [71–76] rose to a 50% range regarding the average value, compared to a 10% variation for the optimized geometry at the same conditions. Further explanation of this geometry optimization is detailed in Appendix **C**. Double-cone samples will be used in Chapter **4**, where a wide variety of initial microstructures and thermomechanical conditions are analyzed.

On the other hand, the advantage of a cylindrical sample is the possible identification of a constitutive law through the stress-strain curves obtained from the compression test. Thus, cylindrical samples will be used implemented in Chapter **5** for the macroscopic analysis. The dimensions of both compression samples are shown in **Figure 2.28**.

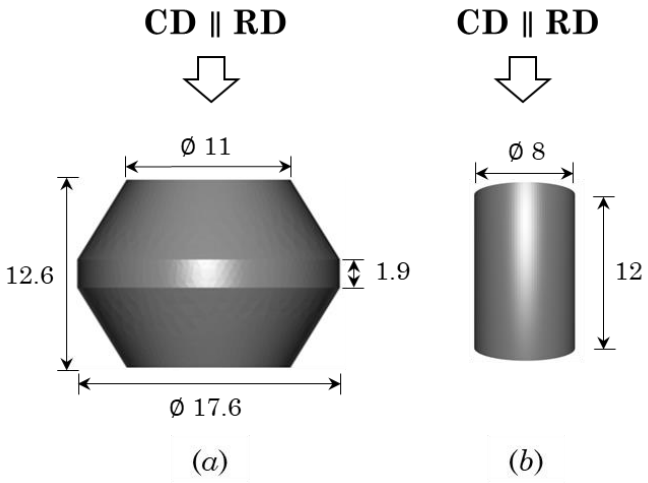



*Figure 2.28. Dimensions of the compression samples (in millimeters): a) Double-cone; b) Cylindrical; the CD is parallel to the RD, as shown in Figure 2.2.*

### *2.9.2 Sampling*

The sampling direction chosen for the as-received and initial states (**Figure 2.2**) was maintained for the compression tests to respect the industrial billets forging direction, thus with compression along RD, *i.e.,* CD ∥ RD (**Figure 2.28**).

Nevertheless, due to their axisymmetry according to the CD axis, the AD x RD reference is not evident to be retrieved after machining the compression samples. For the billets that were heat treated above the $T_\beta$ (*i.e.*, Ti1023_L, Ti64_FL, Ti64_CL), the $\beta$ grains are recrystallized, thus equiaxed (with lamellar $\alpha$ phase). After compression, those prior equiaxed $\beta$ grains obtain a pancake shape (**Figure 2.29***a*).

Consequently, the width and length of the compressed $\beta$ grains are approximately the same in the plane perpendicular to CD, thus AD x TD. On the other hand, for the other billets with equiaxed $\alpha$ phase (Ti1023_El$\beta$, Ti1023_Eq, Ti64_750°*C*, Ti64_Eq), the $\beta$ grains are elongated. After deformation, those grains remain with a cigar shape, with different width and length (**Figure 2.29***b*).

There is then an ambiguity of possibly cutting and analyzing the elongated $\beta$ grains in a plane where they would appear as equiaxed or with a shape factor which would vary significantly depending on the azimuthal position of the longitudinal section prepared for microstructure analysis. This plane is the WD x

HD (in the microscopic coordinate system) and the TD x RD plane (in the macroscopic coordinate system).

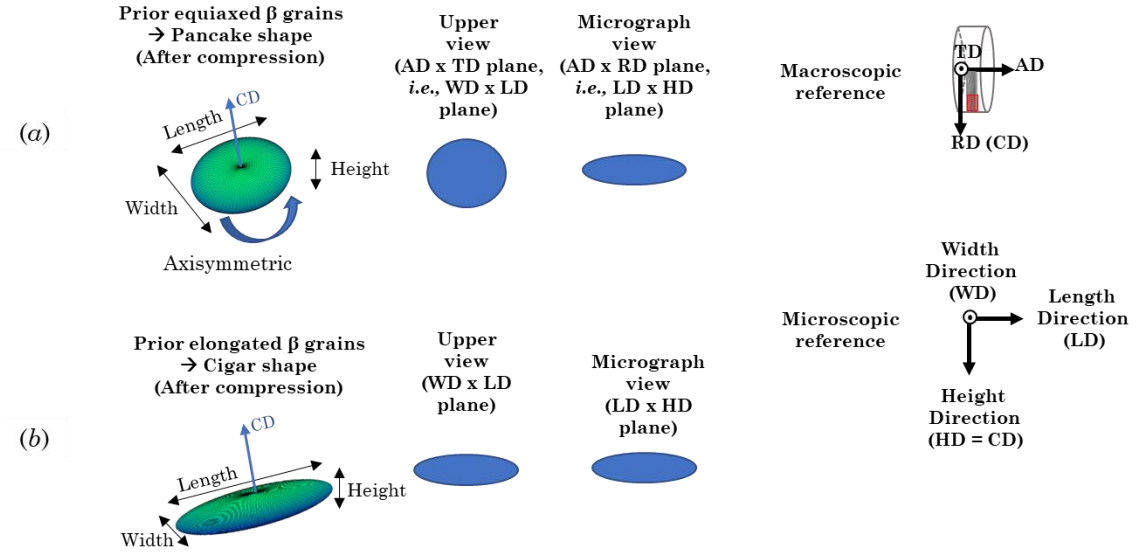



*Figure 2.29. Schematic of the difference in the analysis plane of: a) Pancake shape β grains; b) Cigar shape β grains; Also showing the microscopic (LD x CD x WD) and macroscopic (AD x CD x TD) coordinate systems.*

In order to retrieve the AD direction within the axisymmetric cylindrical or double-cone samples, and thus always analyze microstructures in the same AD x RD plane section, a first polishing step on the upper side of the samples was performed for the $\beta$ elongated microstructures. A schematic example of the procedure to retrieve the AD x RD/CD (or LD x HD/CD in the microscopic coordinate system) plane for the microstructural analysis is shown in **Figure 2.30** for a double-cone sample.

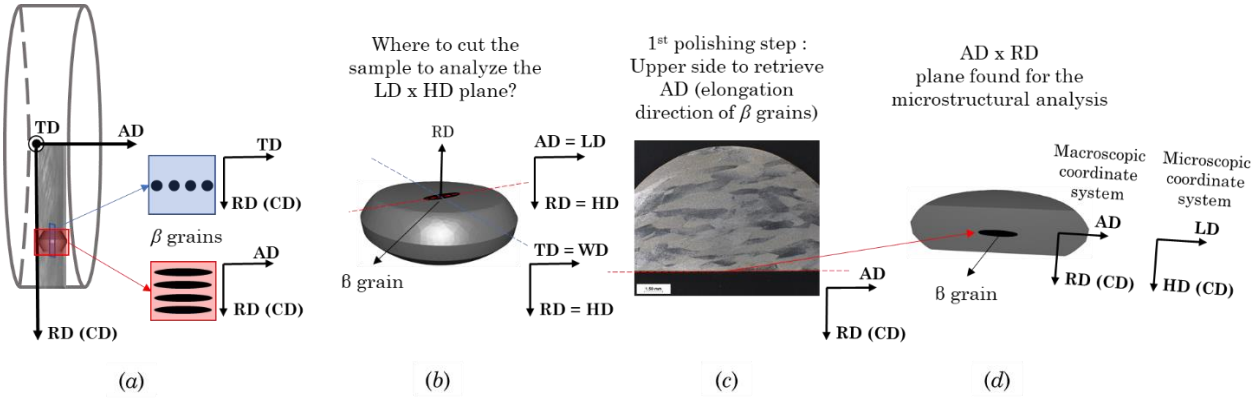



*Figure 2.30. Schematic of the experimental procedure to retrieve the AD x RD plane after the sample compression: a) Sampling; b) Loss of the AD x RD plane; c) Polishing of the upper side of a Ti1023 double-cone sample after deformation; d) AD x RD plane retrieved, showing the elongated β grains for the EBSD analysis.*

### *2.9.3 Double-cone samples*

Double-cone samples were subjected to a 2:1 reduction ($\Delta h = 6.3\ mm$), thus the average axial height (macroscopic) strain ($\varepsilon_{macro}$) being approximately 0.7. Three local equivalent strain levels ($\varepsilon$ = 0.3, 0.8 and 1.3) were selected from a single

double-cone sample, as a function of the radius distance from the center (9.6, 5.9 and 0 $mm$, respectively). The macroscopic strain rate ($\dot{\varepsilon}_{macro}$), detailed in section **4.1**, did not influence the equivalent strain level gradient. This simulation was performed in the *FORGE* software (further details about the simulation parameters are given in the Appendix **C**). **Figure 2.31** exhibits the analyzed zones regarding the different equivalent strain levels obtained.

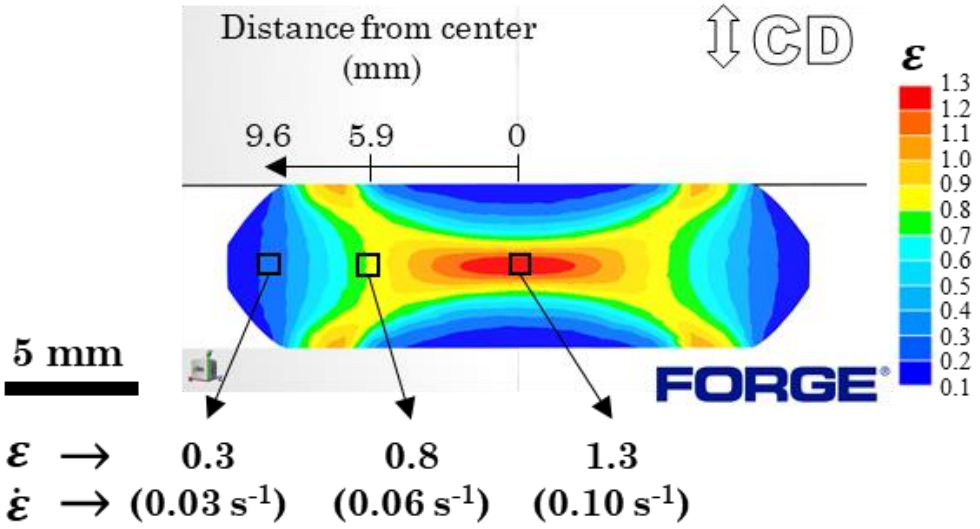



*Figure 2.31. In-diameter cross section of the double-cone sample after compression, with the equivalent plastic strain map (ε), the three analysis zones (black squares) and their local equivalent strain levels and rates.*

Nevertheless, it is clear that to obtain (in a single sample) a gradient of equivalent strain levels, different local strain rates are necessary. However, in this double-cone sample, strain rates are not varying over orders of magnitude but roughly by a factor of 3, thus not having a big impact on the microstructural evolution.

### *2.9.4 Cylindrical samples*

As mentioned previously, cylindrical samples were used in the macroscopic approach (Chapter **5**). As the main objective of this approach is to allow the comparison with the microscopic one (Chapter **4**), the same thermomechanical parameters (temperature, strain level and rate) as those applied to the double-cone samples were maintained.

Cylindrical samples were also subjected to a ~2:1 reduction, same used for the double-cone samples. *FORGE* simulations (with similar parameters described in Appendix **C**) were performed for cylindrical samples. The aim was to determine which macroscopic strain level ($\varepsilon_{macro}$) would generate an equivalent strain level ($\varepsilon$) at the center of the sample (at different time steps) that would be comparable to the three equivalent strain levels selected in the double-cone samples (**Figure 2.32**).

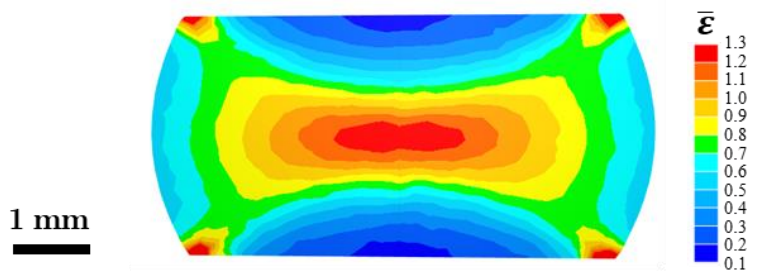



*Figure 2.32. In-diameter cross section of the cylindrical samples after compression (macroscopic strain level = 0.7), with the equivalent plastic strain map ($\bar{\varepsilon}$).*

The comparison between the macroscopic strain and the equivalent strain at the center of the sample is shown in **Table 2.5**.

| Height reduction (%) | Macroscopic strain ($\varepsilon_{macro}$) | Equivalent strain at the center ($\varepsilon_{center}$) |
|---|---|---|
| 18.3 | 0.20 | 0.3 |
| 36.3 | 0.45 | 0.8 |
| 50.4 | 0.70 | 1.3 |

*Table 2.5. Macroscopic strain levels that generate an equivalent strain level at the center of the sample comparable to the double-cone samples.*

At a macroscopic strain ($\varepsilon_{macro}$) of 0.7, both sample geometries presented the same equivalent strain level at the center.

## 2.10 Summary and Conclusions

In this chapter, the different experimental techniques used as well as the methods developed for the needs of the study were presented. More specifically, the methods of microstructural analysis along with the specificities related to the implementation of the thermomechanical tests used were discussed.

Firstly, the as-received materials are presented, along with the heat treatments applied to achieve the initial states (just before deformation). In this work, this is an important element, as several initial microstructures were analyzed in-depth and compared in terms of morphology, temperature, alloy and grain size.

Concerning the EBSD data analysis (main part of this work), some analysis methods available in the *MTEX* toolbox were directly applied (*e.g.,* parent $\beta$ grain reconstruction, pole figure plots, dislocation density estimation from the GND tensor). But also, new analyses were developed, mainly focused on the study of LAGB and HAGB density and also analyzing the intragranular misorientation dependency on grain orientation. These are important features to better understand the dislocation density evolution in titanium alloys, and also to compare the different approaches implemented in this thesis.

One of the biggest challenges of this procedure was to implement the *MTEX* codes for both $\alpha$ and $\beta$ phases and also to adapt them for the different microstructures. It is worth mentioning that a great effort was done to detect parameters to distinguish the $\alpha_P$ and $\alpha_S$ for the Ti64, but also to filter the $\beta$ grains in the Ti1023, yet maintaining some not-indexed zones (where not sufficient EBSD

data was acquired). Furthermore, different strain levels required adapted parameters, as there were microstructural changes from the initial states, as also larger not-indexed zones. All the codes were made available to the other PhD students in the industrial consortium. This development is being (and will be) used in the continuation of this program on titanium alloys.

The methodology of 3D characterizations of titanium alloys was established after some initial tests, opening the possibility of future works based on this technique.

Regarding the thermomechanical tests, one of the main advancements performed was the optimization of the geometry of double-cone samples. The new geometry provides a better stable equivalent strain rate ($\dot{\varepsilon}$) during the compression test. This same geometry will be used for other metals, as its versality was proved in [4] (see Appendix **C**).

## 2.11 Résumé en Français

Dans ce chapitre, les différentes techniques expérimentales utilisées ainsi que les méthodes développées pour les besoins de l'étude ont été présentées. Plus précisément, les méthodes d'analyse microstructurale ainsi que les spécificités liées à la mise en œuvre des essais thermomécaniques utilisés ont été abordées.

Dans un premier temps, les matériaux à réception ainsi que les traitements thermiques appliqués pour atteindre les états initiaux (juste avant déformation) ont été présentés. Dans ce travail, il s'agit d'un élément important, car plusieurs microstructures initiales ont été analysées en profondeur et comparées en termes de morphologie, de température, d'alliage et de taille de grain.

En ce qui concerne l'analyse des données EBSD (partie centrale de ce travail), certaines méthodes d'analyse disponibles dans la boîte à outils *MTEX* ont été directement appliquées (par exemple, la reconstruction du grain parent $\beta$, les diagrammes de figures de pole, l'estimation de la densité de dislocations à partir du tenseur GND). Mais aussi, de nouvelles analyses ont été développées, principalement axées sur l'étude de la densité LAGB et HAGB et analysant également la dépendance de la désorientation intragranulaire à l'orientation des grains. Ce sont des caractéristiques importantes pour mieux comprendre l'évolution de la densité de dislocations dans les alliages de titane, et aussi pour comparer les différentes approches mises en œuvre dans cette thèse.

L'un des plus grands défis de cette procédure était d'implémenter les codes *MTEX* pour les phases $\alpha$ et $\beta$, également de les adapter aux différentes microstructures. Il convient de mentionner qu'un grand effort a été fait pour détecter les paramètres permettant de distinguer les $\alpha_P$ et $\alpha_S$ pour le Ti64, mais aussi pour filtrer les grains $\beta$ dans le Ti1023, tout gérant certaines zones non indexées (où pas suffisamment de données EBSD ont été acquises) . De plus, différents niveaux de déformation nécessitaient des paramètres adaptés, car il y avait des changements microstructuraux par rapport aux états initiaux, ainsi que des zones non indexées plus grandes. Tous les codes ont été mis à disposition des autres doctorants du consortium industriel. Ce développement est (et sera) utilisé dans la poursuite de ce programme sur les alliages de titane.

La méthodologie des caractérisations 3D des alliages de titane a été établie après quelques essais initiaux, ouvrant la possibilité de futurs travaux basés sur cette technique.

Concernant les essais thermomécaniques, l'une des principales avancées réalisées a été l'optimisation de la géométrie des échantillons double-cônes. La nouvelle géométrie fournit une vitesse de déformation équivalent plus stable ($\dot{\bar{\varepsilon}}$) pendant le test de compression. Cette même géométrie sera utilisée pour d'autres métaux, car sa polyvalence a été démontrée dans [4] (voir Appendice **C**).

# 3. CHARACTERIZATION OF AS-RECEIVED AND INITIAL (PRIOR TO HOT DEFORMATION) MICROSTRUCTURES

The workflow for the characterization of the initial states is presented in **Figure 3.1**.




*Figure 3.1. Workflow for the material characterization of the as-received billets and initial states (just before deformation).*

A first step of characterization (through OM) was performed in three of the as-received billet slices to verify possible heterogeneities connected to the forging process and to determine the sampling zones for the following billets. Then, all as-received billets were analyzed through OM, with some verifications by SEM. Heat treatments were applied to obtain the "*initial states*" (*i.e.,* just before deformation) and finally they were characterized by SEM, to assess complete information (*e.g.*, crystallographic orientation, dislocation density, substructures) before studying the hot deformation influence (Chapter **4**).

## 3.1 Verification of possible azimuthal and radial heterogeneities

Different samples were taken from the billet slices received from *Timet*, as shown in **Figure 3.2**. The sampling locations were chosen to check whether between 0 and 90°, or along the radius (between 0R and 1R), there were microstructural differences.

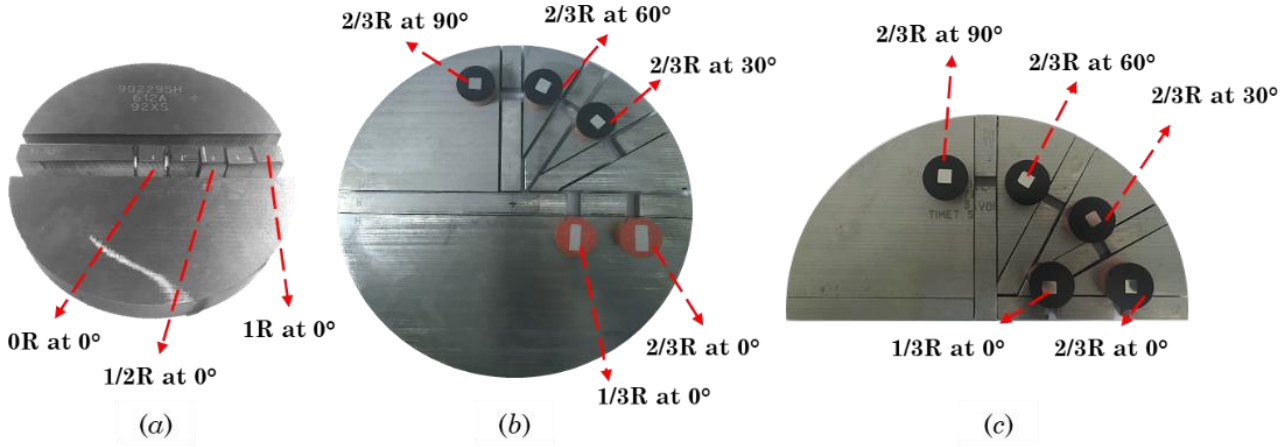



*Figure 3.2. Plan for sampling from the billet slices: a) Ti1023_Elβ; b) Ti1023_Eq; c) Ti64_Eq.*

The mean values of the results ($\boldsymbol{\mu}$) of the verification of possible heterogeneities in the industrial billets are gathered with their standard deviations associated with the different sampling regions ($\sigma_{SR}$) in **Table 3.1**. For each sampling region (SR), 10 micrographs were taken (~1 $mm^2$ of total analyzed area).

| Billet | $\alpha_P$ phase | | | $\beta$ phase | |
|---|---|---|---|---|---|
| | Qualitative analysis | $\overline{GS}_{\alpha_P}$ $[\mu m]$ | $f_{\alpha_P}$ [%] | Qualitative analysis | $\overline{GS}$ $[mm]$ |
| Ti1023_El$\beta$ | Equiaxed and fine grains | **2.4** ± 0.1 | **22** ± 4 | Fine elongated grains according to AD | **0.4** ± 0.1 |
| Ti1023_Eq | Equiaxed and fine grains | **3.2** ± 0.1 | **39** ± 2 | Coarse elongated grains according to AD | **0.6** ± 0.1 |
| Ti64_Eq | Equiaxed and large grains | **19.4** ± 0.8 | **92** ± 2 | Fine elongated grains according to AD | **0.5** ± 0.1 |

*Table 3.1. Summary of the verification of possible radial and azimuthal heterogeneities in the as-received (AR) states ($\boldsymbol{\mu} \pm \sigma_{SR}$).*

After analyzing the results in **Table 3.1**, it appears that the billets can be considered homogeneous, given the low standard deviations between the different sampling regions. Therefore, the sampling region (SR) in each billet will not have a considerable influence on the analyzed microstructure, which is highly useful, as it allows to drastically reduce the microscopic analysis campaigns.

Nevertheless, the borders of the billets were avoided during sampling, as those regions can contain a hardened zone (around 200 $\mu m$ thick) called $\alpha$-case layer (so called because of a higher fraction of $\alpha$ phase). The presence and depth of the $\alpha$-case layer was verified experimentally in a Ti64_Eq sample (**Figure 3.3**). This layer could possibly influence the microstructural analysis, as it increases the primary $\alpha$ phase fraction due to interstitial oxygen diffusion [77]. The $\alpha$-case layer was measured to be extremely thin, approximately 220 $\mu m$, similar to values found in the literature (~200 $\mu m$) [77], and thus does not affect the microstructural analysis.

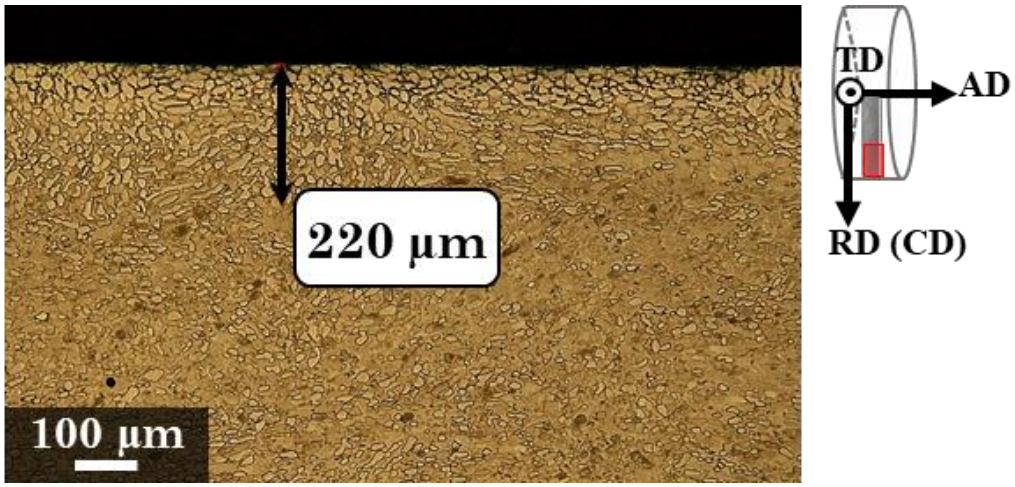



*Figure 3.3. α-case layer observation in a Ti64 alloy heated for 1 hour at 950°C, followed by WQ.*

Regarding the standard deviation related to the $f_{\alpha_P}$ (± 4) of the Ti1023_El$\beta$ billet, this value was the same for the three analyzed samples (22 ± 4, 23 ± 4, 21 ± 4). Therefore, it is possible to say that, in the same sample, the $\alpha_P$ phase fraction of this billet varies more than the other two.

For the billet slices received from *Aubert & Duval* (see **Table 2.1**), to save time, only one sampling point was chosen to analyze the material (2/3R at 0°). The manufacturing process of these billets being similar, the billets from *Timet* not exhibiting azimuthal or radial heterogeneities, it will be considered that the others are also homogeneous (as they present smaller diameter), thus saving time and material.

## 3.2 Characterization of as-received microstructures

All six initial microstructures were characterized in terms of grain size and phase fraction. To facilitate the visualization of the different microstructures, all results are summarized in **Table 3.2**, along with their respective average standard deviations in a single micrograph ( $\bar{\sigma}_M$ , *i.e.,* the average of $\sigma_M$ within all micrographs).

| Billet | Primary $\alpha$ phase | | | $\beta$ phase | | |
|---|---|---|---|---|---|---|
| | Qualitative analysis | $\overline{GS}_{\alpha_P}$ $[\mu m]$ | $f_{\alpha_P}$ [%] | Qualitative analysis | Th $[mm]$ | L $[mm]$ |
| Ti1023_El$\beta$ | Equiaxed and fine grains | **2.4** ± 1.0 | **22** | Fine elongated grains according to AD | **0.4** ± 0.1 | **2.4** ± 1.0 |
| Ti1023_Eq | Equiaxed and fine grains | **3.2** ± 1.7<br>***3.2*** ± *1.6* | **39**<br>***39*** | Coarse elongated grains according to AD | **0.6** ± 0.1 | **1.4** ± 0.1 |
| Ti1023_L | Fine lamellae | **1.0** ± 0.7 | **75** | Fine equiaxed grains | **0.4** ± 0.1 | - |
| Ti64_Eq | Equiaxed and coarse grains | **19.4** ± 3.8<br>***19.4*** ± *3.6* | **91**<br>***92*** | Fine elongated grains according to AD | **0.5** ± 0.1 | **1.7** ± 0.5 |
| Ti64_FL | Fine lamellae | **2.3** ± 0.5 | **92** | Coarse equiaxed grains | **0.6** ± 0.1 | - |
| Ti64_CL | Coarse lamellae | **10.6** ± 1.9 | **91** | Coarse equiaxed grains | **0.7** ± 0.1 | - |

*Table 3.2. Summary of the results ($\boldsymbol{\mu} \pm \sigma$) of the characterization of the as-received states by optical microscopy and by EBSD/SEM (values in italic).*

A comparison between the quantitative results obtained by OM and SEM was performed for the Ti1023_Eq and Ti64_Eq billets. The objective was to check if the

faster OM analysis could be compared to the further (and more detailed) SEM/EBSD analysis. EBSD results are in italics in **Table 3.2**. The two methods are comparable, where all EBSD values fall within the 95% confidence interval ($\mu \pm 2\sigma$ [78]), when compared with those from OM.

The six as-received microstructures are displayed in **Figure 3.4** on two different scales, showing the $\beta$ and $\alpha$ grains.

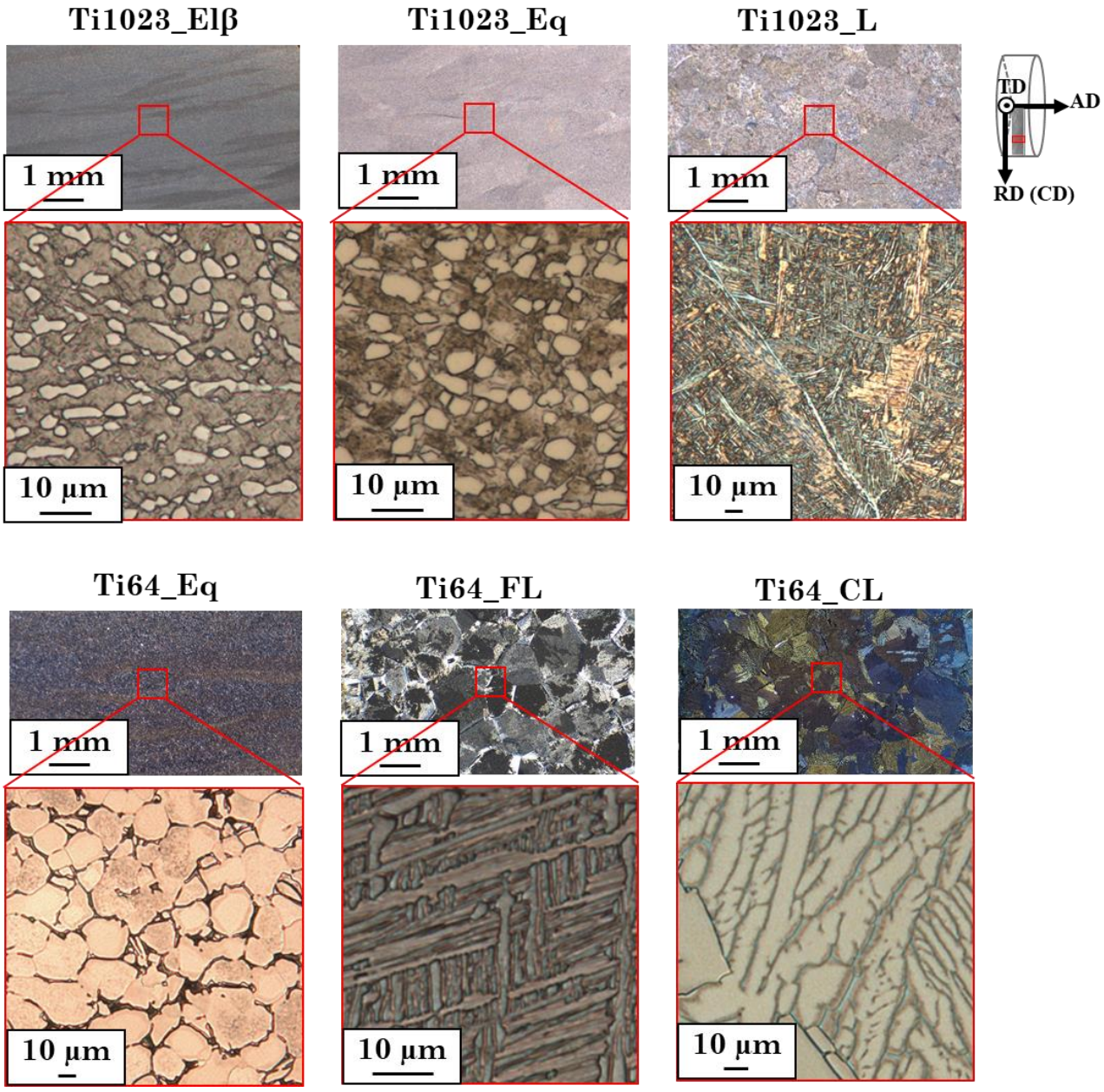



*Figure 3.4. Optical micrographs of the six as-received billet materials, displayed at two different scales, showing the β (or prior-β for the Ti64) and α grains.*

## 3.3 Grain size and phase fractions of initial microstructures

The seven initial microstructures, *i.e.,* prior to deformation, (see the seven heat treatments applied to the six as-received microstructures in Table 2.2) are displayed in **Figure 3.5**. The $\beta$ (or prior-$\beta$ for the Ti64) was characterized by a binocular magnifier, while the $\alpha$ phase by SEM, due to their characteristic dimensions. Equiaxed and lamellar morphologies were selected for each alloy, with varied grain size and morphology. Noteworthily, a few $\alpha$ grains elongated perpendicularly to the forging direction can be observed in the Ti1023_El$\beta$, Ti1023_Eq and Ti64_Eq microstructures. Interestingly, for the Ti64 at 750°C, the temperature was low enough to retain the $\beta$ phase, where its transformation into $\alpha_s$ did not occur, thus allowing the direct assessment of the $\beta$ phase in this microstructure.

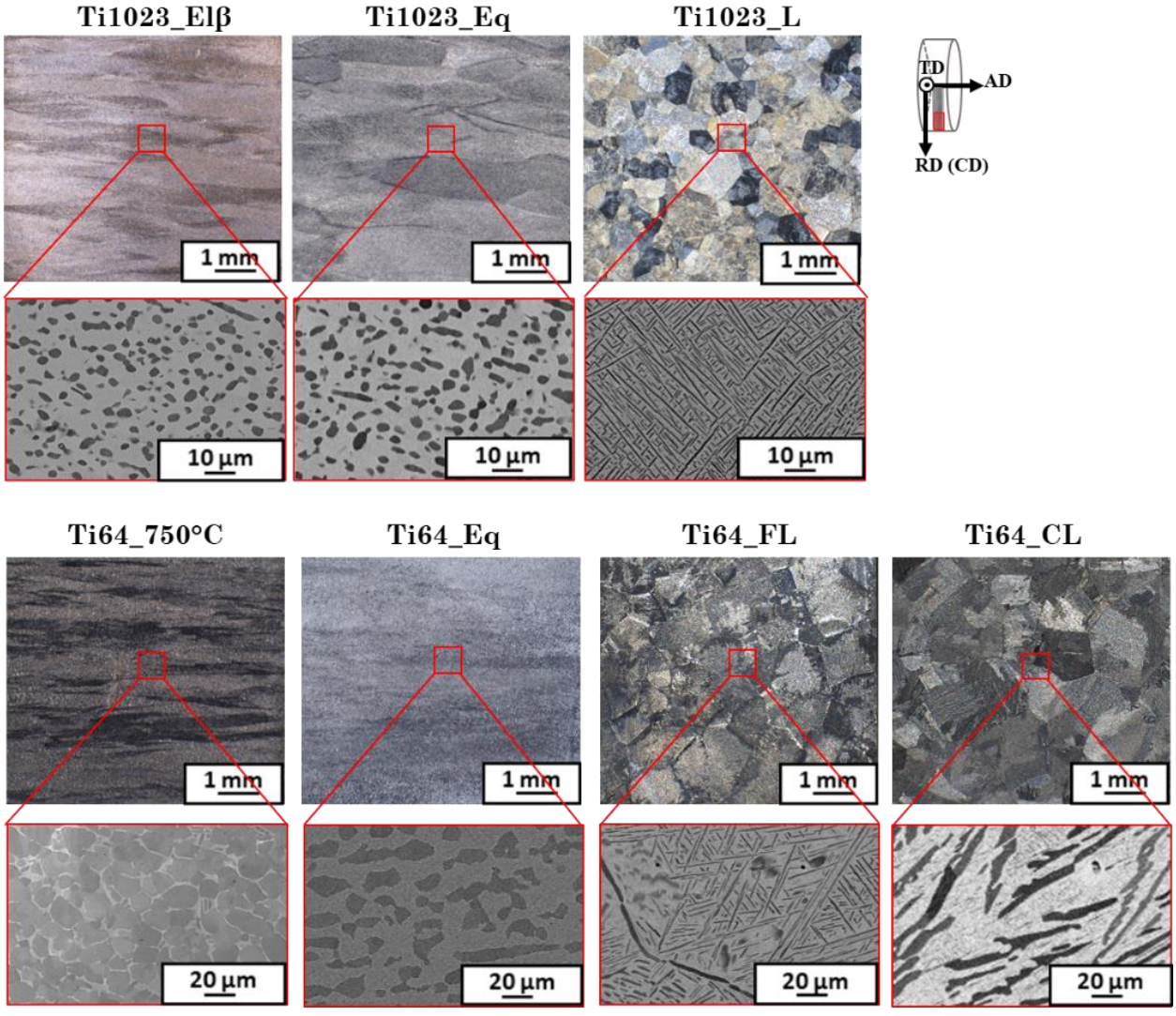



*Figure 3.5. The seven initial microstructures selected for the analysis of the influence of alloy, morphology and grain size on the microstructural evolution.*

A detailed and quantitative characterization of those seven initial microstructures is given in **Table 3.3**.

| Billet | Primary $\alpha$ phase | | | $\beta$ phase | | |
|---|---|---|---|---|---|---|
| | Qualitative analysis | $\overline{GS}$ $[\mu m]$ | $f_{\alpha_P}$ [%] | Qualitative analysis | Th $[mm]$ | L $[mm]$ |
| Ti1023_El$\beta$ | Equiaxed and fine grains | **2.3** ± 1.1 | **23** ± 1 | Fine elongated grains according to AD | **0.4** ± 0.1 | **2.0** ± 0.4 |
| Ti1023_Eq | Equiaxed and fine grains | **3.1** ± 1.3 | **24** ± 1 | Coarse elongated grains according to AD | **0.6** ± 0.1 | **1.5** ± 0.2 |
| Ti1023_L | Fine lamellae | **1.1** ± 0.6 | **24** ± 1 | Fine equiaxed grains | **0.4** ± 0.1 | - |
| Ti64_750°C | Equiaxed and coarse grains | **19.1** ± 7.6 | **81** ± 1 | Fine elongated grains according to AD | **0.4** ± 0.1 | **1.7** ± 0.4 |
| Ti64_Eq | Coarse equiaxed grains | **15.6** ± 5.3 | **35** ± 1 | Fine elongated grains according to AD | **0.5** ± 0.1 | **1.8** ± 0.5 |
| Ti64_FL | Fine lamellae | **1.6** ± 0.7 | **35** ± 1 | Coarse equiaxed grains | **0.7** ± 0.1 | - |
| Ti64_CL | Coarse lamellae | **9.1** ± 1.2 | **35** ± 1 | Coarse equiaxed grains | **0.9** ± 0.1 | - |

*Table 3.3. Summary of the results of the characterization of the initial states ($\boldsymbol{\mu} \pm \bar{\sigma}_M$).*

To check if the initial states are at phase equilibrium, the thermodynamic phase equilibrium and a comparison with the literature was performed. For the Ti64 alloy, experimental results were compared to the Castro & Séraphin model [17], shown in equation **(1.1)**. Nevertheless, the $A$ and $b$ parameters were not found in the literature for the Ti1023. As shown in **Figure 1.5**, Weiss & Semiatin [16] provided experimental data for this alloy ranging from 700°C to 800°C. The former model parameters were then fitted for the Ti1023 based on experimental results and the literature (**Figure 3.6**).

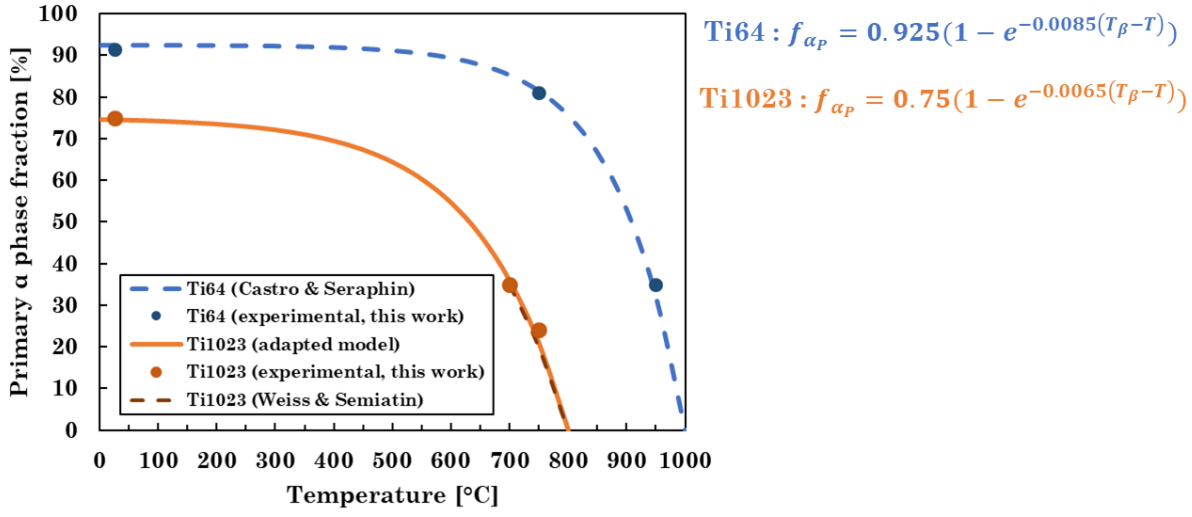



*Figure 3.6. Comparison between models (with their respective equations), literature and experimental results of the $\alpha_P$ phase fraction as a function of temperature.*

Analyzing **Figure 3.6**, experimental results ($f_{\alpha_P}$) shown in **Table 3.2** and **Table 3.3** (dots) of the Ti64 (in blue) are indeed very similar to the Castro &

Séraphin model (dashed blue line), validating the quantification analysis applied. For the Ti1023 alloy, the Weiss & Semiatin results (dashed orange line) is also consistent with the experimental results of this work (orange dots). Consequently, the $A$ and $b$ parameters of equation **(1.1)** were calculated as 0.75 and 0.0065 for the Ti1023, where there is a satisfactory fit between this adapted model (orange line) and the experimental results for this alloy.

Finally, the seven initial microstructures are schematized in **Figure 3.7**, along with their characteristic dimensions, $\alpha_P$ phase fractions and the respective heat treatment temperatures applied (during 1 hour). These schematics will be used throughout the entire manuscript, for the sake of simplicity.

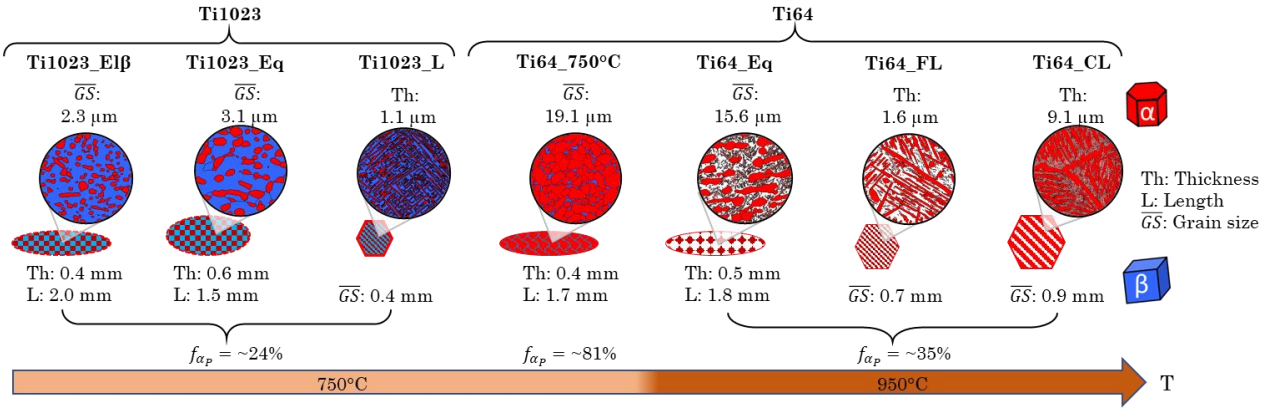



*Figure 3.7. Schematic of the initial microstructures of the Ti1023 and Ti64 alloys, with their characteristic dimensions (for both α and β phases), $\alpha_P$ phase fractions and heat treatment (and subsequent hot deformation) temperatures.*

### *3.3.1 EBSD phase maps and local misorientation analysis*

An EBSD micrograph is shown for each of the seven initial microstructures to illustrate the analyzed zones, with also the LAGB and HAGB indicated by black or yellow lines, respectively. (**Figure 3.8**). For the Ti64_Eq, Ti64_Fl and Ti64_CL billets, the $\beta$ phase was partially reconstructed from the secondary $\alpha$ ($\alpha_S$) phase by the procedure explained in **2.7.1**. The remaining non-indexed areas are due to poor indexing in the $\alpha_S$ laths.

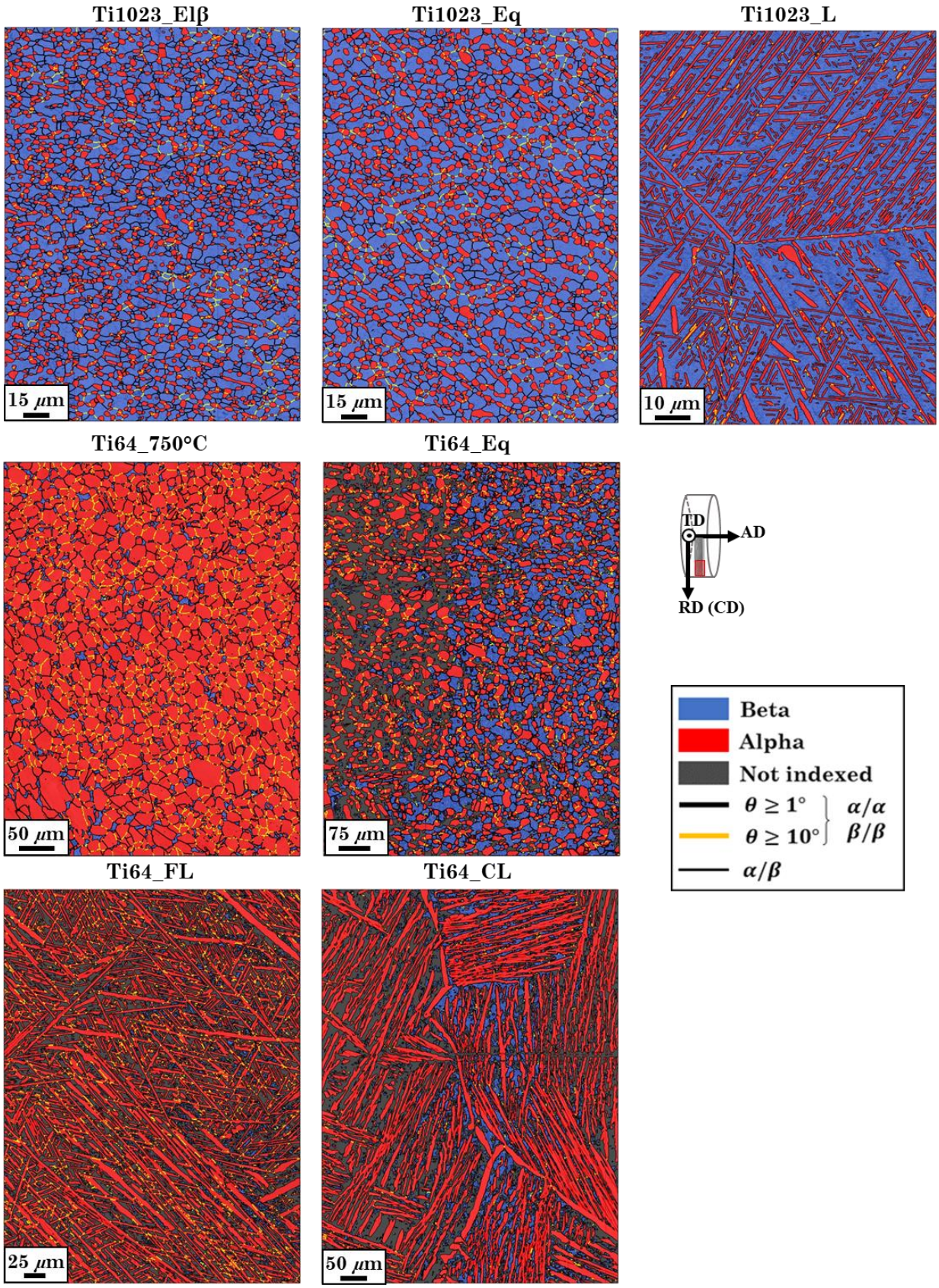



*Figure 3.8. EBSD phase maps of each of the seven initial microstructures, along with the α/α and β/β LAGB (black lines) and HAGB (yellow lines).*

The initial states present low density of HAGB (yellow lines in **Figure 3.8**) at this scale. The only case where there is a high quantity of HAGB is in the Ti64_750°$C$ microstructure, due to its high fraction of primary $\alpha$ phase (81%), where different $\alpha$ grains are interconnected. For the lamellar cases with fine laths (Ti1023_L and Ti64_FL), the presence of HAGB is due to interconnected laths with different orientations (respecting BOR) that create a $\alpha/\alpha$ grain boundary. To prove this, the misorientation angles and axis were calculated for the Ti1023_L at 750°$C$, the histogram of this analysis is shown in **Figure 3.9**.

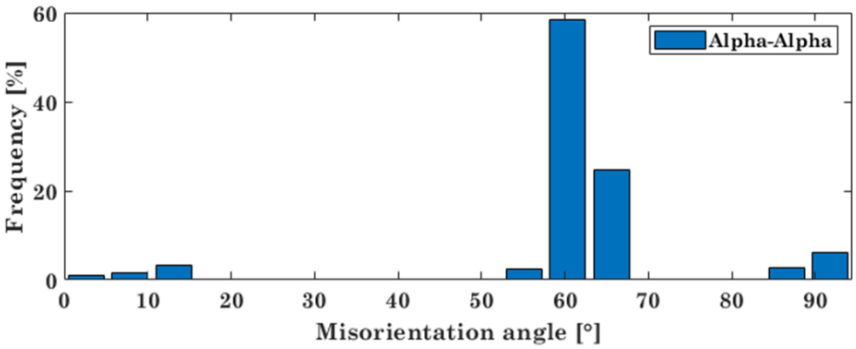



*Figure 3.9. Histogram of the misorientation angles distribution between α – α laths for the Ti1023_L at 750°C.*

Most of the misorientation angles belong to the 5 possible ones between the 12 $\alpha_S$ variants from a same $\beta$ grain, as shown in **Table 3.4**.

| $\theta$ | $\vec{n}$ |
|---|---|
| 10°529 | $\vec{c} = [0001]$ |
| 60° | $\overrightarrow{a_2} = [\bar{1}2\bar{1}0]$ |
| 60°832 | $\overrightarrow{d_1}$ at 80°97 from $\vec{c}$ in plane $(\overrightarrow{d_3}, \vec{c})$ |
| 63°262 | $\overrightarrow{d_2}$ at 72°73 from $\vec{c}$ in plane $(\overrightarrow{a_2}, \vec{c})$ |
| 90° | $\overrightarrow{d_3}$ at 5°26 from $\overrightarrow{a_2}$ in basal plane |

*Table 3.4. List of α/α misorientation angles and axis* [79].

This shows that the HAGB shown in **Figure 3.8** for the Ti64_FL are simply related to the intersection of different $\alpha_S$ laths.

### *3.3.2 GND density of the initial states*

The dislocation density ( $\rho_{EBSD}^{\varphi}$ ) was estimated for each of the initial microstructures by the procedure described in section **2.7.5**. The dislocation density maps for the $\alpha$ and $\beta$ phases, with their average values are shown in **Figure 3.10** (Ti1023) and **Figure 3.11** (Ti64).

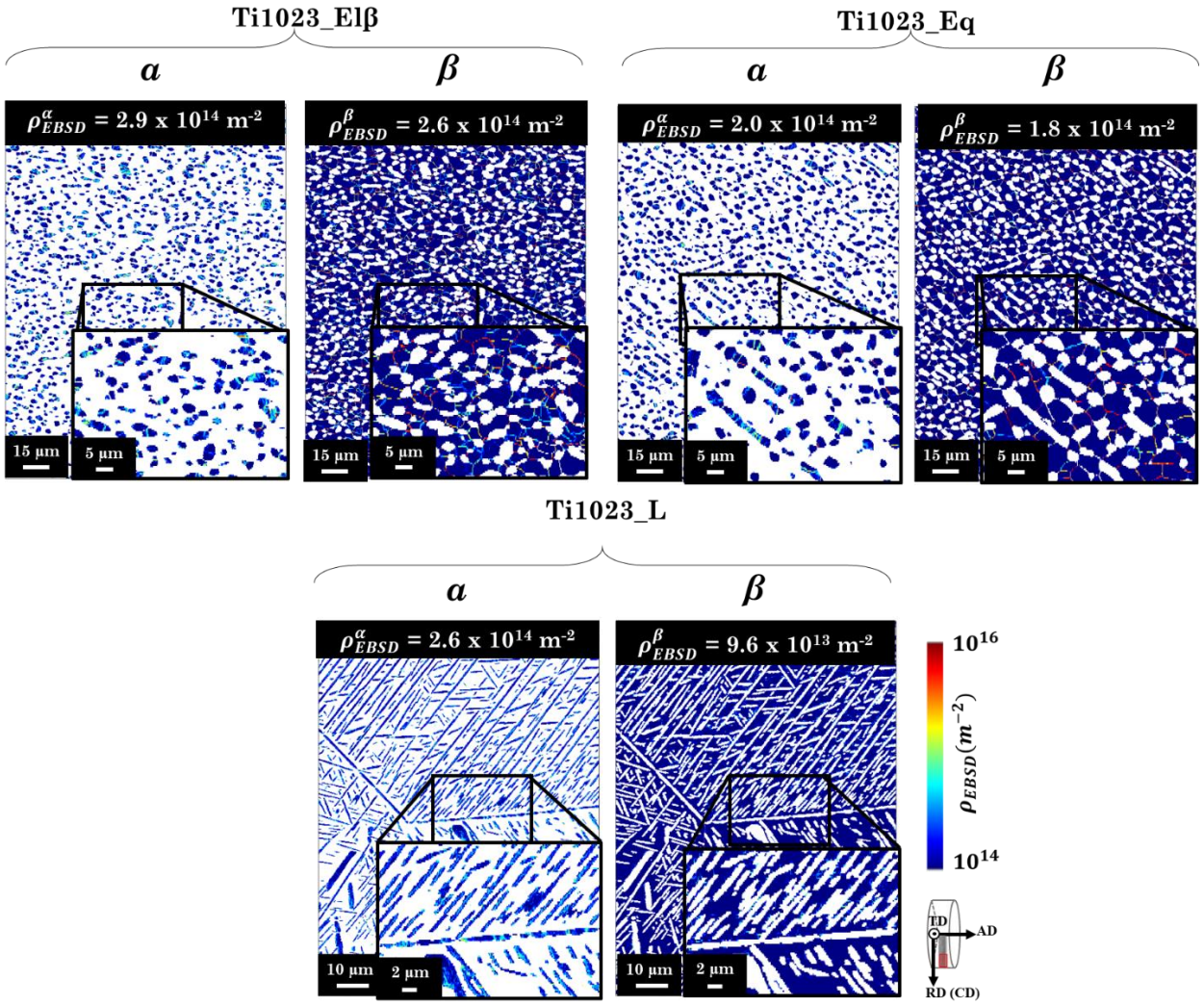



*Figure 3.10. GND density maps for α and β phases (with their average values) in the Ti1023 initial microstructures (ε = 0).*

It is possible to see in **Figure 3.10** that for the equiaxed cases (*i.e.,* Ti1023_El$\beta$ and Ti1023_Eq), the average dislocation density ($\rho^{\varphi}_{EBSD}$) of both phases is similar. Also, there is presence of substructures in both phases and alloys. For the $\beta$ phase the substructures seem to be related to well-defined LAGBs, while in the $\alpha$ phase, those substructures seem to be related to orientation gradients within the grains. Furthermore, as the step sizes used for the EBSD acquisition of those two microstructures were the same, their direct comparison is possible. In addition, it is clear that the alloy which was previously more deformed by the industrial partners (smaller diameter, as shown in Table 2.1) has higher $\rho^{\varphi}_{EBSD}$ values of both phases, which is coherent.

Concerning the lamellar case (Ti1023_L), the average $\rho^{\varphi}_{EBSD}$ value of the $\alpha$ phase is considerably higher than the $\beta$ phase, where basically no substructure is observed in the latter.

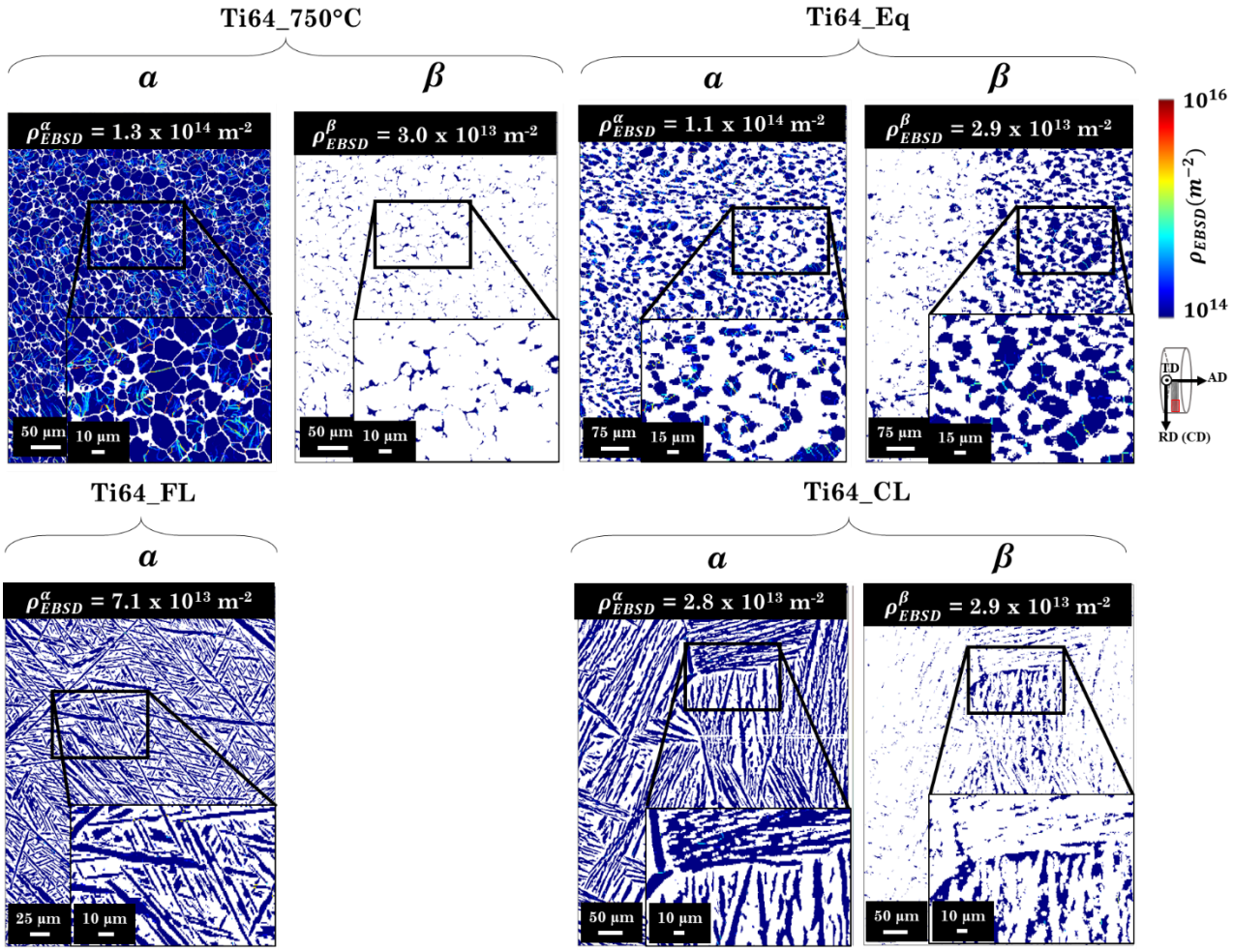



*Figure 3.11. GND density maps for α and β phases (with their average values) in the Ti64 initial microstructures (ε = 0).*

In Figure 3.11, it possible to see that in the equiaxed cases (Ti64_750°C and Ti64_Eq), the average $\rho^{\varphi}_{EBSD}$ of the α phase is considerably higher (around 4 times) than the ß phase one, which present very few substructures. Nevertheless, it is worth mentioning that the $\beta$ phase in the Ti64 alloy is obtained by its reconstruction from the indexed $\alpha_S$ (procedure explained in section **2.7.1**). For the Ti64_Eq and Ti64_CL, only a partial amount of the prior ß phase could be reconstructed, while for the Ti64_FL, this reconstruction was insufficient, so its results were discarded for the sake of representativeness.

### *3.3.3 Complementary 3D analysis of the Ti64_CL and Ti64_FL microstructures*

After FIB milling/ SEM imaging series (section **2.8**), the 2D images were then stacked and the 3D volumes of the Ti64_FL (**Figure 3.12***a*) and Ti64_CL (**Figure 3.12***b*) were reconstructed.

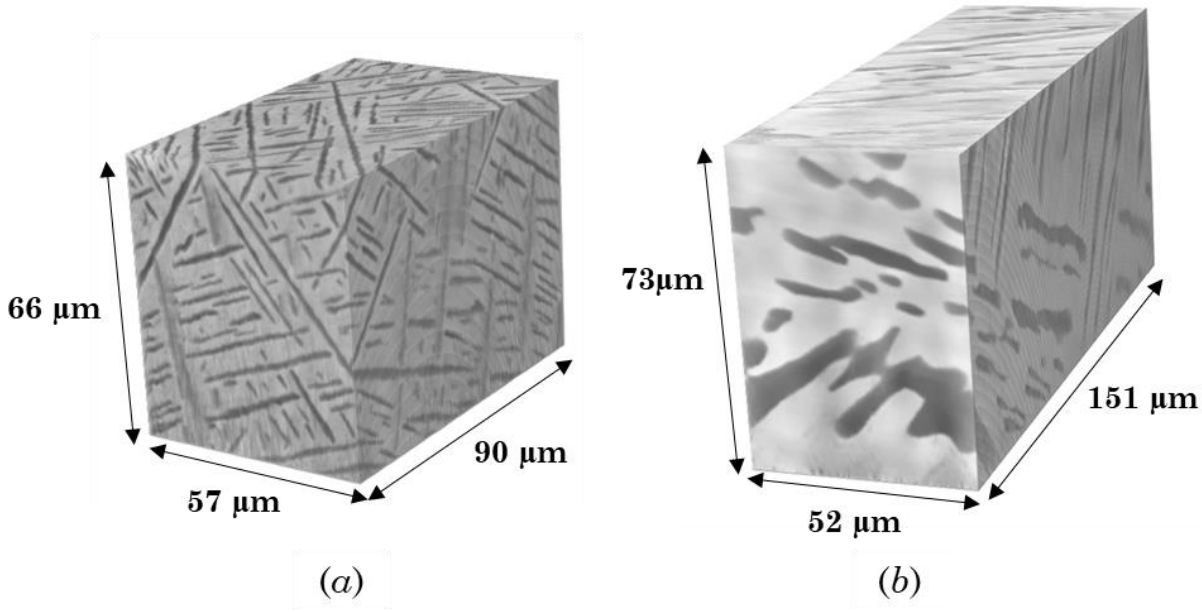



*Figure 3.12. 3D reconstruction of the: a) Ti64_FL; b) Ti64_CL; showing their respective dimensions.*

To enable the analysis of the $\alpha$ laths inside the 3D volume, a 3D segmentation was performed in the *Dragonfly* software [80] (an advanced analysis and visualization software for 3D data). Even if the analyzed volume of the Ti64_CL was bigger than the Ti64_FL, more variants of the $\alpha$ phase could be identified. **Figure 3.13** shows five different $\alpha$ variants, out of six possible planes (see section **1.1.4**), that were identified in the analyzed volume.

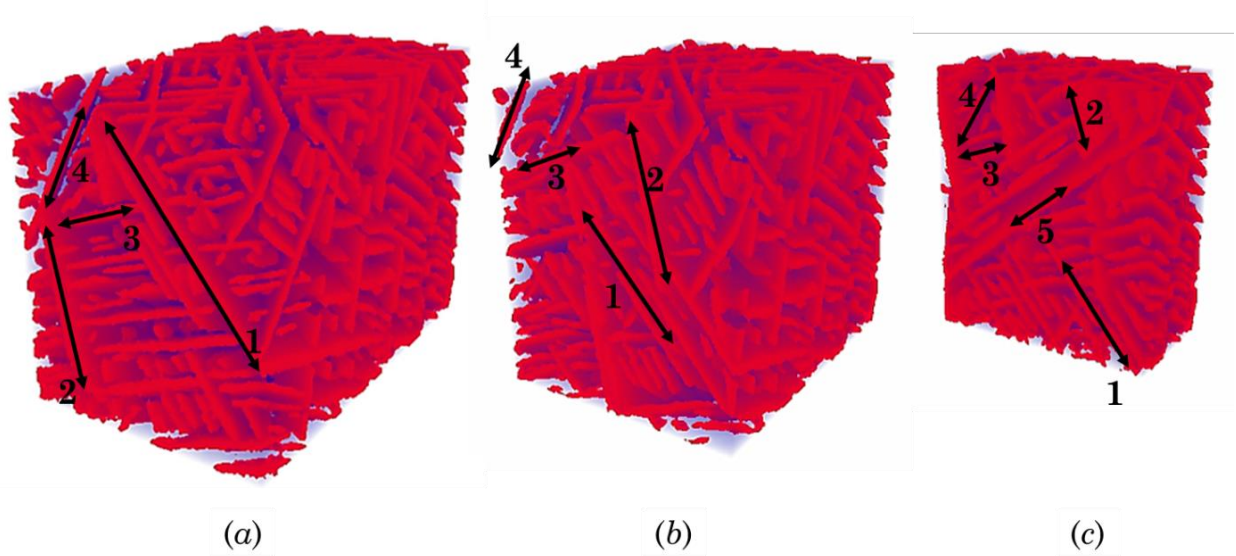



*Figure 3.13. Identification of five different variants of the α phase from the Ti64_FL at: a) 100% volume; b) ~50% volume; c) ~20% volume; enabling the visualization at the interior of the microstructure.*

While for the Ti64_CL, only three different $\alpha$ variants were identified in the analyzed volume (**Figure 3.14**), yet this is most probably linked to the analyzed

volume, which is relatively small (limited by the method) compared to the microstructure.

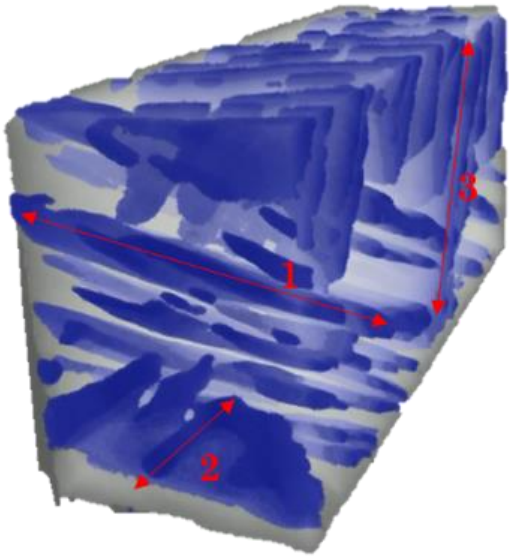



*Figure 3.14. Identification of three different variants of the α phase from the Ti64_CL.*

Furthermore, it seems that the morphology of both microstructures is different. To observe this, a component analysis was performed in the *Paraview* software [81] for the Ti64_FL microstructure, where different feature IDs (connected regions in the volume) were distinguished for the laths (**Figure 3.15**).

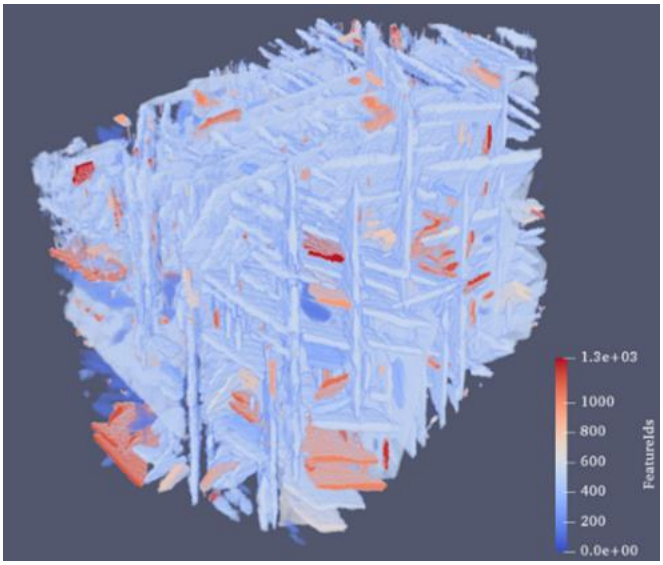



*Figure 3.15. Identification of the feature IDs for the Ti64_FL, showing that basically all the α laths contained in the volume belong to only one feature ID, in other words, are all interconnected.*

The *α* laths of the Ti64_FL seem to be mostly interconnected (or entangled) in **Figure 3.15**, were the *α* laths that have a different feature ID (represented by a different color) are the one at the border of the volume. If the analyzed volume were bigger, those *α* laths at the border would also be likely interconnected to the others. Such interconnected configuration of the *α* laths was shown by [82] in additively manufactured Ti-6Al-4V.

On the other hand, **Figure 3.16** shows that the $\alpha$ laths in the Ti64_CL microstructure do not seem to be interconnected, where a gap between them ($\beta$ phase at 950°C) can clearly be observed.

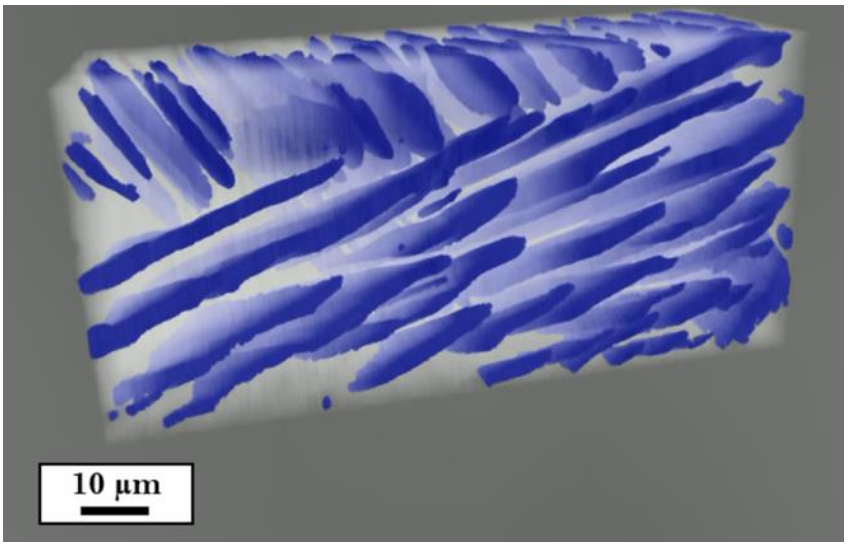



*Figure 3.16. α laths of the Ti64_CL microstructure, showing that they do not seem to possess an interconnected morphology.*

This difference might be mainly connected to the cooling rate applied, where a much faster one was used to obtain the finer laths (Ti64_FL), see **Table 2.1**. Apparently, not only the lath thickness is dependent of the cooling rate [25], but also its 3D morphology, especially concerning the interconnection of the $\alpha$ phase. On the other hand, this interconnexion might also me linked to the spatial resolution in both analyses, as the Ti64_CL laths are much thicker.

## 3.4 Summary and Conclusions

In this chapter, the as-received (six slices of billet) and the initial states (seven microstructures) were fully characterized by OM, SEM and EBSD. Firstly, it was shown that the sampling region in each slice of billet did not have a strong influence on the analyzed microstructure. Thus, it allowed to drastically reduce the microscopic analysis campaigns.

The expected different microstructural features were confirmed by the characterizations. It allowed to establish the set of initial microstructures (in terms of morphology and grain size) to be compared in the following Chapter (**4**) after deformation. Noteworthily, two other as-received microstructures were also characterized, both Ti64 with coarse equiaxed $\beta$ grains (Ti64_FL_C$\beta$ and Ti64_CL_C$\beta$) were removed from the following steps, as the grain size for the finer equiaxed $\beta$ grains (Ti64_FL and Ti64_CL) is already considerably high for the EBSD analysis.

Concerning the phase fraction evolution with temperature, the parameters of a classic model for the Ti64 [17] were adapted for the Ti1023, showing satisfactory agreement with experimental data. These results also helped to establish the deformation temperatures in the second section of Chapter **4** (section **4.2**).

The average dislocation density ($\rho_{EBSD}^{\varphi}$) was calculated for both phases at $\varepsilon = 0$, being in an order of magnitude of approximately $10^{13} - 10^{14}\ m^{-2}$. Also, it was shown that in the initial microstructures, there was already the presence of substructures in both phases. For the $\beta$ phase those substructures seem to be related to well-defined LAGBs, while in the $\alpha$ phase, those substructures seem to be related to orientation gradients within the grains.

Concerning the 3D characterizations, the two lamellar Ti64 microstructures (Ti64_FL and Ti64_CL) have distinct 3D morphological behavior. Apparently, not only the lath thickness is dependent of the cooling rate, but also the interconnection of the $\alpha$ phase. These 3D analyzes show above all that the interpretation of 2D sections must be taken carefully.

## 3.5 Résumé en Français

Dans ce chapitre, les états tels que reçus (six tranches de billette) et les états initiaux (sept microstructures) ont été entièrement caractérisés par OM, SEM et EBSD. Premièrement, il a été montré que la région d'échantillonnage dans chaque tranche de billette n'avait pas une forte influence sur la microstructure analysée. Ainsi, il a permis de réduire drastiquement les campagnes d'analyses microscopiques.

Les différentes caractéristiques microstructurales attendues ont été confirmées par les caractérisations. Elle a permis d'établir l'ensemble des microstructures initiales (en termes de morphologie et de granulométrie) à comparer dans le Chapitre (**4**) suivant après déformation. Il convient de noter que deux autres microstructures telles que reçues ont également été caractérisées, les deux Ti64 avec des grains $\beta$ équiaxes grossiers (Ti64_FL_Cß et Ti64_CL_Cß) ont été retirés des étapes suivantes, car la taille des grains pour les grains $\beta$ équiaxes plus fins (Ti64_FL et Ti64_CL) est déjà considérablement élevée pour l'analyse EBSD.

Concernant l'évolution de la fraction de phase avec la température, les paramètres d'un modèle classique pour le Ti64 [17] ont été adaptés pour le Ti1023, montrant un accord satisfaisant avec les données expérimentales. Ces résultats ont également permis de fixer les températures de déformation pour les travaux de la deuxième section du Chapitre **4** (section **4.2**).

La densité moyenne de dislocations ($\rho_{EBSD}^{\varphi}$) a été calculée pour les deux phases à $\varepsilon = 0$, étant dans un ordre de grandeur d'environ $10^{13} - 10^{14}\ m^{-2}$. Aussi, il a été montré que dans les microstructures initiales, il y avait déjà la présence de sous-structures dans les deux phases. Pour la phase $\beta$, ces sous-structures semblent être liées à des LAGB bien définis, tandis que dans la phase $\alpha$, ces sous-structures semblent être liées à des gradients d'orientation dans les grains.

Concernant les caractérisations 3D, les deux microstructures lamellaires de Ti64 (Ti64_FL et Ti64_CL) ont un comportement morphologique 3D distinct. Les résultats obtenus semblent montrer que, non seulement l'épaisseur des lamelles dépend de la vitesse de refroidissement, mais aussi de l'interconnexion de la phase $\alpha$. Ces analyses 3D montrent surtout que l'interprétation des coupes 2D doit être faite avec précaution.

# 4. MICROSCOPIC APPROACH: MICROSTRUCTURAL EVOLUTION DURING HOT DEFORMATION

The industrial forging process involves deformation at high temperature, thus it is essential to know the correlation between the thermomechanical parameters involved (temperature, time, level and rate of deformation) and the microstructural evolutions. Furthermore, as shown in Chapter **1**, the initial microstructure plays an important role in those evolutions.

Consequently, the approach of this chapter is to distinguish the influence of the initial microstructures and the thermomechanical parameters. To do so, two steps were implemented. The first consisted in varying only the seven initial microstructures selected in section **3.3** (listed and schematized in **Figure 3.7**), for a fixed set of thermomechanical conditions ($T$ and $\dot{\varepsilon}$). Then, based on the initial observations, two initial microstructures for each alloy were subjected to different deformation conditions (two $T$ and two $\dot{\varepsilon}$) to evaluate the effect of these parameters on the development of the deformation substructures and the distribution of the dislocation density.

To do this, double-cone samples were used, allowing the study of different strain levels from a single test. From these double-cone samples, the characterizations consisted in acquiring orientation maps by EBSD, which allow, by analysis of the measured intragranular misorientations, the evaluation of the geometrically necessary dislocation density (GND) field at the granular and intragranular scales, as well as the average dislocation density per phase (procedure described in section **2.7.5**).

## 4.1 Comparison of different initial microstructures for a given set of deformation conditions

The aim of this first series of experiments was to separate and analyze the influence of the initial state on the microstructural evolution throughout the deformation process. The thermomechanical parameters are summarized in **Figure 4.1**. The same temperatures as in section **3.2** were used (*i.e.*, 750°*C* and 950°*C* for the Ti1023 and Ti64 alloys, respectively). Each double-cone sample was submitted to the same heat treatment (prior to deformation) applied to its respective initial state (shown in **Table 2.2**). Double-cone samples were placed between the preheated compression tools and held for 10 minutes to homogenize temperature. The machine was driven at a constant tool velocity, as it was proven to provide a more homogeneous local strain rate in the double-cone samples [4]. The equivalent strain rate at the center of the sample ($\dot{\bar{\varepsilon}}$) was 0.1 $s^{-1}$ (as shown in **Figure 2.31**).

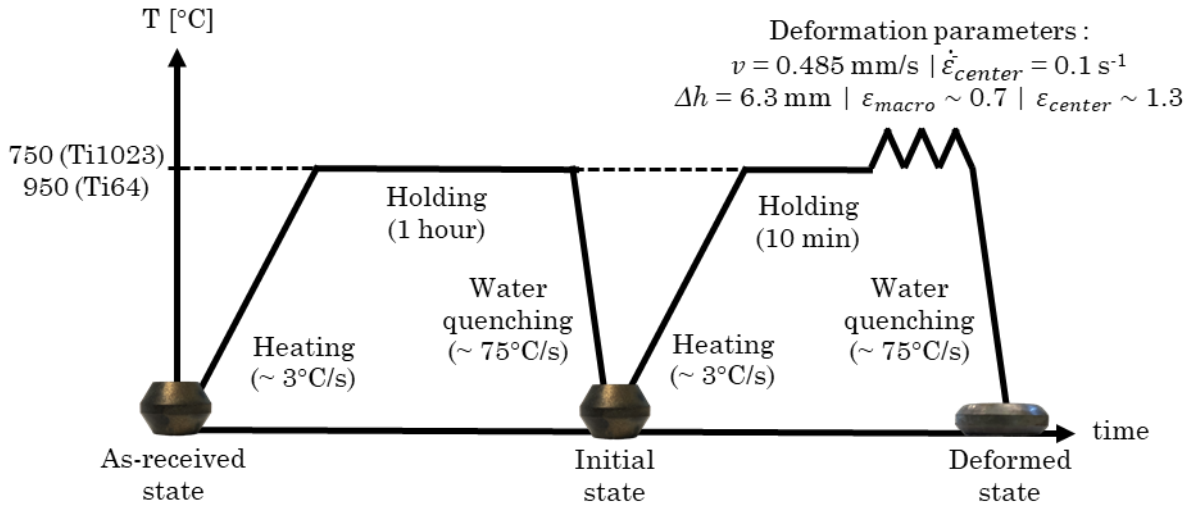



*Figure 4.1. Thermomechanical path for the compression of the double-cone samples.*

### *4.1.1 Topological evolutions*

The influence of the strain level on the microstructural evolutions was analyzed for each of the seven initial microstructures (**Figure 4.2**). As the $\beta$ grains are of the order of millimeters, they will be discussed separately through macrographs (**Figure 4.3**). The initial states are also shown in the figures for comparison.

By analyzing all $f_{\alpha_P}$ values, it is clear that there is no effect of deformation on the phase fraction, *i.e.,* no dynamic transformation was observed for the analyzed conditions. As seen in section **1.2.3.5**, this phenomenon was reported in some works [6,44–46] on the deformation of titanium alloys in the $\alpha + \beta$ domain. Nevertheless, the thermomechanical parameters applied (lower strain rate, torsion test, no holding time prior to deformation) [6,44] and the alloys were different [45,46], which may have influenced the occurrence of this dynamic transformation in other works. For the thermomechanical conditions applied in the double-cone samples (*i.e.,* 0.1 $s^{-1}$, $T\beta$ - 50°$C$ and 10-minute holding time), the fact that no difference between the $f_{\alpha_P}$ values before and after deformation is in accordance to what was shown in the work of Semiatin *et al.* [44].

Several microstructural features can be observed in these micrographs:

- **Ti1023_El$\beta$ and Ti1023_Eq:** For both Ti1023 equiaxed microstructures, similar behaviors were perceived. At $\varepsilon = 0.8$, there is a trend of $\alpha$ grain elongation and alignment perpendicular to the CD direction. With further deformation ($\varepsilon = 1.3$), no kinking or globularization was observed, just some very elongated $\alpha$ grains (but not all, being analyzed furtherly in **Figure 4.7**);
- **Ti1023_L:** At low strain levels ($\varepsilon = 0.3$), a minor $\alpha$ lath kinking is already observed, and becomes more pronounced at $\varepsilon = 0.8$. At higher deformation level ($\varepsilon = 1.3$), there is lath breakage and alignment perpendicular to CD;
- **Ti64_750°C:** A soft elongation and alignment of the globules (perpendicular to the CD) is noticed at $\varepsilon = 0.8$, being more evident with further deformation;
- **Ti64_Eq:** At $\varepsilon = 0.3$, serrated $\alpha/\beta$ phase boundaries can be observed. With higher strain levels, the elongation and alignment of the stretched globules perpendicular to the CD is also evidenced;

- **Ti64_FL:** Throughout the different strain levels, the kinking, breakage and alignment of the laths (perpendicular to the CD) is progressively observed;
- **Ti64_CL:** Similar behavior to the Ti64_FL billet is evidenced. It is interesting to indicate that the grain boundary $\alpha$ layer (in the middle of the micrograph at $\varepsilon = 0.8$) seems to be more kinked/broken than the rest, even though it is/was thicker. Furthermore, different behaviors are observed in individual grains, where those on the left of the prior-$\beta$ grain boundary contains highly kinked laths, while those on the right contains aligned ones. This is very likely to be related to the initial orientation of the laths relative to the applied strain.

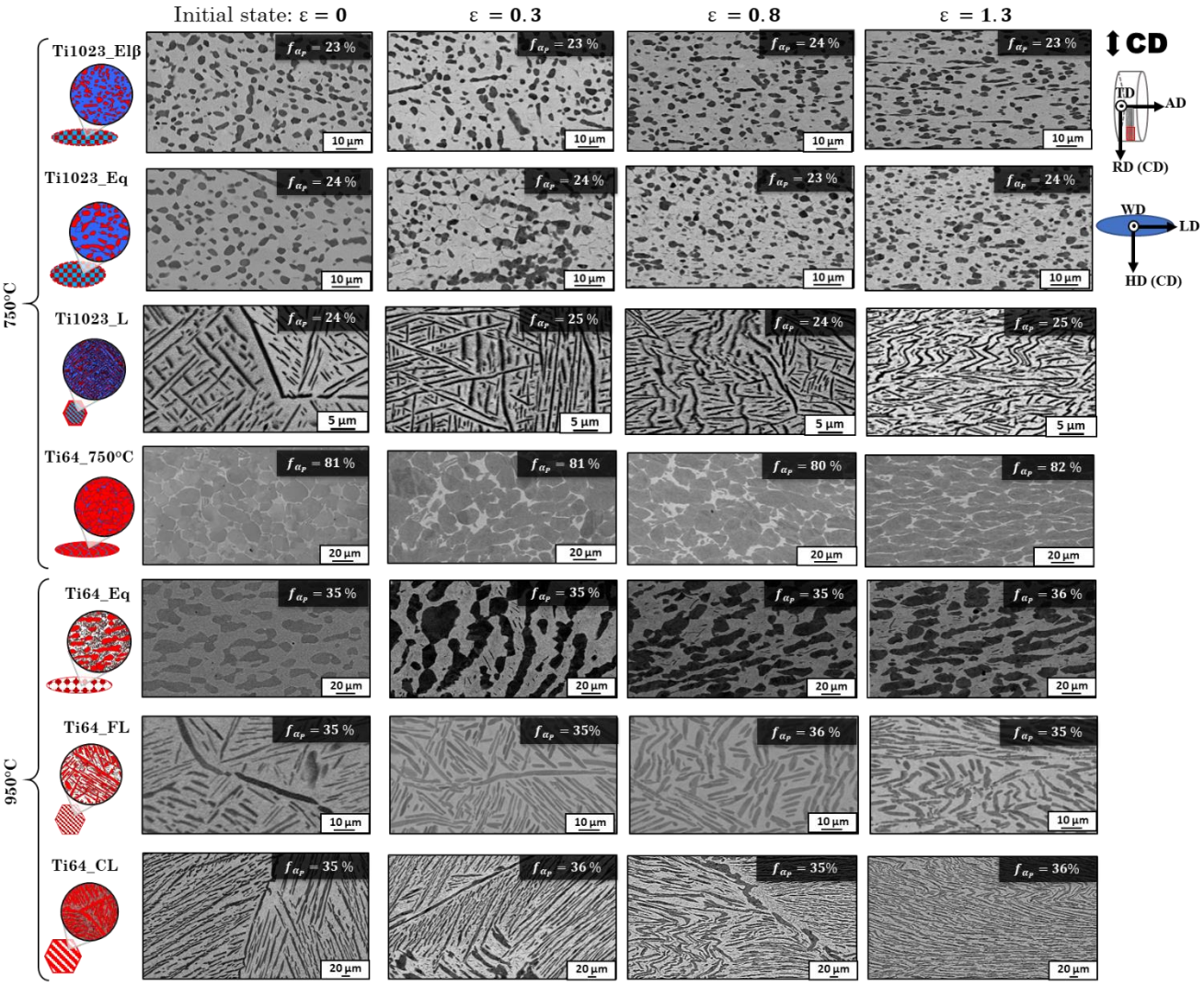



*Figure 4.2. Summary of the evolution (BSE micrographs) of the seven different initial microstructures, during hot-compression with increasing strain level, along with the respective primary α phase fractions. The equivalent strain rate ($\dot{\bar{\varepsilon}}$) at the center of the double-cone samples is 0.1 $s^{-1}$.*

To summarize, for all initial microstructures, a clear trend of alignment of $\alpha$ grains, be they lamellar or elongated nodules, is observed at high strain levels ($\varepsilon = 1.3$). Despite of the high temperatures (50°C below $T_\beta$), considered to be favorable for the globularization mechanism according to literature (**Table 1.2**), only lath kinking was observed. The observed samples have been water quenched just after

deformation, with no post deformation holding, during which the globularization phenomena have been reported [83]. The main morphological difference observed between both alloys is the presence of serrated or jagged boundaries in the Ti64_Eq (**Figure 4.2** at $\varepsilon = 0.3$), which was not observed, or much less obvious, in both equiaxed Ti1023 billets (Ti1023_El$\beta$ and Ti1023_Eq).

It is important to mention that those 2D observations give only a partial view of the microstructure. As seen in section **3.3.3**, the topology might be influenced by the analyzed section. For example, $\alpha$ laths that were cut at a certain angle regarding to their width (*i.e.,* not transversally), give a false impression of a coarser lamellae morphology. Also, elongated $\alpha$ grains that might have been cut transversally, appear as equiaxed in the micrographs. Some of those ambiguities, especially related to the lath kinking, will be addressed in section **4.1.6**.

After deformation, a first polishing step on the upper side of the double-cone samples was applied to retrieved the AD x RD plane (**Figure 4.3***a*). A slight macroscopic anisotropy was noticed in each deformed sample that had an initial microstructure with elongated $\beta$ grains (for both alloys). This anisotropy was exacerbated for the Ti64 alloy (**Figure 4.3***b* and *c*).

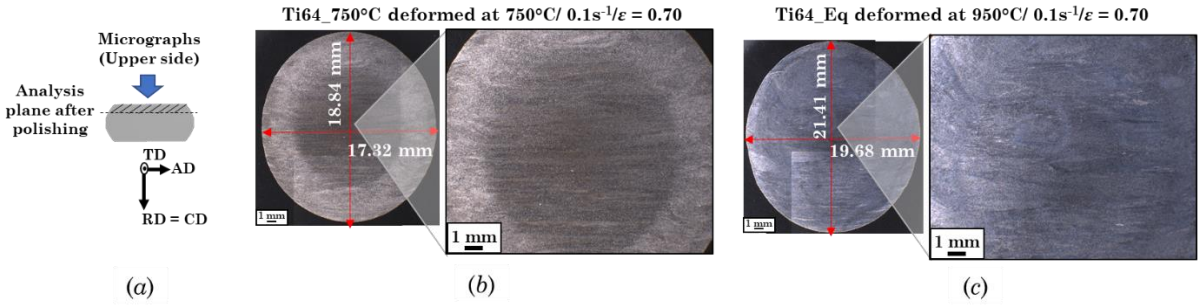



*Figure 4.3. Polishing step to retrieve the AD x RD plane showing: a) The schematic macroscopic reference; b) The upper side of a polished sample of Ti64_750°C; c) The upper side of a polished sample of Ti64_Eq.*

By analyzing **Figure 4.3**, it is clear that the sample elongates perpendicularly to the elongation direction (LD) of the prior-$\beta$ grains (or $\beta$ grains for the Ti1023). The same behavior was observed for the cylindrical samples (with elongated $\beta$ grains) after deformation. Consequently, there seems to be a macroscopic anisotropy of the sample linked to the shape of the $\beta$ grains and/or $\beta$ phase crystallographic texture.

### *4.1.2 Crystallographic texture evolution*

It is important to mention that the EBSD method is not at the right scale to discuss macroscopic texture, especially for the $\beta$ grains (of the order of millimeters). Nevertheless, tendencies in the crystallographic orientations measured at the scale of a few $\beta$ grains have been noticed throughout the deformation, as reported in this section for both phases.

#### *4.1.2.1 α phase*

The morphological behavior of $\alpha$ grain elongation and alignment perpendicular to CD has been shown for all initial microstructures at high strain level (**Figure 4.2**). To complement this information, crystallographic orientations were analyzed through pole figures (**Figure 4.4**). The orientation maps at $\varepsilon = 1.3$ are also shown in **Figure 4.5** for illustration purposes.

For the initial states ($\varepsilon = 0$), most of the microstructures seem to have no distinct $\alpha$ phase texture, except the lamellar microstructures which present a strong local texture linked to the BOR (section **1.1.4**). The $(0001)_\alpha$ planes involved in the BOR coincide with the $\{110\}_\beta$ planes. Nevertheless, for the Ti64_750°*C* and Ti64_Eq (both from the same as-received billet), there is an apparent initial texture, not corresponding to the BOR one. The former has basal planes $(0001)_\alpha$ perpendicular to the CD, while the latter has basal planes oriented ∥ CD ($(0001)_\alpha$ ∥ TD). This latter texture is maintained in the deformed states (*i.e.,* at $\varepsilon = 0.3, 0.8, 1.3$) for the Ti64_Eq.

Interestingly enough, for all the other initial microstructures (except the Ti64_750°*C*), similar texture is developed at high strain levels ($\varepsilon = 1.3$). For the lamellar billets (Ti1023_L, Ti64_FL, Ti64_CL), there is a spread of this texture by the LD-axis. This may be due to the fact explained in **Figure 2.29**, where, for the pancake shape $\beta$ grains, the WD and LD are basically equivalent. Thus, there is no distinction between those axes, as there is for the elongated $\beta$ grains. Accompanied to this texture behavior, the $\langle 11\bar{2}0\rangle_\alpha$ directions are always parallel to the CD, except for the Ti64_750°*C*.

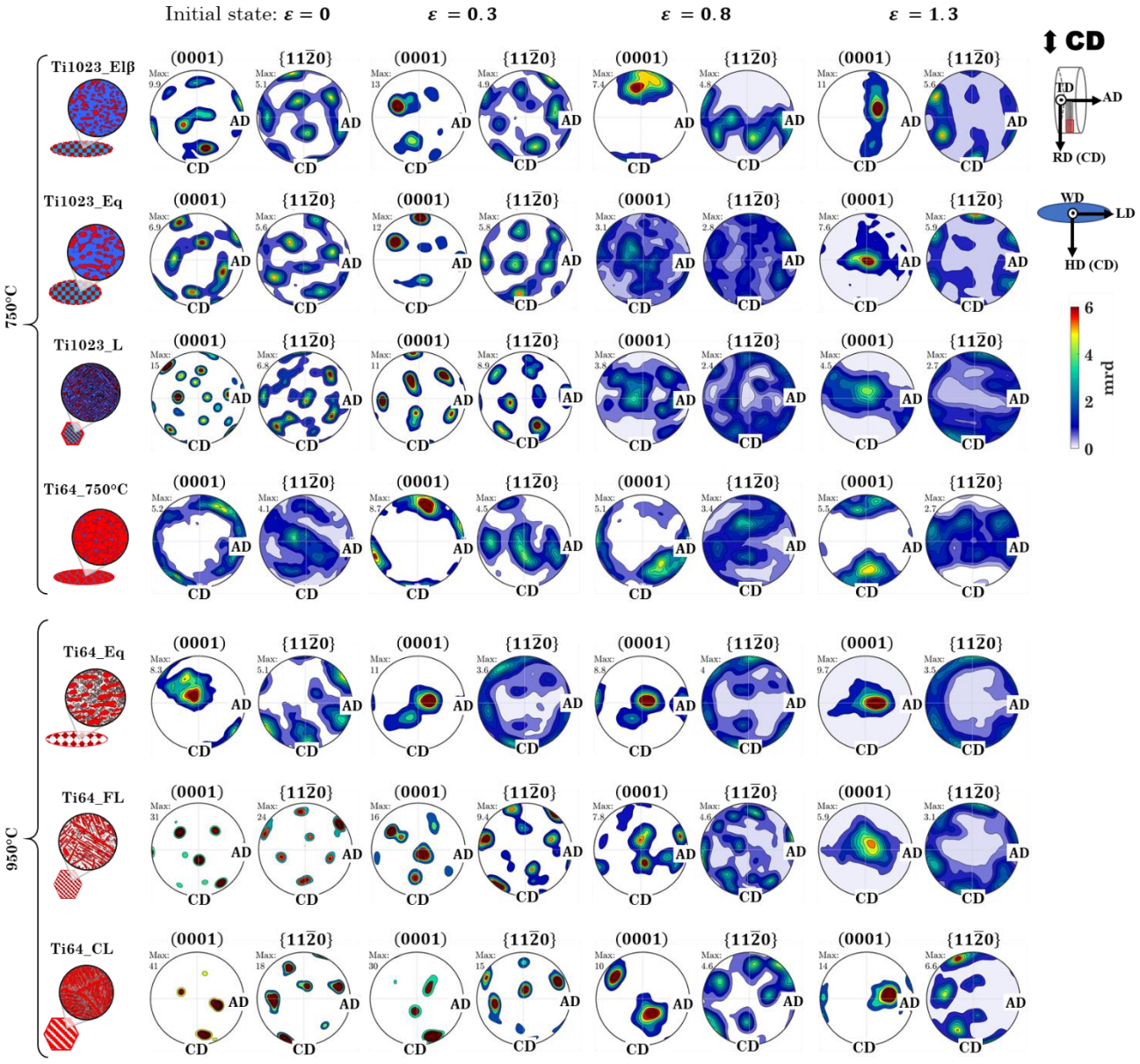



*Figure 4.4. Summary of pole figures obtained by EBSD for the α phase as a function of the initial microstructure and the strain level. The equivalent strain rate ($\dot{\bar{\varepsilon}}$) at the center of the double-cone sample is 0.1 $s^{-1}$.*

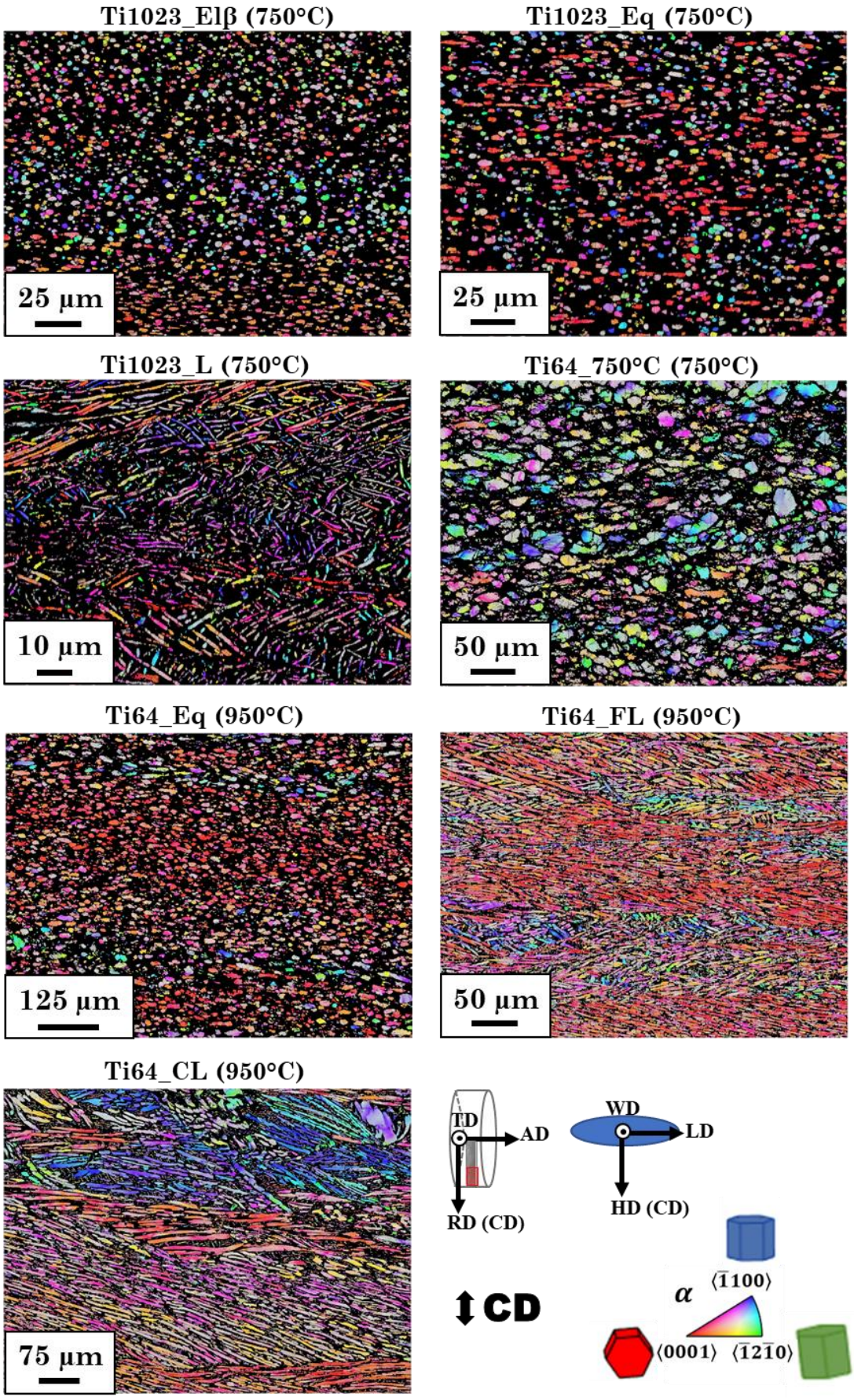



*Figure 4.5. EBSD orientation maps of the α phase with the TD-IPF color coding for all seven initial microstructures after deformation to* $\varepsilon = 1.3$ *at* $10^{-1}\ s^{-1}$.

The $\alpha$-phase texture in the deformed samples is thus in agreement with the literature [3,52], which reported that the [0001] axis tend to align with TD. However, it has been usually shown for one type of initial microstructure separately. Our results (**Figure 4.4**) suggest that there is an intrinsic behavior in the $\alpha$ phase texture, where the basal plane ($(0001)_\alpha$) tend to align parallel to the compression direction (CD), and a $\langle 11\bar{2}0 \rangle$ fiber texture along CD tends to develop (**Figure 4.6**).

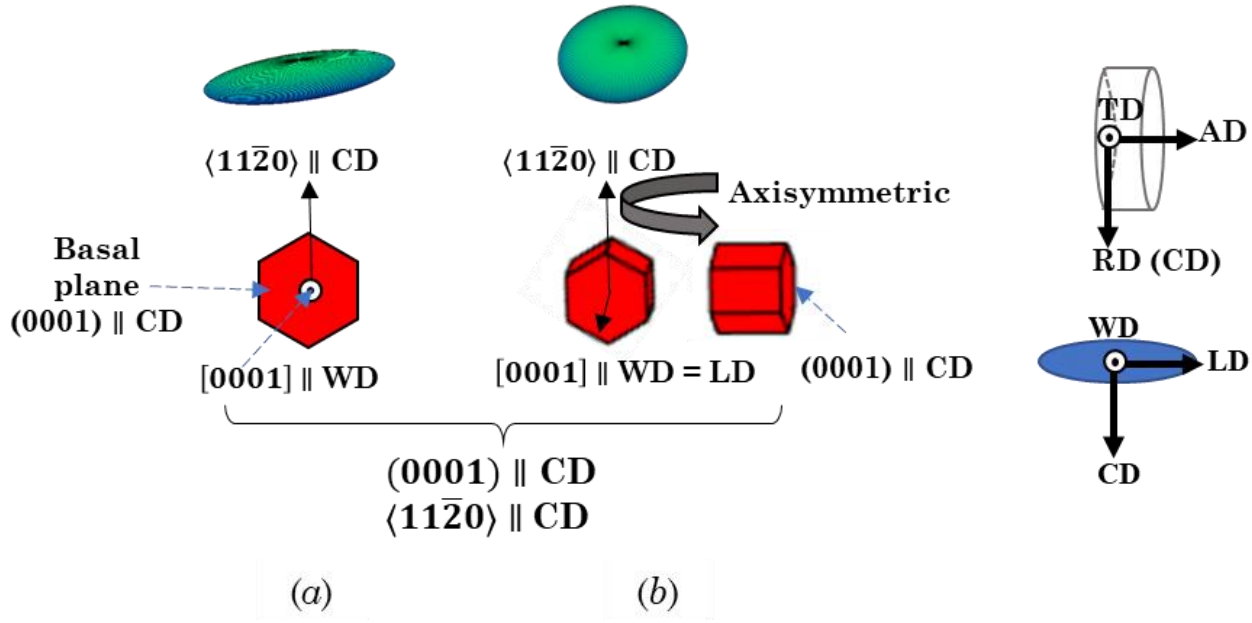



*Figure 4.6. Intrinsic behavior of the α phase according to the β grain shape: a) Cigar; b) Pancake.*

The reason why the Ti64_750°C is the only initial microstructure that does not follow this behavior could be related to the fact that it was the only one that was not deformed at $T_\beta - 50°C$, but at a much lower temperature ($T_\beta - 250°C$). At 750°C, the primary $\alpha$ phase volume fraction of the Ti64 is approximately 81%, being closer to a $\alpha$ alloy than a $\alpha$+$\beta$ alloy, thus the behavior of the microstructure is different.

Furthermore, it is important to mention that this intrinsic behavior of the $\alpha$ phase, observed during deformation at $T_\beta - 50°C$, seems to be independent of the orientation of the $\beta$ phase, as the same trends were observed in the texture evolution of the $\alpha$ phase inside different $\beta$-grain orientations.

Considering the elongation and alignment behavior observed for the initially equiaxed $\alpha$ grains, it is furthermore possible to correlate the morphological and orientation evolutions. An aspect ratio of 2.5 was used as a threshold to separate the most elongated grains. The elongated grains are shown in **Figure 4.7**, with TD-IPF color coding.

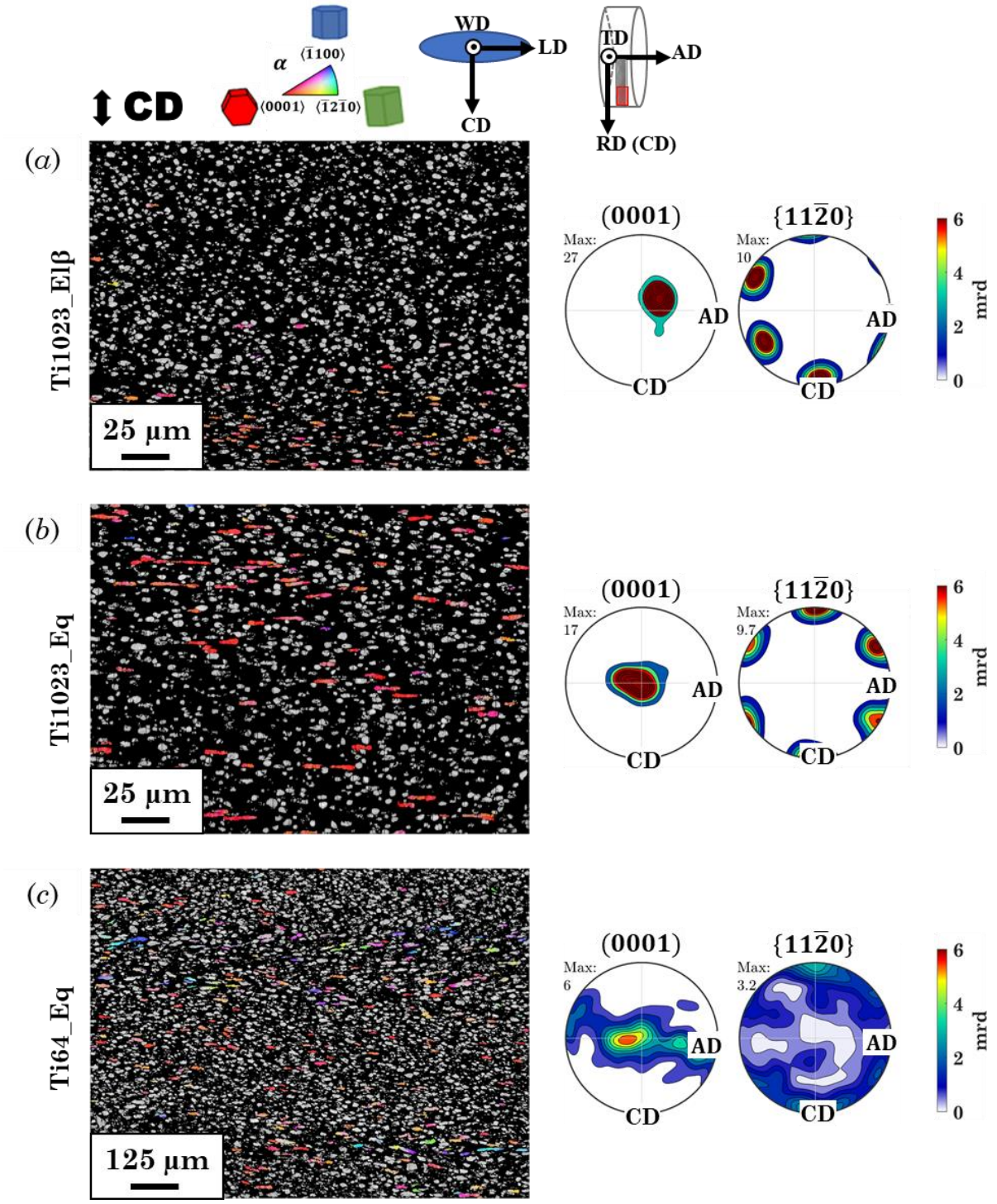



*Figure 4.7. EBSD orientation maps (TD-IPF color coding) and pole figures for the α grains with high aspect ratio (>2.5) for the samples: a) Ti1023_Elβ; b) Ti1023_Eq; c) Ti64_Eq deformed to ε = 1.3 at $T_\beta$ – 50°C/$10^{-1}$ $s^{-1}$.*

For both alloys at $T_\beta$-50°C with equiaxed α grains, the grains that are highly elongated present a very strong crystallographic texture (colored in red), *i.e.*, with basal plane (0001) ∥ CD. By analyzing the pole figures, it is possible to observe that the ⟨11$\bar{2}$0⟩ directions are also parallel to CD. This is the same crystallographic texture described in **Figure 4.6**.

### *4.1.2.2 β phase*

Concerning the $\beta$ phase, crystallographic orientation has been analyzed through CD inverse pole figures (**Figure 4.8**), as described in section **2.7**. The correlation between microstructure evolution and strain level can only be analyzed for the Ti1023 alloy, as the $\beta$ phase reconstruction for the Ti64 alloy could be performed only for the initial states. As mentioned in section **2.7**, due to its scale, the $\beta$ phase crystallographic orientations was analyzed for two or three different grains only. Consequently, the plotted textures cannot be considered representative of the whole microstructure. For the initial states, local textures assessed by EBSD are only the result of the very low number of $\beta$ grains, and should not be interpreted.

On the other hand, similar trends in $\beta$-grain orientations are found after deformation (**Figure 4.9**). It is worth mentioning that a higher number of initial $\beta$ grains are included in EBSD maps of deformed states, as the latter flattened during deformation. For the Ti1023 alloy, at a high strain level ($\varepsilon$ =1.3), the $\beta$ phase develops a ⟨001⟩ ∥ CD texture component and a weaker ⟨$\bar{1}$11⟩ ∥ CD texture component. Similar behavior was reported by [52] for the Ti64 alloy. The strongest texture is observed for the Ti1023_El$\beta$ billet, which has a starting microstructure with highly elongated $\beta$ grains. This is an expected result, as the crystallographic texture tends to increase with increasing deformation.

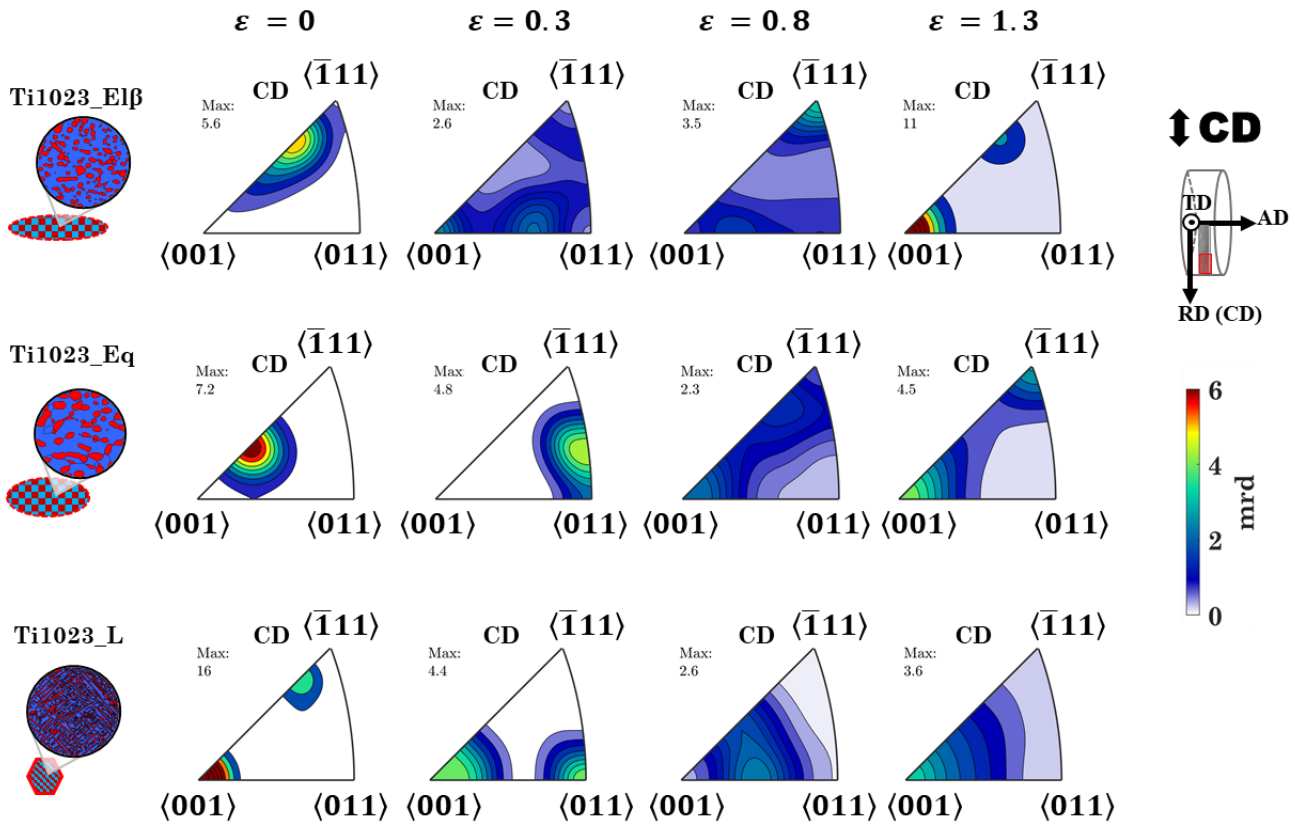



*Figure 4.8. CD-IPF for the β phase of the three different initial Ti1023 microstructures after deformation at $T_\beta$ – 50°C, as a function of the strain level.*

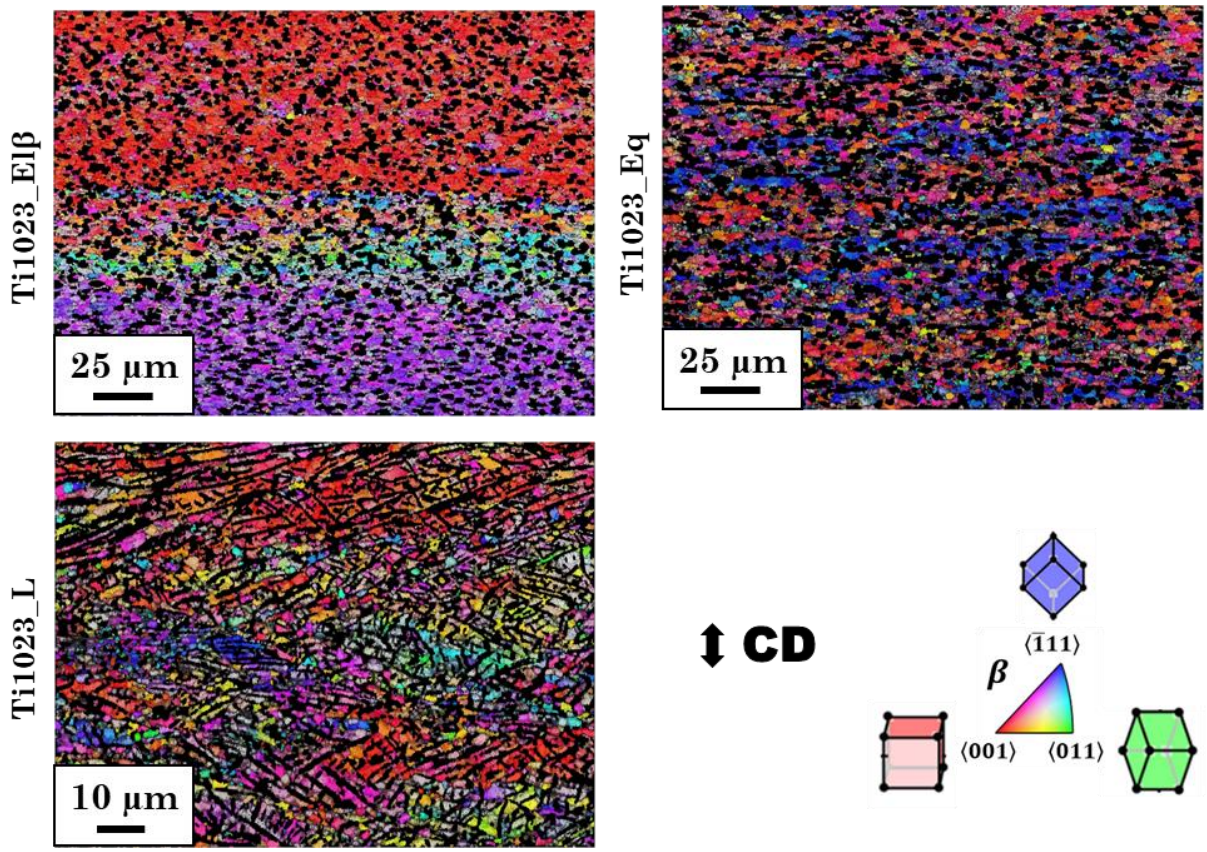



*Figure 4.9. EBSD orientation maps of the β phase, with the CD-IPF color coding, for the three different Ti1023 microstructures, after deformation to* $\varepsilon = 1.3$ *at* $T_\beta - 50°C / 10^{-1}\ s^{-1}$.

### *4.1.3 LAGB and HAGB density*

The analysis explained in section **2.7.3**, regarding the cumulative analysis of the $\rho_{GB}$ (LAGB and HAGB), was performed for all initial microstructures as a function of the strain level. Qualitative and quantitative results are separately presented for the Ti1023 and Ti64 alloys in sections **4.1.3.1** and **4.1.3.2**, respectively.

#### *4.1.3.1 Ti1023 alloy*

The Ti1023 alloy offers the possibility of analyzing the effect of thermomechanical parameters on both phases. The EBSD maps obtained for the three strain levels selected in the double-cone samples are gathered in **Figure 4.10**.

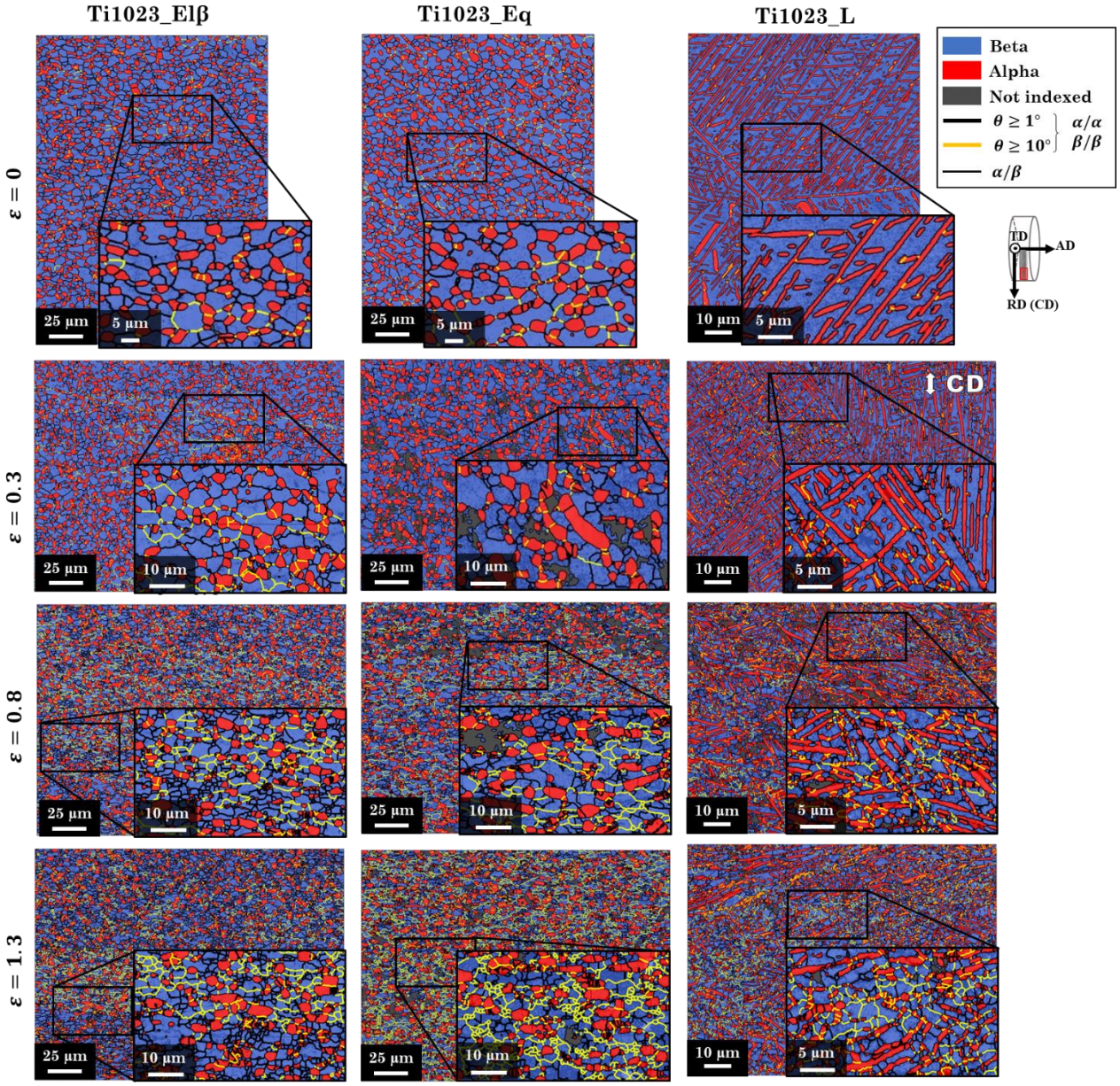



*Figure 4.10. EBSD maps showing LAGBs and HAGBs in the α and β phases of the Ti1023 microstructures deformed at 750°C/$10^{-1}$ $s^{-1}$, as a function of the equivalent strain level.*

By analyzing **Figure 4.10**, it appears that:

- **Ti1023_El*β*:** At $\varepsilon = 0.3$, few HAGB are observed in both phases, especially near *β*-*β* grain boundaries, which is not observed at the initial state (see **Figure 4.11** for more details). With increasing deformation ($\varepsilon = 0.8$), there is a strong increase in the HAGB density, especially in the *β* phase. This seems to be due to the transition of LAGB into HAGB (*i.e.*, continuous dynamic recrystallization). It is interesting to note that there are regions where the *β* phase has higher HAGB density, in contrast to others. Similar behavior is observed at $\varepsilon = 1.3$, where there is a heterogeneous continuous dynamic recrystallization, dependent of the zone. The reason behind this behavior is discussed in **Figure 4.11**, showing that it seems to be linked to the orientation of the *β* grains. For both strain levels (0.8 and 1.3), the *β*

grains that are oriented with the ⟨110⟩ ∥ CD, are the ones which presented higher continuous dynamic recrystallization (inside the yellow rectangles);

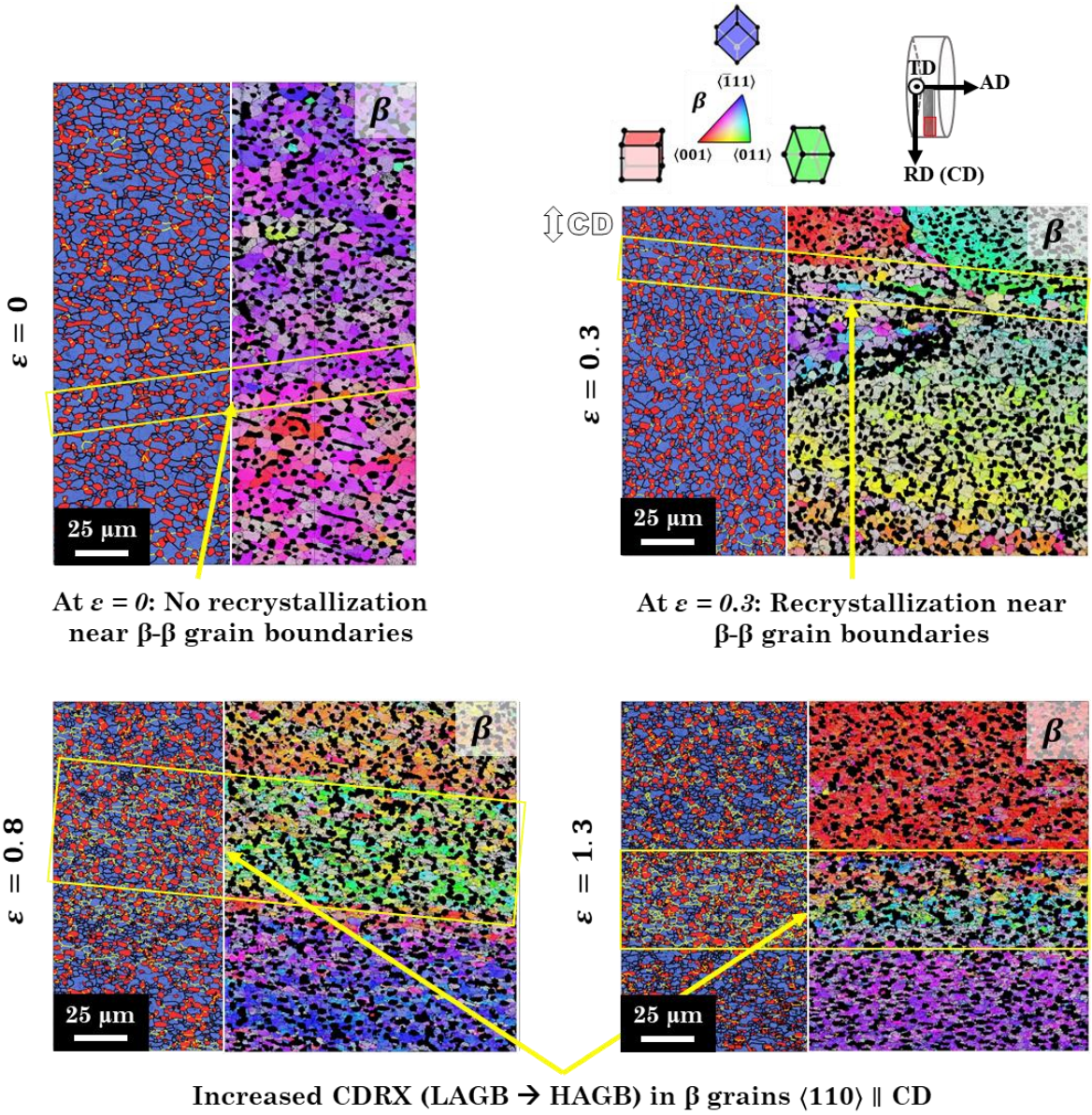



*Figure 4.11. EBSD maps showing both LAGBs and HAGBs (same color coding as **Figure 4.10**), and also the β phase orientation with the CD-IPF color coding, for the Ti1023_Elβ at different stain levels (from 0 to 1.3) at 750°C/$10^{-1}$ $s^{-1}$.*

- **Ti1023_Eq:** At 0 and 0.3 strain level, few HAGB can be noticed in both the phases (**Figure 4.10**). At $\varepsilon = 0.8$, there is a strong increase in the HAGB density, especially in the $\beta$ phase, which presented already LAGB even at $\varepsilon = 0$ . Differently from the Ti1023_El$\beta$, the continuous dynamic recrystallization observed is homogeneous within the $\beta$ grains. With increasing deformation, HAGB can be observed in the whole $\beta$ phase, while for the $\alpha$ phase it has only been slightly increased compared to inferior strain levels (**Figure 4.10**). To verify that this behavior is not linked to the fact that only one $\beta$ grain was observed in the analyzed regions, the same analysis as for the previous microstructure was performed (**Figure 4.12**).

Confirming then that EBSD maps at $\varepsilon = 0.8$ and 1.3 included several $\beta$ grains for this microstructure also. Thus, the continuous dynamic recrystallization when the $\beta$ grains are not initially highly elongated seems to be less dependent of the grain orientation.

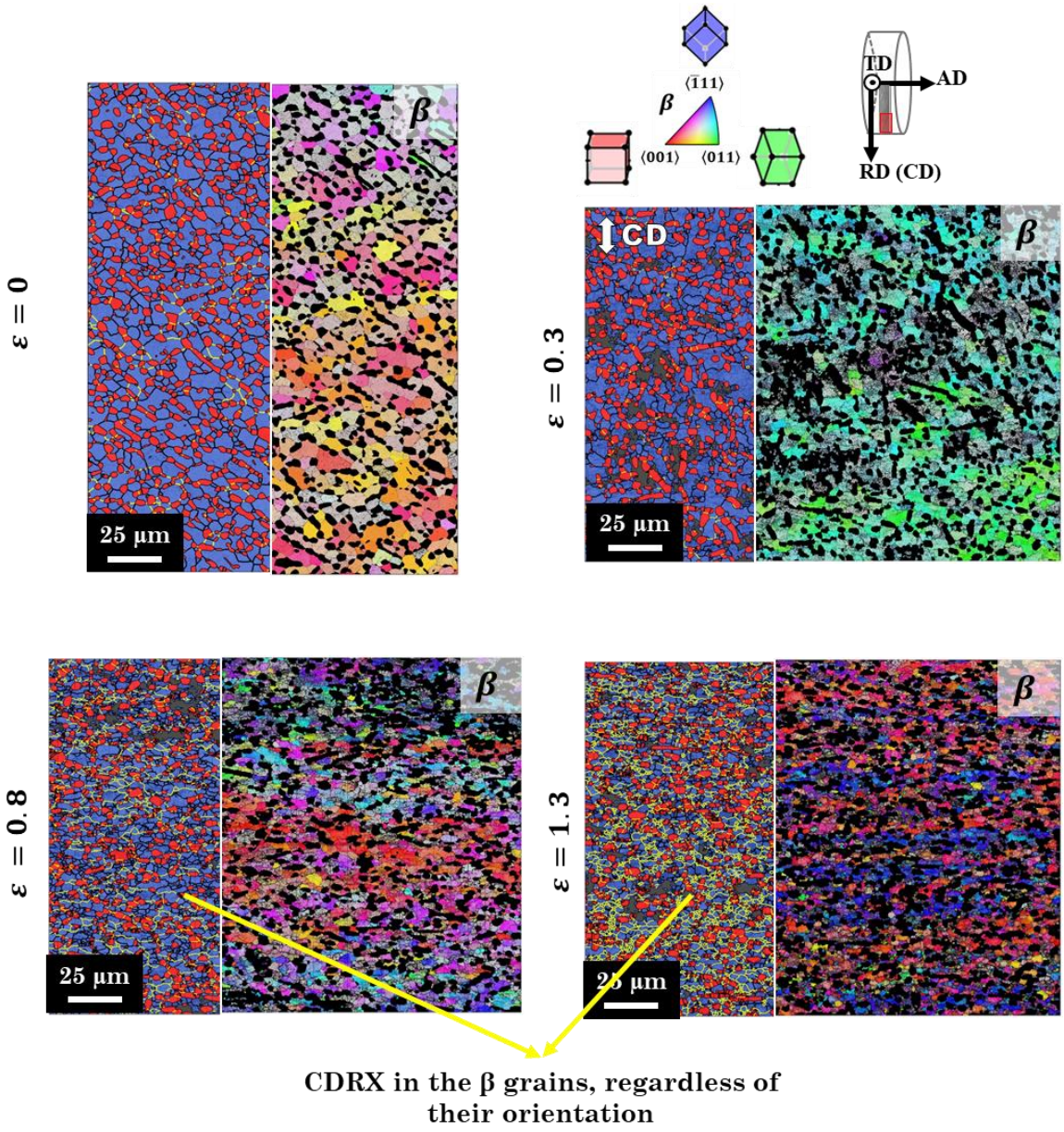



*Figure 4.12. EBSD maps showing both LAGBs and HAGBs (same color coding as **Figure 4.10**), and also the β phase orientation with the IPF color coding by CD, for the Ti1023_Eq at different stain levels (from 0 to 1.3) at 750°C/$10^{-1}$ $s^{-1}$.*

- **Ti1023_L:** At $\varepsilon = 0.3$, the $\alpha/\alpha$ LAGBs (black lines) appear mainly at the $\alpha$ laths at the grain boundaries ($\alpha_{GB}$), inside the yellow rectangles in **Figure 4.13**. With increasing strain level, both phases appear to have more HAGB. At $\varepsilon = 1.3$ (**Figure 4.10**), differently from the previous equiaxed microstructures, it seems that the HAGB density is similar for both phases. Furthermore, continuous dynamic recrystallization seems to occur quite homogeneously in the $\beta$ phase all over the scanned regions.

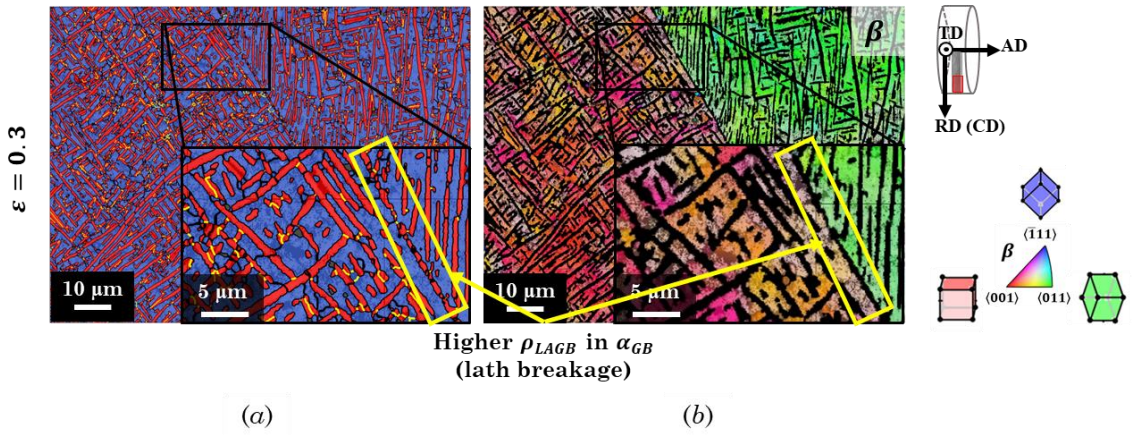



*Figure 4.13. EBSD map of the Ti1023_L deformed to ε = 0.3 at 750°C/10$^{-1}$ s$^{-1}$, showing: a) Both LAGBs and HAGBs (same color coding as **Figure 4.10**); b) β phase orientation with the CD-IPF color coding.*

The quantitative analysis of LAGBs and HAGBs (explained in section **2.7.3**) for the Ti1023 alloy is summarized in **Figure 4.14**, restricted to $\alpha/\alpha$ and $\beta/\beta$ boundaries.

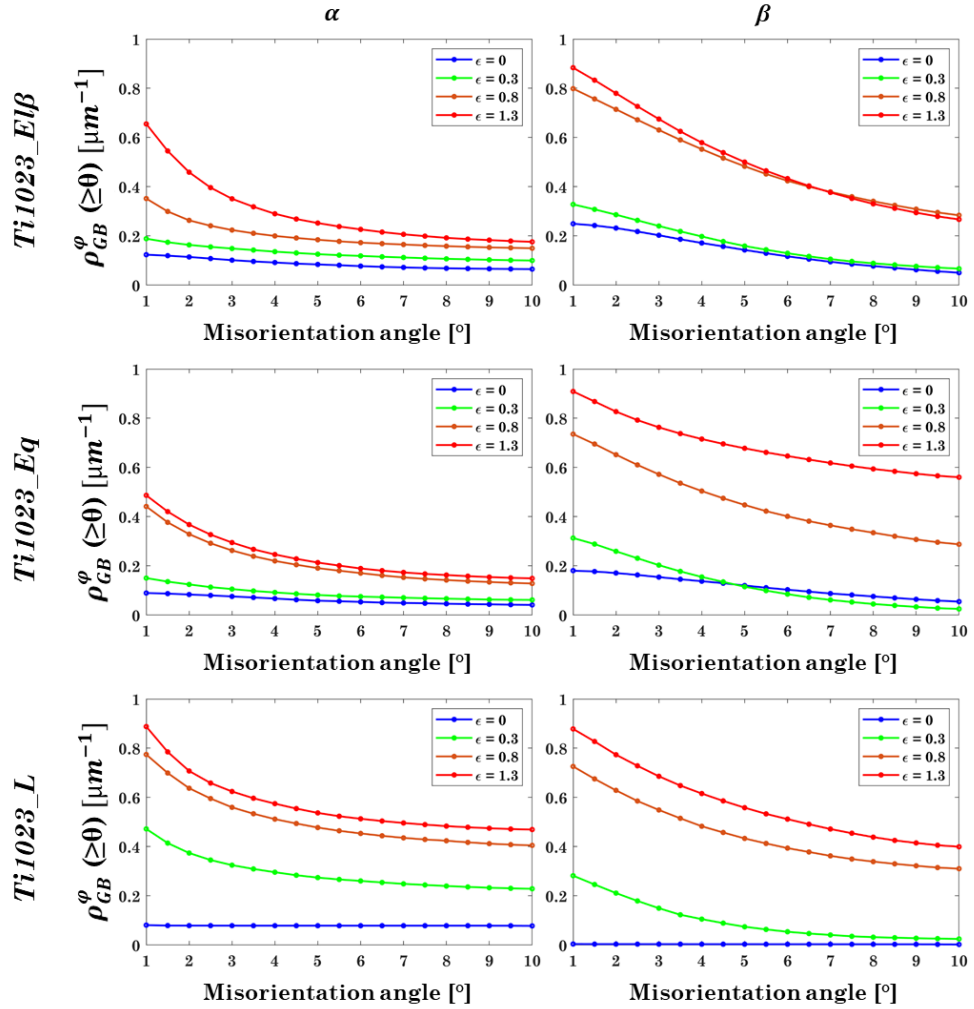



*Figure 4.14. LAGB and HAGB density cumulative analysis for both phases and at different stain levels at 750°C/10$^{-1}$ s$^{-1}$ of the Ti1023 alloy with different initial microstructures.*

For the three Ti1023 initial microstructures, the $\alpha$ phase has a similar behavior. There is a tendency of LAGB with very low misorientation angles (≤ 3°), as it can be observed from the steep slope of the curves, especially at $\varepsilon = 1.3$. For the lamellar microstructure (Ti1023_L), there is a higher density of $\alpha/\alpha$ HAGB (≥ 10°), thus a higher $\rho_{GB}^{\alpha}$. It seems to be harder to form $\alpha/\alpha$ HAGB in microstructures with initial $\alpha$ equiaxed grains, as they have already been highly deformed.

For the $\beta$ phase, different behaviors can be noticed:

- **Ti1023_El$\beta$:** Between $\varepsilon = 0$ and 0.3, there is a slight increase in $\beta/\beta$ LAGB density, while the $\beta/\beta$ HAGB one is maintained. At 0.8 strain level, there is a significant rise in the $\rho_{GB}^{\beta}$, which is consistent with the heterogenous continuous dynamic recrystallization observed in **Figure 4.10**. Then, there is a further increase in the $\beta/\beta$ LAGB density at $\varepsilon = 1.3$, but the $\beta/\beta$ HAGB density is unchanged;
- **Ti1023_Eq:** Similar behavior of the Ti1023_El$\beta$ is observed. However, from 0.8 to 1.3 strain level, there is a higher increase in the HAGB density, consistent with the homogeneous continuous dynamic recrystallization of the $\beta$ phase (see **Figure 4.10**);
- **Ti1023_L:** At low strain levels, the $\alpha$ phase seems to be already substructured, mainly at the grain boundaries ($\alpha_{GB}$), as highlighted in **Figure 4.13**. With further deformation, the same rise remarked on the equiaxed cases (from 0.3 to 0.8 strain level) is observed, due to the $\beta$ phase continuous dynamic recrystallization (**Figure 4.10**). It is worth mentioning that in this microstructure, at $\varepsilon = 1.3$, both phases achieve very similar $\rho_{GB}$ values.

Consequently, it seems that in equiaxed morphologies of the Ti1023, the formation of substructures is privileged in the $\beta$ phase, while for lamellar microstructures, both phases are equally substructured.

#### *4.1.3.1.1 Quantification of α/β boundaries respecting BOR for the Ti1023 microstructures*

After analyzing the $\alpha/\alpha$ and $\beta/\beta$ boundaries, the $\alpha/\beta$ boundaries were also analyzed in terms of the Burgers orientation relationship. The fraction of $\alpha/\beta$ boundaries that corresponds to the BOR (with a 5° tolerance) was obtained according to the procedure explained in section **2.7.2** ($f_{GB_{\alpha/\beta}}^{BOR}$) for the Ti1023 alloys (**Figure 4.15**). For the lamellar microstructure, obtained through cooling from the $\beta$ domain, almost all $\alpha/\beta$ boundaries respect the BOR at $\varepsilon = 0$ (99%), as expected. By analyzing the zoomed area of the Ti1023_L at $\varepsilon = 0$, the only $\alpha/\beta$ boundaries that do not respect the BOR are the ones at the $\beta/\beta$ grain boundaries. The $\alpha$ phase at these zones ($\alpha_{GB}$) respect the BOR with only one of the two adjacent $\beta$ grains. For the equiaxed cases, the forging route was followed to obtain an initial equiaxed microstructure, obviously reduced the $f_{GB_{\alpha/\beta}}^{BOR}$. The billet that has more elongated $\beta$ grains, has lower $f_{GB_{\alpha/\beta}}^{BOR}$. This is also consistent with the forging route, as more deformation was applied to this billet to obtain a smaller diameter (see **Table 2.1**).

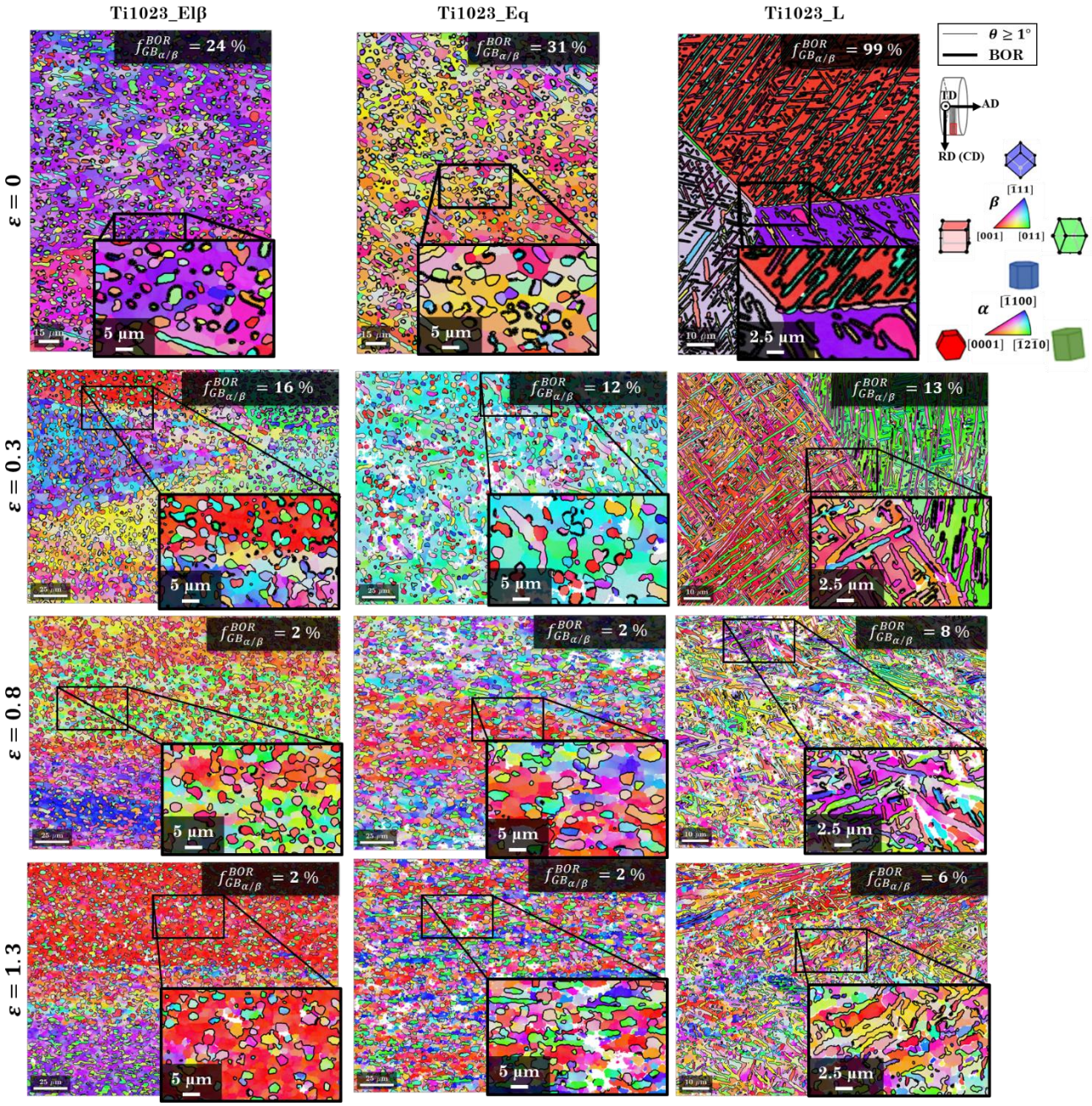



*Figure 4.15. EBSD orientation map, CD-IPF, of the three Ti1023 microstructures as a function of the strain level, showing all α/β grain boundaries (thin black line) and the BOR α/β grain boundaries (thick black line).*

At $\varepsilon = 0.3$ in **Figure 4.15**, the three different microstructures have similar fractions of BOR boundaries and much lower than in initial states (at $\varepsilon = 0$). In all three microstructures deformed to $\varepsilon = 0.3$, the $f_{GB_{\alpha/\beta}}^{BOR}$ is now only 12-16%. With further deformation ($\varepsilon = 0.8$), the equiaxed microstructures achieved $f_{GB_{\alpha/\beta}}^{BOR}$ of about 2% and stagnated at this very low value. In contrast, the decrease of the lamellar Ti1023_L at $\varepsilon = 0.8$ is less pronounced. The reason for this decrease in $f_{GB_{\alpha/\beta}}^{BOR}$ is likely to be related to dislocation accumulation along the $\alpha/\beta$ interfaces, which changes their misorientation.

### *4.1.3.2 Ti64 alloy*

The results for the Ti64 alloy are gathered in **Figure 4.16** and **Figure 4.17** for qualitative analysis of the equiaxed and lamellar microstructures, respectively.

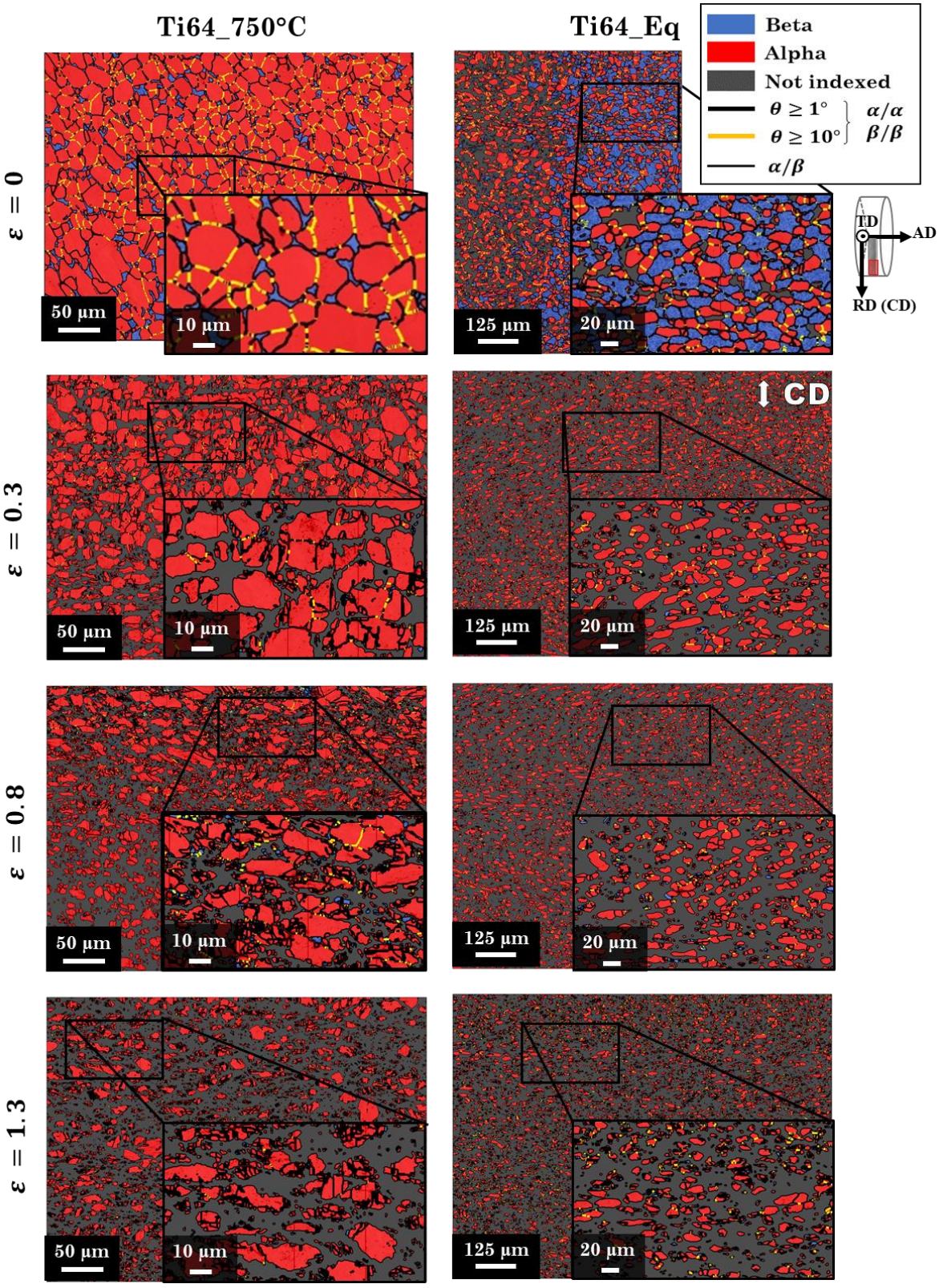



*Figure 4.16. EBSD maps showing the LAGBs and HAGBs in the α and β phases of the equiaxed Ti64 microstructures, as a function of the strain level. Deformation parameters are 950°C and 750°C (for the Ti64_750°C), $10^{-1}$ $s^{-1}$.*

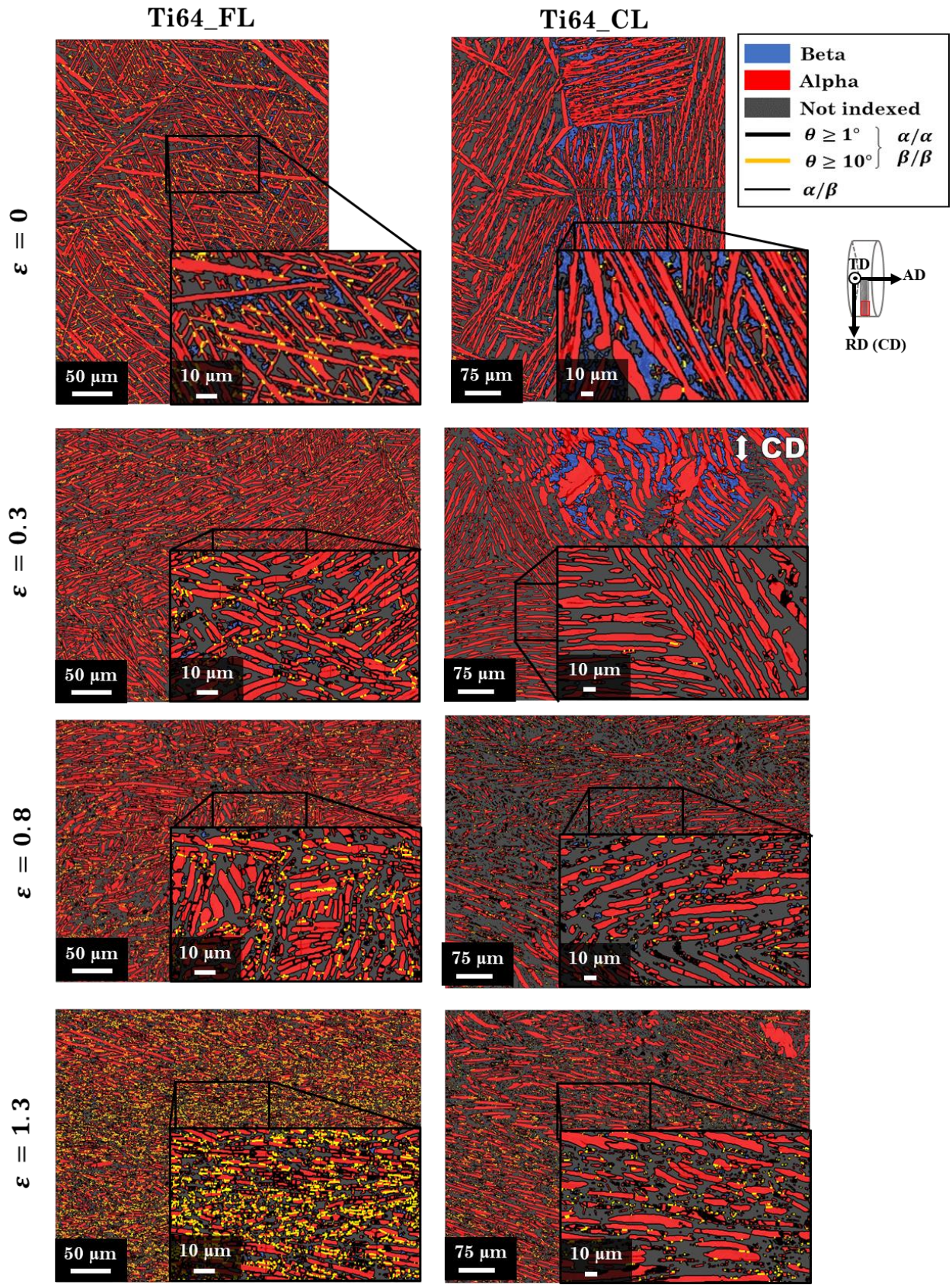



*Figure 4.17. EBSD maps showing the LAGBs and HAGBs in the α and β phases of the lamellar Ti64 microstructures, as a function of the strain level. Deformation parameters are 950°C and 750°C (for the Ti64_750°C), $10^{-1}$ $s^{-1}$.*

The $\beta$ phase is also shown on **Figure 4.16** and **Figure 4.17** to illustrate how much it could be reconstructed from the secondary $\alpha$ variants measured (see section **2.7.1**). Some zones are quite well reconstructed (*e.g.,* Ti64_CL at $\varepsilon = 0.3$), but overall the $\beta$ phase information could not be retrieved well enough to allow for meaningful interpretations. By analyzing **Figure 4.16** and **Figure 4.17**, few HAGB are observed in the $\alpha$ phase for few cases. The higher HAGB density is obtained in the Ti64_FL at high strain levels ($\varepsilon = 1.3$), see **Figure 4.17**. This observation is in accordance to what is reported in the literature regarding globularization (section **1.2.3.2**), which was reported to be promoted by thinner lath width.

To better analyze the distribution of HAGB in the $\alpha$ grains, two EBSD maps with higher spatial resolutions (step size of 200 $nm$) were performed for the Ti64_Eq (**Figure 4.18**) and Ti64_CL (**Figure 4.19**) microstructures after deformation at 950°$C$/ $10^{-1}$ $s^{-1}$/ 1.3 strain level.

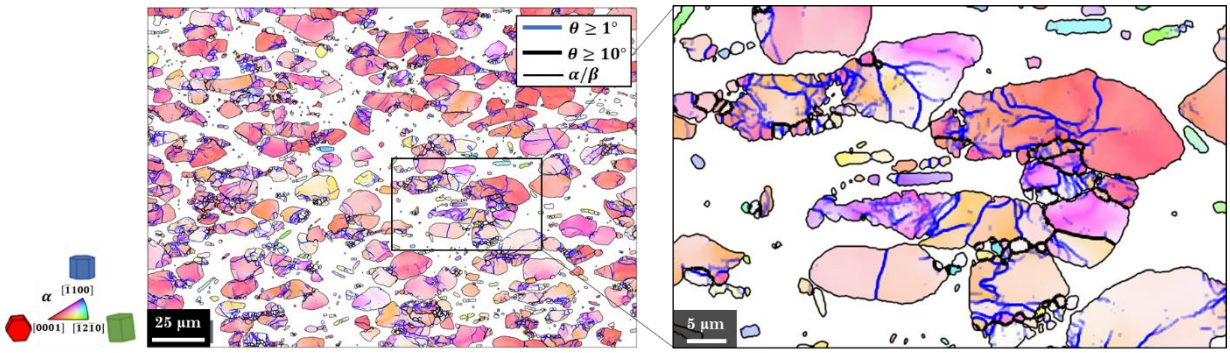



*Figure 4.18. TD-IPF map of the α phase, showing the distribution of α/α LAGBs (blue boundaries) and HAGB (thick black boundaries) in the deformed Ti64_Eq microstructure.*

**Figure 4.18** shows that recrystallization takes place near the $\alpha/\alpha$ and $\alpha/\beta$ grain boundaries (small equiaxed grains surrounded by black boundaries). This recrystallization mechanism is consistent with the one described in [41] as an iso-stress continuous dynamic recrystallization (section **1.2.3.3**).

However, according to the diagram in **Figure 1.24**, the thermomechanical parameters applied (*i.e.,* 950°$C$ and $10^{-1}$ $s^{-1}$) would generate an iso-strain mode. In this case, continuous dynamic recrystallization (HAGB) should be observed inside the $\alpha$ grains, but mainly formation of α/α LAGBs (blue boundaries) is seen in their interior **Figure 4.18**.

On the other hand, the formation of substructures (thus subsequent continuous dynamic recrystallization) seems to be dependent on the grain orientation (as reported in [41]). It appears that the grains with the basal plane parallel to the CD are the ones with higher α/α LAGB density (blue boundaries). In **Figure 4.19** is also possible to observe the formation of HAGBs, especially in the grains with that specific crystallographic orientation. This apparent trend is further analyzed and explained in section **4.1.4**.

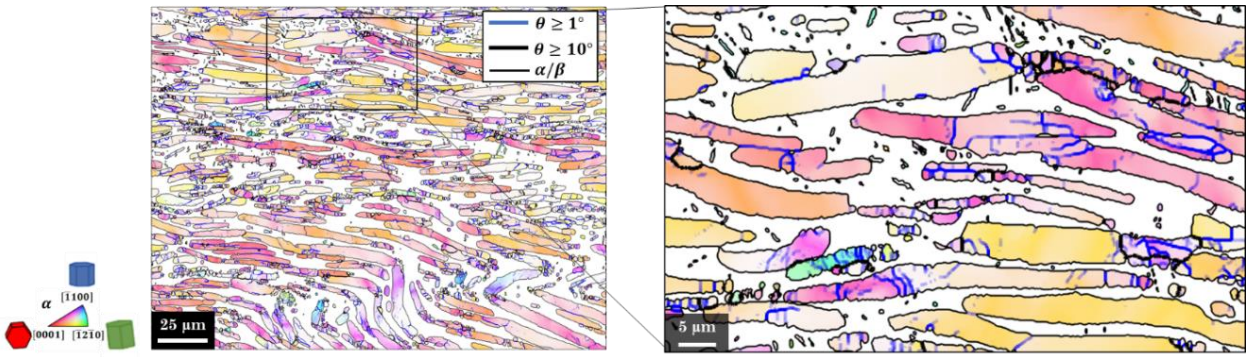



*Figure 4.19. TD-IPF map of the α phase, showing the distribution of α/α LAGB (blue boundaries) and HAGB (thick black boundaries) in the deformed Ti64_CL.*

The quantitative analysis of α/α LAGBs and HAGBs for the Ti64 alloy (similar to the one presented in section **4.1.3.1**) is summarized in **Figure 4.20**.

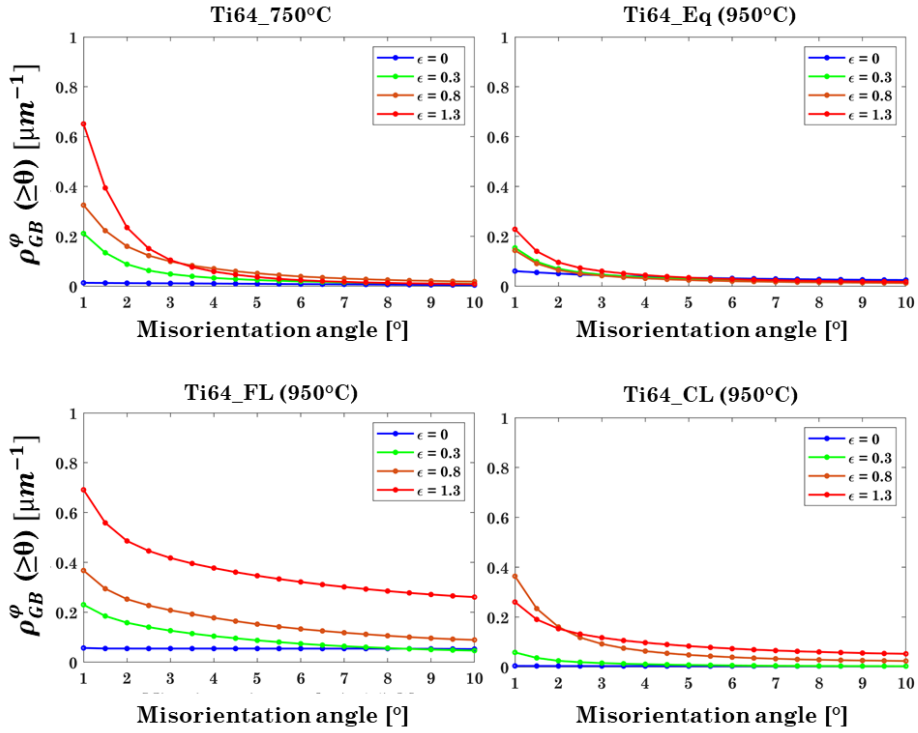



*Figure 4.20. LAGB and HAGB density cumulative analysis for the α phase, at different stain levels, of the Ti64 alloy with different initial microstructures.*

The $\alpha$ phase has a similar behavior in the two equiaxed microstructures (Ti64_750°C and Ti64_Eq). Few HAGBs are observed throughout deformation. This seems to be related to the fact that recrystallization takes place mostly near $\alpha/\alpha$ and $\alpha/\beta$ grain boundaries, forming very small equiaxed grains (~1 $\mu m$), as seen in **Figure 4.18** and **Figure 4.19**. On the other hand, the LAGB density increases significantly with deformation, especially for the Ti64 alloy deformed at 750°C.

For the two lamellar microstructures (Ti64_FL and Ti64_CL), it is clear that fine laths promote high recrystallization of the $\alpha$ phase. Interestingly, the total value of $\rho_{GB}$ for the Ti64_CL at $\varepsilon = 0.8$ is higher than at $\varepsilon = 1.3$. However, looking at the right side of the curve (at 10°), the HAGB level is higher at 1.3 strain level. This could be explained by the local formation of HAGBs (**Figure 4.19**).

#### 4.1.3.2.1 *Quantification of α/β boundaries respecting BOR for the Ti64 microstructures*

After analyzing the $\alpha/\alpha$ and $\beta/\beta$ boundaries, the $\alpha/\beta$ boundaries were also analyzed in terms of the Burgers orientation relationship. To better index the fine secondary $\alpha$ laths ($\alpha_S$) in the Ti64 microstructures, a higher magnified EBSD map was acquired for the Ti64_Eq (x250) and Ti64_CL (x250). For the Ti64_FL, the indexing of $\alpha_S$ could not be improved after enhancing magnification or even applying an additional heat treatment (10min-holding at 650°C, followed by WQ).

The reconstructed EBSD maps, for the initial states of the Ti64_750°C, Ti64_Eq and Ti64_CL microstructures, are shown in **Figure 4.21**, with their respective $f_{GB_{\alpha/\beta}}^{BOR}$ values.

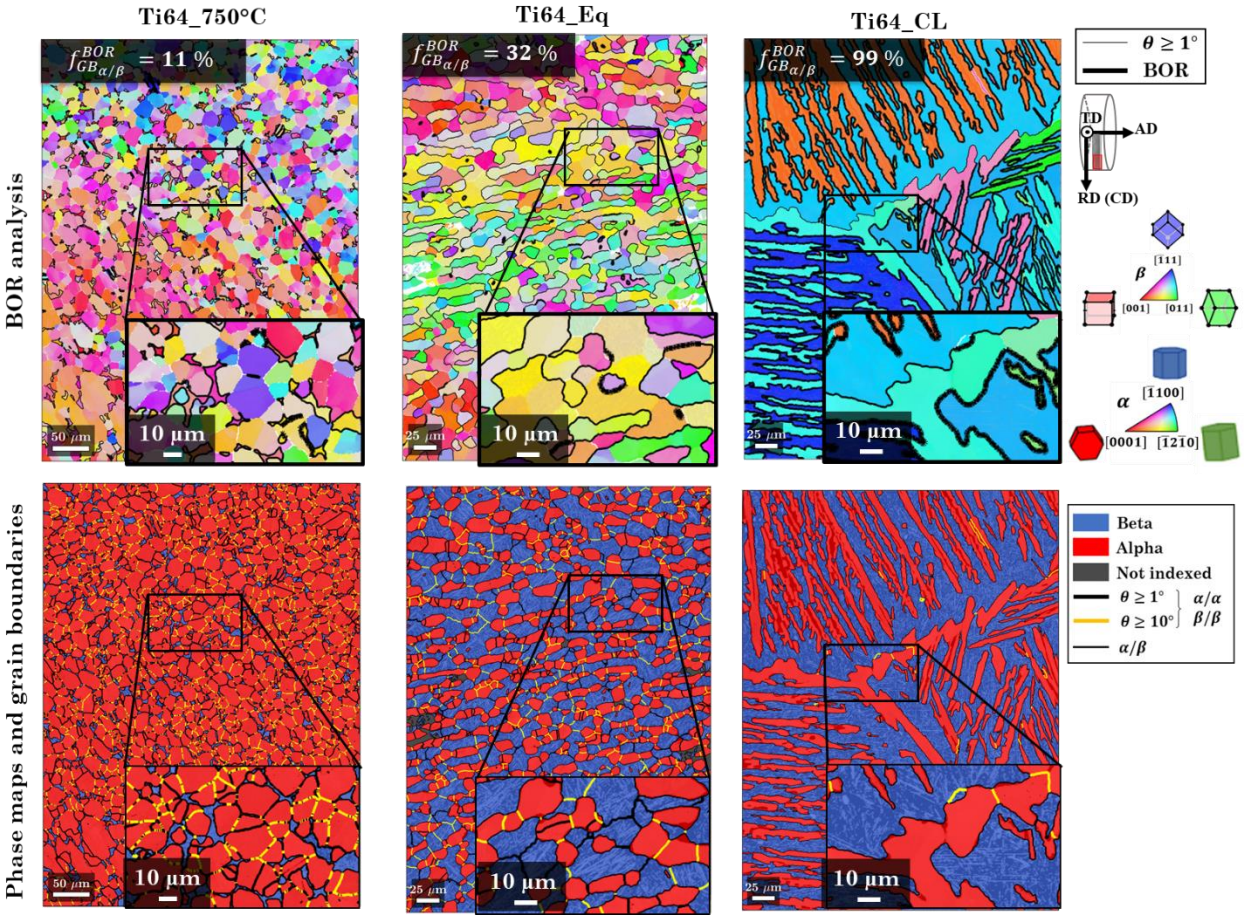



*Figure 4.21. EBSD orientation maps (above), CD-IPF for both phases, of the three Ti64 initial microstructures, showing all α/β grain boundaries (thin black line) and the BOR α/β grain boundaries (thick black line). EBSD phase maps are also shown below for better distinction of α and β phases.*

For the Ti64_CL, a complete reconstruction of the parent $\beta$ phase could be performed, showing a $f_{GB_{\alpha/\beta}}^{BOR}$ of 99%, equivalent to that of the Ti1023_L in **Figure 4.15**. On the other hand, for the Ti64_FL (not shown here), the $\alpha_S$ were extremely fine, leading to a poor indexing rate of those laths. Nevertheless, for the few $\alpha/\beta$ boundaries that were captured, 87% of them respected the BOR.

For the Ti64_Eq, 32% of the $\alpha/\beta$ boundaries respected the BOR, similar $f_{GB_{\alpha/\beta}}^{BOR}$ to that of the Ti1023_Eq (**Figure 4.15**). It shows again that the forging process to obtain initial microstructures with equiaxed $\alpha$ grains, reduced the fraction of $\alpha/\beta$ boundaries respecting BOR. At 750°*C* (Ti64_750°*C*), only 11% of $f_{GB_{\alpha/\beta}}^{BOR}$ was obtained. This might be related to the fact that after quenching from 750°*C*, the ß phase is retained in the Ti64 (as mentioned in section **3.3**), while from 950°*C*, this phase transforms into $\alpha_s$, thus needs to be reconstructed.

To analyze the effect of strain level on the $f_{GB_{\alpha/\beta}}^{BOR}$ evolution, a partial reconstruction of the $\beta$ phase of the Ti64_CL could be performed at $\varepsilon = 0.3$. The $f_{GB_{\alpha/\beta}}^{BOR}$ was then calculated to estimate the behavior of this alloy regarding the BOR $\alpha/\beta$ boundaries. With 61% of the reconstructed $\alpha/\beta$ boundaries corresponding to the BOR, the decrease is minor compared to the one observed for the Ti1023 alloy (**Figure 4.15**). Nevertheless, this analysis should be taken with precaution, as the $\beta$ reconstruction only worked inside one prior-$\beta$ grain, so the statistical relevance of this result is very poor.

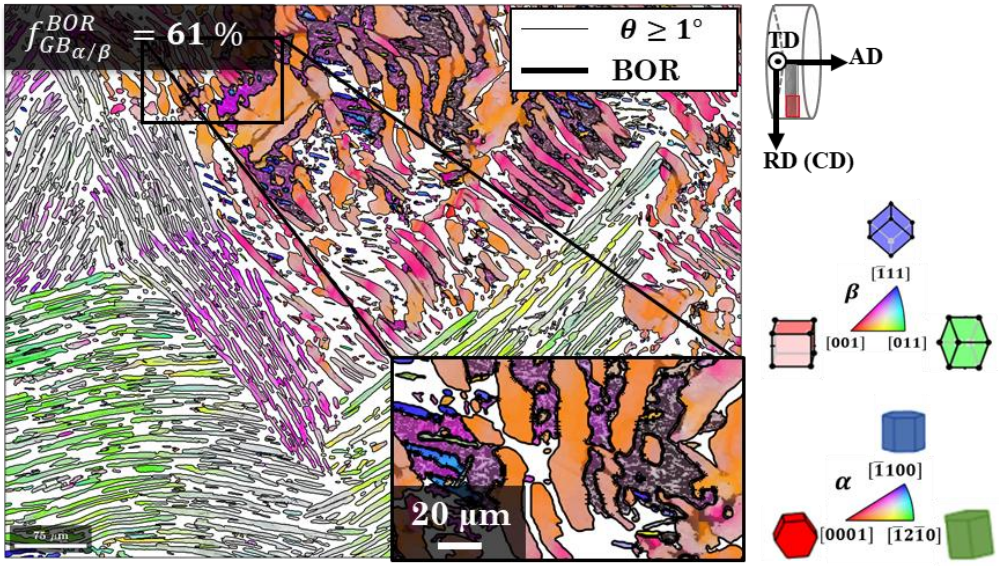



*Figure 4.22. EBSD orientation map, CD-IPF, of the Ti64_CL, after deformation (at 950°C, 0.1 $s^{-1}$ and ε = 0.3), showing all α/β grain boundaries (thin black line) and the BOR α/β grain boundaries (thick black line).*

### *4.1.4 Orientation dependency of substructure formation in α grains*

The analysis detailed in section **2.7.4**, regarding the dependency of the grain orientation on the LAGB density, was performed for different initial microstructures as a function of the strain level (**Figure 4.23**). For all analyzed cases at $\varepsilon = 1.3$, the grains which are oriented with the basal plane parallel to the CD presented more substructures (*i.e.,* higher $\rho_{LAGB}$) than all others. This crystallographic orientation matches the one observed in section **4.1.2.1**. It seems that the developed texture accompanies a configuration where the substructure density is increased in the $\alpha$ grains.

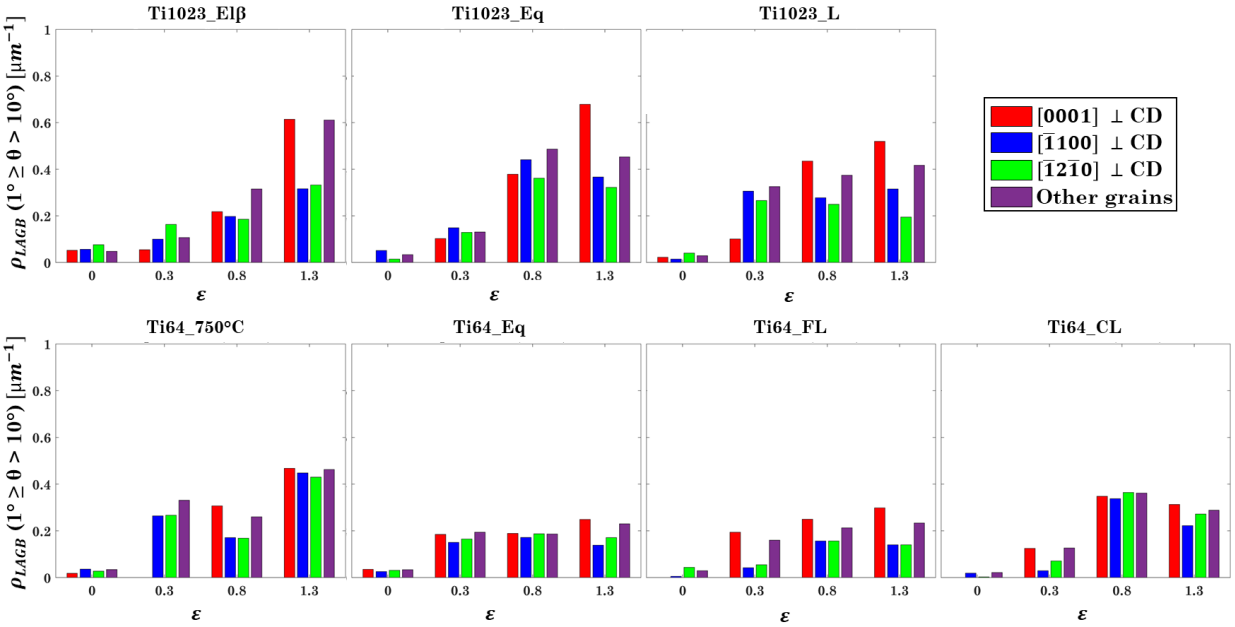



*Figure 4.23. The distribution of the LAGB density ($\rho_{LAGB}$), at different strain levels, for the seven initial microstructures, regarding the three selected specific orientations and the other grains.*

This intrinsic behavior is reinforced by the misorientation axis analysis (**Figure 4.24**). The inverse pole figures (top) shows that the subgrains formation is mainly caused by rotations around the [0001] axis. Furthermore, the pole figures (bottom) show that this misorientation axis is mostly towards the TD (or WD) axis, except for the Ti64_750°*C* (as in section **4.1.2.1**). The combination of those two analyses is in accordance to the previous results (**Figure 4.23**). Both show that, at $\varepsilon = 1.3$, the grains with the (0001) basal plane parallel to the CD (or the [0001]axis perpendicular to the CD), are the ones with higher substructure density.

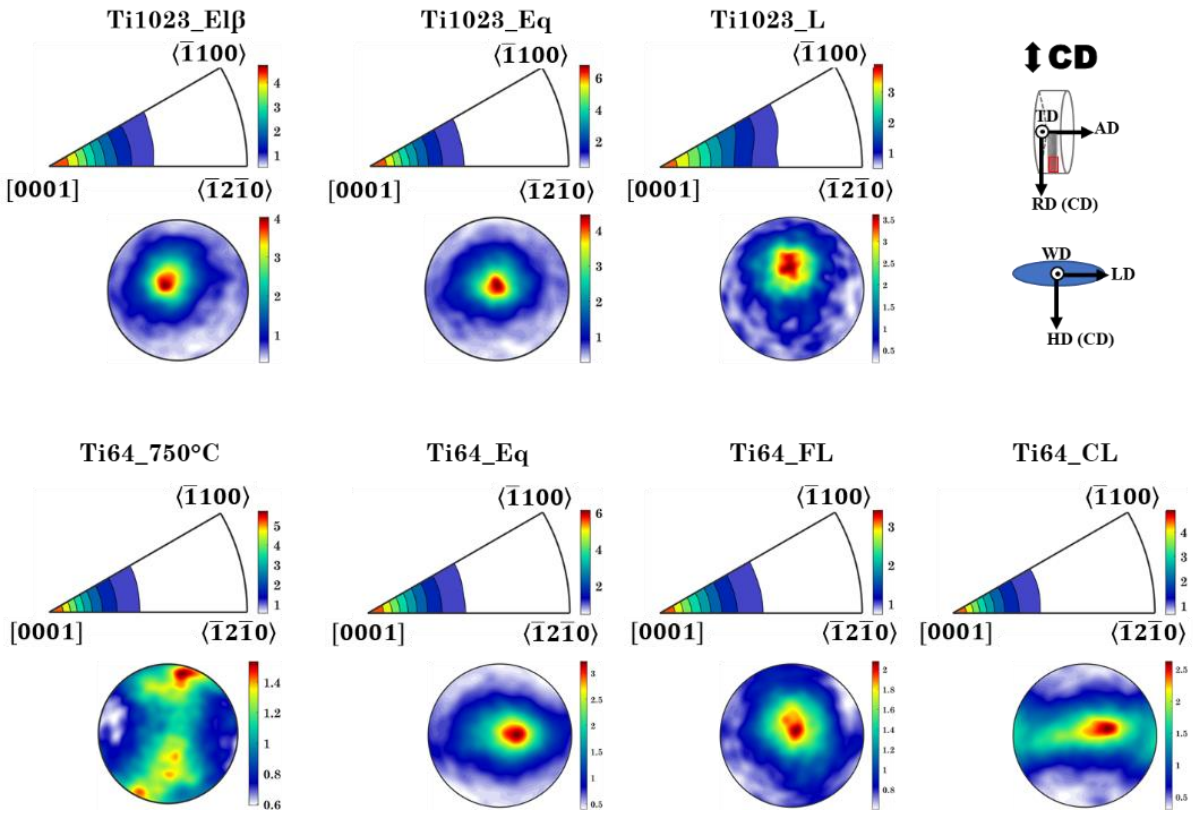



*Figure 4.24. Intragranular misorientation axis analysis (for the α phase and misorientation angles ≥ 1°) in the IPF (top) and the PF (bottom) for all seven initial microstructures, at an equivalent strain level of 1.3.*

This behavior is in agreement with the one observed by [41], for Ti64 with equiaxed $\alpha$ grains. In that mentioned study, the initial grains with the basal plane parallel to the compression direction revealed large fragmentation. Within this thesis, that observation has been generalized to a larger range of initial microstructures.

### *4.1.5 GND density estimation*

The dislocation density ($\rho_{EBSD}^{\varphi}$) for both phases was estimated for each of the initial microstructures by the procedure described in section **2.7.5**. The GND density maps for the $\alpha$ and $\beta$ phases, with their average values, for the Ti1023_El$\beta$, as a function of the strain level, are shown in **Figure 4.25**.

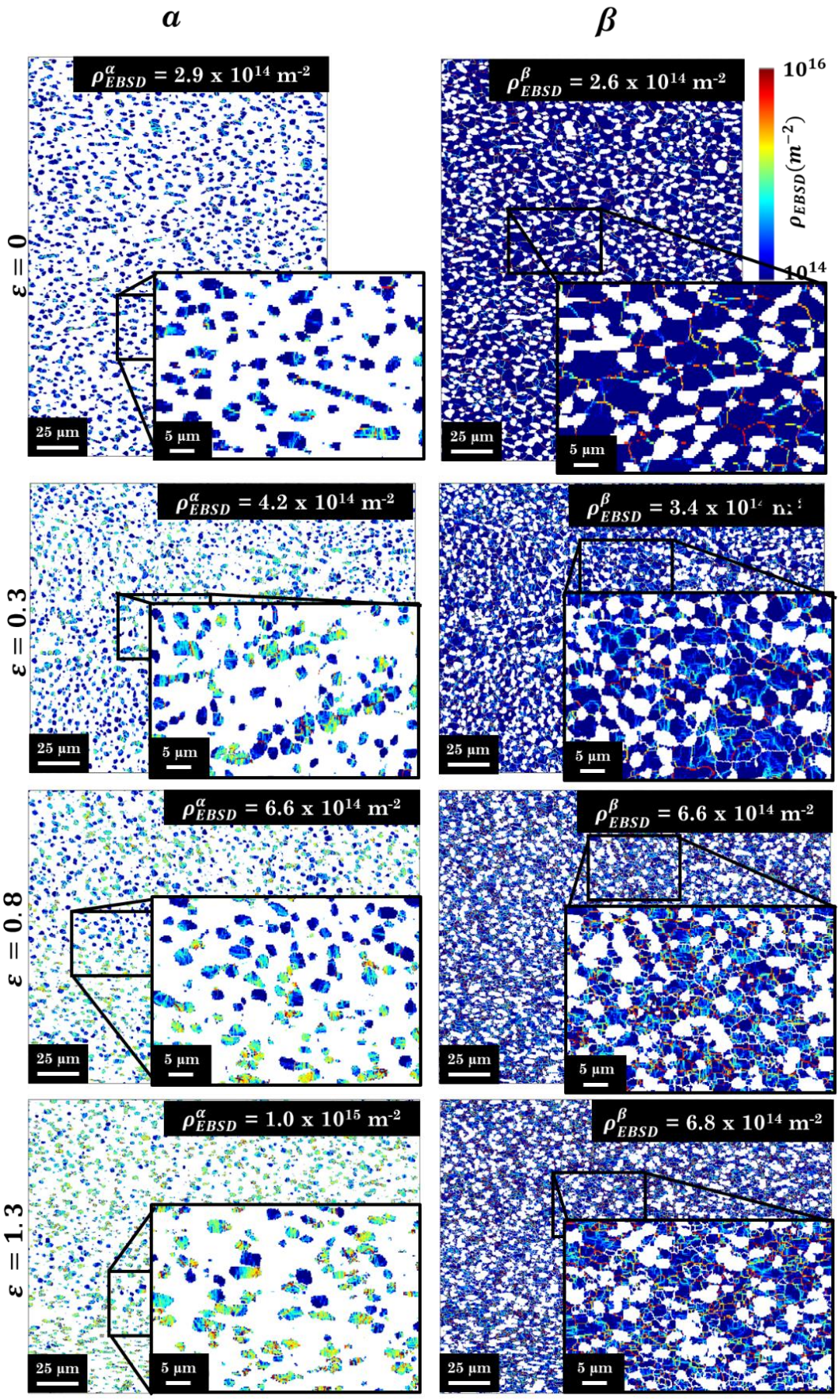



*Figure 4.25. GND density maps for α and β phases (with their average values) in the Ti1023_Elβ microstructure, as a function of strain level at 750°C, 0.1 $s^{-1}$.*

On **Figure 4.25**, it is possible to observe some heterogeneity in the $\alpha$ phase GND density distribution, where there are $\alpha$ grains with higher dislocation density than others. This seems to be mainly linked to the crystallographic orientation of the $\alpha$ grains, as shown in **Figure 4.22**. Interestingly, at 0.8 and 1.3 strain level, the zone where the $\alpha$ phase shows a lower $\rho^{\alpha}_{EBSD}$, is inside the $\beta$ grain with higher continuous dynamic recrystallization rate. This suggests a relation between the $\beta$ grain orientation and the dislocation density evolution in the $\alpha$ phase.

For the sake of simplicity, the dislocation density maps will not be shown for all microstructures and strain levels. However, the average GND density ($\rho^{\varphi}_{EBSD}$) was estimated for both phases, when possible, for each of the seven initial microstructures, as a function of the strain level. The results are summarized in **Figure 4.26**.

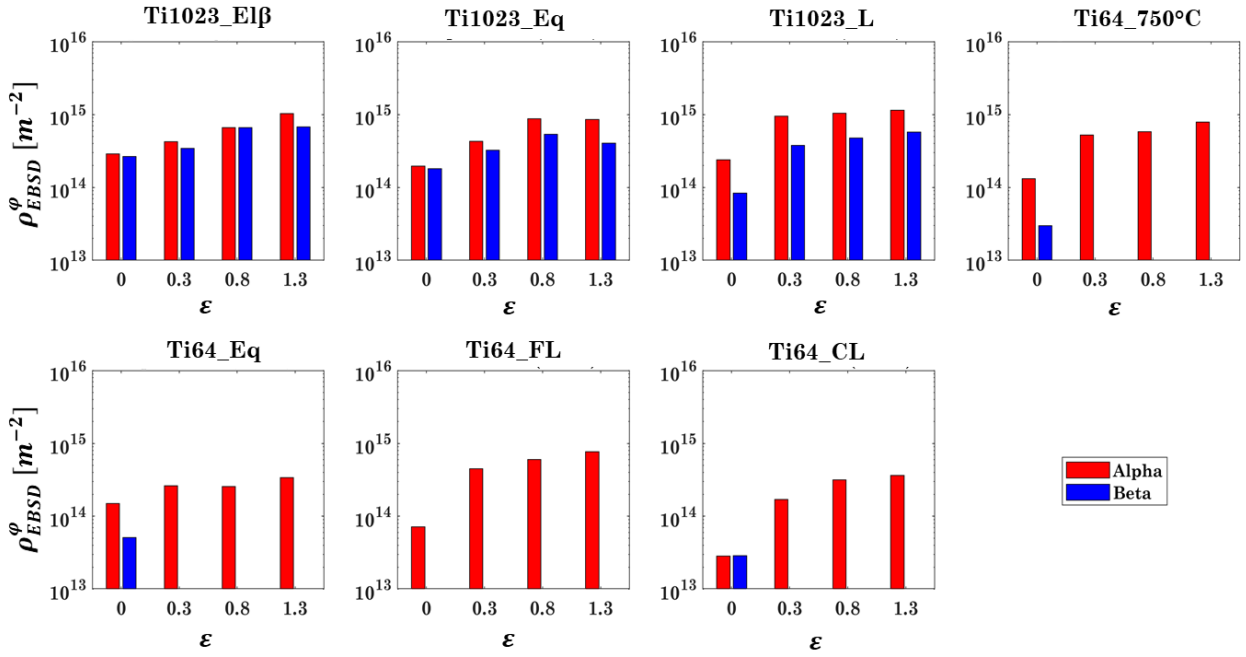



*Figure 4.26. The average GND density for α and β phases, for different initial microstructures and strain levels.*

The exhaustive analysis of the seven initial microstructures suggests that the $\alpha$ phase stores more GNDs (per unit volume) throughout deformation, independently of the alloy, morphology and phase fraction. Noteworthily, the direct comparison of the GND density in the $\alpha$ and $\beta$ phases is intricate, as their crystal structures are different.

Another case where the dislocation density between phases is equivalent is for the Ti1023_El$\beta$ at $\varepsilon = 0.8$. This could to be linked to the fact that the $\beta$ phase evolution is controlled by continuous dynamic recrystallization [25], where LAGBs turn into HAGBs with the increase in strain. When the misorientation angle is equal or above the chosen threshold (10°), those boundaries are not included in the calculation. This is exemplified in **Figure 4.27**.

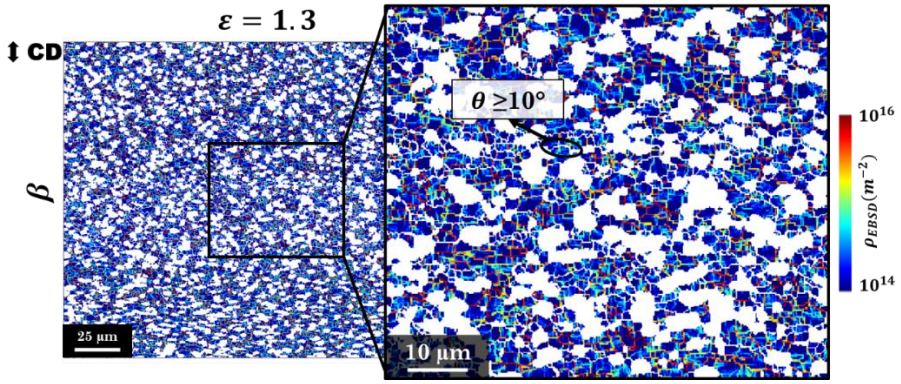



*Figure 4.27. GND density map of the β phase of the Ti1023_Elβ (at 750°C, 0.1 $s^{-1}$ and ε = 1.3), showing in white the β/β HAGB (θ ≥ 10°), which are not considered in the GND density calculation.*

For almost all cases, the evolution trend in the GND density of the $\alpha$ phase ($\rho^{\alpha}_{EBSD}$) is an increase with increasing strain level. This can be clearly seen in the GND density map at $\varepsilon = 1.3$ (**Figure 4.25**), with the presence of higher GND density levels. This behavior also seems to be connected to the texture development with increasing deformation (**Figure 4.6**). The grains that have their basal plane ∥ CD are also the ones with higher $\rho_{LAGB}$ (**Figure 4.23**).

Concerning the $\beta$ phase, the trend in $\rho^{\beta}_{EBSD}$ is to increase with the increase of strain up to $\varepsilon = 0.8$, then a decrease (or stagnation) of the $\rho^{\beta}_{EBSD}$ values as continuous dynamic recrystallization progresses (**Figure 4.26**).

### *4.1.6 3D characterization of deformed Ti64_FL*

After the 3D characterization of the initial microstructures of the Ti64_CL and Ti64_FL (section **3.3.3**), the latter was selected to be analyzed after deformation in order to better understand the observed lath kinking (**Figure 4.2**). The Ti64_FL was selected as more $\alpha$ variants are contained in a given volume.

A double-cone sample was used for this 3D characterization. In order to analyze the highest level of deformation in the sample (ε = 1.3), the ROI was placed at its center. Furthermore, the ROI contained a grain boundary, as it is interesting to analyze how different $\alpha$ lath colonies are deformed, as also the $\alpha_{GB}$ (especially after the behavior observed in **Figure 4.13**). Thus, the first step consisted in marking the ROI (with the FIB) with four crosshairs (**Figure 4.28**).

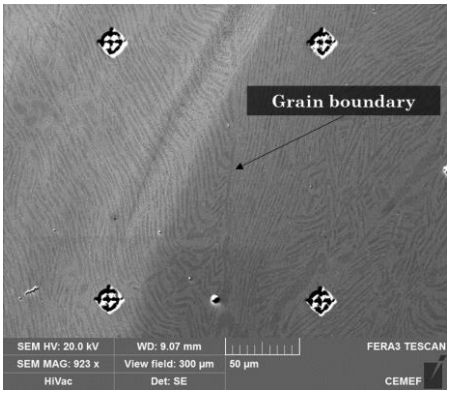



*Figure 4.28. ROI with the four crosshairs engraved (by the FIB) containing a grain boundary (in the middle).*

A 2D EBSD map was then performed on the top ROI surface with a 0.5µ$m$ step size and a 450µ$m$ x 340µ$m$ analysis field to identify the crystallographic orientation of the $\alpha$ laths (**Figure 4.29**). It is clear that the different morphological orientations observed in **Figure 4.28**, correspond to distinct crystallographic orientations in **Figure 4.29**, from different $\alpha$ variant colonies. The non-indexed data is shown in grey, where the four crosshairs can be seen near the corners. Interestingly, the $\alpha_{GB}$ presented more LAGB than the rest of the analyzed microstructure. This behavior was also seen in **Figure 4.13** for the Ti1023.

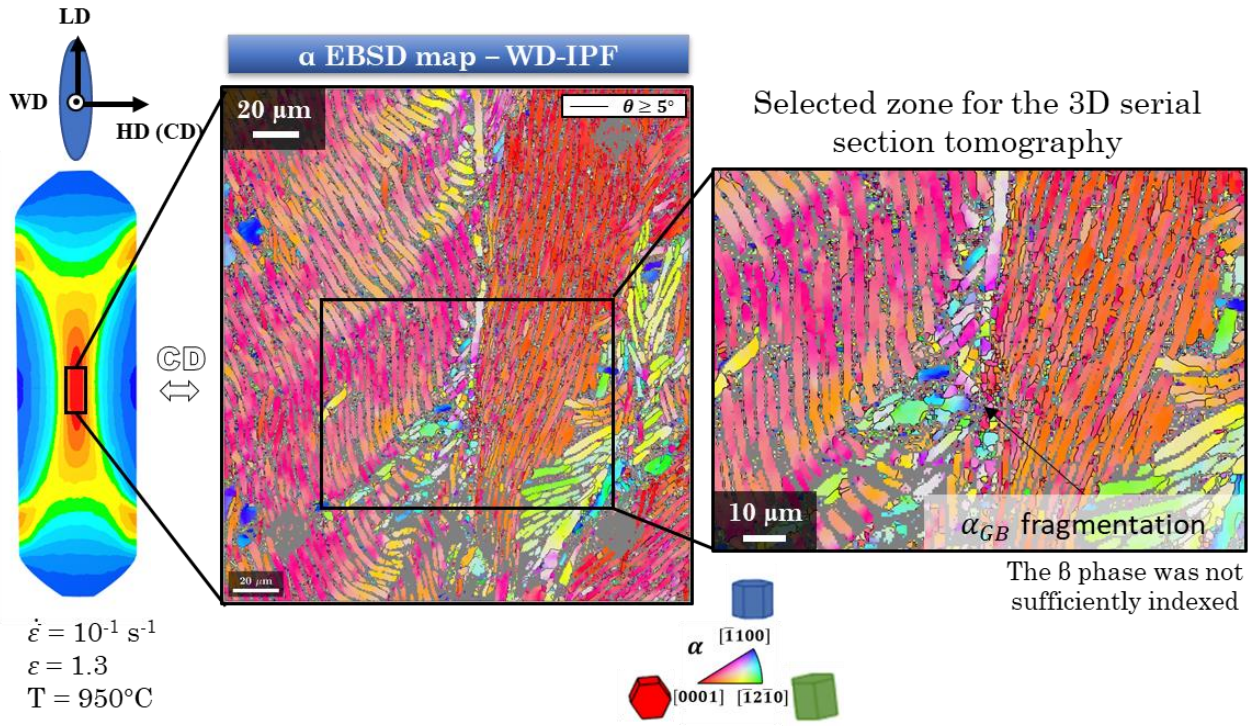



*Figure 4.29. 2D EBSD map of the ROI obtained at the center of a double-cone sample. The selected zone for the following 3D serial sectioning tomography is shown (on right).*

Concerning the serial sectioning tomography procedure in the PFIB-SEM microscope), the parameters used are shown in **Table 4.1**.

| Microstructure | Deposition | Accelerating Voltage (FIB) [$kV$] | Ion Beam current [$\mu A$] | Layer step size [$\mu m$] |
|---|---|---|---|---|
| Ti64_FL | Pt | 30 | 0.1 | 0.25 |

*Table 4.1. PFIB parameters used for the serial sectioning of the deformed Ti64_FL.*

**Figure 4.30** shows the 3D reconstruction of the $\alpha$ laths with the *Dragonfly* software package.

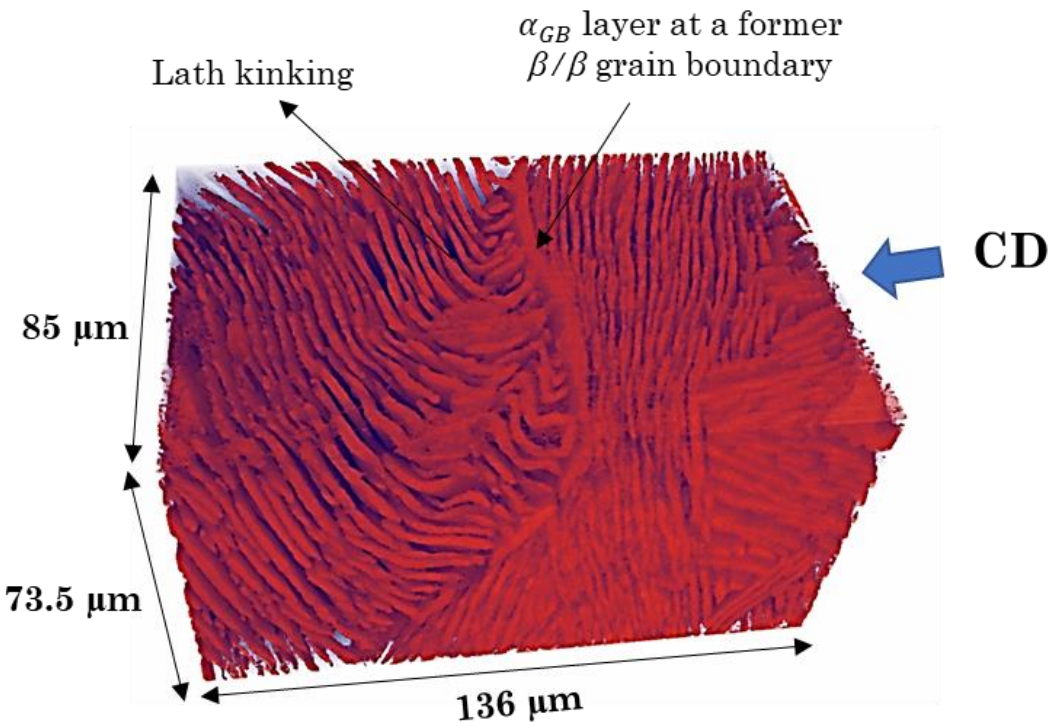



*Figure 4.30. 3D reconstruction of the Ti64_FL α phase after deformation at 950°C, 0.1 $s^{-1}$ and 1.3 strain level, showing the analyzed volume dimensions and the compression direction.*

By analyzing **Figure 4.30**, it is possible to observe the 3D kinking of the laths, where those belonging to the same colony are deformed in a similar way, being a continuous kinking throughout the volume. **Figure 4.31** evidences the 3D fragmentation of the $\alpha_{GB}$ at different positions in the analyzed volume. It is also possible to see that the diagonal $\alpha_{GB}$ is highly fragmented, while the $\alpha$ lath colonies are kinked, but not as fragmented as at the grain boundary (**Figure 4.31***b* and *c*). This same behavior of a higher breakage of the $\alpha_{GB}$ was previously observed (2D EBSD) in the Ti1023 alloys (**Figure 4.13**). Furthermore, no globularization is observed throughout the volume. Those also in agreement with the 2D EBSD observations (**Figure 4.29**).

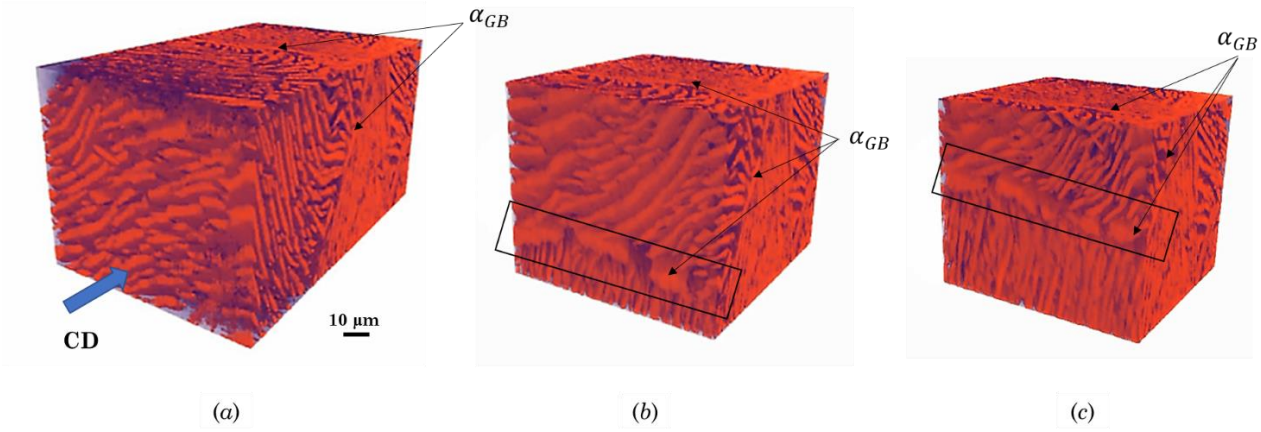



*Figure 4.31. Visualization of the 3D kinking of the α laths, as the fragmentation of the $\alpha_{GB}$ at: a) 100% volume; b) ~75% volume; c) ~50% volume.*

## 4.2 Influence of temperature and strain rate on microstructure evolution

From the previous seven initial microstructures (**Figure 3.7**), four microstructures (Ti1023_El$\beta$, Ti1023_L, Ti64_Eq, Ti64_CL) were selected. The aim was to have two different morphologies (equiaxed and lamellar) for both alloys (Ti64 and Ti1023). The lamellar Ti64 morphology with thicker lamellae was selected to have a nearer $\alpha$ grain size compared to the equiaxed morphology. The Ti1023_El$\beta$ was selected (for the equiaxed case) due to the observed dependency of continuous dynamic recrystallization on the $\beta$ grain orientation, shown in **Figure 4.11**. There was then an interest to analyze this behavior in other temperature and strain rate conditions. The four selected microstructures, with their characteristic dimensions, are schematized in **Figure 4.32**.

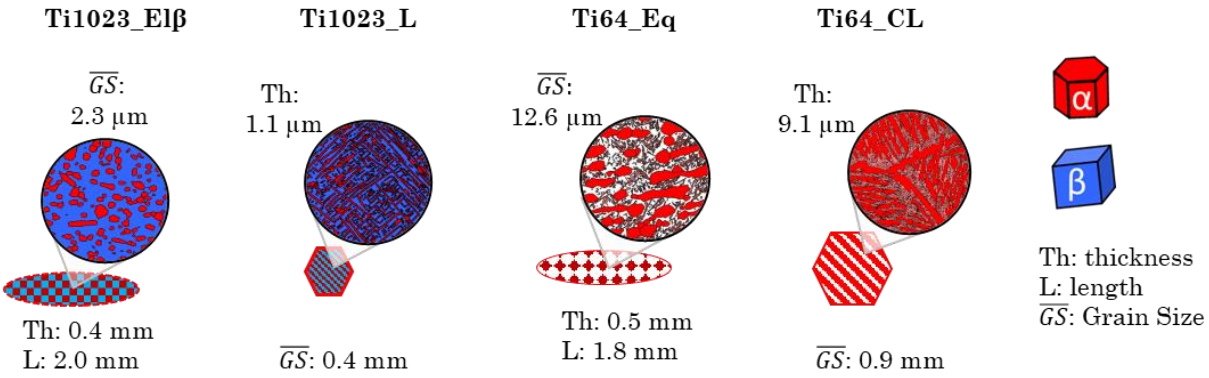



*Figure 4.32. The four microstructures selected out of the seven initial ones to study the influence of temperature and strain rate.*

One temperature (700°$C$) and one strain rate ($10^{-2}s^{-1}$) were selected to be studied. This temperature was selected to be applied on the Ti1023 alloy to allow comparison of the $\alpha$ phase at a similar primary phase fraction as that of the Ti64 at 950°$C$, approximately 35% (see **Figure 3.6**). Both equiaxed and lamellar microstructures of the Ti1023 alloy were first subjected to 1-hour heat treatment at 700°$C$, then WQ. The resulting initial microstructures are shown in **Figure 4.33**. The achieved $f_{\alpha_P}$ of the Ti1023 at 700°$C$ was then indeed 35 $\pm$ 2 %, as estimated from BSE images, following the same procedure explained in **Figure 2.8**.

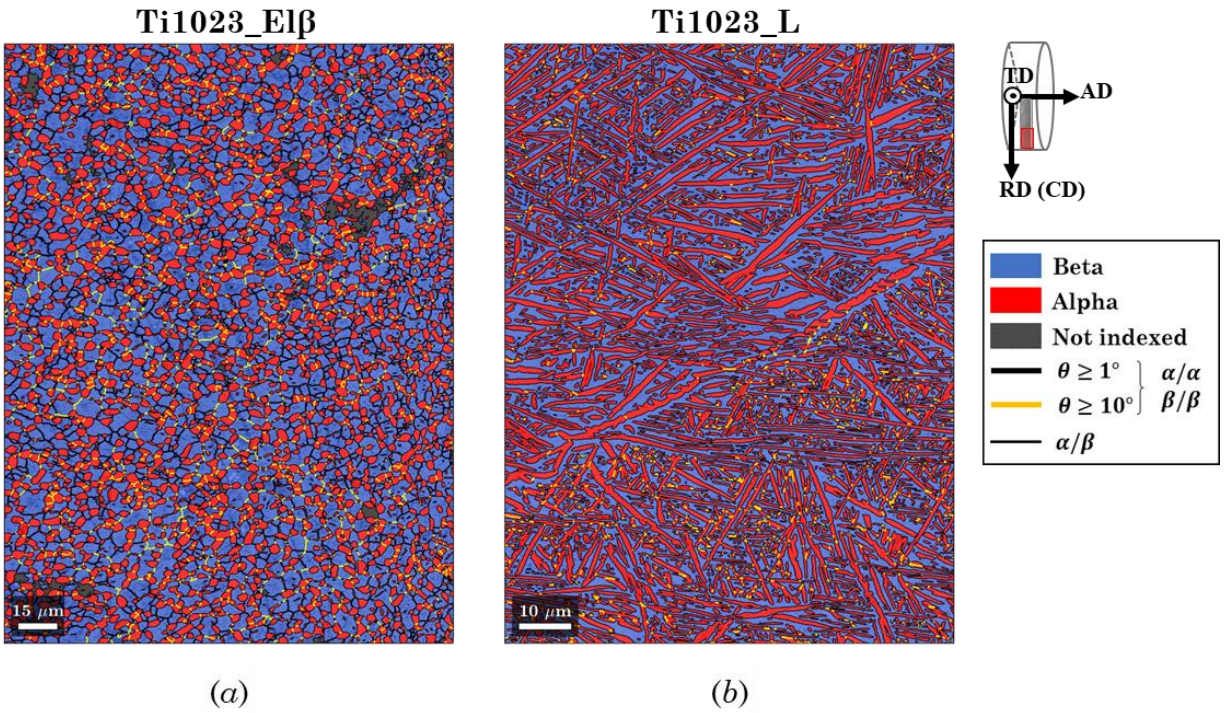



*Figure 4.33. Initial microstructures of the: a) Ti1023_Elβ; and b) Ti1023_L; after holding for 1 hour at 700°C and WQ.*

In total, six double-cone samples were needed for this thermomechanical parameter influence study, as summarized in **Table 4.2**.

| Microstructures (Double-cone samples) | T(°C) | | |
|---|---|---|---|
| | 700 | 750 | 950 |
| Ti1023_El$\beta$ | | | - |
| Ti1023_L | | | - |
| Ti64_Eq | - | - | |
| Ti64_L | - | - | |

*Table 4.2. Experimental plan design for the study of the influence of temperature and strain rate. The conditions selected for each initial microstructure are highlighted in green. The equivalent strain rate ($\dot{\bar{\varepsilon}}$) at the center of the double-cone sample is 0.01 $s^{-1}$.*

EBSD maps were acquired in the same three zones ($\varepsilon$ = 0.3, 0.8 and 1.3) described in **Figure 2.31**, to analyze also the effect of the strain level on microstructure evolution. By comparing these new results with the ones presented in section **4.1**, the influence of strain level, strain rate and temperature could be assessed for both alloys.

### *4.2.1 Topological evolutions*

The influence of the thermomechanical parameters on the four selected microstructures (**Figure 4.32**) was primarily analyzed in terms of morphological and primary $\alpha$ phase fraction evolution, through BSE images. To simplify the comparison between the microstructures obtained with the new temperatures and

strain rates to those from the previous conditions, some of the micrographs shown in **Figure 4.2** are repeated on **Figure 4.34** (for Ti1023) and **Figure 4.35** (for Ti64).

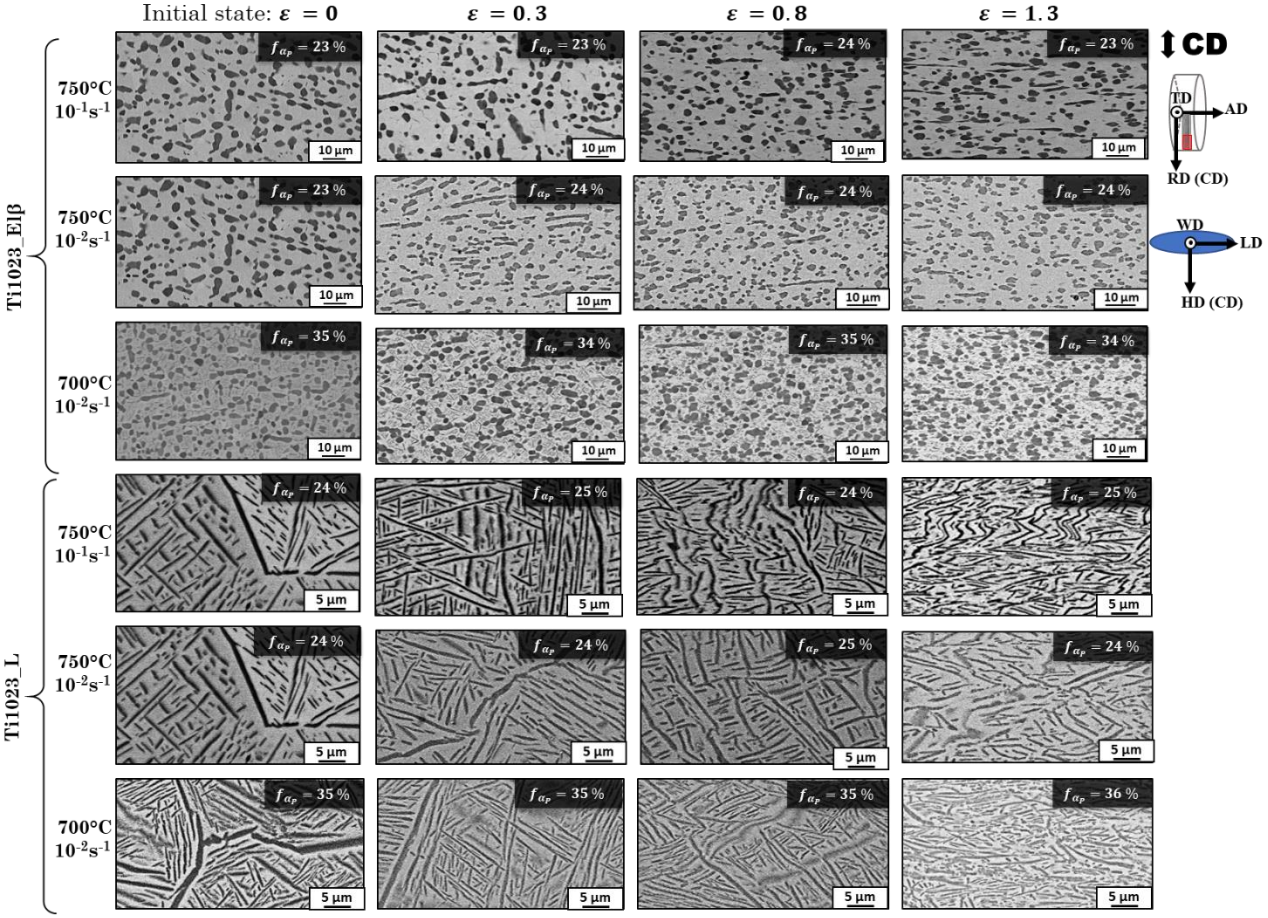



*Figure 4.34. Summary of the influence of thermomechanical parameters on microstructure after hot deformation (BSE micrographs) of Ti1023 samples, along with the respective primary α phase fraction.*

By analyzing all $f_{\alpha_P}$ values, it is clear that there is, again, no effect of hot deformation on phase fractions, *i.e.,* no dynamic transformation was observed for the whole set of analyzed conditions. Furthermore, the alignment of elongated $\alpha$ grains observed in **Figure 4.2** at a high strain level ($\varepsilon = 1.3$), is also seen at lower temperatures and strain rates for the Ti1023 alloy. Regarding the lamellar morphology, only lath kinking was observed, yet no clear start of globularization, except at 700°*C* and $10^{-2}$ $s^{-1}$. This observation is discussed furtherly in section **4.2.3.1** with the analysis of grain boundaries.

**Figure 4.35** summarizes the effect of lowering the strain rate on microstructure evolution of equiaxed and lamellar Ti64 alloy at 950°*C*.

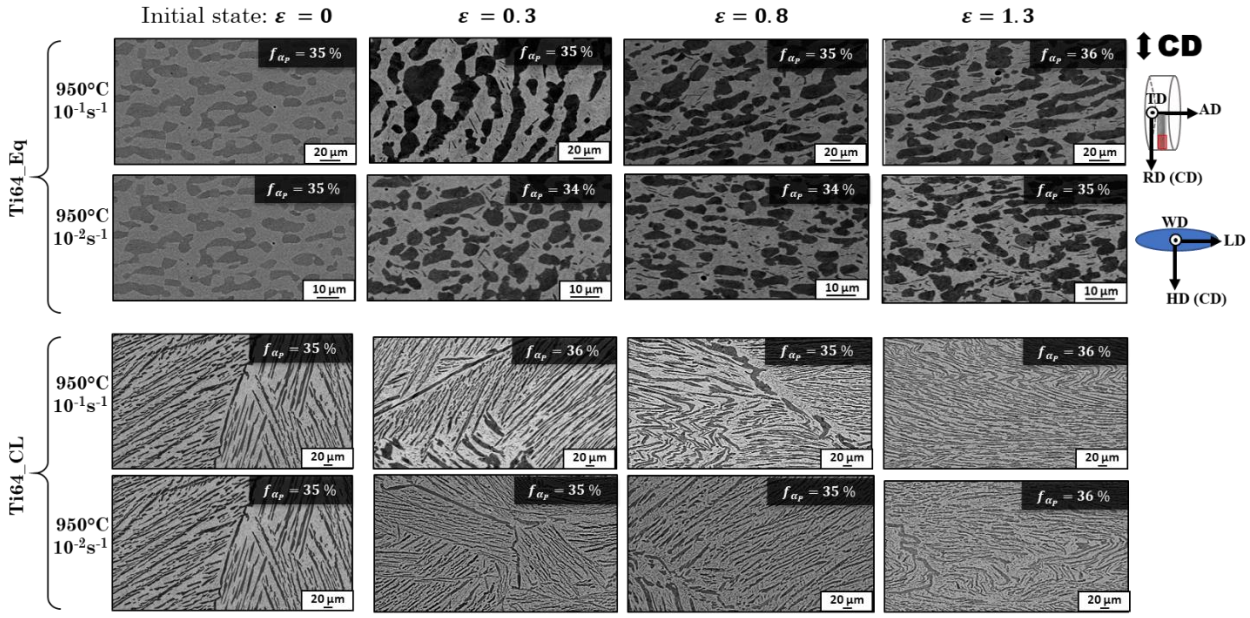



*Figure 4.35. Summary of the influence of strain rate on Ti64 microstructure (BSE micrographs) after hot deformation at 950°C and two strain rates, along with the respective primary α phase fraction.*

The presence of serrated $\alpha/\beta$ boundaries in the Ti64_Eq is less pronounced at $10^{-2}$ $s^{-1}$, but it is also observed. The Ti64_CL behavior seems unchanged at lower strain rates, with kinking and alignment of the thick $\alpha$ laths.

In general, the applied changes in thermomechanical condition do not seem to highly impact the $\alpha$ phase morphology.

The same slight macroscopic anisotropy previously noticed in **Figure 4.3** is observed also at $10^{-2}$ $s^{-1}$ (**Figure 4.36** for a Ti64_Eq), where the sample widens in the direction perpendicular to elongated $\beta$ grains.

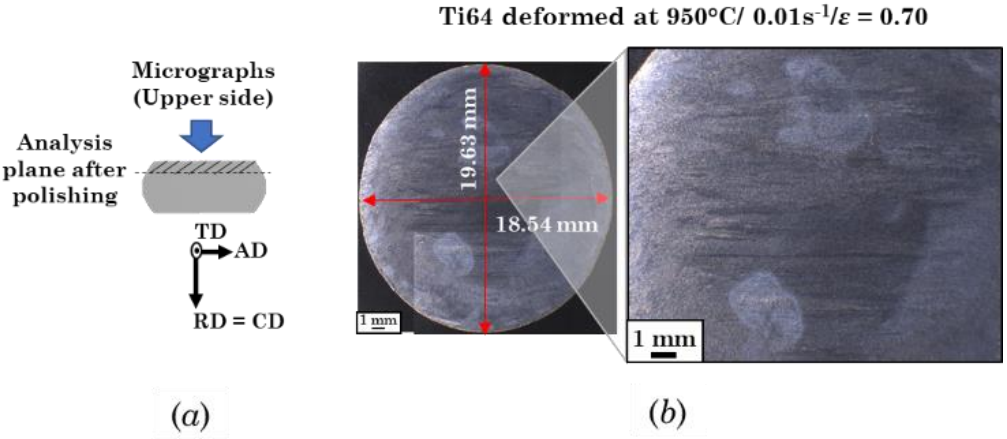



*Figure 4.36. Polishing of the top side of the double-cone samples to retrieve the AD and RD directions: a) Schematic macroscopic reference; b) Upper side of a polished sample of Ti64_Eq after deformation at 950°C and $10^{-2}$ $s^{-1}$.*

The sample elongates perpendicularly to the elongation of the prior-$\beta$ grains. Consequently, the macroscopic anisotropy of the sample linked to the shape and/or texture of the $\beta$ grains is maintained at lower strain rates.

### *4.2.2 Crystallographic texture evolution*

As mentioned in section **4.1.2**, the EBSD method is not at the right scale to discuss macroscopic texture. Tendencies in the crystallographic orientations measured at the scale of a few $\beta$ grains are thus reported in this section for both phases.

#### *4.2.2.1 α phase*

Crystallographic orientations have been analyzed through pole figures (**Figure 4.37**) to study the influence of thermomechanical parameters on texture evolution. These results show that the intrinsic behavior of the $\alpha$ phase observed at $10^{-1}$ $s^{-1}$ (**Figure 4.6**), is globally maintained at $10^{-2}$ $s^{-1}$. The (0001) basal planes tend to align parallel to the CD (*i.e.,* [0001]⊥CD), with the ⟨11$\bar{2}$0⟩ directions ∥ CD. Also, for the lamellar Ti1023, the basal planes ∥ CD, but with the axisymmetry due to pancake shaped $\beta$ grains. Interestingly, when a lower strain rate was applied, the $\alpha$ phase of the Ti64_Eq formed a texture similar to that of lamellar morphology (axisymmetric to CD). This behavior seems to be different from the one observed at $10^{-1}$ $s^{-1}$, where there was a clear alignment of the [0001] ∥ WD. Furthermore, for the Ti64_CL, there is a strong alignment of the [0001] ∥ LD. Nevertheless, this might also be connected to the amount of $\alpha$ colonies being analyzed at the selected spatial resolution.

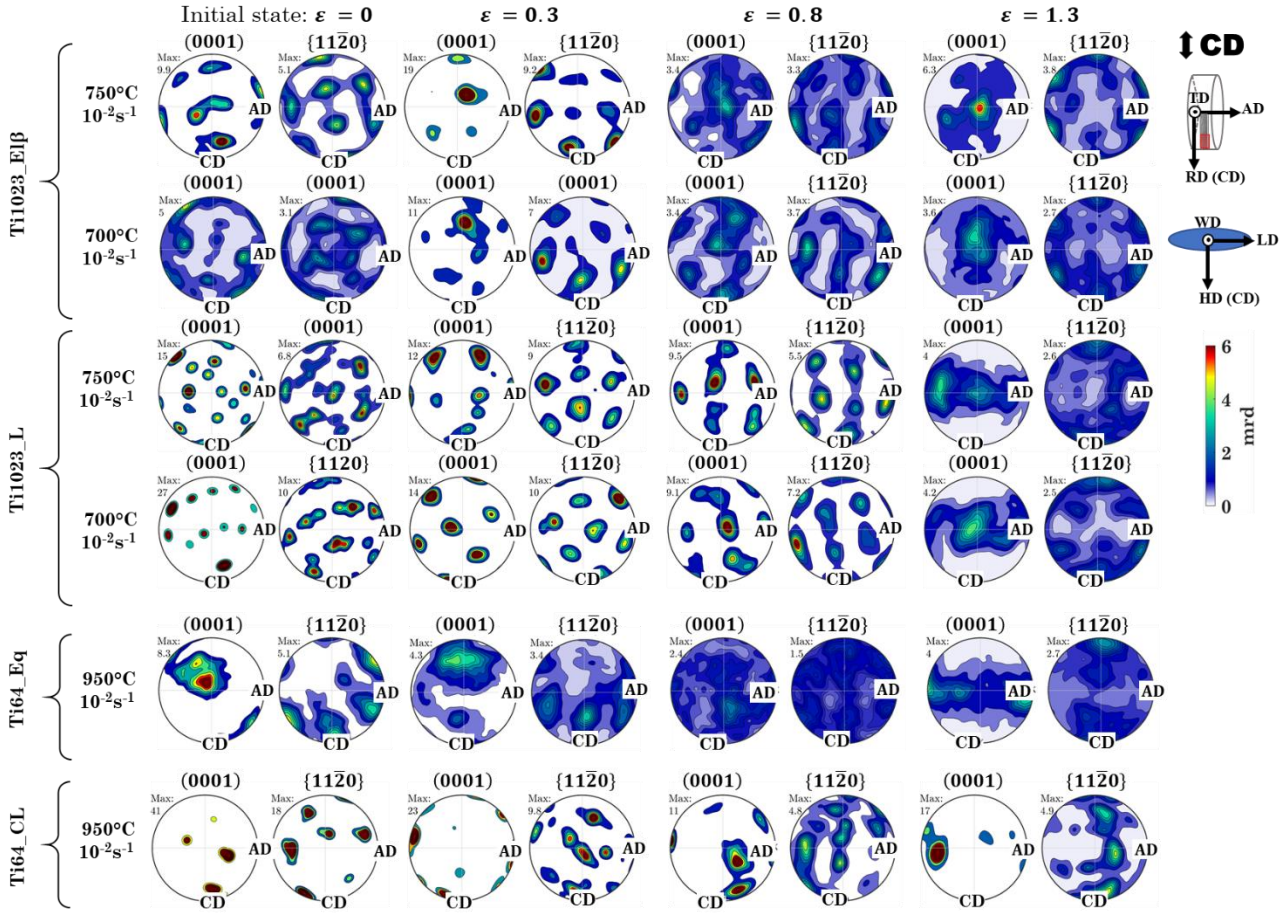



*Figure 4.37. Summary of α phase pole figures, showing texture development as a function of strain level for the four selected microstructures and different deformation conditions.*

Considering the correlation between grain elongation and texture observed for the initially equiaxed $\alpha$ grains in the Ti1023_El$\beta$ (**Figure 4.7**), a similar analysis was performed for the new set of thermomechanical conditions. The aspect ratio of 2.5 was again used as a threshold to separate the most elongated grains. Those are shown in **Figure 4.38**, with TD-IPF color coding.

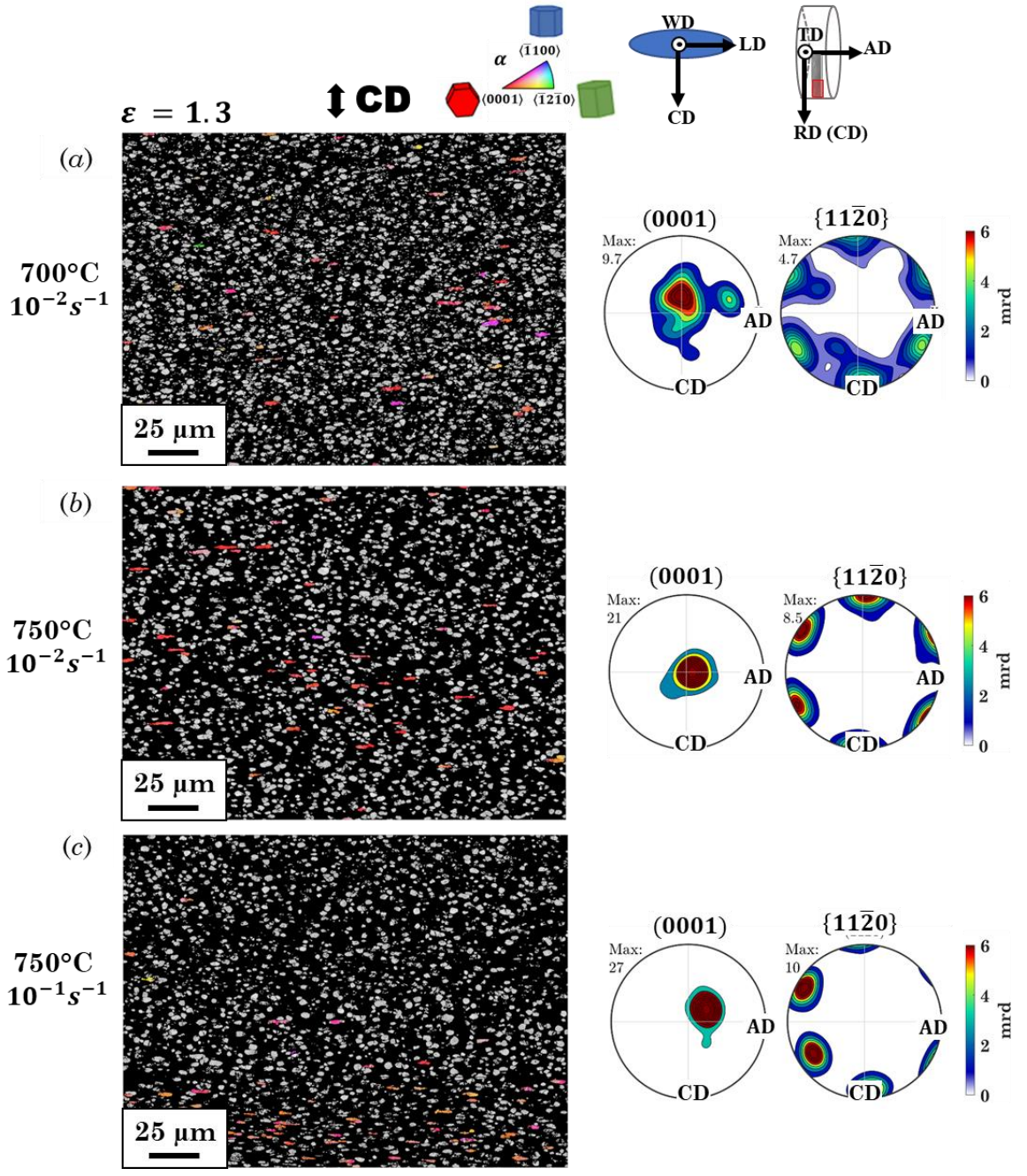



*Figure 4.38. EBSD orientation maps (TD-IPF) and pole figures for the α grains with high aspect ratio (>2.5) for the Ti1023_Elβ at different thermomechanical conditions.*

The grains that are elongated after deformation present a very strong crystallographic texture with [0001] ⊥ CD and ⟨11$\bar{2}$0⟩ ∥ CD (colored in red), same as seen in **Figure 4.7**. This behavior is therefore confirmed here and seems to be independent from the thermomechanical conditions applied to the Ti1023_El$\beta$ (over the applied range) and from $\beta$ grain orientation.

### 4.2.2.2 *β phase*

For the *β* phase, the tendencies observed at $10^{-1}$ $s^{-1}$ (**Figure 4.8**) are also retrieved at $10^{-2}$ $s^{-1}$ (Figure 4.39). At high strain levels ($\varepsilon = 1.3$), the *β* phase develops ⟨001⟩ ∥ CD and ⟨$\bar{1}$11⟩ ∥ CD texture components. It is important to mention that for the Ti1023_El*β* deformed at 750°*C*/ $10^{-2}$ $s^{-1}$, the intensity of the ⟨$\bar{1}$11⟩ ∥ CD component is stronger, in contrast to what was systematically observed before (**Figure 4.8**). It seems that, at lower strain rates and high temperatures, the ⟨$\bar{1}$11⟩ ∥ CD texture component is privileged in the equiaxed microstructure (or this might be connected to statistical fluctuation due to the EBSD map scales). The strongest textures are observed for the Ti1023_El*β* billet (especially at 700°*C*), which had a starting microstructure with highly elongated *β* grains. The Ti1023_L microstructure follows the tendencies observed previously (**Figure 4.8**).

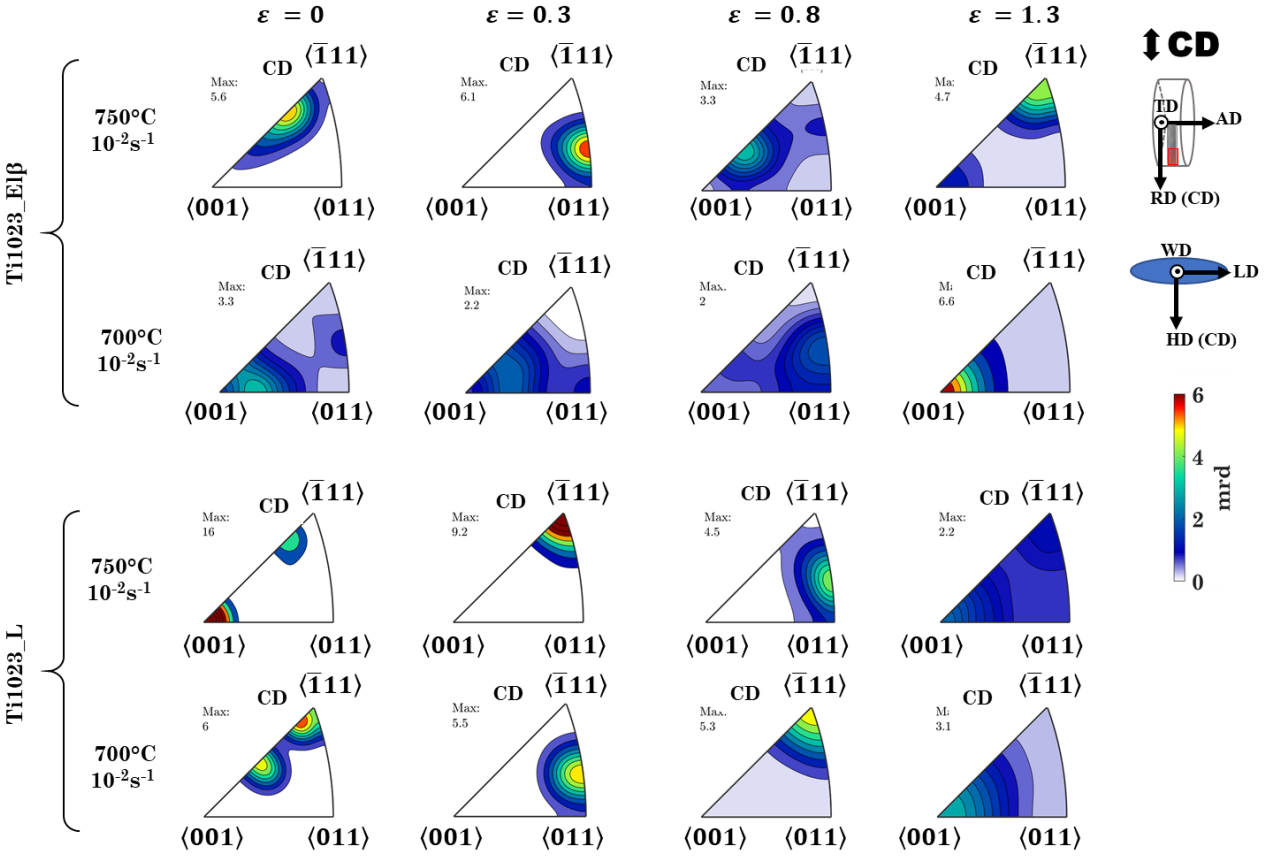



*Figure 4.39. β phase CD-IPF of the Ti1023 alloy as a function of thermomechanical parameters and type of initial microstructures.*

## 4.2.3 *LAGB and HAGB density*

### 4.2.3.1 *Ti1023 alloy*

**Figure 4.40** shows Ti1023_El*β* microstructures as a function of strain applied at different temperatures (700 and 750°*C*) and strain rates ($10^{-1}$ and $10^{-2}$ $s^{-1}$). The deformation conditions of 750°*C*/ $10^{-1}$ $s^{-1}$ already shown in section **4.1.3.1** are displayed again to ease the comparison.

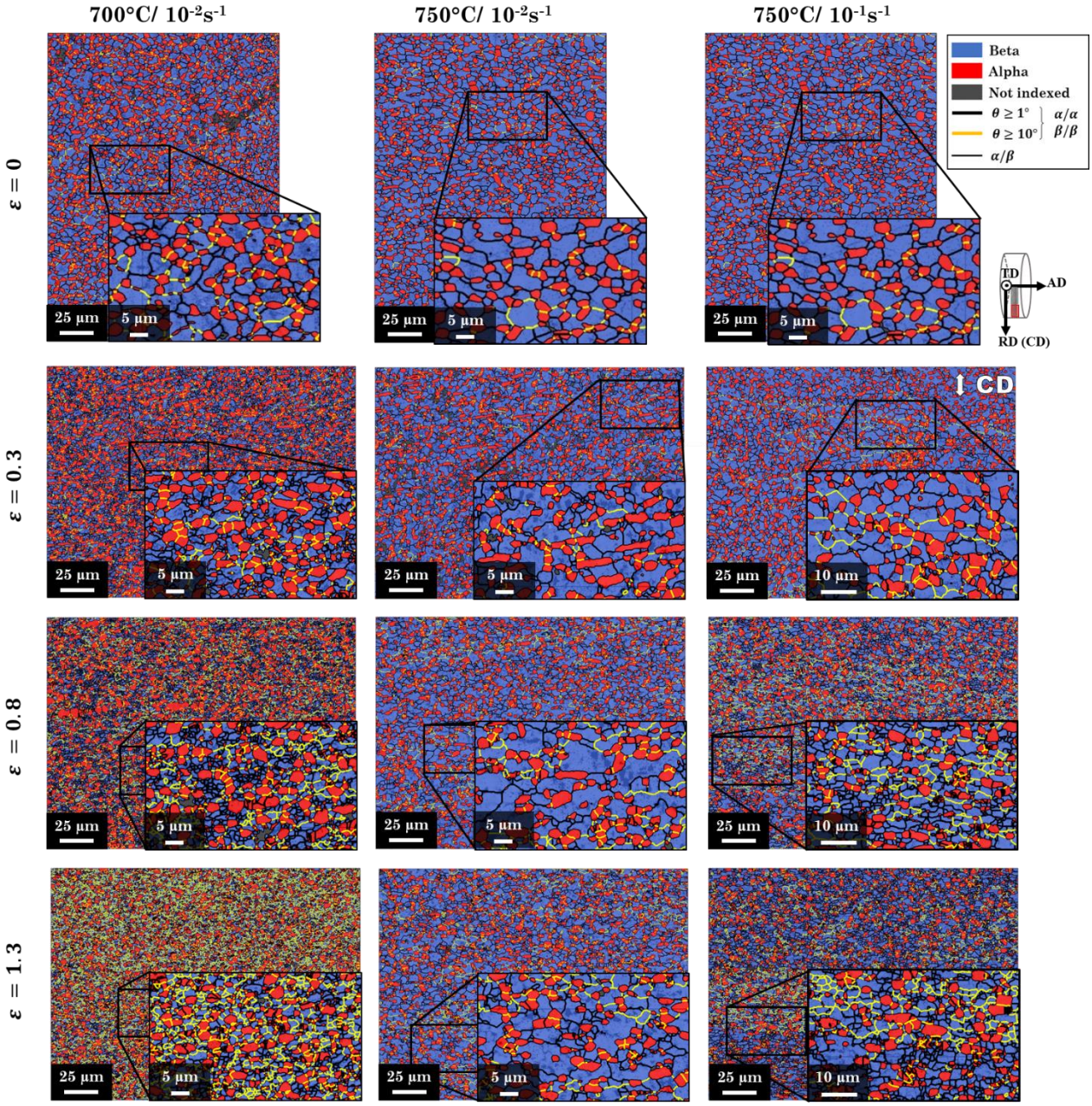



*Figure 4.40. EBSD maps showing LAGBs (black lines) and HAGBs (yellow lines) in the α and β phases of the Ti1023_Elβ microstructures deformed at different strain rates and temperatures, as a function of the equivalent strain level.*

By analyzing **Figure 4.40**, the following observations can be made:

- **At 700°C/10$^{-2}$ s$^{-1}$:** there is minor formation of LAGBs or HAGBs in the equiaxed $\alpha$ phase, a similar behavior to that seen in **Figure 4.33***a*. In the $\beta$ phase, there is on the contrary a clear increase in the LAGB density, especially at $\varepsilon = 0.8$. With further deformation, those LAGB seems to increase their misorientation angle, becoming HAGB (yellow lines), ending into high (and very homogeneous) continuous dynamic recrystallization of the $\beta$ phase;
- **At 750°C/10$^{-2}$ s$^{-1}$:** minor evolution of the microstructure is observed. At those high temperature and low strain rate conditions, only some few

recrystallized zones are observed in the $\beta$ phase. At $\varepsilon = 0.8$, recrystallization seems to take place near $\beta/\beta$ grain boundaries (**Figure 4.41**), as observed for the 0.3 strain level for the $10^{-1}$ $s^{-1}$ condition (**Figure 4.11**). At $\varepsilon = 1.3$, the $\beta$ grains that are oriented with the ⟨110⟩ ∥ CD, are the ones which present higher continuous dynamic recrystallization (inside the yellow rectangles in **Figure 4.41**). It is worth mentioning that this same behavior was observed for the $10^{-1}$ $s^{-1}$ condition (**Figure 4.11**).

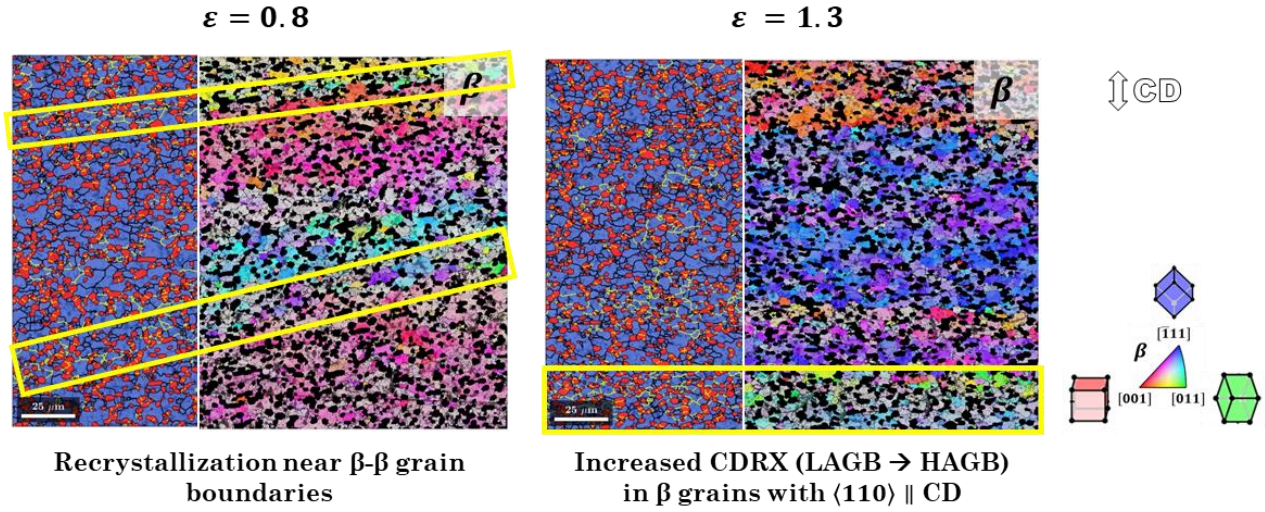



*Figure 4.41. EBSD maps showing both LAGBs and HAGBs (same color coding as **Figure 4.40**, as also the β phase orientation with the IPF color coding by CD, for the Ti1023_Elβ after deformation at 750°C/$10^{-2}$ $s^{-1}$.*

The quantitative analysis of the $\rho_{GB}$ (LAGB and HAGB density, as explained in section **2.7.3**) for the Ti1023_El$\beta$ is summarized in **Figure 4.42**.

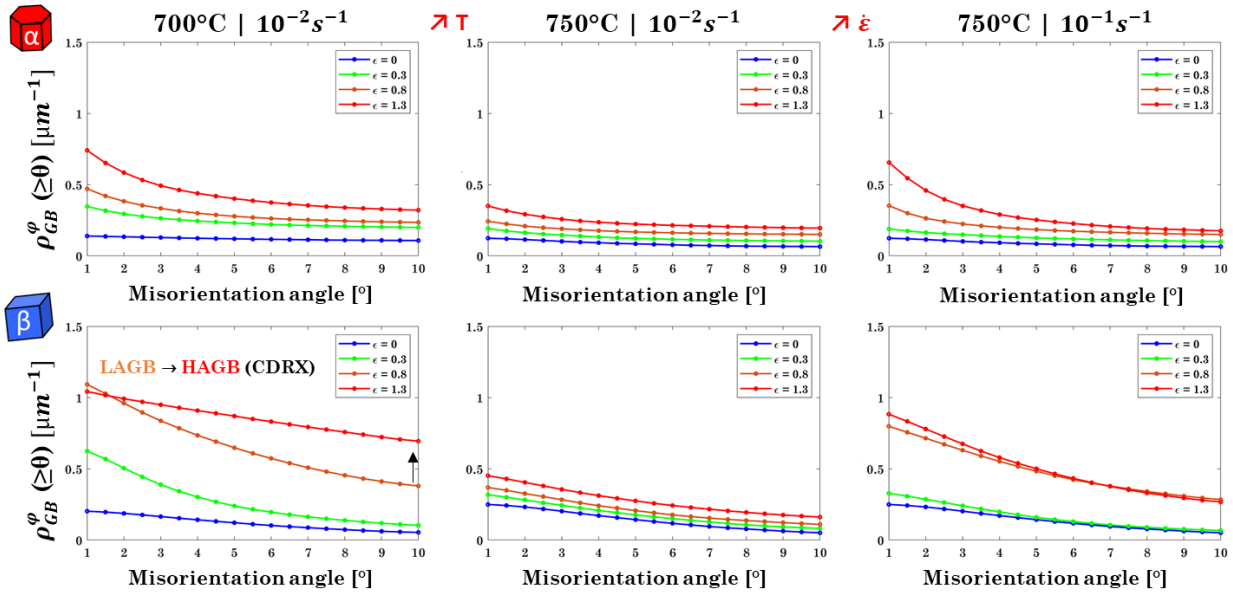



*Figure 4.42. Misorientation angle cumulative distribution analysis for both phases of the Ti1023_Elβ after deformation under different thermomechanical parameters.*

**Figure 4.42** confirms the qualitative analysis done from **Figure 4.40**. For all cases, the $\rho_{GB}$ is low for the $\alpha$ phase, especially at low strain rate and high

temperature. LAGB progressively form, but very few HAGBs even at the highest strain ($\varepsilon = 1.3$).

Concerning the $\beta$ phase, at 700°C/$10^{-2}$ $s^{-1}$, there is a clear continuous dynamic recrystallization behavior, with the LAGB increasing their misorientation angle and becoming HAGB at high strains (see black arrow). The total $\rho_{GB}$ (on the left, ≥1°) is basically unchanged from $\varepsilon = 0.8$ to 1.3, while the amount of HAGB (on the right, ≥10°) drastically increases. At 750°C/$10^{-2}$ $s^{-1}$, a very low $\rho_{GB}$ is observed in the $\beta$ phase, with a slight increase with increasing strain level.

**Figure 4.43** shows Ti1023_L microstructures after deformation at different temperatures (700 and 750°C) and strain rates ($10^{-1}$ and $10^{-2}$ $s^{-1}$).

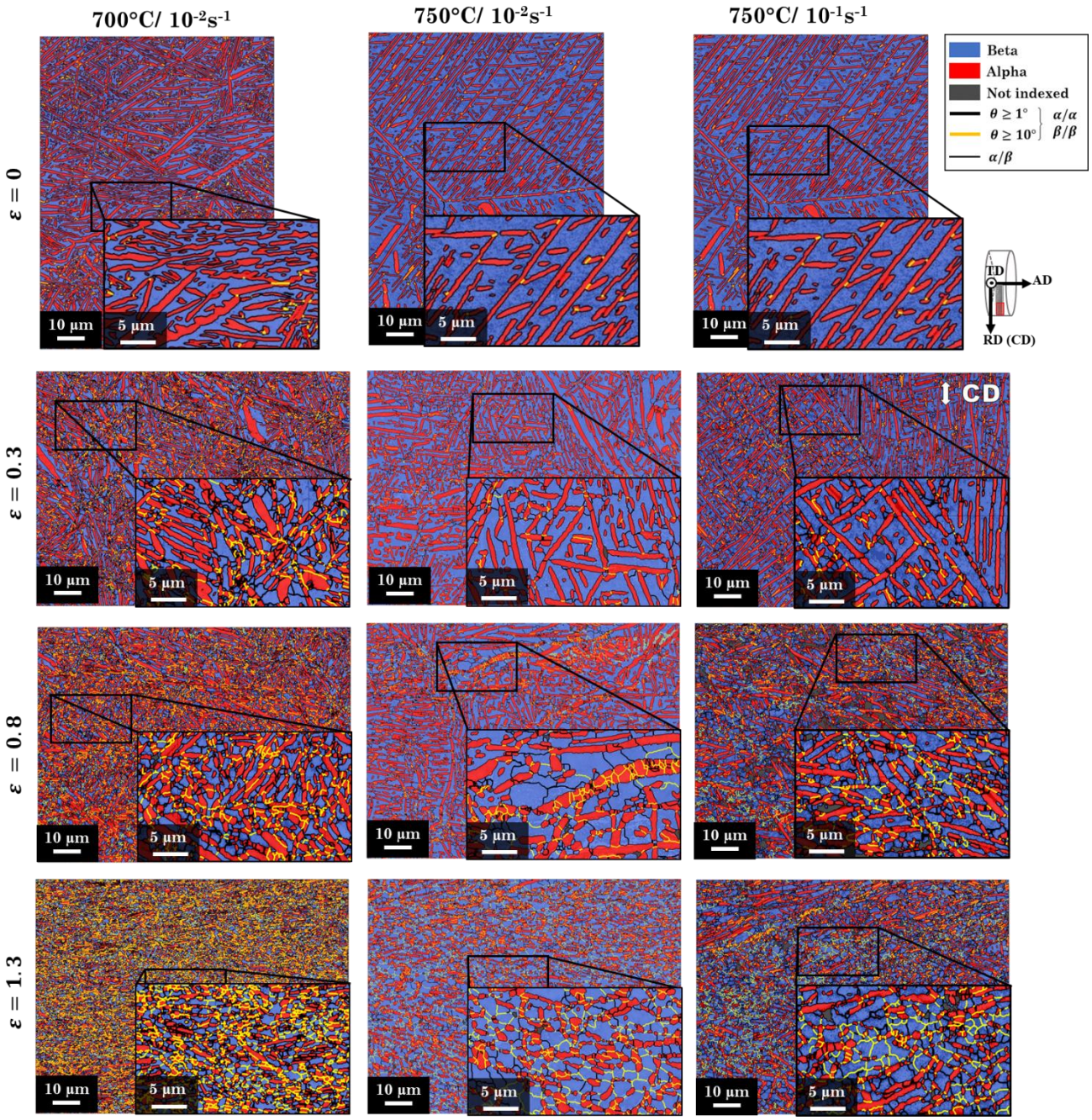



*Figure 4.43. EBSD maps showing LAGBs and HAGBs in the α and β phases of the Ti1023_L microstructures deformed at different strain rates and temperatures, as a function of the equivalent strain level.*

By analyzing **Figure 4.43**, the following observations can be made:

- **At 700°C/10$^{-2}$ s$^{-1}$:** there is a different behavior compared to the equiaxed case. The $\alpha$ phase exhibits a high density of HAGBs, especially at $\varepsilon = 1.3$. For the $\beta$ phase, there is also an increase on the HAGB, but minor when compared to the $\alpha$ phase;
- **At 750°C/10$^{-2}$ s$^{-1}$:** with the increase in strain level, there is a clear increase in HAGB density in both phases. Some $\alpha$ laths are highly recrystallized, especially those at former $\beta/\beta$ grain boundaries ($\alpha_{GB}$), see **Figure 4.44**.

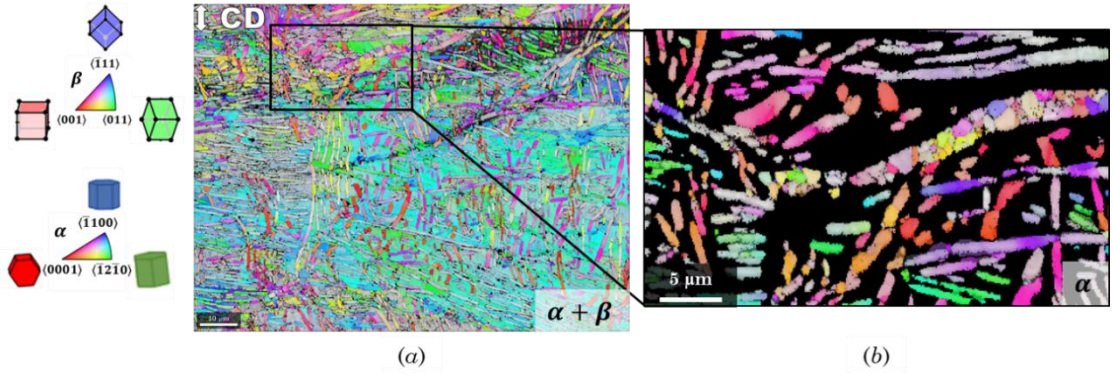



*Figure 4.44. EBSD map (CD-IPF) of the Ti1023_Elβ at ε = 0.8, showing the orientation for: a) both phases, where different β grains can be observed; and b) α phase, zoomed at a former β/β grain boundary to evidence recrystallization inside $\alpha_{GB}$ layer.*

The quantitative analysis for the Ti1023_L is summarized in **Figure 4.45**.

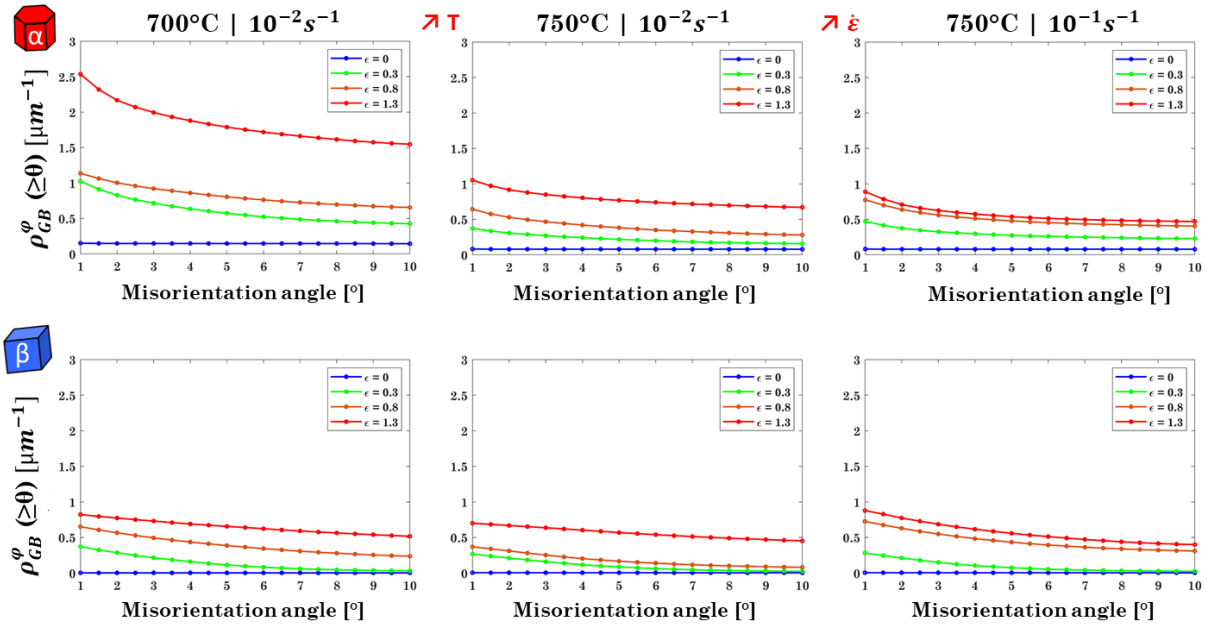



*Figure 4.45. Misorientation angle cumulative distribution analysis for both phases of the Ti1023_L after deformation under different thermomechanical parameters.*

At 700°C, for the $\alpha$ phase, continuous dynamic recrystallization is likely to occur as suggested by the shape of the curves at 0.3 and 0.8, which change in a manner that shows that the total LAGB and HAGB density is basically maintained, but the HAGB density increases, thus LAGB are continuously turning into HAGB. A high $\rho_{GB}$ is especially observed at $\varepsilon = 1.3$. This suggests that low temperatures for

a lamellar Ti1023 microstructures tend to privilege dynamic recrystallization of the $\alpha$ phase.

Similar values of $\rho_{GB}$ are observed for the $\beta$ phase at different thermomechanical conditions, with a minor increase of the LAGB density. This might suggest that the applied conditions do not highly affect the $\beta$ phase in lamellar microstructure, and instead it is the $\alpha$ phase which undergoes most microstructure evolution. Nevertheless, as the dynamic recovery in the $\beta$ phase tends to be swift, the $\rho_{LAGB}$ value might have stagnated due to a partial annihilation of dislocations.

#### *4.2.3.2 Ti64 alloy*

**Figure 4.46** shows Ti64_Eq microstructures after different strain rates ($10^{-1}$ and $10^{-2}$ $s^{-1}$).

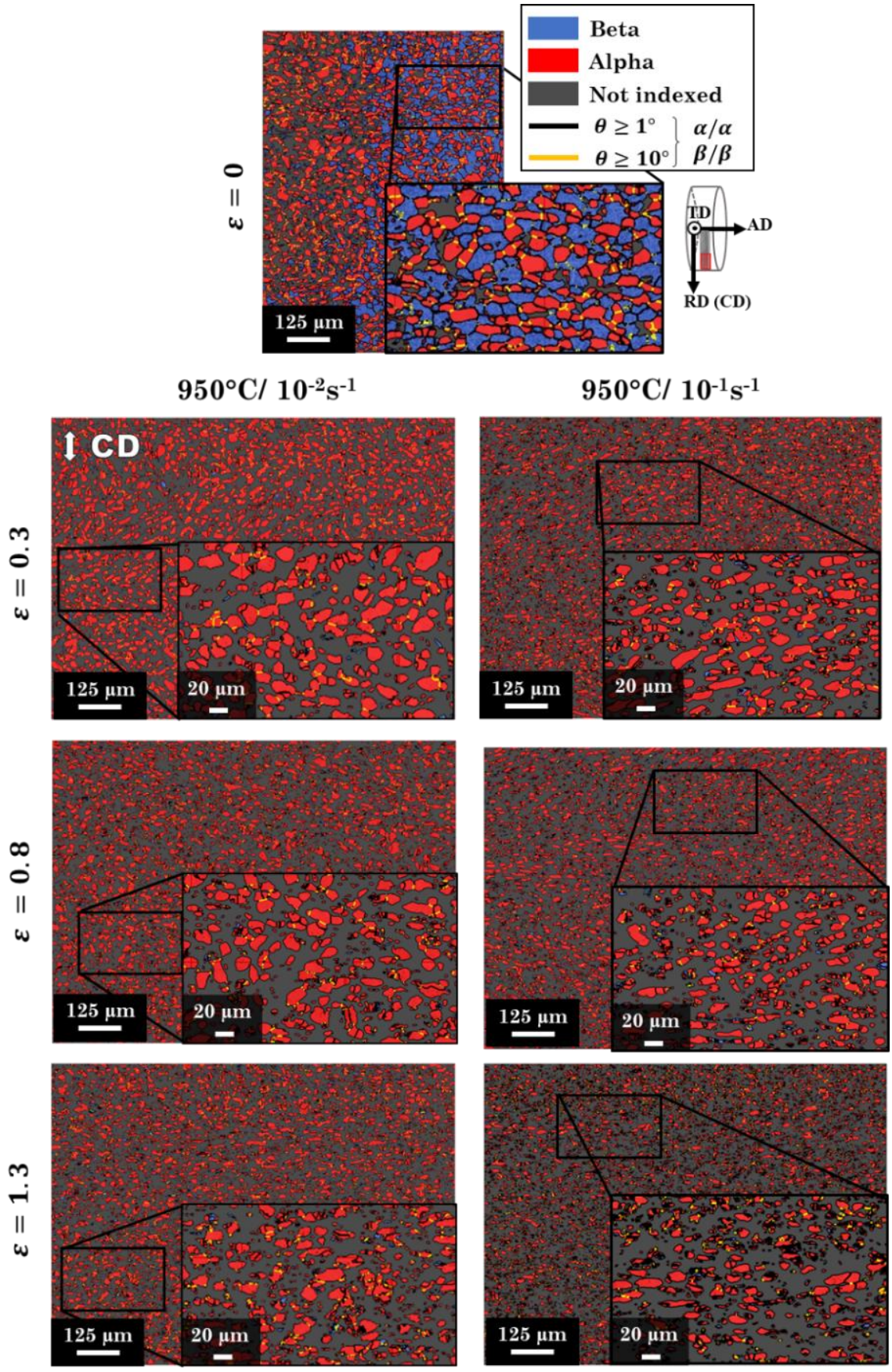



*Figure 4.46. EBSD maps showing the LAGBs and HAGBs in the α phase (and partially reconstructed β) of the Ti64_Eq microstructures deformed at different strain rates and temperatures, as a function of the equivalent strain level.*

Evaluating **Figure 4.46**, it is possible to see that, at $10^{-2}\ s^{-1}$, a similar level of HAGB density is obtained throughout the different strain levels. At $\varepsilon = 0.8$, a higher level of LAGB rate seems to be achieved, while at $\varepsilon = 1.3$ new HAGB seems to appear, especially near the $\alpha/\beta$ boundaries. This might be connected to a discontinuous dynamic recrystallization, which is onset after the stored energy has reached a sufficient level.

Even though, it seems that the $\alpha$ phase is more substructured at $10^{-1}\ s^{-1}$. This behavior is confirmed by the quantitative analysis (**Figure 4.47**), where very low levels of $\rho_{GB}$ are shown for both conditions, yet higher for LAGB (weakly misoriented, *i.e.*, < 3°) at $10^{-1}\ s^{-1}$. Nevertheless, to draw clear conclusions, it would be useful to acquire additional data, with enhanced spatial evolution.

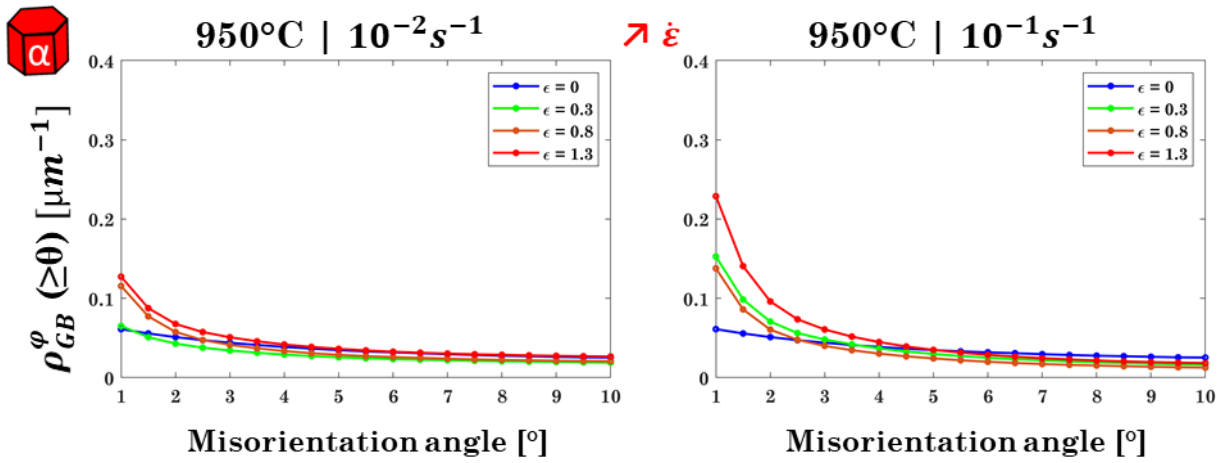



*Figure 4.47. Misorientation angle cumulative distribution analysis for both phases of the Ti64_Eq after deformation under different strain rates.*

**Figure 4.48** shows Ti64_CL microstructures after different strain rates ($10^{-1}$ and $10^{-2}\ s^{-1}$).

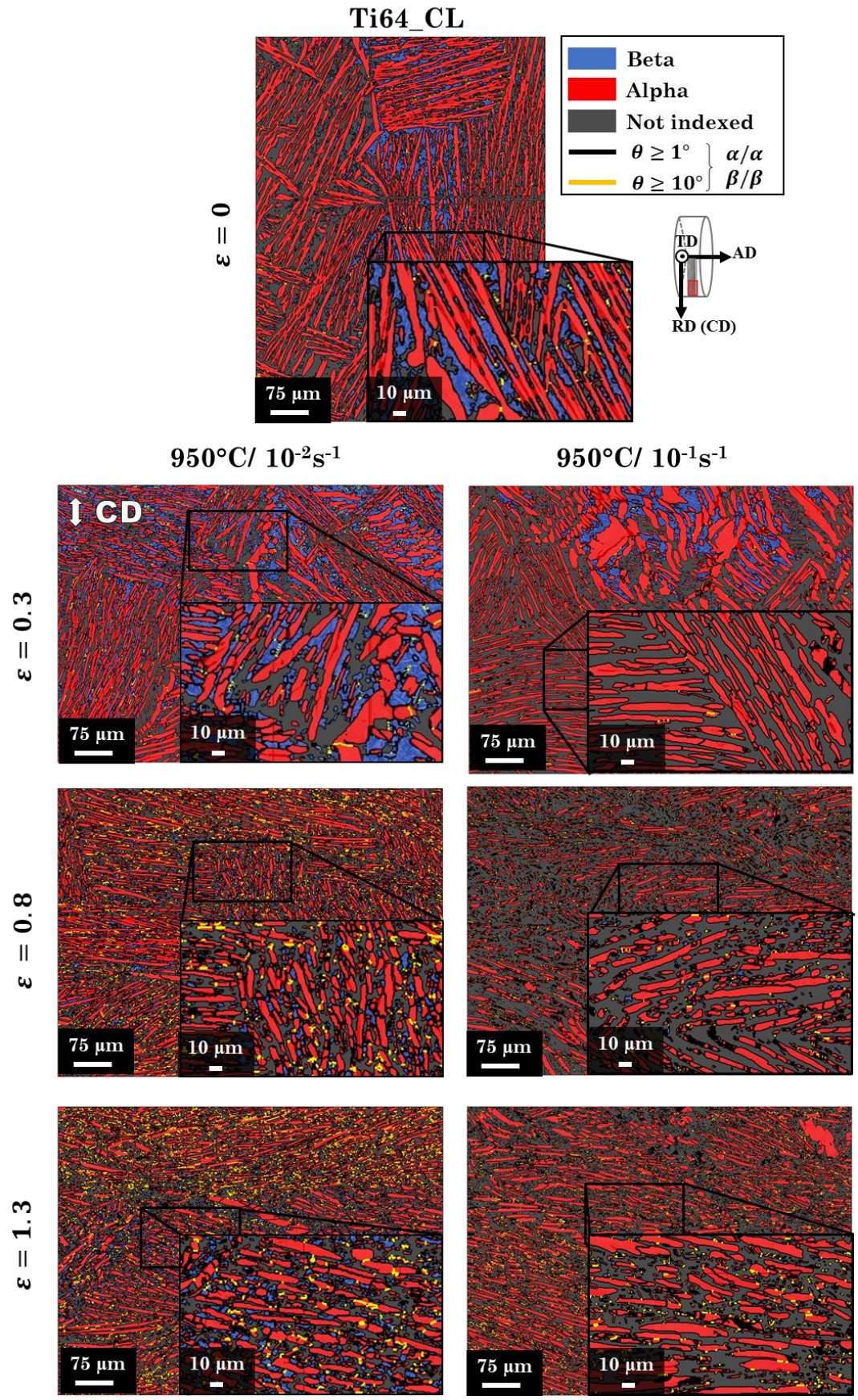



*Figure 4.48. EBSD maps showing LAGBs and HAGBs in the α and β (partially reconstructed) phases of the Ti64_CL microstructures deformed at different strain rates and temperatures, as a function of the equivalent strain level.*

At $\varepsilon = 0.8$ (for the $10^{-2}\ s^{-1}$ condition), a higher level of substructures is observed in the $\alpha$ phase. This seems to be maintained at 1.3 strain level. Comparing to the $10^{-1}\ s^{-1}$, fewer LAGB (black lines) are observed in the deformed microstructure, but with a similar HAGB density (yellow lines).

This behavior is confirmed by the quantitative analysis (**Figure 4.49**), where the total $\rho_{GB}$ is higher at $10^{-1}\ s^{-1}$, but similar levels of HAGB are achieved. Also, for the $10^{-2}\ s^{-1}$ condition, there is almost no difference between the $\rho_{GB}$ at 0.8 and 1.3 strain level (inside only 4 or 5 prior-$\beta$ grains analyzed).

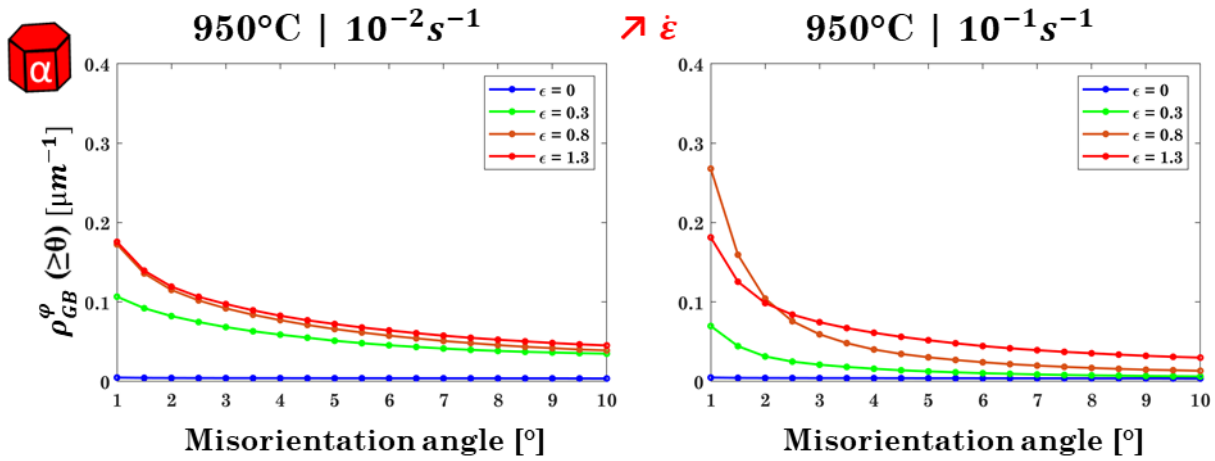



*Figure 4.49. Misorientation angle cumulative distribution analysis for both phases of the Ti64_CL after deformation under different strain rates.*

### 4.2.4 Orientation dependency of substructure formation in α grains

The analysis explained in section **2.7.4** was performed for the four selected microstructures, deformed at different temperatures and strain rates, as a function of the strain level (**Figure 4.50**). The same behavior observed for the seven initial microstructures (**Figure 4.23**) is repeated for the new thermomechanical conditions. For all analyzed cases at $\varepsilon = 1.3$, the grains which are oriented with the basal plane parallel to the CD, presented more substructures (*i.e.*, higher $\rho_{LAGB}$) than the others. This reinforces the fact that the developed texture accompanies (or is accompanied by) a configuration where the substructure density is increased in the $\alpha$ phase.

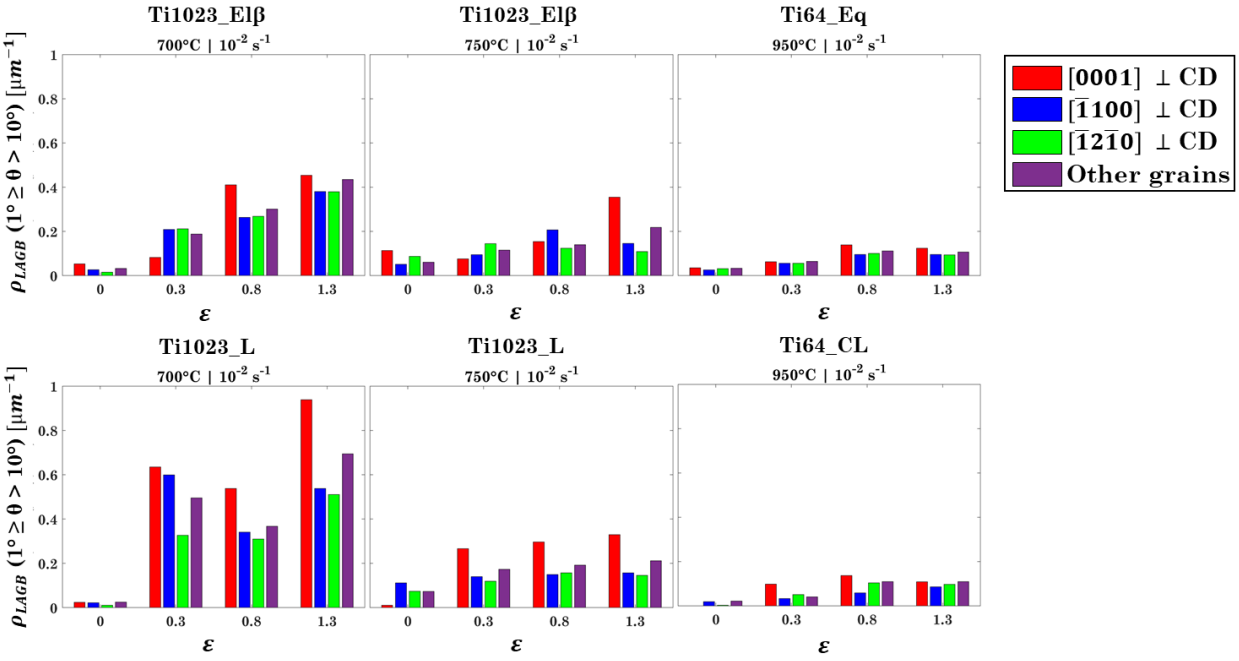



*Figure 4.50. The distribution of the LAGB density in several texture components at different strain levels for the different thermomechanical and microstructural conditions.*

This intrinsic behavior previously observed is also confirmed by the misorientation axis analysis (**Figure 4.51**). The inverse pole figures (top) show that the subgrains formation are mainly caused by rotations around the [0001] axis. Also, the pole figures (bottom) show that this misorientation axis is mostly towards the TD (or WD) axis for the Ti1023 cases, being stronger for the equiaxed ones. For the Ti64 cases, axisymmetric behavior regarding CD is observed, similar to the one seen in **Figure 4.37**. The combination of those two analyses, is in accordance with the previous results (**Figure 4.51**). At $\varepsilon = 1.3$, the $\alpha$ grains with the (0001) basal plane ∥ CD (or the [0001] ⊥ CD), are the ones with higher substructure density.

Also, by comparing the results in **Figure 4.50** with the ones in **Figure 4.23**, the $\rho_{LAGB}$ increased with increasing strain rate, which is consistent with higher dislocation densities and less time for dynamic recovery at higher strain rates. Concerning the Ti1023 microstructures, the $\rho_{LAGB}$ decreased when deformation temperature is increased, which is consistent with lower dislocation densities and faster dynamic recovery at high temperatures.

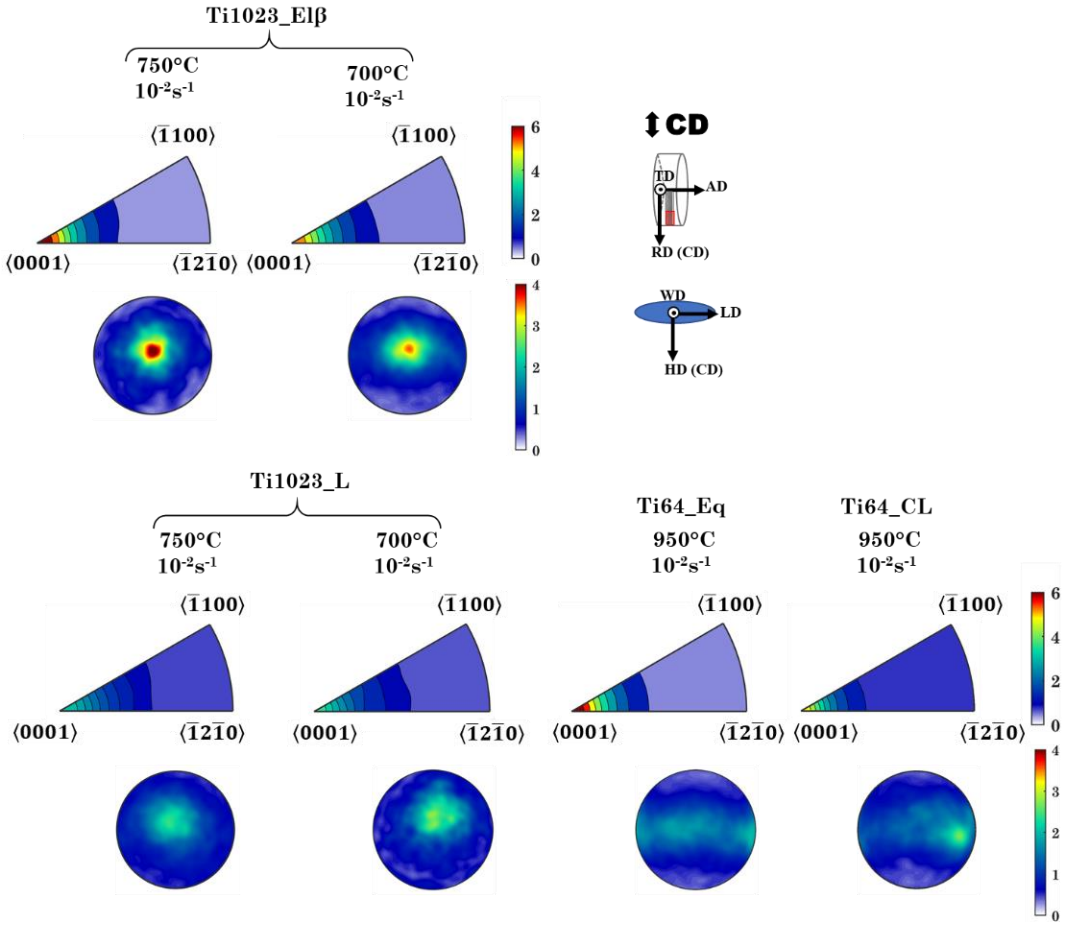



*Figure 4.51. Misorientation axis analysis (for the α phase) in the IPF (top) and the PF (bottom) for the different thermomechanical conditions, at an equivalent strain level of 1.3.*

### 4.2.5 Quantification of α/β boundaries respecting BOR

The $f_{GB_{\alpha/\beta}}^{BOR}$ was also quantified for the different thermomechanical conditions applied to the Ti1023 alloy. For the sake of simplicity, only the quantitative results will be shown on **Figure 4.52**.

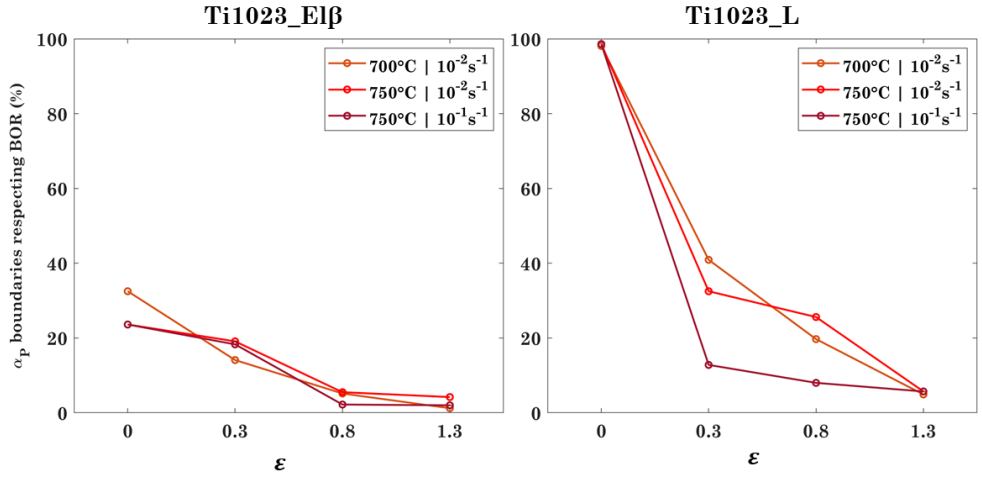



*Figure 4.52. Quantitative analysis of the fraction of α/β boundaries respecting the BOR (5° tolerance) on the Ti1023 alloys after deformation under different thermomechanical conditions.*

For the Ti1023_El$\beta$ at 700°*C*, the initial $f_{GB_{\alpha/\beta}}^{BOR}$ seems to be slightly higher than at 750°*C*. Yet during deformation, it drops to the lowest $f_{GB_{\alpha/\beta}}^{BOR}$ values, then maintains very similar values to the other conditions. Higher strain rate seems to slightly promote faster decrease in the fraction of $\alpha/\beta$ boundaries respecting BOR, but the difference is minor with the available data and would deserve being confirmed with more data.

For the Ti1023_L, the starting point at 700°*C* and 750°*C* are basically the same, which was expected, as almost all $\alpha$ laths from cooling respect the BOR, except the ones at the $\beta/\beta$ grain boundaries, which respect only one of the grains (see **Figure 4.15**). With further deformation, higher strain rate and temperature favor faster decrease in the $f_{GB_{\alpha/\beta}}^{BOR}$. However, at high strain level (1.3), all conditions reached the same fraction of $\alpha/\beta$ boundaries respecting BOR, being quite low and close to the ones measured in equiaxed microstructures. Noteworthily, the $f_{GB_{\alpha/\beta}}^{BOR}$ value for a completely random (synthetically generated) EBSD data was found to be extremely low (0.6%).

### *4.2.6 GND density estimation*

The dislocation density ($\rho_{EBSD}^{\varphi}$) was estimated for each of the thermomechanical and initial microstructures by the procedure described in section **2.7.5**. The dislocation density maps for the $\alpha$ and $\beta$ phases, with their average values, for the Ti1023_El$\beta$, after deformation at three different thermomechanical conditions, are shown in **Figure 4.53**. Lowering temperature or increasing strain rate in the Ti1023_El$\beta$ microstructure had similar influence on the $\alpha$ phase average GND density.

Concerning the $\beta$ phase, increasing strain rate, resulted in a greater increase of the average dislocation density, compared to lowering the temperature. Nevertheless, it is worth mentioning that one of the reasons for this behavior is that, at 700°*C*, a higher HAGB density on the $\beta$ phase was obtained (see **Figure 4.40**). As it was shown in **Figure 4.27**, when the misorientation angle is equal or above the chosen HAGB threshold (10°), those boundaries are not included in the calculation, as they are considered as new grains. This might be the reason why the $\rho_{EBSD}^{\beta}$ measured after deformation at 700°*C* and $10^{-1}$ $s^{-2}$ is lower when compared to deformation at 750°*C* and $10^{-1}$ $s^{-1}$, as more continuous dynamic recrystallization is achieved.

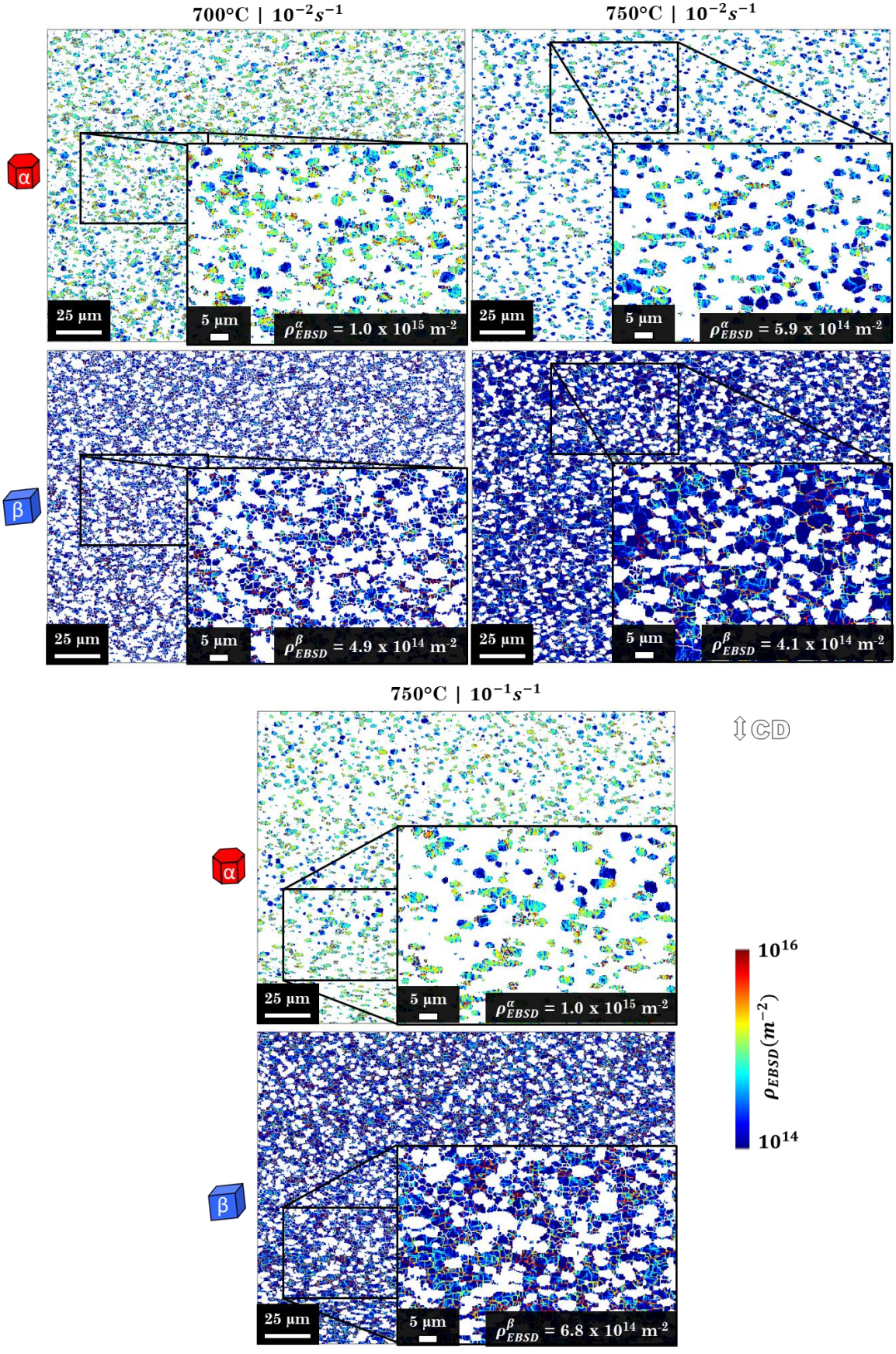



*Figure 4.53. GND density maps for α and β phases (with their average values) of the Ti1023_Elβ deformed to ε=1.3, as a function of the three different thermomechanical conditions.*

The phase average GND density ($\rho_{EBSD}^{\varphi}$) was estimated for each of the four selected microstructures as a function of the different thermomechanical conditions applied. The results for the Ti1023 alloy are summarized in **Figure 4.54**. The estimated initial $\rho_{EBSD}^{\varphi}$ of all cases are similar, the materials having a very low dislocation density level. Increasing the strain level, the tendencies described in section **4.1.5** seem to be maintained, where $\rho_{EBSD}^{\alpha}$ tends to increase, while $\rho_{EBSD}^{\beta}$ tends to stagnate/ decrease.

- **Ti1023_El*β*:** At 700°*C*, $\rho_{EBSD}^{\alpha}$ is rapidly increased, compared to 750°*C*/ $10^{-2}$ $s^{-1}$. Nevertheless, at 750°*C*/ $10^{-1}$ $s^{-1}$, similar dislocation density level is obtained at $\varepsilon$=1.3, as seen in **Figure 4.53**. It appears that increasing temperature (from 700°*C* to 750°*C*) has decreasing effect on the $\rho_{EBSD}^{\alpha}$ values, while the increase in strain rate (from $10^{-2}$ to $10^{-1}$ $s^{-1}$) has an increasing effect. Concerning the $\beta$ phase, the temperature decrease (from 750°*C* to 700°*C*) had more effect on $\rho_{EBSD}^{\beta}$ values, compared to the increment in strain rate (from $10^{-2}$ to $10^{-1}$ $s^{-1}$). Nevertheless, as seen in **Figure 4.54**, at 1.3 strain level, the progress of continuous dynamic recrystallization causes the $\rho_{EBSD}^{\beta}$ at 700°*C* to decrease, as the formed HAGB are not included in the calculation. Also, the new recrystallized $\beta$ grains seem to be slightly smaller when the temperature is lower and the strain rate is higher, their average being approximately 2 $\mu m$ for both 700°*C*/ $10^{-2}$ $s^{-1}$ and 750°*C*/ $10^{-1}$ $s^{-1}$ conditions, while 3 $\mu m$ for the 750°*C*/ $10^{-2}$ $s^{-1}$.
- **Ti1023_L:** A similar behavior is observed for the $\alpha$ phase, compared to the equiaxed one. At 700°*C*/ $10^{-2}$ $s^{-1}$, the $\rho_{EBSD}^{\alpha}$ is immediately increased, while very similar dislocation density levels are observed with increasing strain rate (from $10^{-2}$ $s^{-1}$ to $10^{-2}$ $s^{-1}$, both at 750°*C*). It is worth mentioning that the decrease in the dislocation density from 0.3 to 0.8 strain level might be due to the onset of recrystallization, as already suggested by **Figure 4.45**. As those boundaries are not included in the $\rho_{EBSD}^{\alpha}$ calculation, it has an effect of declining the dislocation density. Concerning the $\beta$ phase, similar effects of the increase in the strain rate or decrease in temperature are observed on the $\rho_{EBSD}^{\beta}$, with a minor increase on the estimated dislocation density.

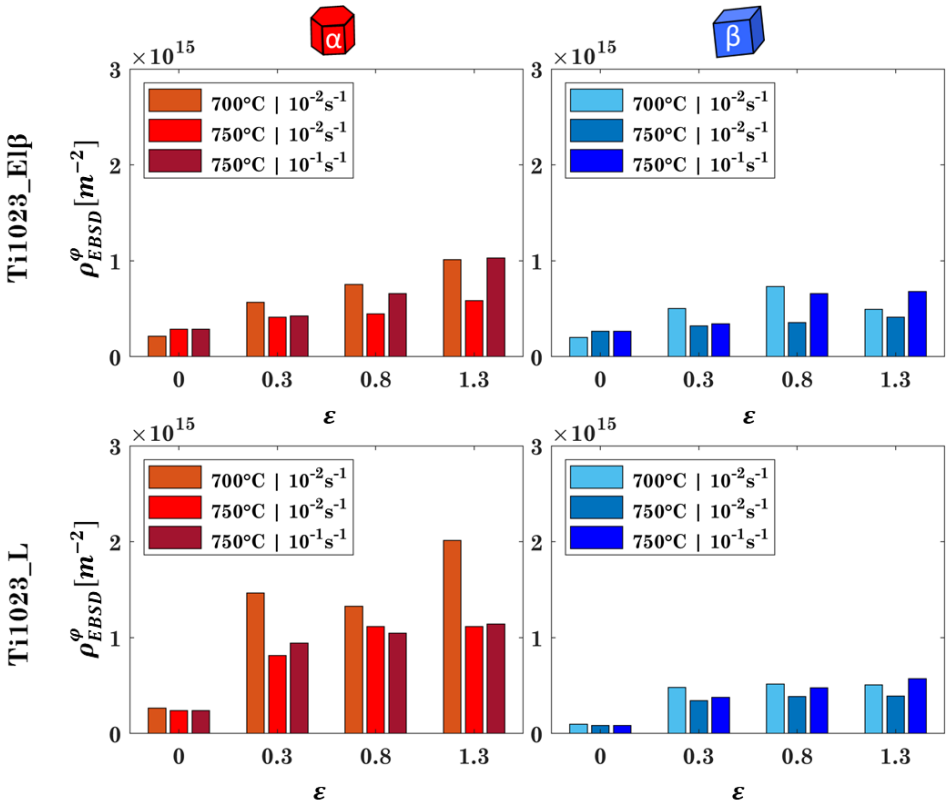



*Figure 4.54. The average GND density for the α and β phases for the Ti1023 alloy deformed under different thermomechanical conditions.*

The results for the Ti64 alloy are summarized in **Figure 4.55**.

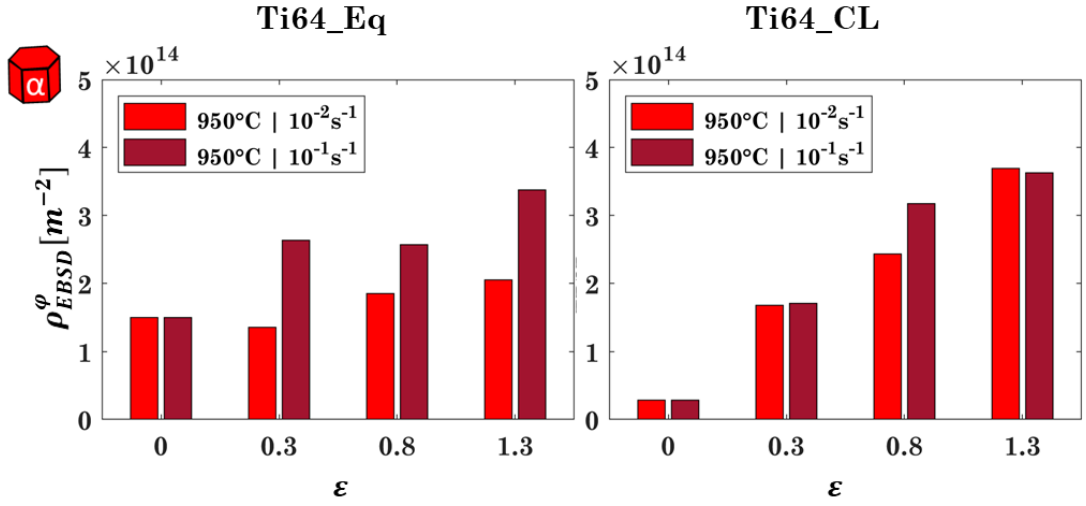



*Figure 4.55. The average GND density for the primary α phase for the Ti64 alloy deformed at 950°C under different strain rates, as a function of the strain level.*

- **Ti64_Eq:** The $\alpha$ phase dislocation density is increased with increasing strain rate (from $10^{-2}$ to $10^{-1}$ $s^{-1}$), showing a clear effect on the $\rho^{\alpha}_{EBSD}$ of the equiaxed $\alpha$ grains in the Ti64 alloy.
- **Ti64_CL:** similar values of $\rho^{\alpha}_{EBSD}$ are obtained at different strain rates throughout deformation. Only at 0.8 strain level does the higher strain rate seem to have a higher impact on the dislocation density, which

could then be due to the development of LAGB, as seen in **Figure 4.49**. Nevertheless, to draw clear conclusions, it would be useful to have a higher statistical representativeness through additional data.

## 4.3 Summary and Conclusions

In this chapter, after a detailed evaluation of different microstructural features for a vast range of initial microstructures submitted to different thermomechanical conditions, the following conclusions can be drawn.

An intrinsic behavior of the $\alpha$ phase was observed at high strain levels ($\varepsilon$ =1.3), summarized in **Figure 4.56**. In nearly all microstructures analyzed, after $\varepsilon$ =1.3 (independently of the temperature or strain rate), the $\alpha$ grains tend to align morphologically perpendicular to the CD. When initially equiaxed, the $\alpha$ grains tend to elongate and align ⊥ CD. By the analysis of those elongated grains specifically, it was observed that they possess a very strong crystallographic orientation, where the basal plane $(0001)_\alpha$ and the $\langle 11\bar{2}0\rangle_\alpha$ directions tend to align parallel to the CD. Interestingly, it was observed for almost all cases, that this same texture was developed in the whole analyzed zones. Also, it appears that the developed preferred crystallographic orientation, is accompanied by a higher deformation of the $\alpha$ grains, as proved by analyzing the LAGB density according to the grain orientation. It was shown that those exact same grains with $(0001)_\alpha$ and $\langle 11\bar{2}0\rangle_\alpha \parallel$ CD, are the ones with the most advanced substructure formation.

On the other hand, initial α lamellae undergo kinking, breakage and alignment in the same morphological direction (⊥ CD) and crystallographic orientation ($(0001)_\alpha$ and $\langle 11\bar{2}0\rangle_\alpha \parallel$ CD).

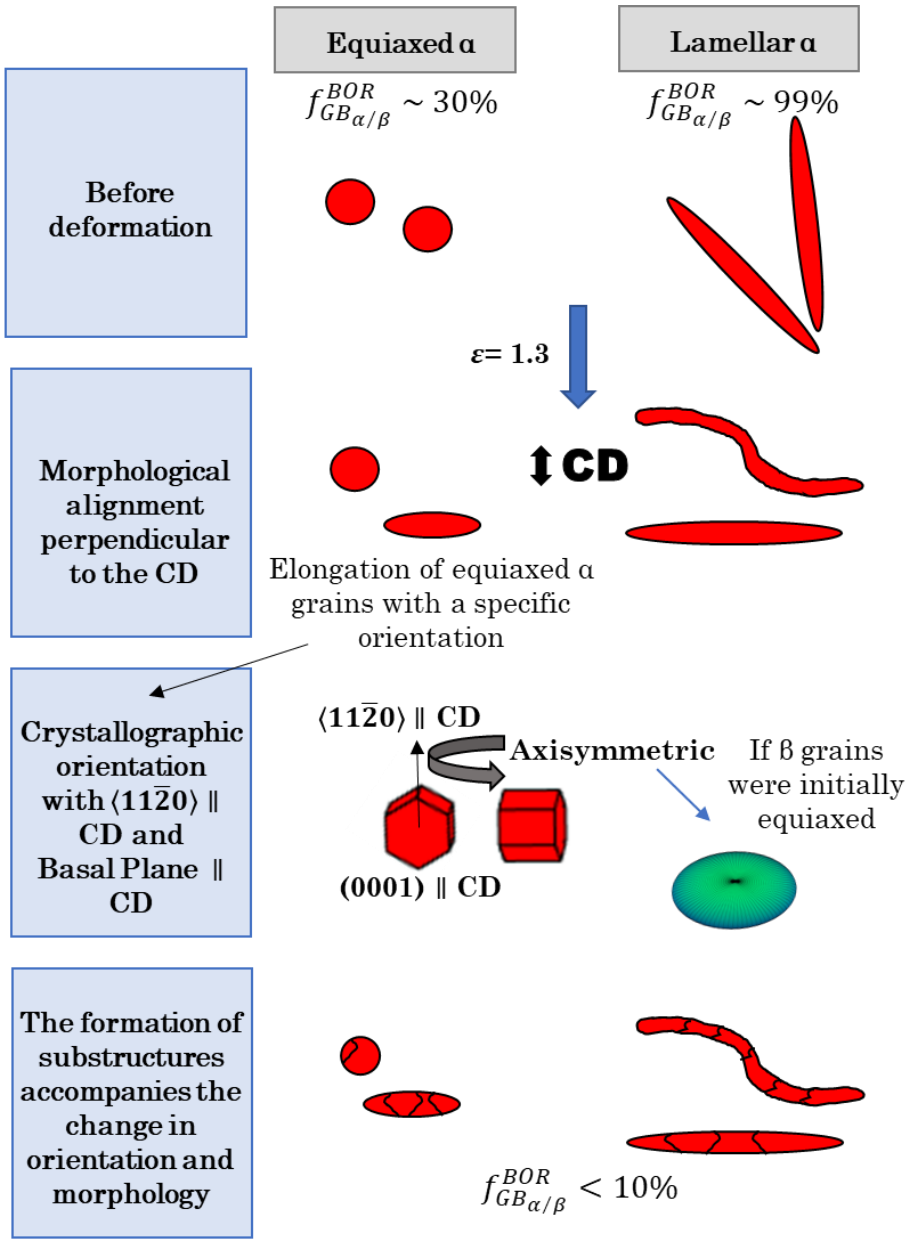



*Figure 4.56. Schematic diagram of the observed intrinsic behavior (meaning independent of the hosting β grain orientation) of the α phase (in both Ti1023 and Ti64 alloys) at 1.3 strain level, when deformed at 50 – 100°C below β-transus and at $10^{-1}$ and $10^{-2}$ $s^{-1}$.*

Interestingly, even if distinct alloys, morphologies, temperatures and strain rates were analyzed, this same intrinsic behavior seems to rule the $\alpha$ phase evolution on two-phase titanium alloys. Only one microstructure did not follow this behavior, the Ti64_750°C. It could be possibly be related to the fact that the Ti64 alloy was deformed at a much lower temperature ($T_\beta - 250°C$). At 750°C, the $f_{\alpha_P}$ of the Ti64 is approximately 81%, being closer to a $\alpha$ alloy than a $\alpha$+$\beta$ alloy, hence the difference in behavior of their microstructure.

The difference between the $\alpha$ phase of two alloys seems to be minor with regard to this observed intrinsic behavior. In the Ti64 alloy, higher spatial resolution EBSD maps showed that dynamic recrystallization of the equiaxed $\alpha$ grains occurs

nearby the $\alpha/\alpha$ and $\alpha/\beta$ grain boundaries, which could not be checked for the Ti1023 alloy, due to the unavailability of EBSD maps with higher spatial resolution.

Concerning the lamellar $\alpha$ phase, besides the underlying behavior explained in **Figure 4.56**, a strong presence of lath kinking and breakage was observed, yet very little dynamic globularization was seen. Nevertheless, by comparing the two Ti64 microstructures with lamellar $\alpha$, it seems easier to form HAGBs on finer $\alpha$ laths. For both alloys, the lamellar $\alpha$ phase at the grain boundaries ($\alpha_{GB}$) was the one which presented more substructuring, with high breakage level after $\varepsilon$ =1.3. On the other hand, the some of the lath colonies were basically kinked (depending on their orientation), behavior confirmed by 3D characterizations.

Furthermore, the intrinsic behavior of the $\alpha$ phase seems to be independent of the $\beta$-grain orientation, as same trends were observed in the texture evolution of the $\alpha$ phase inside different $\beta$-grain orientations.

Regarding the $\beta$ phase, for both Ti1023 microstructures with equiaxed $\alpha$ grains (Ti1023_El$\beta$ and Ti1023_Eq), the $\beta$ grains at the initial state (*i.e.,* $\varepsilon$ =0) were already substructured, with equivalent $\rho_{GB}$ levels. The initial shape of the $\beta$ grains seems to intervene with increasing deformation. For the Ti1023_El$\beta$ microstructure, heterogenous dynamic recrystallization of the $\beta$ grains was observed. At low strain levels ( $\varepsilon = 0.3$ ), recrystallization appeared to be concentrated near $\beta/\beta$ grain boundaries. With further strain (*i.e.,* $\varepsilon$ =0.8 and 1.3), continuous dynamic recrystallization progressed heterogeneously depending on the orientation of the $\beta$ grains. For both strain levels (0.8 and 1.3), the $\beta$ grains that are oriented with the ⟨110⟩ ∥ CD, are the ones that presented the most advanced continuous dynamic recrystallization levels. In constrast, for the Ti1023_Eq microstructure, continuous dynamic recrystallization occurred homogeneously within the $\beta$ phase while deforming up to $\varepsilon = 0.8$ and 1.3. Thus, it appears that a microstructure which contains highly elongated $\beta$ (*e.g.,* Ti1023_El$\beta$) tends to promote heterogeneously recrystallized $\beta$ grains after deformation. Furthermore, at high strain levels ($\varepsilon = 1.3$), the development of ⟨001⟩ ∥ CD and ⟨$\bar{1}$11⟩ ∥ CD texture components were always observed for the three different Ti1023 microstructures.

Concerning the Burgers orientation relationship (BOR), it was shown that the applied deformation has a very strong impact on the fraction of $\alpha/\beta$ boundaries respecting the BOR ($f_{GB_{\alpha/\beta}}^{BOR}$). Even if the microstructures with lamellar $\alpha$ phase initially presented a much higher $f_{GB_{\alpha/\beta}}^{BOR}$ (~99%), after low deformation levels ($\varepsilon$ = 0.3), they reached similar $f_{GB_{\alpha/\beta}}^{BOR}$ values compared to the equiaxed $\alpha$ microstructures. In addition, temperature and strain rate seemed to have a minor impact on the $f_{GB_{\alpha/\beta}}^{BOR}$ evolution compared to the strain level.

Concerning the dynamic phase transformation reported in the literature on the deformation of titanium alloys in the $\alpha + \beta$ domain, it was not observed in these thesis experiments, based on the measured $f_{\alpha_P}$ values before and after deformation. It appears that the thermomechanical conditions applied in the double-cone samples (*i.e.,* strain rates from 0.01 to 0.1 $s^{-1}$, temperatures from $T_\beta$ - 50°$C$ to $T_\beta$ - 100°$C$ and relatively long holding times) do not favor this phenomenon. In some other works, lower strain rates (< 0.01 $s^{-1}$), torsion tests and no holding time prior to deformation seemed to favor dynamic transformation. Also, some of

the studied alloys were different, which may have also influenced the observation of this dynamic transformation.

To summarize the effect of the initial microstructure and thermomechanical parameters on the microstructural evolution, a detailed description of was performed. The influence of those parameters on the LAGB and HAGB density ($\rho_{GB}$) in the Ti1023 and Ti64 alloys are summarized in **Table 4.3** and **Table 4.4**, respectively. The increase or decrease of the $\rho_{GB}$ (density of $\alpha/\alpha$ and $\beta/\beta$ grain boundaries) are represented, respectively, by ↗ and ↘. Also, when two arrows are shown (*e.g.,* ↘↘), it represents a strong effect.

| Thermomechanical parameter | Equiaxed morphology | | Lamellar morphology | |
|---|---|---|---|---|
| | $\alpha$ | $\beta$ | $\alpha$ | $\beta$ |
| ↗ $\dot{\varepsilon}$ ($0.01 \rightarrow 0.1\ s^{-1}$) | ↗ (Very small effect) | ↗ | No effect | ↗ (Very small effect) |
| ↗ $T$ ($700 \rightarrow 750°C$) | No effect | ↘ | ↘↘ | ↘ (Very small effect) |
| ↗ $\varepsilon$ ($0 \rightarrow 1.3$) | ↗ (Very small effect) | At 700°C: ↗ RX homogeneously At 750°C: ↗ RX heterogeneously (first at GB, then inside $\beta$ grains with [110] ∥ CD) | ↗ (Only at 700°C) | ↗ (Especially at GB) |

*Table 4.3. Influence of the thermomechanical parameters and initial morphology on the LAGB and HAGB density in the Ti1023 alloy.*

| Thermomechanical parameter | Equiaxed morphology | Lamellar morphology |
|---|---|---|
| | $\alpha$ | |
| ↗ $\dot{\varepsilon}$ ($0.01 \rightarrow 0.1\ s^{-1}$) | ↗ (Small effect) | ↗ (Very small effect) |
| ↗ $\varepsilon$ ($0 \rightarrow 1.3$) | ↗ (Small effect) | ↗ (Small effect) |

*Table 4.4. Influence of the strain rate and level on the LAGB and HAGB density in the Ti64 alloy with equiaxed or lamellar morphology.*

Some other conclusions can be drawn from **Table 4.3**. For example, regarding the lamellar $\alpha$ Ti1023 microstructure (Ti1023_L), it appears that the temperature reduction (from 750°C to 700°C) had a strong impact in the $\alpha$ phase, yet hardly any substructuring in the $\beta$ phase was observed. On the other hand, in an equiaxed $\alpha$ microstructure (Ti1023_El$\beta$), the changes in temperature and strain rate mainly affect the $\beta$ phase evolution. Concerning the Ti64 microstructures, it appears that

increasing strain level and rate did not affect much the substructure formation in the $\alpha$ phase. It seems that a microstructure with finer $\alpha$ lamellae would promote higher LAGB and HAGB density. However, it appears that the HAGB formation on the Ti64 alloys occurs with the form of very small recrystallized grains (~1 $\mu m$). Consequently, in order to draw further conclusions, other high spatial resolution analysis should be performed.

In terms of dislocation density analysis, the internal energy minimization approach was implemented for all studied cases. It is worth mentioning that the estimated values cannot be simply compared without considering the LAGB and HAGB kinetics, as the method is connected to the threshold applied for separating intragranular misorientation from those at (high angle) grain boundaries. Consequently, as the $\alpha$ phase develops higher LAGB density, compared to the HAGBs, the $\rho_{EBSD}^{\alpha}$ tends to increase with increasing strain. This is reinforced by observation of the developed texture that accompanies a higher substructure development in the $\alpha$ grains. In contrast, the $\beta$ phase undergoes faster dynamic recrystallization, where new HAGB are continuously formed. Being the HAGB criterion the threshold also for the $\rho_{EBSD}^{\beta}$ calculation, there is a tendency to decrease its value.

It is important to recall that the notion of *dislocation density* has a clear and precise definition. The $\rho_{EBSD}$ measured here should be considered as a quantity that is linked to the dislocation density, yet it must be different, as a lower bound (only GNDs being considered). Those conclusions will be analyzed furtherly in section **5.7**, by the comparison between the macroscopic and microscopic approaches for the assessment of the dislocation density in each of both $\alpha$ and $\beta$ phases.

## 4.4 Résumé en Français

Dans ce chapitre, après une évaluation détaillée des différentes caractéristiques microstructurales pour une vaste gamme de microstructures initiales soumises à différentes conditions thermomécaniques, les conclusions suivantes peuvent être tirées.

Un comportement intrinsèque de la phase $\alpha$ a été observé à des niveaux de déformation élevés ($\varepsilon$ =1,3), résumé à la **Figure 4.56**. Dans presque toutes les microstructures analysées, après $\varepsilon$ =1,3 (indépendamment de la température ou de la vitesse de déformation), les grains $\alpha$ ont tendance à s'aligner morphologiquement perpendiculairement à la DC (direction de compression). Lorsqu'ils sont initialement équiaxes, les grains $\alpha$ ont tendance à s'allonger et à s'aligner $\perp$ DC. Par l'analyse de ces grains allongés spécifiquement, il a été observé qu'ils possèdent une très forte texture cristallographique, où le plan basal $(0001)_\alpha$ et les directions $\langle 11\bar{2}0\rangle_\alpha$ ont tendance à s'aligner parallèlement à la DC. Fait intéressant, il a été observé pour presque tous les cas, que cette même texture se développait dans l'ensemble des zones analysées. Aussi, il apparaît que l'orientation cristallographique préférée développée, s'accompagne d'une déformation plus importante des grains $\alpha$, comme le prouve l'analyse de la densité de LAGB en fonction de l'orientation des grains. Il a été montré que ces mêmes grains avec $(0001)_\alpha$ et $\langle 11\bar{2}0\rangle_\alpha \parallel$ DC, sont ceux avec la formation de sous-structures la plus avancée.

D'autre part, les lamelles $\alpha$ initiales subissent un flambement, une cassure et un alignement dans la même direction morphologique ($\perp$ DC) et orientation cristallographique ($(0001)_\alpha$ et $\langle 11\bar{2}0\rangle_\alpha \parallel$ DC).

Il est intéressant de signaler que, même si des alliages, des morphologies, des températures et des vitesses de déformation distincts ont été analysés, ce même comportement intrinsèque semble régir l'évolution de la phase $\alpha$ sur les alliages de titane à deux phases. Une seule microstructure n'a pas suivi ce comportement, le Ti64_750°C. Cela pourrait être lié au fait que l'alliage Ti64 s'est déformé à une température beaucoup plus basse ($T_\beta - 250°C$). À 750°$C$, le $f_{\alpha_P}$ du Ti64 est d'environ 81%, se rapprochant plus d'un alliage $\alpha$ que d'un alliage $\alpha$+$\beta$, d'où la différence de comportement de leur microstructure.

La différence entre la phase $\alpha$ des deux alliages semble être mineure au regard de ce comportement intrinsèque observé. Dans l'alliage Ti64, des cartes EBSD à plus haute résolution spatiale ont montré que la recristallisation dynamique des grains $\alpha$ équiaxes se produit à proximité des joints de grains $\alpha/\alpha$ et $\alpha/\beta$, ce qui n'a pas pu être vérifié pour l'alliage Ti1023, en raison de l'indisponibilité des cartes EBSD avec résolution spatiale suffisamment élevée.

Concernant la phase $\alpha$ lamellaire, outre le comportement sous-jacent expliqué à la **Figure 4.56**, une forte présence de flambement et de cassure des lamelles a été observée, mais très peu de globularisation dynamique. Néanmoins, en comparant les deux microstructures Ti64 avec la phase $\alpha$ lamellaire, il semble plus facile de former des HAGB sur des lamelles $\alpha$ plus fines. Pour les deux alliages, la phase $\alpha$ lamellaire aux joints de grains ($\alpha_{GB}$) est celle qui présente le plus de sous-structuration, très cassées quand $\varepsilon$ =1,3. En revanche, certaines des colonies de

lamelles étaient fondamentalement flambées/ déformées (selon leur orientation), comportement confirmé par les caractérisations 3D.

De plus, le comportement intrinsèque de la phase $\alpha$ semble être indépendant de l'orientation des grains $\beta$, car les mêmes tendances ont été observées dans l'évolution de la texture de la phase $\alpha$ à l'intérieur de différentes orientations des grains $\beta$.

En ce qui concerne la phase $\beta$, pour les deux microstructures Ti1023 avec des grains $\alpha$ équiaxes (Ti1023_El$\beta$ et Ti1023_Eq), les grains $\beta$ à l'état initial (c'est-à-dire $\varepsilon$ =0) étaient déjà sous-structurés, avec des niveaux de $\rho_{GB}$ équivalents. La forme initiale des grains $\beta$ semble intervenir au cours de la déformation. Pour la microstructure Ti1023_El$\beta$, une recristallisation dynamique hétérogène des grains $\beta$ a été observée. Aux faibles niveaux de déformation ($\varepsilon$ = 0,3), la recristallisation semble être concentrée près des joints de grains $\beta/\beta$. Avec une déformation plus importante (c'est-à-dire $\varepsilon$ = 0,8 et 1,3), la recristallisation dynamique continue progresse de manière hétérogène en fonction de l'orientation des grains $\beta$. Pour les deux niveaux de déformation (0,8 et 1,3), les grains $\beta$ qui sont orientés avec le ⟨110⟩ ∥ DC, sont ceux qui ont présenté les niveaux de recristallisation dynamique continue les plus avancés. En revanche, pour la microstructure Ti1023_Eq, la recristallisation dynamique continue s'est produite de manière homogène dans la phase $\beta$ tout en se déformant jusqu'à $\varepsilon$ = 0,8 et 1,3. Ainsi, il apparaît qu'une microstructure qui contient des $\beta$ très allongés (par exemple, Ti1023_El$\beta$) a tendance à favoriser les grains $\beta$ recristallisés de manière hétérogène après déformation. De plus, à des niveaux de déformation élevés ( $\varepsilon$ = 1,3), le développement des composants de texture ⟨001⟩ ∥ DC et ⟨$\bar{1}$11⟩ ∥ DC a toujours été observé pour les trois microstructures différentes de Ti1023.

Concernant la relation d'orientation de Burgers (BOR), il a été montré que la déformation appliquée a un très fort impact sur la fraction des joints $\alpha/\beta$ respectant la BOR ($f_{GB_{\alpha/\beta}}^{BOR}$). Même si les microstructures à phase $\alpha$ lamellaire présentaient initialement un $f_{GB_{\alpha/\beta}}^{BOR}$ très élevé (~99%), après de faibles niveaux de déformation ($\varepsilon$ = 0,3), elles atteignaient des valeurs de $f_{GB_{\alpha/\beta}}^{BOR}$ similaires comparées aux microstructures $\alpha$ équiaxes. De plus, la température et la vitesse de déformation semblaient avoir un impact mineur sur l'évolution de $f_{GB_{\alpha/\beta}}^{BOR}$ par rapport au niveau de déformation.

Concernant la transformation de phase dynamique rapportée dans la littérature sur la déformation des alliages de titane dans le domaine $\alpha + \beta$, elle n'a pas été observée dans ces expériences de thèse, sur la base des valeurs de $f_{\alpha_P}$ mesurées avant et après déformation. Il apparaît que les conditions thermomécaniques appliquées dans les pions double-cônes (c'est-à-dire des vitesses de déformation de 0,01 to 0,1 $s^{-1}$, des températures de $T_\beta$ - 50°$C$ à $T_\beta$ - 100°$C$ et des temps de maintien relativement longs) ne favorisent pas ce phénomène. Dans d'autres travaux, des vitesses de déformation plus faibles (< 0,01 $s^{-1}$), des tests de torsion et l'absence de temps de maintien avant déformation semblaient favoriser la transformation dynamique. De plus, certains des alliages étudiés étaient différents, ce qui peut aussi avoir influencé l'observation de cette transformation dynamique.

Pour résumer l'effet de la microstructure initiale et des paramètres thermomécaniques sur l'évolution microstructurale, une description détaillée a été réalisée. L'influence de ces paramètres sur la densité LAGB et HAGB ($\rho_{GB}$) dans les alliages Ti1023 et Ti64 est résumée dans les tableaux **4.3** et **4.4**, respectivement. L'augmentation ou la diminution des $\rho_{GB}$ (densité des joints de grains $\alpha/\alpha$ et $\beta/\beta$) sont représentées respectivement par ↗ et ↘. De plus, lorsque deux flèches sont affichées (par exemple, ↘ ↘), cela représente un effet plus important.

D'autres conclusions peuvent être tirées du tableau **4.3**. Par exemple, concernant la microstructure du Ti1023 avec $\alpha$ lamellaire (Ti1023_L), il apparaît que la baisse de température (de 750°C à 700°$C$) a eu un fort impact sur la phase $\alpha$, mais pratiquement aucune sous-structuration en phase $\beta$ n'a été observée. D'autre part, dans une microstructure avec $\alpha$ équiaxe (Ti1023_El$\beta$), les changements de température et de vitesse de déformation affectent principalement l'évolution de la phase $\beta$. Concernant les microstructures Ti64, il semble que l'augmentation du niveau et de la vitesse de déformation n'affecte pas beaucoup la formation de sous-structures dans la phase $\alpha$. Il semble qu'une microstructure avec des lamelles $\alpha$ plus fines favoriserait une densité de LAGB et HAGB plus élevée. Cependant, il apparaît que la formation de HAGB sur les alliages Ti64 se produit sous la forme de très petits grains recristallisés (~1 $\mu m$). Par conséquent, afin de tirer d'autres conclusions, d'autres analyses à haute résolution spatiale doivent être effectuées.

En termes d'analyse de densité de dislocations, l'approche de minimisation de l'énergie interne a été mise en œuvre pour tous les cas étudiés. Il convient de mentionner que les valeurs estimées ne peuvent pas être simplement comparées sans tenir compte les cinétiques LAGB et HAGB, car la méthode est liée au seuil appliqué pour séparer la désorientation intragranulaire de celles aux joints de grains (angle élevé). Par conséquent, à mesure que la phase $\alpha$ développe une densité de LAGB plus élevée, par rapport aux HAGB, le $\rho_{EBSD}^{\alpha}$ a tendance à augmenter avec l'augmentation de la contrainte. Ceci est renforcé par l'observation de la texture développée qui accompagne un développement de sous-structure plus élevé dans les grains $\alpha$. En revanche, la phase $\beta$ subit une recristallisation dynamique plus rapide, où de nouveaux HAGB sont formés en continu. Le critère HAGB étant également le seuil pour le calcul de $\rho_{EBSD}^{\beta}$, il y a une tendance à diminuer sa valeur.

Il est important de rappeler que la notion de densité de dislocations a une définition claire et précise. Cependant, cette définition est difficile à utiliser car il n'est pas possible de faire des mesures précises de cette densité et en particulier à l'échelle de cette étude. Dans cette étude nous avons introduit la densité de dislocations mesurées par EBSD ($\rho_{EBSD}$) qui peut être interprétée comme une estimation de l'ordre de grandeur des GND. Ces conclusions seront analysées plus en détail dans la section **5.7**, par la comparaison entre les approches macroscopiques et microscopiques pour l'évaluation de la densité de dislocations dans chacune des phases $\alpha$ et $\beta$.

# 5. MACROSCOPIC APPROACH: RHEOLOGICAL ANALYSIS BASED ON COMPRESSION TESTS

The goal of this chapter is the same as the microstructural approach (Chapter **4**): estimate an average dislocation density per phase, but with a different approach allowing the comparison of the values obtained through different approaches (and scales). To this end, a macroscopic approach (described in sections **5.1** to **5.6**) was implemented, based on stress-strain curves, which were exploited to assess the macroscopic flow stress of each phase. Then, an estimation of the dislocation density distribution between both phases could be performed through this flow stress-based approach.

Furthermore, deformations in the $\beta$ domain were also performed, aiming to compare the stress-strain curves to the estimated ones for the $\beta$ phase (section **5.5.2.1**).

Finally, a comparison is performed for the estimated dislocation densities, between the EBSD (detailed in section **4.1.5**) and the rheological (this chapter) approaches. A discussion is developed on how far the different approaches can be compared to each other and suggestions are given to better correlate them.

## 5.1 A rule of mixtures (ROM) as a ground assumption

In the case of multiphase materials, the correlation between the flow stress with the developed microstructure is highly complex. According to numerous studies regarding deformation mechanisms and metallurgical evolution, phase fraction appears as a very influential parameter on flow stress [6]. When dealing with phase transformation materials, the rule of mixtures (ROM) is so far the simplest and most used method to quantify the macroscopic heterogeneous material behavior, as shown in equation **(5.1)**.

$$\sigma(\varepsilon, \dot{\varepsilon}, T) = ROM[\sigma_\alpha(\varepsilon, \dot{\varepsilon}, T), \sigma_\beta(\varepsilon, \dot{\varepsilon}, T), f_\alpha(T)] \quad (5.1)$$

where $\sigma$ is the flow stress of the alloy, $\sigma_\alpha$ and $\sigma_\beta$ are the individual flow stresses of each phase and $f_\alpha$ is the $\alpha$ phase fraction. It is known that those stresses are dependent on different parameters, thermomechanical ($\varepsilon, \dot{\varepsilon}, T$) and microstructural (*e.g.*, grain size, morphology, phase topology, crystallographic texture). However, this work focuses on the temperature and strain level dependence of $\sigma$, at a given strain rate, aiming to reduce the total number of tests, as different initial microstructures are analyzed. As mentioned previously, the aim of this chapter is to allow a comparison of the dislocation density values obtained in Chapter **4**, by a macroscopic approach. Thus, it does not include the identification of the constitutive behavior of the phases. To this end, the exact same set of thermomechanical parameters described in section **4.1** were applied for selected initial microstructures.

In the case of $\alpha$+$\beta$ titanium alloys, the overall flow stress can be expressed, in a first approximation, as a linear combination of individual flow stresses in each phase [6,84–86], not taking into account interactions between the phases. Aiming to obtain different phase fractions at the same temperature, different holding times were applied, a short one (*off*-equilibrium) and a longer one (*in*-equilibrium), as done in [6]. Hence, at a given temperature, the stresses of the alloy after each applied holding time is expressed, assuming a homogenous deformation (Voigt assumption), by equation **(5.2)**. It is important to mention that this a strong

hypothesis, and most likely it is not valid. However, considering the data and time available, it was the most reasonable choice that could be made.

$$\begin{aligned} \sigma^{in-eq} &= \sigma_\alpha f_\alpha^{in-eq} + \sigma_\beta (1 - f_\alpha^{in-eq}) \\ \sigma^{off-eq} &= \sigma_\alpha f_\alpha^{off-eq} + \sigma_\beta (1 - f_\alpha^{off-eq}) \end{aligned} \quad (5.2)$$

with $f_\alpha$ being the $\alpha$ phase fraction, $\sigma_\alpha$ and $\sigma_\beta$ being the stress in each phase, and $\sigma^{in-eq}$ and $\sigma^{off-eq}$ being the flow stresses measured experimentally for *in* and *off*-equilibrium conditions, respectively. For each point of the experimental $\sigma$ *vs* $\varepsilon$ curve, the resolution of this linear system provides values for individual stresses $\sigma_\alpha$ and $\sigma_\beta$. To do this, some of the compression test conditions applied on the double-cone samples were duplicated on cylindrical samples (*cf.* section **2.9.4**). The selected microstructures and thermomechanical parameters are described in sections **5.2** and **5.3**, respectively.

## 5.2 Selected initial microstructures

From the seven initial microstructures (all shown in **Figure 3.7**), four microstructures (Ti1023_Eq, Ti1023_L, Ti64_Eq, Ti64_CL) were selected to have two different morphologies (equiaxed and lamellar) for each of both alloys (Ti64 and Ti1023). The lamellar Ti64 morphology with thicker lamellae was selected to have a nearer $\alpha$ grain size compared to the equiaxed morphology. These four selected microstructures, with their characteristic dimensions, are schematized in **Figure 5.1**.

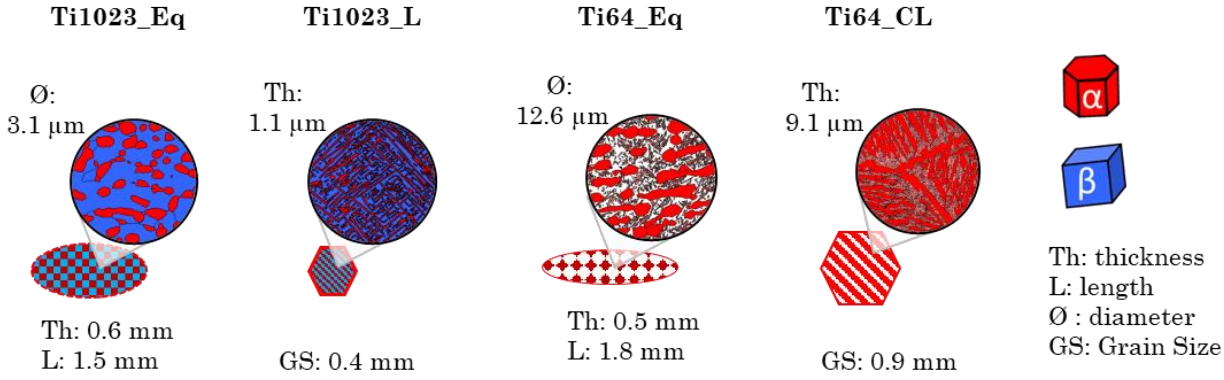



*Figure 5.1. The four selected microstructures from the seven initial ones for the rheological approach.*

## 5.3 Experimental setup and thermomechanical parameters for *in*- and *off*-equilibrium conditions

The experimental design of this analysis, with the information obtained, is displayed in **Figure 5.2**.

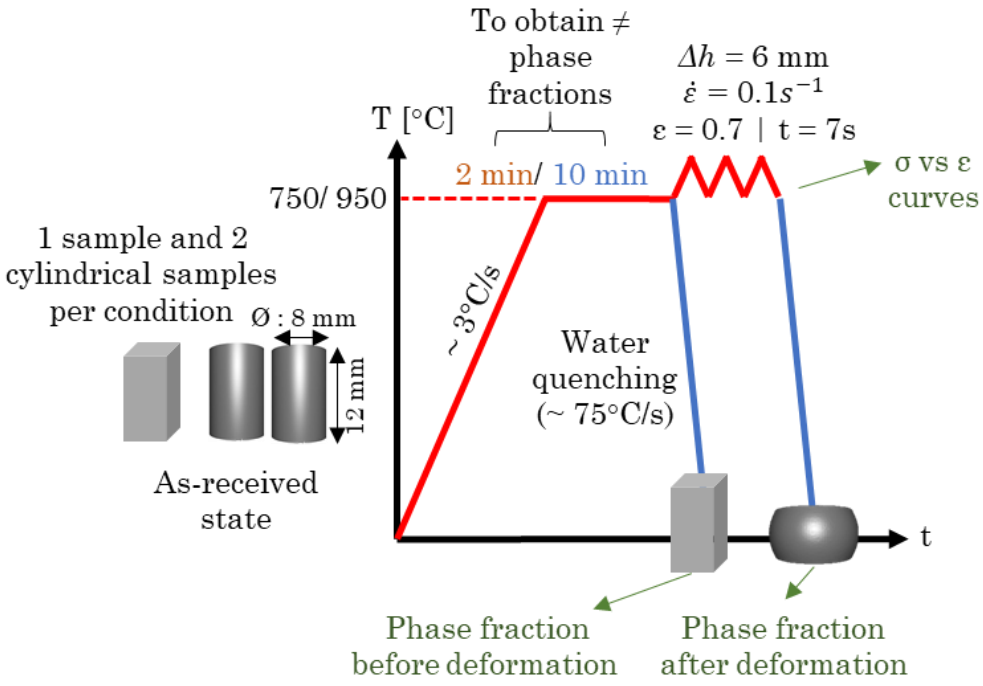



*Figure 5.2. Experimental design of the rheological approach, with the two different holding times to obtain different phase fractions at the same temperature (750°C for Ti1023 and 950°C for Ti64 samples).*

Each deformation condition was repeated twice, for the sake of reproducibility check. Cylindrical sample were coated with boron nitride that served as a lubricant during compression. Initially, each sample was heated at the targeted temperature (750°*C* for the Ti1023 and 950°*C* for the Ti64 alloy) during two different holding times to obtain different phase fractions at the same deformation temperature:

- **2 minutes (*off*-equilibrium):** minimum time for the temperature of the compression machine to stabilize after its opening to place the sample. This time was measured from the moment at which the sample is inserted in the machine;
- **10 minutes (*in*-equilibrium):** time required for phase fraction equilibrium, after experimental verifications in [6].

For the non-deformed states, a simple parallelepipedal sample with similar dimensions was used.

## 5.4 Phase fraction measurements

The microstructures obtained by quenching, before and after deformation, with different holding times, are presented from **Figure 5.3** to **Figure 5.6**, for the four microstructures. The average phase fraction with its standard deviation were obtained after measuring four micrographs for each state, representing a total surface between 0.058 $mm^2$ (for the Ti1023_L) and 0.608 $mm^2$ (for the Ti64_CL).

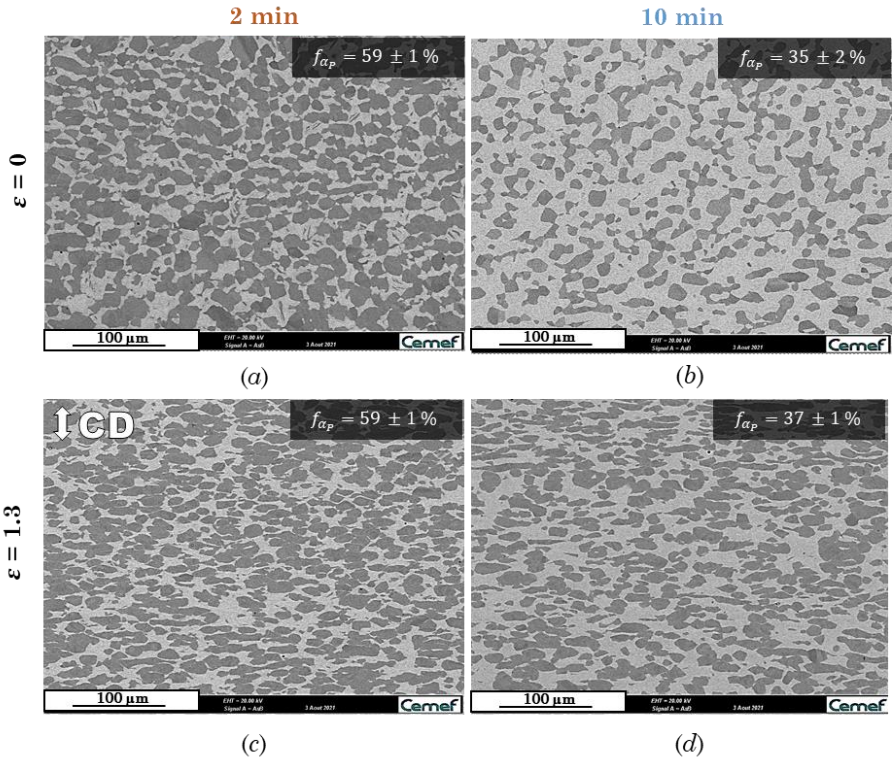



*Figure 5.3. Microstructures (BSE images) of the equiaxed Ti64_Eq obtained by quenching from 950°C, with their respective primary α phase fractions, at different instants: a) 2-minute holding, before deformation; b) 10-minute holding, before deformation; c) 2-minute holding, after deformation; d) 10-minute holding, after deformation.*

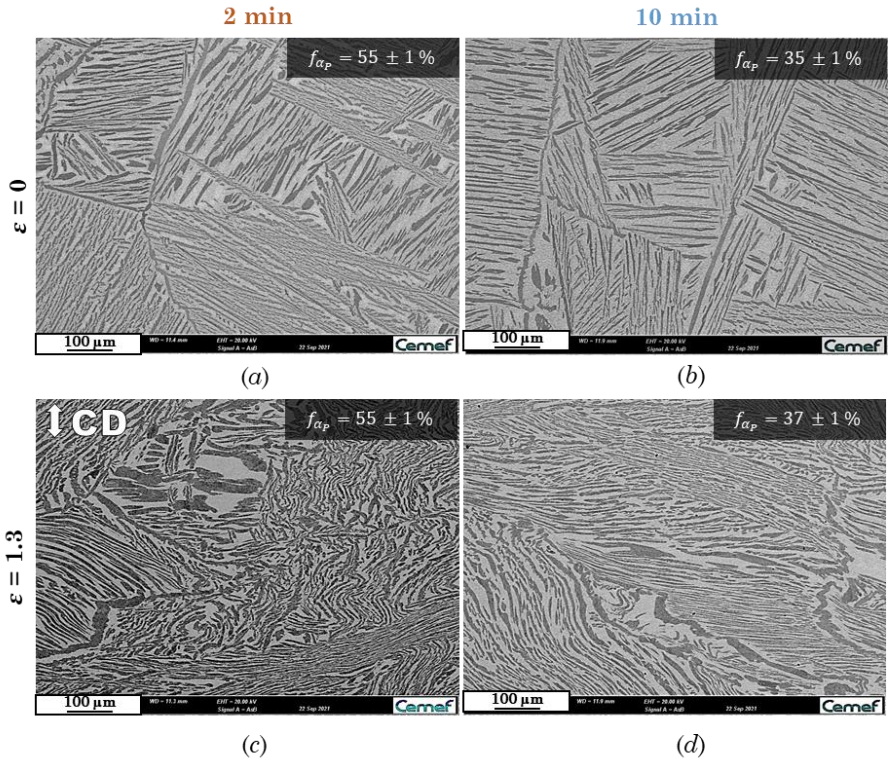



*Figure 5.4. Microstructures (BSE images) of the lamellar Ti64_CL obtained by quenching from 950°C, with their respective primary α phase fractions, at different instants: a) 2-minute holding, before deformation; b) 10-minute holding, before deformation; c) 2-minute holding, after deformation; d) 10-minute holding, after deformation.*

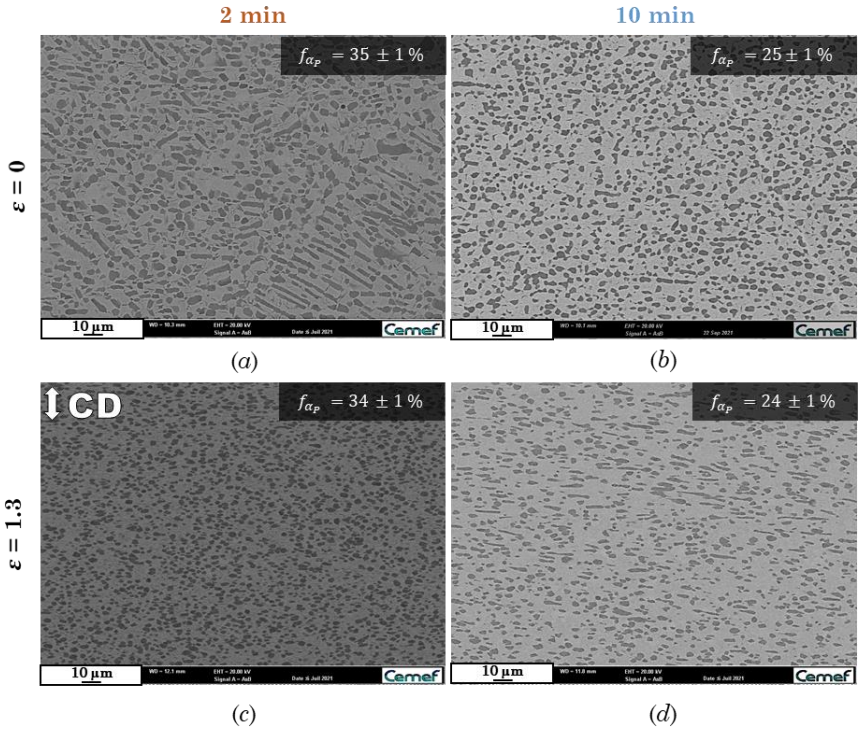



*Figure 5.5. Microstructures (BSE images) of the equiaxed Ti1023_Eq obtained by quenching from 750°C, with their respective primary α phase fractions, at different instants: a) 2-minute holding, before deformation; b) 10-minute holding, before deformation; c) 2-minute holding, after deformation; d) 10-minute holding, after deformation.*

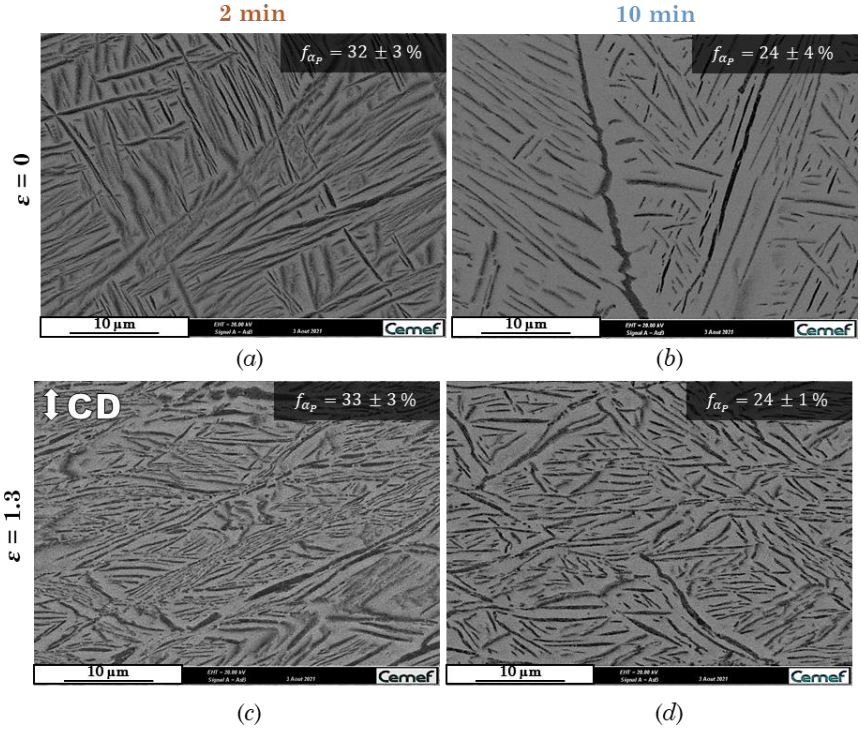



*Figure 5.6. Microstructures (BSE images) of the lamellar Ti1023_L obtained by quenching from 750°C, with their respective primary α phase fractions, at different instants: a) 2-minute holding, before deformation; b) 10-minute holding, before deformation; c) 2-minute holding, after deformation; d) 10-minute holding, after deformation.*

Those figures (**Figure 5.3** to **Figure 5.6**) show that the two different holding times effectively lead to distinct phase fractions.

The phase fractions obtained after 2 or 10-minute holding times and in the deformed states of each microstructure already shown on **Figure 5.3** to **Figure 5.6** are summarized in **Figure 5.7**. As expected [17], after a holding time as short as 2 min, the primary $\alpha$ phase fraction is higher, the thermodynamic equilibrium not being achieved. No change in phase fraction during deformation, *i.e.,* no dynamic phase transformation, was observed, again. The primary $\alpha$ phase fraction ($f_{\alpha_P}$) will thus be considered as constant in equation **(5.2)**, throughout the whole stress-strain curves.

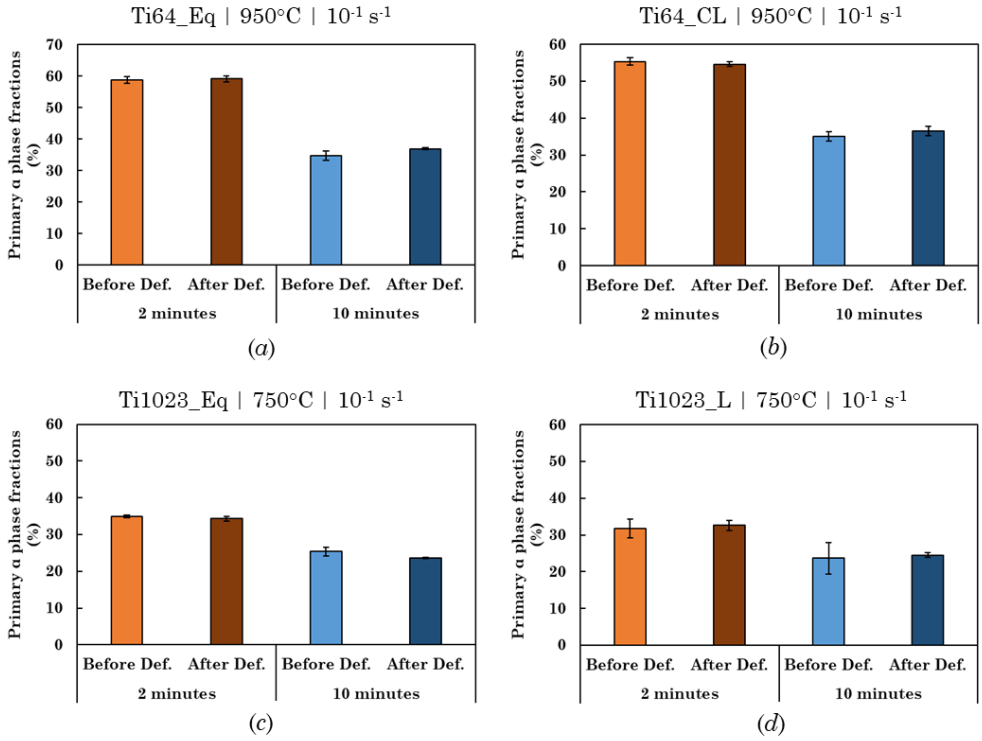



*Figure 5.7. Summary of the phase fractions according to the different holding times and deformation states, for the four selected microstructures*

## 5.5 Analysis of rheological data

### *5.5.1 Experimental stress-strain curves*

The rheology of the microstructures is studied via the compression of cylindrical samples. Due to the rigidity of the assembly of the compression machine, the final height of the deformed sample is slightly greater than the targeted theoretical height, *i.e.,* the height which would result purely from the displacement of the tool entered as a setpoint. This deviation from the theoretical height may vary moderately depending on the tests. To be able to better compare the forces recorded for the various tests, a variation in the effective height of the sample $|\Delta h_{sample}|$ is calculated using the following equation [87]:

$$|\Delta h_{sample}(t)| = |\Delta h_{total}(t)| - \frac{|F(t)|}{\kappa} \tag{5.3}$$

where $F(t)$ is the force measured at time $t$ and κ ($kN/mm$) is the rigidity of the machine for the test considered. $k$ is estimated from the difference between the theoretical final height and the effective final height of the sample for each test. The macroscopic true strain ($\varepsilon$) and the macroscopic true stress ($\sigma$), or flow stress, are then calculated in a conventional way from $|\Delta h_{sample}|$ :

$$\varepsilon(t) = -ln\left(\frac{h_0 - |\Delta h_{sample}(t)|}{h_0}\right) \tag{5.4}$$

$$\sigma(t) = \frac{1}{\pi r_0^2}\frac{h_0 - |\Delta h_{sample}(t)|}{h_0}|F(t)| \tag{5.5}$$

where $h_0$ and $r_0$ are the initial height and radius of the sample (12 and 4 $mm$, respectively).

The experimental true stress / true strain curves of two different samples submitted to the same test conditions (dashed lines) and their average (full lines) are summarized in **Figure 5.8**. It shows good reproducibility of the results, for each of the initial microstructures and applied deformation conditions. Furthermore, as expected, when the $\alpha$ phase fraction is higher (after holding for only 2 minutes), the stress levels are higher, consistent with the $\alpha$ phase being the harder one [6,9].

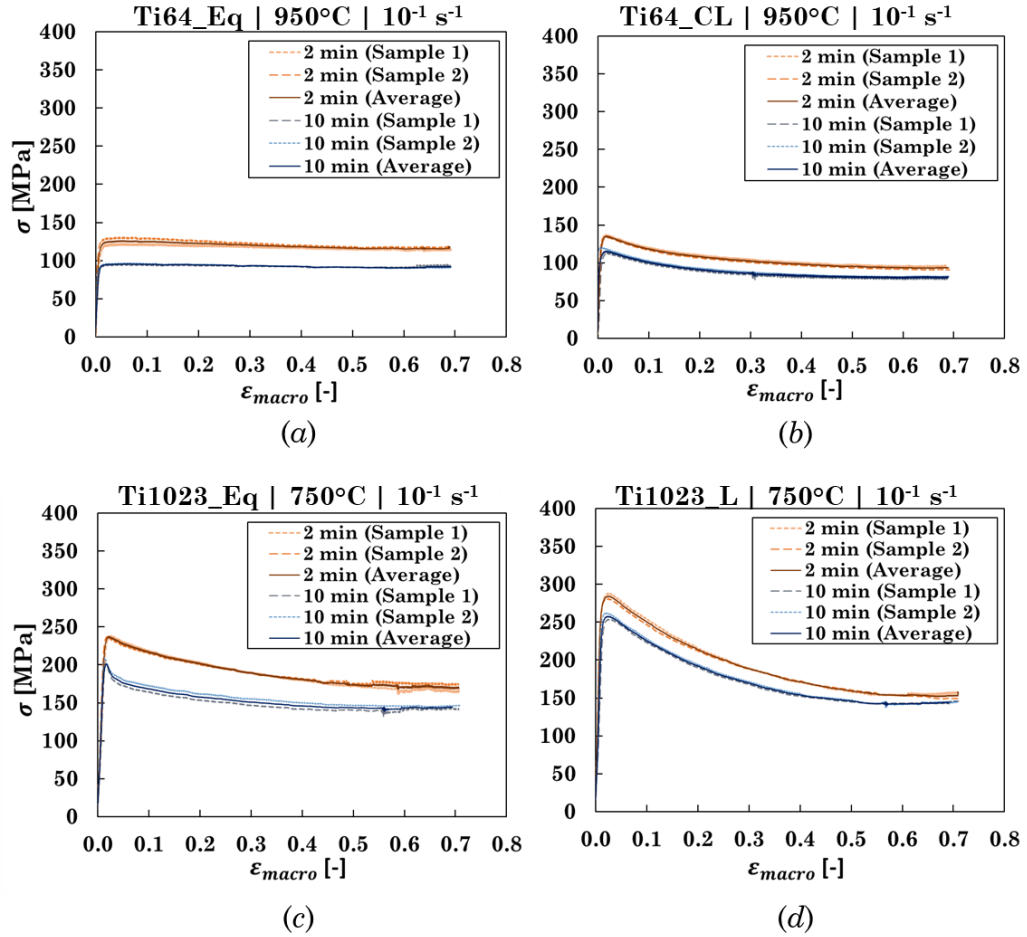



*Figure 5.8. Experimental stress-strain curves for two different samples (dashed lines) and their average (full line), after holding for 2 (orange) and 10 (blue) minutes, for each of the four selected microstructures.*

When comparing the different morphologies (lamellar vs equiaxed), higher stress peaks are observed at low strain levels for the lamellar cases, probably related to the orientation/kinking of laths [25], as visible on **Figure 5.4** and **Figure 5.6**. Nevertheless, after a certain strain level ($\varepsilon_{macro}$ around 0.4), similar stress values are achieved for both morphologies, which could be explained by related to the lath rotation to a softer configuration (alignment perpendicularly to the compression direction), referred to as flow softening mechanism [25]. It was also shown in section **4.1.2** that there is a texture development of the $\alpha$ (**Figure 4.4**) and $\beta$ (**Figure 4.8**) phases during deformation. Similar textures were obtained for lamellar and equiaxed morphologies at high equivalent strain levels, and also similar flow stresses are observed for those two morphologies in both alloys.

### *5.5.2 α and β-phase flow stresses obtained by the rule of mixtures*

The resolution of the linear system presented in equation **(5.2)** allowed the assessment of the values for individual stresses ($\sigma_\alpha$ and $\sigma_\beta$) for each point of the experimental curves (dashed lines on **Figure 5.8**). Those curves of the individual flow stresses were smoothed (**Figure 5.8**) using a Hansel-Spittel law [88].

$$\sigma = \sigma_{y_0} + A \cdot T^{m_9} \cdot \varepsilon^{m_2} \cdot (1+\varepsilon)^{m_5 \cdot T} \cdot \dot{\varepsilon}^{(m_3 + m_8 \cdot T)} \cdot exp(m_1 \cdot T + \frac{m_4}{\varepsilon} + m_7 \cdot \varepsilon) \quad (5.6)$$

The Hansel-Spittel parameters values are shown in Appendix **B**. As mentioned in section **5.1**, those parameters are not from the identification of the behavior of each phase, but are simply used for the purpose of curve smoothing. Multiple thermomechanical variables ($T, \varepsilon, \dot{\varepsilon}$) would be necessary to properly evaluate them, due to the importance of strain rate and temperature effects on the flow stress.

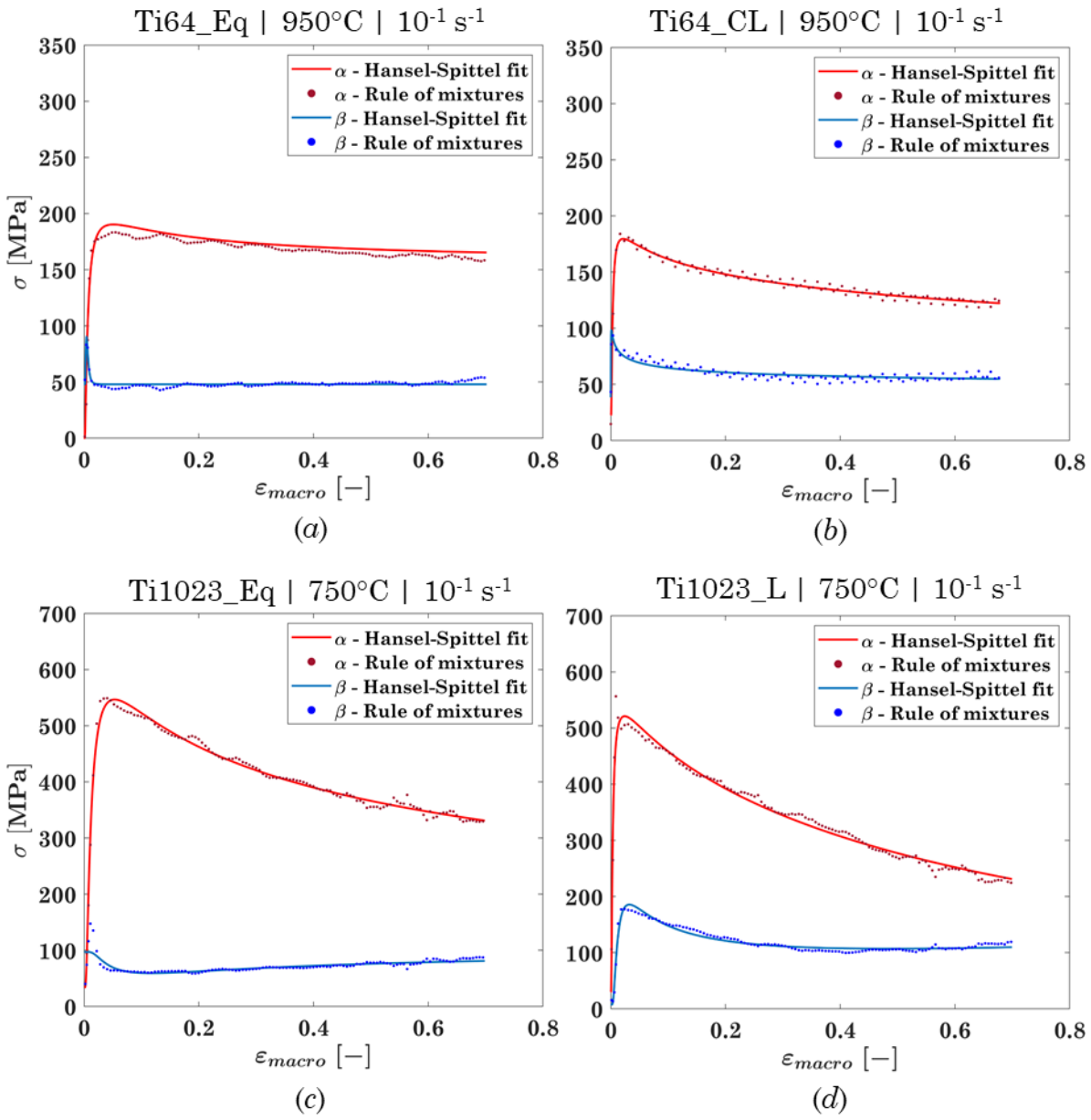



*Figure 5.9. Stress-strain curves for each phase ($\sigma_\alpha$ and $\sigma_\beta$) calculated with the ROM at each point of the experimental curve (dotted lines) and after Hansel-Spittel smoothing (full lines), for each of the four selected microstructures.*

Those smoothed values for each phase were then plotted with the experimental curves (**Figure 5.10**) to compare them. An error margin for the calculated curves was added (shaded areas in **Figure 5.10**) to consider the standard deviations in the phase fraction values measured experimentally.

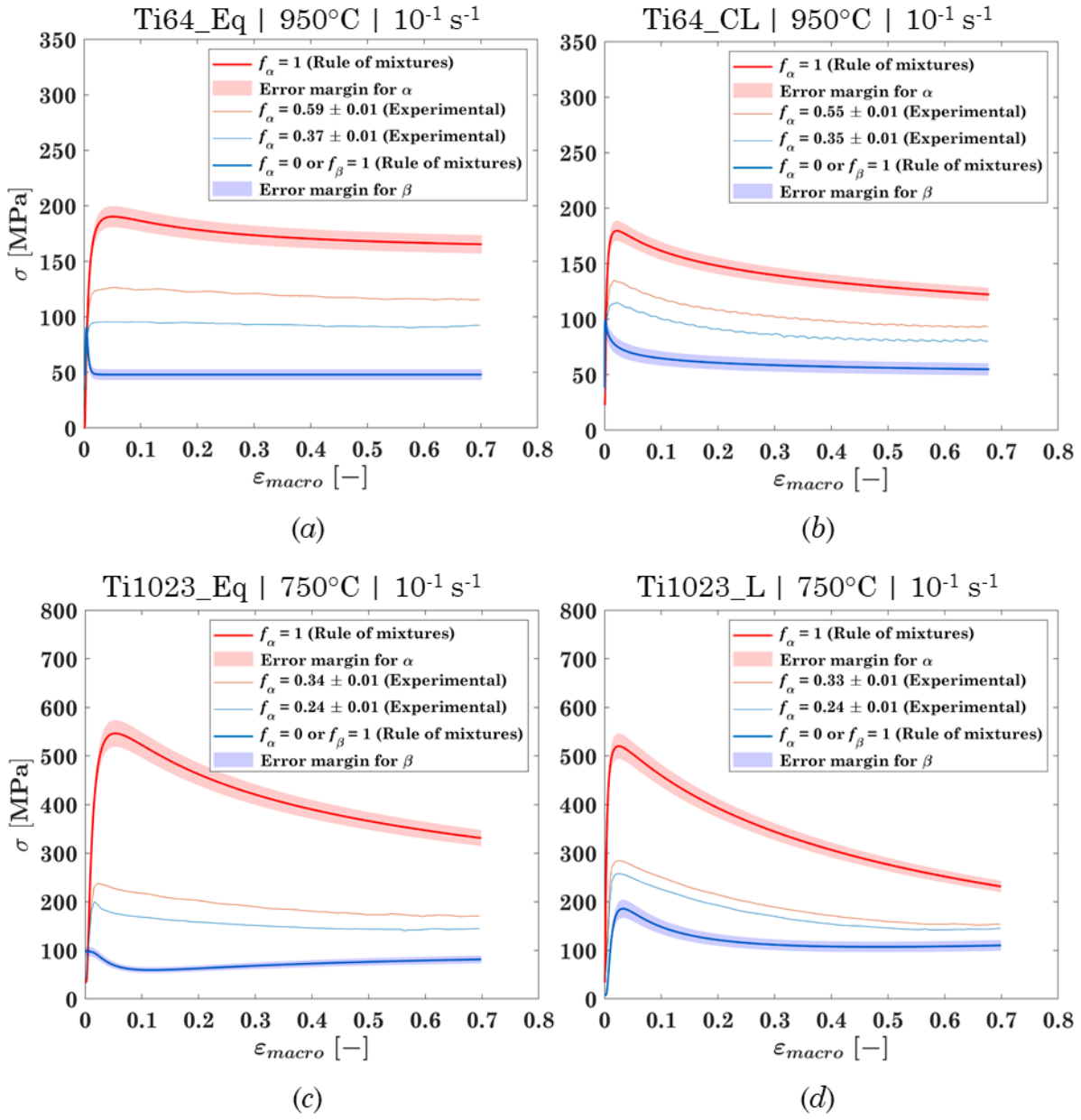



*Figure 5.10. Experimental (orange and light blue, for 2 and 10 minutes holding, respectively) and calculated (red and dark blue, for $\sigma_\alpha$ and $\sigma_\beta$, respectively) curves, with their corresponding error margin (related to the uncertainty in the phase fraction measurements, shaded zones), for each of the four microstructures.*

By analyzing **Figure 5.10**, it appears that the presence of the flow softening, observed on the experimental curves (orange and light blue), can be mainly attributed to the behavior of the $\alpha$ phase (red curves). This behavior was already observed in [6] for an equiaxed Ti64 alloy. The $\sigma_\alpha$ tends to decrease throughout deformation (after passing through a maximum value), while the $\sigma_\beta$ presents a shorter and sharper peak followed by a steady or slightly increasing behavior. This sharp peak observed for the $\beta$ phase will be discussed furtherly in section **5.5.2.1**, discussing deformation of Ti1023 alloy in the $\beta$ domain.

It was shown in **Figure 4.4** that the $\alpha$ phase tends to develop a strong texture during deformation, with the basal plane parallel to the CD, at the

thermomechanical conditions applied. This texture development is likely to be related to the softening behavior of the $\alpha$ phase. This hypothesis is reinforced by the fact that the one flow stress curve that did not show significant softening behavior (for the $\alpha$ phase) was the Ti64_Eq. In **Figure 4.4**, it can be observed that there is no associated texture development, as the initial texture is maintained within the deformation.

Regarding the $\beta$ phase, it was shown in **Figure 4.10** that with increasing strain level, this phase tends to form substructures that progressively transform into HAGB by continuous dynamic recrystallization. This process seems to be behind the steady flow stress of the $\beta$ phase, and an equilibrium between the generation of dislocations, dynamic recovery and recrystallization. In the $\sigma_\beta$ curves for the Ti1023 alloys (**Figure 5.10**), a minor hardening behavior can be observed with increasing strain. This might be related to the fact that the formation of new grains (thus the reduction of the average grain size) tends to increase the flow stress, according to the classical Hall-Petch relation [89,90]. Furthermore, when the $\alpha$ phase is lamellar (Ti64_CL and Ti1023_L), the $\sigma_\beta$ achieved higher values, thus the $\alpha$ phase morphology might have an impact in the ß phase flow stress levels.

Comparing both phases, the $\alpha$ phase flow stress is greater than that of the $\beta$ phase, which is a consistent result, as the former is the harder phase [6,9]. This difference between the flow stress of each phase was quantified (**Figure 5.11**), by calculating the ratio between the individual phase stresses $\sigma_\beta/\sigma_\alpha$, at three macroscopic strain levels ($\varepsilon_{macro}$), as previously shown in **Table 2.5**.

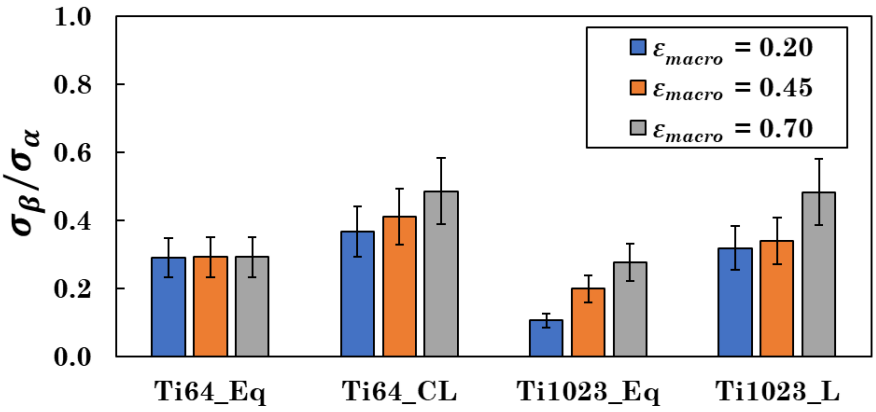



*Figure 5.11. Ratios between the individual flow stresses of each phase as a function of the macroscopic strain level.*

The ratio values varied between 0.1 and 0.5, depending on the strain level, alloy or morphology. There is a clear increasing trend of those values with increasing the strain level, as the $\alpha$ phase presents a softening behavior, while the $\beta$ phase presents a steady/hardening bearing. The only different case is for the equiaxed Ti64, which presents a steady ratio throughout deformation, consistent with both $\sigma_\alpha$ and $\sigma_\beta$ curves being steady. An interesting behavior is observed at high strain level, where the morphology seems to play role in this repartition, independently of the alloy. For the equiaxed microstructures, the ratio was 0.3, while for the lamellar ones, 0.5. As lamellar morphologies presented a stronger softening bearing (**Figure 5.10**), the difference between the individual stresses ($\sigma_\alpha$ and $\sigma_\beta$) is lower.

### *5.5.2.1 Deformation in the β domain*

Few deformations above the $T_\beta$ were performed for the Ti1023_L. The aim is to compare the estimated stress-strain curves for the $\beta$ phase (**Figure 5.10**) with those directly obtained from the deformation in the $\beta$ domain (where there is no $\alpha$ phase). Two cylindrical samples of Ti1023_L were compressed (for reproducibility check), after a 15-minute holding (which allows to obtain a fully $\beta$ state, as checked experimentally), and at two different temperatures above $T_\beta$: 900 and 950°C. The same deformation conditions (strain level and rate) applied previously (**Figure 5.2**) were reproduced for the sake of comparison of results. The thermomechanical path is schematized in **Figure 5.12**.

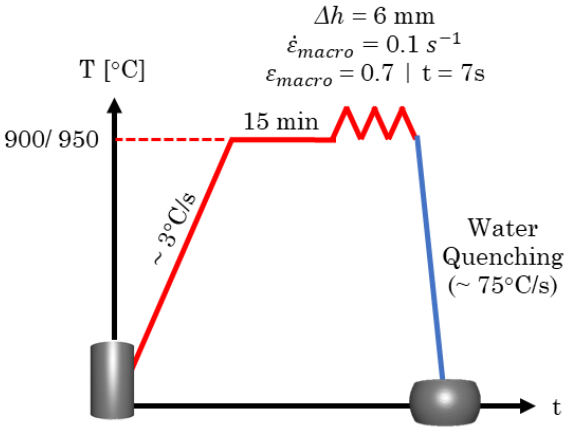



*Figure 5.12. Thermomechanical paths applied for the deformation for Ti1023 alloy in the β domain.*

The stress-strain curves obtained from these deformation experiments in the $\beta$ domain are shown in **Figure 5.13**.

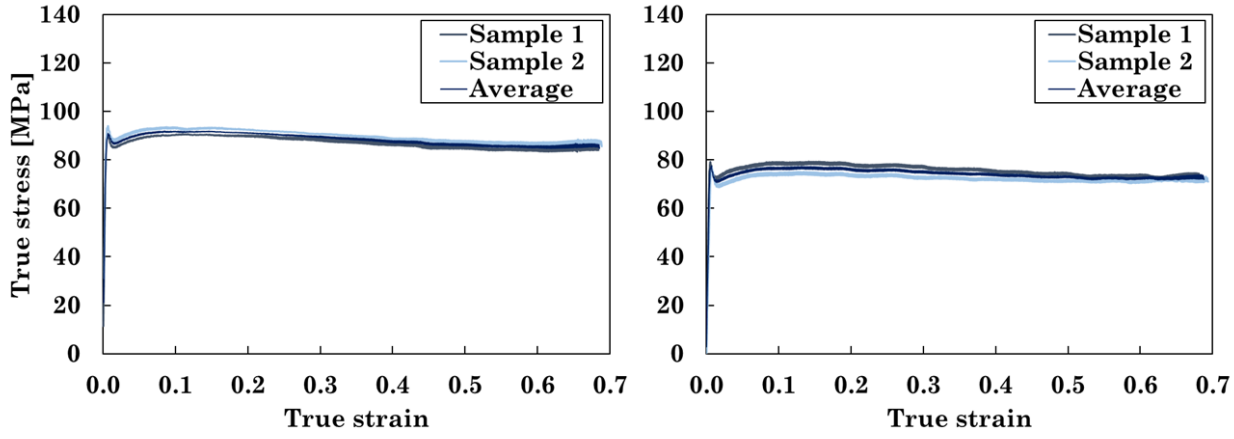



*Figure 5.13. Stress-strain curves of the Ti1023_L microstructure deformed at: a) 900°C; b) 950°C, following the thermomechanical path of **Figure 5.12**.*

Interestingly, the shapes of both curves in **Figure 5.13** agree with the ones estimated (**Figure 5.10**) from the two-phase domain, including the presence of a sharp stress peak at the yield point. This phenomenon could possibly be linked to

interactions between solute and pre-existing dislocations. However, this is a strong hypothesis that require further deformation and microstructural characterization in the $\beta$ domain to be confirmed.

Furthermore, as predicted in **Figure 5.10**, there is no flow softening in the $\beta$ domain. This shows agreement with the hypothesis presented in section **5.7**, that the flow softening in the two-phase range is mainly related to the texture development of the $\alpha$ phase to softer configurations.

As expected, the deformation at 900°*C* (**Figure 5.13***a*) achieved higher stress levels, when compared to the curve at 950°*C* (**Figure 5.13***b*). The comparison of the estimated stress values (**Figure 5.10**) and those shown in **Figure 5.13** shows some consistency, where the $\sigma_\beta$ values are in the same order of magnitude for both alloys and it decreases with increased deformation temperature. Nevertheless, more deformation experiments should be performed in the $\beta$ domain at different temperatures, aiming to between correlate temperature and stress levels. Furthermore, it can be estimated in the $\alpha$+$\beta$ domain, aiming to adjust the ROM presented in equation **(5.2)**.

## 5.6 Estimation of average dislocation density per phase from the estimated phase flow stress

To compare the two different approaches (Microscopic vs Macroscopic), the flow stress values (obtained hereabove in section **5.5**) were used to estimate the average dislocation density per phase, using the Taylor's dislocation model [91], and related by equation **(5.7)**:

$$\sigma_\varphi = \sigma_0 + \psi M_\varphi G_\varphi b_\varphi \sqrt{\rho_\sigma^\varphi} \tag{5.7}$$

where ψ is a material dependent coefficient, $\varphi$ is the phase ($\alpha$ or $\beta$), $M$ is the Taylor factor, $G$ is the shear modulus, $b$ is the Burgers vector magnitude, and $\rho_\sigma^\varphi$ is the dislocation density estimated from the phase flow stress derived from the rheological approach. All parameters, for each of both phases, with their respective values are listed in **Table 5.1**.

| Parameter | $\alpha$ phase | $\beta$ phase | Reference |
|---|---|---|---|
| $\psi$ [-] | 0.1 | 0.1 | [92] |
| $M$ [-] | 5 | 3.05 | [92] |
| $G$ [$GPa$] | 29.2(@750°*C*) and 23.1(@950°*C*) | 17.7(@750°*C*) and 16.5(@950°*C*) | [26] |
| $b$ [$m$] | 2.95 x $10^{-10}$ | 2.86 x $10^{-10}$ | [9] |

*Table 5.1. List of parameters used in the Taylor's dislocation model, with their respective values and references.*

The stress $\sigma_0$ not only represents the yield stress of pure metal, but also considers the contributions of precipitates and solute elements [93]. Assuming that these two contributions remain constant during deformation, $\sigma_0$ can be obtained from the experimental value of the stress at zero plastic strain.

Equation **(5.7)** was applied for the three macroscopic strain levels ($\varepsilon_{macro}$ = 0.2, 0.45, 0.7) that correspond to the equivalent (local) strain levels ($\varepsilon$ = 0.3, 0.8, 1.3) as

shown in **Table 2.5**. Those were chosen for a following comparison of between the Macroscopic and Microscopic approaches, regarding the estimated dislocation density per phase.

The values of $\rho_\sigma$ obtained at different equivalent strain levels and for the four selected microstructures are summarized in **Figure 5.14**.

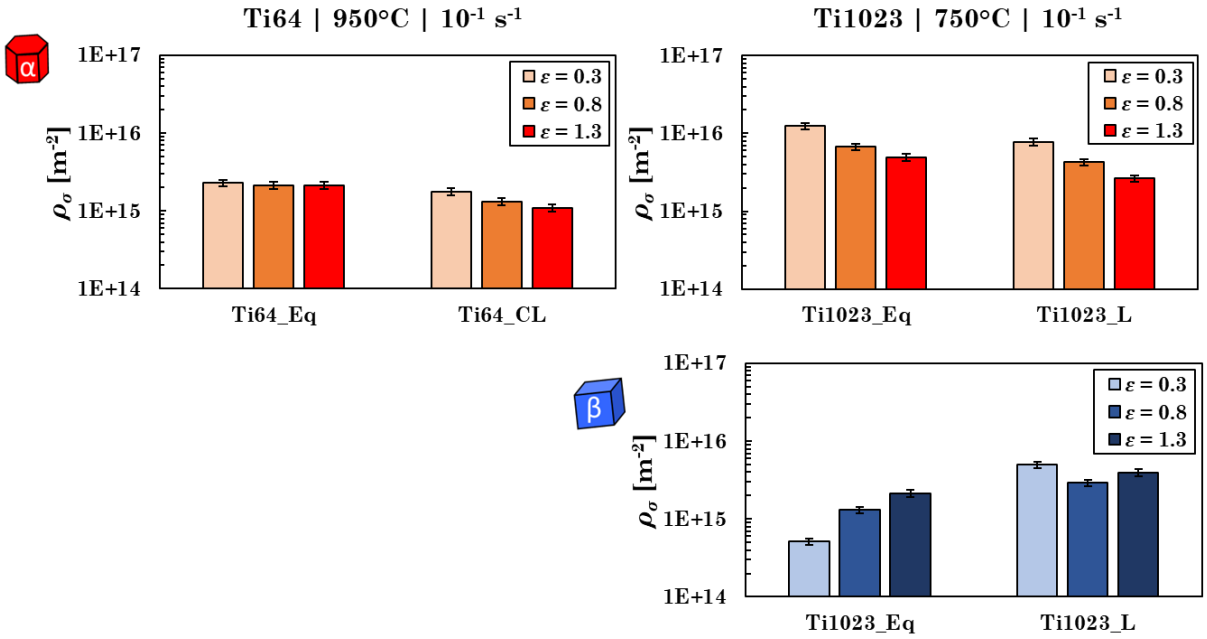



*Figure 5.14. Summary of the estimated average dislocation density per phase obtained from the estimated phase flow stress ($\rho_\sigma$), for the different microstructures and equivalent strain levels.*

The $\rho_\sigma$ values (obviously) follow the tendencies observed in the phase flow stress curves of **Figure 5.10**. For the Ti64_Eq, the dislocation density of the $\alpha$ phase seems to be constant through the investigated strain range. For the lamellar case, there is a decrease in $\rho_\sigma$ consistent with the flow softening. On the other hand, for the Ti1023 alloy, there is also a decreasing tendency for both morphologies. For the $\beta$ phase in the Ti1023_Eq microstructure, the dislocation density increases with increasing strain. Concerning the Ti1023_L, the fluctuation of the $\rho_\sigma$ is also linked to the macroscopic flow stress.

Nevertheless, especially for the $\alpha$ phase, this direct correlation of flow stress and dislocation density proposed in equation **(5.7)**, should be taken carefully. The flow softening seems to be highly linked to the microstructural evolution in the $\alpha$ phase, mainly in terms of morphological orientation and texture development, as discussed in section **5.5.2**. Therefore, the reduction in the flow stress is probably not only linked to a reduction in the dislocation density. This is reinforced by the fact that the analysis of the microstructures obtained after deformation suggests; on the contrary, that the dislocation density in the $\alpha$ phase tends to increase with an increasing deformation (see **Figure 4.26**).

The $\rho_\sigma$ values are further compared to the $\rho_{EBSD}$ values estimated from EBSD data (section **4.1.5**) in the following section (**5.7**).

## 5.7 Comparison between the Macroscopic and Microscopic approaches

The comparison of the estimated dislocation densities, obtained from the EBSD (detailed in section **4.1.5**) and the rheological (described above) approaches, is summarized in **Figure 5.15**.

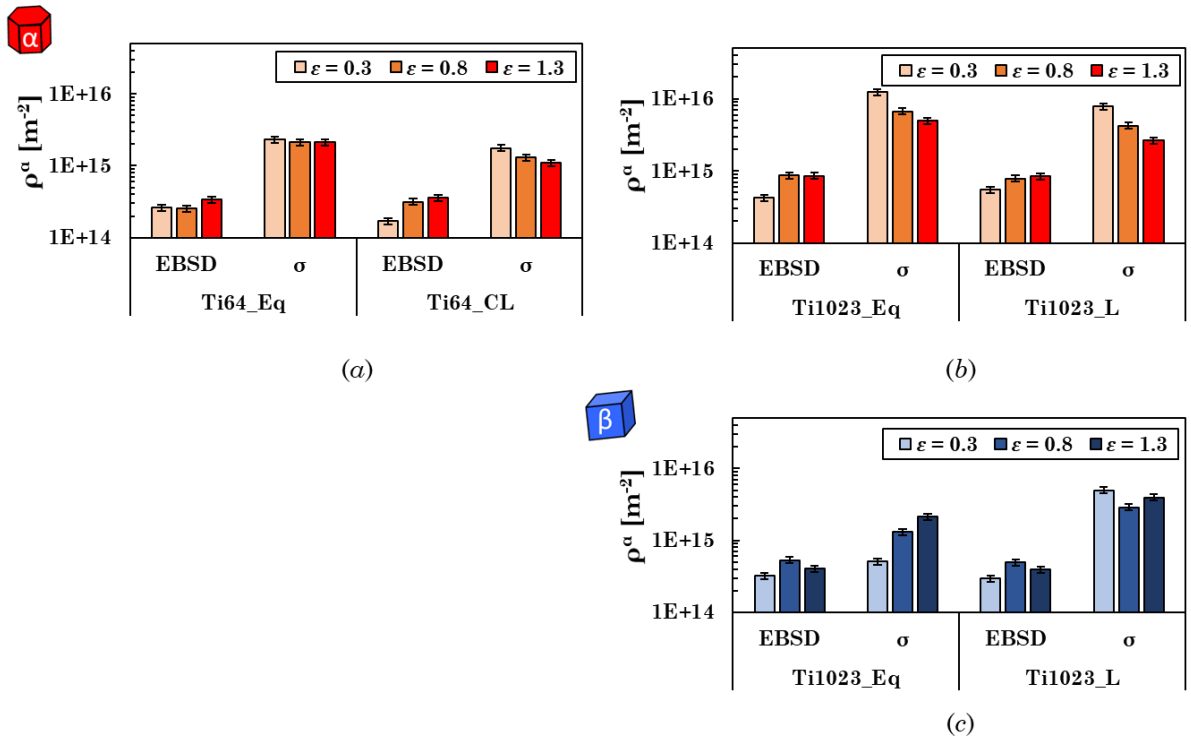



*Figure 5.15. Comparison between the results of EBSD and rheological approaches for the evaluation of the dislocation density evolution at different strain levels for the: a) α phase of the Ti64; b) α phase of the Ti1023; c) β phase of the Ti1023.*

When comparing the dislocation density values between both approaches, those obtained from the macroscopic flow stress appear to be systematically higher, which is somehow consistent, as they take into account both GNDs and SSDs contributions to the flow stress [94], contrary to the dislocation densities estimated from EBSD data which only consider the GNDs [5].

Furthermore, there is a clear difference in their evolution throughout deformation for both phases. Concerning the $\alpha$ phase, the EBSD approach leads to an increase in dislocation density with increasing strain level, while the opposite behavior in the values is obtained from the rheological approach. This is very likely due to the crystallographic texture development of the $\alpha$ phase, where the basal plane tends to align parallel to the compression direction (*cf.* **Figure 4.4** and **Figure 4.56**).

This texture development could be correlated to the flow softening observed in the $\alpha$ stress-strain curves (**Figure 5.10**). This hypothesis is reinforced by the fact that the Ti64_Eq presented this same texture even at low strain levels (**Figure 4.4**). Thus, the $\rho_\sigma$ is stable throughout deformation, where no flow softening is observed (**Figure 5.10***a*). In contrast, as shown in section **4.1.4**, the $\alpha$ grains that are oriented with their basal planes ∥ CD are the ones which presented more

substructure development at high equivalent strain levels ($\varepsilon$ = 1.3), shown in **Figure 4.23**. In this manner, there is an increase tendency on the $\rho_{EBSD}$ with the deformation increase. The correlation between the two approaches, concerning the $\alpha$ phase, is summarized in **Figure 5.16**.

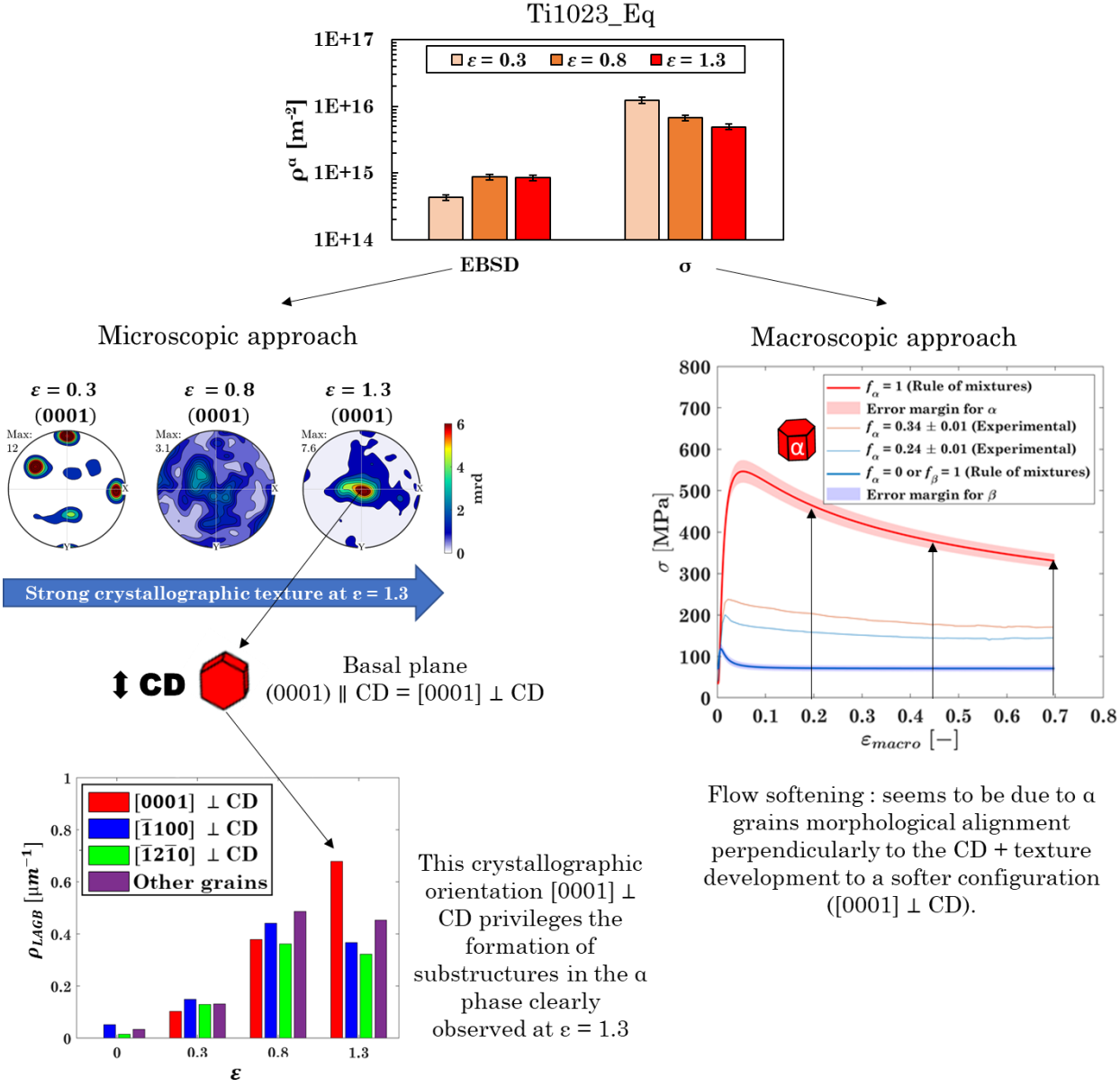



*Figure 5.16. Summary of the correlation between the two approaches regarding the α phase (example for the Ti1023_Eq).*

Concerning the $\beta$ phase, the evolution of the dislocation density also presented differences between the two approaches. For both lamellar and equiaxed morphologies of the Ti1023, at high levels of deformation ($\varepsilon$ = 1.3), a decrease in the values from EBSD data is observed, while an increase can be seen in the values from flow stress analysis. This difference seems to be connected to the occurrence of continuous dynamic recrystallization, where the LAGB increase their misorientation angle and become HAGB (≥ 10°), as detailed in section **4.1.3**. As shown in **Figure 4.27**, the threshold of 10° is used to exclude grain boundaries in the calculation of the $\rho_{EBSD}$. Consequently, those new grain boundaries are not

included in the dislocation density calculation, and the new grains present a lower intragranular dislocation density after recrystallization. Nevertheless, those new grain boundaries serve as barriers for the dislocation movement in the material. They are being considered in the macroscopic approach, thus increasing the estimated $\rho_\sigma$. This may explain the difference in the evolution of the $\rho_{EBSD}$ and $\rho_\sigma$ of the $\beta$ phase, where continuous dynamic recrystallization mechanism leads to a decrease in the $\rho_{EBSD}$ as deformation progresses. However, the average grain size decreases, causing the flow stress, thus the $\rho_\sigma^\beta$, to stagnate/ slightly increase. The correlation between the two approaches, concerning the $\beta$ phase, is summarized in **Figure 5.17**.

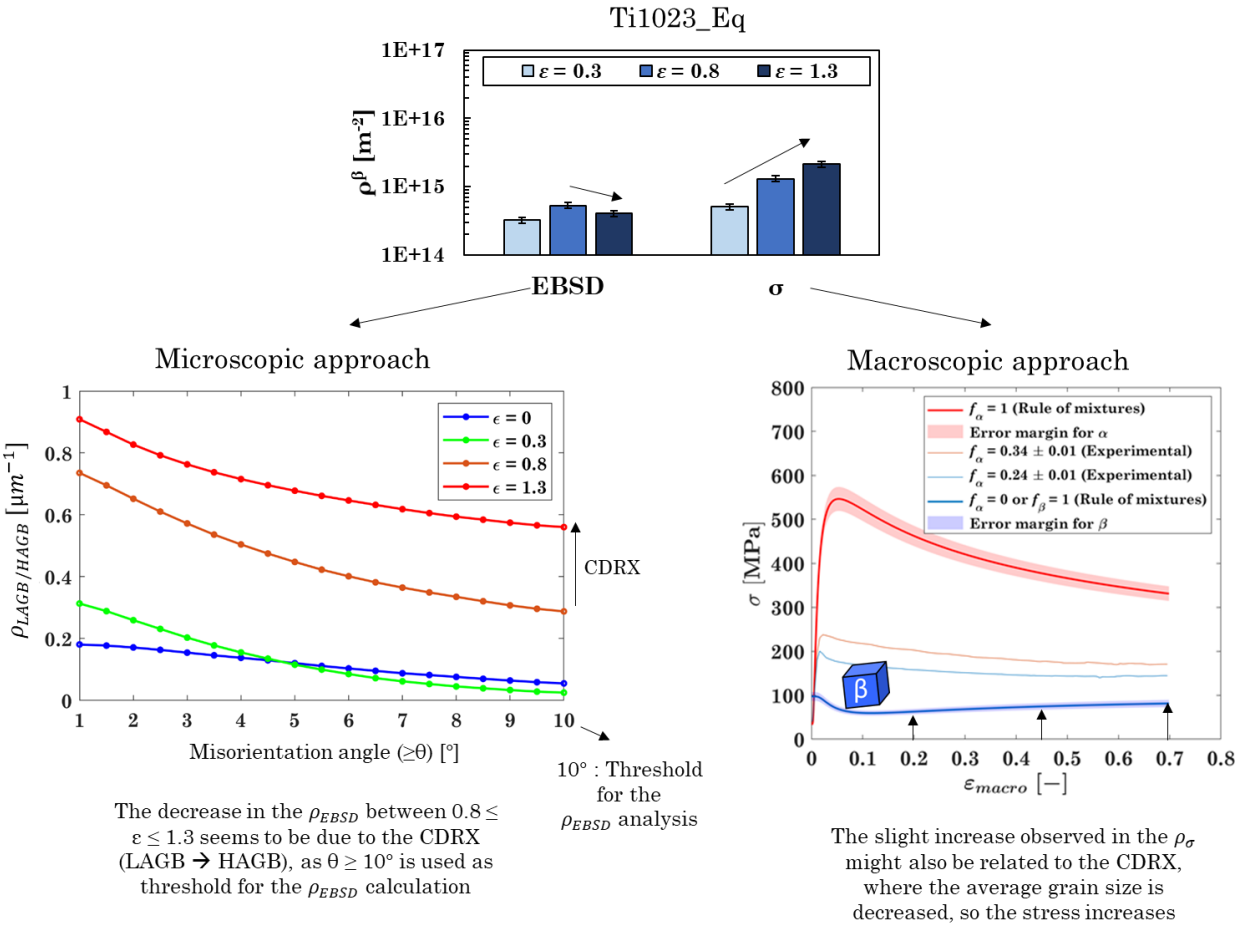



*Figure 5.17. Summary of the correlation between the two approaches regarding the β phase (example for the Ti1023_Eq).*

## 5.8 Summary and Conclusions

In this chapter, a macroscopic approach was implemented, based on stress-strain curves which were analyzed to assess the macroscopic flow stress of each phase. Hence, an estimation of the dislocation density distribution in both phases was performed using the Taylor model.

As expected, for the four microstructures analyzed, the individual stress values of the $\alpha$ phase ($\sigma_\alpha$) were always higher than the $\beta$ ones ($\sigma_\beta$). Interestingly, even if the strong hypothesis of a homogenous deformation was applied, see equation **(5.2)**, the shapes of both $\alpha$ and $\beta$ curves are consistent with other works in the literature [6,95]. It was shown experimentally for the Ti64 alloy [95] that the stress-strain curves tend to present a stronger flow softening at lower temperatures. This behavior tends to disappear when the $\beta$-transus is reached, where the curves have a very flat/steady character. This was also shown experimentally in this work by few deformation experiments in the $\beta$ domain, where the shapes of stress-strain curves agree with the ones estimated from the two-phase domain. Furthermore, no flow softening was observed in the $\beta$ domain, showing agreement with the hypothesis that this phenomenon is mainly related to the texture development of the $\alpha$ phase to softer configurations (easier to be deformed).

The ratio between the estimated flow stresses of both phases ($\sigma_\beta/\sigma_\alpha$) tends to increase with the increasing strain level, as the $\alpha$ phase shows a softening behavior, while the $\beta$ phase presents a steady, or slight hardening, bearing. It was shown that, for a macroscopic strain level ($\varepsilon_{macro}$) of 0.7, for both alloys, the ratio between the softer and the harder phase depended on the phase topology. For the equiaxed ones, the flow stress of the $\beta$ phase is about 70% lower than that of $\alpha$ phase, while 50% lower for the lamellar morphology.

To improve this estimation of flow stress from a ROM, some coefficients can be added in equation **(5.2)**, as proposed by [85,86]. Nevertheless, in order to fit correctly those coefficients, which are dependent on temperature and strain rate, other deformation conditions (*i.e.,* temperature, strain rate) should be performed. Also, different coefficients should be implemented for the different microstructures, as it was seen that the stress-strain curves are highly dependent on the morphology of the microstructure.

Furthermore, two different approaches were used to estimate the dislocation density evolution in each phase: a macroscopic one ($\rho_\sigma$), presented in this chapter, and a microscopic one, presented in Chapter **4** ($\rho_{EBSD}$). The main objective was to identify trends in each approach, explaining the reasons that underlie those differences.

The dislocation density levels obtained from the macroscopic flow stress ($\rho_\sigma$) are higher for all analyzed cases. As this approach considers both GNDs and SSDs, while the dislocation densities estimated from EBSD data concern only the GND, this is a consistent result.

Furthermore, different evolutions when increasing strain were observed when comparing of those two approaches. For the $\alpha$ phase, this divergence is likely to be due to the crystallographic texture developed, which favors the basal plane parallel to the CD, leading to a decrease in $\rho_\sigma$ through a texture effect while α grains are

more and more substructured, thus with increasing $\rho_{EBSD}$. For the $\beta$ phase, the progress of continuous dynamic recrystallization, leads to more and more HAGBs not considered in the microscopic approach (thus decreasing $\rho_{EBSD}$), while they serve as barriers for the dislocation density movement in the material, increasing $\rho_{\sigma}$.

In order to enrich the estimation of the dislocation density distribution in both phases from the macroscopic approach ($\rho_{\sigma}$), equation **(5.7)** could be modified. A parameter that includes the microstructural changes in the $\alpha$ phase could be addressed, especially in terms of texture development. Some attempts were made to correlate the Taylor factor ($M$) or even the Kearns texture factors [96], which are a widely used method for quantifying texture information of hexagonal materials. Nevertheless, no clear tendency was obtained between the texture evolution observed and the estimated dislocation density evolution.

Regarding the $\beta$ phase, a model that includes dynamic recovery and continuous dynamic recrystallization could correlate those two approaches. Some works followed this approach relating stress and substructure size [93,97]. However, it was performed for only one microstructure type. In this work, it was shown that the generalization of parameters between different microstructures is intricate.

The total dislocation density in a polycrystal includes both GNDs and SSDs. Therefore, the comparison of dislocation density levels must be taken with much care. In the literature, the assessment of the SSD density is usually done by applying subtractions of different methods (measuring GNDs + SSDs) from the EBSD one (which can only access GNDs). For example, from measured flow stress based on Taylor's hardening model [94] or even by High-Resolution Synchrotron Diffraction [55]. However, these approaches are not a direct measurement of the SSD density and can lead to misinterpretation such as those discussed in this chapter. The difference between approaches can indeed be related to microstructural evolutions, for example, as variations in morphology or texture throughout the deformation [25,93].

Finally, it was shown in this chapter that the method implemented can influence not only the estimated dislocation density levels, but also their evolutions. Noteworthily, the dislocation density has very precise physical meaning. However, its estimation is not possible in a direct way at the scale of the microstructure. Therefore, the estimations $\rho_{EBSD}$ and $\rho_{\sigma}$ might be seen as a phenomenological description of the actual underlying dislocation density.

## 5.9 Résumé en Français

Dans ce chapitre, afin d'estimer la densité des dislocations totale (GND + SSD) et pouvoir la comparer avec l'approche précédente (qui ne prend en compte que les GND), une approche macroscopique a été mise en œuvre. Elle est basée sur des courbes contrainte-déformation qui ont été analysées pour évaluer la contrainte d'écoulement macroscopique de chaque phase. Par conséquent, une estimation de la distribution de la densité de dislocations dans les deux phases a été réalisée à l'aide du modèle de Taylor.

Comme prévu, pour les quatre microstructures analysées, les valeurs de contraintes individuelles de la phase $\alpha$ ($\sigma_\alpha$) étaient toujours supérieures à celles de la phase $\beta$ ($\sigma_\beta$). Fait intéressant, même si l'hypothèse forte d'une déformation homogène a été appliquée, voir l'équation **(5.2)**, les formes des courbes $\alpha$ et $\beta$ sont cohérentes avec d'autres travaux de la littérature [6,95]. Il a été montré expérimentalement pour l'alliage Ti64 [95] que les courbes contrainte-déformation ont tendance à présenter un adoucissement à l'écoulement plus fort à des températures plus basses. Ce comportement tend à disparaître lorsque le transus $\beta$ est atteint, où les courbes ont un caractère très plat/stable. Cela a également été démontré expérimentalement dans ce travail par quelques expériences de déformation dans le domaine $\beta$, où les formes des courbes contrainte-déformation concordent avec celles estimées à partir du domaine biphasé. De plus, aucun adoucissement de l'écoulement n'a été observé dans le domaine $\beta$, montrant un accord avec l'hypothèse selon laquelle ce phénomène est principalement lié au développement de la texture de la phase $\alpha$ vers des configurations plus douces (plus faciles à déformer).

Le rapport entre les contraintes d'écoulement estimées des deux phases ($\sigma_\beta/\sigma_\alpha$) a tendance à augmenter avec l'augmentation du niveau de déformation, car la phase $\alpha$ montre un comportement d'adoucissement, tandis que la phase $\beta$ présente un palier ou un léger durcissement. Il a été montré que, pour un niveau de déformation macroscopique ($\varepsilon_{macro}$) de 0,7, pour les deux alliages, le rapport entre la phase la plus tendre et la phase la plus dure dépendait de la topologie de la phase. Pour les équiaxes, la contrainte d'écoulement de la phase $\beta$ est d'environ 70% inférieure à celle de la phase $\alpha$, tandis qu'elle est inférieure de 50% pour la morphologie lamellaire.

Pour améliorer cette estimation de la contrainte d'écoulement à partir d'une loi de mélanges, certains coefficients peuvent être ajoutés dans l'équation **(5.2)**, comme proposé par [85,86]. Néanmoins, afin d'ajuster correctement ces coefficients, qui dépendent de la température et de la vitesse de déformation, d'autres conditions de déformation (c'est-à-dire la température et la vitesse de déformation) doivent être effectuées. Aussi, différents coefficients doivent être mis en œuvre pour les différentes microstructures, car nous avons vu que les courbes contrainte-déformation sont fortement dépendantes de la morphologie de la microstructure.

De plus, deux approches différentes ont été utilisées pour estimer l'évolution de la densité de dislocations dans chaque phase : une approche macroscopique ($\rho_\sigma$), présentée dans ce chapitre, et une approche microscopique, présentée au chapitre

**4** ($\rho_{EBSD}$). L'objectif principal était d'identifier les tendances dans chaque approche, en expliquant les raisons qui sous-tendent ces différences.

Les niveaux de densité de dislocations obtenus à partir de la contrainte d'écoulement macroscopique ($\rho_\sigma$) sont plus élevés pour tous les cas analysés. Comme cette approche considère à la fois les GND et les SSD, alors que les densités de dislocation estimées à partir des données EBSD ne concernent que le GND, il s'agit d'un résultat cohérent.

De plus, des évolutions différentes lors de l'augmentation de la contrainte ont été observées lors de la comparaison de ces deux approches. Pour la phase $\alpha$, cette divergence est probablement due à la texture cristallographique développée, qui privilégie la normale du plan basal perpendiculaire à la DC, conduisant à une diminution de $\rho_\sigma$ par effet de texture alors que les grains $\alpha$ sont de plus en plus sous-structurés, donc une augmentation de $\rho_{EBSD}$. Pour la phase $\beta$, la progression de la recristallisation dynamique continue, conduit à de plus en plus de HAGB non pris en compte dans l'approche microscopique (diminuant ainsi $\rho_{EBSD}$), alors qu'ils servent de barrières au mouvement de densité de dislocations dans le matériau, augmentant $\rho_\sigma$.

Afin d'enrichir l'estimation de la distribution de densité de dislocations dans les deux phases à partir de l'approche macroscopique ($\rho_\sigma$), l'équation **(5.7)** pourrait être modifiée. Un paramètre incluant les changements microstructuraux dans la phase $\alpha$ pourrait être abordé, notamment en termes de développement de texture. Certaines tentatives ont été faites pour corréler le facteur de Taylor ($M$) ou même les facteurs de texture de Kearns [96], qui sont une méthode largement utilisée pour quantifier les informations de texture des matériaux hexagonaux. Néanmoins, aucune tendance claire n'a été obtenue entre l'évolution de la texture observée et l'évolution estimée de la densité de dislocations.

En ce qui concerne la phase $\beta$, un modèle incluant la restauration dynamique et la recristallisation dynamique continue pourrait corréler ces deux approches. Certains travaux ont suivi cette approche reliant les contraintes et la taille de la sous-structure [93,97]. Cependant, elle a été réalisée pour un seul type de microstructure. Dans ce travail, il a été montré que la généralisation des paramètres entre différentes microstructures est complexe.

La densité totale de dislocations dans un polycristal comprend à la fois les GND et les SSD. Par conséquent, la comparaison des niveaux de densité de dislocations doit être prise avec beaucoup de soin. Dans la littérature, l'évaluation de la densité de SSD se fait généralement en appliquant des soustractions de différentes méthodes (mesure des GND + SSD) à celle de l'EBSD (qui ne peut accéder qu'aux GND). Par exemple, à partir de la contrainte d'écoulement mesurée basée sur le modèle de durcissement de Taylor [94] ou même par diffraction synchrotron haute résolution [55]. Cependant, ces approches ne constituent pas une mesure directe de la densité SSD et peuvent conduire à des interprétations erronées telles que celles discutées dans ce chapitre. La différence entre les approches peut en effet être liée à des évolutions microstructurales, comme par exemple des variations de morphologie ou de texture tout au long de la déformation [25,93].

Enfin, il a été montré dans ce chapitre que la méthode mise en œuvre peut influencer non seulement les niveaux estimés de densité de dislocations, mais également leurs évolutions. Il convient de noter que la densité de dislocations a

une signification physique très précise. Cependant, son estimation n'est pas possible de manière directe à l'échelle de la microstructure. Par conséquent, les estimations $\rho_{EBSD}$ et $\rho_{\sigma}$ pourraient être considérées comme une description phénoménologique de la densité de dislocation sous-jacente réelle.

# 6. FULL FIELD SIMULATION OF TWO-PHASE MICROSTRUCTURE DEFORMATION

It was shown in section **5.7** that the dislocation densities obtained through the Microscopic and Macroscopic approaches cannot be directly compared, mainly due to the nature of the techniques and their inherent analysis scales. To provide a third approach for the comparison of the dislocation densities in titanium alloys, 3D full field crystal plasticity simulations were conducted. Virtual polycrystals, representative of the measured microstructure (Chapter **3**), were generated or immersed (using 3D EBSD data) into a finite element (FE) mesh. This means that a computational domain that explicitly represents the topology of the two phases is generated. This computational domain, often referred to as *Representative Volume Element* (RVE), is of the order of tens of microns and the mesh is conforming to the topology of the phases. These three-dimensional models were used to analyze the mechanical response of the RVE subjected to monotonic compression.

While the macroscopic domain is considered homogeneous, the RVE resolves explicitly the microstructure (at intra-$\beta$-grain scale, as $\beta$ grains are millimetric, shown in section **3.3**, and the analyzed RVE is micrometric) of the material. To obtain a RVE as close as possible to the real microstructure (in terms of $\alpha$ grain size, phase fraction, orientation and topology), two different strategies were used. In this manner, equiaxed $\alpha$ grains were numerically generated and lamellar $\alpha$ grains immersed. Regarding the latter, a 3D EBSD characterization was thus performed for the Ti64_FL microstructure (section **6.3.1.2.3**).

The framework couples a CPFEM (crystal plasticity finite element method) model with a LS-FE (level-set finite element method) for phenomenological laws. Some of the material parameters were identified (for each phase individually) by inverse analysis from the flow stresses calculated on Chapter **5**. An estimation of dislocation density for each phase ($\rho_{Sim}$), and $\alpha$ texture evolution was performed from these simulations. Noteworthily, the $\rho_{Sim}$ is yet another estimation of dislocation density, not representing the direct measurement of these linear crystalline defects in the material. It can also be seen as a phenomenological variable used to drive the hardening of the material, being linked to the real dislocation density.

It is important to mention that the $\rho_{Sim}$, estimated from the simulations, belongs to a model for the statistically stored dislocations (SSD) only (which evolved from random trapping processes during plastic deformation [98]). Thus, the assessment of geometrically necessary dislocations (GND) is not performed in the full field simulations. This is in contrast with the EBSD technique, which assesses only GND. Thus, the direct comparison of both results is intricate. Therefore, only tendencies in dislocation density evolution throughout deformation and repartition between phases will be analyzed. CPFEM approaches that account for GND exist [99], yet they were not used in this work.

## 6.1 Introduction to crystal plasticity

Current industrial processes demand for polycrystal models with high prediction capability. Crystal plasticity is among the most advanced modeling solutions due to its multiscale nature and concomitant anisotropic stress–strain response in polycrystalline metals subjected to plastic deformation. As a reminder, in metals, the plastic deformation can occur due to the sliding of dislocations on

specific slip systems ($SS$). Also, plastic strain starts when a resolved shear stress (RSS) on a specific slip system trespasses its critical resolved shear stress value (CRSS).

For a two-phase alloy, plastic deformation might occur simultaneously on both phases. Therefore, for such materials, it is mandatory to represent the slip systems ($SS$) of both phases. The $SS$ for the $\alpha$ (HCP) and $\beta$ (BCC) phases have been previously described on **Figure 2.20** and **Figure 2.21**. The following section describes how to model the plastic deformation in the different slip systems of the crystal.

## 6.2 Constitutive model for crystal plasticity finite element method

Crystal plasticity finite element method (CPFEM) is one of the main available options for modeling the dislocation density evolution and the orientation gradients throughout plastic deformation. In CPFEM, the stress–strain response at each integration point is defined by a single crystal model. The specific details of the FEM method have already been described in the literature, and will not be presented in this work. The interested reader can refer to [100–102]. The single crystal model, used in this work, follows an elasto-viscoplastic formulation, according to the work of Marin [103]. This means that in this model each integration point correspond to only one phase.

In order to describe the plastic deformation as a contribution from all different slip systems, the following constitutive model is used, see equation **(6.1)** [104].

$$\underline{\underline{\dot{\varepsilon}}}^{p} = \sum_{SS=1}^{N} \dot{\gamma}^{SS} (\underline{\boldsymbol{s}}^{\boldsymbol{SS}} \otimes \underline{\boldsymbol{n}}^{\boldsymbol{SS}}) \tag{6.1}$$

where $\underline{\underline{\dot{\varepsilon}}}^{\mathrm{p}}$ is the plastic strain rate tensor, $\dot{\gamma}^{SS}$ is the slip rate on the slip system $SS$, $N$ is the total number of slip systems, $\underline{\boldsymbol{s}}^{\boldsymbol{SS}}$ and $\underline{\boldsymbol{n}}^{\boldsymbol{SS}}$ express, respectively, the slip direction and the slip plane normal of the slip system ($SS$), and $\otimes$ is the outer product. Solving crystal plasticity equations consists in computing the slip rate of every edge-type slip system (where both plane and direction are known) on every material point such that the mechanical equilibrium is preserved.

### *6.2.1 Flow and hardening rules*

The used framework is based on several flow and hardening laws found in the literature [105]. The flow rule used is a traditional power law, defined in equation **(6.2)**:

$$\dot{\gamma}^{SS} = \dot{\gamma}_0^{SS} \left( \frac{|\tau^{SS}|}{k^{SS}} \right)^{\frac{1}{m}} sign(\tau^{SS}) \tag{6.2}$$

where $\dot{\gamma}_0^{SS}$ is the reference slip rate and $m$ the strain rate sensitivity coefficient, both considered as material parameters. Also, $\tau^{SS}$ represents the resolved shear stress (RSS) and $k^{SS}$ the critical RSS (CRSS) on the slip system ($SS$). The RSS ($\tau^{SS}$) is computed as the projection of the local stress tensor ($\underline{\underline{\sigma_{local}}}$) into the slip system, as shown in equation **(6.3)**.

$$\tau^{SS} = \left(\underline{\underline{\sigma_{local}}} \cdot \underline{\boldsymbol{n}}^{SS}\right) \cdot \underline{\boldsymbol{s}}^{SS} \tag{6.3}$$

While the CRSS ($k^{SS}$) is driven by a phenomenological law that uses the dislocation density as a stable variable, defined by a Taylor's dislocation model [91], shown in equation **(6.4)**:

$$k^{SS} = k_0 + \psi G b \sqrt{\rho_{Sim}} \tag{6.4}$$

where $k_0$ is the microscopic yield stress of the material, defined as $k_0 = \sigma_0/M$, being $\sigma_0$ the macroscopic yield stress and $M$ the Taylor factor. $\psi$ is a material dependent parameter, $G$ the shear modulus, $b$ the Burger's vector magnitude and $\rho_{Sim}$ the dislocation density.

The evolution of $\rho$ is driven by a phenomenological law (involving hardening and dynamic recovery) that uses the Yoshie-Laasraoui-Jonas law [106], shown in equation **(6.5)**:

$$\dot{\rho_{Sim}} = \left(\frac{K_1}{M} - \frac{K_2}{M}\rho_{Sim}\right) \sum_{SS=1}^{n} |\dot{\gamma}^{SS}| \tag{6.5}$$

being $K_1$ and $K_2$ material parameters related to the generation of dislocations (hardening) and dynamic recovery (DRV), respectively. However, it is worth mentioning that the current model does not include the DRX phenomena. Hence, only the beginning of deformation ($\varepsilon_{macro}$~ 0.1 maximum) was considered, where the recrystallization can be neglected for sure.

Furthermore, for the implementation of this model for BCC crystals, it is sufficient to consider only one CRSS for all the slip systems [107]. Contrastingly, for HCP crystals, different CRSS values must be considered [25,52]. The ratio of the CRSSs in the $\alpha$ phase are approximately 1:1:1.5:3, for prismatic $\langle a \rangle$, pyramidal $\langle a \rangle$, basal $\langle a \rangle$, pyramidal $\langle c+a \rangle$ slip systems [25]. Also, between phases, the CRSS ratio is typically ~1/3 between $\beta$ phase and for prismatic $\langle a \rangle$ slip in the $\alpha$ phase [52], being also in agreement with $\sigma_\beta/\sigma_\alpha$ in Figure 5.11 (same order of magnitude).

In this manner, for the HCP crystal, two parameters were added to represent, respectively, the CRSS ratios between the basal $\langle a \rangle$ / prismatic $\langle a \rangle$ slip systems ($R^{CRSS}_{Basal}$) and the pyramidal $\langle c+a \rangle$ / prismatic $\langle a \rangle$ ($R^{CRSS}_{Pyramidal\,\langle c+a \rangle}$) ones. The proposed values of 1.5 and 3.0 [25] for the $R^{CRSS}_{Basal}$ and $R^{CRSS}_{Pyramidal\,\langle c+a \rangle}$, respectively, also depend on deformation temperature, thus being inserted in the identification of initial parameters.

Finally, **Table 6.1** summarizes all the parameters needed for the implementation of this CPFEM model.

| Parameters | Unit | Origin |
|---|---|---|
| $m$ | [-] | [103] |
| $\dot{\gamma}_0^{SS}$ | $[s^{-1}]$ | [103] |
| $\psi$ | [-] | [91] |
| $M$ | [-] | [91] |
| $G$ | $[MPa]$ | [91] |
| $\upsilon$ | [-] | [108] |
| $b$ | $[mm]$ | [91] |
| $\rho_0$ | $[mm^{-2}]$ | [106] |
| $K_1$ | $[mm^{-2}]$ | [106] |
| $K_2$ | [-] | [106] |
| $k_0$ | $[MPa]$ | [91] |
| $R_{Basal}^{CRSS}$ | [-] | [25] |
| $R_{Pyramidal\ \langle c+a\rangle}^{CRSS}$ | [-] | [25] |

*Table 6.1. List of parameters needed in the developed model.*

The Poisson's ratio ($\upsilon$) is necessary to calculate the Young's modulus ($E$) from the shear modulus ($G$), which are related by $E = 2G(1+\upsilon)$ [108].

## 6.3 Simulation

In order to correctly implement the full field simulations, three key points are necessary: a computational domain, the constitutive laws of each phase and the boundary conditions. Those three are described, respectively, in sections **6.3.1**, **6.3.2** and **6.3.3**.

### *6.3.1 Computational domain*

Full field models describe the microstructure topology at the polycrystal scale and allow to consider local phenomena and interactions between neighboring grains. A level-set (front capturing approach) was implemented in this work. It describes the grain interfaces implicitly with auxiliary functions (distance functions [109]). The main limitation of this approach is its complexity and numerical cost.

For the definition of the 3D computational domain (at intra-$\beta$-grain scale), two different strategies were used regarding the microstructure morphology. The equiaxed $\alpha$ grains were generated but experimentally measured $\alpha$ lamellae were immersed into the FE mesh (procedures detailed in sections **6.3.1.1** and **6.3.1.2**). The Ti64 alloy was selected for the full field simulations, as the 3D characterizations of the initial lamellar morphology were performed for this alloy, as presented in section **2.8**.

#### *6.3.1.1 Equiaxed α morphology*

The equiaxed $\alpha$ morphology was the most straightforward case to be implemented. The equiaxed $\alpha$ grains were considered as spheres in this framework. 124 $\alpha$ grains (spheres of 10 $\mu m$ diameter) were randomly generated in *Matlab*, inside a specified volume of 90 x 57 x 66 $\mu m$ (**Figure 6.1**).

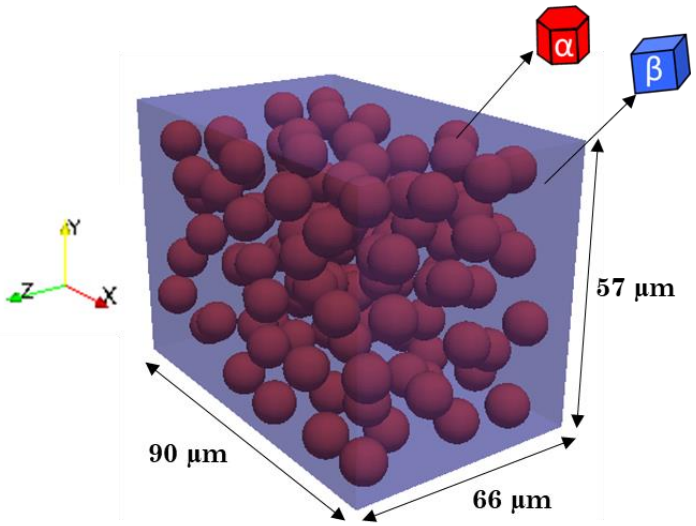



*Figure 6.1. The 124 α grains (spheres) randomly generated inside a single β grain defined by the volume specified.*

None of the spheres are in contact with each other, because to distribute both phases in the geometry (computational domain), each element is assigned a Boolean value (1 or 0). Thus, all spheres are identified by connected components between those elements, distinguishing all spheres.

A conforming mesh [110] (2.5 $\mu m$) was generated using *Gmsh* software [111]. In this strategy, a surface mesh of the grain boundaries is firstly considered, thus the volume mesh is generated inside the grains, based on surface meshes. This method has the particularity to generate a mesh coincident with grain boundaries, which is interesting when modelling polycrystal deformation [112].

However, it is intricate to generate a conforming mesh in *Gmsh* when objects intersect the borders. In this manner, the $\alpha$ spheres (**Figure 6.1**) also do not touch the borders of the domain. Respecting these conditions, a maximum primary $\alpha$ phase fraction of 18% could be achieved, as close as possible to the experimental one (35%). It is important to mention that those conditions are not a limitation of the methodology, yet they are a simpler strategy to create the computational domain.

**Figure 6.2** shows that the conforming mesh provided an adequate representation of the morphology, with more than $2x10^6$ elements.

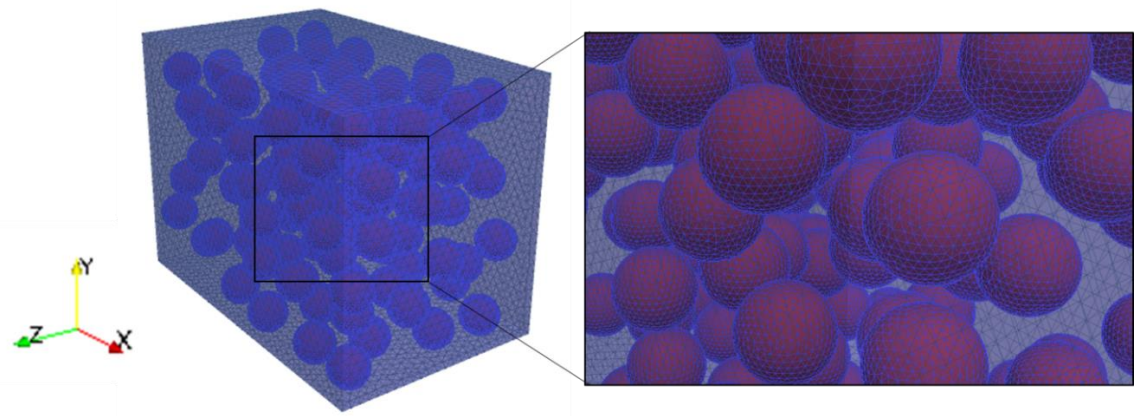



*Figure 6.2. RVE with the highlighted mesh to show the different elements in the model.*

The element size is heterogeneous in the immersed domain, especially for the $\beta$ phase, allowing satisfactory description of the $\alpha/\beta$ interface with a finer mesh, and a larger mesh size farther from the $\alpha$ grains (**Figure 6.3**), reducing computation time.

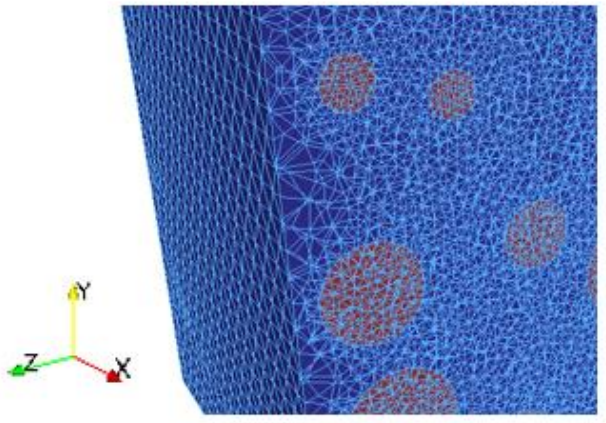



*Figure 6.3. Zoom in a cross section of the volume of the RVE (regarding X-axis), showing the heterogeneous mesh.*

Concerning crystallographic orientations, each of the $\alpha$ grains was assigned an average grain orientation obtained from a set of $\alpha$ grains measure in a prior-$\beta$ grain by 2D EBSD analysis, for the Ti64_Eq at 950°*C* before deformation. The consequent pole figures of the $\alpha$ phase are shown in **Figure 6.4**.

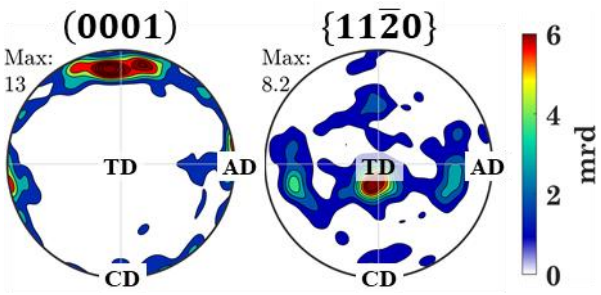



*Figure 6.4. Pole figures of the α phase, showing the initial orientation of the numerical α grains, obtained from 2D EBSD data.*

In order to analyze texture evolution throughout deformation, a coupling between the EBSD data post-processing tools available in *MTEX* [51] and the simulation results was performed. It enabled the plot of pole figures from the initial orientations (described by Euler angles). Furthermore, an analysis of the influence of the $\alpha$ grain crystallographic orientation on the dislocation density and stress-strain curves (at the RVE scale) was performed. Three different $\alpha$ grain orientations were selected: basal [0001], pyramidal $\langle 0\bar{1}1\bar{1}\rangle$ and prismatic $\langle 1\bar{1}00\rangle$ directions parallel to TD, thus perpendicular to the CD. It is important to mention that, for the case where the [0001] is perpendicular to CD, the $\langle 11\bar{2}0\rangle$ was intentionally oriented parallel to CD, to obtain the same orientation seen in **Figure 4.56**. For the $\beta$ phase, only one orientation was chosen for the RVE: (100) plane parallel to the CD. The $\alpha$ and $\beta$ orientations are schematized in **Figure 6.5**.

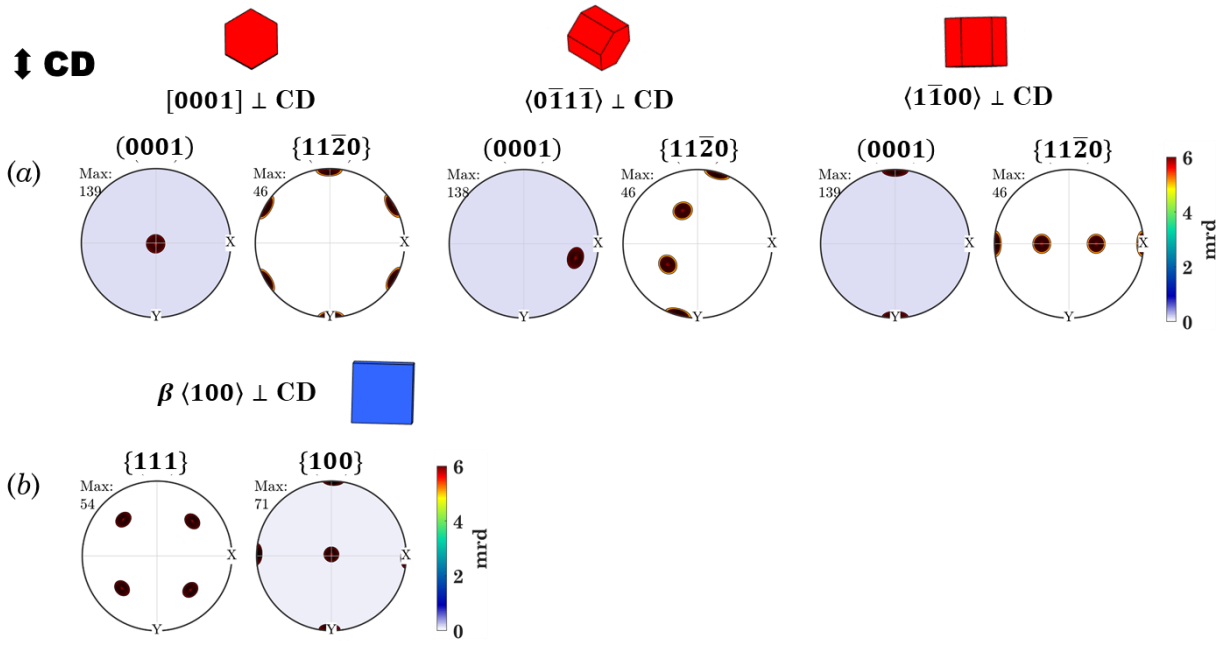



*Figure 6.5. The pole figures and the crystal shapes (hexagonal and cubic) representing the crystallographic orientations for the: a) α phase; b) β phase; along with the CD.*

### *6.3.1.2 Lamellar α morphology*

For the lamellar case, the numerical implementation was less straightforward, as 3D EBSD analysis was necessary to obtain the RVE. The synthetic generation of a lamellar RVE would have been quite complex with the numerical framework used in its current state. Therefore, an alternative has been preferred consisting in using 3D EBSD in order to build the numerical RVE. The idea is to interpolate the experimental data in the FE mesh. To this end, the mesh should be adapted to the topology of the microstructure. This mesh adaptation process is computationally expensive, but was the best option available to accurately represent the complex topology of the lamellar morphology.

The 3D analysis has some differences when applied to serial section tomography using backscattered electron (BSE) imaging (section **2.8**), as briefly explained below. In the following section, the reconstructed volume for the full field simulations immersion will be described as well.

#### *6.3.1.2.1 Procedure description*

When acquiring 3D EBSD data by FIB-SEM microscopy, thin slices of the sample material are milled by FIB and the new surfaces are analyzed by 2D EBSD. FIB milling and 2D EBSD mapping are sequentially repeated, hundreds of times, aiming to analyze the total volume of interest. The main difference to the procedure explained in section **2.8** involves the fulfillment of an extra geometrical condition. At the EBSD position, the surface of interest must be tilted 70° from horizontal in front of the detector. Additionally, the FIB milling condition for the ion beam is a tilt of 55° of the top surface from horizontal surface (see **Figure 2.23**). A so-called static configuration [113] is provided by the TESCAN FERA 3 PFIB-SEM. It has the great advantage that serial sectioning combined with EBSD can be performed

without moving the sample, significantly improving the quality of the final result and the analysis time.

For the 3D EBSD analysis, a Ti64_FL sample was taken from the industrial billet (**Figure 6.6***a*), heat treated at 950°*C* for one hour and WQ (see **Table 2.2**). Then, two perpendicular surfaces were polished (**Figure 6.6***b*). This step of polishing proved necessary because the acquisition was performed of the edge of the sample (see **Figure 6.6***c*), where a flat topology of the top surface is needed to reduce curtaining effect. Similar preparation conditions shown in section **2.8** are performed around the ROI (*i.e.,* Pt deposition and stairs milling). The FIB + EBSD analysis zone is shown in **Figure 6.6***d*, after FIB polishing step at 100 *nA*.

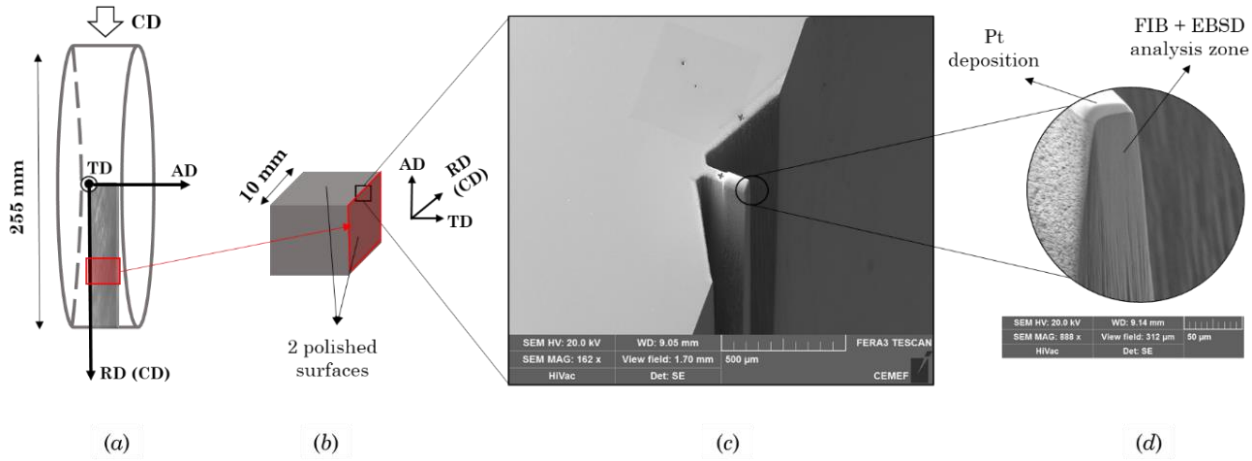



*Figure 6.6. The different scales in the 3D EBSD analysis implementation: a) The industrial billet sampling; b) The sample with the two polished surfaces; c) A zoom in the analysis zone after FIB removal of material on both sides (to avoid shadowing in further EBSD acquisitions); d) The 3D EBSD analysis surface, after polishing, with the Pt deposition on top.*

Finally, the FIB milling conditions for 3D EBSD analysis was launched at an ion beam current of 100 *nA*, during 188 slices of 0.3 *μm* each, every milling step being followed by an ion polishing step at 100 *nA*. The whole process took 40 hours approximately, while, for each section, ~1 minute was spent in the milling, ~12 minutes for the EBSD map acquisition, and ~10 seconds for the in-beam SE image acquisition. In **Figure 6.7**, the first slice and its corresponding EBSD map are shown.

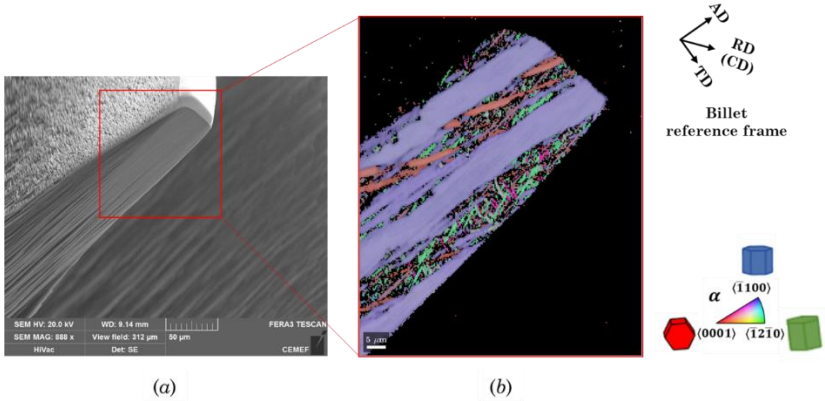



*Figure 6.7. First layer of the 3D EBSD analysis: a) SE image where the curtaining effect can be clearly seen; b) Raw EBSD map with AD-IPF color coding.*

#### *6.3.1.2.2 Reconstruction and post-processing*

The reconstruction of the 3D volume was performed in the *Dream3D* software [110] through a series of steps. The pipeline begins with the import of the 2D EBSD files that were exported from the EBSD data acquisition software. In this step, the thickness of each slice is assigned (0.3 $\mu m$), and all the maps are located one over the other. Secondly, bad quality indexation points are removed by applying a threshold in the band contrast. Then, grains are segmented using a misorientation tolerance of 10°. Finally, the average orientation of each grain is calculated and the IPF is generated.

The 3D volume and its properties can be visualized in the *Paraview* software [81] (**Figure 6.8**). In **Figure 6.8***a*, the reconstructed volume of the raw data can be observed, with the outline (white lines) of the cropped area and post-processed data (shown in **Figure 6.8***b*). The scattered voxels on top (removed during crop) are poorly indexed data, which were outside the ROI (see **Figure 6.7**). The final volume of the reconstruction is 25.2 x 45.3 x 55.8$\mu m^3$. **Figure 6.8***c* shows the laths that have an average width higher than 0.5 $\mu m$, threshold used (after manual checks) to remove the indexed $\alpha_S$, which is not present at 950°*C*. It is also worth mentioning that most probably the primary laths are thinner at 950°C, and that the spatial resolution applied is not sufficiently high to index the very thin $\beta$-layer between α laths. Thus, thicker α laths are being shown, instead of a layering of fine $\alpha$ laths with $\beta$ phase between them.

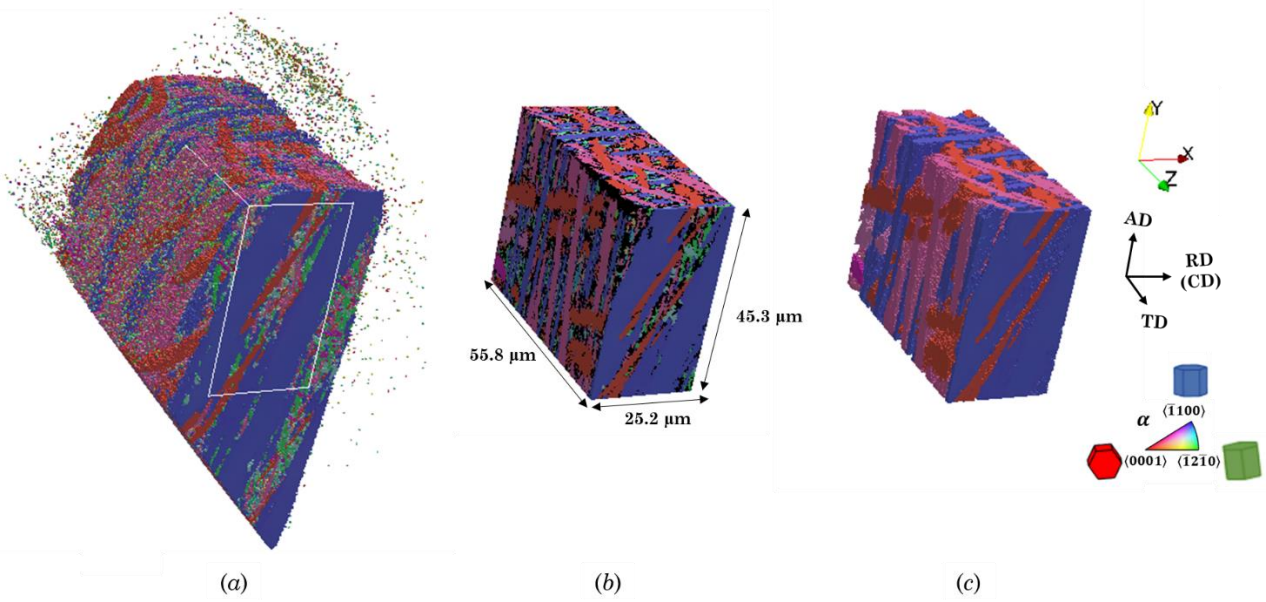



*Figure 6.8. 3D EBSD map with TD-IPF of the: a) Raw data; b) Cropped and post-processed data; c) Laths selected using a minimum average width criterion set to 0.5 µm.*

Five main crystallographic orientations, corresponding to different lath colonies, can be distinguished in the analyzed volume (**Figure 6.9**). The mainly captured orientations were n°1 to 3, while only a small zone of orientations n°4 and 5 were captured in the 3D EBSD analysis.

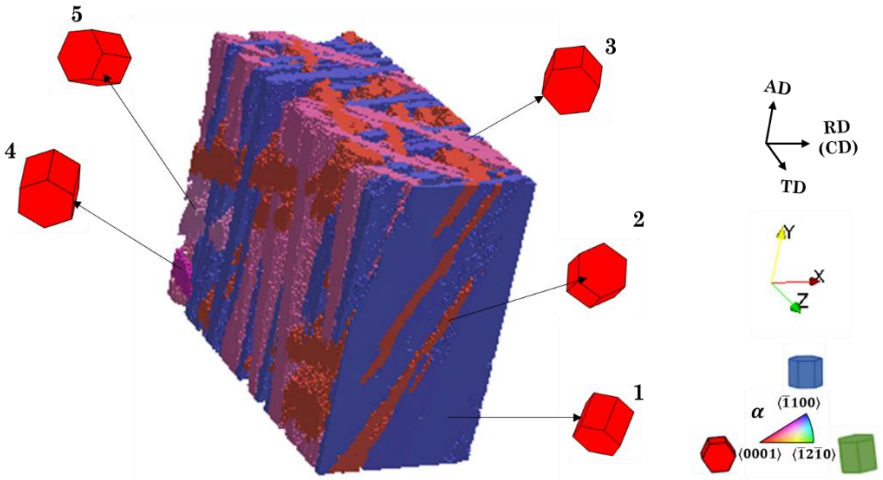



*Figure 6.9. 3D EBSD map of the Ti64_FL at 950°C, with TD-IPF and the respective shapes of the lath colonies.*

**Figure 6.10** evidences the complexity of the entangled morphology of the lamellar Ti64_FL, with the intersection of $\alpha$ laths containing different crystallographic orientations. Interestingly, at their intersection, only one crystallographic orientation is selected in a given 2D section.

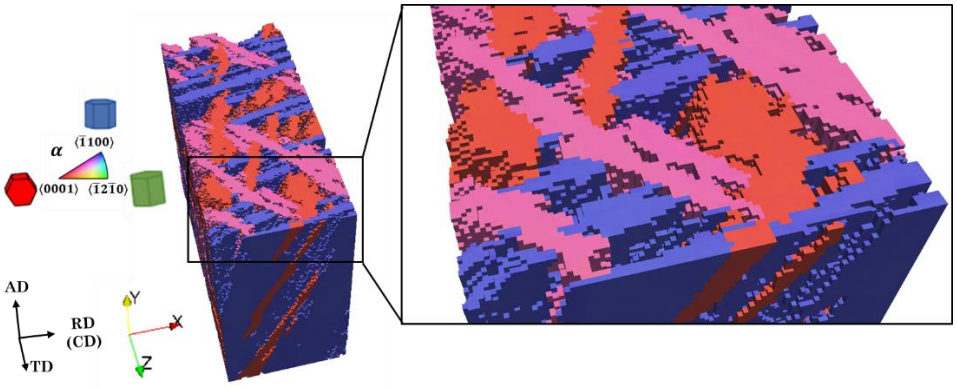



*Figure 6.10. Upper view of the 3D EBSD map (TD-IPF), evidencing the entangled morphology of the α laths with different crystallographic orientations.*

The complexity of this microstructure is the reason behind the necessity of an immersion of 3D lamellar microstructure to provide the most realistic input data possible to the full field simulations.

#### *6.3.1.2.3 Immersion of the microstructure from the 3D EBSD data*

The 3D EBSD data can be seen as a structured hexahedral mesh. Since the voxel (hexahedron) size is constant, then given a point in space (x,y,z), it is simple to find the voxel that contains it. For each point (node) of the FE mesh, the orientations of the voxel that contains it are assigned. Consequently, from the 3D data analysis, a list of the three Euler angles ($\phi_1, \Phi, \phi_2$, according to the Bunge convention ZXZ), for each voxel of $\alpha$ phase, was exported from *Dream3D* software. This list was inserted in the simulation, along with the volume studied (25.2 x 45.3 x 55.8 $\mu m$), to immerse the 3D microstructure. The result of this immersion can be observed in **Figure 6.11**.

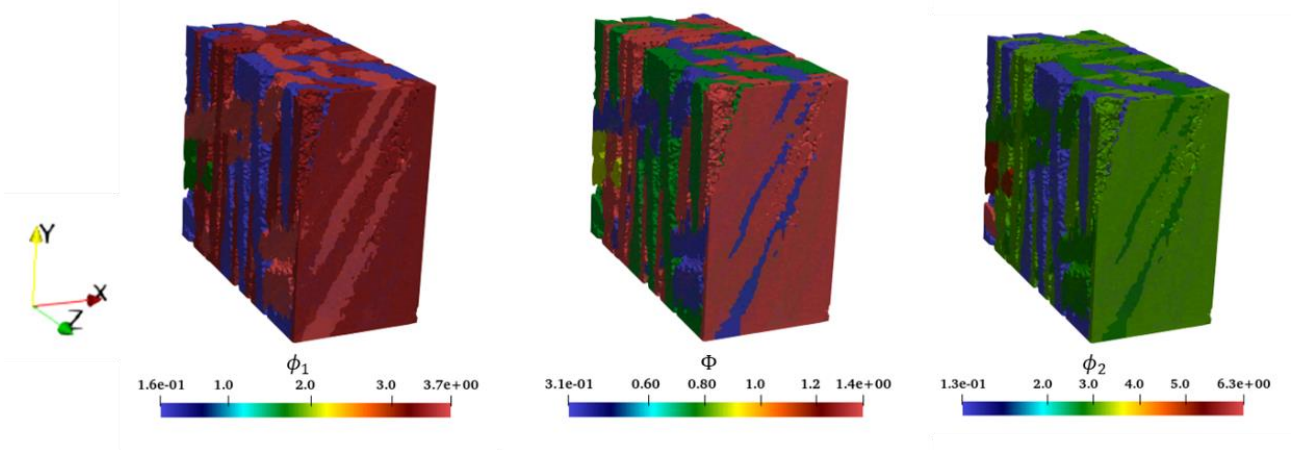



*Figure 6.11. The three Euler angles ($\phi_1, \Phi, \phi_2$) shown for the different laths inside the studied volume. The five different lamellae orientations identified in the 3D EBSD characterization can be spotted.*

**Figure 6.11** shows a satisfactory immersion of the real 3D microstructure in the simulations, where the morphology and the different orientations are preserved (see **Figure 6.8***c*).

**Figure 6.12** shows the RVE dimensions, along with the $\alpha$ and $\beta$ phase distribution.

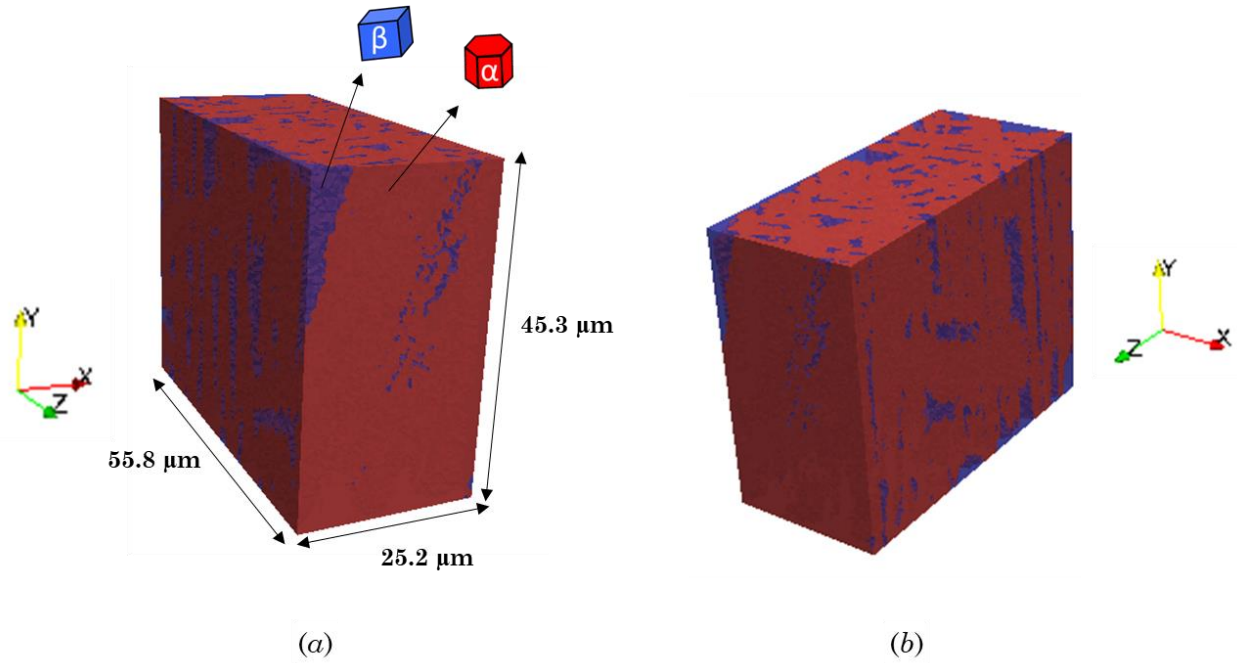



*Figure 6.12. RVE dimensions for the lamellar case (Ti64_FL), along with α and β phases from two different views (a and b).*

Finally, the pole figures of the numerical $\alpha$ laths at the initial state (before deformation), obtained experimentally from 3D EBSD data are shown in **Figure 6.13**. For the $\beta$ phase, the same crystallographic orientation selected for the equiaxed morphology was applied: [100] direction ⊥ CD, but it would be possible also to consider the $\beta$ grain orientation deduced from the $\alpha$ BOR variants.

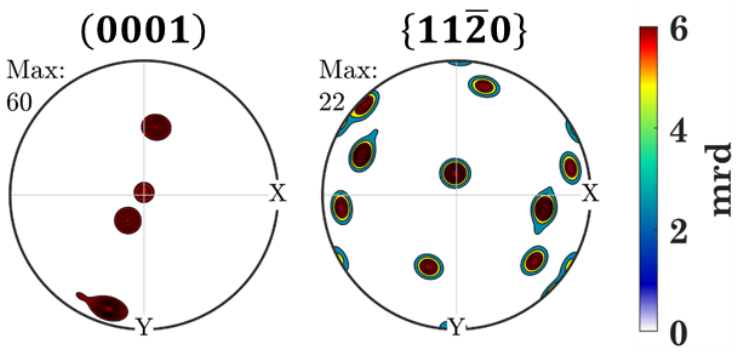



*Figure 6.13. Pole figures showing the initial orientation of the numerical α laths obtained from 3D EBSD data.*

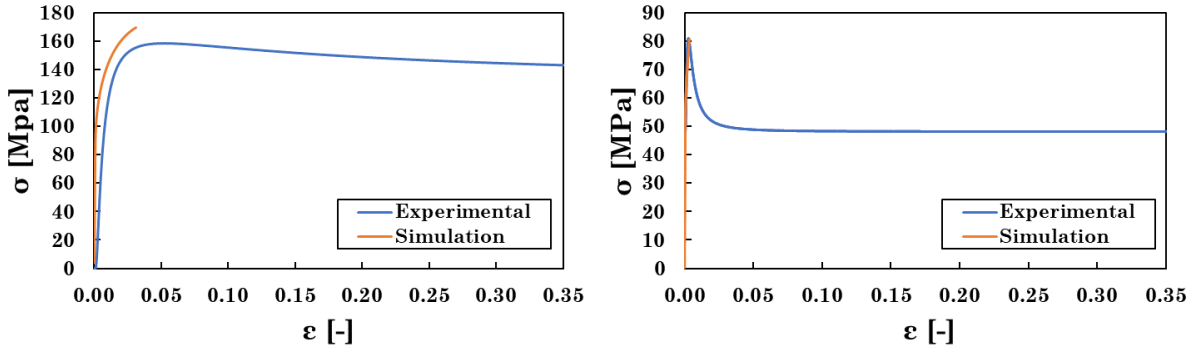
### *6.3.2 Constitutive laws*

Properly identifying some of the parameters needed in equations **(6.4)** and **(6.5)**, would require several experimental data and identification by inverse analysis through simulations. As the experimental stress-strain curves presented in Chapter **5** are from only one set of temperature and strain rate, this cannot be implemented. Also, for a correct identification by inverse analysis, several simulations including the complete RVE should be performed. Such an optimization process based on full field RVE simulations at several thermomechanical conditions is highly time and computing costly.

To tackle this problem, a material point was used within monophasic simulations (with the same crystal plasticity model used in the full field simulations), to identify the needed parameters by inverse analysis. This procedure was performed, for each phase separately, in the *MOOPI* software (developed in CEMEF [114] for optimization and parameters identification). The individual flow stresses calculated in Chapter **5** were used for the correlation between experimental data and the monophasic simulations. The objective is to impose a small deformation (below dynamic recrystallization onset) and endeavor to reproduce the stress estimated experimentally by the flow rules in equation **(5.2)**. It is worth mentioning again that this is a strong hypothesis, since it neglects the mechanical coupling between the two phases, yet has the advantage of being simple and swift.

Furthermore, the three main $\alpha$ orientations shown in **Figure 6.5** were tested in this step, as also the one of the $\beta$ phase. Regarding the hardening law, three parameters ($k_0, K_1, K_2$) were identified for each phase. Also, for the HCP crystal, the ratios between the CRSS of the different slip systems ($R^{CRSS}_{Basal}$ $R^{CRSS}_{Pyramidal\,\langle c+a\rangle}$) were added in this inverse analysis.

Several simulations were automatically launched, for each phase separately, to find the desired parameters within the established ranges. For the $\alpha$ phase, the mean stress values as also the average of the parameters were calculated. **Figure 6.14** shows the results of this identification process, where the simulated curves are fitted to the very beginning of the experimental curves (no recrystallization) obtained in Chapter **5**.




(*a*) (*b*)

*Figure 6.14. Stress-strain curves comparing the experimental data and the simulation after the identification of the model parameter for the: a) α phase; b) β phase.*

The parameters fitted from this identification process ($k_0, K_1, K_2, R^{CRSS}_{Basal}, R^{CRSS}_{Pyramidal\,\langle c+a\rangle}$), as also other parameters used in the developed model, are detailed in **Table 6.2**.

| Parameters | | $\alpha$-phase | $\beta$-phase | Reference |
|---|---|---|---|---|
| Obtained from literature | $m$ [-] | 0.1 | 0.1 | [109] |
| | $\dot{\gamma}_0^{SS}[s^{-1}]$ | 1 | 1 | [99] |
| | $\psi$ [-] | 0.1 | 0.1 | [92] |
| | $M$ [-] | 5 | 3.05 | [92] |
| | $G$ [$MPa$] | 23100 (@950°C) | 16500 (@950°C) | [26] |
| | $b$ [$mm$] | 2.95 x $10^{-7}$ | 2.86 x $10^{-7}$ | [9] |
| | $v$ [-] | 0.33 | 0.33 | [115] |
| Obtained experimentally | $\rho_0$ [$mm^{-2}$] | 1 x $10^{8}$ | 1 x $10^{8}$ | See Figure 4.26 |
| Fitted | $K_1[mm^{-2}]$ | 1.1 x $10^{12}$ | 9.0 x $10^{11}$ | [99] |
| | $K_2$[-] | 99.7 | 20.0 | [99] |
| Fitted from a range established in the literature | $k_0$ [$MPa$] | 65.2 | 38.5 | [25,52] |
| | $R^{CRSS}_{Basal}$ [-] | 1.4 | - | [25,52] |
| | $R^{CRSS}_{Pyramidal\,\langle c+a\rangle}$ [-] | 2.88 | - | [25,52] |

*Table 6.2. List of parameters used in the developed model.*

### *6.3.3 Boundary conditions and limitations*

One of the main difficulties when studying material's mechanical response at the microscale is the choice of the boundary conditions. Different approaches can be taken. In theory, the mechanical response of the material at the microscale could be studied using Direct Numerical Simulations. This would mean meshing the microstructure of the entire material, then applying macroscopic boundary conditions directly to that mesh. This method obviously incurs a huge cost, being

only suitable for very small samples (hundreds of $\mu m$). Therefore, for larger samples and industrial applications, researchers have explored ways in which micromechanics could be considered, without the huge computational cost of Direct Numerical Simulations.

The most accurate way of obtaining representative boundary conditions would be to measure them from experimental data. The idea is to use multiple 3D images of the same region at different loading states during an interrupted test. These images could be used to measure the displacement field using Digital Volume Correlation [116,117]. This approach is again very costly and is not suitable to the destructive 3D imaging technique used in this work. A simpler alternative consists in using the macroscopic constitutive law of the material to simulate the test at the macroscopic scale, then the thermomechanical loading can be tracked over the ROI. Although this method would require a deep characterization of the boundary conditions of the computational domain.

In this work, the macroscopic boundary conditions of an uniaxial compression were imposed to the RVE. In this manner, the deformation of the macroscopic material is considered the same as at the microscopic level. This method is a much simpler alternative to the problematic, as the aim of this chapter is mostly to compare the tendencies observed in the experimental chapters (**4** and **5**). Nevertheless, it is important to mention that this is a strong hypothesis. All different RVEs were uniaxially compressed (according to Y-axis) at a 0.1 $s^{-1}$ strain rate until 0.1 strain level. The fact that the same deformation parameters were applied to all RVEs allowed the comparison between different $\alpha$ grains orientations and morphologies described in sections **6.3.1.1** and **6.3.1.2**.

## 6.4 Results, comparison to experimental data and discussions

The results presented in this section are mainly focused on the dislocation density distribution ($\rho_{Sim}$) between $\alpha$ and $\beta$ phases, and also the influence of $\alpha$ grain crystallographic orientation in the $\rho_{Sim}$. The slight texture evolution of the $\alpha$ grains are presented by pole figures after deformation. Finally, the stress-strain curves are shown and compared between the different cases. The results are also compared to the ones seen experimentally in Chapters **4** and **5**.

### *6.4.1 Equiaxed α morphology*

**Figure 6.15** shows the change in shape and noteworthily in surface roughness of the RVE after deformation. It is obviously related to crystal plasticity anisotropy and the two-phase nature of the system, which impact the deformation. This can be seen by the rugosity in **Figure 6.15***b* surfaces, where the positions of the harder equiaxed $\alpha$ grains can be perceived.

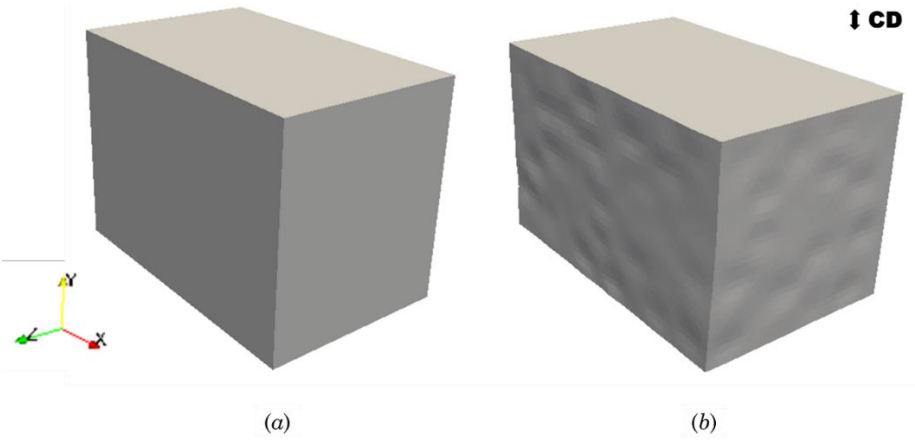



*Figure 6.15. RVE shape of the equiaxed case: a) before; b) after deformation.*

Regarding the dislocation density estimated by the simulations ($\rho_{Sim}$), **Figure 6.16** shows its distribution within the RVE, at the end of deformation, for the equiaxed $\alpha$ grains with experimental orientations from 2D EBSD data. Only half of the volume (along X-axis) is displayed, to show the dislocation density evolution in both phases in the mid plane of the RVE, as the $\alpha$ grains are fully contained inside the $\beta$ phase.

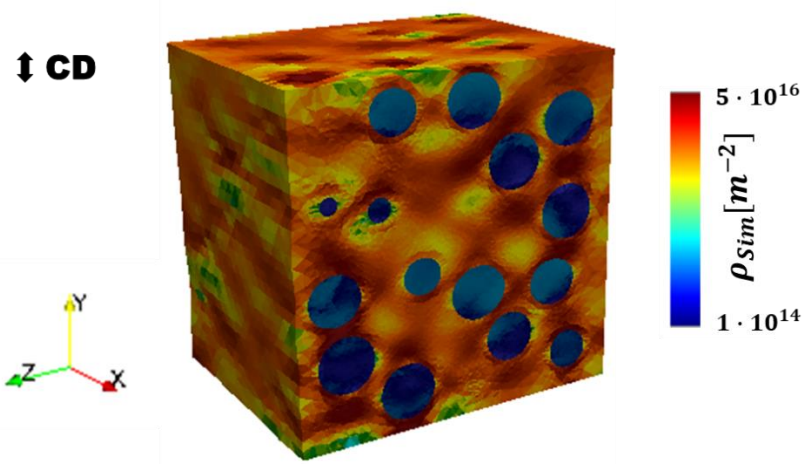



*Figure 6.16. Dislocation density distribution in half of the RVE (cut along X-axis), containing the equiaxed α grains with orientation from 2D EBSD data.*

By analyzing **Figure 6.16**, it is clear that the $\beta$ phase contains more dislocations than the $\alpha$ phase. This is consistent with the CRSS values ($k_0$), as the CRSS of the $\beta$ phase is lower than the $\alpha$ ones (see **Table 6.2**). Additionally, the shear modulus ($G$) of the $\alpha$ phase is also higher. In this manner, the slip first occurs in the $\beta$ phase, as the resolved shear stress necessary to produce slip is lower in this phase. This behavior seems in contrast to the results of Chapter 4 from EBSD analysis, where the $\rho_{EBSD}$ of the $\alpha$ phase, after deformation, was always superior to the $\beta$ phase one (see **Figure 4.26**). Nevertheless, as mentioned in the introduction of this chapter, a direct comparison of both dislocation densities ($\rho_{EBSD}$ and $\rho_{Sim}$) is intricate, as they estimate different types of dislocations. Also, from experimental data, the dislocation density in the $\beta$ phase could not be calculated for the Ti64 alloy, as explained in section **2.7.1**. Finally, the lowest strain level analyzed

experimentally was 0.3, which is considerably higher than the one applied in this chapter (0.1).

On **Figure 6.16**, it can also be observed that the $\alpha$ phase has an effect on the $\rho_{sim}$ distribution in the $\beta$ phase, where quite strong gradients of dislocation density can be observed, in the $\beta$ phase, in the vicinity of the $\alpha$ grains, which is coherent with the fact that those regions recrystallize in an easier way (see Figure 1.25).

**Figure 6.17** shows the quantitative analysis of the average $\rho_{sim}$ evolution in both phases throughout deformation, where, at the end of deformation, the ratio between the $\beta$ and $\alpha$ phases is 4.3.

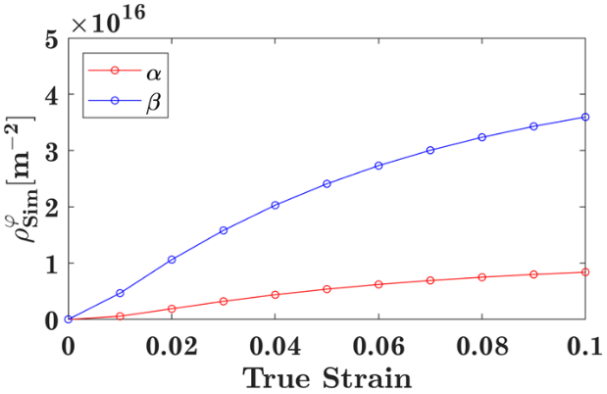



*Figure 6.17. Average dislocation density ($\rho_{Sim}$) evolution throughout deformation of the α and β phases.*

Furthermore, a gradient of dislocation density can be observed inside each $\alpha$ grains (**Figure 6.16**), this is also coherent to what was seen experimentally in the $\alpha$ grains (Figure 4.25), yet in this case it is possibly because each element is taken separately in the FEM calculation. Also, it is possible to see that different $\alpha$ grains contain varying levels of $\rho_{Sim}$.

**Figure 6.18** shows how the crystallographic orientation of the $\alpha$ grains, evolved throughout deformation, even if in a very subtle manner, owing to the fact that the total strain level applied is only 0.1.

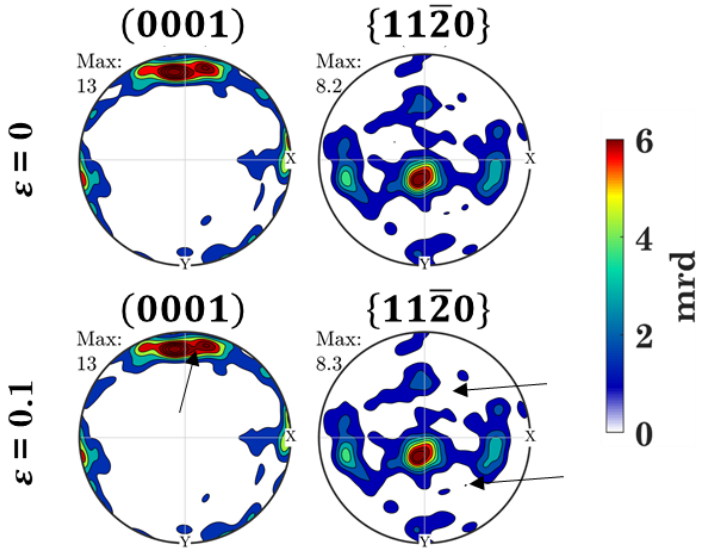



*Figure 6.18. Pole figures of the α grains with initial orientation from 2D EBSD data before and after deformation; some differences in texture are highlighted by the black arrows.*

### 6.4.1.1 Orientation dependency of dislocation density evolution

The dislocation density ($\rho_{Sim}$) maps, at the end of deformation, for the equiaxed $\alpha$ grains with three different initial orientations (basal, pyramidal and prismatic planes parallel to the CD) are displayed in **Figure 6.19** along with the quantitative analysis of the average $\rho_{Sim}$ evolution, on both phases.

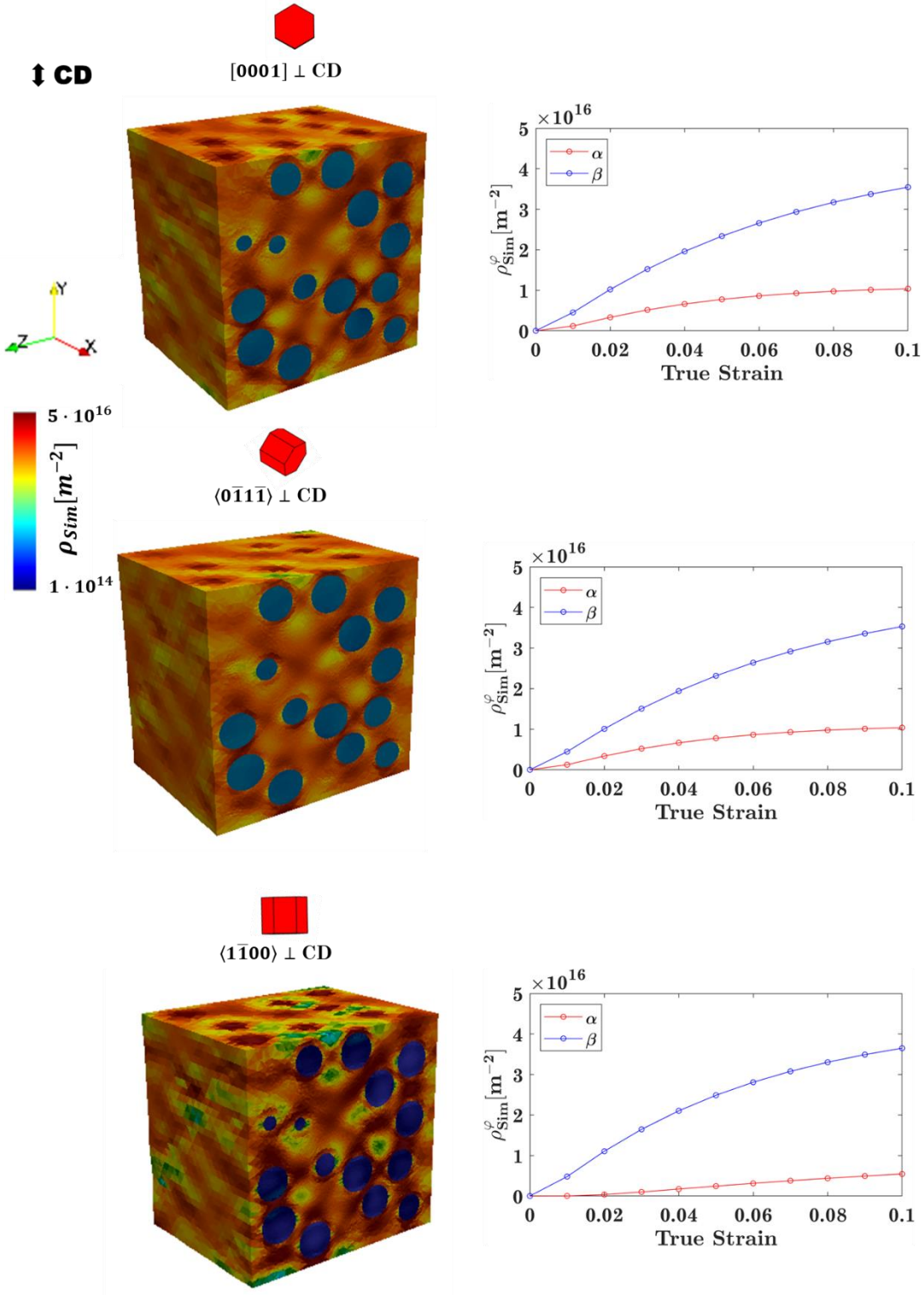



*Figure 6.19. Dislocation density maps on half of the RVE (regarding X-axis), containing the equiaxed α grains with three different initial orientations, along with their average dislocation density ($\rho_{Sim}$) evolutions of the α and β phases.*

For the basal [0001] and pyramidal $\langle 0\bar{1}1\bar{1}\rangle$ ⊥ CD, similar levels of $\rho_{Sim}$, within both phases were obtained, mainly related to the Schmid factor [118]. This was also seen experimentally in Chapter **4**, where grains with basal planes ∥ CD (*i.e.*, [0001] ⊥ CD) showed higher dislocation density levels than the ones with prismatic planes ∥ CD (**Figure 4.23**).

Meanwhile, for the prismatic configuration, compared to the two others, a slightly higher $\rho_{Sim}$ was achieved in the $\beta$ phase, while it was drastically reduced in the $\alpha$ phase. It seems that, when the $\beta$ phase is oriented with [100] ⊥ CD, a prismatic $\langle 1\bar{1}00\rangle$ ⊥ CD does not privilege the development of dislocations in the $\alpha$ phase. This is coherent, as all systems with $\langle a\rangle$ as Burgers vector have a RSS equal to zero when $\langle a\rangle$ ⊥ CD. In this manner, more dislocations are developed in the $\beta$ phase to accommodate the deformation applied.

### *6.4.1.2 Schmid factor investigation*

To investigate the reason behind similar dislocation levels between the basal and pyramidal configurations, as also a lower one for the prismatic one, the Schmid factor of each of the 30 edge-type slip systems (**Figure 2.20**) of the $\alpha$ phase were calculated (**Figure 6.20**). It is worth to recall that the fitted ratios between the $\alpha$ phase slip systems are: 2.88 and 1.4 for the $R^{CRSS}_{Pyramidal\ \langle c+a\rangle}$ and $R^{CRSS}_{Basal}$, respectively.

The list of the 30 slip systems, in their respective order, is detailed in **Table 6.3**.

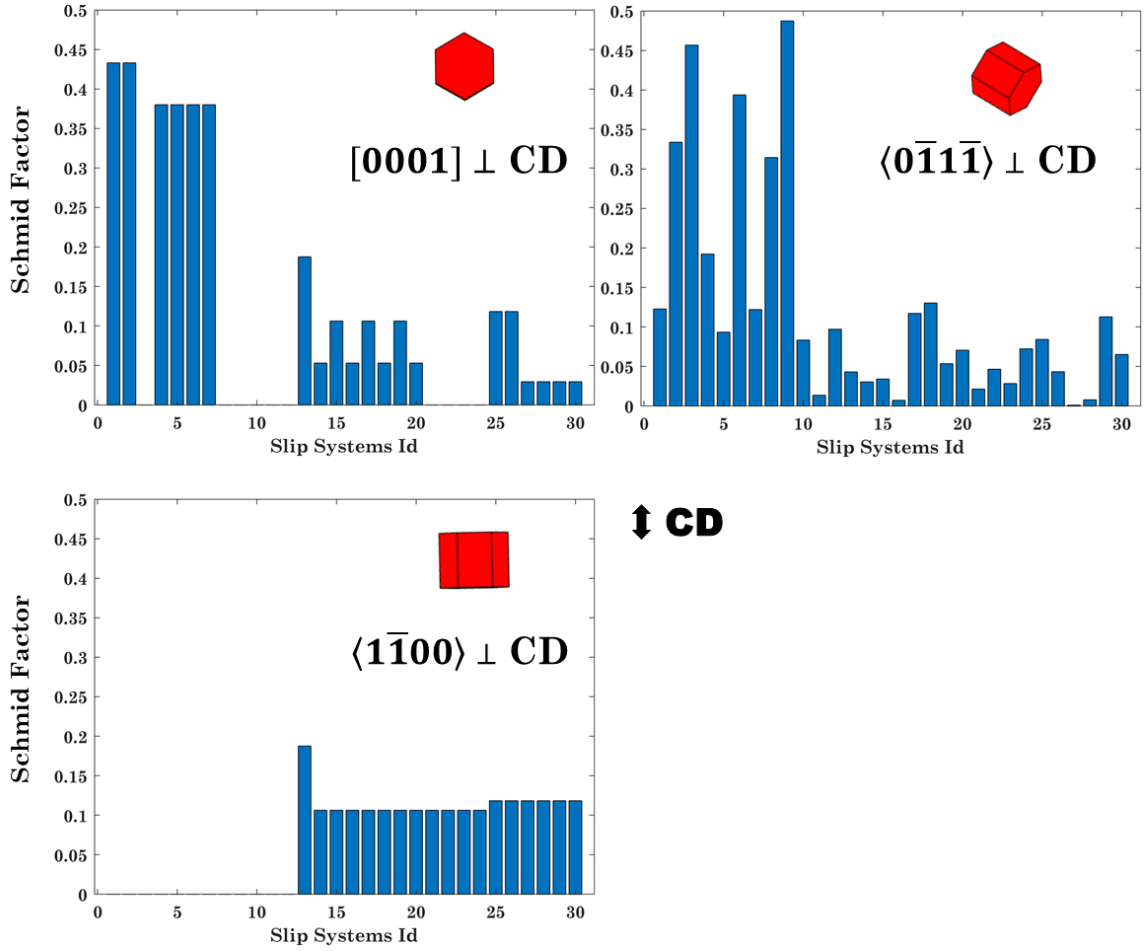



*Figure 6.20. Schmid factor for each of the 30 slip systems for the three orientation configurations of the α phase.*

| Id | Slip Systems |
|---|---|
| 1 to 3 | Prismatic $\langle a \rangle$ |
| 4 to 9 | Pyramidal $\langle a \rangle$ |
| 10 to 12 | Basal $\langle a \rangle$ |
| 13 to 24 | Pyramidal $\langle c+a \rangle$ 1st |
| 25 to 30 | Pyramidal $\langle c+a \rangle$ 2nd |

*Table 6.3. List of slip systems Id.*

In the basal [0001] and pyramidal $\langle 0\bar{1}1\bar{1} \rangle \perp$ CD, the most active slip systems are $\langle a \rangle$-type. It seems to be the reason why the dislocation density levels were similar in those two cases (**Figure 6.19**). Contrastingly, for the prismatic $\langle 1\bar{1}00 \rangle \perp$ CD, the active slip systems are $\langle c+a \rangle$-type, which can explain much lower $\rho_{sim}$ were obtained for this configuration, as the CRSS $\langle c+a \rangle$ are much higher than the $\langle a \rangle$ ones (see **Table 6.2**). It is worth mentioning that the $\underline{\underline{\sigma}}$ was assumed to be equal to the macroscopic stress applied. In reality, there are local changes on the stress, so the local Schmid factor should be different, yet this simplification still allows the obtention of some insights.

**Figure 6.21** displays only the $\alpha$ grains, to better analyze this phase.

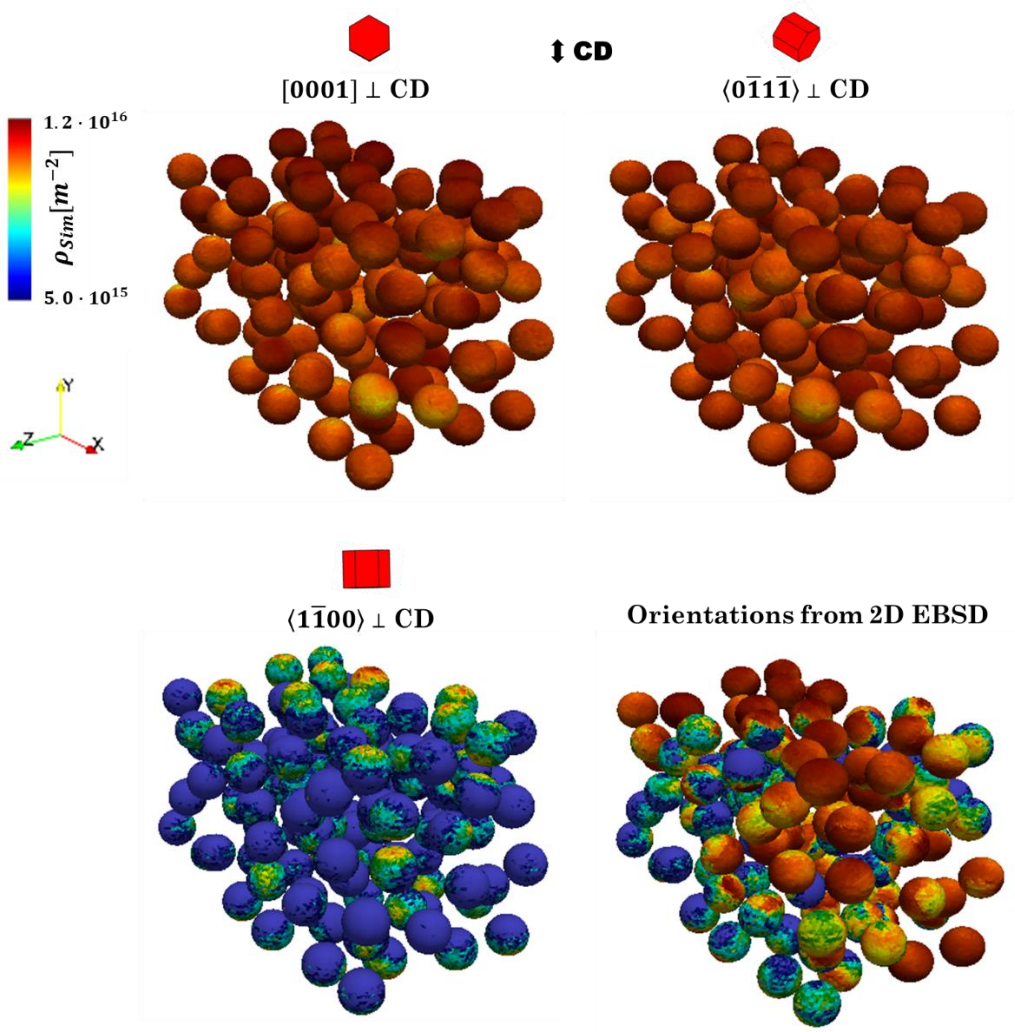



*Figure 6.21. Dislocation density distribution (α phase only) on the equiaxed α grains with three different initial orientations and from 2D EBSD data.*

It is possible to see that, when all $\alpha$ grains have the same initial orientation, the dislocation density gradient between different grains is reduced (compared to the one from 2D EBSD data). The observed difference in $\rho_{Sim}$ levels within distinct $\alpha$ grains in the latter seems to be connected to the crystalline orientations. This behavior was also seen in the experimental analysis from EBSD data (Chapter **4**), where the different $\alpha$ grain orientations affected the substructure evolution (section **4.1.4**).

As could be expected, the boundary conditions have also an impact on the results. For instance, the grains on the upper side of the RVE, where the compression was applied, have, on average, a higher dislocation density level. In this manner, it is clear that different initial orientations of the $\alpha$ grains have a strong impact in the dislocation density evolution, depending on the crystallographic orientation according to the CD.

### *6.4.2 Lamellar α morphology*

**Figure 6.22** shows the change in shape of the RVE after deformation, where the volume is heterogeneously deformed, due to the presence of the $\alpha$ laths.

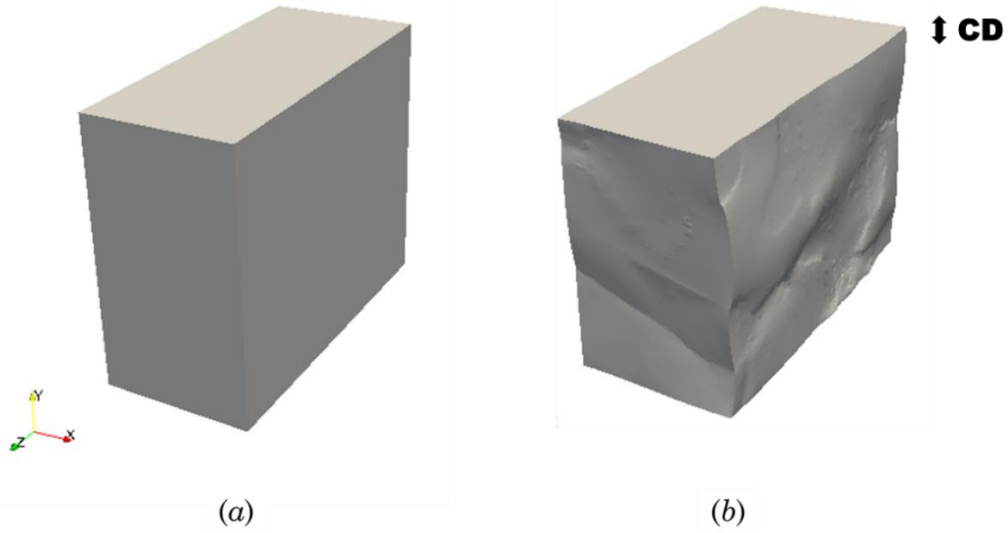



*Figure 6.22. RVE shape of the lamellar case: a) Before; b) After deformation.*

Regarding the dislocation density ($\rho_{Sim}$), **Figure 6.23** shows its repartition within the RVE at the end of deformation, along with the quantitative analysis of the average dislocation density evolutions, for both phases. The $\beta$ phase has again a higher $\rho_{sim}$ compared to the $\alpha$ phase.

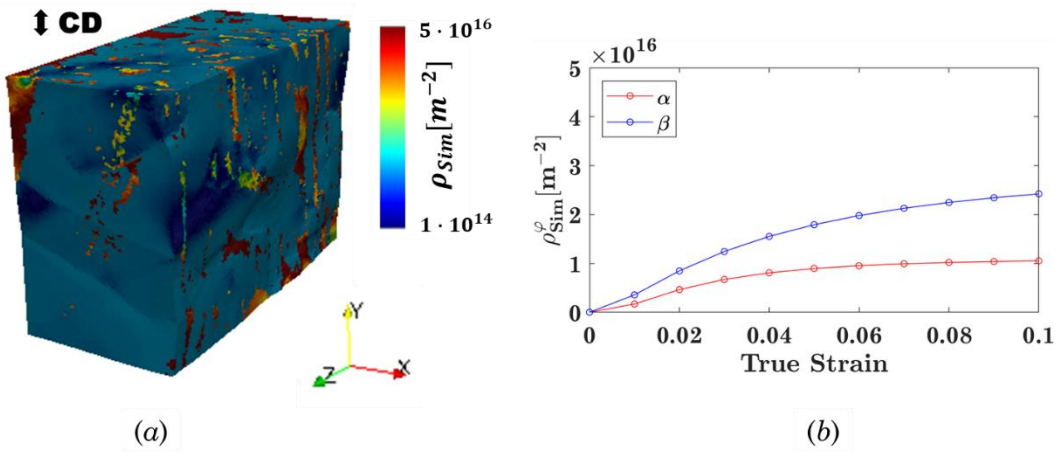



*Figure 6.23. a) Dislocation density distribution on the RVE containing the α laths; b) Average dislocation density ($\rho_{Sim}$) evolutions of the α and β phases for the lamellar RVE.*

Concerning the $\alpha$ phase, the dislocation density at the end of deformation reached similar values compared to the equiaxed RVE, except for the $\alpha$ grains with prismatic plane ∥ CD. However, for the $\beta$ phase, the average dislocation density was inferior to the equiaxed cases, around 1.5 times inferior. It seems that on the Ti64, the $\rho_{sim}$ on the $\beta$ phase is unfavored by a lamellar morphology.

Analyzing the $\alpha$ phase separately (**Figure 6.24**), it is clear that the gradient of $\rho_{sim}$ is high (**Figure 6.24***a*). The Φ Euler angle is also shown (**Figure 6.24***b*) to allow the visualization of different laths and orientations.

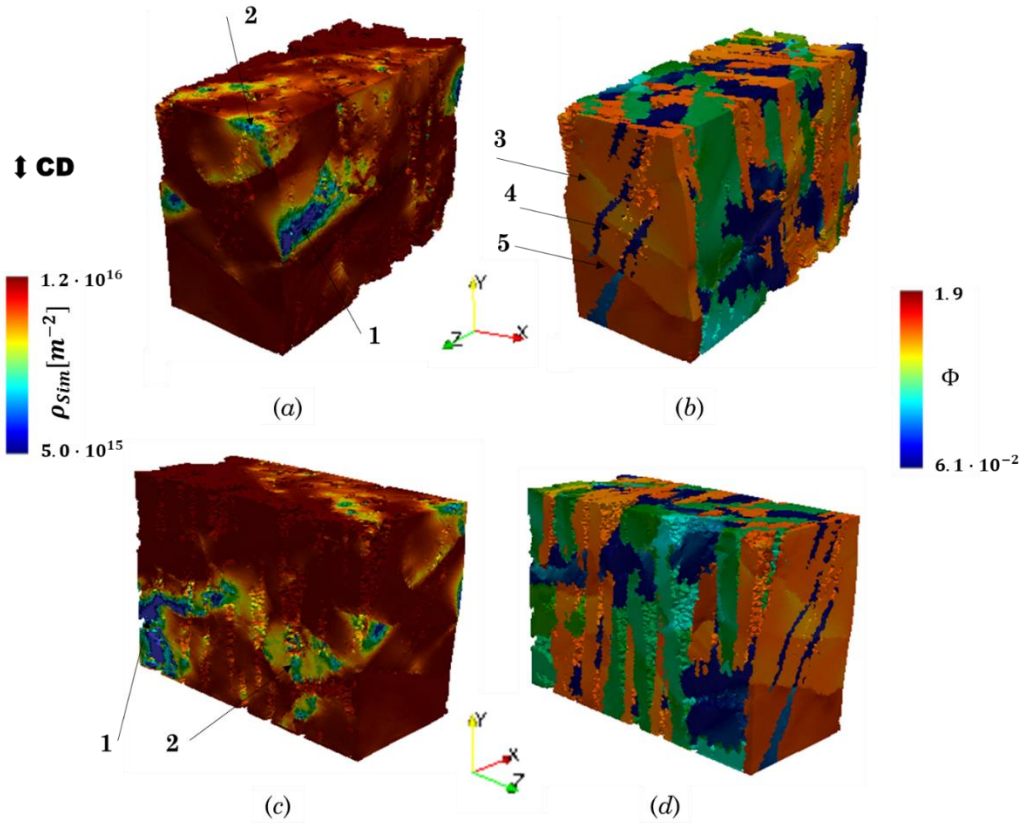



*Figure 6.24. Lamellar α phase inside the RVE showing the: a) and c) Dislocation density map; b) and d) Φ Euler angle color coding (to distinguish laths).*

It seems that the dislocation density evolution in the lamellar $\alpha$ is connected to the intersection of different lamellar orientations. The lower values of $\rho_{sim}$ (blue to green zones, see arrows 1 and 2 in **Figure 6.24***a*) appear mostly in those regions. The highest $\rho_{sim}$ values observed (dark red) are mostly within one lamellar colony. In **Figure 6.24***b*, it is also possible to observe lath kinking, accompanied by an orientation gradient within the lath colony (arrows 3 to 5). This behavior was experimentally shown for the Ti64_FL, where after deformation, lath kinking could be observed (**Figure 4.30**) with an orientation gradient throughout the $\alpha$ laths (**Figure 4.31**).

Once again, the regions presenting lower values of $\rho_{sim}$ (blue to green zones, see arrows 1 and 2 in **Figure 6.24***c*) appear mostly in the intersection of different lath orientations. Especially for orientations n°4 and 5 in **Figure 6.9**.

Regarding the texture evolution throughout deformation of the $\alpha$ grains, it is possible to see that there is a weakening of the initial strong texture, which tends to spread the peaks found for the different lamellar colonies (**Figure 6.25**). Also, for the $\alpha$ laths, more than for the equiaxed grains, the rotation does not come only from plastic activity, but also from a "geometrical" rotation (as shown in Figure 4.56).

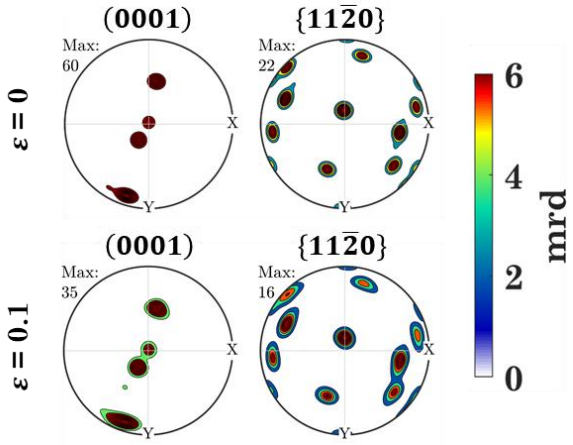



*Figure 6.25. Pole figures of the α laths before and after deformation.*

### *6.4.3 Stress-strain curves*

To study the mechanical response of the RVEs, stress-strain curves were plotted for the five tested cases (**Figure 6.26**).

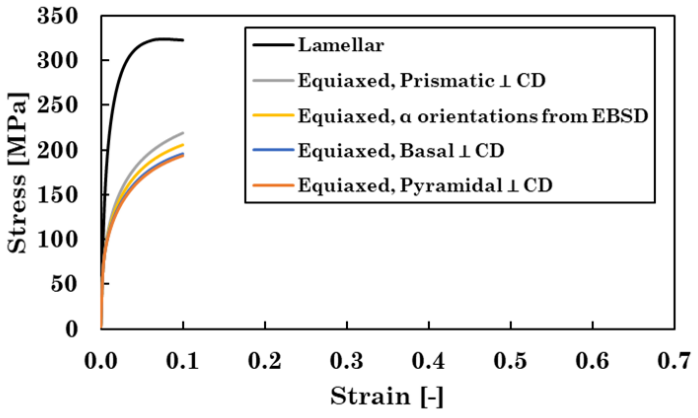



*Figure 6.26. Stress-strain curves for the five different cases analyzed.*

For the equiaxed cases, the prismatic $\langle 1\bar{1}00\rangle \perp$ CD configuration is the one that generated the higher stress levels. This result was expected, as this same configuration produced the lowest dislocation density level for the $\alpha$ phase (see Figure 6.19). Hence, when the $\alpha$ grains are oriented with the prismatic $\langle 1\bar{1}00\rangle \perp$ CD, they are harder to deform. This can be also seen by the $\alpha$ orientation from EBSD data, which had an initial texture similar to the prismatic case (**Figure 6.18**). In the former, the dislocation density value was slightly higher than the prismatic one, but inferior to basal [0001] and pyramidal $\langle 0\bar{1}1\bar{1}\rangle \perp$ CD. This is coherent as the stress has to be much higher to generate dislocations in the prismatic case.

These results strengthen the hypothesis raised in the comparison between the macroscopic and microscopic approaches (section **5.7**) concerning the $\alpha$ phase. It was suggested that the texture development of the $\alpha$ phase (where the basal plane tends to align parallel to the CD, *i.e.,* [0001] $\perp$ CD) is related to a microstructural evolution to a softer configuration. Thus, in the microscopic approach, the dislocation density level ($\rho_{EBSD}$) is increased with the increase in deformation. Contrastingly, in the macroscopic approach, the stress drops with the increase in deformation (as the developed texture is into a softer configuration), so the $\rho_{\sigma}$ decreases.

Interestingly, it seems that the lamellar morphology implied higher stress values (around 1.5 times), when compared to the equiaxed one (**Figure 6.26**), yet is might also be linked to a higher primary $\alpha$ phase fraction in this case, due to the 3D immersion. Also, a sharper peak is observed for the lamellar case. Both behaviors were also observed in the experimental stress-strain curves from Chapter **5** (see **Figure 5.8**). However, to go further in this analysis and compare the stress values obtained in the full field simulations (**Figure 6.26**) with the ones from Chapter **5**, it would be necessary to perform some experimental tests for the Ti64_FL. In Chapter **5**, the stress-strain curves were obtained for the Ti64_CL, which presents thicker laths. According to [25], the lath thickness is inversely proportional to the stress values. Since for the experimental results for the Ti64_CL, the stress curves achieved lower values (**Figure 5.8**) than the ones observed for the simulations for the Ti64_FL (**Figure 6.26**), it seems that the results are coherent.

## 6.5 Summary, Conclusions and Perspectives

After analyzing five different $\alpha$ phase configurations, consistent trends arise from the full field simulations, even if this part of the work still remains preparatory for future analysis and improvements. Regarding the dislocation density ($\rho_{sim}$), it was shown that the $\beta$ phase presented higher levels than the $\alpha$ phase, for all configurations. This behavior seems to be mainly connected to the lower CRSS and $G$ values of the $\beta$ phase, which promotes plastic activity in this phase. Also, similar tendencies were reproduced in the simulations, regarding the dependency of dislocation density evolution on $\alpha$ grain orientation previously observed in Chapter **4**. For example, grains with the normal of the basal planes perpendicular to the compression direction ([0001] $\perp$ CD), presented higher dislocation density levels than the ones with prismatic $\langle 1\bar{1}00 \rangle \perp$ CD. Other configurations can be tested in the future, especially in terms of the $\beta$ phase orientation, while only one was adopted in this analysis, and also in terms of $\alpha/\beta$ orientation relationships.

Regarding the lamellar morphology, the successful immersion of the real lamellar microstructure, from 3D EBSD data, in the full field simulations is already an achievement. Some interesting behaviors were observed from this first initial simulation. The presence of lath kinking and the development of an orientation gradient within a lath throughout deformation is in accordance to what was seen experimentally. Concerning the dislocation density evolution in the $\alpha$ laths, the strongest gradients appeared in the vicinity of lath colonies with different crystallographic orientations. From those orientation gradients, it could be possible to calculate a $\rho_{GND}$, by a similar procedure explained in section **2.7.5**.

In terms of the stress-strain curves, they seem to be consistent with what was seen experimentally in Chapter **5**, where the lamellar microstructure presented a higher and sharper stress peak, compared to the equiaxed cases. The expected inverse relation between the stress levels of the RVE and the dislocation densities obtained in the equiaxed $\alpha$ grains was also observed. Those that presented lower levels of $\rho_{sim}$, were the ones that produced higher stresses. Also, the $\alpha$ grains with prismatic $\langle 1\bar{1}00 \rangle \perp$ CD are harder to deform, when compared to the other orientations, consistent with the Schmid factor analysis and the CRSS values. Interestingly, these results strengthen the hypothesis raised for the dislocation density evolutions in $\alpha$ phase (section **5.7**). Where the comparison of the macroscopic and microscopic approaches for this phase seems to be mainly related to the texture development of the $\alpha$ phase (basal plane alignment parallel to the CD, *i.e.,* [0001] $\perp$ CD).

In terms of perspectives, a change in the parameters shown in **Table 6.2**, coupled with the inverse analysis in the *MOOPI* software, might help the correlation of the experimental and simulations results. Furthermore, the implementation of recrystallization in the current model (section **6.2**) has a crucial impact on this correlation and would allow for considering higher strain levels in the simulation. Nevertheless, as mentioned previously, a model that includes the GNDs should also be implemented to narrow this gap between experimental and simulation results. Noteworthily, the $\rho_{Sim}$ can be seen as a phenomenological estimation of the real dislocation density.

Furthermore, the analysis of the full field simulation results with *MTEX* implemented on this work was successful, allowing the plot of pole figures from simulation results. With the implementation of recrystallization in the model, it might allow a satisfactory prediction of the texture development of titanium alloys. Also, to analyze local phenomena, an interphase model should be implemented, including the diffusion of chemical elements through the interphase boundaries. The simulation of the dissolution of the α phase during heating should also be implemented, as the 3D data are acquired at room temperature, it is highly possible that the $\alpha$ laths are less thick or long at high temperatures. Furthermore, there is also the spatial resolution aspect, where the very thin $\beta$-layer between α laths is not indexed.

Finally, the immersion of real 3D microstructures is still currently a laborious task, thus the immersion process could be improved by an automated tool from the acquired 3D EBSD data.

## 6.6 Résumé en Français

Après avoir analysé cinq configurations de phase $\alpha$ différentes, des tendances cohérentes ressortent des simulations en champ complet, même si cette partie du travail reste encore préparatoire à de futures analyses et améliorations. Concernant la densité de dislocations ($\rho_{sim}$), il a été montré que la phase $\beta$ présentait des niveaux plus élevés que la phase $\alpha$, pour toutes les configurations. Ce comportement semble être principalement lié aux valeurs CRSS et $G$ plus faibles de la phase $\beta$, ce qui favorise l'activité plastique dans cette phase. De plus, des tendances similaires ont été reproduites dans les simulations, concernant la dépendance de l'évolution de la densité de dislocations sur l'orientation des grains $\alpha$ précédemment observée au Chapitre **4**. Par exemple, les grains avec la normale des plans basaux perpendiculaire à la direction de compression ([0001] ⊥ DC), présentaient des niveaux de densité de dislocations plus élevés que ceux avec prismatique $\langle 1\bar{1}00\rangle$ ⊥ DC. D'autres configurations pourront être testées dans le futur, notamment en termes d'orientation de phase $\beta$, alors qu'une seule a été retenue dans cette analyse, et également en termes de relations d'orientation $\alpha/\beta$.

Concernant la morphologie lamellaire, l'immersion réussie de la microstructure lamellaire réelle, à partir de données EBSD 3D, dans les simulations plein champ est déjà une tâche laborieuse. Des comportements intéressants ont été observés dès cette première simulation initiale. La présence de flambement des lamelles et le développement d'un gradient d'orientation à l'intérieur d'une lamelle tout au long de la déformation est conforme à ce qui a été observé expérimentalement. Concernant l'évolution de la densité de dislocations dans les lamelles $\alpha$, les gradients les plus forts apparaissent au voisinage des colonies de lamelles avec des orientations cristallographiques différentes. A partir de ces gradients d'orientation, il pourrait être possible de calculer un $\rho_{GND}$, par une procédure similaire expliquée dans la section **2.7.5**.

En termes de courbes contrainte-déformation, les simulations sont faites jusqu'à une déformation inférieure au seuil de recristallisation. Dans tous les cas, elles semblent être cohérentes avec ce qui a été vu expérimentalement au Chapitre **5**, où la microstructure lamellaire présentait un pic de contrainte plus élevé et plus net, par rapport aux cas équiaxes. La relation inverse attendue entre les niveaux de contrainte du VER (volume élémentaire représentatif) et les densités de dislocations obtenues dans les grains $\alpha$ équiaxes a également été observée. Ceux qui présentaient des niveaux inférieurs de $\rho_{sim}$ étaient ceux qui produisaient des contraintes plus élevées. De plus, les grains $\alpha$ avec $\langle 1\bar{1}00\rangle$ (prismatique) ⊥ DC sont plus difficiles à déformer, par rapport aux autres orientations, conformément à l'analyse du facteur de Schmid et aux valeurs de CRSS. De manière intéressante, ces résultats renforcent l'hypothèse émise pour les évolutions de la densité de dislocations en phase $\alpha$ (section **5.7**). Là où la comparaison des approches macroscopiques et microscopiques pour cette phase semble être principalement liée au développement de la texture de la phase $\alpha$ (alignement de la normale du plan basal perpendiculaire à la DC, c'est-à-dire [0001] ⊥ DC)

En termes de perspectives, une modification des paramètres présentés dans le tableau **6.2**, couplée à l'analyse inverse dans le logiciel *MOOPI*, pourrait aider à la corrélation des résultats expérimentaux et des simulations. De plus, la mise en œuvre de la recristallisation dans le modèle actuel (section **6.2**) a un impact crucial

sur cette corrélation et permettrait de considérer des niveaux de déformation plus élevés dans la simulation. Néanmoins, comme mentionné précédemment, un modèle qui inclut les GND devrait également être mis en œuvre pour réduire cet écart entre les résultats expérimentaux et de simulation. Il convient de noter que la $\rho_{Sim}$ peut être vue comme une estimation phénoménologique de la densité réelle de dislocations.

De plus, l'analyse des résultats de simulation en champ complet avec *MTEX* mise en œuvre sur ce travail a été une réussite, permettant le tracé des figures de pôles à partir des résultats de simulation. Avec la mise en œuvre de la recristallisation dans le modèle, cela pourrait permettre une prédiction satisfaisante du développement de la texture des alliages de titane. Aussi, pour analyser les phénomènes locaux, un modèle d'interphase doit être implémenté, incluant la diffusion des éléments chimiques à travers les frontières d'interphase. La simulation de la dissolution de la phase $\alpha$ lors du chauffage doit également être mise en œuvre, les données 3D étant acquises à température ambiante, il est fort possible que les lamelles $\alpha$ soient moins épaisses ou longues à haute température. De plus, il y a aussi l'aspect de la résolution spatiale, où la très fine couche $\beta$ entre les lamelles $\alpha$ n'est pas indexée.

Enfin, l'immersion de microstructures 3D réelles est encore actuellement une tâche laborieuse, ainsi le processus d'immersion pourrait être amélioré par un outil automatisé à partir des données EBSD 3D acquises.

# 7. GENERAL CONCLUSIONS AND PERSPECTIVES

## 7.1 Conclusions, perspectives and synthesis

The thesis work that has been presented throughout this manuscript focuses on the description of microstructure evolution during hot deformation in the two-phase domain of the Ti64 and Ti1023 alloys, according to the thermomechanical parameters and initial microstructure.

The assessment of dislocation density distribution, amongst the different phases ($\alpha$ and $\beta$), is of utmost importance to unravel the complex metallurgical mechanisms and kinetics which ultimately control de microstructure and properties of forged components. It is important to remind that the definition of dislocation density as it is presented in metallurgy books (defined as the total length of dislocation line per unit volume of crystal [23]) is a physical concept. Noteworthily, none of the presented methods in this work provide access to the real dislocation density. In fact, all the existing approaches only allow to obtain partial or imprecise estimates of the dislocation density distributions, not being a direct measurement of these linear crystalline defects.

In this work, three distinct and complementary approaches are implemented to address microstructure and dislocation density evolution in two-phase titanium alloys: experimental at the microscopic and at the macroscopic scale, as well as by numerical simulation. The main results are described in the sections below (from **7.1.1** to **7.1.4**).

### *7.1.1 Methodology and characterization of microstructures*

The development of experimental methods and data processing, adapted to the complexity of the underlying physical phenomena, was performed and presented in Chapter **2**. It allowed to characterize (by OM, SEM and EBSD) the initial microstructures (*i.e.,* just before deformation) for each of the two alloys studied (Ti64 and Ti1023), varying the morphology of the phases (globular and lamellar) and the characteristic sizes of each type of grain.

Some analysis available in the *MTEX* toolbox were directly applied, yet most importantly, new ones were developed and adapted for the different microstructures and deformation states (Chapter **3**). Those new analyses are mainly focused on the study of LAGBs and HAGBs density, also studying the intragranular misorientation dependency on grain orientation. All the *MTEX* codes were made available to the other PhD students in the industrial consortium.

Furthermore, the methodology of 3D characterizations of titanium alloys by FIB-SEM was established after some initial tests, opening the possibility of future works focused on this technique. Also, the optimization of the geometry of double-cone samples was performed. This same geometry will be useful for further works on many different alloys, as its versality was proved in [4].

### *7.1.2 Microscopic approach: Microstructural evolution during hot deformation*

Regarding the microscopic approach (Chapter **4**), a detailed evaluation was performed (for both phases) of different microstructure evolution features, for a vast range of initial microstructures (different alloys, globular *vs* lamellar

morphologies, characteristic $\alpha$ and $\beta$ grain sizes) submitted to different thermomechanical conditions. Interestingly, even though all these different conditions studied, an intrinsic behavior of the $\alpha$ phase evolution was observed at high strain levels ($\varepsilon$ =1.3). In basically all microstructures analyzed after $\varepsilon$ =1.3 (independently of the temperature or strain rate and of the globular *vs* lamellar initial morphology), the basal planes of the $\alpha$ phase tended to align ∥ CD. This crystallographic alignment was also accompanied by a morphological one, where some of the initially equiaxed $\alpha$ grains were also elongated ⊥ CD. It was seen that those specific grains possess a very strong texture, where the basal plane $(0001)_\alpha$ and the $\langle 11\bar{2}0\rangle_\alpha$ directions tend to align ∥ CD. This same texture was developed in the whole analyzed zones, it appears then that the developed crystallographic orientation, is accompanied by a higher deformation of the $\alpha$ grains. The LAGB density analysis, according to the grain orientation, reinforced this hypothesis, where it was also shown that those exact same grains with $(0001)_\alpha$ and $\langle 11\bar{2}0\rangle_\alpha$ ∥ CD, are the ones with higher substructure formation.

Concerning the lamellar $\alpha$ phase, besides this underlying behavior explained above, lath kinking and breakage was observed. On the other hand, very few dynamic globularization was seen which is consistent with literature, globularization being a process that requires long-term annealing. However, it appears that it is easier to dynamically globularize the fine $\alpha$ laths, also in agreement with literature, while the coarser ones tended to be kinked. For both alloys, the lamellar $\alpha$ phase at the grain boundaries ($\alpha_{GB}$) was the one which presented more substructure formation. On the other hand, the lath colonies were basically kinked, those behaviors being confirmed by 3D characterizations of the Ti64 alloy.

This intrinsic behavior of the $\alpha$ phase seems to be independent of the $\beta$-grain orientation, as same trends were observed in the texture evolution of the $\alpha$ phase inside different $\beta$-grain orientations. Concerning the $\beta$ phase, also at high strain levels ($\varepsilon$ = 1.3), the development of $\langle 001\rangle$ ∥ CD and $\langle \bar{1}11\rangle$ ∥ CD texture components were always observed for the different Ti1023 microstructures. Depending on the initial level of elongation of $\beta$ grains, homogeneous or heterogeneous dynamic recrystallization was observed. The latter behavior was seen in the Ti1023_El$\beta$ microstructure (with highly elongated $\beta$), where the $\beta$ grains that were oriented with the $\langle 110\rangle$ ∥ CD, were the ones that presented more advanced continuous dynamic recrystallization.

A Burgers orientation relationship (BOR) analysis was also performed in this thesis. It was shown that the applied strain level has a very strong impact on the fraction of $\alpha/\beta$ boundaries respecting the BOR ($f_{GB_{\alpha/\beta}}^{BOR}$), stronger than the temperature and strain rate influence. Even if the lamellar $\alpha$ microstructure initially presented a much higher $f_{GB_{\alpha/\beta}}^{BOR}$, after low strain levels ($\varepsilon$ = 0.3), they reached similar $f_{GB_{\alpha/\beta}}^{BOR}$ values compared to the equiaxed $\alpha$ microstructures. Noteworthily, this fast reduction might also be related to the higher distortion on the local orientation at high strains.

The effect of the initial microstructure and thermomechanical parameters on the microstructural evolution was also addressed. The influence of those parameters on the LAGB and HAGB density ($\rho_{GB}$) was evidenced in both alloys.

For the lamellar $\alpha$ Ti1023 microstructure, for example, it was shown that the reduction in temperature (from 750°$C$ to 700°$C$) had a very strong impact in the $\alpha$ phase, yet hardly any in the $\beta$ phase substructuring. Contrastingly, in an equiaxed $\alpha$ microstructure, the changes in temperature and strain rate mainly affect the $\beta$ phase evolution. Concerning the Ti64 microstructures, increasing strain level and strain rate did not affect much the substructure formation in the $\alpha$ phase. However, after some higher-resolution EBSD analysis, it appears that the HAGB formation on the Ti64 alloys occurs by the formation of very small recrystallized grains (~ 1 $\mu m$). Consequently, in order to draw further conclusions, other high-resolution analysis should be performed.

The GND density ($\rho_{EBSD}$) was estimated for all studied cases, in terms of initial microstructure and thermomechanical conditions. It is worth reminding the comparison of the estimated $\rho_{EBSD}$ values needs to be accompanied by the LAGB and HAGB kinetics. The method is indeed connected to the threshold applied for its calculation. The $\alpha$ phase developed higher LAGB density, compared to the HAGBs that appear inside the $\alpha$ grains, consequently the $\rho_{EBSD}^{\alpha}$ increased with increasing strain. This observation was reinforced by the texture development, that accompanied a higher substructure development in the $\alpha$ grains. On the other hand, the $\beta$ phase showed increasing higher recrystallization rate, with new HAGBs continuously being formed inside $\beta$ grains with strain. As the HAGBs are ignored in the $\rho_{EBSD}^{\beta}$ calculation, there is a tendency to decrease its value in the $\beta$ phase with increasing deformation.

### *7.1.3 Macroscopic approach: Rheological analysis based on compression tests*

A macroscopic approach (Chapter **5**) was implemented based on stress-strain curves and a rule of mixtures (ROM), which were exploited to assess the macroscopic flow stress of each phase. An estimation, using the Taylor model, of the dislocation density distribution in both phases was also performed.

For four selected microstructures (two alloys with globular or lamellar topology), the individual flow stress values of the $\alpha$ phase ($\sigma_{\alpha}$) were higher than the $\beta$ phase ones ($\sigma_{\beta}$). Interestingly, even if the strong hypothesis of a homogenous deformation was applied, the estimated shapes of both $\alpha$ and $\beta$ curves are consistent with other works. The stress-strain curves of titanium alloys tend to present a stronger flow softening at lower temperatures, which tends to disappear above the $\beta$-transus, where the curves have a very flat/steady character.

This behavior was estimated in this work by the stress-strain curves for both phases, as also confirmed experimentally for the $\beta$ phase, thanks to additional deformation experiments in the $\beta$ domain. The sharp peaks observed in the estimated curves also appeared in the $\beta$ phase stress-strain curves. Nevertheless, this phenomenon requires further deformation experiments and related microstructural characterization, in the $\beta$ domain to be explained. Furthermore, the absence of flow softening in the $\beta$ domain seems to agree with the hypothesis that this softening behavior observed in the stress-strain curves is mainly related to the texture development of the $\alpha$ phase to softer configurations (*i.e.,* easier to be deformed).

To improve this estimation of flow stress from a ROM and properly identify a constitutive behavior law, more deformation conditions (temperature and strain rate) should be applied. Nevertheless, it is important to remind that the applied ROM is most likely not valid. Hence, different coefficients in the ROM should be added, also accounting for the different microstructures, as it was seen that the experimental stress-strain curves are highly dependent on the morphology of the microstructure.

Furthermore, the $\sigma_\alpha$ and $\sigma_\beta$ values were used to estimate the dislocation density evolution in each phase ($\rho_\sigma^\varphi$). It was then compared to the one estimated by the microscopic one ($\rho_{EBSD}^\varphi$). The main objective was to identify trends in each approach, to compare them and in the end to explain the exhibited differences. The dislocation density levels obtained from the macroscopic flow stress ($\rho_\sigma$) were higher for all analyzed cases, which is a consistent result. Indeed, this approach considers both GNDs and SSDs, while the dislocation densities estimated from EBSD data concern only the GNDs. However, the given ratios between $\rho_\sigma^\alpha$ and $\rho_\sigma^\beta$ are most probably inaccurate, since the stresses are not very precise.

More importantly, different trends in the dislocation density evolution were observed in this comparison. For the α phase, the $\rho_{EBSD}^\alpha$ values increased with increasing strain level, while $\rho_\sigma^\alpha$ decreased. It is worth mentioning that the model used to compute $\rho_\sigma^\varphi$ does not allow to capture the effect of texture development, yet this divergence seems to be related to microstructural changes in the $\alpha$ phase. Being most likely due to the crystallographic texture development, which favors the basal plane ∥ CD and is accompanied by a higher LAGB formation (as seen in Chapter **4**). For the $\beta$ phase, the $\rho_{EBSD}^\beta$ values decreased at a very high strain level ($\varepsilon$ = 1.3), while $\rho_\sigma^\beta$ remained steady or slightly increased with increasing strain level. This contrast appears to be related to the continuous dynamic recrystallization, as HAGBs formed intergranularly are not considered in the microscopic approach. However, those boundaries serve as barriers for the dislocation density movement in the material.

Finally, the comparison of those two approaches showed that the method implemented can influence not only the dislocation density level yet also its evolution trend. Some suggestions were provided to narrow the gap between this comparison for each phase. Nevertheless, the comparison of those methods is still intricate and must be done with much care.

### *7.1.4 Full field simulation of the deformation of two-phase microstructures*

Full field simulations were implemented to help in the description of the dislocation density and eventually texture development of $\alpha$ and $\beta$ phases. The aim of these simulations is to verify whether the tendencies observed experimentally (Chapters **4** and **5**) are reproduced by the simulations. In this manner, meshes conforming to the measured phase topologies of the Ti64 alloy were generated (synthetically or by immersing real microstructures obtained from 3D EBSD data). Representative volume elements (RVE) according to the real microstructures

(morphologies and orientations) were also studied in an intergranular ß grain scale at $\varepsilon = 0.1$.

After the analysis of five different $\alpha$ phase configurations, it was shown that the $\beta$ phase presented higher levels of dislocation density ($\rho_{Sim}$) than the $\alpha$ phase. This behavior differs from what was observed experimentally. It seems to be mainly connected to the lower critical resolved shear stress and shear modulus of the $\beta$ phase implemented in the model, which promotes slip on this phase. Also, it seems that the dynamic recovery is underestimated in the current model. On the other hand, similar behavior on the $\alpha$ grains and their dislocation density evolution (previously observed in Chapter **4**) were reproduced in the simulations. For example, $\alpha$ grains with basal planes ∥ CD, presented higher dislocation density levels than the ones with prismatic planes ∥ CD.

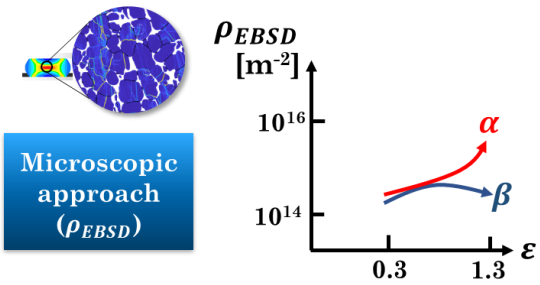
Regarding the lamellar morphology, a successful immersion was performed, from 3D EBSD data, for a real lamellar microstructure (Ti64 alloy). The presence of lath kinking and the development of orientation gradients inside $\alpha$ laths throughout deformation is in accordance with the experimental behavior.

The exploited stress-strain curves seem to be coherent with what was seen experimentally in Chapter **5**. For example, the lamellar microstructure presented a higher stress values, compared to the equiaxed cases. Also, as expected, the RVEs that presented higher levels of $\rho_{Sim}$ were the ones that presented a softer behavior (easier to deform). These results strengthen the hypothesis raised regarding the comparison of the macroscopic and microscopic approaches for the $\alpha$ phase. It indeed seems to be mainly related to the crystallographic and morphological textures development of this phase (*i.e.,* basal plane alignment parallel to the CD and more elongated grains). This seems to be caused by a microstructural evolution towards a softer configuration, the $\rho_{EBSD}$ is increased with the strain level increase. Meanwhile, the $\rho_{\sigma}$ decreases, as the stress drops (easier to deformed). The reason for this will be reminded in section **7.1.5**.

As mentioned previously, this full field simulations approach still remains preparatory for future analysis and improvements. In terms of perspectives, the implementation of recrystallization in the current model has a crucial impact on the correlation between experiments and simulations. The analysis of the full field simulations results with *MTEX* implemented in this work was successful, allowing to plot pole figures from simulation results. Consequently, with the implementation of the recrystallization in the model, it might allow simulations up to higher strain levels and prediction of the texture development of titanium alloys. Furthermore, the boundary conditions implemented in this work were not representative of the real deformed microstructure at the microscopic scale, which most probably had an impact on the results. The most accurate way of obtaining representative boundary conditions would be to measure them from experimental data. However, his approach is costly and is not suitable to the destructive 3D imaging capabilities of CEMEF.

### 7.1.5 *Summary of the comparison between the three different approaches and final considerations*

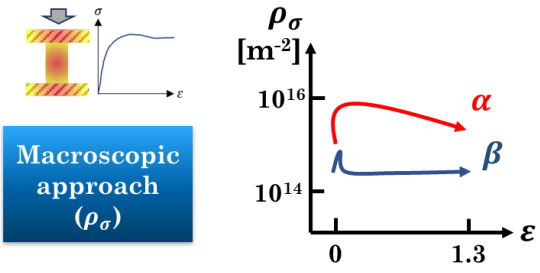
For each of the phases, key microstructural elements, mainly in terms of texture development ($\alpha$ phase) and dynamic recrystallization ($\beta$ phase), are given. The aim is to better correlate these approaches to have a better estimation of the dislocation density, thus microstructural evolution.




**Dislocation density values estimated from intragranular misorientations (< HAGB threshold)**

**$\alpha$ : Increase related to the developed crystallographic texture : (0001) and $\langle 11\bar{2}0\rangle \parallel$ CD → configuration accompanied by higher LAGB density inside those grains.**

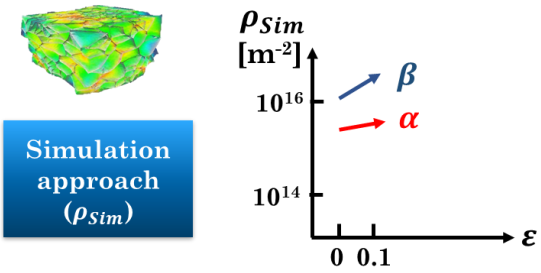
**$\beta$ : Decrease related to the dynamic recrystallization → HAGB not accounted in the model + lower LAGB density inside the new grains.**




**Dislocation density values estimated using the Taylor relationship ($\sigma_\varphi = \sigma_0 + \psi M_\varphi G_\varphi b_\varphi \sqrt{\rho_\sigma^\varphi}$)**

**$\alpha$ : Decrease also related to the developed crystallographic texture (which is not accounted for in the model) : (0001) and $\langle 11\bar{2}0\rangle \parallel$ CD → softer configuration, those grains are easier to be deformed (flow softening).**

**β : Sharp and short peak, followed by a steady behavior due to continuous dynamic recrystallization.**




**Dislocation density values estimated using full field simulations based on Crystal Plasticity modeling**

**$\alpha$ : Increasing behavior, also related to grains with (0001) and $\langle 11\bar{2}0\rangle \parallel$ CD, compared to when the prismatic plane $\parallel$ CD → the former being a softer configuration, thus lower stress values.**

**$\beta$ : Increasing behavior and higher values compared to the $\alpha$ phase, probably related to lower *CRSS* and *G* values. Also, the applied boundary conditions are not representative of the real local deformation state of the material, which might have induced a spurious increase of the dislocation density.**

*Figure 7.1. Summary of the comparison between the three different approaches ($\rho_{EBSD}, \rho_\sigma, \rho_{Sim}$), evidencing the key tendencies in the microstructural aspects that were observed in this work and the reasons for the apparent discrepancies in the dislocation densities estimated through each approach.*

To conclude, the results of this thesis along with the discussion conducted, notably compare the three different approaches (**Figure 7.1**) and show that any direct comparison should be avoided. In fact, the definition of dislocation density from the perspective of crystallography is very precise and it is something one could physically measure (in theory). However, the methods used in the work only allow to indirectly estimate the effect of dislocations, either by analyzing measured intragranular misorientations ($\rho_{EBSD}$), macroscopic hardening ($\rho_{\sigma}$) or slip hardening ($\rho_{Sim}$). Therefore, the use of the term *dislocation density* might be misleading, since the quantities do not directly correspond to estimations of this physical quantity. Noteworthily, $\rho_{EBSD}$ is a lower bound (underestimation) of the real dislocation density, while $\rho_{\sigma}$ and $\rho_{Sim}$ are, at best, phenomenological quantities linked to the real value.

This thesis was the first from a multi-year work program (2019-2025) comprising a total of six PhD theses. Several elements and tools were provided here for a better understanding of the behavior of titanium alloys during hot deformation in the two-phase domain, and of the influence of thermomechanical parameters (temperature, strain level and rate) and initial microstructure. The different aspects analyzed in this work, and in the ongoing and future theses of the CONTiNUUM consortium, will provide indications to the industrial financial partners (*Airbus*, *Aubert & Duval*, *Safran* and *Timet*) to help optimizing their forging routes. With this aim, to start connecting this thesis and the others, some preliminary experiments were already performed, aiming at being further studied in the other PhD works, and presented in section **7.2**.

## 7.2 Preliminary experiments addressing perspectives of this work related to the industrial process

As mentioned in the general introduction, this work aims to describe the evolutions of microstructure during the stages of hot deformation. It was shown in **Figure 1.26** that different thermomechanical processing steps are involved in the industrial process, several of these steps being studied in detail in the PhD works of the consortium (*e.g.*, cooling, holding, *etc.*). In the present work, focused on hot deformation, the samples have been quenched immediately after deformation, but the actual microstructures of (slow cooled) industrial pieces undergo post-dynamic evolutions that must be considered as well. Also, industrial process usually involves multi-pass deformation, contrary to the monotonic deformation experiments performed here. The influence of the cooling rate and the thermomechanical path in microstructure evolutions are evaluated, respectively, in sections **7.2.1** and **7.2.2**, through few additional experiments.

### *7.2.1 Tests followed by slow cooling*

In fact, industrial billets have much larger sections (~ 200 $mm$ diameter) than the laboratory samples (~ 10 $mm$), thus cannot be water quenched at the same rate. Hence, slower cooling rates must be *studied* to acknowledge the industrial case. A slow cooling (~ $5°C/min$, representative of the actual cooling rate achieved in a real scale billet) was performed for each of the four selected microstructures selected in Chapter **5** (Ti64_Eq, Ti64_CL, Ti1023_Eq, Ti1023_L), to allow comparison of microstructures right after deformation (*i.e.,* water quenched) and after slow cooling, to evaluate post-dynamic evolutions. A similar thermomechanical path to the one shown in (**Figure 5.2**) was used, where the only difference was the slower cooling rate at ~ $5°C/min$ (**Figure 7.2**), compared to ~ $75°C/s$ previously applied (*i.e.,* by water quenching).

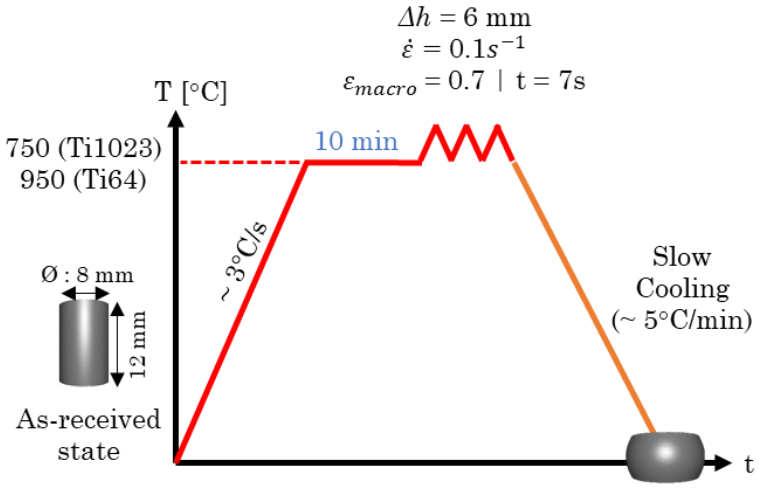



*Figure 7.2. Thermomechanical path of the slow cooling tests.*

The results of the slow cooling rate for each of the Ti64 and Ti1023 microstructures are shown and compared to those obtained after water quenching in **Figure 7.3** and **Figure 7.4**, respectively, through BSE images taken at the center of the cylindrical sample.

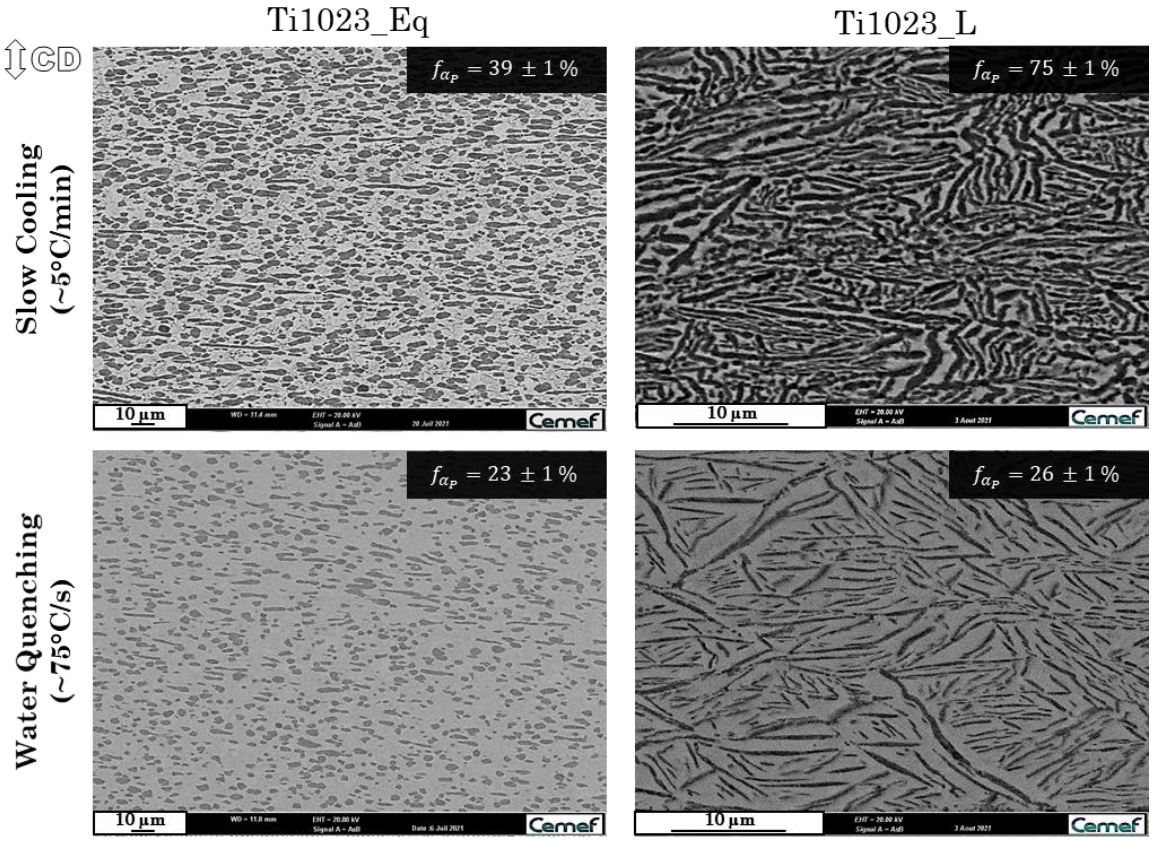



*Figure 7.3. BSE images for the comparison deformed Ti1023 microstructures which have been either water quenched (about 75°C/s) or slow cooled (at 5°C/min).*

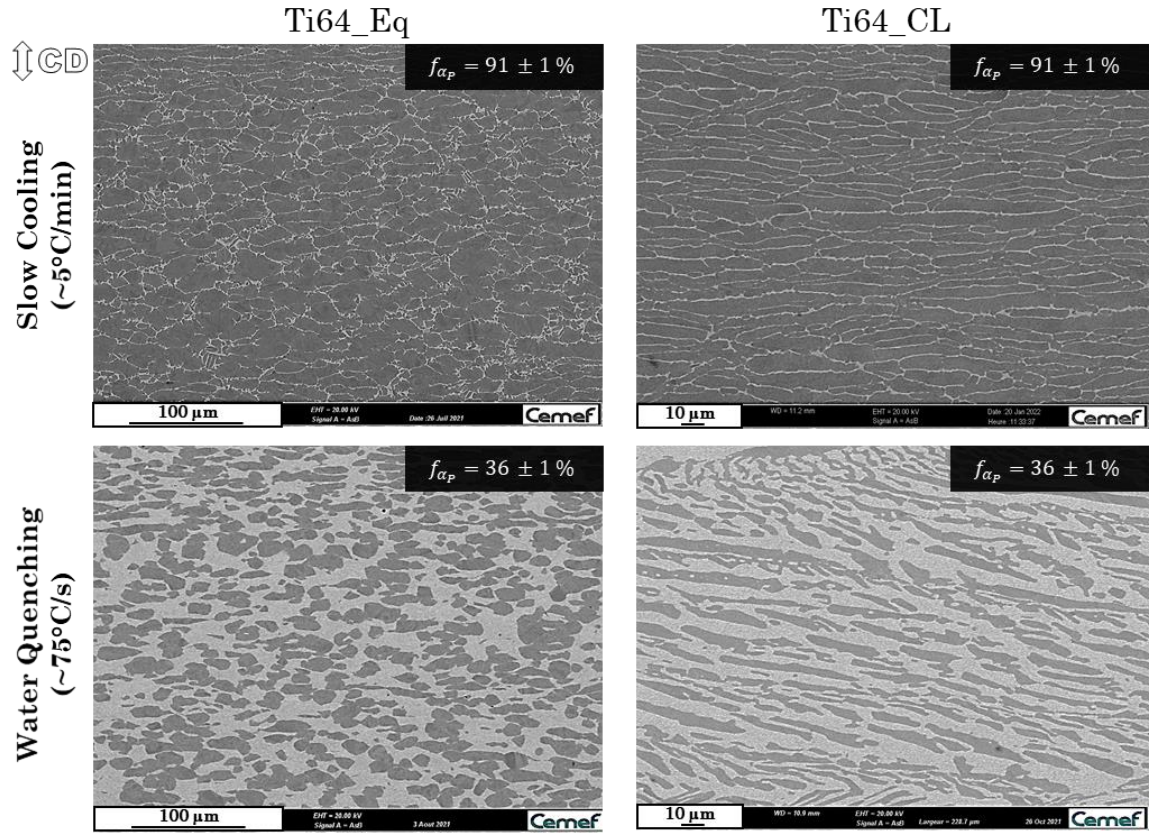



*Figure 7.4. BSE images for the comparison deformed Ti64 microstructures which have been either water quenched (about 75°C/s) or slow cooled (at 5°C/min).*

After slow cooling, the primary $\alpha$ phase fractions of all microstructures achieved the as-received values (**Table 3.2**). This suggests that the slow cooling rate applied is comparable to the industrial process.

In terms of GND density evolution due to slow cooling, different behaviors were observed for the $\alpha$ and $\beta$ phases. An example of the dislocation density maps is shown in **Figure 7.5** for the Ti1023_Eq.

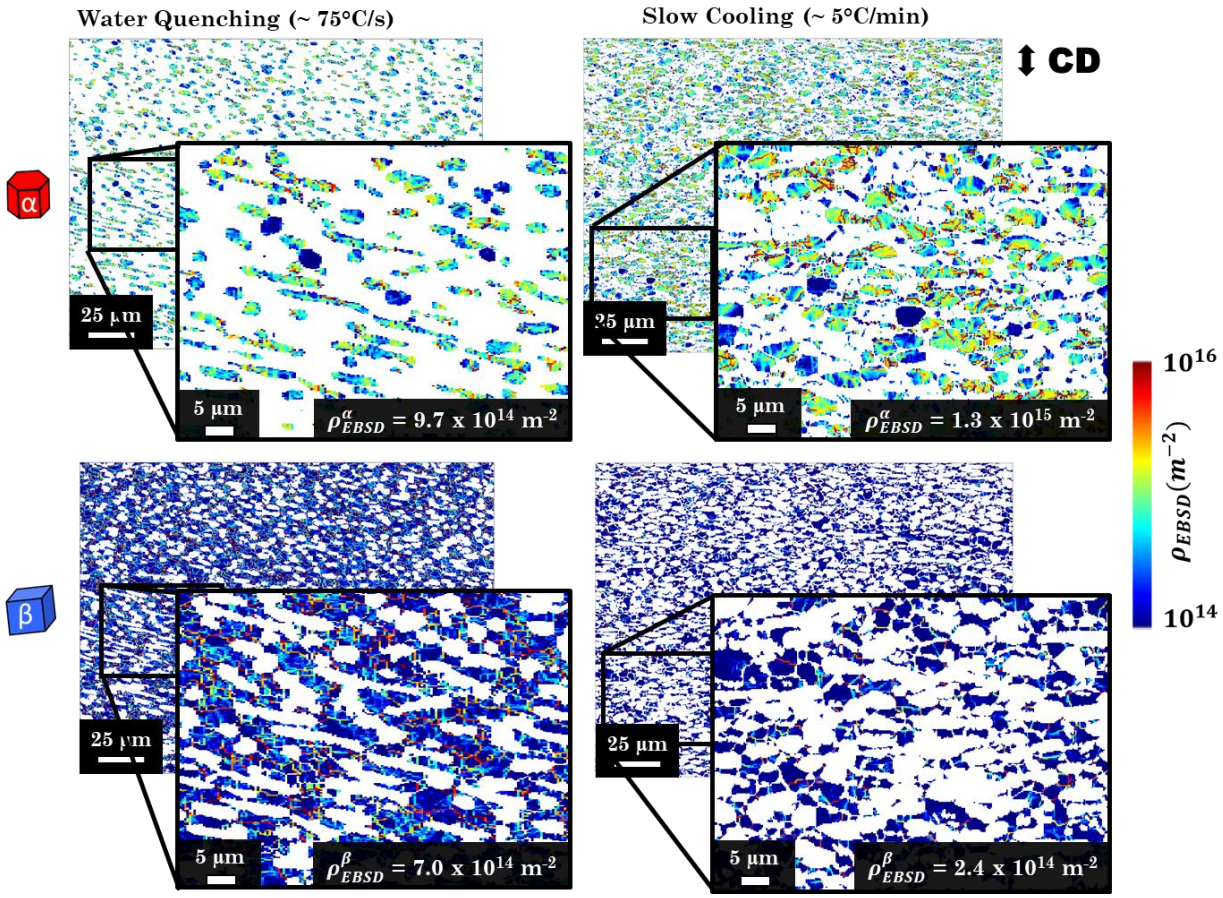



*Figure 7.5. GND density maps of the Ti1023_Eq at 1.3 strain level, deformed at 0.1 s$^{-1}$ and 750°C, and water quenched or slow cooled.*

The average GND density ($\rho_{EBSD}$) in the $\alpha$ phase of the Ti1023_Eq is basically unchanged by the slow cooling (**Figure 7.5**), the slight increase observed in the $\rho^{\alpha}_{EBSD}$ values being most likely due to statistical fluctuation, as the analyzed areas are rather small. Contrastingly, for the $\beta$ phase, there is a more significant decrease in the $\rho^{\beta}_{EBSD}$ value after slow cooling, which might be connected to more time for recovery (rearrangement and annihilation of dislocations) but also to the $\beta$ phase, being consumed by the growth of the primary $\alpha$ grains as temperature decreases. This is evidenced by less substructures in the $\beta$ grains after the slow cooling. Concerning the Ti64 microstructures, only the $\alpha$ phase can be analyzed. For the Ti64_Eq, the $\rho^{\alpha}_{EBSD}$ remains basically unchanged after slow cooling, with a minor decrease in its value (**Figure 7.6**), which again cannot be considered to be representative with such limited analyzed areas.

Interestingly enough to be mentioned, most of the grown primary $\alpha$ grains, in both alloys, have significant levels of $\rho_{EBSD}$ and substructures. Only few of them have very low $\rho_{EBSD}$ , which could be expected for grains which have developed

while the material was no longer being deformed. The mechanisms behind this observation could deserve being studied.

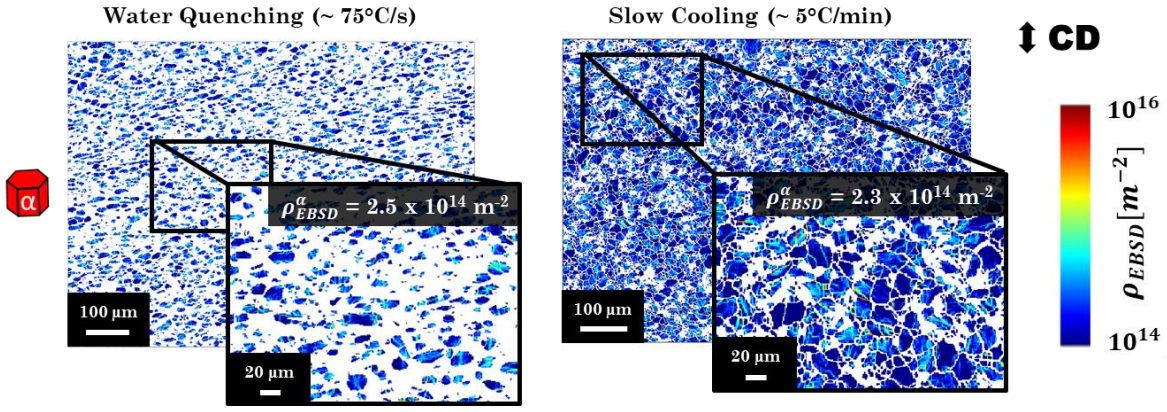



*Figure 7.6. GND density maps of the Ti64_Eq at 1.3 strain level, deformed at 0.1s$^{-1}$ and 950°C, and water quenched or slow cooled.*

**Figure 7.7** summarizes, for the four different microstructures, the influence of the cooling rate on the average GND density. For the Ti1023_L (**Figure 7.7***a*), similar behavior to the one of Ti1023_Eq is observed for both phases. On the other hand, for the Ti64_CL, the $\rho^{\alpha}_{EBSD}$ reduced, probably related to the lath growth.

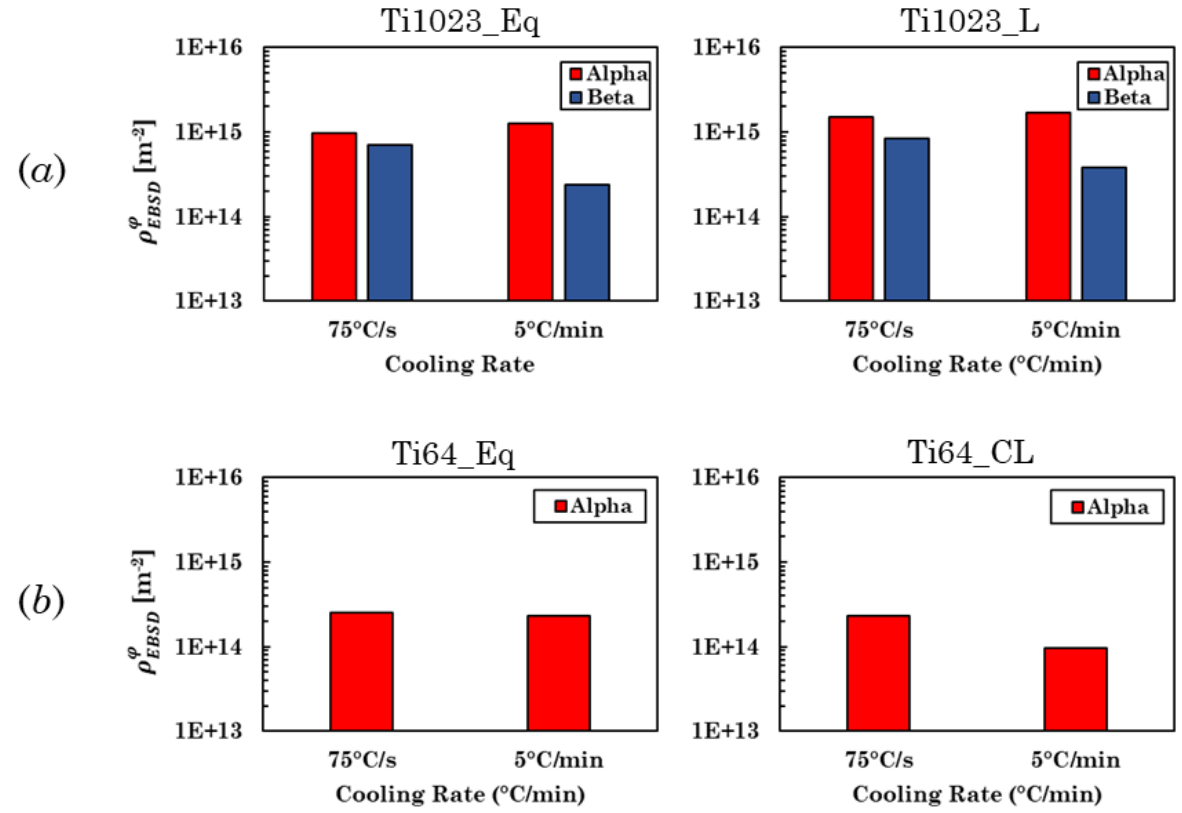



*Figure 7.7. Summary of the influence of the cooling rate on the average dislocation density in the four microstructures.*

Through the cumulative analysis of the LAGB and HAGB density, previously presented (section **2.7.3**), it is possible to evaluate if the reduction in $\rho_{EBSD}$ is

connected to the change of LAGB into HAGB or to a global reduction in $\rho_{GB}$. **Figure 7.8** shows this analysis for the $\alpha$ and $\beta$ phases in the Ti1023 microstructures.

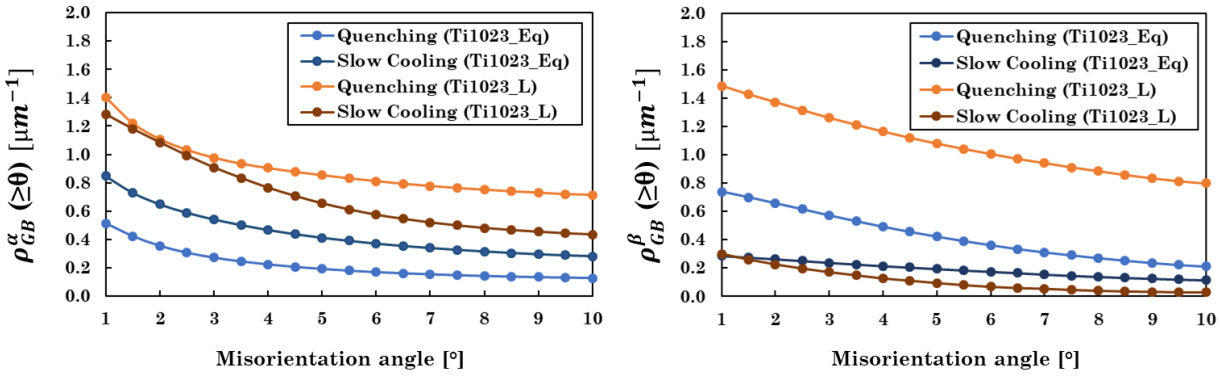



*Figure 7.8. Cumulative analysis of the LAGB and HAGB density, as a function of the misorientation angle, in the: a) α phase; b) β phase of Ti1023 microstructures.*

For the $\alpha$ phase (**Figure 7.8***a*), the total $\rho_{GB}$ in the Ti1023_L is similar at the two cooling rates. Although, the HAGB density is lower at slower cooling. This could be related to the increase in primary $\alpha$ phase fraction, which lowers the amount of HAGB per area. Interestingly, for the Ti1023_Eq, the $\rho^{\alpha}_{GB}$ is globally increased. Thus, it seems that a slower cooling rate for $\alpha$ equiaxed grains tends to promote the substructure formation.

Concerning the $\beta$ phase (**Figure 7.8***b*), for both morphologies, the total $\rho_{GB}$ is reduced, especially for the Ti1023_L. This can be related to the fact that the change in primary $\alpha$ phase fraction for the lamellar microstructure was more important (from 26% to 75% after slow cooling).

Regarding the reduction in the $\rho_{EBSD}$ of the $\alpha$ phase in the Ti64_CL, **Figure 7.9** shows its dislocation density maps after water quenching or slow cooling. It appears that the reduction in the $\rho_{EBSD}$ of the $\alpha$ phase is connected to some grains (especially those that have grown during cooling) with very low dislocation densities (fully dark blue grains).

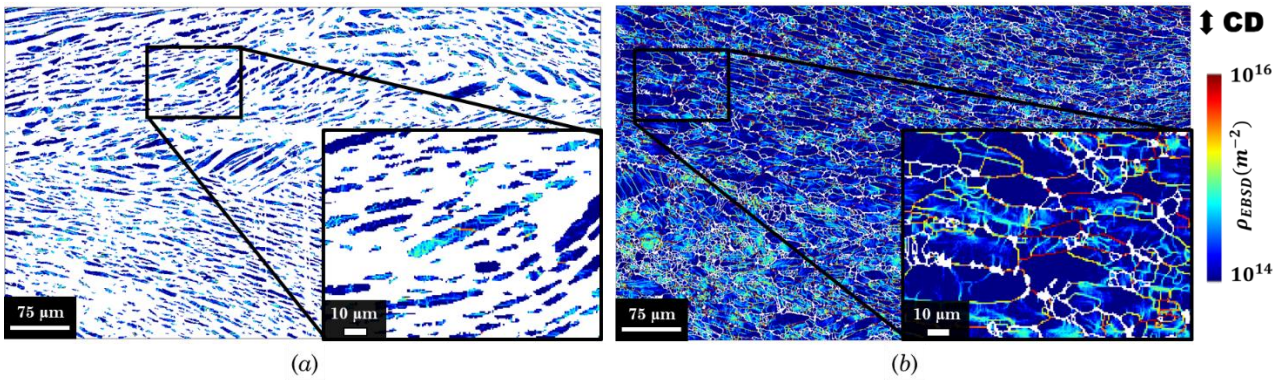



*Figure 7.9. Dislocation density maps of the Ti64_CL at 1.3 strain level, deformed at 0.1 $s^{-1}$ and 950°C, followed by: a) Quenching; b) Slow cooling.*

The $\alpha$ laths grew, accompanied by the substructure development inside them, which the latter can be confirmed in **Figure 7.10** by higher $\rho_{GB}$ levels in the Ti64_L

curves. Similar behavior can be observed for the Ti64_Eq. Once more the strongest difference between the water quenching and slow cooling can be perceived for the lamellar microstructure. It seems then that the formation of LAGBs and HAGBs upon cooling is privileged in a lamellar $\alpha$ configuration.

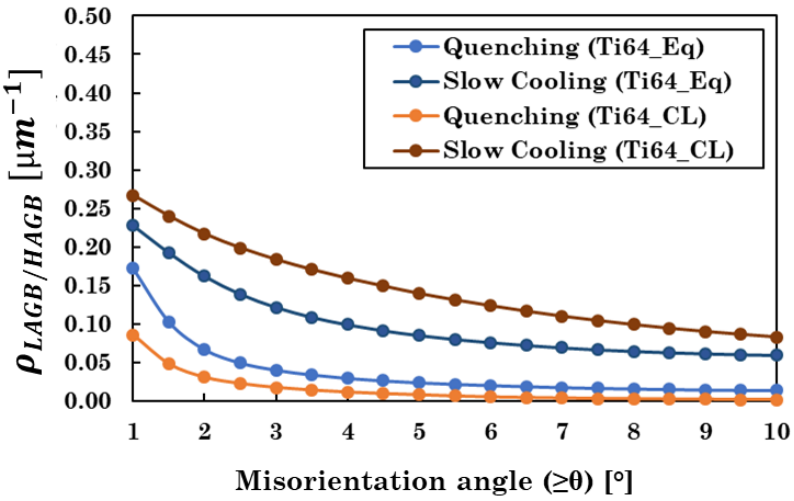



*Figure 7.10. Cumulative analysis of the LAGB and HAGB density, as a function of the misorientation angle, in the α phase of Ti64 microstructures.*

The texture development of the $\alpha$ phase after slow cooling was also analyzed through pole figures (**Figure 7.11**). Interestingly, the intrinsic $\alpha$ phase texture observed in section **4.2.2.1** (basal planes ∥ CD) is no longer observed. There is an apparent loss of texture in the $\alpha$ phase during the slow cooling. Thus, this phase does not maintain the preferred orientations obtained after deformation.

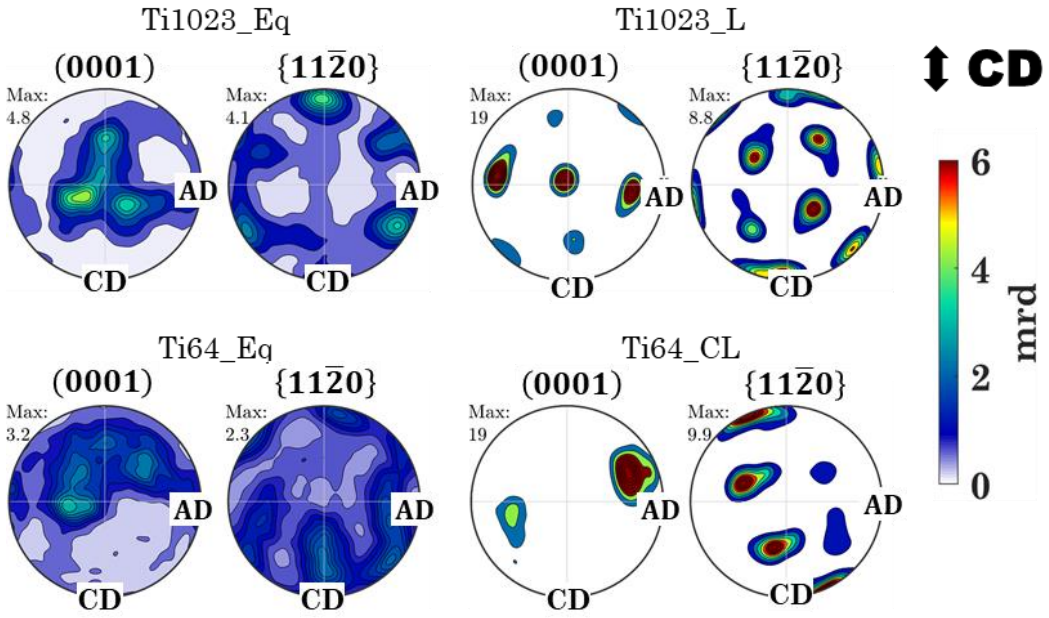



*Figure 7.11. α phase pole figures of the four selected microstructures after slow cooling.*

It seems then that the $\alpha$ grains growth favors minor orientations of the deformation texture of after nucleation of few grains with different orientations. **Figure 7.12** shows the $\beta$ phase pole figures of the Ti1023_L. By comparing the pole

figures of the planes involved in the BOR, *i.e.*, $\{0001\}_\alpha$ (**Figure 7.11**) and $\{110\}_\beta$ **Figure 7.12**, it appears that the BOR is respected in this $\alpha$ phase growth during slow cooling, *i.e.*, with $(0001)_\alpha$ poles at the same positions as the $(110)_\beta$ poles.

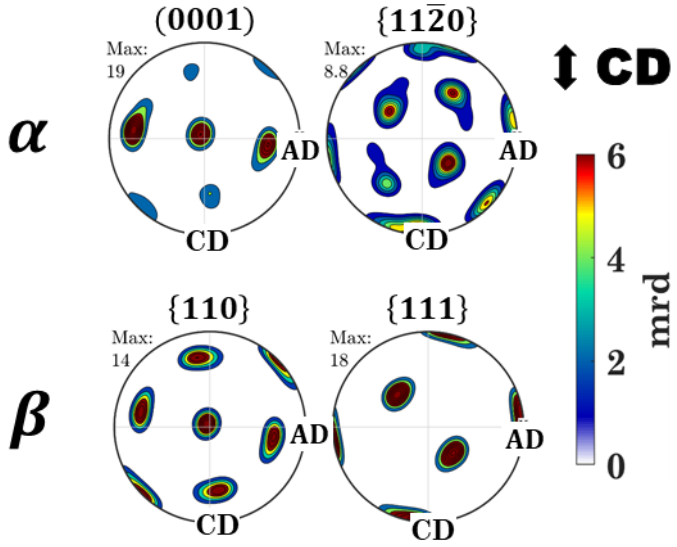



*Figure 7.12. β phase pole figure of the Ti1023_L microstructure after slow cooling.*

## 7.2.2 Influence of the thermomechanical path

### 7.2.2.1 Post-deformation holding

The influence of the post-deformation holding was also addressed with a preliminary experiment in this work to be compared with the changes associated to slow cooling (**7.2.1**). During slow cooling, both stored energy and thermomechanical driving forces are at play. During isothermal holding, no change in phase fractions is expected (since no dynamic phase transformation has been observed). The comparison of both kind of experiments, isothermal post-deformation holding *vs* slow cooling, should therefore allow for decoupling the effects of stored energy and of phase transformation. The thermomechanical paths are schematized in **Figure 7.13**.

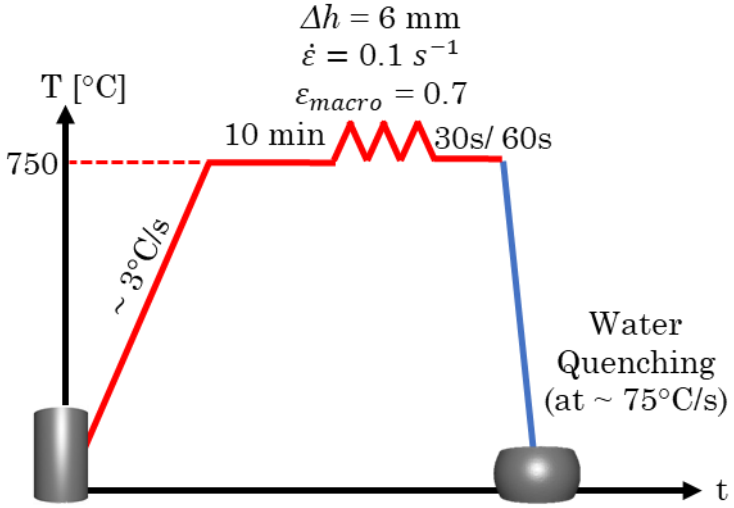



*Figure 7.13. Thermomechanical path of the analysis of the post-deformation holding.*

Two different post-deformation holding times were applied (30 and 60 seconds), as shown in **Figure 7.13**. Short holding times have been chosen since post-dynamic evolutions can have very fast kinetics, as shown previously in Ni base superalloys [119,120]. Those results were compared to EBSD analysis performed at the center of the cylindrical samples presented in Chapter **5** (hereafter referred to as *no-holding*), where no holding time was intentionally applied after the deformation (*i.e.,* experimental quenching delay of maximum 2 seconds).

**Figure 7.14** shows the EBSD maps with the LAGB and HAGB for the four different cases studied, while **Figure 7.15** gathers its qualitative analysis.

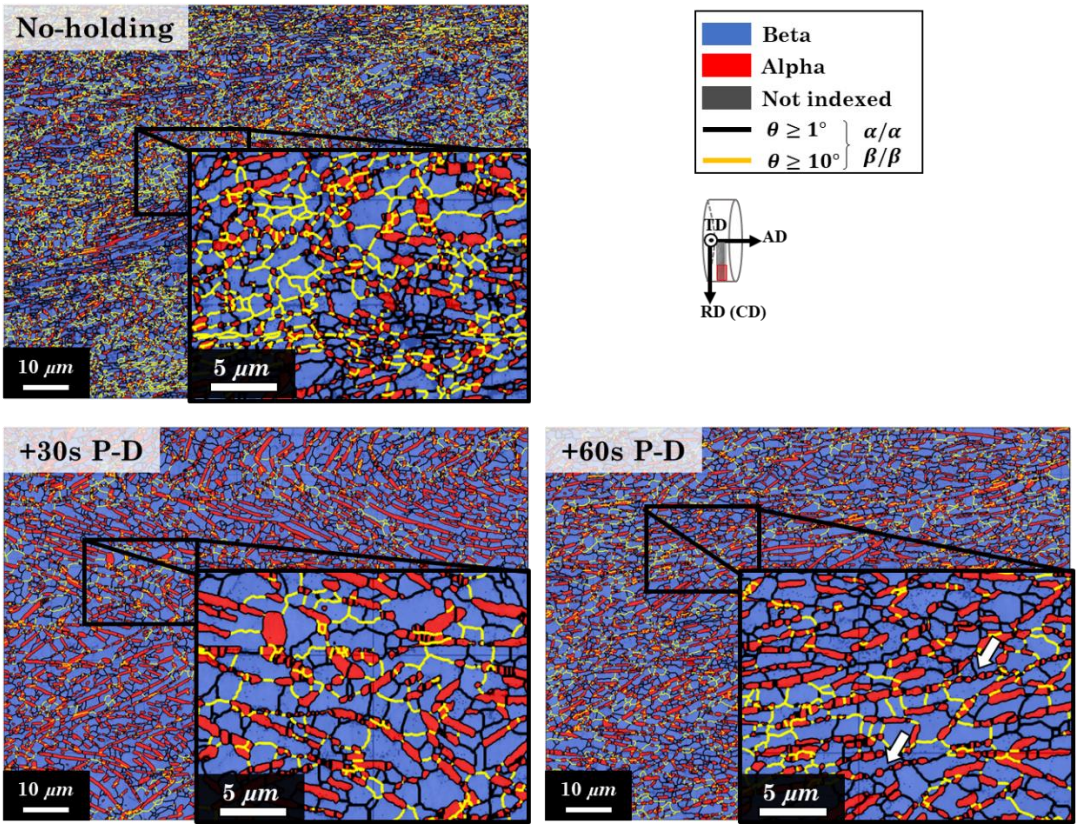
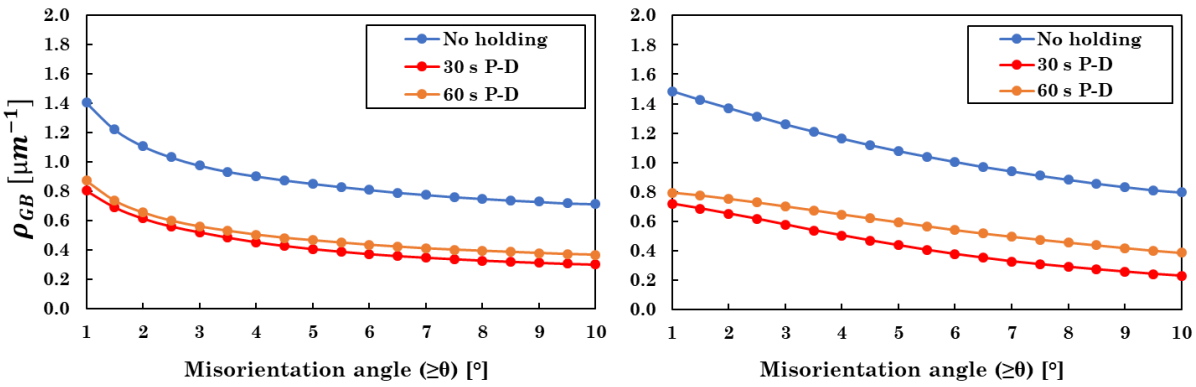



*Figure 7.14. EBSD maps showing the LAGB and HAGB in the α and β phases of the Ti1023_L microstructures deformed at 1.3 strain level (center of the samples), with thermomechanical paths described in **Figure 7.13**.*




(*a*) (*b*)

*Figure 7.15. Cumulative analysis of the LAGB and HAGB density, as a function of the misorientation angle, for the: a) α phase; b) β phase; after the different thermomechanical paths described in **Figure 7.13**.*

By analyzing **Figure 7.15, w**hat first attract attention is a clear and very rapid evolution after only 30 seconds, which induces indisputable changes. A very clear decrease in all LAGBs and HAGBs can be observed. It seems that then, between 30 and 60 seconds, the quantity of LAGBs and HAGBs increases slightly, yet with a relatively small difference. This should be confirmed with more data and better statistical quality. Furthermore, the reduction in the $\rho_{HAGB}$ seems to be due to the coarsening of substructures, as visible on the EBSD maps of **Figure 7.14**.

As expected for such short holding times, no clear globularization was observed. Nevertheless, some lath shearing and the formation of smaller substructures in the $\alpha$ laths can be observed (arrowed on **Figure 7.14**), especially after holding 60 seconds after deformation, and in the thinnest laths. This could be the onset of globularization.

In terms of dislocation density, the results are summarized in **Figure 7.16**. The highest $\rho_{EBSD}$ levels are the ones of the reference (no-holding), where there is a clear tendency to reduce the $\rho_{EBSD}$ with longer post-deformation holding times. This is probably due to the dynamic recovery and coarsening of substructures, being more evident for the $\beta$ phase.

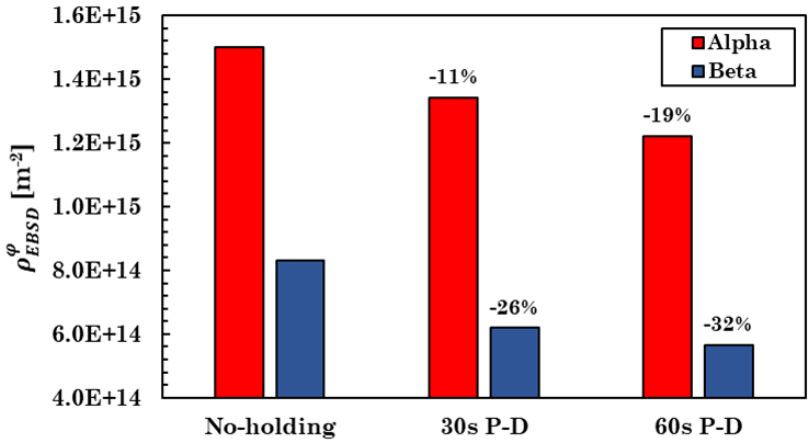



*Figure 7.16. Dislocation density values of the different thermomechanical paths analyzed, along with the reduction (in %) in the $\rho_{EBSD}$ levels compared to the reference state (no-holding).*

### *7.2.2.2 Two-step forging*

A two-step deformation is also interesting in the industrial context, as billet forging is a multiple-step deformation process. Hence, half of the total deformation ($\varepsilon_{macro}$ = 0.35) was firstly applied, followed by one hour holding at the same temperature (750°C), then the other half of deformation ($\varepsilon_{macro}$ = 0.35) was applied (**Figure 7.17**). The results were also compared to EBSD analysis performed at the center of the cylindrical samples deformed up to $\varepsilon_{macro}$ = 0.7 (or 1.3 local $\varepsilon$ value at the center) in a single step and presented in Chapter **5** (hereafter referred to as single-step deformation).

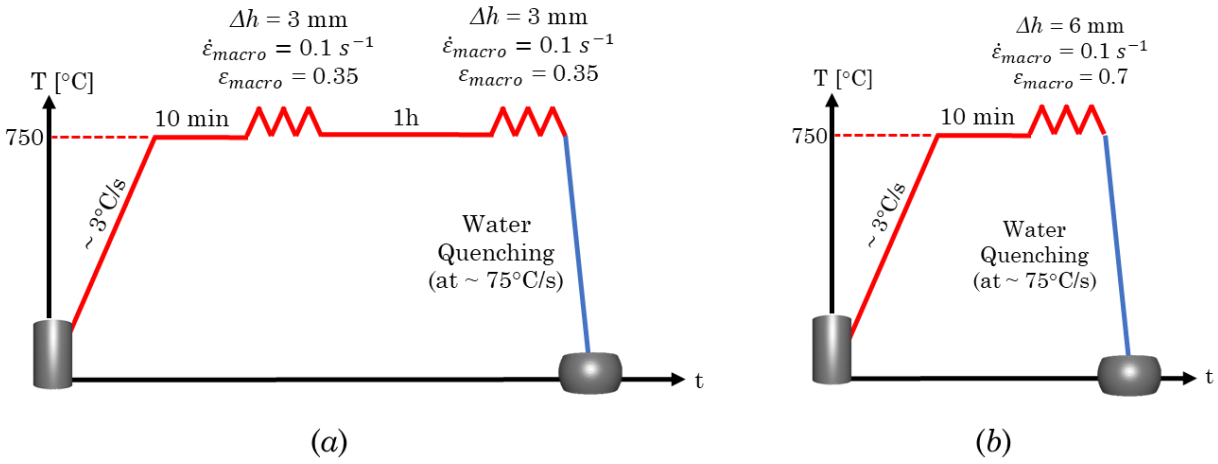



*Figure 7.17. Thermomechanical path of the: a) Two-step hot-compression test; and b) corresponding single step experience (from Chapter **5**).*

**Figure 7.18** shows the EBSD maps with the LAGB and HAGB for the two different cases studied, while **Figure 7.19** gathers its qualitative analysis.

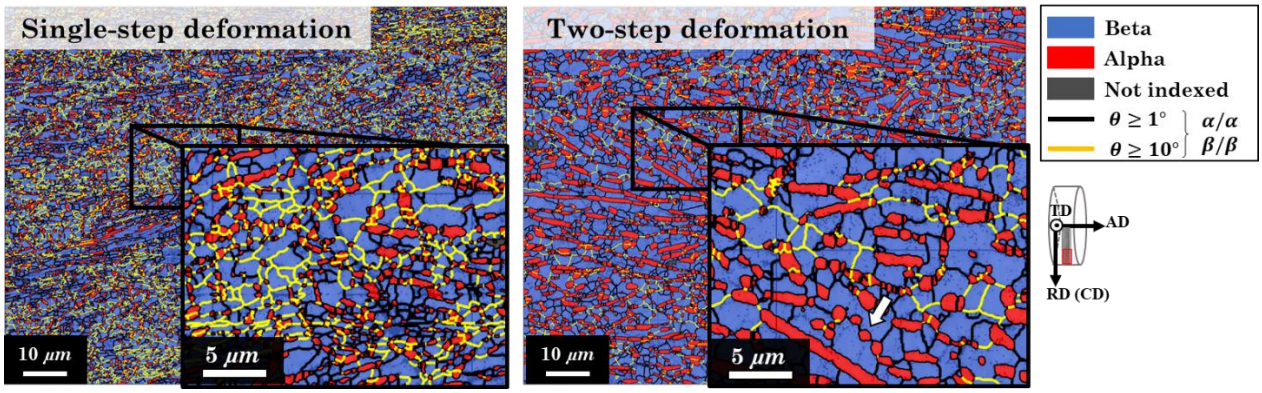



*Figure 7.18. EBSD maps showing the LAGB and HAGB in the α and β phases of the Ti1023_L microstructures deformed at 1.3 strain level (center of the samples), with thermomechanical path described in **Figure 7.17**.*

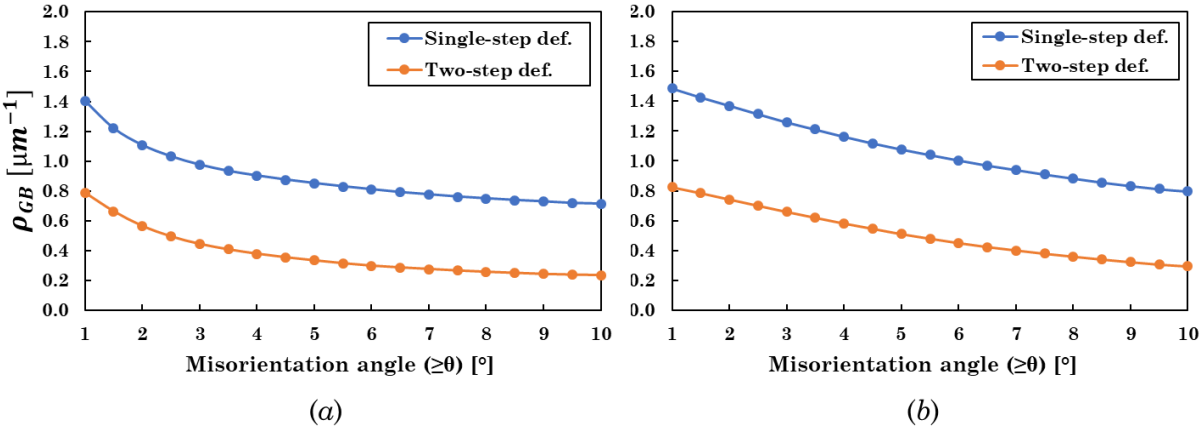



*Figure 7.19. Cumulative analysis of the LAGB and HAGB density, as a function of the misorientation angle, for the: a) α phase; b) β phase; after the thermomechanical path described in **Figure 7.17**.*

Interestingly, for the two-step deformation, with a one-hour holding in between deformation steps, $\alpha$ laths are much thicker, compared to the single-step case as well as the $\beta$ grain substructures which seem to have coarsened (**Figure 7.18**), leading to lower LAGB and HAGB densities (**Figure 7.19**). Furthermore, after the long holding time (1 hour) between deformations, the globularization phenomenon was observed (arrowed in **Figure 7.18)**.

In terms of dislocation density, the results are summarized in **Figure 7.20**. Once again, the highest $\rho_{EBSD}$ levels are the ones of the reference (single-step), where there is a clear tendency to reduce the $\rho_{EBSD}$ with long post-deformation holding times in between deformation. This behavior is again more evident for the $\beta$ phase, as seen in **Figure 7.7** and **Figure 7.16**.

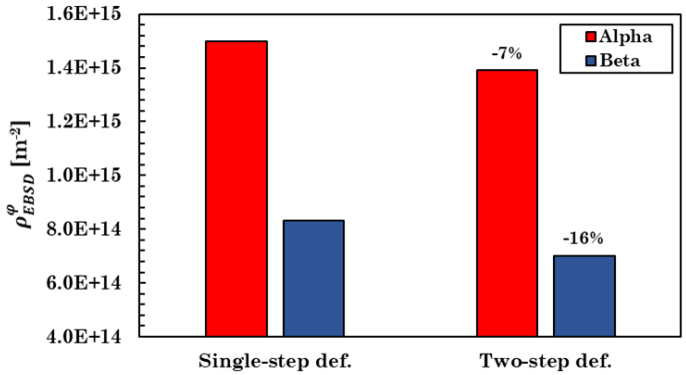



*Figure 7.20. Dislocation density values of the two-step deformation, along with the reduction (in %) in the $\rho_{EBSD}$ levels compared to the reference state (single-step).*

To summarize, those two sections (**7.2.1** to **7.2.2**) were mainly performed to create a link between this work and complementary topics which will be further addressed in the other theses of the consortium. Some trends have been identified for different thermomechanical processing steps, especially the effect of time and temperature on the microstructure evolution after deformation.

Furthermore, the same tools to analyze the microstructural features (especially those developed in *MTEX*) will be used in the forthcoming works in order to allow assessing, as far as possible, the quantitative impact of the deformed structures on the following metallurgical evolution kinetics.

# APPENDIXES

# A. Analyzed microstructures that were not selected for further studies in this PhD work

As mentioned in section **2.1**, after the microstructural characterization of the as-received states, a first selection of microstructures was done to optimize the amount of analyzed microstructures. The two analyzed microstructures that were not selected for further studies in this PhD work are detailed in Table A.1 and shown in Figure A.1.

| Billet name | Expected microstructure | Supplier | Ø (*mm*) | H (*mm*) | HT realized by the suppliers |
|---|---|---|---|---|---|
| Ti64_FL_C$\beta$ | $\alpha$: Fine lamellae<br>$\beta$: Highly coarse grains | Aubert & Duval | 255 | 20 | 1150°*C* \| 2 hours \| Air cooling |
| Ti64_CL_C$\beta$ | $\alpha$: Coarse lamellae<br>$\beta$: Highly coarse grains | Aubert & Duval | 255 | 20 | 1150°*C* \| 2 hours \| Slow cooling (1°*C*/*min* up to 700°*C*) |

*Table A.1. Summary of the as-received (AR) billet slices, supplied by industrial partners, that were not selected for further studies in this PhD work.*

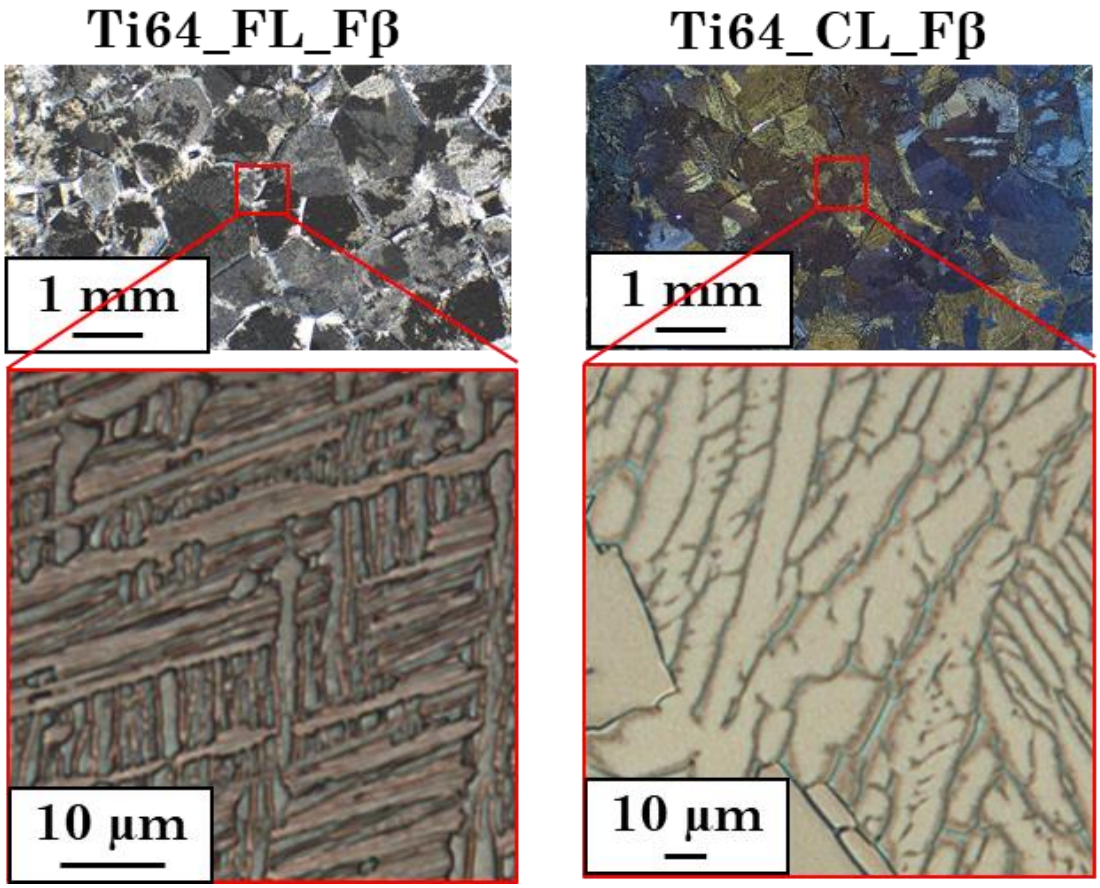



*Figure A.1. Optical micrographs of the six as-received billet materials that were not selected for further studies in this PhD work, displayed at two different scales, showing the β (or prior-β for the Ti64) and α grains.*

Both Ti64 with coarse equiaxed $\beta$ grains (Ti64_FL_C$\beta$ and Ti64_CL_C$\beta$) were removed from the following steps of this PhD work, as the grain size for the fine equiaxed $\beta$ grains (Ti64_FL_F$\beta$ and Ti64_CL_F$\beta$) is considerably high for the EBSD analysis. The preliminary characterization results of those non-selected materials are nevertheless provided in this appendix (Table A.2) in view of a possible use in the forthcoming works of the consortium CONTiNUUM.

| Billet | Primary $\alpha$ phase | | | $\beta$ phase | |
|---|---|---|---|---|---|
| | Qualitative analysis | $\overline{GS}$ ($\mu m$) | $f_{\alpha_P}$ (%) | Qualitative analysis | $\overline{GS}$ ($mm$) |
| Ti64_FL_C$\beta$ | Fine lamellae | **2.0** ± 0.4 | **92** ± 1 | Highly coarse equiaxed grains | **1.0** ± 0.1 |
| Ti64_CL_C$\beta$ | Coarse lamellae | **16.6** ± 1.1 | **93** ± 1 | Highly coarse equiaxed grains | **1.0** ± 0.2 |

*Table A.2. Summary of the results of the characterization of the as-received states ($\boldsymbol{\mu} \pm \sigma$), which were not selected for further studies in this PhD work.*

# B. About dislocation density estimation and dislocation mode analysis from EBSD data: application to hot-deformed titanium alloys

This appendix is a first state of a paper to be submitted for publication. The described work demonstrates that analyzing dislocation modes as arising from the Nye tensor analysis and energy minimization principal can be misleading as the results for a given phase appear to be dependent on grain orientation. Furthermore, the relevance of comparing values in different phases is also discussed. Based on this piece of work, it was decided to not perform such kind of analysis in this PhD work.

## *B.1 Introduction*

Dislocations are of utmost importance in mechanical behavior and microstructural evolution of metallic materials. Thus, analyzing how the dislocation density is distributed amongst the different dislocation modes (planes and directions for edge and screw dislocations), may provide important information to understand the active deformation mechanisms, the development of crystallographic texture, but also recrystallization mechanisms [121]. Furthermore, crystal plasticity finite element method (CPFEM) models have proven to provide accurate predictions of deformation, dislocation and texture evolution [103,122]. Examination of intragranular orientations, thus dislocation density distributions among different slip modes, could also be useful to guide the calibration of parameters in CPFEM models.

When dealing with dual phase materials, different crystal structures must be defined in the dislocation assessment. For titanium alloys, the concerned structures are HCP ($\alpha$) and BCC ($\beta$). Furthermore, HCP crystals are highly anisotropic, especially due to the $\langle a \rangle$ and $\langle c + a \rangle$-type slip, which have different Burger's vectors, and several possible slip planes with distinct critical resolved shear stresses (CRSSs) [25,64].

The number of possible dislocation modes for the HCP is 39 (30 edge-type + 9 screw-type [64]), while for the BCC is 52 (48 edge-type + 4 screw-type [12]), as presented in Figure B.1and Figure B.2, respectively.

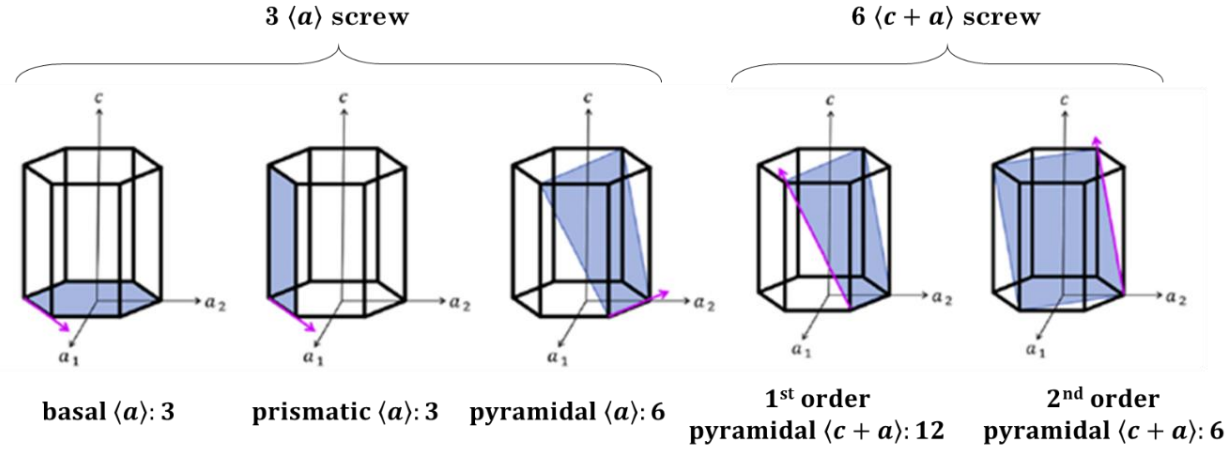



*Figure B.1. Slip systems and dislocation modes in a HCP crystal* [13].

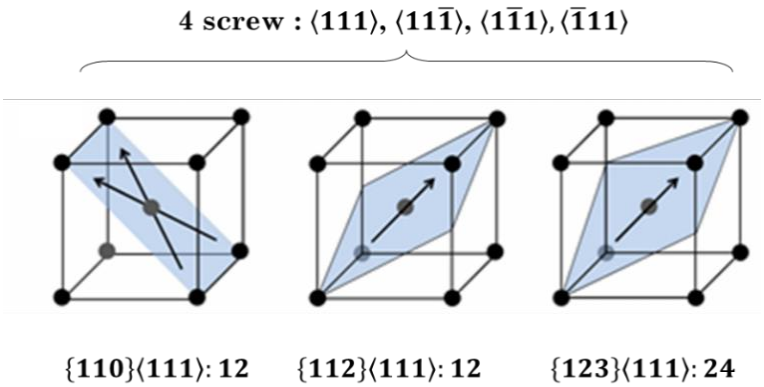



*Figure B.2. Slip systems and dislocation modes in a BCC crystal [12].*

The aim of this work is to analyze, both using experimental and synthetic data, how the different dislocation modes contributes to the total dislocation density in each phase and how the grain orientation, filtering of the raw data, or crystal symmetry can influence this distribution. One of the main objectives is also to discuss the relevance and limits of the internal energy minimization approach that many works have been using in order to estimate dislocation density (*e.g.*, [55,64,123,124]).

## *B.2 Experimental orientation maps*

### *B.2.1 Materials*

Two-phase $\alpha$+$\beta$ titanium alloy Ti-10V-2Fe-3Al (metastable-$\beta$), hereafter referred to as Ti1023, with equiaxed $\alpha$ phase (Ti1023_Eq, as shown in ***Table 2.1***) was supplied by *Timet Savoie*. In order to analyze the real to-be-deformed microstructures (at hot temperatures), a sample was heat treated at 750°*C*, followed by water quenching. The resulting microstructure was characterized using a binocular microscope (to visualize the large $\beta$ grains) and BSE imaging in the SEM (to visualize the primary $\alpha$ phase topology), shown in **Figure B.3**.

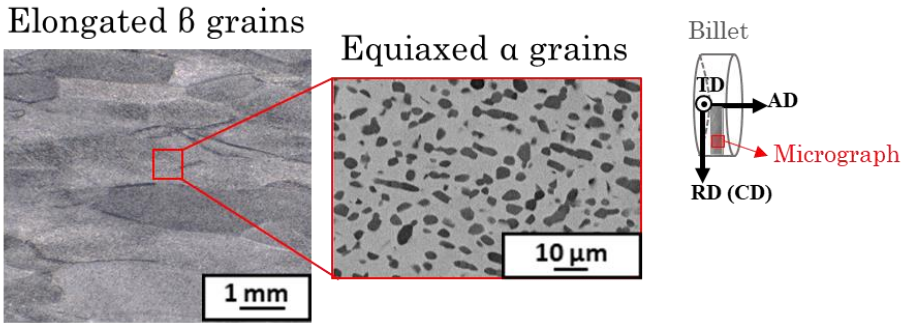



*Figure B.3. The Ti1023 microstructure, showing both β (on the left) and α grains (on the right), along with the macroscopic reference.*

Primary $\alpha$ phase fraction is about 24%, it is mostly equiaxed with an average grain size of 3.1 $\pm$ 1.3 $\mu m$, while $\beta$ grains were 0.6 $\pm$ 0.1 $mm$ thick with 1.5 $\pm$ 0.2 $mm$ in length (as shown in **Table 3.3**). $\beta$ grains tend to elongate along the axial direction of the billet (AD), perpendicular to the forging direction (radial direction of the billet, RD/CD, see **Figure B.3**).

### *B.2.2 EBSD measurement and analysis*

EBSD maps were acquired using a Zeiss SUPRA 40 FEG-SEM equipped with a Bruker Crystalign system and a sensitive EBSD detector. The following SEM and EBSD acquisition settings were applied: 70° sample tilt; 20 kV acceleration voltage; working distance of 14 $mm$; 120 $\mu m$ aperture size; magnification of 1000 (analysis field of 112.5 $\mu m$ x 85 $\mu m$); step size of 0.1 $\mu m$.

Microstructural analysis were performed with *MTEX* [51] (a free access *MATLAB* toolbox specifically developed for the post-processing of EBSD data). Three different datasets were created:

- **Raw**: direct analysis of the raw EBSD data, including measurement noise and non-indexed points;
- **Filtered**: Filtering of the raw EBSD orientation data is performed using the half-quadratic filter [67], that preserves the substructures while reducing the orientation noise and filling the small non-indexed zones [68]. The purpose of this filtering step is to avoid the overestimation of the GND density by misinterpretation of local misorientation related to the experimental orientation determination inaccuracy. A misorientation angle ($\theta$) threshold of 10° defined a high-angle grain boundary (HAGB). This value is selected because it appears to be a satisfactory compromise after manual checks. Indeed, this value is high enough to consider misorientation substructures as intragranular phenomena and low enough to consider grain boundaries as intergranular features. This value is used in order to define grain boundaries and exclude them in the intragranular misorientation analysis;
- **Mean orientation**: to separate the contribution of subgrain boundaries and the contribution of intra-subgrain orientation fluctuations (due to GNDs really present or due to measurement noise). In this manner, a threshold of 2° was used to define the subgrain boundaries. Then, a mean orientation of the subgrain was given for each of them, thus smoothing/eliminating the misorientation angle between two neighboring points that was inferior than 2°. The dislocation density calculation was then done considering only subgrain boundaries that exceed 2°, defined as observed and thus true substructures.

### *B.2.3 Qualitative analysis from the experimental datasets*

A comparison between the different orientation maps is shown in **Figure B.4** for the raw, filtered and mean orientation datasets. The raw image contains both noise and non-indexed data for both phases, which are corrected in the filtered data. In the latter, it is possible to see the presence of very low misorientation angles ($\theta < 2°$). Those have been smoothed in the mean orientation analysis, where a single orientation can be seen for each subgrain.

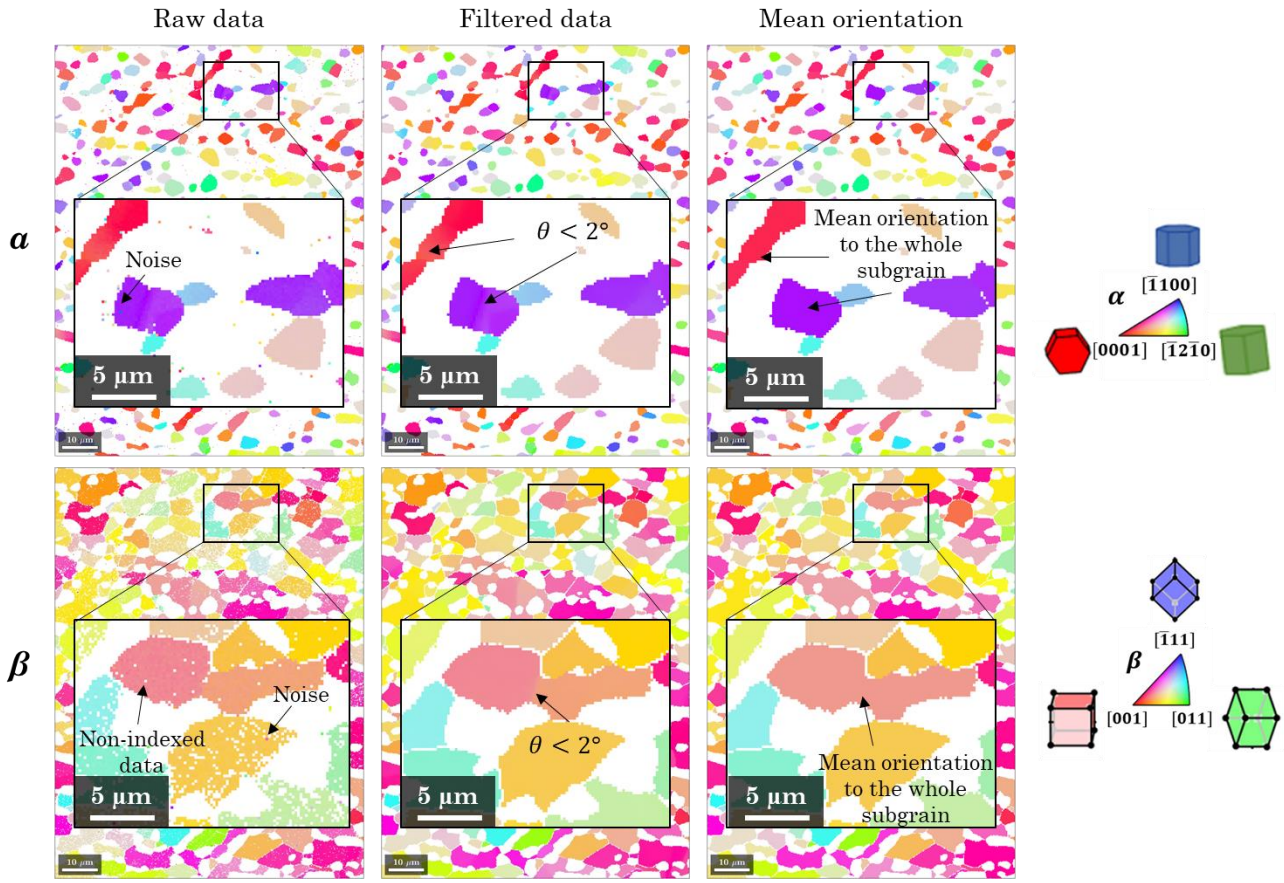



*Figure B.4. Orientation maps (TD-IPF) for the α and β phases of the Ti1023 alloy after heat treatment at 750°C (1 hour), and quenching: raw and filtered data, along with the mean orientation of the subgrains inside each of them.*

Finally, for all three cases, the GND tensor method [58,59], explained in section **2.7.5**, is applied for each phase separately, respecting its crystal structure. The arithmetic mean of all measurements across the microstructure is then calculated for each dislocation mode, giving the average dislocation density per dislocation mode, which allows in turn to obtain the average dislocation density of each phase ($\rho_{EBSD}$ $[m^{-2}]$).

## *B.3 Synthetic orientation maps*

The aim of generating synthetic EBSD data is analyze a data set with complete control of the considered configuration and the possibility to introduce controlled fluctuation. Two different initial orientations of each phase where added to a synthetic EBSD data (**Table B.1**), with their directions parallel to the transverse direction (TD), shown in Figure B.3.

| Synthetic map n° | $\alpha$ orientation regarding TD | $\beta$ orientation regarding TD |
|---|---|---|
| 1 | $(0001)[11\bar{2}0]$ | $(110)[1\bar{1}1]$ |
| 2 | $(0\bar{1}1\bar{1})[1\bar{2}13]$ | $(111)[\bar{1}\bar{1}\bar{1}]$ |

*Table B.1. α and β orientations implemented in the different synthetic orientation maps.*

A random slight misorientation was then applied to each pixel, creating noise in the data. This was performed by using a unimodal orientation distribution function (ODF), which is specified by a radially symmetrical function (Ψ) centered at a modal orientation (g) in space (x), which belong to the 3D rotation group (SO(3)), as shown in equation **(B.1)**.

$$f(g;x) = \Psi\big(\angle(g,x)\big), \qquad g,x \in SO(3) \tag{B.1}$$

The function used was the "de la Vallée Poussin", which is the default kernel of *MTEX* toolbox [51]. The angle chosen for the misorientation angle threshold was 8°, slightly inferior to the one used for the HAGB threshold and the dislocation density calculation (10°).

The two synthetic orientation maps, containing both $\alpha$ and $\beta$ phases are shown in **Figure B.5**.

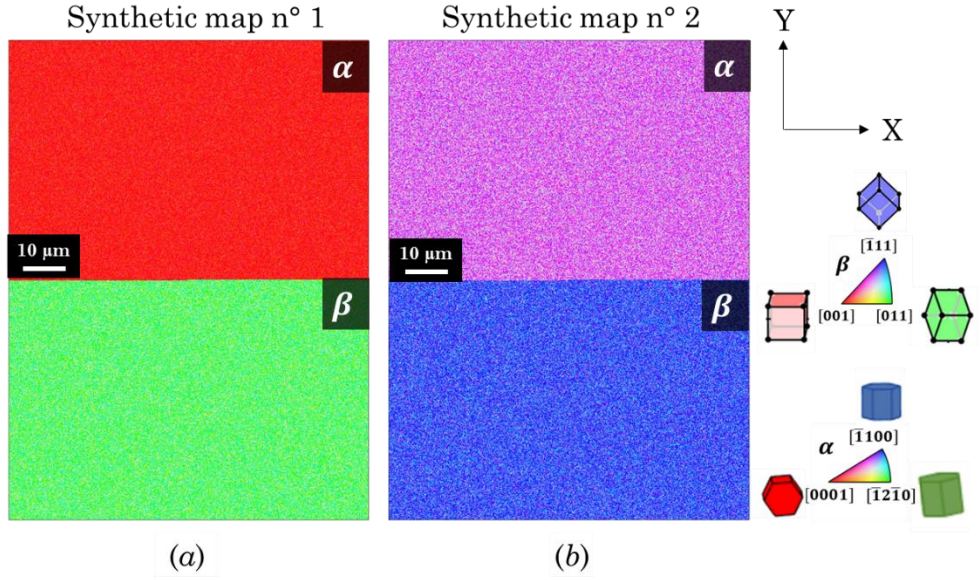



*Figure B.5. Synthetic orientation maps (TD-IPF) n°: a) 1, with α* (0001)[11$\bar{2}$0] *and β* (110)[1$\bar{1}$1] *; b) 2, with α* (0$\bar{1}$1$\bar{1}$)[1$\bar{2}$13] *and β* (111)[$\bar{1}\bar{1}\bar{1}$].

To better illustrate the effect of the introduced noise in the given orientations for both phases, the pole figures, inverse pole figures (IPF) of the misorientation axes, and the histogram of misorientation angles are shown in Figure B.6 and Figure B.7 for the synthetic map n°1 and 2, respectively.

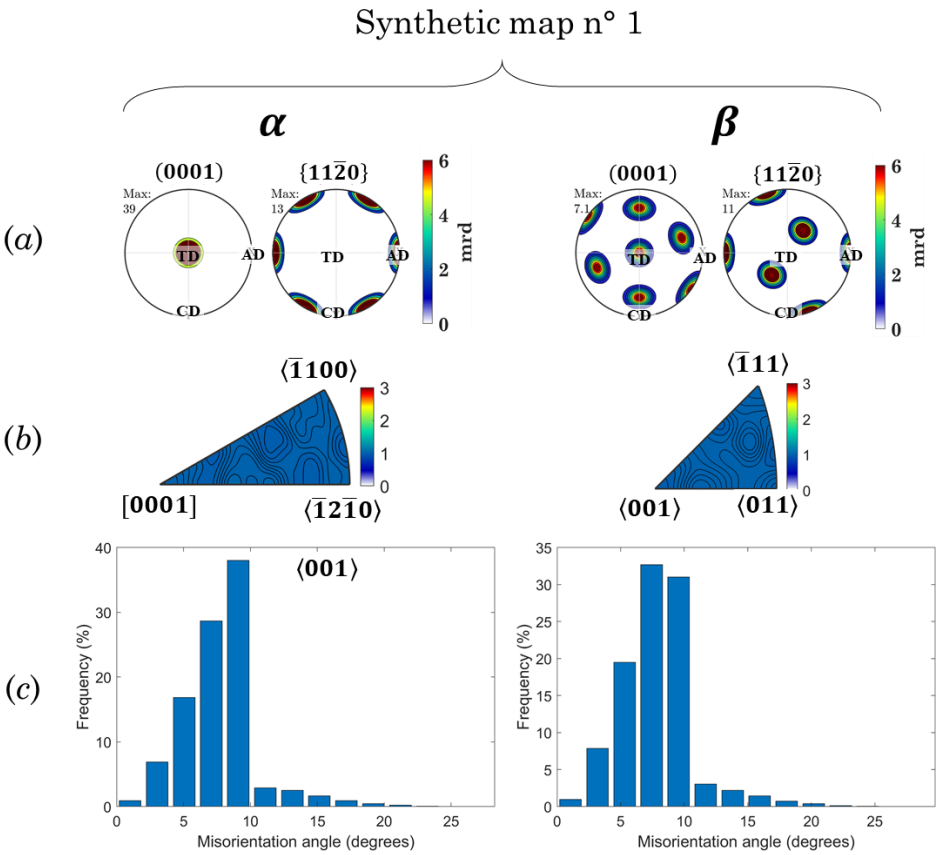



*Figure B.6. Synthetic orientation map n° 1, showing: a) Pole figures; b) IPF of the misorientation axes; c) Histogram of misorientation angles; for both α and β phases.*

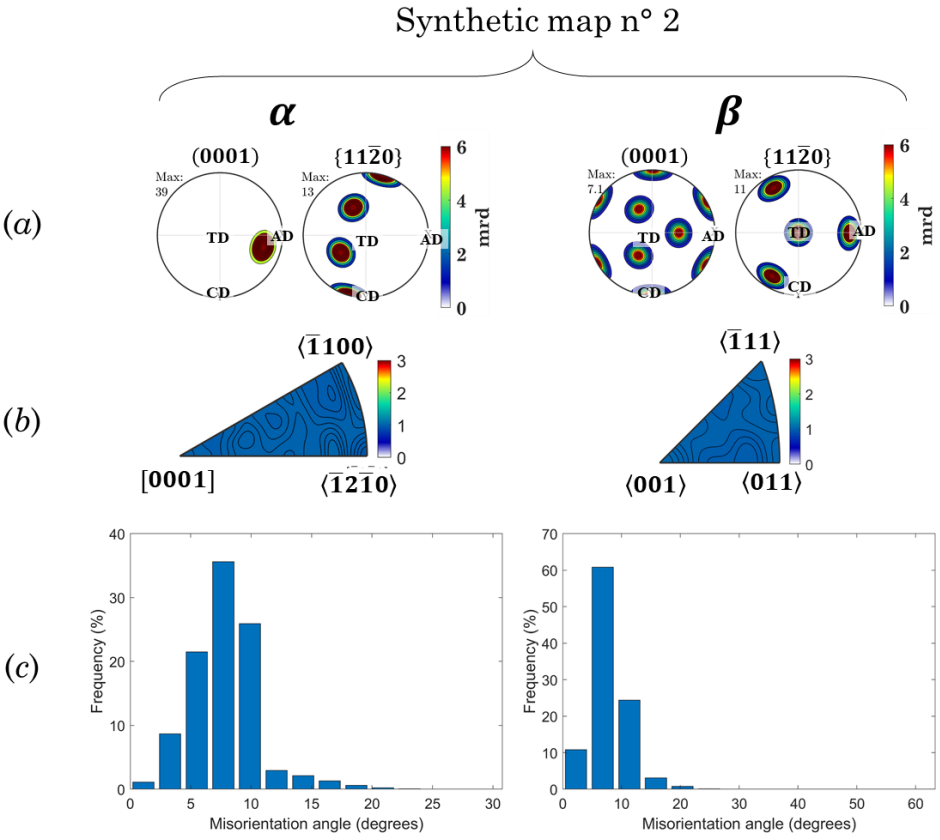



*Figure B.7. Synthetic orientation map n° 2, showing: a) Pole figures; b) IPF of the misorientation axes; c) Histogram of misorientation angles; for both α and β phases.*

By analyzing the pole figures in Figure B.6*a* and Figure B.7*a*, it is possible to observed the chosen orientations in **Table B.1**, with a slight spread (misorientation). In the IPF of the misorientation axes (Figure B.6*b* and Figure B.7*b*), it is clear that there is a homogeneous distribution, with no preferred axes being selected for the generation of misorientation. Finally, in the histogram of misorientation angles (Figure B.6*c* and Figure B.7*c*), it is possible to observe the peaks around the chosen angle (8°). It is important to point out that the same orientation spread/ noise has been introduced in all considered synthetic data set, so that the effects of the grain orientation and of orientation noise can be decoupled (the noise level in orientation data actually being orientation dependent).

Then, the GND tensor method is applied with the same parameters as explained in section **B.2.2**, for the sake of comparison.

## *B.4 Results*

### *B.4.1 Dislocation density maps of the experimental dataset*

The total dislocation density distribution maps (for all different dislocation modes) from the three different data sets obtained from the raw experimental data are summarized in **Figure B.8**. The raw data tends to overestimate the total dislocation density in the microstructure, as the measurement noise [5] is analyzed leading to higher local dislocation densities. In the filtered data, the substructures are better revealed, showing very low dislocation densities in the regions inside subgrains. While for the mean orientation dataset, only higher angle grain boundaries are shown ($\theta \geq 2°$), showing zero density values for the intragranular zones.

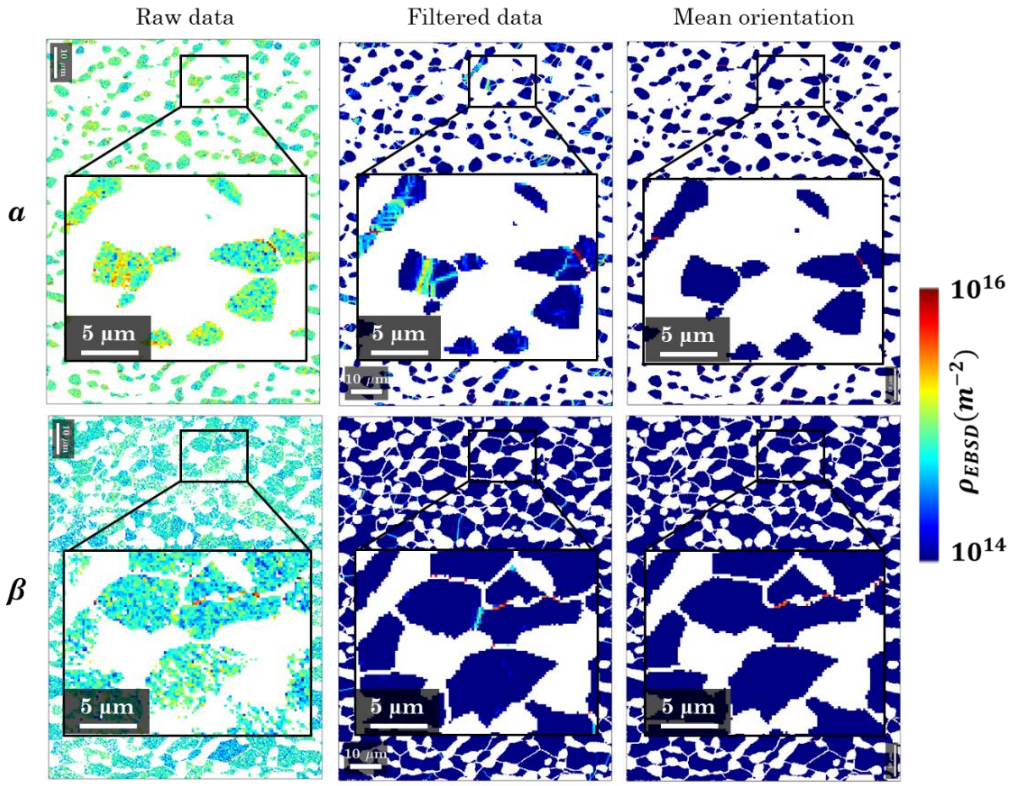



*Figure B.8. Dislocation density maps for the α and β phases for the raw, filtered and mean orientation experimental datasets.*

As mentioned previously, this total dislocation density corresponds to the contribution of the different dislocation modes for each phase. As show in **Figure B.9** and **Figure B.10**, for the $\alpha$ and $\beta$ phase, respectively, after filtering of the data.

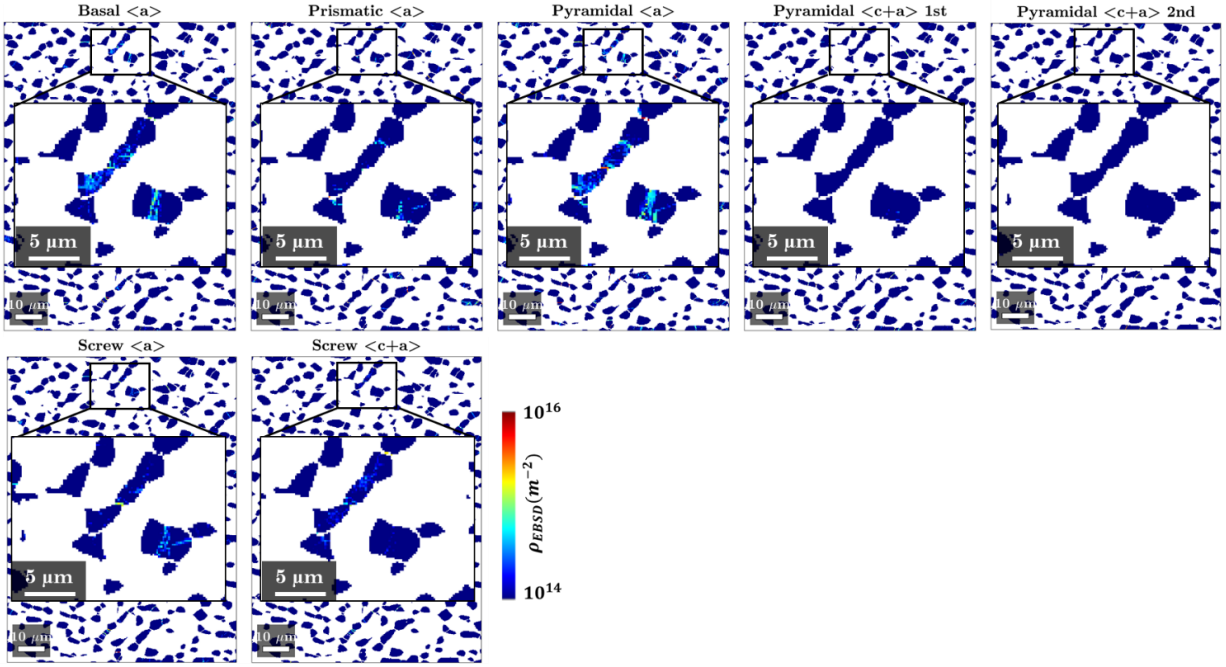



*Figure B.9. Dislocation density contributions of the different dislocation modes of the α phase after filtering of the data.*

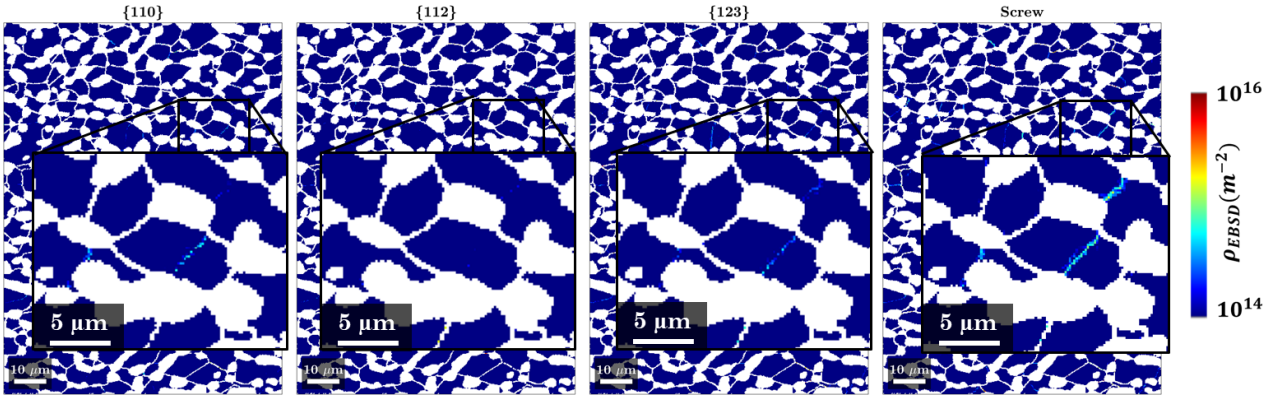



*Figure B.10. Dislocation density contributions of the different dislocation modes of the β after filtering of the data.*

By analyzing the $\alpha$ phase (**Figure B.9**), it is clear that the main contributions to the total dislocation density come from the $\langle a \rangle$-type dislocation modes, especially the basal and pyramidal ones. While for the $\beta$ phase (**Figure B.10**), the {110} and {123} slip planes are the most activated, along with the screw-type. Nevertheless, screw dislocations are not possible to distinguish within which plane slip occurred, only the direction. So, to compare both dislocation types (*i.e.,* edge and screw), the sum from all edge-type dislocation modes has been performed (**Figure B.11**).

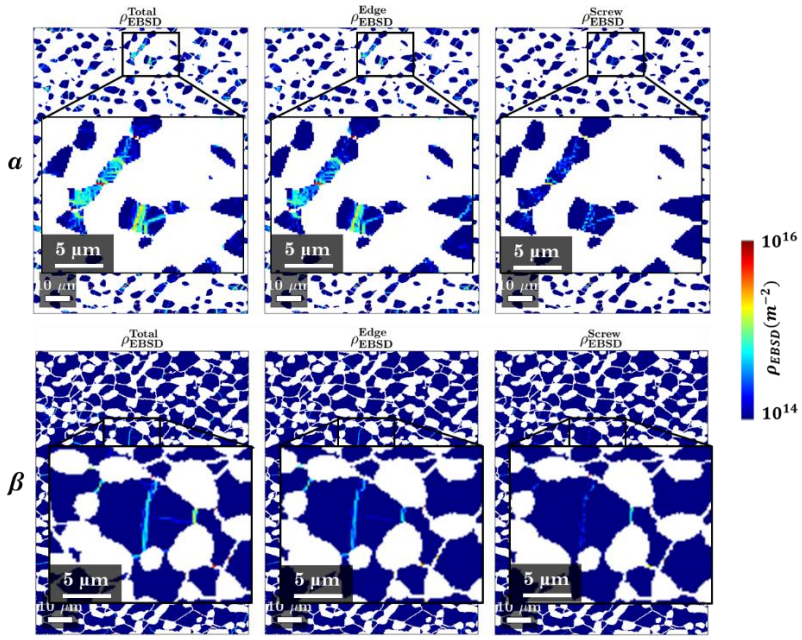



*Figure B.11. Dislocation density contributions of the different dislocation types (edge and screw) for the α and β phases after filtering of the data.*

For both phases, it is evident that the main dislocation type responsible for the slip in the Ti1023 microstructure are the edge ones.

### *B.4.2 Quantitative analysis from the different experimental and synthetic datasets*

The contributions of the different dislocation modes for the different datasets shown previously (experimentally and synthetically obtained) were quantified and are summarized in **Figure B.12**.

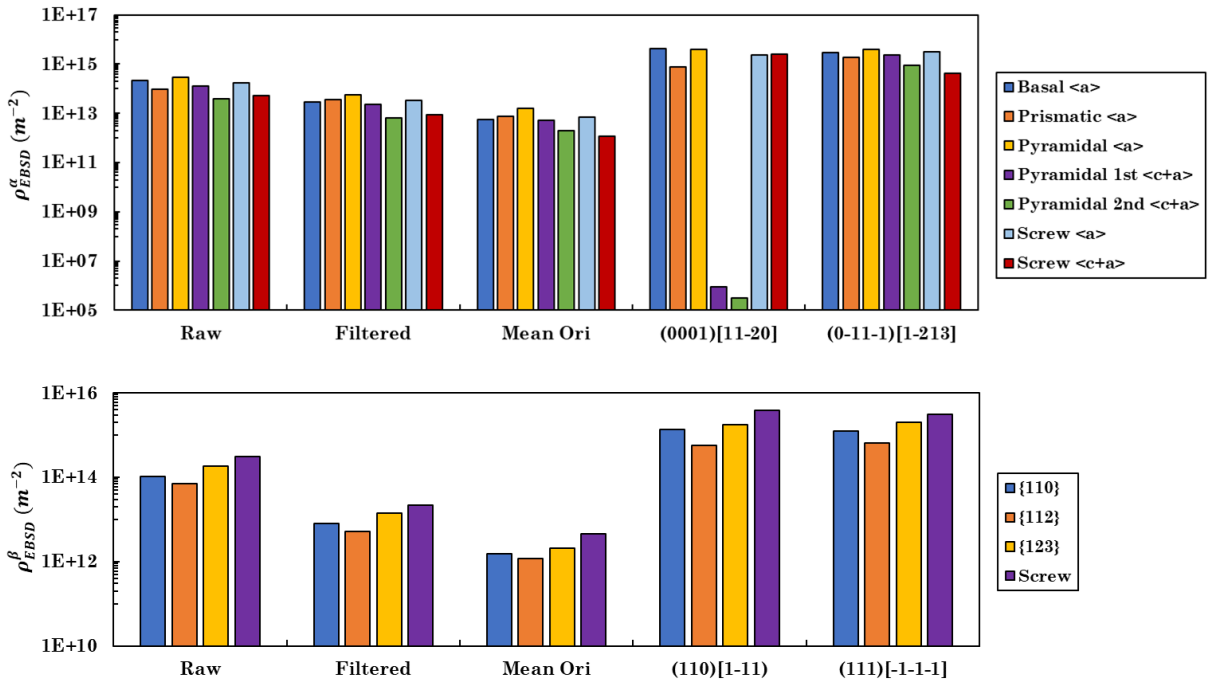



*Figure B.12. Summary of the contributions of the different dislocation modes to the total dislocation density calculated from different datasets, for the α and β phases.*

As expected, for both $\alpha$ and $\beta$ alloys, the analysis from the raw data gave higher values than the filtered one of the one with locally averaged orientations, as the former contained measurement noise. What is interesting to point out in the $\alpha$ phase is that the $\langle a \rangle$-basal slip presented higher values than the $\langle a \rangle$-prismatic in the raw data, behavior that changed after filtering. This tendency is confirmed in the dataset with averaged orientation, where only observed substructures were considered.

An interesting bearing is that when the synthetically generated orientation map belonged to a $\langle a \rangle$-basal system (*i.e.,* $(0001)[11\bar{2}0]$), the $\langle c+a \rangle$-edge slip systems do not come out from the analysis, showing values much inferior (order of magnitude of 10) than the other dislocation modes. Nevertheless, the $\langle a \rangle$ and $\langle c+a \rangle$ screw modes appear to be significant, but it should be noted that they include all screw contributions. Furthermore, it was the single case where the $\langle a \rangle$-basal slip system has high density, while the $\langle a \rangle$-pyramidal edge dislocations are the dominant mode for the other datasets. This behavior of the dominant $\langle a \rangle$-pyramidal dislocation mode was shown in distinct works for the Ti64 ($\alpha$+$\beta$ alloy) [64,124] and the Ti-5553 [125] (near-$\beta$ alloy), based on Crystal Plasticity Finite Element Method and on this dislocation mode analysis.

Concerning the $\beta$ phase, the orientation of the grains or the filtering of the data does not seem to change the contribution of the different dislocation modes, where for the edge dislocations, the planes {123} were always the most activated, followed by the {110} and {112} dislocation modes. Even though screw dislocation come out with the highest densities among all possible dislocation modes, it should be reminded that they include screw contributions. Thus, edge dislocations remain the main type in the both phases when gathered.

## *B.5 Discussions*

Besides the case where the orientation map belonged to the synthetic dataset generated based on the $(0001)[11\bar{2}0]$ orientation, the $\langle a \rangle$-pyramidal mode was the most active slip in the $\alpha$ phase. Nevertheless, when the $\alpha$ orientation chosen to the synthetic dataset generated based on the $(0\bar{1}1\bar{1})[1\bar{2}13]$ orientation, the contribution of the different dislocation modes was not significantly changed compared to the experimental datasets. This shows a clear dependency of the grain orientation on the dislocation density contributions of the different dislocation modes for the $\alpha$ phase.

The observed influence of the orientation may be related to the fact that 2D EBSD data does not assess the orientation changes along the normal direction to the sample surface, being considered as uniform. In order to surpass this assumption, 3D EBSD data would be necessary to assess the real dislocation mode that was responsible for the slip in the microstructure.

The intrinsic behavior observed for the $\beta$ phase, where the distribution seems to be independent from the dataset (*i.e.,* orientation or filtering), could be related to the crystallographic structure, where the {123} planes account to half of the possible edge-type dislocations (**Figure 2.21**). This relationship of the crystal structure and the dislocation distribution might also be addressed to the $\alpha$ phase analysis. The $\langle a \rangle$-pyramidal mode having higher densities could be due to the fact that it includes 6 possible slip systems, differently from the basal and prismatic,

which accounts for 3 each (**Figure 2.20**). In this manner, it appears to exist and influence of the crystal symmetry and the multiplicity of each dislocation type. Furthermore, the $\langle c + a \rangle$ edge-type systems (*i.e.*, pyramidal 1st and 2nd) accounting for one order of magnitude lower than the $\langle a \rangle$ ones due to the norm of the Burgers vector. The latter have an inferior value, then minimizes more efficiently the internal energy associated to dislocations and is thus more selected in the optimization algorithm of equation ***(2.14)***.

## *B.6 Conclusions*

Analyzing dislocation densities and their distribution in the different dislocation modes provide crucial information in understanding the active deformation mechanisms and the development of crystallographic texture. One of the most used approaches in the literature is the internal energy minimization one. Nevertheless, the analysis of the most active dislocation modes must be taken with precaution, as it was shown in this work (through experimental and synthetic data) that it is highly dependent on the orientation of the grain (for the $\alpha$ phase), thus on the crystallographic structure. If not taken carefully, this analysis might lead to misinterpretation of the crystal plasticity behavior of the microstructure. 3D EBSD data might be necessary to avoid the assumption that orientations along the normal plane of the 2D EBSD data are considered as uniform, which is likely to be the main reason for the grain orientation dependence of the results of such analysis.

# C. An optimized geometry of double-cone compression test samples for a better control of strain rate

This appendix is the content of the following published paper:

— **M. Brozovic Gariglio**, N. Bozzolo, D. Pino Muñoz, *An Optimized Geometry of Double-Cone Compression Test Samples for a Better Control of Strain Rate*, Metall. Mater. Trans. A Phys. Metall. Mater. Sci. 52 (2021) 4125–4136. doi:10.1007/*s*11661-021-06373-8.

Matheus Brozovic Gariglio, Nathalie Bozzolo, Daniel Pino Muñoz

*Mines ParisTech – PSL University, CEMEF – Centre for Material Forming, CNRS UMR 7635 CS 10207, 1 rue Claude Daunesse, 06904 Sophia Antipolis cedex, France*

ABSTRACT

Double-cone samples offer the great advantage of drastically reducing the number of required tests to correlate between processing parameters and microstructural evolution, as their characteristic geometry results in an equivalent strain gradient after compression. Their usual drawback is a relatively poor control of the equivalent strain rate ($\dot{\varepsilon}$), which varies along the radius and in time. To tackle this drawback, a parametric optimization of the geometry of these double-cone samples for compression tests was performed based on FE simulations. This optimization aims at minimizing the average equivalent strain rate standard deviation in time, among five numerical tracking points placed along the radius. The optimized geometry provides, for all cases tested, an average variation in time within a 10% range regarding the mean equivalent strain rate at the center of the sample. Another advantage is a homogeneous plastic strain path along the radius at the mid-height plane of the double-cone sample, as also throughout the deformation. The optimized geometry was compared with other found in literature and systematically showed improvement in terms of strain rate control, especially at the center of the sample, where the variation for the tested geometries rose up to 50% regarding the average strain rate value, compared to a 10% variation for the optimized geometry at the same conditions.

*Keywords:* Double-cone sample, thermomechanical processing, strain rate, compression test.

## C.1 Introduction

The correlation between the processing parameters (temperature, time, strain level and rate) and microstructural changes is a key element for the manufacture of advanced materials parts, which often involves deformation processing at high temperatures. Double-cone samples have been widely used to study microstructural evolution as a function of the equivalent strain ($\bar{\varepsilon}$) for different alloys, as for the René 65™ nickel based superalloy [126], the 9310 steel [71] and the Ti-6Al-4V alloy [127]. The characteristic geometry of these samples is aimed at generating controlled heterogeneities in the strain field (especially along the radial direction at the mid-height plane after compression), but it also necessarily induces heterogeneities in the strain rate field.

Even though the strain rate is often not a parameter of first order (if not varying over orders of magnitude), it has an impact on the microstructural evolution kinetics, as reported by Ding *et al.* [34], regarding the Ti-6Al-4V alloy, or recently by Nicolaÿ *et al.* [119], concerning the Inconel 718. In most studies, the local value of the strain rate has been disregarded, considering the macroscopic strain rate [72], or the imposed tool velocity [128], to be homogeneous in the whole specimen. Maire [112] pointed out that the strain rate is actually heterogeneous, both along the radial direction at mid-height and during the compression test, preventing to associate the resulting local microstructure with an exact strain rate value. The aim of this work is to define, based on FE simulations, an optimized double-cone sample geometry that provides at best a homogeneous equivalent strain rate ($\dot{\bar{\varepsilon}}$) during the compression test, while preserving a sufficiently wide range of equivalent strain ($\Delta\bar{\varepsilon} \geq 1$) along the radius at the mid-height plane. The optimization method is presented first, then the performance of the proposed optimized geometry is discussed with regards to other geometries found in the literature, and with regards to different deformation conditions (temperatures, alloys, friction coefficients and strain rates). Finally, a comparison of the final dimensions between experimental and simulated double-cone samples for hot deformed titanium alloys is discussed.

## C.2 Finite Element Model

### C.2.1 Initial geometry

The reference geometry used for optimization, represented in **Figure C.1***a*, is the one used in several published works to study the correlation between deformation and microstructural changes on nickel based alloys [126,129], titanium alloys [83] and on the 304L steel [122]. This geometry can be fully described using five parameters: $R_1$, $R_2$, $R_3$, $H_1$ and $H_2$ (**Figure C.1***b*). As shown in the thesis of Vernier [87], the peripheral zone of these compressed samples can hardly be interpreted (very low local deformation levels) and the deformation mode is significantly different from simple compression, therefore this area has simply been removed for the initial geometry optimization ($R_3 = R_1$ in **Figure C.1***c*). This first modification also allows material savings and reduction in the number of dimensions ($R_1$, $R_2$, $H_1$ and $H_2$) to be considered for the parametric optimization.

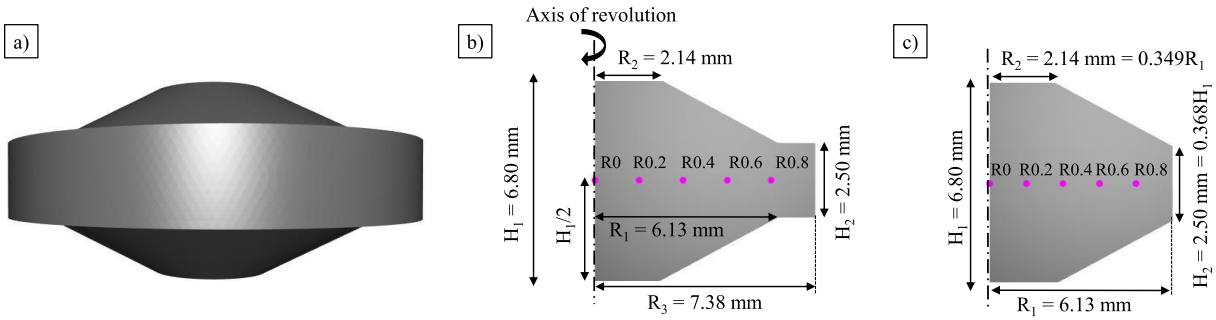



*Figure C.1. a) 3D model of the reference geometry; b) In-diameter half cross section with dimensions of the reference geometry; c) Initial geometry for optimization (In-diameter half cross section with dimensions).*

To analyze the thermomechanical history along the radius of the double-cone samples, five tracking points (sensors) were numerically placed at mid-height: at the center (referred to as R0) and at 20%, 40%, 60% and 80% of the higher radius ($R_1$), referred to as R0.2, R0.4, R0.6 and R0.8, respectively. Placement of tracking points is updated according to the actual $R_1$ value for each new geometry.

In order to analyze the equivalent strain level and rate at each of these tracking point positions, finite element simulations were run. The FE model is presented in the next section.

### *C.2.2 FE simulations*

Compression test simulations were performed with the FORGE® (X64) finite element software. The equivalent strain rate ($\dot{\bar{\varepsilon}}$) and equivalent strain ($\bar{\varepsilon}$) are computed using Equations **(C.1)** and **(C.2)**, respectively:

$$\dot{\bar{\varepsilon}} = \sqrt{\frac{2}{3}\,\dot{\varepsilon}_{ij} : \dot{\varepsilon}_{ij}} \tag{C.1}$$

$$\bar{\varepsilon} = \int_0^t \dot{\bar{\varepsilon}}\, dt \tag{C.2}$$

where $\dot{\varepsilon}_{ij}$ is the plastic strain rate tensor.

The boundary conditions were chosen to numerically reproduce an experimental compression test setup. Two rigid tools were used in the simulation, where the upper tool compresses the sample (placed on top of the lower tool) at a constant velocity ($v$, in $mm/s$) so that the final macroscopic strain ($\varepsilon$) is 0.69 (height reduction by $\Delta h$ = 3.40 $mm$). A constant velocity of the tool leads to a macroscopic strain rate ($\dot{\varepsilon}$) that evolves in time. However, a comparison with a variable tool velocity is provided later in this work (section **C.4.4**), explaining the choice of deforming the double-cone samples at a constant tool velocity regarding the equivalent strain rate. After performing one test simulation, the tool velocity was adjusted ($v = \Delta h/t$) according to the final equivalent strain obtained at the center of the sample ($\bar{\varepsilon}_{R0}$), so that the average equivalent strain rate during the compression ($\langle\dot{\bar{\varepsilon}}_{R0}\rangle$), estimated by Equation **(C.3)**, is as close as possible to the desired value in the following simulations (here 0.1 $s^{-1}$).

$$\langle \dot{\bar{\varepsilon}}_{R0} \rangle = \frac{\bar{\varepsilon}_{R0}}{t} \tag{C.3}$$

The alloy considered in the simulations for sample geometry optimization is the Ti-6Al-4V alloy, with a constitutive behavior law described by a Hansel-Spittel equation [88] and parameters provided by the Aubert & Duval company. Deformation temperature was set to 950°*C*, to be representative of a typical industrial forging of this alloy. To account for the friction between the sample and the tools, when considering high plastic deformation in metal forming, the friction law that is generally used is Tresca [130]. In the case of a Von Mises' plasticity criterion, it is expressed by Equation **(C.4)**:

$$\tau = m\frac{\sigma_y}{\sqrt{3}} \tag{C.4}$$

where $\tau$ is the shear stress at the interface, $m$ is the Tresca friction coefficient and $\sigma_y$ is the flow stress.

The friction coefficient depends on many experimental parameters, as the lubricant used, temperature, strain rate and pressure of the tools. Thus, it was determined by inverse analysis, through the measure of the barreling value, as described by Shahriari *et al.* [131] and Li *et al.* [132], after isothermal hot compression of cylindrical samples (diameter 8 *mm*, length 12 *mm*) of a Ti-6Al-4V alloy supplied by *Timet Savoie*. The value found for the friction coefficient using boron nitride as lubricant was 0.3.

Since FORGE® does not provide an axisymmetric formulation, thus a 3D model has been set up, but, taking advantage of the axial symmetry of the sample, the simulations were carried out on one sixth of each of the geometries to reduce computation time. The mesh was created using *GMSH*® [111]. A mesh and time step convergence analysis were performed to ensure the validity of the numerical study. The selected element size is of 0.23 *mm*, which induced a relative error of 1.8% in terms of the equivalent strain at the center ($\bar{\varepsilon}_{R0}$), with respect to the finest mesh tested (0.09 *mm*). The time step was set to 0.2 seconds for a good compromise between computation time and accuracy of results. It induced a relative error of 3.9% in terms of the average equivalent strain rate standard deviation in time (called ⟨SD⟩ in the following), with respect to the smallest time step tested (0.05 seconds).

Among simulations of different geometries, all parameters mentioned above (temperature, friction coefficient, element size, time step, tool velocity) where kept constant to isolate the effect of sample geometry on the optimization results.

## *C.3 Methodology and resulting optimized geometry*

The basic principle of the applied optimization procedure is to minimize the average equivalent strain rate standard deviation in time (⟨SD⟩) of each tracking point placed at mid-height along the radius, by modifying the double-cone sample dimensions. The *SD* and its average, are defined by Equations **(C.5)** and **(C.6)**, respectively:

$$SD = \sqrt{\frac{\sum_{i=1}^{N}(\dot{\bar{\varepsilon}}_i - \langle \dot{\bar{\varepsilon}} \rangle)^2}{N-1}} \tag{C.5}$$

$$\langle SD \rangle = \frac{\sum_{j=1}^{s} SD_j}{s} \tag{C.6}$$

where $N$, the number of calculation steps, is fixed and related to the tool velocity, $\langle \dot{\bar{\varepsilon}} \rangle$ is the average equivalent strain rate throughout the compression test at each tracking point, and $s$ is the number of tracking points ($s$=5 as defined in section **C.2.1**).

The parametric optimization was performed in two steps, first manually, through a design of numerical experiments, then automatically, using FORGE®, following the recommendations provided in the software documentation [133]. Through the assumption that these geometries can be fully described by setting an arbitrary $H_1$ hence applying different ratios to obtain $R_1$, $R_2$ and $H_2$, the number of optimization parameters can be reduced to three ($R_1/H_1$, $R_2/R_1$ and $H_2/H_1$). This is valid since the constitutive law used does not include any length scale. The preliminary manual step consists in setting different values for the ratios $R_2/R_1$ and $H_2/H_1$ ($R_1$ and $H_1$ fixed), and analyzing the evolution of ⟨SD⟩ to determine which geometry minimized it. This first manual step aims at targeting an improved starting geometry for the automatic step (where the final ratio $R_1/H_1$ will be optimized) and drastically reduces the number of simulations in this latter step of the optimization process.

Since the goal of this kind of geometry is to induce different levels of strain along the radius and allow in-depth analysis of the strain level effect in the microstructure, an additional constraint was considered. This constraint consists of having a minimum range of strain of 1.0 between tracking points R0 and R0.8 ($\bar{\varepsilon}_{R0.8} - \bar{\varepsilon}_{R0} \geq 1.0$). When the achieved strain range did not respect this constraint, the geometry was discarded. Another constraint imposed is related to the geometry dimensions, values under 1 *mm* were not accepted, for the sake of further machining feasibility or simplicity.

### *C.3.1 Manual geometry improvement*

The design of numerical experiments for the manual geometry improvement was built in two successive steps as explained below. **Table C.1** provides the ⟨SD⟩ values obtained for all the fourteen manually defined and tested geometries.

| ⟨SD⟩ ($s^{-1}$) | | $R_2/R_1$ | | | | |
|---|---|---|---|---|---|---|
| | | 0.250 | *0.349* | 0.500 | 0.625 | 0.750 |
| **$H_2/H_1$** | 0.150 | - | - | 0.013 | 0.012 | ~~0.012~~ |
| | 0.250 | *0.020* | *0.016* | *0.014* | 0.013 | ~~0.012~~ |
| | *0.368* | *0.021* | *0.017* | *0.015* | - | - |
| | 0.500 | *0.023* | *0.019* | *0.016* | - | - |

*Table C.1. Results in terms of ⟨SD⟩ values of the two successive steps in the design of numerical experiments. The initial geometry value (bold) is part of the first step (italic), non-valid values regarding additional constraints are crossed and the finally retained improved result is in upright and bold font.*

In the first step (italic font in **Table C.1**), nine geometries were analyzed (**Figure C.2**). The ratios of $R_2/R_1$ = 0.349 and $H_2/H_1$ = 0.368 correspond to the initial geometry (italic bold), while lower and higher arbitrary values (0.250 and 0.500) were added to analyze the ⟨SD⟩ minimization tendencies. ⟨SD⟩ was minimized as $R_2/R_1$ increased and $H_2/H_1$ decreased, so the geometry that led to the

smallest ⟨SD⟩ value was the one when $R_2/R_1 = 0.500$ and $H_2/H_1 = 0.250$ (⟨SD⟩ = 0.014 $s^{-1}$).

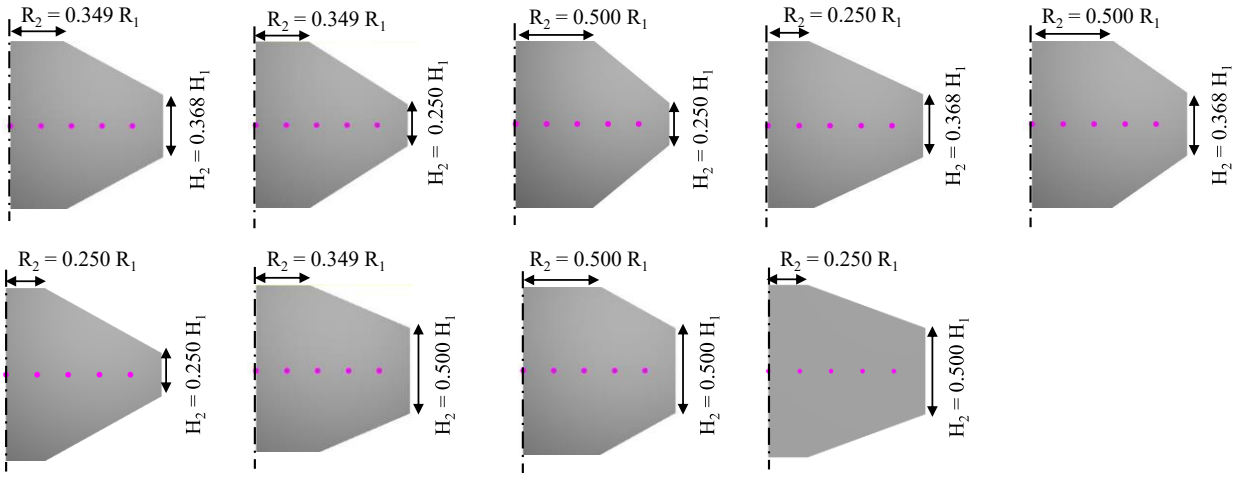



*Figure C.2. Geometries tested in the first step of the design of numerical experiments (symmetrical representation with dimensions), where $R_1$ and $H_1$ are fixed and equal to 6.13 and 6.80 mm respectively, according to* ***Figure C.1****c.*

The values of $R_2/R_1 = 0.625$ and 0.750 and $H_2/H_1 = 0.150$ were then included in a second step of the design of numerical experiments (upright font in **Table C.1**). It is worth mentioning that the value of $H_2/H_1 = 0.150$ was chosen to keep fulfilled the constraint of a minimum 1 *mm* dimension ($H_2$ = 1.02 *mm*), for machining feasibility matter, as mentioned previously. Smallest ⟨SD⟩ values were obtained when $R_2/R_1$ = 0.750, but the imposed constraint of having an acceptably large equivalent strain range along the radius ($\bar{\varepsilon}_{R0.8} - \bar{\varepsilon}_{R0} \geq 1.0$) was not satisfied, as its value in both cases was approximately 0.7. Thus, these results are not valid for this optimization (crossed in **Table C.1**). Hence, the best geometry out of these all 14 tested ones (upright and bold font in **Table C.1** and shown in **Figure C.3**), which leads to the minimum ⟨SD⟩ value (= 0.012 $s^{-1}$), and fulfills the two other constraints is that with $R_2/R_1 = 0.625$ and $H_2/H_1 = 0.150$.

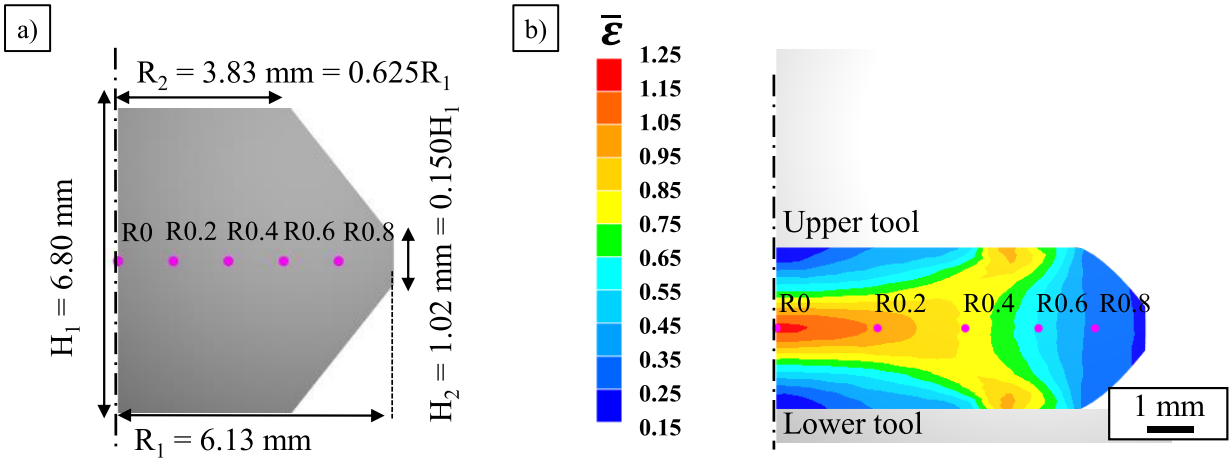



*Figure C.3. Improved geometry resulting from the design of numerical experiments of* ***Table C.1****: a) In-diameter half cross section with dimensions; b) Equivalent plastic strain map ($\bar{\varepsilon}$) after compression.*

### *C.3.2 Automatic geometry optimization*

After the improved starting geometry was found in the manual step, the automatic optimization aimed at finding the optimal ratio $R_1/H_1$. While fixing $H_1$ and the best ratio $R_2/R_1 = 0.625$ previously found, the bounds for the automatic optimization were arbitrarily set, but defining a wide range, by applying a proportionality law regarding the radial direction (*i.e.,* radii scale) from 0.500 to 1.500. Thus, the software varies the larger radius of the starting geometry between $0.500R_1$ (3.065 *mm*) and $1.500R_1$ (9.195 *mm*), simultaneously with the variation of its smaller radius between $0.500R_2$ (1.915 *mm*) and $1.500R_2$ (5.745 *mm*), as shown in **Figure C.4**. The single parameter for this automatic optimization is the radii scale (*i.e.,* the $R_1/H_1$ ratio), thus simplifying this step.

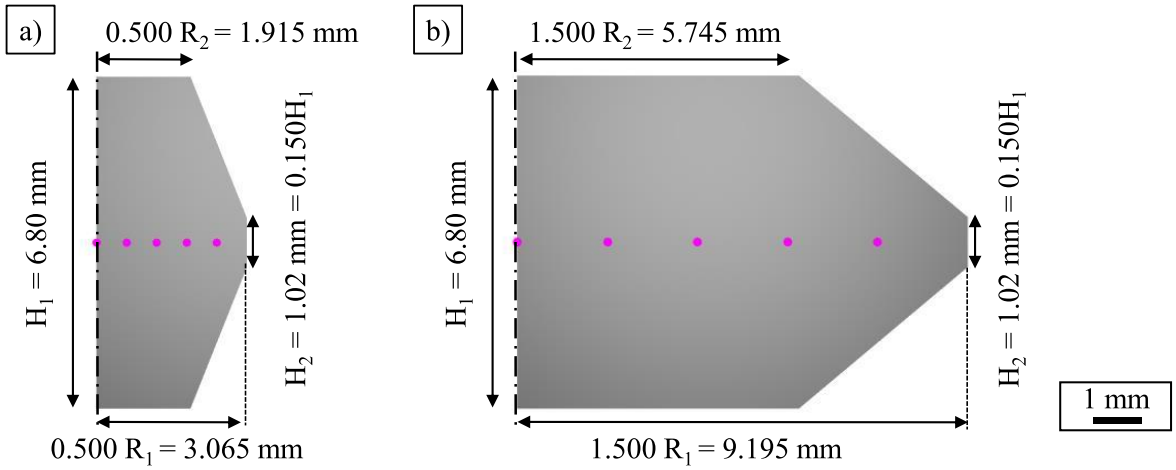



*Figure C.4. In-diameter half cross section of the two boundary geometries chosen for the automatic optimization: a) Lower bound (0.500 $R_1$); b) Upper bound (1.500 $R_1$).*

The algorithm used in the software to find the optimal geometry is based on genetic methods [133]. The ⟨SD⟩ was calculated in this step by implementing Equations **(C.5)** and **(C.6)** in the optimization toolbox. The total number of simulations chosen to minimize ⟨SD⟩ was set to 24, being a good compromise between the convergence of results and computation time. **Figure C.5** shows the convergence of results after the automatic simulations performed between the chosen bounds, with the minimization of ⟨SD⟩ at 0.011 $s^{-1}$, when the radii scale was set at 0.777 ($R_1/H_1 = 0.700$).

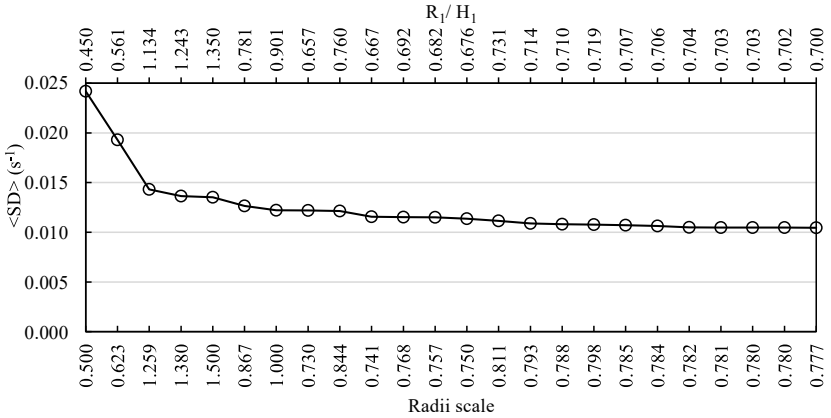



*Figure C.5. Result of automatic optimization using FORGE® software after 24 simulations.*

The final optimized geometry (**Figure C.6**) was then obtained (with the dimensions rounded to two decimal places, for machining accuracy consistency). The optimal parameters of the double-cone geometry are then $R_1/H_1 = 0.700$, $R_2/R_1 = 0.625$ and $H_2/H_1 = 0.150$. It is worth mentioning that homothetic copies of this geometry can be done by setting an arbitrary $H_1$ hence applying the ratios mentioned above to obtain $R_1$, $R_2$ and $H_2$. However, the equivalent strain field must be verified regarding possible friction effects.

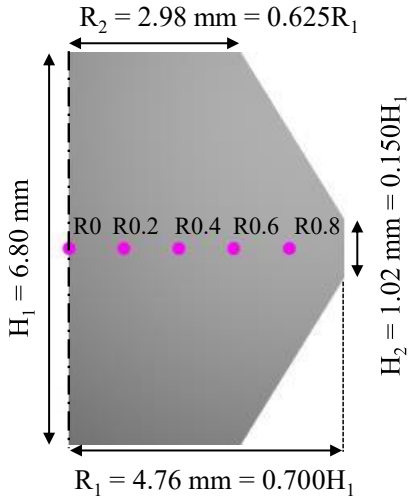



*Figure C.6. Final optimized geometry (In-diameter half cross section with dimensions).*

## *C.4 Evaluation of the new geometry*

### *C.4.1 Comparison between the reference and the optimized geometries*

The behavior of the reference (**Figure C.1***b*) and the optimized (**Figure C.6**) geometries were compared to better analyze the impact of the optimization. **Figure C.7** shows the equivalent plastic strain maps ($\bar{\varepsilon}$) for both geometries after compression to half height (3.40 *mm*) at a constant tool velocity of 0.26 *mm/s* (13 seconds, for $\langle \dot{\bar{\varepsilon}}_{R0} \rangle$ equal to 0.1 $s^{-1}$), as shown in Equation **(C.3)**.

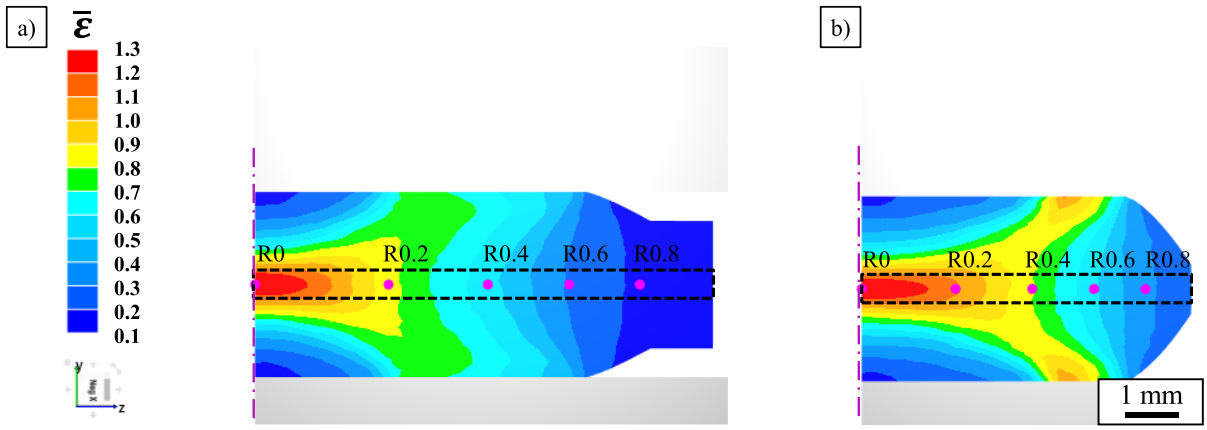



*Figure C.7. Equivalent strain map ($\bar{\varepsilon}$) for: a) the reference geometry after compression; b) the optimized geometry after compression; Both with their analysis zones along the radial direction at mid-height (dotted black rectangles).*

The optimized geometry covers a fairly wide range of equivalent strain, between 0.25 and 1.31 along the radius (fulfilling the constraint $\bar{\varepsilon}_{R0.8} - \bar{\varepsilon}_{R0} \geq 1.0$). Higher or lower levels of deformation can be achieved in the sample by deforming it more or less, respectively. The evolution of the equivalent strain during the test is quasi linear at each tracking point position for both geometries, as shown in **Figure C.8**.

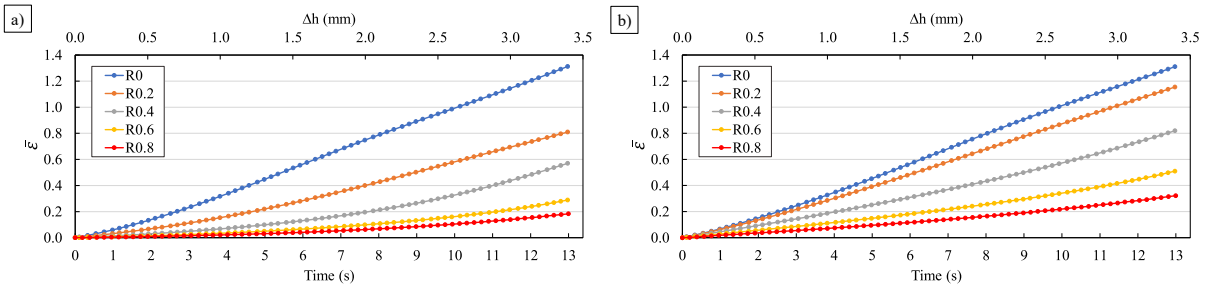



*Figure C.8. Evolution of the $\bar{\varepsilon}$ at tracking point positions R0, R0.2, R0.4, R0.6 and R0.8 during the compression test within a) the reference geometry; b) the optimized geometry.*

By analyzing the evolution of the equivalent strain rate ($\dot{\bar{\varepsilon}}$) in time at each tracking point position (**Figure C.9**), it is evident that the optimized geometry leads to a more homogeneous field during the compression test.

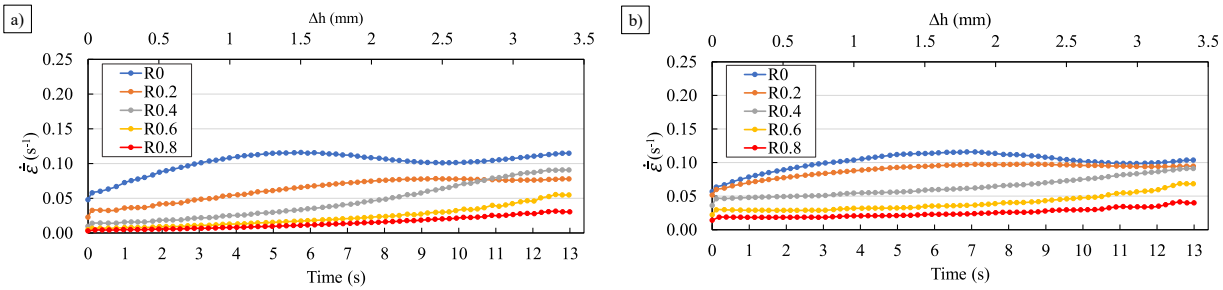



*Figure C.9. Evolution of the equivalent strain rates ($\dot{\bar{\varepsilon}}$) at tracking point positions R0, R0.2, R0.4, R0.6 and R0.8 during the compression test within a) the reference geometry; b) the optimized geometry.*

This difference is quantified in **Table C.2**, with the calculation of the standard deviation of $\dot{\bar{\varepsilon}}$, for the five tracking points separately ($SD_j$) and their average ($\langle SD \rangle$). The optimized geometry provides a stable evolution of $\dot{\bar{\varepsilon}}$ during the compression test, homogenizing the $SD$ values at 0.01 $s^{-1}$ for each tracking point position. The most remarkable difference can be seen for the tracking point at R0.4, where the $SD$ decreased from 0.03 (reference) to 0.01 $s^{-1}$ (optimized). The $\langle SD \rangle$ was also reduced from 0.02 to 0.01 $s^{-1}$ after the geometry optimization.

| Geometry | Variables ($s^{-1}$) | R0 | R0.2 | R0.4 | R0.6 | R0.8 | $\langle SD \rangle$ ($s^{-1}$) |
|---|---|---|---|---|---|---|---|
| Reference | $\langle \dot{\bar{\varepsilon}} \rangle$ | 0.10 | 0.06 | 0.04 | 0.02 | 0.01 | - |
| | $SD$ | 0.02 | 0.02 | 0.03 | 0.01 | 0.01 | 0.02 |
| Optimized | $\langle \dot{\bar{\varepsilon}} \rangle$ | 0.10 | 0.09 | 0.06 | 0.04 | 0.03 | - |
| | $SD$ | 0.01 | 0.01 | 0.01 | 0.01 | 0.01 | 0.01 |

*Table C.2. Average equivalent strain rates ($\langle \dot{\bar{\varepsilon}} \rangle$) with their respective standard deviation in time (SD) at each tracking point position, and the average value ($\langle SD \rangle$), for the reference and the optimized geometries.*

The evolution of the plastic deformation has first been locally analyzed in terms of the equivalent plastic strain. However, it is important to acknowledge that the plastic strain is a tensor that expresses the strain path. Two ratios between plastic strain tensor components ($\varepsilon_{zz}/\varepsilon_{yy}$ and $\varepsilon_{xx}/\varepsilon_{yy}$) were also analyzed at each tracking point position. In fact, the proposed optimized geometry leads to strain paths at the different tracking point positions that are much more stable compared to those obtained in the original geometry, especially for the tracking points at R0.6 and R0.8 (see **Figure C.10**). In this manner, the plastic deformation, being related to the strain path of the material [134], is more homogeneous both in space and time, revealing another advantage of the new geometry.

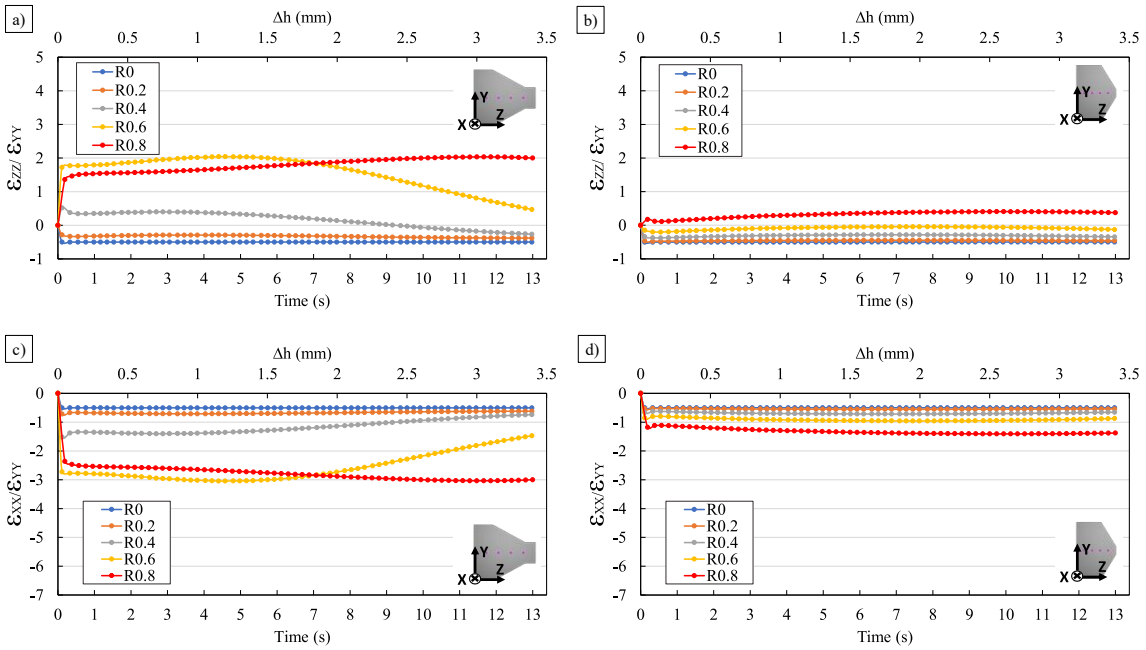



*Figure C.10. Evolution of plastic strain tensor component ratios at the different tracking point positions and for the two geometries: a) $\varepsilon_{zz}/\varepsilon_{yy}$ of the reference geometry; b) $\varepsilon_{zz}/\varepsilon_{yy}$ of the optimized geometry; c) $\varepsilon_{xx}/\varepsilon_{yy}$ of the reference geometry; d) $\varepsilon_{xx}/\varepsilon_{yy}$ of the optimized geometry.*

### *C.4.2 Comparison between the optimized geometry and other geometries found in the literature*

It was shown in **Table C.2** that the optimized geometry provided a more homogenous strain rate for the double-cone specimen, when compared to a reference geometry that was often implemented in other works [83,122,126,129]. Yet it was worth to analyze also other geometries that can be found in the literature and compare them to the one proposed in this work. Aoki *et al.* [73] use a double-cone sample ($R_1/H_1$ = 0.571, $R_2/R_1$ = 0.375, $H_2/H_1$ = 0.214) to describe the influence of hot-working conditions on grain growth of superalloy 718, while Wang *et al.* [74] employ, for the same alloy, another geometry ($R_1/H_1$ = 0.500, $R_2/R_1$ = 0.300, $H_2/H_1$ = 0.400) to analyze microstructure heredity during hot-working. Furthermore, a unique double-cone geometry ($R_1/H_1$ = 0.627, $R_2/R_1$ = 0.253, $H_2/H_1$ = 0.253) was implemented in four distinct works to correlate microstructure evolution and thermo-mechanical processing parameters. Weston and Jackson [75] use this geometry to evaluate the performance of a new processing route for forged

components, whilst Semiatin *et al.* [76] and Weaver and Semiatin [72] employed it to describe nickel based superalloy recrystallization behavior. Finally, Kozmel *et al.* [71] report, within the same geometry, the kinetics of sub-micron grain size refinement in 9310 steel.

Those three other double-cone geometries were thus tested with the exact same parameters described in section **C.2.2**, throughout the optimization procedure, to isolate the effect of the geometry in the equivalent strain rate evolution in time. Tracking points positions were adapted according to each geometry, with respect to their radius $R_1$.

| Geometry parameters | Variables ($s^{-1}$) | R0 | R0.2 | R0.4 | R0.6 | R0.8 | ⟨SD⟩ ($s^{-1}$) | References |
|---|---|---|---|---|---|---|---|---|
| $R_1/H_1$ = 0.571 | $\langle\dot{\varepsilon}\rangle$ | 0.10 | 0.08 | 0.05 | 0.03 | 0.02 | - | [73] |
| $R_2/R_1$ = 0.375 | $SD$ | 0.04 | 0.03 | 0.02 | 0.01 | 0.01 | 0.02 | |
| $H_2/H_1$ = 0.214 | | | | | | | | |
| $R_1/H_1$ = 0.500 | $\langle\dot{\varepsilon}\rangle$ | 0.10 | 0.08 | 0.05 | 0.03 | 0.02 | - | [74] |
| $R_2/R_1$ = 0.300 | $SD$ | 0.05 | 0.05 | 0.03 | 0.02 | 0.02 | 0.03 | |
| $H_2/H_1$ = 0.400 | | | | | | | | |
| $R_1/H_1$ = 0.627 | $\langle\dot{\varepsilon}\rangle$ | 0.10 | 0.08 | 0.05 | 0.03 | 0.02 | - | [71,72,75, |
| $R_2/R_1$ = 0.253 | $SD$ | 0.05 | 0.04 | 0.03 | 0.02 | 0.01 | 0.03 | 76] |
| $H_2/H_1$ = 0.253 | | | | | | | | |
| $R_1/H_1$ = 0.700 | $\langle\dot{\varepsilon}\rangle$ | 0.10 | 0.09 | 0.06 | 0.04 | 0.03 | - | This work |
| $R_2/R_1$ = 0.625 | $SD$ | 0.01 | 0.01 | 0.01 | 0.01 | 0.01 | 0.01 | |
| $H_2/H_1$ = 0.150 | | | | | | | | |

*Table C.3. Average equivalent strain rates ($\langle\dot{\varepsilon}\rangle$) with their respective standard deviations in time (SD), at each tracking point position, and the average value ($\langle SD\rangle$), regarding three geometries used in six distinct works.*

Comparing the results of the three tested geometries found in the literature with those obtained with the optimized geometry proposed in this work (**Table C.3**), it is clear that the latter provides an improved control of the equivalent strain rate along the radius and during the compression test. The $SD_{R0}$ values (at the specimen center) for these tested geometries are especially heterogeneous in time, showing a variation up to a 50% range regarding the average value ($\langle\dot{\varepsilon}_{R0}\rangle$), compared to a 10% variation for the optimized geometry at the same conditions.

### *C.4.3 Comparison between the reference and the optimized geometries for different alloys and conditions*

It was shown above that the optimized geometry allows to obtain a better control of the equivalent strain rate (**Table C.2**) when considering deformation of the Ti-6Al-4V alloy at 950°*C*, with a friction coefficient equal to 0.3. To check if the optimized geometry also allows this better control in other conditions, simulations have been performed and compared between both the reference and the optimized geometries. A wide range of conditions was applied, varying the alloy, the friction coefficient, the temperatures and the average equivalent strain rates at the center ($\langle\dot{\varepsilon}_{R0}\rangle$), by changing the constant tool velocity, as shown in Equation **(C.3)**.

The tested alloys and temperatures have been chosen to assess a possible influence of the flow stress behavior notably with regards to work-hardening. The behavior laws for the steels tested (304 and 316L) and for the Ti-6Al-4V at room temperature (25°*C*) where obtained from the *JMATPRO*® software. The ones for the Ti-6Al-4V and the Ti-10V-2Fe-3Al at their typical hot-forging temperature

ranges were obtained from a Hansel-Spittel equation provided by Aubert & Duval. Those steels where chosen as they have a much higher hardening behavior when compared to titanium alloys, so the objective was to check whether the optimized geometry was valuable also for these cases. **Figure C.11** shows the differences between titanium and steel alloys hardening behavior at room temperature, as also the softening behavior of the Ti-6Al-4V and the Ti-10V-2Fe-3Al at high temperatures.

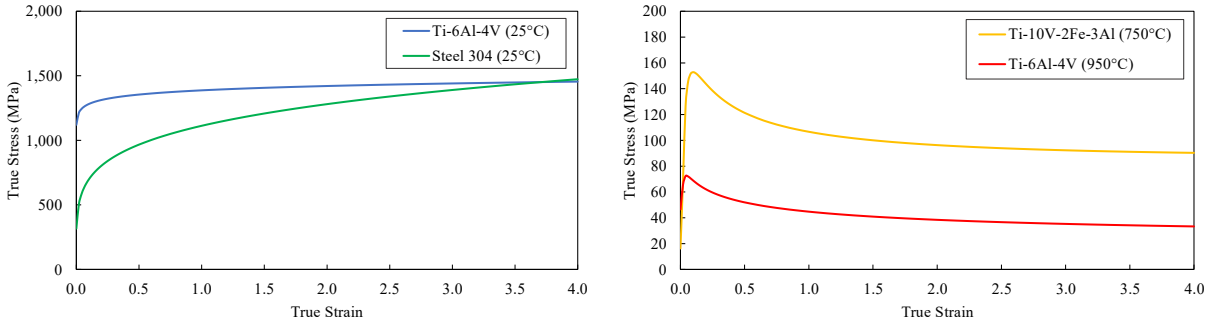



*Figure C.11. True stress vs True strain curves showing the differences in the behavior laws depending on the alloy and temperature for some of the considered cases.*

By analyzing the summary of the performed comparisons (**Table C.4**), the optimized geometry appears to provide, for all cases tested (different temperatures, alloys, friction coefficients and strain rates), an average variation in time within a 10% range regarding the average equivalent strain rate at the center of the sample ($\langle\dot{\bar{\varepsilon}}_{R0}\rangle$). Thus, providing a better control of the equivalent strain rate when compared to the reference geometry.

| Friction coefficient | T (°C) | Alloy | $\langle\dot{\bar{\varepsilon}}_{R0}\rangle$ ($s^{-1}$) | $\langle SD\rangle$ ($s^{-1}$) | |
|---|---|---|---|---|---|
| | | | | Reference | Optimized |
| 0.3 | 950 | Ti-6Al-4V | 0.010 | 0.002 | 0.001 |
| 0.3 | 950 | Ti-6Al-4V | 0.10 | 0.02 | 0.01 |
| 0.3 | 950 | Ti-6Al-4V | 1.0 | 0.2 | 0.1 |
| 0.1 | 950 | Ti-6Al-4V | 0.10 | 0.02 | 0.01 |
| 0.4 | 950 | Ti-6Al-4V | 0.10 | 0.02 | 0.01 |
| 0.8 | 950 | Ti-6Al-4V | 0.10 | 0.02 | 0.01 |
| 0.3 | 750 | Ti-10V-2Fe-3Al | 0.10 | 0.02 | 0.01 |
| 0.4 | 900 | Steel 316L | 0.10 | 0.02 | 0.01 |
| 0.4 | 25 | Steel 304 | 0.10 | 0.02 | 0.01 |
| 0.4 | 25 | Ti-6Al-4V | 0.10 | 0.02 | 0.01 |

*Table C.4. Summary of the comparison between the reference and the optimized geometries for different conditions, showing their average equivalent strain rates at the center ($\langle\dot{\bar{\varepsilon}}_{R0}\rangle$) with their respective average standard deviations in time ($\langle SD\rangle$).*

The new geometry turned out to be significantly versatile for the different tested conditions. However, before using it for a new material or condition (*e.g.*, much higher strain rates or temperatures, or compression without lubricant), it is advisable to analyze a simulation of the test to check the equivalent strain level and rate throughout the specimen radius, and, if necessary, customize the geometry to suit the current case. With the method being set and described in this work, the optimization of a new geometry is rather straightforward.

### *C.4.4 Variable tool velocity verification*

Further simulations, with the same parameters as presented in section **C.2.2**, were performed to check the validity of the new geometry for the case where the upper tool compresses the sample at a variable tool velocity. This velocity is calculated to obtain a constant macroscopic strain rate (in a cylindrical sample) during compression, by taking the sample height reduction into account, as shown in Equation **(C.7)**.

$$v(t) = -h_0 \cdot \dot{\varepsilon} \cdot exp(\dot{\varepsilon} \cdot t) \qquad \text{(C.7)}$$

where $h_0$ is the initial height of the sample and $\dot{\varepsilon}$ is the constant macroscopic strain rate ($\dot{\varepsilon} < 0$).

The results (**Table C.5**) show that the optimized geometry also provides a better equivalent strain rate homogeneity throughout the test, decreasing the ⟨SD⟩ from 0.02 to 0.01 $s^{-1}$, for a macroscopic strain rate of 0.1 $s^{-1}$. Nevertheless, at tracking points placed at positions R0 and R0.2, the local standard deviation is not changed, remaining slightly elevated. Therefore, to obtain a very homogeneous equivalent strain rate, throughout the compression test of double-cone samples, all along their radius, it is better recommended to perform it at a constant tool velocity.

| Geometry | Variables ($s^{-1}$) | R0 | R0.2 | R0.4 | R0.6 | R0.8 | ⟨SD⟩ ($s^{-1}$) |
|---|---|---|---|---|---|---|---|
| Reference | $\langle\dot{\varepsilon}\rangle$ | 0.19 | 0.12 | 0.08 | 0.04 | 0.03 | - |
| | $SD$ | 0.03 | 0.02 | 0.03 | 0.02 | 0.01 | 0.02 |
| Optimized | $\langle\dot{\varepsilon}\rangle$ | 0.19 | 0.17 | 0.11 | 0.07 | 0.05 | - |
| | $SD$ | 0.03 | 0.02 | 0.01 | 0.01 | 0.01 | 0.01 |

*Table C.5. Average equivalent strain rates ($\langle\dot{\varepsilon}\rangle$) with their respective standard deviation in time (SD), at each tracking point position, and the average value (⟨SD⟩), regarding compression test simulation with a tool velocity varying to achieve a constant macroscopic strain rate (in a cylindrical sample).*

For the sake of comparison with the double-cone geometry, a simulation of a classic cylindrical compression sample (diameter 8 $mm$, length 12 $mm$) has also been made to analyze the equivalent strain rate evolution at its center (R0), throughout a test at a macroscopic strain rate of 0.1 $s^{-1}$, to a macroscopic strain of 0.70 (~50% height reduction). **Figure C.12** reveals that even in the case of a compression of a simple cylindrical sample, the nominal strain rate of 0.1 $s^{-1}$ is not respected at the center, where the $\dot{\bar{\varepsilon}}_{R0}$ presented an evolution during the compression test, being equal to $0.17 \pm 0.02$ $s^{-1}$. This evolution is mainly due to the friction between the samples and the tools [135]. Thus, the optimized geometry, deformed at a constant tool velocity, is better than the cylindrical sample at obtaining a homogeneous equivalent strain rate throughout the compression test. Nevertheless, it is important to mention that the advantage of the cylindrical sample is the possible identification of a constitutive law through the stress-strain curves obtained from the compression test.

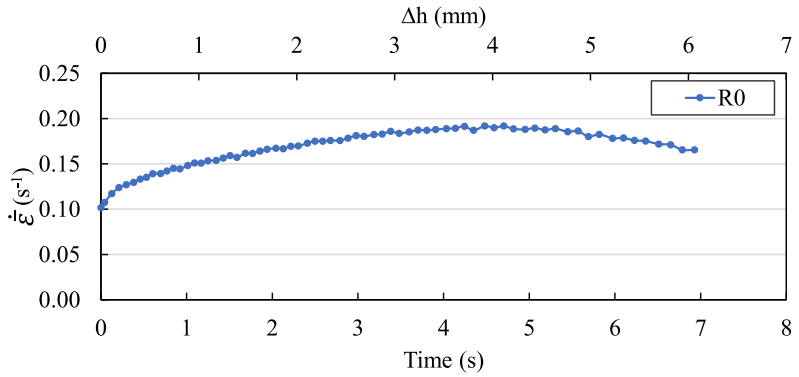



*Figure C.12. Evolution of the equivalent strain rate ($\dot{\bar{\varepsilon}}$) at the center of a cylindrical sample (R0) throughout the compression test at a variable tool velocity.*

### *C.4.5 Experimental verification for hot-deformed titanium alloys*

The validity of the performed simulations has also been double-checked by comparing the simulated shape evolution of the double-cone samples with that of real hot-compression tests. For that purpose, double-cone samples were machined from two different billets of titanium alloys (Ti-6Al-4V and Ti-10V-2Fe-3Al) supplied by *Timet Savoie* and *Aubert & Duval*, with the dimensions of the optimized geometry (**Figure C.6**). Hot compression tests were conducted with the same thermomechanical parameters used in the simulations. Deformation temperatures were set at 950°*C* and 750°*C* for the Ti-6Al-4V and the Ti-10V-2Fe-3Al samples, respectively. These temperatures were chosen to be 50°*C* below the $\alpha + \beta$ / $\beta$ phase transus temperature for each material. The Ti-6Al-4V was also deformed at 750°*C* to evaluate this alloy deformation behavior at a lower temperature. Samples were pre-heated for one hour to ensure thermochemical phase equilibrium and temperature homogeneity. Constant tool velocities of 0.026 $mm/s$ and 0.26 $mm/s$ were applied, compressing the samples to half of their initial height ($\Delta h$ = 3.40 $mm$) and boron nitride was used as lubricant, the same one used for the choice of the friction coefficient value implemented in the simulations. **Figure C.13** shows a schematic of the thermomechanical path. Deformed samples were then cut in half through their diameter, images of the final geometry profile were obtained with a binocular magnifier and measured using the *ImageJ*® software.

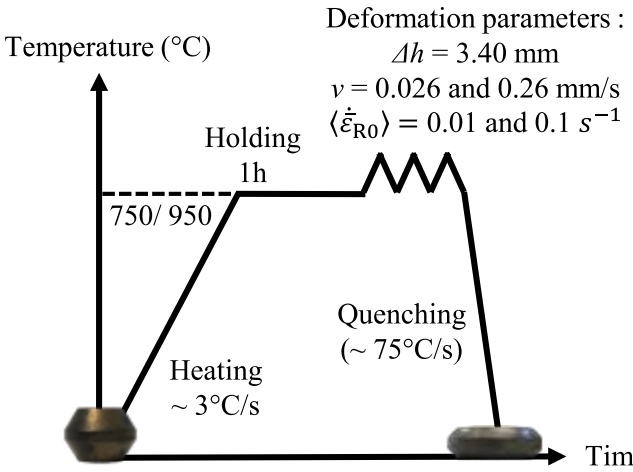



*Figure C.13. Thermomechanical path for the compression of the double-cone samples.*

Dimensions of the real deformed samples and the ones obtained through simulation are compared in **Table C.6**.

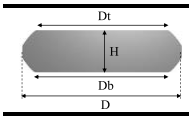
|  | Alloy | T (°C) | $\langle\dot{\bar{\varepsilon}}_{R0}\rangle$ ($s^{-1}$) | Dimensions (*mm*) | | | |
|---|---|---|---|---|---|---|---|
| | | | | H | D | Dt | Db |
| Experimental | Ti-6Al-4V | 950 | 0.1 | 3.44 | 12.23 | 9.56 | 9.55 |
| | Ti-10V-2Fe-3Al | 750 | 0.1 | 3.43 | 12.04 | 9.71 | 9.63 |
| | Ti-6Al-4V | 750 | 0.1 | 3.44 | 11.64 | 9.41 | 9.40 |
| | Ti-6Al-4V | 950 | 0.01 | 3.44 | 12.13 | 9.77 | 9.61 |
| | Ti-10V-2Fe-3Al | 750 | 0.01 | 3.39 | 12.00 | 9.62 | 9.58 |
| Simulation | Ti-6Al-4V | 950 | 0.1 | 3.41 | 12.12 | 9.60 | 9.58 |
| | Ti-10V-2Fe-3Al | 750 | 0.1 | 3.41 | 12.12 | 9.62 | 9.61 |
| | Ti-6Al-4V | 750 | 0.1 | 3.41 | 12.12 | 9.48 | 9.46 |
| | Ti-6Al-4V | 950 | 0.01 | 3.41 | 12.12 | 9.68 | 9.66 |
| | Ti-10V-2Fe-3Al | 750 | 0.01 | 3.41 | 12.12 | 9.70 | 9.68 |
| Relative error (%) | Ti-6Al-4V | 950 | 0.1 | 0.95 | 0.85 | 0.39 | 0.34 |
| | Ti-10V-2Fe-3Al | 750 | 0.1 | 0.63 | 0.67 | 0.96 | 0.17 |
| | Ti-6Al-4V | 750 | 0.1 | 0.95 | 3.97 | 0.80 | 0.63 |
| | Ti-6Al-4V | 950 | 0.01 | 0.95 | 0.09 | 0.95 | 0.56 |
| | Ti-10V-2Fe-3Al | 750 | 0.01 | 0.48 | 0.98 | 0.89 | 0.95 |

*Table C.6. Comparison of the final dimensions between experimental and simulation results.*

The relative errors between the simulated final shapes and the deformed samples were consistently below 1% for four of the five tested cases. Thus, the choice of the former parameters, especially the friction coefficient and constitutive laws, are satisfactory, also proving that these latter are representative of the materials. A comparison between the simulated and experimental deformed shapes of the Ti-10V-2Fe-3Al alloy deformed at 0.1 $s^{-1}$ is shown in **Figure C.14**, showing that both shapes are highly equivalent.

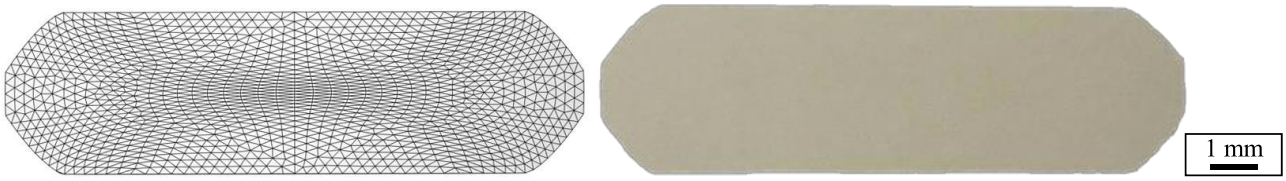



*Figure C.14. Comparison between the simulated (left) and experimental (right) deformed shapes of the Ti-10V-2Fe-3Al alloy deformed at 750°C and 0.1$s^{-1}$.*

The only sample where there was a slight difference (4%) between one of the simulated and experimental dimensions was the Ti-6Al-4V deformed at 750°*C*. This variation can be explained through the plastic anisotropy of titanium alloys [136], that was not considered in the behavior laws. The simulated final shape of this sample had indeed a slightly elliptical form (shape factor of 1.08), suggesting an anisotropic effect for the present tested sample. Nevertheless, the relative error is yet only 4%, thus not likely to have an important impact in the effective strain levels and rates. In such case the correlation between simulation and experiments could be improved by using a suitable anisotropic behavior law in the FE model.

## C.5 Conclusions

An optimized geometry for compression test double-cone samples was defined based on FE simulations, starting from a geometry formerly used in the literature, and was also compared with others that were applied in several works. The main results are summarized as follows.

The optimized geometry is better than all those found in the literature that have been tested, providing a more homogeneous equivalent strain rate ($\dot{\bar{\varepsilon}}$) throughout the compression test and along the radius at the mid-height of the sample. This improvement is particularly true at the center of the sample, where the variation for the tested geometries rose to a 50% range regarding the average value, compared to a 10% variation for the optimized geometry at the same conditions. When compared to the chosen reference geometry, it also provided a more stable strain path both in space and time. Besides, it is simpler from a machining point of view and requires less material than the reference one.

Optimization was performed using mechanical behavior data of Ti-6Al-4V alloy at 950°*C*, yet the optimized geometry proved to be suitable for other alloys and conditions, including cold and hot deformation, varied friction coefficient values and a two order of magnitude range regarding the local strain rate. In the requirement to design custom testing samples for a particular application, the methodology applied and detailed in this work could also be applied.

When the identification of a constitutive behavior law through stress-strain curves is dispensable, the optimized geometry is also recommended instead of the classic cylindrical sample. However, it is advisable to perform the compression test at a constant tool velocity, as it was shown to provide a more stable evolution of the local strain rate in time.

Thanks to the improved equivalent strain rate control and plastic strain path, this optimized double-cone sample geometry opens the possibility of a more accurate correlation between the processing parameters and microstructural evolutions.

# D. Hansel-Spittel smoothing parameters for the rheological analysis

The Hansel-Spittel law has been used in this work, not to properly describe the constitutive behavior of the studied alloys and their $\alpha$ and $\beta$ phases, yet to smooth experimental stress-strain curves, with the parameters given below in Table D.1 ($\alpha$ phase) and Table D.2 ($\beta$ phase).

| Alpha | | | | | | | | | | |
|---|---|---|---|---|---|---|---|---|---|---|
| Microstructure | A | m1 | m2 | m3 | m4 | m5 | m7 | m8 | m9 | σy0 |
| Ti64 Equiaxed | 19564 | -0.0061 | -0.1379 | -0.3783 | -0.0065 | 0.0003 | -0.0257 | 0.0000 | 0.0091 | 0 |
| Ti64 Lamellar | 403 | -0.0032 | -0.1496 | -0.9134 | -0.0033 | -0.0002 | -0.0109 | 0.0002 | 0.0075 | 23 |
| Ti1023 Equiaxed | 17159 | -0.0022 | -0.2611 | 0.0052 | -0.0147 | -0.0004 | 0.0347 | 0.0013 | -0.0091 | 34 |
| Ti1023 Lamellar | 48004 | 0.0165 | -0.1052 | -2.4448 | -0.0033 | -0.0013 | -0.2455 | 0.0126 | -0.1616 | 30 |

*Table D.1. α-phase Hansel-Spittel smoothing parameters used for the smoothing of the individual stresses obtained from the ROM from experimental curves.*

| Beta | | | | | | | | | | |
|---|---|---|---|---|---|---|---|---|---|---|
| Microstructure | A | m1 | m2 | m3 | m4 | m5 | m7 | m8 | m9 | σy0 |
| Ti64 Equiaxed | 105653 | -0.0144 | -5.8580 | 4.6818 | -0.0253 | -0.0006 | -0.3308 | 0.0041 | -0.0494 | 48 |
| Ti64 Lamellar | 3116 | -0.0011 | -0.2313 | 0.1925 | -0.0002 | -0.0001 | 0.0172 | 0.0017 | 0.0060 | 39 |
| Ti1023 Equiaxed | -698 | -0.0056 | -0.1061 | -0.3456 | -0.0180 | 0.0002 | 0.0349 | 0.0005 | 0.0049 | 83 |
| Ti1023 Lamellar | 13338 | -0.0075 | -0.7219 | -0.2174 | -0.0212 | 0.0030 | -0.1010 | 0.0006 | -0.0064 | 8 |

*Table D.2. β-phase Hansel-Spittel smoothing parameters used for the smoothing of the individual stresses obtained from the ROM from experimental curves.*

# SCIENTIFIC COMMUNICATIONS AND PRIZES

This PhD work has led to the following communications and prizes.

# Articles

— **M. Brozovic Gariglio**, N. Bozzolo, D. Pino Muñoz, *An Optimized Geometry of Double-Cone Compression Test Samples for a Better Control of Strain Rate*, Metall. Mater. Trans. A Phys. Metall. Mater. Sci. 52 (2021) 4125–4136. doi:10.1007/*s*11661-021-06373-8.

— **M. Brozovic Gariglio**, N. Bozzolo, D. Pino Muñoz, *About dislocation density estimation from EBSD data: application to hot-deformed titanium alloys.* (Presented in Appendix **B**, to be sent for publication).

— The results concerning the comparison between the macroscopic and microscopic approaches presented in section **5.7** will soon be synthesized in the form of an article.

# Presentations

— **M. Brozovic Gariglio**, N. Bozzolo, D. Pino Muñoz, *Estimation of the dislocation density distribution, by microscopic and macroscopic approaches, in titanium alloys after hot deformation in the α+β domain*, World Titanium Conference, Edinburgh, Scotland, June 12-16 2023. ***Oral***

— **M. Brozovic Gariglio**, N. Bozzolo, D. Pino Muñoz, *About dislocation density distribution in titanium alloys after hot deformation in the α+β domain*, Symposium on Advances in Titanium Technology at TMS, Anaheim, California, USA, February 27–March 3 2022. ***Poster***

— **M. Brozovic Gariglio**, N. Bozzolo, D. Pino Muñoz, *Stored energy distribution in α and β phases of hot-deformed titanium alloy microstructures*, Plasticité, Toulouse, France, April 6-7 2021. ***Oral***

# Prizes

— **1st Prize from France Titane (The French Titanium Association):** *Annual prize aimed at rewarding the best work of theses in France, concerning both metallurgy and the properties of titanium and its alloys.* Lyon, France, October 10th 2023. ***Oral***

— **Medal and 1st Pierre Laffitte Prize from the Côte d'Azur and Paris Sciences & Lettres Universities:** *Annual prize intended to reward research for industry, the Economy of the Common Good and the Environment***.** Sophia Antipolis, France, October 22nd 2021. ***Oral***

# BIBLIOGRAPHY

[1] B. Halse, Strategic Research Agenda, 2004.

[2] M. Perrut, P. Caron, M. Thomas, A. Couret, High temperature materials for aerospace applications: Ni-based superalloys and γ-TiAl alloys, Comptes Rendus Phys. 19 (2018) 657–671. https://doi.org/10.1016/j.crhy.2018.10.002.

[3] G. Lütjering, J.C. Williams, Titanium : Engineering Materials and Processes, 2007. https://doi.org/10.1007/978-3-540-73036-1.

[4] M. Brozovic Gariglio, N. Bozzolo, D. Pino Muñoz, An Optimized Geometry of Double-Cone Compression Test Samples for a Better Control of Strain Rate, Metall. Mater. Trans. A Phys. Metall. Mater. Sci. 52 (2021) 4125–4136. https://doi.org/10.1007/s11661-021-06373-8.

[5] A. Seret, C. Moussa, M. Bernacki, J. Signorelli, N. Bozzolo, Estimation of geometrically necessary dislocation density from filtered EBSD data by a local linear adaptation of smoothing splines, J. Appl. Crystallogr. 52 (2019) 548–563. https://doi.org/10.1107/S1600576719004035.

[6] M. Saby, E. Massoni, N. Bozzolo, A metallurgical approach to individually assess the rheology of alpha and beta phases of Ti-6Al-4V in the two-phase domain, Mater. Charact. 89 (2014) 88–92. https://doi.org/10.1016/j.matchar.2014.01.001.

[7] C.R. Brooks, Heat Treatment, Structure, and Properties of Nonferrous Alloys, American Society for Metals (ASM), Ohio, USA, 1982.

[8] C. Barbosa, Metais não ferrosos e suas ligas : microestrutura, propriedades e aplicações, 1st ed., E-Papers, 2014.

[9] M. Peters, C. Leyens, Titanium and Titanium Alloys: Fundamentals and Applications, 2003. https://doi.org/10.1002/3527602119.

[10] W.F. Smith, W.F. Smith, J. Hashemi, Foundations of Materials Science and Engineering (SI Units), 2011. http://books.google.com/books?id=2pVbSAAACAAJ&pgis=1.

[11] A. Zarkades, F.R. Larson, Elasticity of Titanium Sheet Alloys, in: Sci. Technol. Appl. Titan., 1970: pp. 933–941. https://doi.org/10.1016/b978-0-08-006564-9.50104-4.

[12] J. Carroll, Crystal Plasticity Predictions of Material Deformation in Body Centered Cubic Tantalum, in: ICMAT, Singapore, 2019.

[13] Z. Zheng, D.S. Balint, F.P.E. Dunne, Rate sensitivity in discrete dislocation plasticity in hexagonal close-packed crystals, Acta Mater. 107 (2016) 17–26. https://doi.org/10.1016/j.actamat.2016.01.035.

[14] G. Wang, Z. Chen, J. Li, J. Liu, Q. Wang, R. Yang, Microstructure and Mechanical Properties of Electron Beam Welded Titanium Alloy Ti-6246, J. Mater. Sci. Technol. 34 (2018) 570–576. https://doi.org/10.1016/j.jmst.2016.10.007.

[15] W.G. Burgers, On the process of transition of the cubic-body-centered modification into the hexagonal-close-packed modification of zirconium, Physica. 1 (1934) 561–586. https://doi.org/10.1016/S0031-8914(34)80244-3.

[16] I. Weiss, S.L. Semiatin, Thermomechanical processing of beta titanium alloys - An overview, Mater. Sci. Eng. A. 263 (1999) 243–256. https://doi.org/10.1016/S0921-5093(97)00783-1.

[17] R. Castro, L. Séraphin, Contribution à l'étude métallographique et

structurale de l'alliage de titane TA6V, Les Mémoires Sci. La Rev. Métallurgie. 12 (1966) 1025–1058.

[18] S.R. Seagle, Titanium processing, Encycl. Br. (2019). https://www.britannica.com/technology/titanium-processing (accessed February 3, 2020).

[19] J.H. Schmitt, T. Iung, Durcissement des alliages métalliques - Impact de la microstructure sur la déformation plastique, Tech. l'Ingénieur. Matériaux (2016) 1–26.

[20] B. Chenal, J. Driver, Écrouissage D ' Alliages D ' Aluminium, Tech. L'ingénieur. 33 (2008) 1–18.

[21] F. Montheillet, Métallurgie en mise en forme à chaud, Tech. L'ingénieur. M3031 V1 (2009) 1–14.

[22] F.J. Humphreys, M. Hatherly, Recrystallization and Related Annealing Phenomena, Second Edi, Elsevier, 2004. https://doi.org/10.1016/B978-0-08-044164-1.X5000-2.

[23] D. Hull, D.J. Bacon, Introduction to dislocations, Fifth Edit, Elsevier, Liverpool, UK, 2011. https://doi.org/10.1016/B978-075064681-9/50006-7.

[24] T. Baudin, Analyse EBSD - Déformation et recristallisation des matériaux métalliques, Tech. l'Ingénieur. 33 (2011) M4 139. http://www.techniques-ingenieur.fr.rp1.ensam.eu/res/pdf/encyclopedia/42343210-m4139.pdf.

[25] S.L. Semiatin, An Overview of the Thermomechanical Processing of Alpha/Beta Titanium Alloys: Current Status and Future Research Opportunities, Metall. Mater. Trans. A Phys. Metall. Mater. Sci. (2020) 1–102.

[26] M. Semblanet, Traitement thermomécanique de l'alliage Ti17 : Forgeage en α + ß et maintien post-forgeage en ß, Thèse de doctorat de l'Ecole Nationale Supérieure des Mines de Saint-Etienne, 2014.

[27] S. Gourdet, F. Montheillet, An experimental study of the recrystallization mechanism during hot deformation of aluminium, Mater. Sci. Eng. A. 283 (2000) 274–288. https://doi.org/10.1016/S0921-5093(00)00733-4.

[28] K. Huang, R.E. Logé, A review of dynamic recrystallization phenomena in metallic materials, Mater. Des. 111 (2016) 548–574. https://doi.org/10.1016/j.matdes.2016.09.012.

[29] P. Audrérie, Etude du comportement rheologique et des evolutions microstructurales au cours de traitements thermomecaniques d'alliages de titane, Thèse de doctorat de l'Ecole Nationale Supérieure des Mines de Paris, 1993.

[30] J.G. Malcor, F. Montheillet, Evolution structurale de l'alliage de titane Ti-6%Al-4%V au cours d'une déformation dans le domaine du forgeage à chaud, Mem. Etudes Sci. La Rev. Metall. 81 (1984) 181–187.

[31] L. Pallot, Thermomechanical processing of alloy Ti-17. Experimental investigation and modeling of dynamic recrystallization in the Beta range, Ecole Nationale Supérieure des Mines de Saint-Etienne, 2013. https://tel.archives-ouvertes.fr/tel-00849211.

[32] D.L. OuYang, M.W. Fu, S.Q. Lu, Study on the dynamic recrystallization behavior of Ti-alloy Ti-10V-2Fe-3V in ß processing via experiment and

simulation, Mater. Sci. Eng. A. 619 (2015) 26–34. https://doi.org/10.1016/j.msea.2014.09.067.

[33] D. Luquiau, Caractérisation du comportement et de l'endommagement de l'alliage de titane Ti-10V-2Fe-3AI en fatigue, Thèse de doctorat de l'Université de Technologie de Compiègne, 1996. https://doi.org/1996COMP923.

[34] R. Ding, Z.X. Guo, A. Wilson, Microstructural evolution of a Ti-6Al-4V alloy during thermomechanical processing, Mater. Sci. Eng. A. 327 (2002) 233–245. https://doi.org/10.1016/S0921-5093(01)01531-3.

[35] R.M. Miller, T.R. Bieler, S.L. Semiatin, Flow softening during hot working of Ti-6Al-4V with a lamellar colony microstructure, Scr. Mater. 40 (1999) 1387–1393. https://doi.org/10.1016/S1359-6462(99)00061-5.

[36] G.Z. Quan, W.Q. Lv, J.T. Liang, S.A. Pu, G.C. Luo, Q. Liu, Evaluation of the hot workability corresponding to complex deformation mechanism evolution for Ti-10V-2Fe-3Al alloy in a wide condition range, J. Mater. Process. Technol. 221 (2015) 66–79. https://doi.org/10.1016/j.jmatprotec.2015.02.002.

[37] S. Mironov, M. Murzinova, S. Zherebtsov, G.A. Salishchev, S.L. Semiatin, Microstructure evolution during warm working of Ti-6Al-4V with a colony-α microstructure, Acta Mater. 57 (2009) 2470–2481. https://doi.org/10.1016/j.actamat.2009.02.016.

[38] T. Seshacharyulu, S.C. Medeiros, J.T. Morgan, J.C. Malas, W.G. Frazier, Y.V.R.K. Prasad, Hot deformation and microstructural damage mechanisms in extra-low interstitial (ELI) grade Ti-6Al-4V, Mater. Sci. Eng. A. 279 (2000) 289–299. https://doi.org/10.1016/S0921-5093(99)00173-2.

[39] T. Seshacharyulu, S.C. Medeiros, W.G. Frazier, Y.V.R.K. Prasad, Microstructural mechanisms during hot working of commercial grade Ti-6Al-4V with lamellar starting structure, Mater. Sci. Eng. A. 325 (2002) 112–125. https://doi.org/10.1016/S0921-5093(01)01448-4.

[40] F. Warchomicka, M. Stockinger, H.P. Degischer, Quantitative analysis of the microstructure of near ß titanium alloy during compression tests, J. Mater. Process. Technol. 177 (2006) 473–477. https://doi.org/10.1016/j.jmatprotec.2006.04.022.

[41] P.M. Souza, P.D. Hodgson, B. Rolfe, R.P. Singh, H. Beladi, Effect of initial microstructure and beta phase evolution on dynamic recrystallization behaviour of Ti6Al4V alloy - An EBSD based investigation, J. Alloys Compd. 793 (2019) 467–479. https://doi.org/10.1016/j.jallcom.2019.04.183.

[42] J.S. Kim, J.H. Kim, Y.T. Lee, C.G. Park, C.S. Lee, Microstructural analysis on boundary sliding and its accommodation mode during superplastic deformation of Ti-6Al-4V alloy, Mater. Sci. Eng. A. 263 (1999) 272–280. https://doi.org/10.1016/s0921-5093(98)01157-5.

[43] S. Balachandran, S. Kumar, D. Banerjee, On recrystallization of the α and ß phases in titanium alloys, Acta Mater. 131 (2017) 423–434. https://doi.org/10.1016/j.actamat.2017.04.008.

[44] S.L. Semiatin, N.C. Levkhulic, C.A. Heck, A.E. Mann, A.L. Pilchak, J.S. Tiley, Transient Plastic Flow and Phase Dissolution during Hot compression of two phase Ti alloys - Semiatin et al.pdf, Metall. Mater. Trans. A Phys.

Metall. Mater. Sci. (2020) 42.

[45] J.J. Jonas, C. Aranas, A. Fall, M. Jahazi, Transformation softening in three titanium alloys, Mater. Des. 113 (2017) 305–310. https://doi.org/10.1016/j.matdes.2016.10.039.

[46] B. Guo, S.L. Semiatin, J.J. Jonas, Dynamic transformation during the high temperature deformation of two-phase titanium alloys, Mater. Sci. Eng. A. 761 (2019) 138047. https://doi.org/10.1016/j.msea.2019.138047.

[47] M.D. Abràmoff, P.J. Magalhães, S.J. Ram, Image processing with ImageJ, Biophotonics Int. 11 (2004) 36–41. https://doi.org/10.1201/9781420005615.ax4.

[48] A. Campbell, P. Murray, E. Yakushina, S. Marshall, W. Ion, New methods for automatic quantification of microstructural features using digital image processing, Mater. Des. 141 (2018) 395–406. https://doi.org/10.1016/j.matdes.2017.12.049.

[49] International Organization for Standardization, ISO 643:2019 - Steels - Micrographic determination of the apparent grain size, 2019. https://www.iso.org/standard/72193.html.

[50] P.V.C. Hough, A method and means for recognition complex patterns; US Patent: US3069654A, US Pat. (1962) 6.

[51] F. Bachmann, R. Hielscher, H. Schaeben, Texture analysis with MTEX- Free and open source software toolbox, Solid State Phenom. 160 (2010) 63–68. https://doi.org/10.4028/www.scientific.net/SSP.160.63.

[52] C. Nguyen, M. Balzer, T. Witulski, M. Böhm, B. Dod, M. Preuss, J. Quinta, Understanding the ß-phase texture development in Ti-6Al-4V during compression in the α + ß regimes, 14th World Conf. Titan. (2019) 2–7.

[53] F. Niessen, T. Nyyssönen, A.A. Gazder, R. Hielscher, Parent grain reconstruction from partially or fully transformed microstructures in MTEX, J. Appl. Crystallogr. 55 (2022) 180–194. https://doi.org/10.1107/S1600576721011560.

[54] L. Germain, N. Gey, R. Mercier, P. Blaineau, M. Humbert, An advanced approach to reconstructing parent orientation maps in the case of approximate orientation relations: Application to steels, Acta Mater. 60 (2012) 4551–4562. https://doi.org/10.1016/j.actamat.2012.04.034.

[55] O. Muránsky, L. Balogh, M. Tran, C.J. Hamelin, J.S. Park, M.R. Daymond, On the measurement of dislocations and dislocation substructures using EBSD and HRSD techniques, Acta Mater. 175 (2019) 297–313. https://doi.org/10.1016/j.actamat.2019.05.036.

[56] W.T. Read, W. Shockley, Dislocation Models of Crystal Grain Boundaries, Phys. Rev. (1950) 275–289.

[57] M. Calcagnotto, D. Ponge, E. Demir, D. Raabe, Orientation gradients and geometrically necessary dislocations in ultrafine grained dual-phase steels studied by 2D and 3D EBSD, Mater. Sci. Eng. A. 527 (2010) 2738–2746. https://doi.org/10.1016/j.msea.2010.01.004.

[58] J.F. Nye, Some geometrical relations in dislocated crystals, Acta Metall. 1 (1953) 153–162. https://doi.org/10.1016/0001-6160(53)90054-6.

[59] E. Kröner, The fundamental relationship between dislocation density and

stress functions, Zeitschrift Für Phys. 142 (1955) 463–475. https://doi.org/10.1007/BF01375082.

[60] C. Fressengeas, V. Taupin, L. Capolungo, An elasto-plastic theory of dislocation and disclination fields, Int. J. Solids Struct. 48 (2011) 3499–3509. https://doi.org/10.1016/j.ijsolstr.2011.09.002.

[61] W. Pantleon, Resolving the geometrically necessary dislocation content by conventional electron backscattering diffraction, Scr. Mater. 58 (2008) 994–997. https://doi.org/10.1016/j.scriptamat.2008.01.050.

[62] B.S. El-Dasher, B.L. Adams, A.D. Rollett, Viewpoint: Experimental recovery of geometrically necessary dislocation density in polycrystals, Scr. Mater. 48 (2003) 141–145. https://doi.org/10.1016/S1359-6462(02)00340-8.

[63] A.J. Wilkinson, D. Randman, Determination of elastic strain fields and geometrically necessary dislocation distributions near nanoindents using electron back scatter diffraction, Philos. Mag. 90 (2010) 1159–1177. https://doi.org/10.1080/14786430903304145.

[64] F.P.E. Dunne, R. Kiwanuka, A.J. Wilkinson, Crystal plasticity analysis of micro-deformation, lattice rotation and geometrically necessary dislocation density, Proc. R. Soc. A Math. Phys. Eng. Sci. 468 (2012) 2509–2531. https://doi.org/10.1098/rspa.2012.0050.

[65] H.J. Frost, M.F. Ashby, Deformation-mechanism maps: the plasticity and creep of metals and ceramics, Pergamon Press, New York, 1982.

[66] R. Hielscher, R. Kilian, Geometrically Necessary Dislocations, (2018). https://mtex-toolbox.github.io/GND.html.

[67] R. Bergmann, R.H. Chan, R. Hielscher, J. Persch, G. Steidl, Restoration of manifold-valued images by half-quadratic minimization, Inverse Probl. Imaging. 10 (2016) 281–304. https://doi.org/10.3934/ipi.2016001.

[68] F. Ram, S. Zaefferer, T. Jäpel, D. Raabe, Error analysis of the crystal orientations and disorientations obtained by the classical electron backscatter diffraction technique, J. Appl. Crystallogr. 48 (2015) 797–813. https://doi.org/10.1107/S1600576715005762.

[69] L. Kwakman, G. Franz, M.M.V. Taklo, A. Klumpp, P. Ramm, Characterization and failure analysis of 3D integrated systems using a novel plasma-FIB system, AIP Conf. Proc. 1395 (2011) 269–273. https://doi.org/10.1063/1.3657902.

[70] T.L. Burnett, R. Kelley, B. Winiarski, L. Contreras, M. Daly, A. Gholinia, M.G. Burke, P.J. Withers, Large volume serial section tomography by Xe Plasma FIB dual beam microscopy, Ultramicroscopy. 161 (2016) 119–129. https://doi.org/10.1016/j.ultramic.2015.11.001.

[71] T. Kozmel, E.Y. Chen, C.C. Chen, S. Tin, Kinetics of sub-micron grain size refinement in 9310 steel, Metall. Mater. Trans. A Phys. Metall. Mater. Sci. 45 (2014) 2590–2600. https://doi.org/10.1007/s11661-014-2212-6.

[72] D.S. Weaver, S.L. Semiatin, Recrystallization and grain-growth behavior of a nickel-base superalloy during multi-hit deformation, Scr. Mater. 57 (2007) 1044–1047. https://doi.org/10.1016/j.scriptamat.2007.07.033.

[73] C. Aoki, T. Ueno, T. Ohno, K. Oikawa, Influence of hot-working conditions on grain growth of superalloy 718, J. Mater. Process. Technol. 267 (2019) 26–

33. https://doi.org/10.1016/j.jmatprotec.2018.12.002.

[74] J. Wang, D. Liu, X. Ding, H. Wang, Microstructure Heredity of Inconel 718 Nickel-Based Superalloy during Preheating and Following Deformation, Crystals. 3 (2020) 10–12. https://doi.org/10.3390/cryst10040303.

[75] N.S. Weston, M. Jackson, FAST-forge − A new cost-effective hybrid processing route for consolidating titanium powder into near net shape forged components, J. Mater. Process. Technol. 243 (2017) 335–346. https://doi.org/10.1016/j.jmatprotec.2016.12.013.

[76] S.L. Semiatin, D.S. Weaver, P.N. Fagin, M.G. Glavicic, R.L. Goetz, N.D. Frey, R.C. Kramb, M.M. Antony, Deformation and recrystallization behavior during hot working of a coarse-grain, nickel-base superalloy ingot material, Metall. Mater. Trans. A Phys. Metall. Mater. Sci. 35 A (2004) 679–693. https://doi.org/10.1007/s11661-004-0379-y.

[77] B. Sefer, J.J. Roa, A. Mateo, R. Pederson, M.-L. Antti, Evaluation of the Bulk and Alpha-Case Layer Properties in Ti-6Al-4V at Micro-And Nano-Metric Length Scale, Proc. 13th World Conf. Titan. (2016) 1619–1624. https://doi.org/10.1002/9781119296126.ch271.

[78] E. Depiereux, Distribution Normale, Univ. Namur. (2012). https://webapps.fundp.ac.be/umdb/biostats/?q=book/export/html/212 (accessed June 1, 2020).

[79] L. Germain, Contribution to the study of texture heterogeneities in IMI 834 billets, Université de Metz, 2005. https://www.theses.fr/2005METZ018S.

[80] Object Research Systems (ORS), Dragonfly, (2020). http://www.theobjects.com/dragonfly.

[81] J. Ahrens, B. Geveci, C. Law, ParaView : An End-User Tool for Large-Data Visualization, (n.d.).

[82] R. DeMott, N. Haghdadi, Z. Gandomkar, X. Liao, S. Ringer, S. Primig, Formation and 3D morphology of interconnected α microstructures in additively manufactured Ti-6Al-4V, Materialia. 20 (2021) 101201. https://doi.org/10.1016/j.mtla.2021.101201.

[83] D. Polychronopoulou, Spheroidization in α/ß titanium alloys : numerical modeling and experimental analysis, PSL Research University - Prepared at MINES ParisTech, 2018. https://pastel.archives-ouvertes.fr/tel-02196069.

[84] J. Zhong, M. Dargusch, C. Davies, Modelling the high temperature deformation of Ti-6Al-4V, Mater. Sci. Forum. 654–656 (2010) 879–882. https://doi.org/10.4028/www.scientific.net/MSF.654-656.879.

[85] J. Luo, M. Li, X. Li, Y. Shi, Constitutive model for high temperature deformation of titanium alloys using internal state variables, Mech. Mater. 42 (2010) 157–165. https://doi.org/10.1016/j.mechmat.2009.10.004.

[86] O. Bouaziz, P. Buessler, Mechanical behaviour of multiphase materials: An intermediate mixture law without fitting parameter, Rev. Metall. Cah. D'Informations Tech. 99 (2002). https://doi.org/10.1051/metal:2002182.

[87] S. Vernier, Microstructural evolution of the nickel-based superalloy AD730 during the industrial forging process, PSL Research University - Prepared at MINES ParisTech, 2018. https://pastel.archives-ouvertes.fr/tel-02149391.

[88] A. Hansel, T. Spittel, Kraft-und Arbeitsbedarf bildsamer

Formgebungsverfahren, Deutscher Verlag für Grundstoffindustrie, Leipzig, 1978.

[89] E.O. Hall, The deformation and ageing of mild steel: III Discussion of results, Proc. Phys. Soc. Sect. B. 64 (1951) 747–753. https://doi.org/10.1088/0370-1301/64/9/303.

[90] N.J. Petch, The Cleavage Strength of Polycrystals, J. Iron Steel Inst. 173 (1953) 25–28.

[91] G.I. Taylor, The mechanism of plastic deformation of crystals. Part I. Theoretical, in: Proc. R. Soc. A Math. Phys. Eng. Sci., 1934: pp. 362–387.

[92] R.H. Buzolin, M. Lasnik, A. Krumphals, M.C. Poletti, A dislocation-based model for the microstructure evolution and the flow stress of a Ti5553 alloy, Int. J. Plast. 136 (2021) 102862. https://doi.org/10.1016/j.ijplas.2020.102862.

[93] C. Poletti, L. Germain, F. Warchomicka, M. Dikovits, S. Mitsche, Unified description of the softening behavior of beta-metastable and alpha+beta titanium alloys during hot deformation, Mater. Sci. Eng. A. 651 (2016) 280–290. https://doi.org/10.1016/j.msea.2015.10.109.

[94] C. Zhu, T. Harrington, G.T. Gray, K.S. Vecchio, Dislocation-type evolution in quasi-statically compressed polycrystalline nickel, Acta Mater. 155 (2018) 104–116. https://doi.org/10.1016/j.actamat.2018.05.022.

[95] G.Z. Quan, H.R. Wen, S.A. Pu, Z.Y. Zou, D. Sen Wu, Identification of Stable Processing Parameters in Ti-6Al-4V Alloy from a Wide Temperature Range Across ß Transus and a Large Strain Rate Range, High Temp. Mater. Process. 34 (2015) 715–729. https://doi.org/10.1515/htmp-2014-0129.

[96] J.J. Kearns, On the relationship among "f" texture factors for the principal planes of zirconium, hafnium and titanium alloys, J. Nucl. Mater. 299 (2001) 171–174. https://doi.org/10.1016/S0022-3115(01)00686-9.

[97] B. Derby, The dependence of grain size on stress during dynamic recrystallisation, Acta Metall. Mater. 39 (1991) 955–962. https://doi.org/10.1016/0956-7151(91)90295-C.

[98] A. M.F., The deformation of plastically non-homogeneous materials, Philos. Mag. 21 (1969) 37–41.

[99] D. Ruiz Sarrazola, Full field modeling of discontinuous dynamic recrystallization in a CPFEM context, PSL Research University - Prepared at MINES ParisTech, 2020. https://pastel.archives-ouvertes.fr/tel-03338762.

[100] R.J. Asaro, A. Needleman, Overview no. 42 Texture development and strain hardening in rate dependent polycrystals, Acta Metall. 33 (1985) 923–953. https://doi.org/10.1016/0001-6160(85)90188-9.

[101] E.B. Marin, P.R. Dawson, On modelling the elasto-viscoplastic response of metals using polycrystal plasticity, Comput. Methods Appl. Mech. Eng. 165 (1998) 1–21.

[102] O.C. Zienkiewicz, R.L. Taylor, The Finite Element Method for Solid and Structural Mechanics, 6th ed., Butterworth-Heinemann, 2014.

[103] E.B. Marin, On the formulation of a crystal plasticity model, Sandia Rep. (2006) 4170. http://www.osti.gov/servlets/purl/890604-gUvhWh/.

[104] F. Bassani, G.L. Liedl, P. Wyder, Encyclopedia of condensed matter physics, 2005. https://doi.org/10.5860/choice.43-4384.

[105] F. Roters, P. Eisenlohr, L. Hantcherli, D.D. Tjahjanto, T.R. Bieler, D. Raabe, Overview of constitutive laws, kinematics, homogenization and multiscale methods in crystal plasticity finite-element modeling: Theory, experiments, applications, Acta Mater. 58 (2010) 1152–1211. https://doi.org/10.1016/j.actamat.2009.10.058.

[106] A. Yoshie, H. Morikawa, K. Itoh, Y. Onoe, Formulation Hot Rolling of Static Process Recrystallization of Steel Plate, (1987).

[107] K. Venkatraman, M. Ben Haj Slama, V. Taupin, N. Maloufi, A. Guitton, Tuning critical resolved shear stress ratios for bcc-titanium Ti21S via an automated data analysis approach, Model. Simul. Mater. Sci. Eng. 29 (2021). https://doi.org/10.1088/1361-651X/abfeb0.

[108] G.E. Dieter, Mechanical metallurgy, SI Metric, McGraw-Hill Book Company, 2011. https://doi.org/10.5962/bhl.title.35895.

[109] D.A. Ruiz Sarrazola, D. Pino Muñoz, M. Bernacki, A new numerical framework for the full field modeling of dynamic recrystallization in a CPFEM context, Comput. Mater. Sci. 179 (2020) 109645. https://doi.org/10.1016/j.commatsci.2020.109645.

[110] M.A. Groeber, M.A. Jackson, DREAM.3D: A Digital Representation Environment for the Analysis of Microstructure in 3D, 3 (2014) 5. http://www.immijournal.com/content/3/1/5.

[111] C. Geuzaine, J.F. Remacle, Gmsh: A 3-D finite element mesh generator with built-in pre- and post-processing facilities, Int. J. Numer. Methods Eng. 79 (2009) 1309–1331. https://doi.org/10.1002/nme.2579.

[112] L. Maire, Full field and mean field modeling of dynamic and post-dynamic recrystallization in 3D – Application to 304L steel, PSL Research University - Prepared at MINES ParisTech, 2018. https://pastel.archives-ouvertes.fr/tel-02418810.

[113] J. Guyon, N. Gey, D. Goran, S. Chalal, F. Pérez-Willard, Advancing FIB assisted 3D EBSD using a static sample setup, Ultramicroscopy. 161 (2016) 161–167. https://doi.org/10.1016/j.ultramic.2015.11.011.

[114] J.L. Chenot, P.O. Bouchard, L. Fourment, P. Lasne, E. Roux, Optimization of metal forming processes for improving final mechanical strength, Comput. Plast. XI - Fundam. Appl. COMPLAS XI. (2011) 42–55.

[115] Y. COMBRES, Traitements thermiques des alliages de titane, Trait. Des Métaux. 33 (2013). https://doi.org/10.51257/a-v3-m1335.

[116] M. Shakoor, A. Buljac, J. Neggers, F. Hild, T.F. Morgeneyer, L. Helfen, M. Bernacki, P.O. Bouchard, On the choice of boundary conditions for micromechanical simulations based on 3D imaging, Int. J. Solids Struct. 112 (2017) 83–96. https://doi.org/10.1016/j.ijsolstr.2017.02.018.

[117] V.M.T. Navas, A. Buljac, F. Hild, T.F. Morgeneyer, M. Bernacki, P.-O. Bouchard, An examination of local strain fields evolution in ductile cast iron through micromechanical simulations based on 3D imaging, J. Theor. Comput. Appl. Mech. (2022) 0–18. https://doi.org/10.46298/jtcam.7501.

[118] E. Schmid, W. Boas, Kristallplastizität, 1935. https://doi.org/10.1007/978-3-662-34532-0.

[119] A. Nicolaÿ, G. Fiorucci, J.M. Franchet, J. Cormier, N. Bozzolo, Influence of

strain rate on subsolvus dynamic and post-dynamic recrystallization kinetics of Inconel 718, Acta Mater. 174 (2019) 406–417. https://doi.org/10.1016/j.actamat.2019.05.061.

[120] M. Zouari, R.E. Logé, N. Bozzolo, In situ characterization of inconel 718 post-dynamic recrystallization within a scanning electron microscope, Metals (Basel). 7 (2017). https://doi.org/10.3390/met7110476.

[121] R. Wang, C. Lu, K.A. Tieu, A.A. Gazder, Slip system activity and lattice rotation in polycrystalline copper during uniaxial tension, J. Mater. Res. Technol. 18 (2022) 508–519. https://doi.org/10.1016/j.jmrt.2022.02.110.

[122] D.A. Ruiz Sarrazola, L. Maire, C. Moussa, N. Bozzolo, D. Pino Muñoz, M. Bernacki, Full field modeling of dynamic recrystallization in a CPFEM context – Application to 304L steel, Comput. Mater. Sci. 184 (2020) 109892. https://doi.org/10.1016/j.commatsci.2020.109892.

[123] C. Fressengeas, B. Beausir, C. Kerisit, A.L. Helbert, T. Baudin, F. Brisset, M.H. Mathon, R. Besnard, N. Bozzolo, On the evaluation of dislocation densities in pure tantalum from EBSD orientation data, Mater. Tech. 106 (2018). https://doi.org/10.1051/mattech/2018058.

[124] T. Ben Britton, S. Birosca, M. Preuss, A.J. Wilkinson, Electron backscatter diffraction study of dislocation content of a macrozone in hot-rolled Ti-6Al-4V alloy, Scr. Mater. 62 (2010) 639–642. https://doi.org/10.1016/j.scriptamat.2010.01.010.

[125] B. Tang, M. Zhang, R. Yang, W. Chen, H. Kou, J. Li, Microplasticity behavior study of equiaxed near-b titanium alloy under high-cycle fatigue loading: Crystal plasticity simulations and experiments, J. Mater. Res. Technol. 8 (2019) 6146–6157. https://doi.org/10.1016/j.jmrt.2019.10.009.

[126] M.A. Charpagne, T. Billot, J.M. Franchet, N. Bozzolo, Heteroepitaxial recrystallization: A new mechanism discovered in a polycrystalline γ-γ′ nickel based superalloy, J. Alloys Compd. 688 (2016) 685–694. https://doi.org/10.1016/j.jallcom.2016.07.240.

[127] F. Warchomicka, C. Poletti, M. Stockinger, T. Henke, Microstructure evolution during hot deformation of Ti-6Al-4V double cone specimens, Evolution (N. Y). 3 (2010) 215–218. https://doi.org/10.1007/s12289-010-0745-9.

[128] G. He, L. Tan, F. Liu, L. Huang, Z. Huang, L. Jiang, Strain Amount Dependent Grain Size and Orientation Developments during Hot Compression of a Polycrystalline Nickel Based Superalloy, Materials (Basel). 10 (2017) 161. https://doi.org/10.3390/ma10020161.

[129] E. Alabort, R.C. Reed, D. Barba, Combined modelling and miniaturised characterisation of high-temperature forging in a nickel-based superalloy, Mater. Des. 160 (2018) 683–697. https://doi.org/10.1016/j.matdes.2018.09.048.

[130] H.S. Valberg, Applied metal forming: Including FEM analysis, Cambridge University Press, Cambridge, UK, 2010.

[131] D. Shahriari, M.H. Sadeghi, G.R. Ebrahimi, K.T. Kim, Effects of lubricant and temperature on friction coefficient during hot forging of Nimonic 115 superalloy, (2011) 375–383. https://doi.org/10.4149/km.

[132] Y. Li, E. Onodera, A. Chiba, Friction coefficient in hot compression of cylindrical sample, Mater. Trans. 51 (2010) 1210–1215. https://doi.org/10.2320/matertrans.M2010056.

[133] Transvalor, Optimisation (FORGE NxT documentation), Biot, France, 2019.

[134] K.C. Chan, W.B. Lee, Effect of prestrain on the evolution of yield locus of polycrystalline metals, Adv. Eng. Plast. Its Appl. (1993) 547–553.

[135] J. Obiko, Friction correction of flow stress-strain curve in the upsetting process, IOP SciNotes. 2 (2021) 14401. https://doi.org/10.1088/2633-1357/abdd96.

[136] D. Banerjee, J.C. Williams, Perspectives on titanium science and technology, Acta Mater. 61 (2013) 844–879. https://doi.org/10.1016/j.actamat.2012.10.043.

## RÉSUMÉ

Les alliages de titane sont beaucoup employés dans l'industrie aéronautique, pour leurs propriétés de résistance à la température et à la corrosion, mais surtout leur faible densité. Ces propriétés sont fortement liées à la microstructure, elle-même issue des opérations de forgeage à chaud mises en œuvre pour fabriquer les pièces. L'optimisation des propriétés nécessite donc de maîtriser l'impact des paramètres thermomécaniques sur les évolutions microstructurales. Le caractère biphasé ($\alpha$/ß) de certains alliages de titane offre, pour une nuance donnée, une très grande variété de microstructures possibles et donc une certaine souplesse dans l'ajustement des propriétés. Deux alliages de titane sont étudiés dans ce travail : l'alliage Ti-6Al-4V ($\alpha$+$\beta$) utilisé dans les turboréacteurs, et l'alliage Ti-10V-2Fe-3Al (ß-métastable) utilisé dans les trains d'atterrissage. L'objectif principal de ce travail est d'évaluer et de décrire comment la densité de dislocations se réparti entre les phases $\alpha$ et ß, en fonction des paramètres thermomécaniques et de la microstructure initiale. Trois approches distinctes et complémentaires sont mises en œuvre : expérimentales à l'échelle microscopique et à l'échelle macroscopique, ainsi que par simulation numérique. Une grande part des résultats de cette thèse est issue d'analyses microstructurales fines, principalement sous la forme de cartographies d'orientation obtenues par diffraction d'électrons rétrodiffusés (EBSD), mais aussi sous la forme de caractérisations tridimensionnelles complémentaires. Des techniques avancées de post-traitement des données EBSD sont utilisées pour évaluer les densités de dislocation à partir des désorientations intragranulaires mesurées. L'approche macroscopique est quant à elle basée sur l'analyse de courbes contrainte-déformation issues d'essais de compression à chaud. Enfin, des simulations de déformation plastique en champ complet sont réalisées sur des microstructures artificielles et expérimentales. La discussion compare les résultats obtenus par ces trois approches et montre que toute comparaison directe devrait être évitée. Pour chacune des phases, des éléments microstructuraux clés, principalement en termes de texture cristallographique et de recristallisation dynamique, sont donnés en vue de relier ces approches pour avoir une meilleure estimation de la densité de dislocations, donc des évolutions microstructurales. Ces travaux apportent des éléments pour mieux comprendre le comportement des alliages de titane, aidant les partenaires financiers industriels (*Airbus, Aubert & Duval, Safran* et *Timet*) à optimiser le procédé de forgeage.

## MOTS CLÉS

Microstructure, titane, déformation à chaud, biphasé, EBSD, densité de dislocations

## ABSTRACT

Titanium alloys are widely used in the aeronautical industry, thanks to their properties of resistance to temperature and corrosion, but above all their low density. These properties are strongly linked to the microstructure, itself resulting from the hot forging operations implemented to manufacture industrial parts. The optimization of the properties therefore requires controlling the impact of the thermomechanical parameters on the microstructure evolution. The two-phase ($\alpha$/ß) nature of certain titanium alloys offers, for a given grade, a very wide variety of possible microstructures, thus a certain flexibility in the adjustment of the properties. Two titanium alloys are studied in this work: the Ti-6Al-4V ($\alpha$+ß) alloy used in turbojet, and the Ti-10V-2Fe-3Al (metastable-ß) alloy used in landing gears. The main objective of this work is to evaluate and describe how the dislocation density is distributed between the $\alpha$ and $\beta$ phases, depending on the thermomechanical parameters and the initial microstructure. Three distinct and complementary approaches are implemented: experimental at the microscopic and at the macroscopic scale, as well as by numerical simulation. A large part of the results of this thesis come from fine microstructural analyses, mainly in the form of orientation maps obtained by electron backscattered diffraction (EBSD), but also in the form of complementary three-dimensional characterizations. Advanced EBSD data post-processing techniques are used to assess dislocation densities from measured intragranular misorientations. The macroscopic approach is based on the analysis of stress-strain curves from hot compression tests. Finally, full-field plastic deformation simulations are performed on artificial and experimental microstructures. The discussion compares the results obtained by these three approaches and shows that any direct comparison should be avoided. For each of the phases, key microstructural elements, mainly in terms of crystallographic texture and dynamic recrystallization, are given in order to link these approaches to better estimate the dislocation density, therefore of microstructure evolution. This work provides elements for a better understanding of the behavior of titanium alloys, assisting the industrial financial partners (*Airbus, Aubert & Duval, Safran* and *Timet*) to optimize the forging routes.

## KEYWORDS

Microstructure, titanium, hot deformation, two-phase, EBSD, dislocation density